JAERI-M
92-036

DEPARTMENT OF CHEMISTRY PROGRESS REPORT

(JANUARY 1989-DECEMBER 1991)

March 1992

Department of Chemistry

日 本 原 子 力 研 究 所
Japan Atomic Energy Research Institute

JAERI-Mレポートは，日本原子力研究所が不定期に公刊している研究報告書です。
入手の問合わせは，日本原子力研究所技術情報部情報資料課（〒319-11茨城県那珂郡東海村）あて，お申しこしください。なお，このほかに財団法人原子力弘済会資料センター（〒319-11 茨城県那珂郡東海村日本原子力研究所内）で複写による実費頒布をおこなっております。

JAERI-M reports are issued irregularly.
Inquiries about availability of the reports should be addressed to Information Division Department of Technical Information, Japan Atomic Energy Research Institute, Tokai-mura, Naka-gun, Ibaraki-ken 319-11, Japan.

編集兼発行　日本原子力研究所
印　　刷　いばらき印刷㈱

JAERI-M 92-036

Department of Chemistry Progress Report (January 1989 - December 1991)

Department of Chemistry

Tokai Research Establishment
Japan Atomic Energy Research Institute
Tokai-mura, Naka-gun, Ibaraki-ken

(Received February 7, 1992)

The research activities in Department of Chemistry during the last 3 years from 1989 to 1991 were compiled. The researches and works of Department of Chemistry are mainly those concerned with important basic matters and items which are committed to further development of nuclear fuels and materials, to establishment of the nuclear fuel cycle, and to new development of advanced nuclear researches such as laser, ion-beam and photo-chemistry. Intensive efforts were also made on chemical analysis service of various fuels and nuclear materials.

Keywords: Progress Report, Fuels, Nuclear Materials, Environmental Safety, Basic Research, Radionuclides, Laser, Ion-beam, Photochemistry

---

JAERI－M 92－036

化学部プログレスレポート
（1989年１月～1991年12月）

日本原子力研究所東海研究所
化学部

（1992年２月７日受理）

化学部の1989から1991年にわたる研究活動をまとめた。研究内容は核燃料・材料の開発，核燃料サイクルの確立ならびにレーザー，イオンビーム及び光化学のような原子力高度化研究に資するための基礎研究である。所内外からの燃料及び各種材料の依頼分析及び関連研究も進めた。

東海研究所：〒319-11　茨城県那珂郡東海村白方字白根2-4
化学部プログレスレポート編集委員会：
佐伯　正克（委員長），渡部　和男（分析センター），中島　幹雄（放射化学第１），
篠原　伸夫（放射化学第２），日夏　幸雄（燃料化学），馬場　祐治（固体化学），
横山　　淳（物理化学），白石　浩二（レーザー化学），室村　忠純（原研・大学プロジェクト共同研究），
安達　武雄（高燃焼度燃料溶解試験），吉田　善行（常温核融合追試試験）

Contents

目　　次

FOREWORD

This report covers research activities during the period January 1989 to December 1991 at the Department of Chemistry, JAERI, Tokai. The research field in which we have worked during this period can be divided mainly into actinide chemistry and photo- and beam-chemistry.

Resesarch on actinides has been performed in collaboration with researchers from universities under the JAERI-Universities Co-working Project since 1986. Much progress has been made in nuclear properties of transcurium elements (e.g., Fm, Md) with the aid of the 20 MV tandem accelerator combined with sophisticated radiation detection techniques. Solid state chemistry of the oxides of actinides and solution chemistry of actinides have been studied and a new spent fuel reprocessing called SREEP based on electrochemical extraction processes has been proposed.

For the near future promotion of advanced research, we are studying laser induced photochemical reactions of lanthanide compounds to find processes applicable to elemental separations. Research using ion beams for creating new materials and also for finding a better utilization of the nuclear energy is being done using various techniques such as electron microscope, electron spectroscopy, SIMS, and Mossbauer spectroscopy.

Other activities are (i) Continuation of dissolution experiments of spent fuels (35,000 MWD/t; Gd-contained) to obtain information on insoluble residue and others. (ii) volatile radioactive (tritium and iodine) chemistry, and (iii) analytical chemistry.

Enzo TACHIKAWA
Director,
Department of Chemistry

1. ANALYTICAL CHEMICAL STUDIES ON NUCLEAR FUELS AND REACTOR MATERIALS

H. Aoyagi, Y. Baba, H. Fukushima, Y. Sasaki, H. Takeishi and Z. Yoshida

1.1 Studies on Atomic Spectroscopy

1.1.1. Isotopic analysis of lithium by hollow cathode excitation

Isotope sepctrum shift in 670.77 nm resonance line of lithium was used for the analysis of iosotopes ^{6}Li and ^{7}Li. A pressure scanned Fabry-Perot interferometer crossed with a grating monochromator was used to resolve isotopic components of the lithium resonance line. The interferometer with spacers of 4.5 mm thick gave optimum isolation of the isotopic components. The spacers were cemented to mirror plates to maintain those plates parallel, so that the interferometer kept high resolution without any adjustment throughout this work.

The water-cooled hollow cathode tube specially designed was used to reduce Doppler broadening. A lithium acetate solution containing 0.14 mg of lithum was evaporated in a graphite electrode, which was then loaded in the cathode cavity of the hollow cathode tube. The hollow cathode tube was driven by the pulsed current operation with the repetition rate of 400 Hz, pulse duration of 0.62 msec, peak current of 8.6 mA, and average current of 2 mA. Stable and intense signals of the isotopic components could be obtained with the discharge operated in a stream of pure argon at 1.05 torr, under these pulsed conditions. The light intensities of the components under this pulsed operation were about 200 times as large as that under equivalent dc current operation. Variation in the $^{6}Li/^{7}Li$ intensity ratio

Table 1 Comparison of optical and mass spectrometric results.

Sample	Intensity ratio $^{6}Li/^{7}Li$	n	$\sigma_{(n-1)}$	C.V. (%)	Analytical value $^{6}Li/^{7}Li$ (atomic ratio)	Analytical value ^{6}Li (atomic %)	Mass spectrometric value (atomic %)
A	0.07912	6	0.00005	0.06	0.08020	7.42	7.43±0.03
	0.07897	6	0.00005	0.06	0.08005	7.41	
B	0.05290	7	0.00004	0.08	0.05364	5.09	5.13±0.02
	0.05279	6	0.00002	0.04	0.05353	5.08	
C	0.02193	7	0.00001	0.05	0.02226	2.18	2.20±0.03
	0.02187	6	0.00004	0.07	0.02220	2.17	
D	0.07841	6	0.00005	0.06	0.07948	7.36	7.38±0.02
	0.07828	6	0.00004	0.05	0.07935	7.35	

n is the number of determinations of intensity ratio, σ the standard deviation and C.V. coefficient of variation.

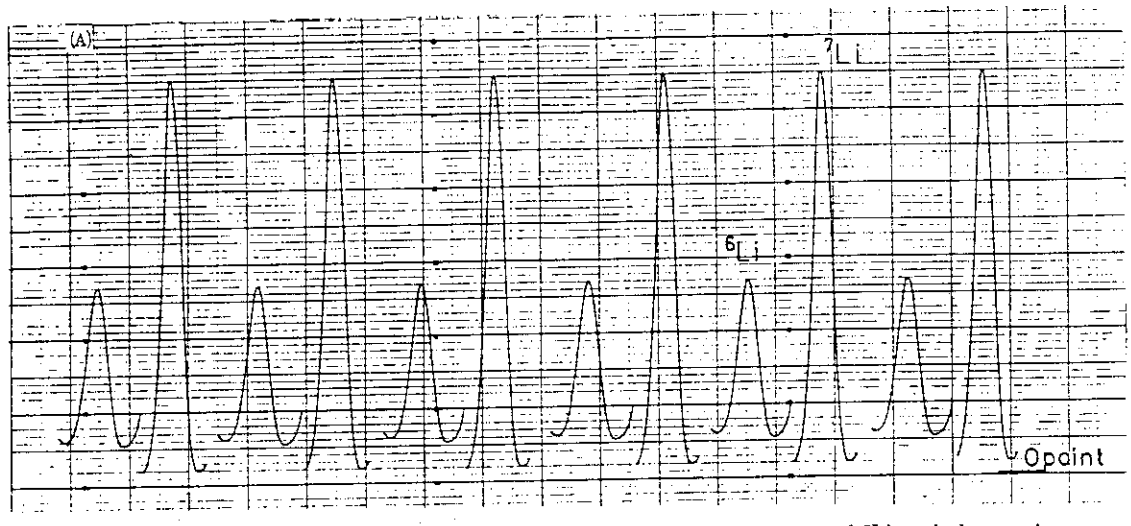

Fig. 1 Recorder traces of a series of scannings for the strong component of ^{7}Li and the weak component of ^{6}Li. (A) a sample of 7.4 atomic % ^{6}Li.

was not detected in a countinuous operation up to 2 hours. The analysis time required for a single determination was usually about 30 minutes. The coefficient of variation was from 0.27 to 0.02 % for ^{6}Li atomic contents between 0.51 and 99.3 %. In Table 1, the analytical values obtained by the present method are shown in comparison with those obtained by a surface ionization mass spectrometric method. Fig.1 shows typical recorder traces on a sample of 7.4 atomic % ^{6}Li scanned at a rate of 0.2 order/minute.

1.1.2. Application of wire filament electrothermal vaporization in inductively coupled plasma atomic emission spectrometry
—— Determination of trace rare earth elements in uranium ——

A wire filament electrothermal vaporization device was constructed for trace element analysis and its analytical performance was examined for the determination of nanogram amounts of rare earth elements (REEs) in uranium[1]. The filament was tungsten wire of 0.1 mm in diameter and was placed in a small glass evaporation chamber (about 1 ml in volume), which was connected to a plasma torch with Teflon tube of 1 mm i.d. and 40 cm long. The small volume of the evaporation chamber minimised sample aerosol dilution with argon carrier gas. A microliter sample was vaporized on a filament heated by an instantaneous discharge current of a condenser. The use of both the instantaneous heating and the small evaporation chamber reduced broadening of temporal emission signal of analyte and made considerable improvement in signal to noise ratio. Nine REEs (Nd, Sm, Eu, Gd, Dy, Ho, Er, Tm, Lu) which had high neutron absorption were investigated.

U_3O_8 sample, 0.590 g, was dissolved with concentrated nitric acid. Separation and preconcentration of the REEs from the sample solution were achieved by 9 M hydrochloric acid anion exchange, and 2.3 M and 6 M nitric acid gradient cation exchange. A sample aliquot of 5 μl was deposited on the filament, and dried slowly by ohmic heating of the filament with a low current(3 A), and then vaporized by passing an instantaneous discharge current through the filament from a condenser (0.2 F). The vaporized sample was introduced into the plasma torch with a continuous argon flowing at a rate of 1 l/min. The emiission signal appeared about 100 msec after the initiation of the discharge and disappeared completely within 200 msec.

The spectral interference effect in the presence of other REEs was examined for the selected analytical lines. No appreciable spectral interference was observed in the presence of 2 μg/ml of each REE in the final solution. The recovery of the nine REEs investigated ranged from 88 to 93 %, when solutions of 20 ng/ml each of the nine REEs were added to a solution containing 0.5 g of uranium (40 ppb each). The relative standard deviations were from 3.6 to 5.1% for the nine REEs with a 10 ng/ml concentration. The detection limits of all the nine elements were 10^{-13} g level.

Reference

1) H.Fukushima, S.Tamura and K.Oho, "Determination of trace rare earth elements in uranium by wire filament electrothermal vaporization and inductively coupled plasma atomic emission spectrometry," Thirty-ninth Annu. Conf. on Anal. Chem. Soc. Japan (Nagoya), 1A15, Oct. 1990.

Publication List

[1] H.Fukushima, "Isotopic analysis of lithium by hollow cathode excitation," Bunkou Kenkyu (in Japanese) 39 (1990) 102.

1.2. Research on Surface Analysis and Surface Chemical Reaction

Ion beam is widely used for the probe of various surface analytical techniques such as secondary ion mass spectrometry and ion scattering spectroscopy. It is also used for surface modifications of materials to produce various surface functional devices. The aim of this study is to clarify the mechanism of chemical reactions induced by ion beams at material surfaces. It was found that the yield of atmospheric gas trapping induced by Ar^+-ion bombardment is appreciably higher than that of the direct ion implantation. For example, the yield of nitride formation at titanium surface by one Ar^+-ion bombardment was obtained to be 20.[1] By comparing the yields of nitrogenation among various metal targets, the mechanism of metal-nitrogen reaction induced by Ar^+-ion was elucidated. The mechanism of the trapping of atmospheric oxygen in metal surfaces by Ar^+-ion bombardments was also clarified. The details of this work is described in section 11.1.

References

1) Y. Baba, "Surface Chemical Reaction Induced by Ion Beam," Kagaku to Kogyo (in Japanese), 42 (1989) 200.

Publication list

[1] Y. Baba, "Surface Chemical Reaction Induced by Ion Beam," Kagaku to Kogyo (in Japanese), 42 (1989) 200.

[2] Y. Baba and T.A. Sasaki, "Nitride Formation at Metal Surfaces by Ar^+ Ion Bombardment in Nitrogen Atmosphere," Mater. Sci. Eng. A 115 (1989) 203.

[3] Y. Baba, T.A. Sasaki and I. Takano, "Trapping of Atmospheric Oxygen on Metal Surfaces under Ar^+ Ion Bombardment," Surf. Sci. 221 (1989) 609.

[4] W. Wurth, J. Stöhr, P. Feulner, X. Pan, K.R. Bauchspiess, Y. Baba, E. Hudel, G. Rocker and D. Menzel, "Bonding, Structure, and Magnetism of Physiorbed and Chemisorbed O2 on Pt(111)," Phys. Rev. Lett. 65 (1990) 2426.

[5] Y. Baba, G. Dujardin, P. Feulner, and D. Menzel, "Formation and Dynamics of Exciton Pairs in Solid Argon Probed by Electron-Stimulated Ion Desorption," Phys. Rev. Lett. 66 (1991) 3269.

1.3 Chemical Analysis of Oxidation State of Copper or Oxygen and its Distribution in Superconducting La-Sr-Cu Oxide.

Determination of nonstoichiometric composition of high Tc superconducting oxides has a fundamental significance for the elucidation of the superconducting mechanism. The chemical methods so far proposed[1] are not enough sensitive, and no attempt has been made to apply the chemical method to the measurement of distribution of the composition in the sample solid. The objective of the present research is to develop a more sensitive and precise chemical method for the determination of the oxidation state as well as its distribution in $La_{2-x}Sr_xCuO_y$ samples.

Fig. 1 shows an apparatus for the continuous dissolution of the sample and for the successive detections. Column electrode was essentially identical to that described previously[2]. Column electrode E_1 was employed for the coulometric determination of Fe^{3+} generated through the redox reaction (1)

$$Fe^{2+} + (CuO)^{+} + 2H^{+} \rightarrow Fe^{3+} + Cu^{2+} + H_2O \quad (1)$$

Column electrode E_2 was for the determination of Cu^{2+} and column electrode E_{prep} was used to convert Fe^{3+} to Fe^{2+} in the dissolving solution immediately before the introduction into the dissolution room.

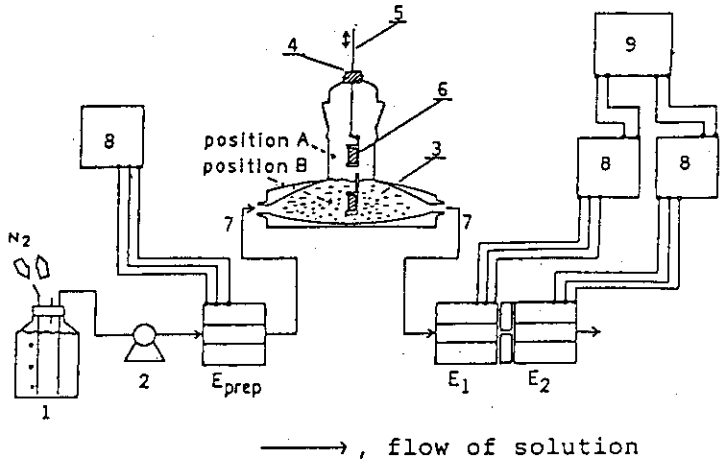

Fig. 1 Apparatus.
(1) reservoir for the dissolving solution,
(2) pump, (3) sample dissolution room,
(4) isoprene rubber seal, (5) Pt wire,
(6) sample holder of Pyrex glass,
(7) Teflon tubing (1 mm i.d.),
(8) potentiostat, (9) two-pens recorder.
column electrodes: E_{prep}; -0.25 V,
E_1; +0.25 V, E_2; -0.25 V.

Fig. 2 shows typical curves showing relationship between current and dissolution time, i.e., i_1-t at E_1 and i_2-t at E_2, obtained for a sample of $La_{2-x}Sr_xCuO_y$ with (1)x=0 (2)x=0.15 and (3)x=0.25. The ratio $(CuO)^+/Cu_{total}$ in the bulk of the samples, defined as X_b, can be expressed by the ratio $Q_1/0.5Q_2$, where Q_1 and Q_2 are the coulomb numbers calculated by the integration of i_1-t and i_2-t curves, respectively. The X_bs for samples with $0 < x < 0.6$ were determined and the results are plotted against x in Fig. 3. Oxygen content y in $La_{2-x}Sr_xCuO_y$ was calculated from X_b based on eq. (2).

$$y = 4 + (X_b - x)/2 \quad (2)$$

The y values are in good agreement with the results reported previously[3,4]. The y values are slightly higher than 4 for samples with x of less than 0.1, this suggests the excess oxygen locating at interstitial site in

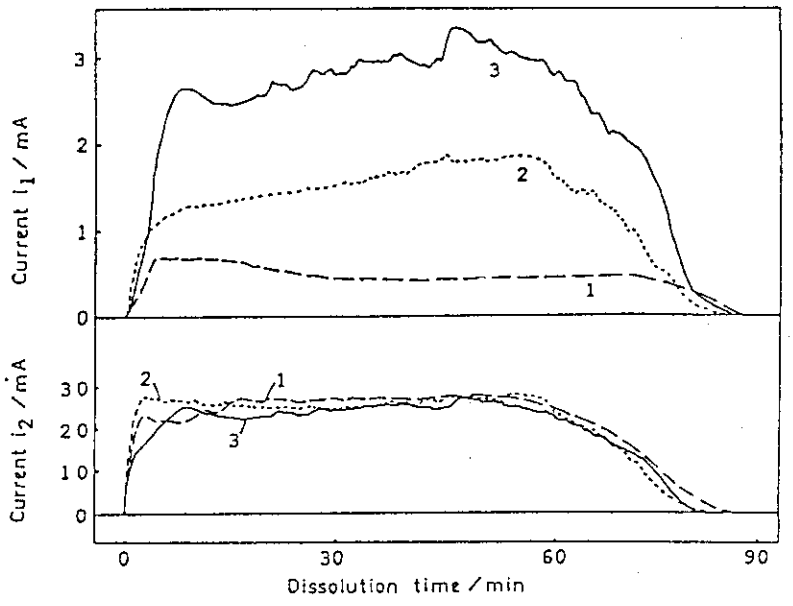

Fig. 2 i_1-t and i_2-t curves observed during the dissolution of $La_{2-x}Sr_xCuO_y$. strontium content, x; (1) 0, (2) 0.15, (3) 0.25. sample weight; 205 ± 5 mg.

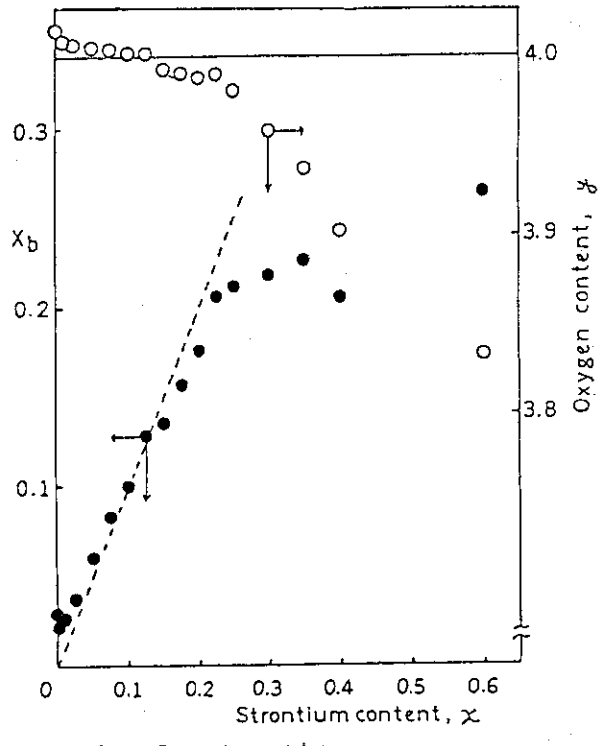

Fig. 3 $(CuO)^+/Cu_{total}$ ratio, X_b, (●) and oxygen content, y, (○) as a function of the strontium content, x, in $La_{2-x}Sr_xCuO_y$.

the unit cell. The gradual decrease of y in the region of x of more than 0.15 reflects the formation of the oxygen vacancy.

The ratio $i_1/0.5i_2$ at a definite time in both i-t curves corresponds to the $(CuO)^+/Cu_{total}$ ratio, X_t, at a given dissolution time of the sample solid. Variation of X_t with time, i.e., X_t-distribution curve, may provide the information on the distribution of $(CuO)^+$ in the sample pellet. The experimental error in the determination of X_t was small, because the residual currents of E_1 and E_2 are steady during the measurement. The X_ts observed at earlier stage of the dissolution correspond to $(CuO)^+/Cu_{total}$ ratios near the surface of the sample pellet. The samples prepared under various conditions were analyzed and the distribution of $(CuO)^+$ near the surface was examined. Fig. 4a shows results for the samples of $La_{2-x}Sr_xCuO_y$ with x=0, 0.01, 0.1, 0.15 and 0.25 analyzed within 1 day after the preparation. Here, the samples with x=0, 0.1, 0.15 and 0.25 showed the superconducting property. It is clear that the X_t values in the surface region of 50 - 150 um in depth were much lower than the X_b. Results in Fig. 4b were obtained by the same procedure as that for 4a but with the sample pellets stored for 5 months after the preparation. Remarkable differences between two series of results in Figs. 4a and 4b are as follows; (i) X_b decreases with standing after the preparation, (ii) the thickness of the region where X_t is lower than X_b increases with standing,

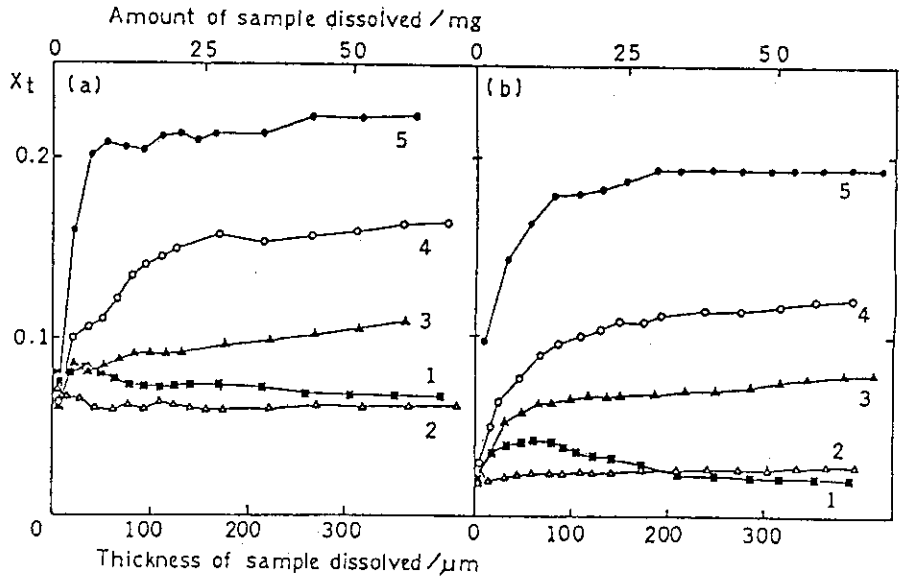

Fig.4. X_t-distribution curves for $La_{2-x}Sr_xCuO_y$.
Samples: (a)analyzed within 1 day after the preparation; (1)x=0, X_b=0.0695, (2)x=0.01, X_b=0.0625, (3)x=0.1, X_b=0.137, (4)x=0.15, X_b=0.167, (5)x=0.25, X_b=0.236 :(b)analyzed 5 months after the preparation; (1)x=0, X_b=0.0234, (2)x=0.01, X_b=0.0285, (3)x=0.1, X_b=0.0923, (4)x=0.15, X_b=0.123, (5)x=0.25, X_b=0.198.

and (iii) X_t at the outermost surface decreases with standing. It is noteworthy that the X_ts for the sample with x=0.01 of nonsuperconducting property (see curve 2) show almost homogeneous distribution. In addition, the peculiar distribution which showed the maximum of X_t at around 30-50 um depth from the surface was observed in the sample with x=0 as shown in curve 1.

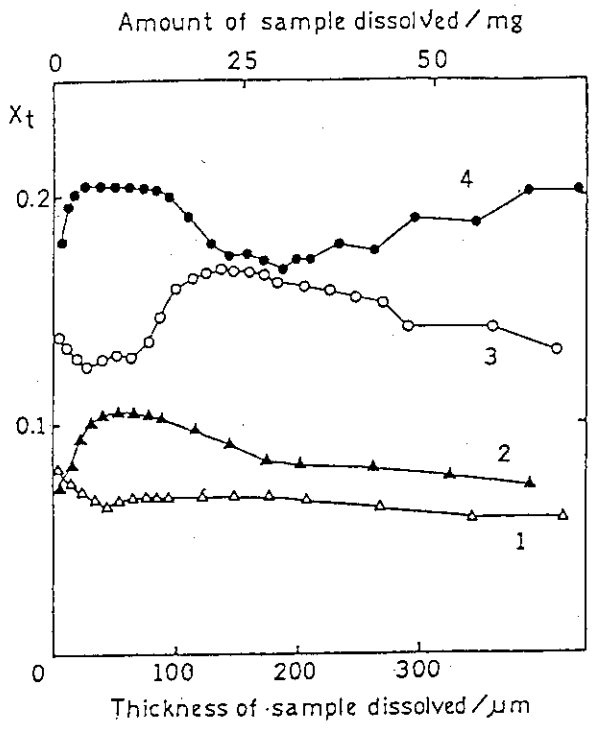

Fig.5. X_t-distribution curves for $La_{2-x}Sr_xCuO_y$ prepared in various atmosphere.
Samples; (1)x=0, X_b=0.0728, (2)x=0, X_b=0.0855, (3)x=0.15, X_b=0.130, (4)x=0.15, X_b=0.198.
Sintering atmosphere;
(1),(3) Ar, (2),(4) O_2

Fig. 5 illustrates results for the distribution of X_ts in the sample pellets which were annealed at 860 °C for 30 hrs in the flow of Ar or O_2 gas are illustrated in Fig. 5. The effect of atmosphere in the annealing process was observed particularly for the sample with x=0.15. The X_b for the sample annealed in O_2 is higher than that annealed in Ar, and X_ts show a maximum and a minimum near the surface depending on the annealing atmosphere. The sample with x=0 annealed in Ar had the homogeneous distribution of X_t, and was nonsuperconducting. The sample with x=0 annealed in O_2 gas giving curve 2 is still superconductor.

The present method has a advantage to be high sensitivity in the determination of X_b. It is evaluated that more than 2 X 10^{-7} mole of $(CuO)^+$ in the sample can be determined. This corresponds to a detection limit of X_b to be 0.0003 with 200 mg of a sample. Another advantage is that the oxidation state near the surface as well as in the bulk, i.e., the distribution of $(CuO)^+$ in the sample, can be measured.

REFERENCES

1)M.W. Shafer, T. Penny and B.L. Olson, Phys. Rev. B36(1987)4047.
2)H. Aoyagi, Z. Yoshida and S. Kihara, Anal. Chem., 59(1987)400.
3)Z. Tan, M.E. Filipkowski, J.I. Budnick, E.K. Heller, D.L. Brewe, B.L. Chamberland, C.E. Bouldin, J.C. Woicik and D. Shi, Phys. Rev. Lett., 64(1990)2715.
4)K. Yoshimura, Y. Nishizawa, Y. Ueda and K. Kosuge, J. Phys. Soc. Jpn., 59(1990)3073.

PUBLICATION LIST

[1] Y. Sasaki, H. Aoyagi, H. Takeishi and Z. Yoshida, Determination of concentration and distribution of $(CuO)^+$ in high-Tc superconducting $La_{2-x}Sr_xCuO_y$ pellet by flow-coulometry, Physica C in press.
[2] Y. Sasaki, H. Aoyagi, H. Takeishi and Z. Yoshida, Chemical analysis of oxidation state of copper or oxygen and its distribution in superconducting La-Sr-Cu oxide, Anal. Sci. in press.

1.4 Ion Exchange Separation of Trace Amounts of Uranium and Thorium in Tantalum.

With the increase of accumulation in LSI, it is very important to reduce such impurities as alpha emitters because alpha particles cause errors in LSI[1]. Uranium and thorium are typical alpha emitters. These elements in tantalum metal, which has high melting point and is used in LSI, were determined by neutron activation analysis followed by ion exchange separation method[2,3].

Determination of distribution coefficients

The distribution coefficient,Kd, of uranium, thorium and tantalum in hydrofluoric and hydrofluoric-boric acid media was determined by batch method. These Kd values were shown in Table 1.

Column operation

From the results of Kd, it is clear that cation exchange separation with $HF-H_3BO_3$ is suitable for the concentration of uranium and thorium from the tantalum metal. In this case, the recovery of uranium and thorium, as well as the remaining amount of tantalum in the numbers of column operation are important. In table 2, decontamination factor of tantalum and recovery of uranium and thorium were shown. Based on results in Table 1 and 2, the scheme for the separation of uranium and thorium from tantalum using cation exchange resin with

Table 1
Cation exchange distribution coefficients of U, Th and Ta in Hf and HF – H_3BO_3 media

Element	HF, M				
	0.1	0.2	0.5	1	2
U	8	<3	<3	<3	<3
Th	50	16	8	6	5
Ta	<3	<3	<3	<3	<3

Element	HF, M – 0.65M H_3BO_3				
	0.1	0.2	0.5	1	2
U	$4 \cdot 10^3$	$2 \cdot 10^3$	500	190	60
Th	$4 \cdot 10^3$	$3 \cdot 10^3$	$2 \cdot 10^3$	700	160
Ta	10	6	<3	<3	<3

Table 2
Recoveries of U and Th, and amount of Ta remained in cation exchange separation

Number of column operation	Amount of Ta remained	Decontamination factor of Ta	U and Th recovered, %	
			U	Th
1	1 mg	10^3	98 ± 2	98 ± 2
2	20 μg	$5 \cdot 10^4$	97 ± 5	96 ± 5
3	400 ng	$2.5 \cdot 10^6$	95 ± 7	94 ± 7

Amount of Ta: 1 g, U and Th: radioactive tracers, errors: 1 σ

HF and HF-H_3BO_3 media was recommended as shown in Fig. 1. Uranium and thorium in some tantalum metals supplied from the several companies were determined.

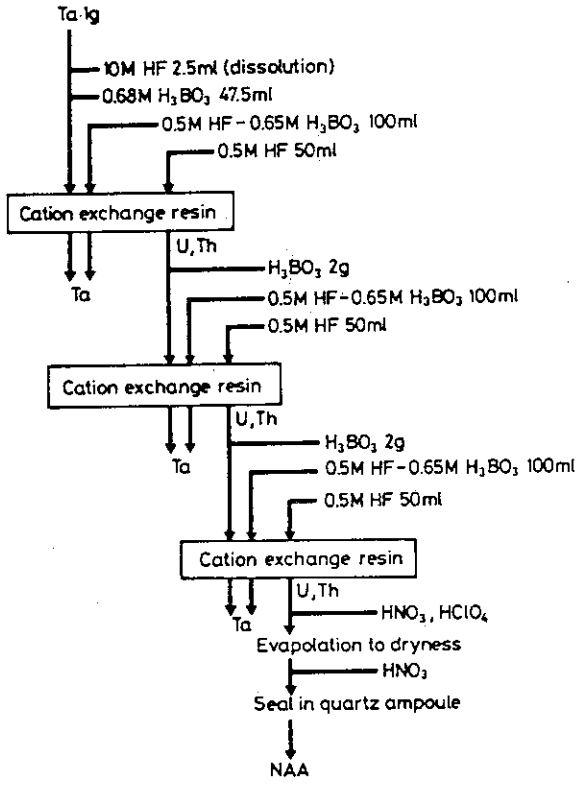

Fig. 1 Separation scheme for U and Th in Ta

References

1) T.C.May and M.H.Woods, 16th Annual Proc. on Reliability Physics, 1978, p33
2) T.Adachi, H.Yoshida, K.Izawa, S.Kihara, H.Hashitani, Bunseki Kagaku 33(1984)11.
3) T.Adachi, H.Yoshida, K.Izawa, H.Hashitani, Bunseki Kagaku, 33(1984)455.

Publication List

[1] Y.Sasaki, H. Takeishi, T. Adachi, K. Izawa, Ion exchange separation of trace amounts of uranium and thorium in tantalum for neutron activation analysis, J. Radioanal. Nucl. Chem., Articles, 139(1990)143.

2. DEVELOPMENT OF CERTIFIED REFERENCE MATERIALS

S. Iso, M. Itoh, A. Hoshino *, K. Takashima, K. Tamura, S. Tamura, Y. Toida and K. Watanabe

* Institute for Environmental Sciences

INTRODUCTION

The International Atomic Energy Agency (IAEA) held an advisary group meeting titled "Chemical and Isotopic Reference Materials in the Nuclear Fuel Cycle" in 1980. Among the participated thirty four countries, only nine, including Japan, can supply the certified reference materials (CRMs) related to this field, as previously reported [1]. The International Organization for Standardization (ISO) and the IAEA have discussed a possible cooperation agreement on the evaluation of analytical methods and procedures. The importance of certified reference materials increases greatly and urgently because of rapid popularization of sophisticated high-precision analytical instruments in this decade. The domestic and international networks of measurement-compatibility have been necessitated in terms of trade, environmental protection, development of new materials, and world health, etc. [2].

The JAERI has so far devoted an effort to develop a few tens of certified reference materials which are minimal needful for the quality control of nuclear industry in this country [3]. Within the last several years, we have issued five new CRMs of zirconium, hafnium and Zircaloys ; namely, JAERI-Z19 (Hafnium metal) Z20 (Zircaloy-2 for gas assay), Z21 (Zirconium metal), Z22 (Zircaloy-2 for chemical analysis) and Z23 (Zircaloy-4 for chemical analysis). The preparation of these CRMs was planned by the Committee on Analytical Chemistry of Nuclear Fuels and Reactor Materials, JAERI.

In this report, a continued effort to issue the CRMs related to quality control of nuclear materials is concisely presented, i.e., zirconium-, hafnium-, zircaloy- and graphite- reference materials.

2.1 Zirconium, Hafnium and Zircaloy certified reference materials (CRMs) : JAERI-Z19, Z20, Z21, Z22 and Z23

2.1.1 Preparation, analysis and certification

The hafnium reference material (JAERI-Z19) has been prepared aiming mainly at a use in destructive analysis by an inductively coupled plasma atomic emission spectrometry (ICP-AES). The raw material was obtained from Nippon Mining

Co., Ltd. Purity test, chipping, sieving, washing and bottling were carried out in JAERI. Homogeneity was examined by isotope dilution mass spectrometry and ICP-AES. Purity of hafnium was determined by subtracting amounts of zirconium, iron, oxygen, nitrogen and other impurities from the total amount. Hafnium purity was determined to be 97.8%. Each glass bottle contains 2 grams of hafnium metal chips. This reference material was planned to prepare in 1984 and issued in 1987 [4].

The zircaloy reference material (JAERI-Z20), Zircaloy-2, is in a form of block, 6 mm in square and 50 mm long. It is intended for calibrating inert gas fusion method for the analysis of oxygen and nitrogen. For the certification, oxygen was determined by inert gas fusion method and nitrogen was determined by titration method or spectrophotometry with thymol. Certified values for oxygen and nitrogen are 0.128 and 0.0036%, respectively. The value for hydrogen, 5.3 ±1 ppm, was not certified, but was given for information only. JAERI-Z20 was planned to prepare in 1984 and issued in 1990.

Zirconium and zirconium alloy reference materials (JAERI-Z21 to Z23) are intended for use in the evaluation of ICP-AES method employed for the determination of impurities in zirconium alloys. The raw material of the JAERI-Z21 and Z23 were prepared by Nippon Mining Co., Ltd., and that of Z22 was purchased from Western Zirconium Co., USA. Certified values are basd on results obtained by two or more independent and reliable methods in collaborative analysis. These CRMs were planned to prepare in 1986 and issued in 1990.

Certified values for JAERI-Z19 to -Z23 and methods for certification are shown in Table 1 and 2, respectively.

References

1) S.Deron and J.D.Navratil:IAEA Report AG-256, April, 1980.
2) Science Council of Japan:A Report of the Study-Liaison Committee on Reference Materials, April, 1991.
3) Anal.Chem.Lab.,JAERI:A Catalogue of CRMs for Chemical Analysis of Nuclear and Reactor Materials, 1991(Revised).
4) K.Takashima, S.Tamura, K.Watanabe, M.Ouchi, S.Iso, M.Ito, H.Takeishi, Y.Toida K.Tamura, K.Kato and A.Hoshino: "Preparation of hafnium reference material JAERI-Z19"(in Japanese), JAERI-M 88-116(1988).

Publication list

[1] The Committee on Analytical Chemistry of Nuclear Fuels and Reactor Materials JAERI:"Preparation of Certified Reference Material for Determination of Oxygen and Nitrogen in Zirconium Alloys, JAERI-Z20",(in Japanese), JAERI-M 90-026(1990).

[2] Idem :"Preparation and Certification of Certified Reference Materials JAERI-Z21, Z22 and Z23 for Analysis of Zirconium and its Alloys", (in Japanese), JAERI-M 91-044(1991).

[3] K.Takashima and K.Kato: "Direct determination of tin and aluminium in zirconium by ICP-vacuum ultraviolet AES ", Bunseki Kagaku, 39(1990)533, (in Japanese).

[4] K.Takashima, A.Hoshino and S.Tamura:"Proceedings of Int. Symp. of Certified Reference Materials", May 1989, Beijing, Int. Academic Publisher(Pergamon-CNPIEC) Beijig-New York, P.244(1989).

[5] K.Kato : "Simultaneous multielement analysis of zirconium alloys by chlorination separation of matrix/ICP-AES", Bunseki Kagaku, 39(1990)439, (in Japanese).

Table 1 Specification and certified values for JAERI-Z19 to Z23

Elements	Specification(%)*				Certified values(%)*				
	Zircaloy-2		Zircaloy-4		Z19	Z20	Z21	Z22	Z23
Sn	1.20	1.70	1.20	1.70	--	--	0.03	1.43	1.52
Fe	0.07	0.20	0.18	0.24	(11ppm)	--	0.102	0.144	0.226
Cr	0.05	0.15	0.07	0.13	--	--	0.013	0.096	0.112
Ni	0.03	0.08	--		--	--	(0.0005)	0.050	(0.0010)
Fe+Ni+Cr	0.18	0.38	0.28	0.37					
Hf	<100		<100		97.8%	--	82ppm	35ppm	73ppm
H	< 25		< 25		(6ppm)	(5.3ppm)	--	--	--
N	< 80		< 80		--	0.0036%	--	--	--
O	900	1500	900	1500	(250ppm)	0.128%	--	--	--
C	< 0.027%		< 0.027%		(136ppm)	--	--	--	--
B	< 0.5		< 0.5		--	--	<0.2	<0.2	<0.2
Cd	< 0.5		< 0.5		--	--	<0.1	<0.1	<0.1
U	< 3.5		< 3.5		--	--	<0.1	1.1	<0.2
Cu	< 50		< 50		--	--	2	8	8
Co	< 20		< 20		--	--	<2	<2	<2
Mn	< 50		< 50		--	--	11	6	17
Ni	--		< 70		--	--	--	--	--
Pb	--		--		--	--	2	2	3
Al	< 75		< 75		--	--	22	40	42
Si	<120		<120		--	--	18	90	23
Ti	< 50		< 50		--	--	9	3	6
Mo	--		--		--	--	--	--	--
W	<100		<100		--	--	<10	<10	<10

* ppm for minor or impurity elements.

Table 2 A list of chemical methods used for certification

Elements	Method used
Sn :	Iodate titration after reduction with aluminum. 8-Quinolinol extraction photometry, GF-AAS, ICP-AES.
Fe :	1,10-Phenanthroline photometry, Thiocyanate photometry, ICP-AES.
Cr :	Diphenylcarbazide photometry, Diphenylcarbazide photometry after separation of iron by ion exchange, ICP-AES.
Ni :	Dimethylglyoxime extraction photometry, Dimethylglyoxime bromine photometry, ICP-AES.
Hf :	IDMS after ion exchange separation, ICP-AES.
B :	Curcumine photometry, IDMS after methyl borate distillation.
Cd :	Graphite furnace atomic absorption spectrometry(GF-AAS), AAS after separation of ion exchange or DDTC extraction.
U :	Arsenazo III photometry after ion exchange separation, IDMS after TPAN/MIBK extraction.
Cu :	ICP-AES or AAS after ion exchange separation.
Co :	ICP-AES, ICP-MS, AAS, GF-AAS after ion exchange separation.
Mn :	ICP-AES or AAS after ion exchange separation, ICP-AES.
Pb :	ICP-AES or AAS after ion exchange separation, GF-AAS.
Al :	ICP-AES or ICP-MS after ion exchage separation, ICP-AES with iron correction.
Si :	Molybdenum blue photometry.
Ti :	Diantipirylmethane photometry, Thiocyanate photometry, ICP-AES after ion exchange separation, ICP-AES.
W :	Thiocyanate extraction photometry, ICP-AES, ICP-MS.

2.1.2 Determination of boron, zirconium, hafnium, and uranium in CRMs JAERI-Z8, Z19, Z21 to Z23 and NIST SRM 360b by isotope dilution surface ionization mass spectrometry

INTRODUCTION

As one of the highly accurate and principle independent methods available at present in chemical analysis, isotope dilution surface ionization mass spectrometry (IDSIMS) has been eagerly utilized to determine several elements in the certified reference materials (CRMs) prepared in this laboratory.[1-6] The elements chosen to analyze by this method were those difficult to analyze precisely and accurately by other methods. The capability to analyze accurately these in nuclear materials is very important. Compatibility of certificate values for alloying and impurity elements in the CRMs of Zircaloys internationally available has been discussed elsewhere.[7]

In this paragraph, a brief description will be given for the analytical results obtained for the elements in four JAERI CRMs and one NIST SRM recently issued.

EXPERIMENTAL

Reagents and apparatus : Water was double distilled in a fused silica distillator. The sulfuric acid was purified by sub-boiling in a fused silica vessel. Hydrochloric, nitric and hydrofluoric acids were of precision analysis grade. Glycerol solution(10 v/v %) was deionized by cation exchange. Methanol, use in boron analysis, was purified by alkaline added distillation in a fused silica flask. The sodium carbonate solution put in a methyl borate reservoir was made from a Merck Suprapur reagent. The enriched isotopes, 89 atom. % ^{91}Zr (ZrO_2) and 87 atom. % ^{177}Hf (HfO_2), were purchased from Oak Ridge National Lab., USA, and they were decomposed by heating in a sulfuric and hydrofluoric acid mixture to make the spike solutions. Their concentrations were calibrated by using the CRM JAERI-Z15 (99.9 wt. % Zr, 2 ppm Hf) and the CRM JAERI-Z19 (97.8 wt. % Hf, 2.13 wt. % Zr). The boron spike solution was prepared by dissolving a weighed aliquot of the NIST SRM 952 (95 atom.% ^{10}B, 99.97 ± 0.02 wt.% boric acid) in water and neutralized with a sodium carbonate solution. When necessary, its concentration was calibrated by isotope dilution using the NIST SRM 951 (natural 19.83 atom.% ^{10}B, 100 ± 0.01 wt.% boric acid). The uranium spike solution was made by dissolving a weighed aliquot of the NIST SRM U-900 (90.196 atom.% ^{235}U, U_3O_8) in diluted nitric acid and calibrated with a solution of the CRM JAERI U-4 (99.99 wt.%

uranium metal, natural 0.711 atom.%^{235}U).[8]
Zone-melting refined tantalum and rhenium ribbons (0.025 mm thick x 0.75 mm wide, 4N5 or better purity) were obtained from H.Cross, Co., USA, and spot-welded on filament beads, rinsed in acetone-water, dried at 60 °C, and then prebaked in a vacuum for 1 to 3 h at about 1700 °C. To minimize the contamination of zirconium and hafnium from glasswares, platinum and plastics tools,[9,10] all of them were carefully washed by immersing in a 2M hydrofluoric-2M sulfuric acid container, and then in a 6M hydrochloric acid tank for several days.
The mass spectrometers employed were a CEC 21-702B, 12 inch deflection radius - 60 degree magnet, and a VG MM54-10, 27 cm deflection radius - 90 degree magnet followed with a 10 cm radius - 90 degree static electric filter. The latter was equipped with a Daly type scintillation detecor besides a Faraday cup collector. The isotope ratios of the elements concerned were measured by direct detection systems thrououghout this work. The ion pairs, such as $Na_2{}^{11}BO_2^+/ Na_2{}^{10}BO_2^+$ (corrected for a value of $^{17}O/^{16}O = 0.000385$ to convert into $^{11}B/^{10}B$ ratio), $^{90}Zr^+/^{91}Zr^+$, $^{92}Zr^+/^{91}Zr^+$, $^{178}Hf^+/^{177}Hf^+$, $^{179}Hf^+/^{177}Hf^+$, $^{180}Hf/^{177}Hf^+$, $^{235}U^+/^{238}U^+$, were utilized in the isotope dilution analyses. Since the mass fractionation in raw isotope ratios observed by surface ionization techniques would not be ignored, the multiple isotope dilution averaging were practiced whenever possible.[11, 12]

In this work, the material and combination of filaments in an ion source of the mass spectrometer were chosen correspondingly to the elements, i.e., single tantalum for boron, triple tantalum for zirconium, single rhenium for hafnium, and triple rhenium or tantalum-rhenium-tantalum for uranium.
Chemical procedures : Procedures adopted for sample decompositions and the chemical separation of elements have been described in details elsewhere.[1-4] The amounts of samples taken in analyses were one to two grams. The decomposition of samples was carried out mostly by heating with the sulfuric acid except that a hydrofluoric and nitric acid mixture was employed in the analysis of uranium. Samples for boron were decomposed by a low temperature decomposition technique[13] followed by methyl borate distillation. Zirconium and hafnium were mutually separated by a strongly basic anion exchange resin chromatography.[11] When much molybdenum was present, zirconium fractions were evaporated to small volumes of 10 ml and purified of it by either aqueous ammonium or diammonium hydrogenphosphate precipitation.[14] The precipitate was decomposed by heating with sulfuric and nitric acids. Uranium was

separated by tetra-n-propylammonium hydroxide - methyl isobutyl ketone extraction.[15] The uranium extracted in the organic phase was backextracted with a 0.1 M nitric acid to the aqueous phase and aluminum accompanied was precipitated with ammonium carbonate solution (20 w/v %).[1] This modification was necessary to make the samples for mass spectrometry.

RESULTS AND DISCUSSION

The isotope analyses of boron, zirconium and hafnium were carried out by a carbonized sample technique.[16] The results obtained by this technique for natural isotopic compositions of zirconium and hafnium were in excellent agreements with those reported by others.[17-19] The high-precision mass spectrometry on uranium has been done in a manner similar to that described previously.[20]

The averages and standard deviations observed for concentrations of employed spike solutions were typically seen as follows (μg of the element per g of the solution) : Boron ; 35.79 ± 0.01 (wt. per wt. base), Zirconium ; 102.50 ± 0.13 (N=5), Hafnium ; 25.38 ± 0.044 (N=6), Uranium ; 14.544 ± 0.026 (N=5), where N is the number of independent determinations. These sizes of standard deviations seemed to be a measure of the attainable repeatability precisions of the IDSIMS, exclusiving the uncontrollable blank flactuation and inhomogeneity of the element contents if any.

A summary of analytical results for the elements concerned is shown in Table 1. The results for boron, hafnium and uranium may give a good reference to those obtained by the other methods. The results for zirconium in Z19 seem somewhat scattered, although the results obtained by ICP-AES were in a good agreement with the average value of isotope dilution analyses. A comparative homogeneity test using two pure hafnium wires commercially available was carried out. The content of zirconium in the sample A, 1 mm dia. wire, 0.2 g taken of a distance of every 25 cm, was determined to be 2.968 ± 0.007 (for six positions), and that in the sample B, 2.3 mm dia. wire, 1.2 g taken of a distance of every 25 cm, to be 0.1560 ± 0.0009 (for six positions), % Zr. Therefore, there may exist an unknowing reason why the results on Z19 were ragged (Table 2). However, the ambiguity in certified values given to Z19 (97.8 % Hf, 2.13 % Zr) would be sufficiently small when it is utilized as a chemical standard in common analyses.

(S.Tamura, Y.Toida, K.Tamura and K.Takashima)

References

1) The Committee on Analytical Chemistry of Nuclear Fuels and Reactor Materials, JAERI : JAERI 4050, July, 1969.
2) Idem : JAERI-M85-038, Feb., 1985.
3) Idem : JAERI-M91-044, Feb., 1991.
4) K.Takashima, S.Tamura, K.Watanabe, M.Ouchi, S.Iso, M.Ito, H.Takeishi, Y. Toida, K.Tamura, K.Kato and A.Hoshino : JAERI-M88-116, June, 1988.
5) A.Hoshino, K.Takashima and S.Tamura : Proc.First Int. Symp. on Advanced Nuclear Energy Research, " Near-Future Chemistry in Nuclear Energy Field ", Oh-arai, Japan, Feb., 1989.
6) K.Takashima, A.Hoshino and S:Tamura : " Proc. of Int. Symp. of Certified Reference Materials ", May, 1989, Beijing, Int. Academic Publisher (Pergamon-CNPIEC) , Beijing— New York, p.244 (1989).
7) K.Takashima, S.Tamura and A.Hoshino : Fiftieth Meeting of Anal. Chem. Soc. Japan (Shimane), IC05, June 1989.
8) H.Hashitani, A.Hoshino and T.Adachi : JAERI-M5343, Aug.,1973.
9) M.Shima : Geochim. Cosmochim. Acta, 43(1979), 353.
10) P.J.Patchett and M.Matsumoto : Contrib. Mineral. Petrol., 75(1980),263.
11) S.Tamura, K.Tamura and K.Kato : Thirtieth Ann. Conf. Anal. Chem. Soc. Japan (Kyoto), 3G06 (1981).
12) K.Tamura and S.Tamura : Thirty ninth Ann. Conf. Anal. Chem. Soc. Japan (Nagoya), 3C19(1990).
13) S.Tamura, Y.Toida and K.Tamura : JAERI-M89-058, p.17 (1989).
14) G.Hevesy and K.Kimura : J. Am. Chem. Soc., 47(1925), 2540.
15) W.J.Maeck, G.L.Booman, M.C.Elliott and J.M.Rein : Anal. Chem., 30(1958), 1902.
16) S.Tamura : Mass Spectroscopy, 23(1975), 49.
17) J.Minster and L.Ph.Ricard : Int. J. Mass Spectrom. Ion Processes, 37(1981), 259.
18) M.Nomura, K.Kogure and M.Okamoto : ibid., 50(1983), 219.
19) P.J.Patchett : Geochim.Cosmochim. Acta, 47(1983), 81.
20) S.Tamura and H.Hashitani (Edited by) : JAERI-M82-053, May 1982.

Publication List
A part of this work was published in a report below.

The Committee on Analytical Chemistry of Nuclear Fuels and Reactor Materials, JAERI : " Preparation and Certification of Certified Reference Materials JAERI-Z21, Z22 and Z23 for Analysis of Zirconium and its Alloys ", Edited by K.Takashima, JAERI-M91-044, Feb., 1991.

Table 1 Determination of boron, zirconium, hafnium and uranium in CRMs JAERI-Z8, Z19, Z21 to Z23 and NIST SRM 360b by isotope dilution surface ionization mass spectrometry

Sample description	Elements determined, average ± std. dev. (no. of runs)			
	Boron *a) ppm	Zirconium *b) %	Hafnium *c) ppm	Uranium *d) ppm
Z8 Zircaloy-2	0.03 ± 0.01 (3)	---	---	0.27 ± 0.01 (3)
Z19 Hafnium	0.20 ± 0.08 (9)	2.130 ± 0.033 (6)	---	---
Z21 Zircaloy-2	0.21 ± 0.06 (3)	---	82.30 ± 0.25 (5)	0.01_5 ± 0.01_3 (3)
Z22 Zircaloy-2	0.18 ± 0.04 (3)	---	35.42 ± 0.48 (5)	1.11 ± 0.12 (3)
Z23 Zircaloy-2	0.17 ± 0.09 (3)	---	72.86 ± 0.21 (5)	0.15 ± 0.01 (3)
360 b Zircaloy-4	0.31 ± 0.06 (3)	---	79.32 ± 0.68 (5)	1.18 ± 0.01 (3)

*a) Sample taken : 1 g. Blank, 0.08 ± 0.02 μg B (N=4), was deducted.
*b) Sample taken : 2 g. Blank, 0.39 ± 0.23 μg Zr(N=4), was not deducted. See Table 2.
*c) Sample taken : 1 g. Blank, 0.025 ± 0.003 μg Hf (N=2), was not deducted.
*d) Sample taken : 1 g. Blank, 0.070 ± 0.004 μg U (N=4), was deducted.

Table 2 Comparative homogeneity tests on the contents of zirconium in pure hafnium samples

Sample (Position number)	Zirconium found (wt,% Zr)		
	A(ø1 mm wire) *a)	B(ø2.3 mm wire) *b)	Z 19(chip) *c)
1	2.963 ±0.017	0.1552 ±0.0007	2.124 ± 0.005
2	2.973 ±0.020	0.1570 ±0.0024	2.176 ± 0.005
3	2.972 ±0.013	0.1558 ±0.0008	2.126 ± 0.002
4	2.959 ±0.016	0.1568 ±0.0012	2.152 ± 0.003
5	2.962 ±0.013	0.1552 ±0.0008	+ 2.077 0.007
6	2.976 ±0.010	0.1560 ±0.0022	2.124 ± 0.004
Average Std.dev.	2.968 ± 0.007(6)	0.1560 ± 0.0009(6)	2.130 ±0.033(6)

*a, b) Pure hafnium wires commercially available. Sample positions in wires were of a distance of every 25 cm along length. Samples taken for A were 0.2 g, for B 1.2 g. Standard deviations for A and B were calculated on eight to twelve pairs of isotope ratios of $^{90}Zr/^{91}Zr$ and $^{92}Zr/^{91}Zr$ in a single loading of mass spectrometric analysis.

*c) For Z 19, the position numbers mean the separate bottle numbers. A whole content, 2 g, in the bottle was decomposed to analyze. The average values were given for duplicate loadings of mass spedtrometric analysis.

2.1.3 Verification of Certified Hydrogen values in CRMs by Isotope Dilution Mass Spectrometry

Introduction

It is well known that metals such as titanium, zirconium, and its alloys are markedly embrittled by the formation of hydrides. The maximum permissible value for hydrogen in zirconium and its alloys for nuclear applications is 0.0025% by weight. Rapid extraction methods are commonly used for the determination of hydrogen. For its accurate determination by the techniques, all the hydrogen must be extracted. In order to test the accuracy of the extraction results, independent analysis techniques are required. The isotope dilution mass spectrometry (IDM) has been investigated for the accurate determination of hydrogen in metals and alloys[1]. The results were found to be dependent on the recovery of the isotopically equilibrated hydrogen because of isotope effect on the solubilities in the solid samples. Equilibrium pressure measurements of hydrogen and deuterium over these metals also showed definite isotope effect on solubilities[2]. To overcome the isotope effect in the IDM, recovery of the equilibrated hydrogen must be quantitative. The isotope dilution procedure was modified for the accurate and precise determination of hydrogen in metals and alloys[3].

In the present paper, we applied the IDM to a number of Certified Reference Materials (CRMs) to verify certified hydrogen values in titanium zirconium and its alloy reference materials; and obtained the results that were in good agreement with the certified values for National Institute of Standards and Technology (NIST), but higher than that for BCR sample. We traced the cause of the high result for Community Bureau of Reference (BCR) sample and found that the hydrogen concentration near the sample surface was higher than the average content.

Experimental

Typically 0.5g of sample was loaded on a sample holder, which was attached to a silica reaction tube in a vacuum system. The silica tube was outgassed for at least 30 min by heating at 900° C. Then the temperature of the tube was lowered to 850° C. The sample was dropped into the silica tube by rotating the sample holder. Deuterium in a known volume vessel was expanded

into the silica tube and reacted with the sample for 20 min. The equilibrated hydrogen gas was then transferred to a 5-litter gas-collecting vessel by a mercury transfer diffusion pump for subsequent mass spectrometric analysis.

Results and discussion

Hydrogen amounts in different sample weights for some of CRMs were determined to check whether there exists a systematic error in the IDM. The results (Fig. 1) indicate no systematic error.

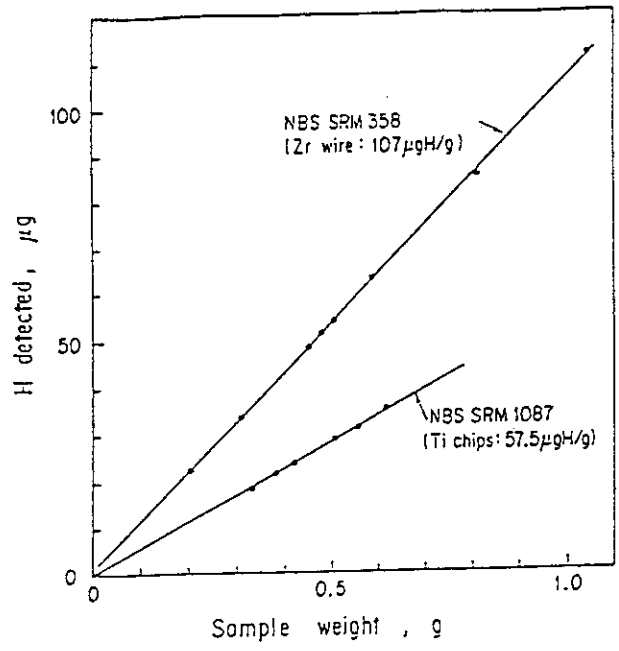

Fig. 1 Analyzed amount of H dependent on the weighed samples of SRMs 358 and 1087

A summary of hydrogen results on CRMs is shown in Table 1. The results are in good agreement with the certified values for NIST samples and tentative values for JAERI samples, but higher than the certified value for BCR CRM318. In an attempt to trace the cause of the high result for BCR318, some of CRMs were etched with a mixture of concentrated nitric and hydrofluoric acids before analysis. Effect of the etching on the hydrogen result is significant for BCR CRM318: the result obtained for the etched sample is in agreement with the certified value; while the effect is insignificant for NIST SRM352b and JAERI Z20 (Table 2). The hydrogen concentration of the etched part (10% in weight) of BCR CRM318 is estimated to be about 45 ug/g: about three times as high as the average concentration. We also applied the inert-gas fusion technique to BCR CRM318, but obtained no significant difference between the results obtained for the as-received and the etched ones. We assume that there might exist hydrogen, which could not be extracted as hydrogen molecules by the extraction methods, in the vicinity of the sample surface. Because the extraction methods detect only hydrogen gas evolved, while the IDM detects all of the hydrogen which can dilute deuterium concentration.

Table 1. Determination of hydrogen in CRMs

Sample	Hydrogen (μg/g) Certified	Found±1s (%RSD)		n
NIST SRM				
352b,Ti	46.9±0.8	47.9±0.4	(2)	6
1086,Ti	116 ±3	114 ±1.1	(1)	4
1087,Ti	57.5±2.5	56.0±0.9	(2)	7
352c,Ti	49.0±0.9	50.3±1.4	(3)	11
357,Zr	19 ±3	20.0±0.9	(5)	6
358,Zr	107 ±3	107 ±1.8	(2)	8
BCR CRM				
318,Ti	12.2±0.8	17.5±0.4	(2)	6
JAERI				
Z21,Zr	(4.0 *)	4.0±0.2	(5)	5
Z10,Zry-2	(8.2±1.1)	9.3±0.4	(4)	5
Z20,Zry-2	(5.3±1.1*)	9.2±0.6	(6)	7
Z23,Zry-4	(6.7±0.8*)	7.9±0.3	(4)	5
Z19,Hf	(6.0±0.7*)	6.4±0.2	(3)	7

Values in parentheses are not certified.
*Results obtained by fusion extraction.

Table 2. Effect of acid etching

(μgH/g)

Sample (Form)	As-received	Acid-etched	
BCR SRM318,Ti (disc,7 x1mm)	17.5 ± 0.5 (n=6)	14.5 ± 0.8	(n=4)
NIST SRM352b,Ti (platelet,3x3x1mm)	48.0 ± 1.3 (n=3)	47.9 ± 0.4	(n=3)
JAERI-Z20,Zry-2 (bar, 6x6x50mm*)	9.2 ± 0.7 (n=3)	8.5 (0.5)	(n=2)

* Sample was cut in 0.3 - 0.5 g pieces before analysis.

References

1) K. Watanabe, M. Ouchi, Bunseki Kagaku, 34 (1985) 677.

2) K. Watanabe, J. Nucl. Mat., 136 (1985) 1.

3) K. Watanabe, M. Ouchi, K. Gunji, Frezenius Z. Anal. Chem., 323 (1986) 225.

Publication List

[1] K. Watanabe, M. Ouchi, K. Gunji, "Determination of hydrogen in metals and alloys by isotope-equilibration mass spectrometry", Proc. of the 38th ASMS Conf. on Mass Spectrometry and Allied Topics, p. 69 (1990).

2.2 High Purity Graphite RMs : JAERI-G5 and G6

2.2.1 Preparation

The high purity graphite is a very useful material in the field of nuclear reactor technology. JAERI is constructing High Temperature Engineering Test Reactor (HTTR) at the Oarai Research Establishment in which a variety of high purity graphite is used in large amounts as a moderator and replaceable and fixed reflectors. Knowledge of the content of trace element in these materials is essential to evaluate their characteristics before and after the irradiation.

Accordingly, we have been preparing reference materials (RMs) necessary to establish accurate analytical methods for the pure graphite. These RMs consist of two kinds of graphite powdered, one is a purified, JAERI-G5 (ash content <10 ppm), the other is an unrefined, JAERI-G6 (ash content ca. 200 ppm). The raw material (PD-11) was specially prepared at Sakuragawa Works, Hitachi Chemical Co., Ltd. Physical properties of PD-11 are shown in Table 1, and the contents of metallic impurities are summarized in Table 2. The procedure for the preparation of G5 and G6 are shown in Fig. 1. The preparation of these RMs started at 1988 and the issuance will be authorized in 1992.

Table 1 Physical property of graphite(PD-11)

Bulk density, g/cm ^{3}	1.76
Electrical resistivity, μohm-cm	1060
Thermal conductivity, W/m℃	125
Flexural strength, kg/cm ^{2}	430
Young's modulus, kg/mm ^{2}	850
Hardness, Shore	48
Lattice(002), Å	6.735
Isotropic factor	1.30

Table 2 Metallic impurities in graphite(PD-11)

Total ash	200ppm	Molybdenum	0.7ppm
Aluminium	4	Nickel	0.3
Boron	2	Strontium	0.2
Calcium	32	Titanium	15
Iron	13	Vanadium	3

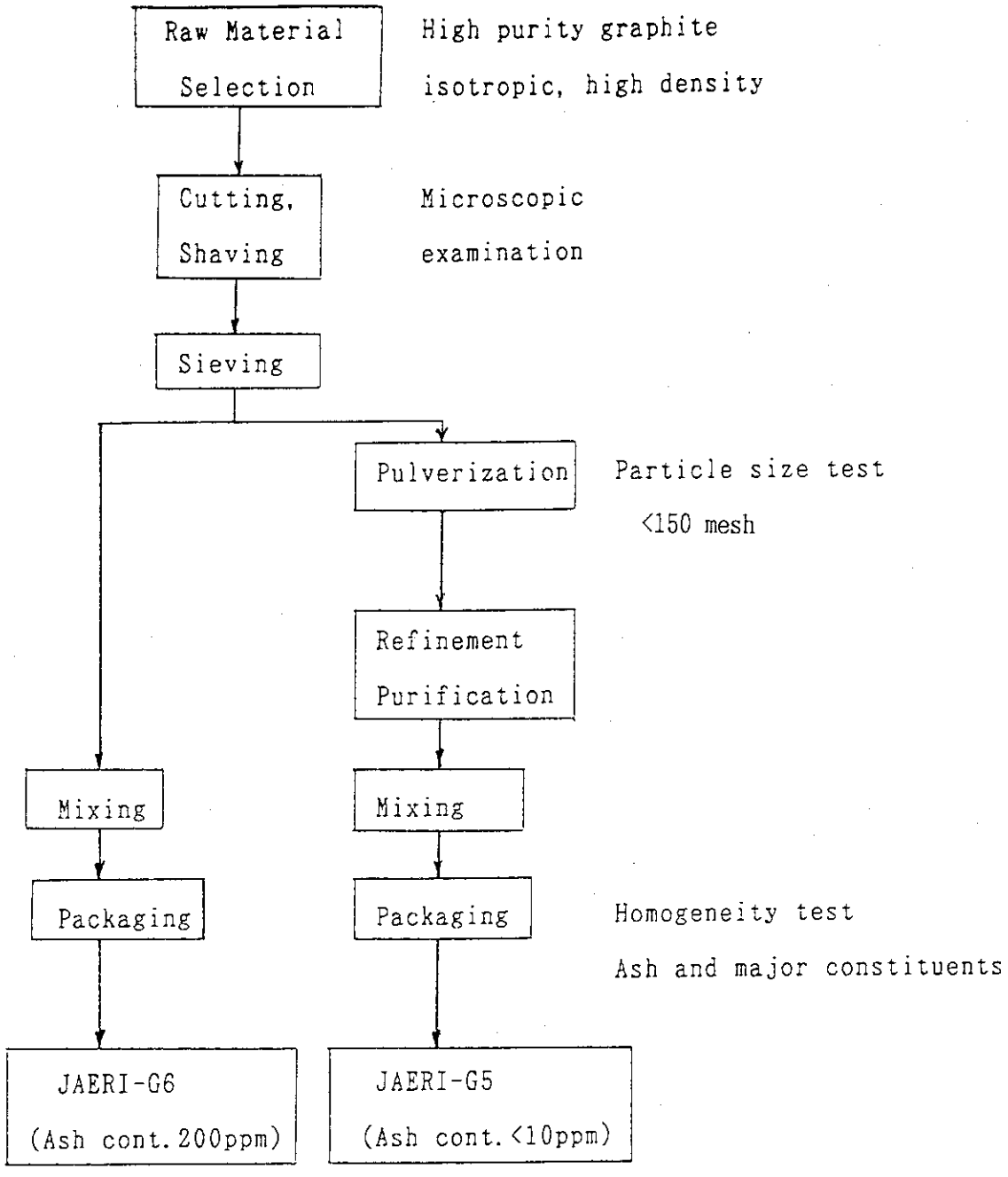

Fig. 1 Procedure for the Preparation of JAERI-G5 and G6

2.2.2 Studies on the determination of metallic impurities

An acid extraction technique in a sealed PTFE (polytetrafluoroethylene) vessel was studied to develop a simple method for determining the metallic impurities in the high purity graphite reference materials using inductively coupled plasma emission spectrometry (ICP-AES). The results are compared with those obtained by analyzing ashed graphite samples prepared by a low temperature ashing in an oxygen-plasma asher or a high temperature ashing in an electric muffle furnace. It was found that most of major metallic impurities (Al, Ca, Fe, Mo, Ni, Ti, V) except strontium were extracted quantitatively into a mixture of hydrochloric and nitric acids by heating the graphite sample in the sealed PTFE vessel at 200°C overnight. Table 1 summarizes the results for the graphite reference materials; JAERI G3, G5 and G6. The results obtained by the acid extraction methods are in good agreement with those obtained by the dry-ashing techniques. The results suggest that most of impurity elements exist between graphitic layers of grain boundaries as extractable chemical forms.

When the graphite sample was extracted in an open-beaker with the acid mixture at its boiling temperature or in the sealed PTFE vessel below 150°C, 5~10% low results were obtained in comparison with those obtained by the acid extraction using the sealed PTFE vessel at 200°C. The results for JAERI G3 are shown in Table 2, together with those obtained by a wet ashing method[1]. Although the open-beaker extraction method yields low results, it is useful for a semiquantitative determination of impurities in graphite because of its simplicity.

Reference

1) H. Hashitani, H.Yoshida,T.Adachi,K.Izawa,Bunsekikagaku, 35(1986)911.

Table 1 Determination of metallic impurities in the graphite reference materials

(μg/g)

Element	SAMPLE JAERI G3			JAERI G5		JAERI G6		
	Dry ashing	Acid extraction	Mean*)	Dry ashing	Mean*)	Dry ashing	Acid extraction	Mean*)
Al	1.3, 1.0	1.4, 1.4	1.0±0.2	0.07, 0.07	0.1 ±0,04	2.2*, 2.3*		2.1 ±0.4
Ca	217, 217	210, 212	208 ±9	0.1, 0.005	0.18±0.17	38.6, 39.7	34.3, 34.5	35.9 ±1.8
Cr			1.4±0.4		0.01	0.14*, 0.17*		0.25±0.13
Cu	0.4, 0.5	0.3, 0.3	0.3±0.2	N.D. N.D.	0.02	0.39*, 0.38*		0.52±0.33
Fe	44.7, 44.3	44.0, 44.3	41 ±3.2	0.11, 0.09	0.20±0.11	12.5, 13.8	11.5, 11.9	11.0 ±1.2
Mg	0.2, 0.2	0.3, 0.2	0.2±0.05	0.007, 0.005	0.08±0.04			
Mn	0.4, 0.3	0.08, 0.07	0.2±0.2	N.D. N.D.		0.03*, 0.03*		0.03±0.0
Mo	3.1, 3.1	2.9, 3.0	4 ±1	N.D. N.D.		0.37*, 0.45*		0.35±0.05
Ni	29.4, 29.7	28.1, 28.6	28 ±1.3	N.D. N.D.		0.33*, 0.34*		0.26±0.07
Sr	4.6, 4.7	3.6, 3.7	4.3±0.4	0.0001, 0.0001		0.57, 0.58	0.30 0.34	0.57±0.05
Ti	5.5, 5.4	5.2, 5.4	5.3±0.2	N.D. N.D.		19.1, 19.8	18.2, 19.2	17.0 ±3.4
V	42.2, 44.0	44.9, 45.2	42 ±3	N.D. N.D.		3.3, 3.4	3.0, 3.2	2.9 ±0.3

*) Mean value obtained by cooperative analysis at the Sub-Committee on the Analysis of High Purity Graphite Materials as of Feb. 25, 1991.
N.D.: not detected

Table 2 Determination of impurities in JAERI G3 by the extraction methods and the ashing methods

(μg/g)

Method	Ca	Fe	Ni	Sr	Ti	V
Open beaker extraction						
HCl-HNO_3/1hr.	187, 186	42.4, 41.5	28.5, 28.3	1.3, 1.3	4.8, 4.7	41.1, 41.7
HCl-HNO_3/9hrs.	197, 197	43.1, 43.1	28.3, 28.1	1.4, 1.5	4.7, 4.8	41.9, 44.1
Sealed vessel extraction						
HCl-HNO_3/100℃, 1night	193, 192	42.1, 41.3	28.5, 28.4	1.4, 1.4	4.9, 4.9	42.7, 42.6
HCl-HNO_3/150℃, 1night	206, 199	42.7, 42.4	29.1, 29.1	1.9, 1.9	5.3, 5.2	44.0, 43.8
HCl-HNO_3/200℃, 1night*1	206±2.2	44.4±0.5	29.6±0.6	3.5±0.1	5.6±0.1	45.0±0.4
Dry ashing						
Ashed at 800～950℃*2	215±1.0	44.8±0.7	30.1±0.2	4.6±0.0	5.6±0.0	41.1±1.7
Wet ashing[1)]	213	43.4	29.8	--	6.8	43.8

*1 mean of 6 determinations

*2 mean of 5 determinations

3. Solution Chemistry and Analytical Chemistry of Actinide Elements

T. Adachi, H. Aoyagi, K. Gunji, Y. Kato, T. Kimura, N. Kohno, Y. Meguro, H. Muto, Y. Nakahara, S. Nakayama[1)] M. Ohnuki, Y. Sasaki, T. Sonobe, T. Suzuki, H. Takeishi, S. Uno, Z. Yoshida, W. Cheng[2)], S. Kihara[3)], Y. Li[4)] and C.M. Wai[5)]

[1] Dept. of Environmental Safety Research, JAERI,
[2] Anal. Chem. Lab., Institute of Atomic Energy of China,
[3] Institute for Chemical Research, Kyoto University,
[4] Dept. of Environmental Engineering, Tsinghua Univ., Beijing,
[5] Dept. of Chemistry, Univ. of Idaho, USA,

Actinide elements in the 5f series show chemical behavior[1-3)] that is intermediate between that of 4f and d-transition elements, e. g., the variability in oxidation states from III to VI of the lighter elements such as U, Np and Pu reflects a closer resemblance to d-transition elements, whereas transplutonium are more similar to lanthanide elements in the 4f series. Fundamental data on the solution chemistry as well as separation and anaytical methods for actinide ions are indispensable in the field of nuclear technology. Following studies have been performed ; 1) electroanalytical study to elucidate the redox behavior of U, Np and Pu ions, 2) development of new separation methods of actinide and lanthanide by solvent extraction, and 3) speciation of actinide ions in various solutions.

3.1 Electroanalytical Chemistry of U, Np, and Pu

3.1.1 Flow-coulometry of Uranium, Neptunium, and Plutonium Ions with Multi-step Column Electrodes

The overall feature of the oxidation-reduction behavior of U, Np and Pu ions in acidic aqueous media has been elucidated on the basis of results on the electrolysis at a column electrode.[4-6)] This electrode shows the following advantages : 1) coulometric electrolysis can be attained rapidly, 2) quantitative electrolysis proceeds with small overpotential even if the electrode reaction is irreversible, and 3) the electrolysis is carried out in a flow-system. In this study a detailed discussion was made, in particuler, on the irreversible electrode reduction of AnO_2^+ and the oxidation of An^{4+} (An : U, Np or Pu). Based on the above fundamental results, rapid

methods were developed for the coulometric determination of Pu, and for the speciation of Np or U and Pu in mixtures. The configuration of a column electrode is illustrated in Fig. 1. The working electrode was a bundle of ca. 2.5×10^5 glassy carbon fibers(Tokai Carbon GC-20, 11.5 μm in diameter) packed in a porous Vycor glass cylinder (Corning, 8 i.d., 10 o.d., and 50 mm long) which worked as an electrolytic diaphragm. An electrolysis was performed with the aid of a Pt counter electrode and a Ag-AgCl/1M LiCl reference electrode(SSE). The preparation of ions at desired oxidation states was made with twin- or triple-column electrodes in series via a neoprene seal. A current-potential curve by flow-coulometry, called a coulopotentiogram hereafter, was recorded by scanning the applied potential, while the deaerated solution was driven at a constant flow-rate through the column electrode by a pump. Coulopotentiograms for the redox of 10^{-3}M U, Np and Pu ions in (A)perchloric, (B)nitric and (C)sulfuric acid solutions are summarized in Fig. 2. The numbers on the ordinate in the figures indicate n values calculated from the current measured using eq. (1),

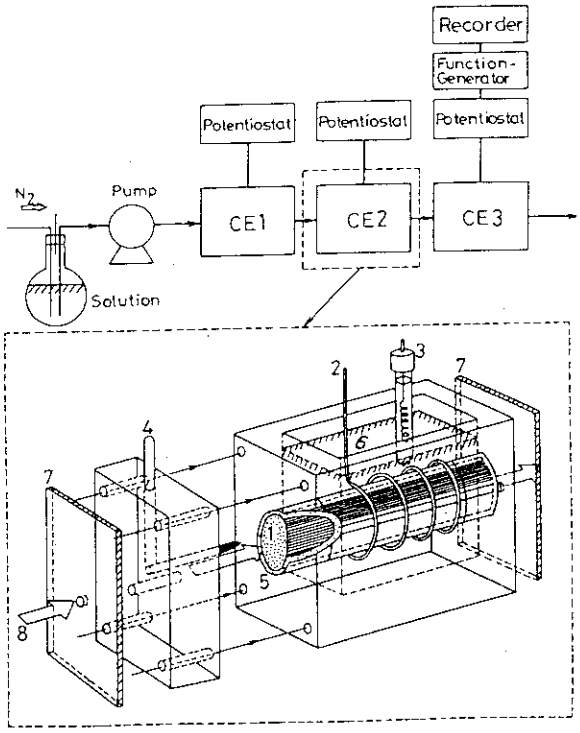

Fig. 1 Column electrode and electrolysis system
1: working electrode; 2: Pt counter electrode; 3: SSE reference electrode; 4: contact GC rod for working electrode; 5: electrolytic diaphragm; 6: outer solution; 7: Neoprene seal; 8: sample solution

$$I = nFCf \qquad (1)$$

where, I, n, F, C and f are the current(ampere) flowing through the column electrode, the number of electrons, the Faraday constant, the concentration of the ions(M), and the fow-rate of the solution(L/sec), respectively. Two-electron reduction and oxidation between UO_2^{2+} and U(IV) occur at the column electrode as shown by curves 1(U) and 2(U) in Fig. 2. The $E_{1/2}$ for the reduction of UO_2^{2+} to U(IV) is almost independent of f or the hydrogen-ion concentration, C_{H^+}, of the solution which implies that the reduction of UO_2^{2+} to UO_2^{+} is the rate-determining step, which is followed by rapid disproportionation of UO_2^{+} into U^{4+} and UO_2^{2+}. The rate of two electron oxidation of U(IV) to UO_2^{2+} is controlled by the slow oxidation step which involves the formation of uranium-oxygen bond, and therefore, the $E_{1/2}$ for the oxidation of U^{4+} depends on f and C_{H^+}. Since the formation of

sulfate complex is much favored with U^{4+} than with UO_2^+, the oxidation reaction is affected by sulfate ion as well. General aspect of the redox behavior of Np and Pu ions is similar to each other. One-electron wave for the reduction of MO_2^{2+}(M : Np or Pu) to MO_2^+ and two-electron wave for the further reduction of MO_2^+ to M(III) are observed in the coulopotentiograms as given by curves 1(Np) and 1(Pu) in Fig. 2. The redox process, MO_2^{2+}/MO_2^+, is reversible. Curve 4(Np) and 3(Np) or 4(Pu) and 3(Pu) indicate that the redox between M^{4+} and M^{3+} is also reversible and diffusion-controlled. $E_{1/2}$ for these reversible processes shift to more negative in the presence of such an anion as sulfate ion, that complexes both MO_2^{2+} and M^{4+}. Two-electron reduction of MO_2^+ into M^{3+} is influenced by f and C_{H^+}. If the f is sufficiently small, the quantitative electrolysis of MO_2^+ to M^{3+} can be made with considerably small over potential, because the chromatographic electrolysis occurs during the stay of the solution in the column electrode. The irreversible reduction of MO_2^+ is promoted by the presence of such complexing agent as sulfate or phosphate ions, which is also advantageous to attain the quantitative electrolysis of MO_2^+ to M^{3+}. It should be stressed that two-step reduction waves due to M(V)→M(IV)→M(III) can be observed in the coulopotentiograms for the reduction of M(V) in the acid solution contain-

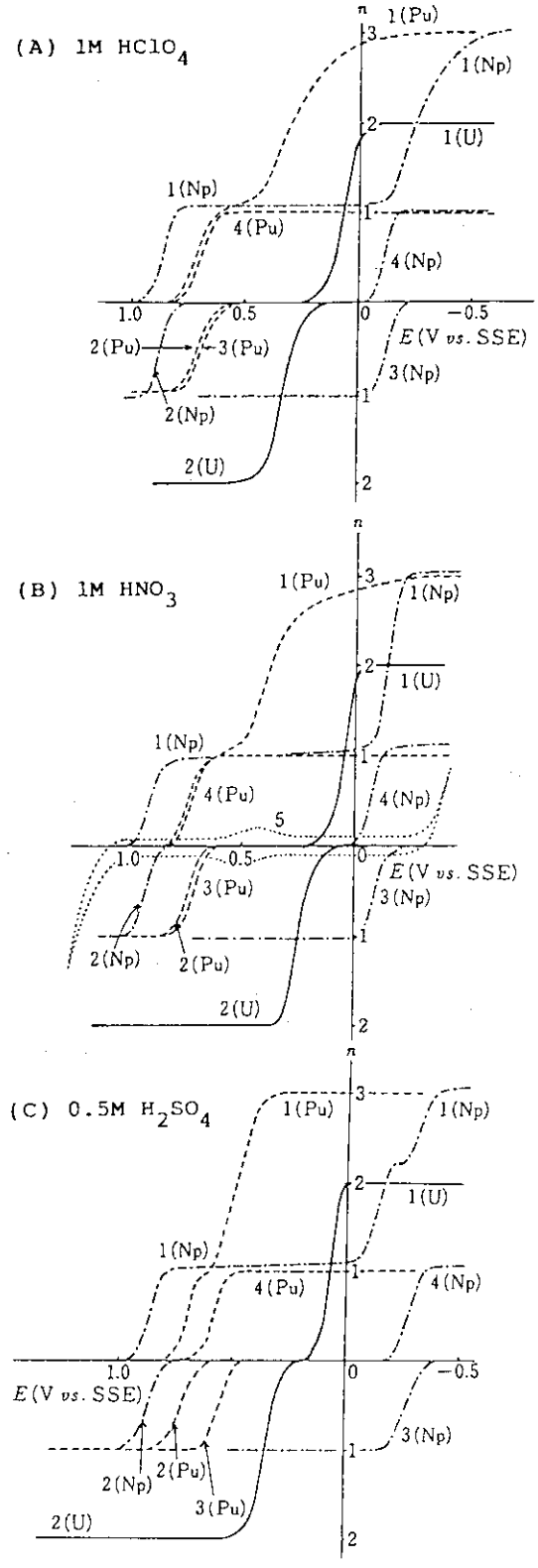

Fig. 2. Coulopotentiograms for U, Np and Pu. Scan rate: 0.2 mV/sec, Flow-rate: 1.5 ml/min.
1: reduction of UO_2^{2+}, NpO_2^{2+} or PuO_2^{2+}, 2: oxidation of U^{4+}, NpO_2^+ or PuO_2^+, 3: oxidation of Np^{3+} or Pu^{3+}, 4: reduction of Np^{4+} or Pu^{4+}

ing a complex-forming anion, e. g., for the reduction of NpO_2^+ in sulfuric acid solution, (cf. curve 1(Np)), in Fig. 2(C) or for the reduction of PuO_2^+ in phosphate media.

Based on the redox behavior of U, Np and Pu ions as described above, new procedure for the determination or the speciation of these ions has been developed. For the determination of Np, U and Pu in nitric acid solution, we recommend the procedure of the three series (A-C) of measurements as illustrated in Fig. 3. Each electrolytic system is composed of a twin column

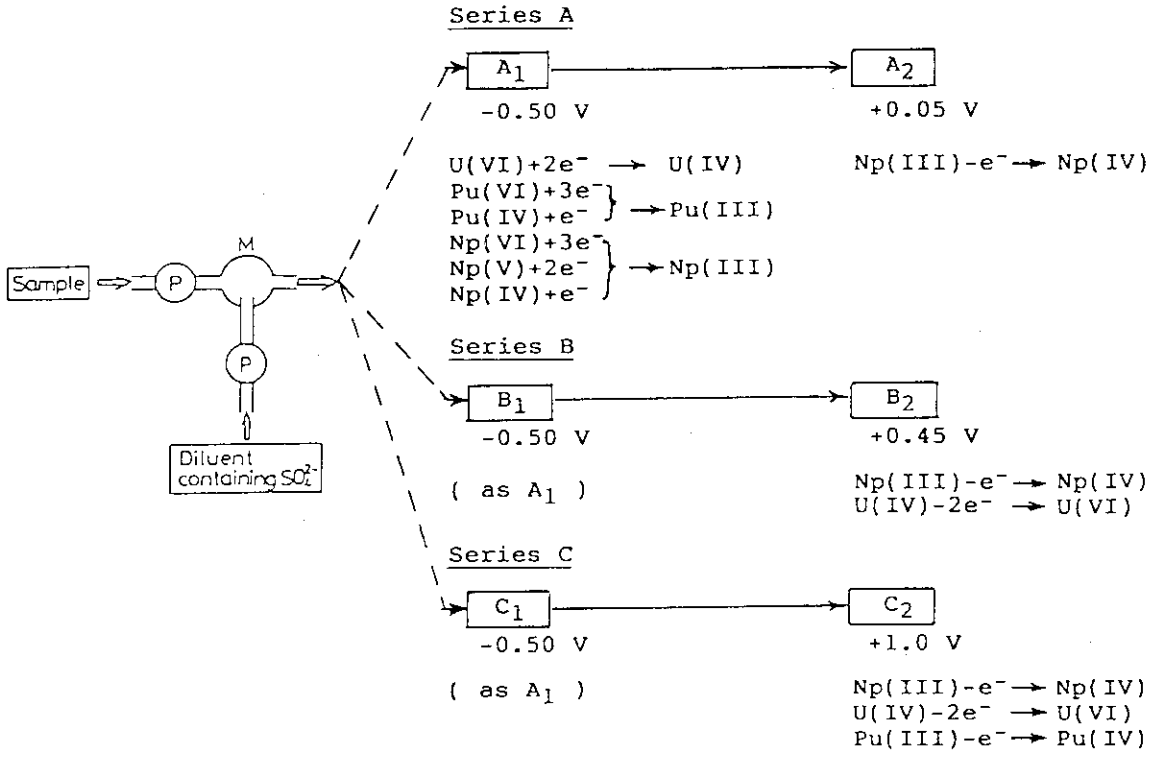

Fig. 3. Schematic diagrams of column electrode electrolysis system for the determination of U, Np and Pu ions in nitric acid solution.
M : mixing chamber, P : pump.

electrodes, a mixing chamber and two plunger-type pumps. The mixing chamber is necessary to mix the sample solution with diluent containing sulfate ion. As stated earlier sulfate media is preferable for the quantitative reduction of NpO_2^{2+} or NpO_2^+ to Np^{3+} and of PuO_2^{2+} to Pu^{3+} efficiently at more positive potential region. Immediately after the mixing, the solution is introduced into the electrolysis system. The potentials applied to the electrodes are indicated in Fig. 3 together with the electrode reactions expected at each column electrode. The first column electrodes, A_1, B_1 and C_1 at -0.50 V in each series are employed for the preparation of the oxidation states of ions, i. e., all Np, U and Pu species are converted into Np^{3+}, U^{4+} and Pu^{3+}. The current $I(A_2)$, $I(B_2)$ and $I(C_2)$ at the respective

electrodes are measured. Taking electrode reactions at each column electrode into account, current are correlated to the concentration C of ions in the sample solution using eqs.(2) to (4). Solving simultaneous eqs., we obtain the total concentration of Np, U and Pu.

$$C_{Np,total} = I(A_2)/Frf \quad (2)$$

$$C_{U,total} = \{I(B_2) - I(A_2)\}/2Frf \quad (3)$$

$$C_{Pu,total} = \{I(C_2) - I(B_2)\}/Frf \quad (4)$$

Here, r is the diluting ratio of the sample solution at the mixing chamber. The speciation of NpO_2^{2+}, NpO_2^{+} and Np^{4+} in nitric acid solution is possible on the basis of the identical principle using a triple-column electrodes system. In this procedure the presence of Np^{3+} in the sample is neglected, since Np^{3+} is fairly unstable and easily oxidized to Np^{4+} in nitric acid solution. The concentration of Np ions at different oxidation states can be calculated from the currents flowing through the column electrodes, A_1 at +1.20 V, A_2 at +0.50 V and A_3 at -0.35 V using eqs.(5) to (7).

$$C_{Np(V)} = I(A_1)/Frf \quad (5)$$

$$C_{Np(VI)} = \{-I(A_2) + I(A_1)\}/Frf \quad (6)$$

$$C_{Np(IV)} = \{-I(A_3) + 2I(A_2)\}/Frf \quad (7)$$

The detection limits in the determination or the speciation of U, Np and Pu ions by these methods were confirmed to be 10^{-6} to 10^{-5} M.

3.1.2 Electrode Processes of Plutonium Ions in Phosphate Media

Phosphate media are expected to be promising for voltammetric determination or differentiation of plutonium ions of various oxidation states, since PuO_2^{2+} and Pu^{4+} form stable and soluble complexes with $H_2PO_4^{-}$ and HPO_4^{2-} in acidic media[2-3] and the complex formation results in significant shift of redox potentials. The fundamental studies on the voltammetric behavior of plutonium ions in phosphate media are very few. In the present work, the electrolytic behavior of plutonium ions in a phosphate media has been studied by flow-coulometry with column electrodes and voltammetry with a GC disk electrode. The coulopotentiograms illustrated in Fig. 4 was obtained employing 1.4 M H_3PO_4 + 1 M HNO_3 medium. The reduction of PuO_2^{2+} (Coulopotentiogram 1) gave three-step waves with n=1.10±0.05, 1.12±0.07, and 0.75±0.05 for the 1st, 2nd, and 3rd wave respectively, and three electron reduction of PuO_2^{2+} to Pu(III) was attained even at +0.35 V, which was much more positive than the value in the phosphate-free media. Half wave potentials, $E_{1/2}(c)$s, for the 1st and the 3rd waves did not depend on C_{H^+},

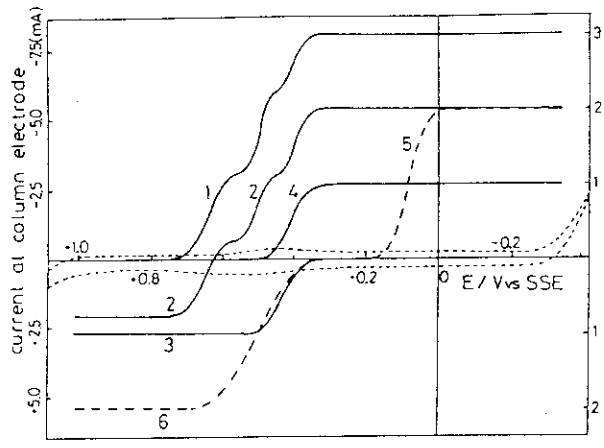

Fig. 4. Coulopotentiograms for 1.12×10^{-3}M Plutonium ions in 1.4M H_3PO_4 + 1M HNO_3. Plutonium ions : 1PuO_2^{2+}; 2PuO_2^{+}; 3Pu^{3+}; 4Pu^{4+}; 5UO_2^{2+}; 6U^{4+}

whereas $E_{1/2}(c)$ for the 2nd wave shift into a more positive direction with the increase of C_{H^+}. Coulopotentiogram 3 for Pu(III) was recorded with the twin-column electrodes system with the 1st column at +0.20 V. The oxidation wave with n=1.0 was identical to that recorded with the Pu^{3+}-solution which had been prepared by adding phosphoric acid to Pu^{3+}-nitrate solution. In addition the $E_{1/2}(c)$ of the wave was independent on C_{H^+}. Hence, the wave was due to the oxidation of Pu^{3+} to Pu^{4+}.

Coulopotentiogram 4 for Pu^{4+} was recorded by the triple-electrode system with the 1st column at +0.20 V and the 2nd column at +0.80 V. The observed one-electron reduction wave, $E_{1/2}(c)$ of which was not affected by C_{H^+}, was identical to $E_{1/2}(c)$ of the oxidation wave in coulopotentiogram 3, indicating that the redox process, Pu^{4+}/Pu^{3+}, is reversible. Since $E_{1/2}(c)$ of the 1st wave in coulopotentiogram 1 was independent of C_{H^+}, and since $E_{1/2}(c)$ of coulopotentiogram 4 was identical to $E_{1/2}(c)$ of the 3rd wave in coulopotentiogram 1, the step-wise reduction, $PuO_2^{2+} \rightarrow PuO_2^{+} \rightarrow Pu^{4+} \rightarrow Pu^{3+}$, is responsible for the three-step waves in coulopotentiogram 1. The disproportionation of PuO_2^{+} and/or Pu^{4+} may be the reason why the n values of the three waves were not precisely 1.0. The redox process, PuO_2^{2+}/PuO_2^{+} is reversible even in the phosphate media, and $E_{1/2}(c)$ of the oxidation wave with n=0.7 of PuO_2^{+} in coulopotentiogram 2 is identical to that of the 1st wave of coulopotentiogram 1. Voltammograms for PuO_2^{2+}, Pu^{4+} or Pu^{3+} at a GC disc electrode in 1.4 M H_3PO_4 + 1M HNO_3 medium are illustrated in Fig. 5, and their characteristics are summarized in Table 1. Dependences of E_p and I_p on v, and of $E_{1/2}(v)$ and $I_l(v)$ on w, and the slope of log-analysis, support the assumption that redox processes, PuO_2^{2+}/PuO_2^{+} and Pu^{4+}/Pu^{3+}, are reversible in the phosphate media. The 2nd peak current of voltammogram 1 in Fig. 5, which stands for the reduction of PuO_2^{2+} at the stationary electrode, was about twice the 1st peak current, and hence, the 2nd peak is assigned to the reduction of PuO_2^{+} to Pu(III). The well-defined 2nd peak in the voltammogram lies at a more positive potential than that of the 2nd wave observed in phosphate free media. This suggests that the presence

Table 1. Characteristics of the voltammograms of plutonium ions in 1.4M H_3PO_4 + 1M HNO_3.

Plutonium ion	v	Stationary disc electrode				ω	Rotating disc electrode								
		1st peak		2nd peak			1st wave			2nd wave			3rd wave		
		E_p	I_p	E_p	I_p		$E_{1/2}(v)$	$I_\ell(v)$	Slope of log-analysis	$E_{1/2}(v)$	$I_\ell(v)$	Slope of log-analysis	$E_{1/2}(v)$	$I_\ell(v)$	Slope of log-analysis
PuO_2^{+}	2	+0.61	7.2	+0.43	17.8	250	+0.65	33.2	59	+0.36	47.4	64	−0.08	20.6	80
	5	+0.62	11.0	+0.41	30.0	500	+0.65	47.0	61	+0.37	51.4	74	−0.01	35.8	80
	10	+0.61	15.8	+0.39	48.1	1000	+0.64	63.2	66	+0.36	53.8	82	−0.01	53.8	81
						1500	+0.65	77.5	60	+0.39	62.0	90	+0.03	65.8	96
Pu^{4+}	2	+0.39	5.4			250	+0.42	25.3	60						
	5	+0.38	9.4	none		500	+0.42	35.8	61	none					
	10	+0.39	13.0			1000	+0.42	56.9	61						
						1500	+0.42	65.8	60						
Pu^{3+}	2	+0.45	6.9			250	+0.41	36.3	60						
	5	+0.45	10.5	none		500	+0.42	49.2	57	none					
	10	+0.45	15.8			1000	+0.42	69.6	58						
						1500	+0.42	89.1	61						

v = potential scan rate (mV s^{-1})
E_p = peak potential at the stationary disc electrode (versus SSE)
I_p = peak current at the stationary disc electrode (μA)
ω = rotation rate of the rotating disc electrode (rpm)
$E_{1/2}(v)$ = half-wave potential at the rotating disc electrode (V versus SSE)
$I_\ell(v)$ = limiting current at the rotating disc electrode (μA)
Slope of log-analysis = slope of log $(I_\ell - I)/I$ versus E plot (mV)

of phosphoric acid enhances the rate of the reduction of PuO_2^{+} to Pu(III), though the reduction is still irreversible. The most remarkable feature of the redox behavior of plutonium ions in phosphate media was observed in the reduction of PuO_2^{2+} at the rotating disc electrode, as shown in voltammogram 4 in Fig. 5, in which three waves appear. Since $I_1(v)$s for the three waves are almost identical to each other at of w 1500 rpm, three-step reductions are due to $PuO_2^{2+} \rightarrow PuO_2^{+} \rightarrow Pu(IV) \rightarrow Pu(III)$. Slopes of log analyses for the 2nd and 3rd waves were 64 to 90 mV and 80 to 96 mV, respectively, and $I_1(v)$s for these waves were not proportional to $w^{1/2}$, which indicates that both waves are different from those of a reversible process controlled by diffusion. The ratio of $I_1(v)$ of the 2nd wave to that of the 3rd wave increases with lowering w. $E_{1/2}(v)$s for the 2nd and 3rd waves depend strongly on the composition of the media. It is presumed that the electrode processes for the 2nd and the 3rd waves may involve two H^{+}, since $E_{1/2}(v)$s for the 2nd and the 3rd

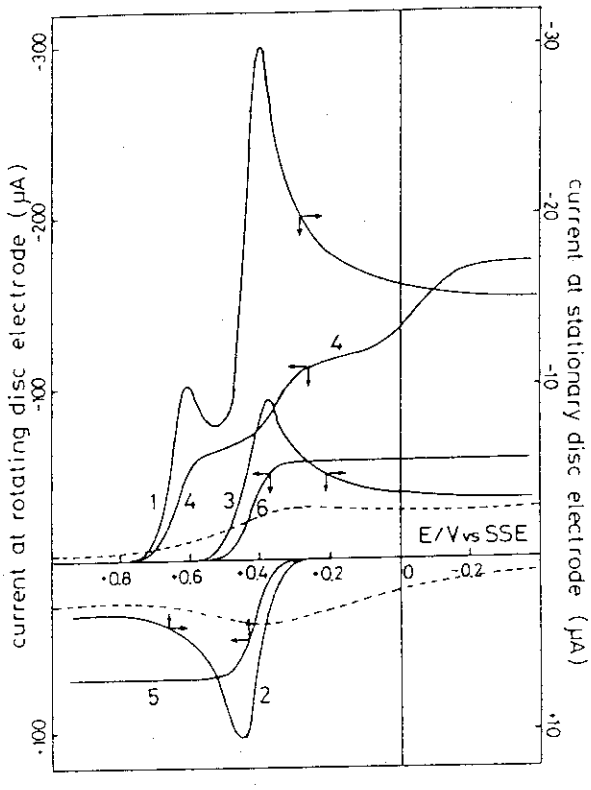

Fig. 5. Voltammograms for 1.12×10^{-3}M Pu ions in 1.4 M H_3PO_4 + 1 M HNO_3. Plutonium ions : 1,4 PuO_2^{2+} ; 2,5 Pu^{3+} ; 3,6 Pu^{4+}.

waves shift by 220 mV and 260 mV to more negative direction with decreasing a_{H^+} by one order, and the slope of log-analyses is 90 to 96 mV. This indiates that the species participating in the reduction of PuO_2^+ in the phoshate media may differ from those in the phosphate-free media. It is noteworthy that the characteristics of the 3rd wave due to the reduction of Pu(IV) to Pu(III) are completely different from the reduction wave of Pu^{4+} to Pu^{3+} as given by curve 6 in Fig. 5. The differences lead to the assumption that the intermediate Pu(IV)-species, taking part in the successive reduction of PuO_2^{2+}, may differ from Pu^{4+}. The presence of phosphoric acid promotes the reduction of PuO_2^+ to Pu^{3+}, which may make possible the voltammetric and coulometric determination of plutonium, avoiding the interference from the electrode reaction of uranium and/or hydrogen evolution. For example, coulopotentiograms for the redox between UO_2^{2+} and U^{4+} in 1.4 M H_3PO_4 + 1 M HNO_3 are added to Fig. 4 as curves 5 and 6. From the comparison of the coulopotentiograms for uranium with those for plutonium, it is obvious that all plutonium species are completely reduced to Pu^{3+} at +0.20 to +0.30 V, where neither the reduction nor the oxidation of uranium takes place (we denoted the potential range as $E_{(\text{no redox U})}$. The presence of a wide $E_{(\text{no redox U})}$ indicates that one can determine plutonium and uranium dissolved in 1.4 M H_3PO_4 + 1 M HNO_3 using the twin-column electrode system, where 1st column is set at +0.25 V for the determination of PuO_2^{2+} and/or Pu^{4+} and the 2nd column at -0.10 V for the determination of UO_2^{2+}.

References

1) J.J. Katz, G.T. Seaborg, L.R. Morss(Ed.),"The Chemistry of the Actinide Elements", 2nd Ed., Chap. 15 (Chapman and Hall, New York,1986)
2) J.M. Cleveland , "The Chemistry of Plutonium", (Gordon and Breach, New York,1970) p.92-140.
3) C. Keller, "The Chemistry of the Transuranium Elements",(Verlag Chemie, Weinheim,1971) p.409.
4) H. Aoyagi, Z. Yoshida, S. Kihara, Anal. Chem., 59(1987)400.
5) Z. Yoshida, H. Aoyagi, S. Kihara, Fresenius J. Anal. Chem., 340(1991)403.
6) S. Kihara, Z. Yoshida, H. Aoyagi, Bunseki Kagaku, 40(1991)309.

Publication List

[1] Z.Yoshida, H. Aoyagi, Y. Kato, Y. Li, S. Kihara,"Redox, Disproportionation and Complex Formation Reactions of Neptunium Ions," in: Proc. The 3rd Intern. Symp. on Adv. Nucl. Energy Res.,(Mito, Ibaraki,1991) p.268.

[2] S. Kihara, Z. Yoshida, H.Aoyagi, "Analytical Chemical Study on Actinoids Ions by Column Electrolysis", Bunseki Kagaku, 40(1991)309. (in Japanese)

[3] Z.Yoshida, H. Aoyagi, S. Kihara, " Electrode Processes of Plutonium Ions in Phosphate Media", Fresenius J. Anal. Chem., 340(1991)403.

[4] Z. Yoshida, H. Aoyagi, Y. Sasaki, S. Kihara, "Flow-coulometry of Uranium, Neptunium and Plutonium Ions with Multi-step Column Electrodes" in: Proc. Intern. Cong. on Analytical Sciences 1991, Makuhari, in press.

[5] Z. Yoshida, H. Aoyagi, S. Kihara, "Stripping Coulometry of Trace Amount of Uranium", in:Proc. Intern. Trace Analysis Symp. '90, 439(1990).

3.2 Solvent Extraction of Actinides and Lanthanides using Crown Ethers

3.2.1 Solvent Extraction of Americium(III), Curium(III), and Europium(III) with 2-Thenoyltrifluoroacetone and Crown Ethers

Since trivalent lanthanide and actinide elements which are contained in spent fuel show almost identical chemical properties, mutual separation of these metal ions is quite difficult. The development of an efficient method for their partitioning is important subject in the field of nuclear technology. Solvent extraction is one of the most promising methods for the separation of metal ions, and synergistic extraction is useful for the separation of metal ions with high coordination numbers such as actinides and lanthanides. There have been developed various synergistic extraction systems, enhancement of selectivity is expected by employing such multidentate adduct as CEs. Although several studies have been carried out on the synergistic extraction of actinides and lanthanides with CEs[1,2], the systematic elucidation of the extraction mechanism, the solvent effect and the chemical form or the stability of extracted species have not yet been achieved. In the present study the extraction of Am(III), Cm(III), and Eu(III) were investigated using benzene(Bz), cyclohexane(Cy) and 1,2-dichloroethane(DCE) solution of HTTA and CEs, i.e., 15-crown-5(15C5), 18-crown-6 (18C6), dicyclohexano-18C6(DC18C6), dibenzo-18C6(DB18C6), dicyclohexano-24-crown-8(DC24C8) and dibenzo-24C8 (DB24C8).

The distribution ratios(D) of Am^{3+} were determined between Bz solution containing HTTA and CE and aqueous solution of pH 3.1 - 4.9. The results of log D were plotted against pH in Fig. 1 at C_{HTTA} = 0.01M and C_{CE} = 0.01M. Here C_{HTTA} and C_{CE} denote the initial concentration of HTTA and CE, respectively. The dotted line in Fig. 1 was for distribution(D_0) of Am^{3+} with HTTA in the absence of CE. The D of Am^{3+} with CE was larger than that without CE for all CEs examined, which indicates the synergistic effect. The plots gave a straight line with a slope of 2.7 for 15C5, 2.7 for 18C6, 2.6 for DC18C6, 2.8 for DB18C6, 2.8 for DC24C8 and 2.7 for DB24C8. The log D - log $[HTTA]_{org}$ plots gave straight lines with slopes, 2.8 for Am^{3+}/HTTA/18C6 and 3.1 for Am^{3+}/HTTA/DC24C8, and the log D - log $[CE]_{org}$ plots had linear portion with slopes, 1.0 for 15C5, 0.91 for 18C6, 0.89 for DC18C6, 1.0 for DB18C6, 0.88 for DC24C8, and 0.92 for DB24C8 in Am^{3+}/HTTA/CE extraction system. Here, $[HTTA]_{org}$ and $[CE]_{org}$ denote the concentrations of HTTA and CE in Bz. From these results, the extracted species was found to be $Am(TTA)_3(CE)$. The adduct formation constants($\beta_{s,1}$), defined by eq.(1), were calculated from eq.(2) and are summarized in Table 1.

$$Am(TTA)_{3org} + CE_{org} \underset{}{\overset{\beta_{s,1}}{\rightleftharpoons}} Am(TTA)_3(CE) \qquad (1)$$

$$\beta_{s,1} = (D - D_0)/D_0[CE]_{org} \qquad (2)$$

The strength of the adduct complex could not be explained alone the basicity of CE, as pointed out previously[1]. For example, $\beta_{s,1}$ for DC18C6 is smaller than that for 18C6, although DC18C6 with electron-donating cyclohexano- substituent is expected to form the adduct complex more favorably than 18C6. This implies the steric hindrance due to a large substituent in the adduct complex formation. The $\beta_{s,1}$ values for CEs with a DC- or DB-substituent and with a different number of ether groups show that the larger $\beta_{s,1}$ is obtained for CE with the more ether groups such as DC24C8 or DB24C8. Considering that an ionic diameter of Am^{3+} is between the cavities of 15C5 and 18C6, one sees that the size-fitting effect of CE may not play an important role in the formation of $Am(TTA)_3(CE)$.

Ds for the extraction of Am^{3+} were determined using Cy or DCE instead of Bz and plots of log D - pH obtained are given in Figs. 2 and 3 (C_{HTTA} = 0.01M, C_{CE} = 0.01M). The synergistic effect by CE can be

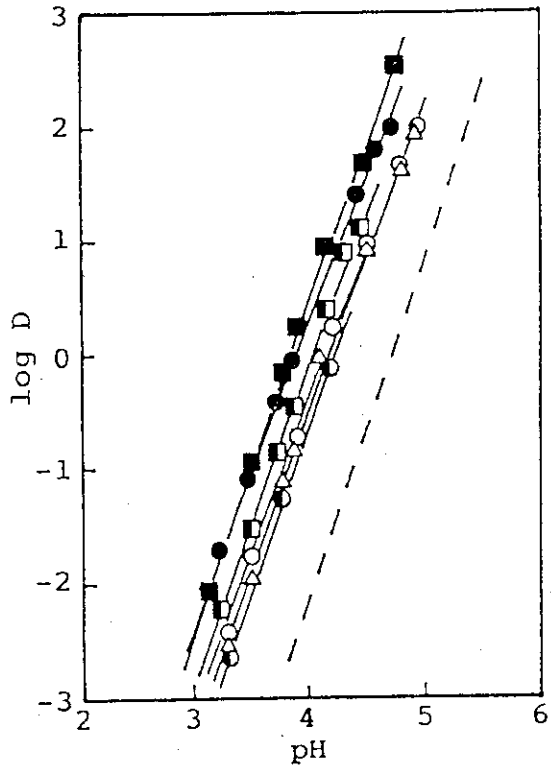

Fig. 1 Effect of pH on log D for Am^{3+} in Bz with 0.01M HTTA and 0.01M CEs.
(△)15C5; (○)18C6; (●)DC18C6; (◐)DB18C6; (■)DC24C8; (◧)DB24C8.

Table 1 The $\beta_{s,1}$ for synergistic extraction of Am^{3+} in Bz and Cy with HTTA and CEs between 0.1M $LiClO_4$ aqueous and organic solutions.

CE	log $\beta_{s,1}$	
	Bz	Cy
15C5	4.59±0.19	5.15±0.21
18C6	4.98±0.18	5.39±0.13
DC18C6	4.50±0.16	4.69±0.10
DB18C6	3.53±0.08	-
DC24C8	4.55±0.11	5.27±0.19
DB24C8	4.02±0.12	-

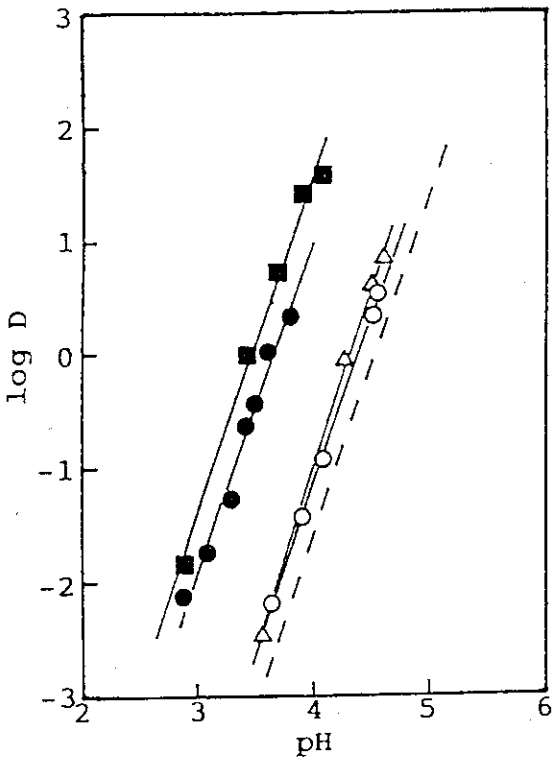

Fig. 2 Effect of pH on log D for Am^{3+} in Cy with 0.01M HTTA and 0.01M CEs.
(△)15C5; (○)18C6; (●)DC18C6; (■)DC24C8.

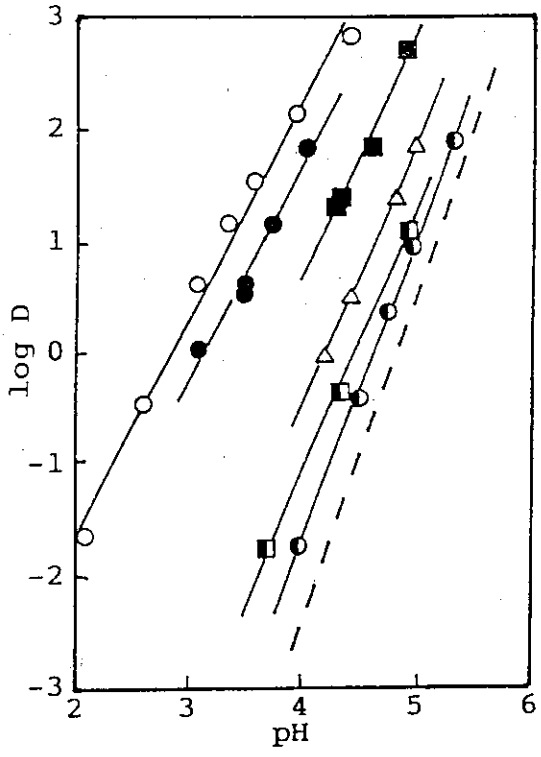

Fig. 3 Effect of pH on log D for Am^{3+} in DCE with 0.01M HTTA and 0.01M CEs.
(△)15C5; (○)18C6; (●)DC18C6; (◐)DB18C6; (■)DC24C8; (◧)DB24C8.

observed with Cy, and the extracted species was confirmed to be $Am(TTA)_3(CE)$. The adduct formation constants for four kinds of CEs were determined and added in Table 1. The $\beta_{s,1}$ value with the CE in Cy was larger than that with the respective CE in Bz, which agrees with a general concept that the adduct complex is liable to be formed in the solvent of less polarity.

The most remarkable feature of the extraction behavior with DCE having a comparatively high dielectric constant(Fig. 3) is that the slope of log D - pH plots are 2.0 for 18C6, 1.9 for DC18C6, 2.4 for 15C5, 2.3 for DC24C8 and 2.4 for DB24C8, instead of 3. The slope of log D - log $[HTTA]_{org}$ plot was 2.0, when extraction was carried out using DCE with 18C6(C_{HTTA} = 10^{-3} - 0.03M, C_{CE} = 0.01M, pH = 3.5). These suggest that Am^{3+} can be extracted as ionic species, i.e., $Am(TTA)_2(CE)_n^+$ containing two TTA^-, into the DCE phase. In this connection, log D was less than -4 when Am^{3+} was extracted at pH 3.6 using DCE containing 0.01M CE in the absence of HTTA. Although the slopes of the log D - log $[CE]_{org}$ plots with 0.01M HTTA and

10^{-8} - 0.1M CE were scattered between 0.5 to 1.3, it is presumed that the extracted species may contain one molecule of CE. It is noteworthy that larger D values can be obtained at lower pH region in the ion-pair extraction of $Am(TTA)_2(CE)^+$ using DCE with HTTA and 18C6 or DC18C6 than in the synergistic extraction of $Am(TTA)_3(CE)$ using Bz or Cy. Furthermore extractability depends more strongly on the kind of CE than in the case of using Bz or Cy. In the ion-pair extraction system with DCE, D for 18C6 is larger than D for 15C5 and D for DC18C6 is larger than D for DC24C8, which implies that the effect of size-fitting between Am^{3+} and CE may be involved in the formation of $Am(TTA)_2(CE)^+$ complex.

Distribution ratio for the extraction of Am^{3+}, Cm^{3+}, and Eu^{3+} in DCE were determined, and the results of log D vs. pH for 18C6 were given in Fig. 4 (C_{HTTA} = 0.01 M, C_{18C6} = 0.01 M) together with result of D_0 with HTTA in the absence of 18C6(dotted line). The slopes of the plot were ca. 2. Separation factors(SF) which were calculated as the ratio of distribution between two metal ions were listed in Table 2. The SF for Am/Eu using 18C6 was ca. 30 which was larger than that for other CEs. This suggests that cavity size of CE takes a important role in this extraction system.

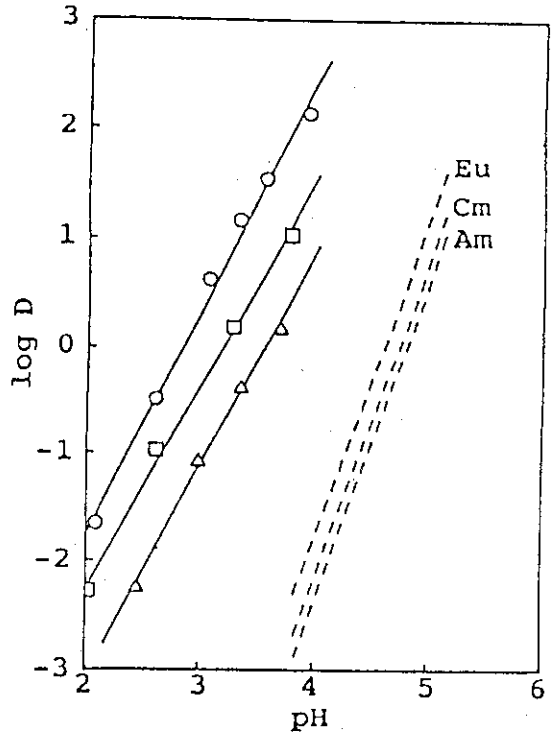

Fig. 4 pH-log D plots for extraction of Am^{3+}, Cm^{3+}, and Eu^{3+} with 0.01 M HTTA and 0.01 M 18C6 in DCE. ○:Am^{3+}, □:Cm^{3+}, △:Eu^{3+} ---:extraction with HTTA in the absence of 18C6

Table 2 The separation factor of metal ions on extraction in DCE

CE	Am/Cm	Cm/Eu	Am/Eu
none	0.68(1.5)	0.44(2.3)	0.30(3.4)
18C6	4.5	6.4	29
DC18C6	4.3	4.0	17
15C5	1.8	0.60	1.1
DC24C8	1.4	2.1	2.9

( ):reciprocal number

Trivalent actinide was extracted as 1:3:1 complex by HTTA and CEs in benzene or cyclohex-

ane which has low dielectric constant and adduct complex formation was affected strongly by the steric effect of CE. On the other hand, using DCE having high dielectric constant, extraction mechanism was different and it can be concluded that the ion-pair extraction with the synergistic effect has a possibility of the mutual separation of trivalent actinides and lanthanides.

3.2.2 Selective Extraction and Separation of Actinides with Ionizable Crown Ethers

Properly designed macrocyclic polyethers containing ionizable functional group can be made highly selective for solvent extraction of trivalent lanthanide and actinide ions. In the case of sym-dibenzo-16-crown-5-oxyacetic acid, the extraction of lanthanides was found independent of counter anion and reversible with respect to pH[3]. The distribution coefficients for the lanthanides are several order of magnitudes greater than those for the alkali metal ions and the alkaline earth metal ions of similar ionic radius[4]. This type of ionizable crown ethers have been applied to the extraction of the trivalent lanthanides ions from seawater and separation of ^{90}Y from ^{90}Sr by paper chromatography[4,5]. The chelation of actinides with ionizable crown ethers is unknown in the literature. The present study deals with the solvent extraction of Th, U, Np, Pu, Am, and Cm ions by sym-dibenzo-16-crown-5 host with oxyacetic acid moieties and their potential applications to the separation of the f-block elements.

The stable oxidation states of Th, U, and Am in aqueous solution under normal conditions are quadravalent, hexavalent and trivalent, respectively. Extraction efficiencies of Th(IV), U(VI) and Am(III) with sym-dibenzo-16-crown-5-oxyacetic acid as a function of pH are shown in Fig. 5. The concentration of the macrocycle used in the experiments was 5×10^{-3} M in chloroform and these of Th and U were 5×10^{-5} M and that of Am was 10^{-8} M in acetate buffered solution. According to Fig. 5, extraction of Th(IV) occurs at pH as low as 2 and reaches 90% at pH above 3.2. Extraction of U(VI) becomes significant at pH above 4 and becomes quantitative at pH above 5. The extraction of Am(III) is quantitative at pH above 6. A linear relationship between log D and log [CE] for Th(IV) was observed with a slope of 2.2 indicating the extracted species is coordinated with 2 ligands. It is known that Th^{4+} undergoes hydrolysis to form $Th(OH)^{3+}$ and $Th(OH)_2^{2+}$ at pH around 3 which corresponds to the pH range for Th extraction. The correlation seems to suggest that the extracted Th-complex is of

the form $Th(OH)_2(CE)_2$. From the same examination, the extracted U complex and Am complex is probably of the form $UO_2(OH)(CE)$ and $Am(OH)(CE)_2$, respectively. The extraction of actinides appears to depend on the formation of a proper aqueous hydroxide species capable of forming a neutral and stable complex with the ionizable crown ether.

The pH dependence on the extraction of Np(VI), Pu(VI) and Cm(III) by sym-dibenzo-16-crown-5-oxyacetic acid is shown in Fig. 6. The extraction behavior of Pu(VI) is similar to that of U(VI). The concentration of Pu used in this experiment was relatively high(1×10^{-3} M) compared with the other actinide experiments. Pu(VI) also forms 1 : 1 complex according to the slope determined by a log D vs. log [CE] plot. The extraction curve of Cm(III) is similar to that of Am(III).

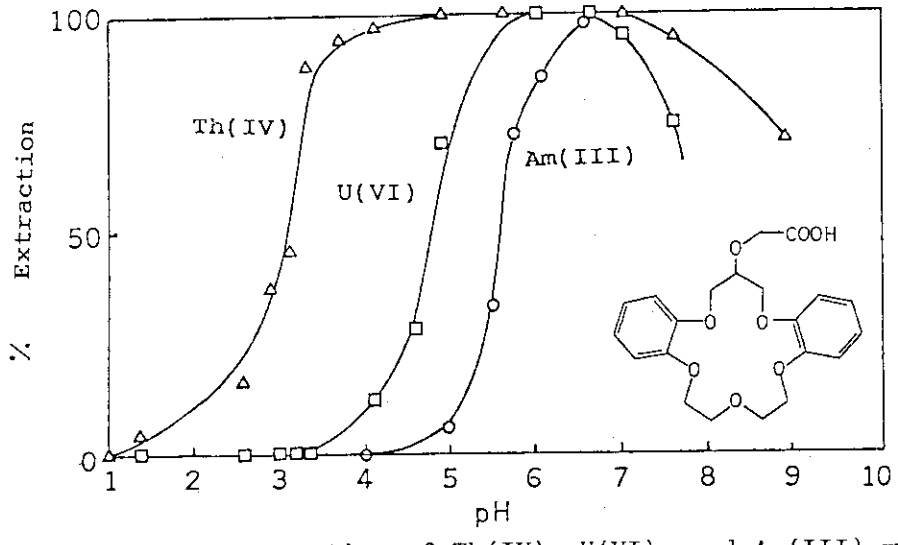

Fig. 5 Solvent extraction of Th(IV), U(VI), and Am(III) with sym-dibenzo-16-crown-5-oxyacetic acid as a function of pH.

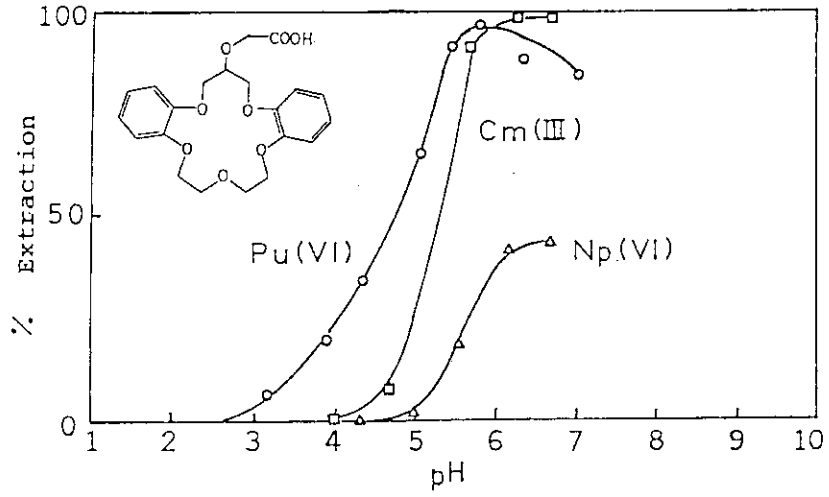

Fig. 6 Solvent extraction of Np(VI), Pu(VI), and Cm(III) with sym-dibenzo-16-crown-5-oxyacetic acid as a function of pH.

The ionizable crown ethers discussed in this study may have important applications in analytical chemistry for the separation and preconcentration of actinides. Since the extraction is reversible with respect to pH, actinides can be recovered from the organic phase by stripping with a dilute acid.

Reference

1) J. N. Mathur, P. K. Khopkar, Solvent Extr. Ion Exch., 6(1988)111.
2) D. D. Ensor, M. Nicks, D. J. Pruett, Sep. Sci. Technol., 23(1988)1345.
3) J. Tang, C. M. Wai, Anal. Chem., 58(1986)3233.
4) C. M. Wai, H. S. Du, Anal. Chem,, 62(1990)2412.
5) J. Tang, C. M. Wai, Talanta 36(1986)1129.

Publication List

[1] Y. Meguro, W. Cheng, H. Imura, Z. Yoshida, "Synergistic Extraction of Americium(III) with 2-Thenoyltrifluoroacetone and Crown Ether," J. Radioanal. Nucl. Chem., in press.
[2] Y. Meguro, H. Muto, Z. Yoshida, "Solvent Effect on Synergistic Extraction of Americium(III)/2-Thenoyltrifluoroacetone/Crown Ether," Anal. Sci., in press.
[3] C. M. Wai, H. S. Du, Y. Meguro, Z. Yoshida, "Selective Extraction and Separation of Actinides with Ionizable Crown Ether," Anal. Sci., in press.

3.3 REDOX REACTIONS OF NEPTUNIUM IONS IN CARBONATE MEDIA

Elucidating the behavior of various actinide species in ground water system is indispensable for the safety assessment of nuclear waste disposal in deep ground. The interaction of the ions with the geological media depends on their oxidation states and chemical forms in the path of migration. Neptunium is of particular concern because of its long decay period, relatively high concentration in the spent fuel, and high radiation toxicity. Carbonate is supposed to be the dominant ligand to react with neptunium ions in ground water[1-3].

In the present work, we observed the redox process of neptunium ions in perchloric acid solution and in concentrated carbonate solution by means of a controlled-potential electrolysis in combination with spectrophotometry.

Experimental

The electrolytic cell consisted of Pt gauze working electrode, Pt wire counter electrode and Ag/AgCl(sat. KCl) reference electrode. A pair of light transmission probes were placed at the wall of the cell so that a light path was 3 cm. The probes were connected by optical fibers with Optical Waveguide Spectrum Analyzer. The spectrum of the solution was recorded, immediately after the sample solution was electrolyzed.

Results and discussion

Sample solution, 1 M $HClO_4$ containing 2.09 x 10^{-4} M NpO_2^{2+}, was electrolyzed at a given potential ranging between +1.2 and -1.0 V, and then absorption spectrum of the solution was measured. Concentrations of Np(V), Np(IV), and Np(III) were determined from the absorption peak intensities using calibration curves. The relation between the electrolysis potential, E, and the fraction, F %, of neptunium ions of various oxidation states is shown in Fig. 1.

The redox reaction between NpO_2^{2+} and NpO_2^{+} is concluded to be reversible even in the carbonate solution, since $E_{1/2}$(VI->V) and $E_{1/2}$(V->VI) are identical to each other. The $E_{1/2}$(VI->/<-V) being +0.25 V in 1 M Na_2CO_3 solution, shifted by 0.69 V negatively from the $E_{1/2}$(VI->/<-V) in perchloric acid solution (Fig. 2). Since $E_{1/2}$(VI->/<-V) is independent on the carbonate concentration, it can be concluded that complexes, $NpO_2(CO_3)_3^{5-}$ and $NpO_2(CO_3)_3^{4-}$, may participate in the redox reaction[4].

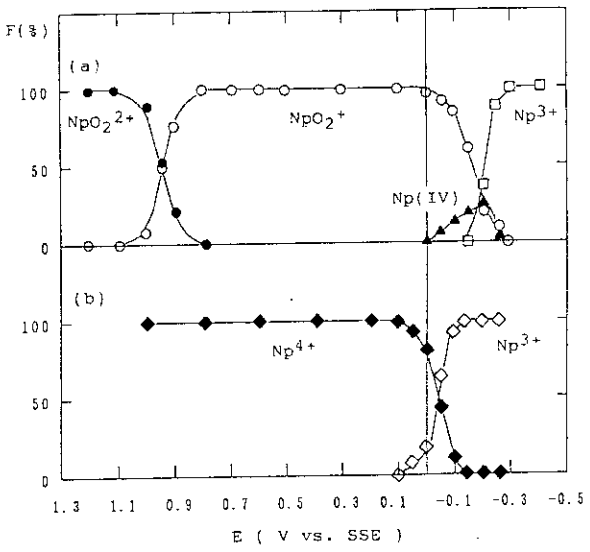

Fig. 1 E-F(%) diagrams for the redox of neptunium ions in 1 M $HClO_4$ solution.
Oxidation state of neptunium ion before the electrolysis ;
(a) Np(VI) or Np(V), (b) Np(IV) or Np(III).

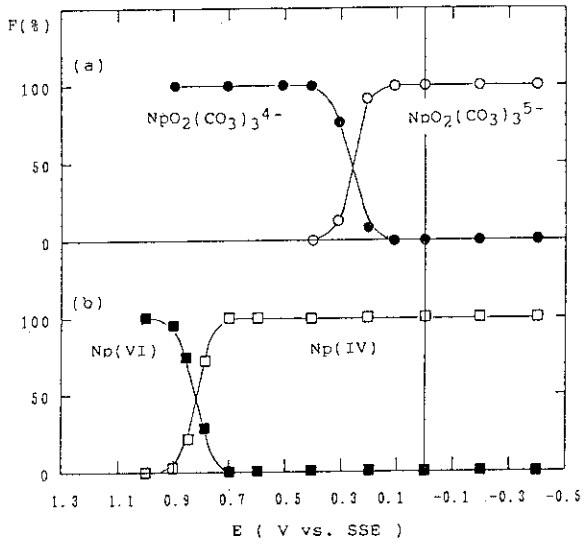

Fig. 2 E-F(%) diagrams for the redox of neptunium ions in 1 M Na_2CO_3 solution of pH 10.8±0.1.
Oxidation state of neptunium ion before the electrolysis ;
(a) Np(VI) or Np(V), (b) Np(IV).

The further reduction of NpO_2^+ to Np(IV) and/or Np(III) in the carbonate solution of pH 10 to 11 was not observed even at -1.0 V.

The oxidation reaction of Np^{4+} to NpO_2^{2+}, which involves the process of the formation of Np-O bond, is significantly promoted due to the decrease of the concentration of hydrogen ion even in the carbonate solution, though Np^{4+} is stabilized by the formation of strong carbonate complex. As a result, the oxidation of Np^{4+} into NpO_2^{2+} takes place at around +0.8 to +0.85 V.

The generation of NpO_2^{2+} due to the oxidation of Np^{4+} in 0.2, 0.5, or 1.0 M Na_2CO_3 solution of pH 10.1 or 10.8 was investigated, and the results are given in Fig. 3. The oxidation behavior of Np^{4+} in Na_2CO_3 solution of less than 0.2 M at pH 10.8 could not be studied, since Np^{4+} precipitated.

The $E_{1/2}$(IV->VI) of curve 4 obtained with 0.2 M Na_2CO_3 solution (pH 10.1 ± 0.03) shifts largely to more negative direction from those with 0.5 or 1.0 M Na_2CO_3 (pH 10.1 or 10.8). Such a drastic potential shift with the slight change in the concentration of carbonate and pH can be explained by considering participation of different kinds of neptunium complex species. Because Np(VI)-species is $NpO_2(CO_3)_3^{4-}$ in 0.2 to 1.0 M

Na_2CO_3 solutions (pH 10 - 11) as concluded above, different Np(IV)-species might be formed. Different absorption spectrum were obtained for Np(IV) in 0.5 or 1.0 M Na_2CO_3 solutions of pH 10-11 and in 0.2 M Na_2CO_3 solution of pH 10.1.

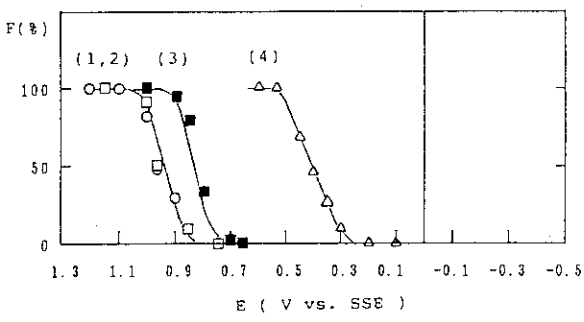

Fig. 3 E-F(%) plots for the generation of Np(VI) by the oxidation of Np(IV) in carbonate solutions.

Media: (1) ○ 0.5 M Na_2CO_3, pH 10.10±0.03,
(2) □ 1.0 M Na_2CO_3, pH 10.10±0.03,
(3) ■ 1.0 M Na_2CO_3, pH 10.80±0.07,
(4) △ 0.2 M Na_2CO_3, pH 10.10±0.03.

References

1) L. Maya, Inorg. Chem. 23(1984)3926.
2) D. M. Wester and J. C. Sullivan, J. Inorg. Nucl. Chem. 43(1981)2919.
3) P. G. Varlashkin, D. E. Hobart, G. M. Begun and J.R. Peterson, Radiochim. Acta 35(1984)91.
4) G. A. Simakin, Radiokhimiya 19(1977)518.

Publication List

[1] Z. Yoshida, H. Aoyagi, Y. Kato, Y. Li, S. Kihara, "Redox, Disproportionation, and Complex Formation Reactions of Neptunium Ions," Proc. 3rd Internat. Symp. on Adv. Nucl. Ener. Res., Mito, 1991, p.268.

3.4 Development of Photoacoustic Spectroscopy for Speciation of Actinide Elements in Aqueous and Solid Phase

3.4.1 Introduction

Concerning the chemical behavior of actinide elements in the environment, not only determination of total concentration of the elements but also speciation of their chemical forms or species is required, because the nature of the species influences various features such as solubility, complexation, redox reaction, adsorption, precipitation, and so on. Since the behavior and relative safety significance of various actinide species differ greatly, selective and sensitive analytical methods with minimal disturbance of species equilibria are needed for the speciation, especially to assist predictive studies of the behavior of the species in natural systems.

Photoacoustic spectroscopy (PAS) has favorable characteristics for the speciation of the actinide elements in both solid and liquid phases, that is to say, high sensitivity and capability of measurement without pretreatment of a sample.[1,2] While considerable progress has been made recently on the measurement of the actinide species in aqueous solution,[3-6] little progress has been made in the identification and measurement of the species in solid phase.[7] For these reasons, we have developed three types of PAS: Fourier transform laser-induced photoacoustic spectroscopy (FT-LPAS), ultraviolet, visible and near-infrared photoacoustic spectroscopy (UV-VIS-NIR PAS), and Fourier transform infrared photoacoustic spectroscopy (FT-IR PAS).

In the present paper, the usefulness of FT-LPAS for the speciation of the actinide elements in aqueous solution and of UV-VIS-NIR PAS and FT-IR PAS for that in solid phase is demonstrated by using tetravalent and hexavalent uranium.

3.4.2 Application of the FT-LPAS system to the speciation of uranium in $NaHCO_3/NaClO_4$ solutions

As an application of the FT-LPAS system to aqueous solution, the PA spectra of U(VI) in $NaHCO_3/NaClO_4$ solutions were measured and compared with absorption spectra measured by conventional spectrophotometry.

Figure 1(a) shows the absorption spectra of 1.0×10^{-2} M U(VI) in various solutions at one week after the sample preparation. The spectral shape and absorbance of samples (ii), (iii) and (iv) varied with the

elapse of time due to the effect of hydrolysis, while those of samples (i) and (v) were stable. Though the spectrum of sample (ii) was similar to that of sample (i) initially, the absorbance increased gradually and the precipitate was formed three weeks after the preparation. In the case of sample (iii), the precipitate was also formed and the absorbance decreased. The spectral change of sample (iv) was slight, but the absorbance increased. On the basis of the spectral shape and molar absorptivity in the literature,[8-11] the primary species in the sample solutions (Fig. 1(a)) were estimated as follows: (i) $UO_2(CO_3)_3^{4-}$, (ii) $UO_2(CO_3)_2^{2-}$, (iii) $(UO_2)_3(OH)_5^{+}$, (iv) $(UO_2)_2(OH)_2^{2+}$, (v) UO_2^{2+}. In the cases of samples (ii) and (iv), other species might also be present.

FT-LPAS can provide spectra for U(VI) species in lower concentration, as shown in Fig. 1(b). The figure 1(b) shows the PA spectra of 1.0×10^{-4} M U(VI) in the wavelength range of 420 to 460 nm (1 nm step). The time for data acquisition at each wavelength is 3.2 seconds and the time to take the spectrum is about 20 minutes, including the time for wavelength scanning and signal processing under the present conditions. The reproducibility of the spectra is found to be satisfactory but accumulation of the data will be required further to reduce errors at each wavelength. Species estimated from the PA spectra is as follows: (i) $UO_2(CO_3)_3^{4-}$, (ii) UO_2^{2+}.

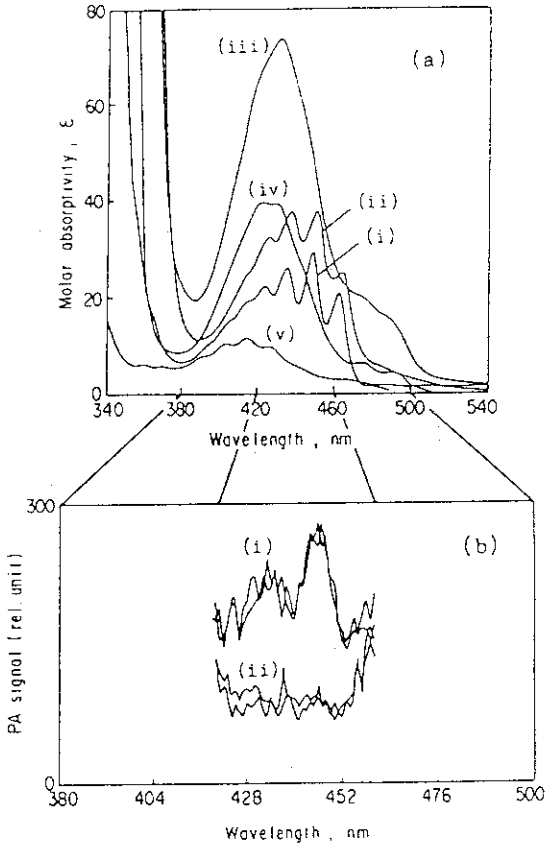

Fig. 1 Absorption and photoacoustic spectra of uranyl ion in $NaHCO_3/NaClO_4$ solutions:
(a) Absorption spectra; 1.0×10^{-2} M U(VI);
(i) 0.1 M $NaHCO_3$, pH 9.36;
(ii) 0.05 M $NaHCO_3/NaClO_4$, * pH 8.36;
(iii) 0.02 M $NaHCO_3/NaClO_4$, * pH 4.77;
(iv) 0.01 M $NaHCO_3/NaClO_4$, * pH 4.14;
(v) 0.1 M $NaClO_4$, pH 2.91;
*, with precipitates:
(b) Photoacoustic spectra; 1.0×10^{-4} M U(VI); (i) 0.01 M $NaHCO_3/NaClO_4$, pH 9.11; (ii) 0.1 M $NaClO_4$, pH 4.77.

As mentioned above, the dominant U(VI) species in 0.01 M $NaHCO_3/NaClO_4$ solution depend on the uranium concentration: $(UO_2)_2(OH)_2^{2+}$ and $UO_2(CO_3)_3^{4-}$ at 10^{-2} M and 10^{-4} M U(VI), respectively, while the species UO_2^{2+} in 0.1 M $NaClO_4$ solution is almost independent of the U(VI)

concentration. Since these solutions were not buffered, the pH values differed considerably as noted in Fig. 1. In order to further examine these results, percentage distribution diagrams of uranyl-hydroxy-carbonate complexes vs. pH in 0.01 M $NaHCO_3/NaClO_4$ solutions of 10^{-2} M and 10^{-4} M U(VI) have been computed with a computer program MINTEQ[12] using currently available thermodynamic data for uranium species such as UO_2OH^-, $(UO_2)_2(OH)_2^{2+}$, $(UO_2)_3(OH)_5^+$, $UO_2CO_3^0(aq)$, $UO_2(CO_3)_2^{2-}$, $UO_2(CO_3)_3^{4-}$, $(UO_2)_2CO_3(OH)_3^-$, $UO_2(OH)_2(aq)$, and others. A comparison between the experimental data and the results of the computation indicates that the species estimated from the spectral data are in fair agreement with those predicted from the calculated percentage distribution diagram and that the difference of the species, $(UO_2)_2(OH)_2^{2+}$ and $UO_2(CO_3)_3^{4-}$ in 0.01 M $NaHCO_3/NaClO_4$ solution, is due to the pH value, rather than the uranium concentration.

3.4.3 Application of the UV-VIS-NIR and FT-IR PAS systems to the speciation of uranium precipitates

As an application of UV-VIS-NIR PAS and FT-IR PAS to the speciation of actinide elements in solid phase, the PA spectra of U(IV) and U(VI) precipitates were measured in the wavelength range of 250 nm to 25 μm. Uranium oxalates and ammonium uranates of U(IV) and U(VI) were chosen as objects of the study on the basis of the following facts and considerations.

1. The precipitates are produced easily from acidic solutions at room temperature.
2. Both the U(IV) and U(VI) precipitates are insoluble in aqueous solutions.
3. The resulting precipitates are crystalline and/or amorphous products.

Uranium(IV) was prepared from 0.5 M $UO_2(NO_3)_2$-1 M HNO_3 solution by photochemical reduction using ethanol as a reducing agent and UV light from a high pressure mercury lamp (100 W). The progress of the photoreduction was monitored with a spectrophotometer. The uranium oxalates and ammonium uranates of U(IV) and U(VI) were produced from 0.5 M U(IV or VI)-1 M HNO_3 by adding 0.5 M $H_2C_2O_4$ and 1.5 M NH_4OH, respectively. The precipitates were washed with water and lyophilized. The resulting products were analyzed by X-ray diffraction, UV-VIS-NIR PAS and FT-IR PAS.

The results of X-ray diffraction show that the chemical forms of the U(IV) and U(VI) oxalates are $U(C_2O_4)_2 \cdot 6H_2O$ and $UO_2C_2O_4 \cdot 3H_2O$, respective-

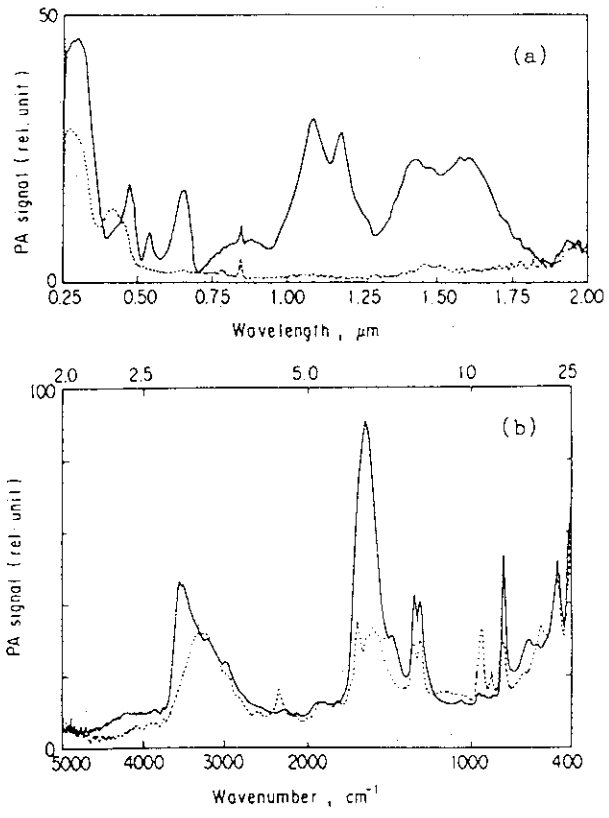

Fig. 2 Photoacoustic spectra of uranium oxalates: (a) UV-VIS-NIR PAS; (b) FT-IR PAS: ——, U(IV); ---, U(VI).

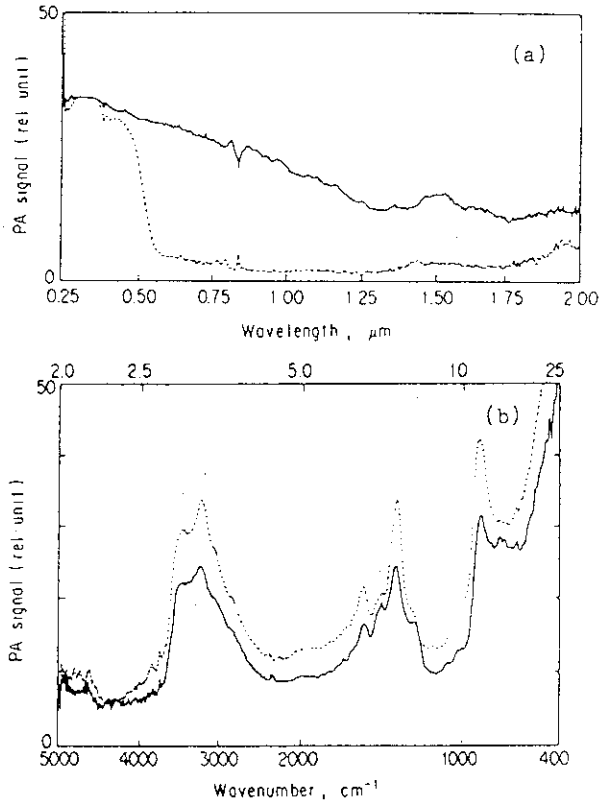

Fig. 3 Photoacoustic spectra of ammonium uranates: (a) UV-VIS-NIR PAS; (b) FT-IR PAS: ——, U(IV); ---, U(VI).

ly. However, the chemical forms of the ammonium uranates could not be determined because the precipitates were non-crystalline.

The PA spectra of the uranium oxalates are shown in Fig. 2. In the cases of the UV-VIS-NIR PA spectra, the absorption bands and relative absorbancies of the U(IV) and U(VI) oxalates are quite similar to those of U^{4+} and UO_2^{2+} in $HClO_4$ solution. The broad absorption bands which might be due to $C_2O_4^{2-}$ are also observed in UV range of both spectra. On the other hand, the absorption bands such as ν_{OH} (3200-3500 cm^{-1}), $\nu_{as,CO}$ (1600-1700 cm^{-1}), $\nu_{s,CO}$ (1312, 1350 cm^{-1}), δ_{OCO} (810 cm^{-1}), etc. owing to H_2O and $C_2O_4^{2-}$ in the precipitates are observed in both the FT-IR PA spectra. Furthermore, the absorption bands of $\nu_{as,OUO}$ (934 cm^{-1}) and $\nu_{s,OUO}$ (868 cm^{-1}) owing to UO_2^{2+} are observed in the spectrum of the U(VI) oxalate.

The PA spectra of the ammonium uranates are shown in Fig. 3. The UV-VIS-NIR PA spectrum of the U(VI) precipitate exhibits intense and broad absorption bands in the range 250-580 nm, which might be due to UO_2^{2+}. The spectrum of the U(IV) precipitate also shows broad and intense ab-

sorption bands in the wide range of wavelength, from UV to NIR, but the oxidation state could not be estimated from the spectrum. The absorption bands of the U(IV) precipitate in the region of UV to VIS may be due to an electron transfer process and/or the $5f^2$-$5f^16d$ transition, while the absorption of the U(IV) oxalate is ascribed to transitions within the $5f^2$ configuration. The FT-IR PA spectra of the both precipitates resemble with each other and the absorption bands such as ν_{OH} (3200-3500 cm^{-1}), δ_{OH} (1620 cm^{-1}), $\nu_{3,NH4}$ (3230 cm^{-1}), $\nu_{4,NH4}$ (1420 cm^{-1}), etc. owing to H_2O and NH_4^+ in the precipitates are observed in the spectra. However, the slight difference in the absorption band of 900 cm^{-1}, which may be due to UO_2^{2+}, is observed in the spectra.

3.4.4 Conclusions

FT-LPAS system has been developed for the speciation of actinide elements in aqueous solution at lower concentration where conventional spectrophotometry is not suitable. It was applied to the measurement of uranium complexes in $NaHCO_3/NaClO_4$ solutions, and the usefulness for the speciation of the species in aqueous solution has been demonstrated. Further improvements of the system are currently being pursued for more sensitive and quantitative direct speciation.

UV-VIS-NIR PAS and FT-IR PAS have also been developed for the speciation of actinide elements in solid samples. These systems were applied to the measurement of uranium precipitates prepared from aqueous solution. The systems make it possible to measure the PA spectra in the wavelength range of 250 nm to 25 μm with a few mg of solid samples, and on particular these were applicable to the amorphous materials which can not be analyzed by X-ray diffraction.

REFERENCES

1) C.K.N. Patel and A.C. Tam, Rev. Mod. Phys. 53(1981)517.
2) A.C. Tam, Rev. Mod. Phys. 58(1986)381.
3) R. Klenze and J.I. Kim, Radiochim. Acta 44/45(1988)77.
4) J.V. Beitz, D.L. Bowers, M.M. Doxtader, V.A. Maroni and D.T. Reed, Radiochim. Acta 44/45(1988)87.
5) P.M. Pollard, M. Liezers, J.W. McMillan, G. Phillips, H.P. Thomason and F.T. Ewart, Radiochim. Acta 44/45(1988)95.
6) R. Klenze, J.I. Kim and H. Wimmer, Radiochim. Acta 52/53(1991)97.
7) G. Heinrich, H. Gusten and H.J. Ache, Appl. Spectrosc. 40(1986)363.

8) C.A. Blake, C.F. Coleman, K.B. Brown, D.G. Hill, R.S. Lowrie and J.M. Schmitt, J. Am. Chem. Soc. 78(1956)5978.
9) S. O'Cinneide, J.P. Scanlan and M.J. Hynes, J. Inorg. Nucl. Chem. 37(1975)1013.
10) J.P. Scanlan, J. Inorg. Nucl. Chem. 39(1977)635.
11) R.M. Rush and J.S. Johnson, J. Phys. Chem. 67(1963)821.
12) A.R. Felmy, D.C. Girvin and E.A. Jenne, EPA-600/3-84-032 (1984).

Publication List

[1] T. Kimura and S. Nakayama, "Speciation of Actinoids by Photoacoustic Spectroscopy," Reiza Kenkyu, (in Japanese), 18(1990)279.
[2] T. Kimura and S. Nakayama, "Development of Photoacoustic Spectroscopy for Speciation of Actinide Elements in Aqueous Solution and in Solid Phase," Proc. 3rd. Int. Symp. Adv. Nucl. Energ. Res. (1991) p.262.
[3] S. Nakayama and T. Kimura, "Applications of Photoacoustic Spectroscopy to Speciation of Lanthanide Elements in Aqueous Solutions and of Solid Phase," J. Nucl. Sci. Technol. 28(1991)780.

3.5 Spent Fuel Analysis

In recent years, the demands for the utilization of the nuclear fuels to higher burnup have been growing larger. It is thus important to determine the amount of actinides and fission products in spent nuclear fuels as accurately as possible for the several nuclear fields such as; 1) Reactor operation, 2) Spent fuel storage and transportation, 3) Spent fuel reprocessing, 4) Waste managemnt, and 5) Safegurds. Aiming to determine actinides more than $1X10^{-10}$/ initial U atom in 1 to 10 mg spent fuel sample, a method consisted of anion exchang separation and determination by both mass spectrometry and α -ray spectrometry has been developed.

a) Ion exchange separation Ion exchange separation was done in two steps. At first stage U, Np, Pu and mixtures of trivalent lanthanides and actinides together with fission products were separated using anion exchange resin in HCl solution[1]. Pu, Np and U were further purified by repeating the same procedure. At second stage Nd, Am and Cm were separated from each other using anion exchange resin in mixture of methanol and nitric acid[2].

b) Mass spectrometry For the determination of Nd, U and Pu, isotope dilution mass spectrometry(IDMS) was adopted using mixtures of ^{150}Nd, ^{233}U and ^{242}Pu as a spike. A surface ionization type mass spectrometer, VG 54-38 was used for the isotopic measurements of Am and Cm isotopes. Based on the investigations concerning measurement conditions and interferring ions at measurement, automatic measurement programs for Am and Cm was completed[3].

c) α -ray spectrometry Sources of α -ray spectrometry of ^{232}U, ^{234}U, ^{237}Np, ^{238}Pu, ^{241}Am, ^{242m}Am, ^{243}Am, ^{242}Cm, ^{243}Cm and ^{244}Cm nuclides were prepared for six kind of solutions, i.e., solution before ion exchange separation and fractions of U, Np, Pu, Am and Cm[4].

Following ratios of peak area can be obtained from α -ray spectrum: (^{238}Pu + ^{241}Am)/(^{239}Pu + ^{240}Pu) and ^{244}Cm/(^{239}Pu + ^{240}Pu) with the samples before separation, ^{232}U/^{238}U and ^{234}U/^{238}U with the U fraction, ^{238}Pu/(^{239}Pu + ^{240}Pu) and

$^{236}Pu/(^{239}Pu + ^{240}Pu)$ with the Pu fraction, $^{243}Am/^{241}Am$ with the Am fraction, $^{242}Cm/^{244}Cm$ and $^{243}Cm/^{244}Cm$ with the Cm fraction.

Since the atomic ratio of $(^{238}Pu + ^{240}Pu)/U$ was accurately known from the results by mass spectrometry, the ratios of peak area $(^{238}Pu + ^{241}Am)/(^{239}Pu + ^{240}Pu)$, $^{244}Cm/(^{239}Pu + ^{240}Pu)$, $^{238}Pu/(^{239}Pu + ^{240}Pu)$ and $^{236}Pu/(^{239}Pu + ^{240}Pu)$ could be converted to the ratios of the activities $(^{238}Pu + ^{241}Am)$, ^{244}Cm, ^{238}Pu and ^{236}Pu to the unit amount of U. In the same way ratios of the activities ^{232}U and ^{234}U to the unit amount of U could be calculated. By using $^{244}Cm/U$ and $^{241}Am/U$, activities of ^{243}Am, ^{242}Cm and ^{243}Cm could be determined.

The $^{237}Np/U$ ratio was determined from the α -ray spectrum with Np fraction, taking chemical yield, counting efficiency and amount of sample into account, because the above mentioned technique based on the activity ratio was not able to apply.

By the proposed method amounts and/or isotopic ratios of such actinides as U(232, 234, 235, 236, 238), Np-237, Pu(236, 238, 239, 240, 241, 242, 244), Am(241, 242m, 243) and Cm(242, 243, 244, 245, 246, 247) can be determined. Since it has been scarcely reported on the amount of these nuclides in high burnup fuels, analytical results for these nuclides could contribute to many nuclear technological fields.

References

1) H. Umezawa, et al., Private communucation(1972).
2) S. Usuda, N. Kohno, Separation Sci. Technol. 23(1988)1119.
3) K. Gunji et al., Private communication(1990).
4) N. Shinohara, N. Kohno, Appl. Radiat. Isot.,40(1989)41.

Publication List

[1] N. Shinohara, N. Kohno,"Rapid Preparation of High-Resolution Sources for Alpha-Ray Spectrometry of Actinides Spent Fuel," Appl. Radiat. Isot.,40(1989)41.
[2] Y. Nakahara, T. Suzuki, K. Gunji, N. Kohno, H. Takano, Z. Yoshida, T. Adachi,"Amount of nuclides constituting PWR spent fuels, conparison of observed with calculated values", Radiochim. Acta, 50(1990)141.

4. Analytical Chemical Service and Scientific Glassblowing Utilization

K. Gunji, S. Iso, M. Itoh, N. Kohno, H. Muto, M. Ohnuki, M. Ouchi, T. Sonobe, T. Suzuki, K. Takashima, T Takeishi, K. Tamura, S. Tamura and Y. Toida (analytical chemical service)
R. Sato, T. Ideta and K. Obara (Scientific glass-blowing)

A wide variety of analytical service and glassblowing service work were carried out on request from other laboratories and R & D programs within JAERI.

4.1 Analytical Chemical Service

4.1.1 Elemental and Isotopic Analysis

The function of analysis services in the elemental and isotopic analyses cover the following items; (i) wet chemical analysis including inductively coupled plasma atomic emission spectroscopy(ICP-AES), atomic absorption spectroscopy, flame spctrophotometry, absorption spectrophotometry, electrochemical analysis, etc., sometimes in combination with various chemical separation methods, (ii) gas analysis using gas chromatography, mass spectrometry and thermal analysis usually combined with various separation techniques such as inert gas fusion, (iii) X-ray fluorescence spectrometry, electron probe microanalyzer (EPMA), optical emission spectroscopy using direct current arc excitation source, and (iv) isotope mass spectrometry.

Thirty to fifty requests have been received and treated in each fiscal year during these three years. Requests made in 1988- , 1989- and 1990-fiscal year are shown in Table 1, together with those on the burnup measurements. Some of the typical service analyses carried out in 1988-1991 are described below.

In the field of analysis of nuclear fuels, various analyses were performed, e.g., the determination of titanium,

nickel, chromium, iron, hydrogen and carbon in uranium oxide in relation to the study on the cause of spontaneous emission of smoke from uranium metal during its storage, the determination of carbon and oxygen content and isotopic analysis of uranium silicide, and the determination of metallic impurities in thorium oxide. Concerning the nuclear materials, such analyses were actively performed as the fractional determination of acid soluble and insoluble boron in Hastelloy XR, the quantitative determination of impurities in the control rod material of research reactor, hydrogen in zircaloy, impurities of lithium carbonate and sintered lithium oxide, elemental analysis of concrete materials and rocks, as well as isotopic analyses of uranium in uranium hexafluoride, of lithium in the lithium compounds. In addition to these services described above, requests for qualitative EPMA analysis of sample materials are increasing.

In the field of downstream of nuclear fuel cycle, the following analytical services were carried out; determination of impurities in the waste solution of the reprocessing process, determination of long-lived nuclides such as carbon-14, tritium, cobalt-60, plutonium-239, etc. present in biological shielding concrete, ion exchange resin and fuel storage pool water of JPDR, measurements of deuterium content in the groundwater as a study on its movement, analyses of the simulated spent fuel pellets and their insoluble residues, analyses of the coolant in the high level liquid waste tank, determination of cesium in pure water for the evaluation of source terms, determination and isotopic analysis of plutonium in plutonium nitrate solution, and radiometric analysis of manganese-54 in high burnup fuel clad.

Table 1 Analytical chemical service requestes in each fiscal year: 1988～1990

<fiscal year>	Upstream related	downstream related	burnup
1988			
No. of requests	17	8	7
No. of samples	102	95	39
No. of components	333	124	620
1989			
No. of requests	20	21	7
No. of samples	133	238	18
No. of components	624	496	246
1990			
No. of requests	22	20	3
No. of samples	68	1158	4
No. of components	597	2158	70

4.1.2 Burnup Measurements

Following the previous work[1], burnup measurements and high-energy neutron monitoring(^{54}Mn in cladding) of the sample specimens have been done, as follows:

- High burnup uranium dioxide fuels from commercial PWR reactor[2]
- Pulse irradiated fuels from Nuclear Safety Research Reactor Experiment using spent PWR , BWR and JMTR UO_2 fuels
- Pulse irradiated fuels from Nuclear Safety Research Reactor Experiment using Plutonium-Uranium Mixed Oxide[3], Silicide Plate-type and PWR UO_2 fuels[4]
- Isotopic composition measurements of cadmium as control rod and burnable neutron absorber[5]

In relation to the burnup measurements of high burnup PWR fuels, determination of uranium, neptunium, plutonium, americium and curium by α -ray spectrometry[6] , and isotopic composition measurements of americium and curium by mass spectrometry[7] have been carried out. By the combination of these methods 22 actinide nuclides existed in the spent fuels more than $1x10^{-10}$/Initial U atom can be determined accurately.

The half-life of highly purified ^{242}Cm has been remeasured by three independent methods[8]. The overall weighted mean of the measurements was 161.41d ± 0.28d. The remeasured value agrees well with the authors' previous result, but is shorter by about 1 % than the values reported by others[9].

References

1) Department of Chemistry Progress Report(Jan. 1986 - Dec. 1988), p75(1989).
2) K. Gunji, N. Kohno, T. Sonobe, M. Ohnuki, Y. Meguro, T. Suzuki and T. Adachi, Private communication(1990).
3) S. Yanagihara, T. Suzuki and T. Inabe, J. Nucl. Sci. Technol. 26(1989)787.
4) K. Yanagisawa, K. Soyama, H. Ichikawa, T. Nemoto, O.

Hoshino, H. Uno, M. Umeda, T. Suzuki, H. Kanazawa, Y. Kimura and H. Mimura, JAERI-M 91-114(1991).
5) K. Gunji and H. Takeishi, Private communication(1991).
6) N. Kohno, K. Gunji, N. Shinohara, M. Ohnuki, T. Sonobe, Y. Meguro and T. Adachi, Private communication(1990).
7) K. Gunji, N. Kohno, S. Okazaki, T. Sonobe, M. Ohnuki, Y. Meguro, and T. Adachi, Private communication(1990).
8) S. Usuda, T. Suzuki, N.Kohno and H. Umezawa, JAERI-M 90-030(1990).
9) S. Usuda and H. Umezawa, J. Inorg. Nucl. Chem., 43(1981)3081.

Publication List

[1] S. Yanagihara, T. Suzuki and T. Inabe,"Fission Density in Plutonium-Uranium Mixed Oxide Fuel Irradiated by Pulsed Power in NSRR Experiments," J. Nucl. Sci. Technol. 26(1989)787.
[2] S. Usuda, T. Suzuki, N.Kohno and H. Umezawa,"Remeasurement of ^{242}Cm half life," JAERI-M 90-030(1990).
[3] K. Yanagisawa, K. Soyama, H. Ichikawa, T. Nemoto, O. Hoshino, H. Uno, M. Umeda, T. Suzuki, H. Kanazawa, Y. Kimura and H. Mimura,"Technical Developement of the Silicide Plate-type Fuel Experiment at Nuclear Safety Research Reactor," JAERI-M 91-114(1991).

4.2 Glassblowing

The glassblowing shop, established in 1958, produces and rapairs various experimental apparatuses, instruments and vessels made of glass. The members of glassblowing shop not only make large instruments using large-scaled lathers or drills but also produce precise parts by hand with excellent skill. The glassblowing shop also contributes to the progress of glassblowing technique by developing a new method which is characteristic to the field of nuclear technology. The detailed facilities and activities of glassblowing shop are described elesewhere[1].

The numbers of request for glassblowing were 201 and 174 in FY 1989 and 1990, respectively. The typical items of work made at the requests in these three years are summarized as follows;

1) Construction of an apparatus for the measurement of the ratio of hydrogen isotopes. This experimental device was employed to investigate the effect of isotopic ratio $\{T_2/(T_2+HT+DT)\}$ on the conversion reaction of trace quantity of tritium gas in air to tritiated water.

2) Construction of the following experimental devices;

·compact type-scrubber to remove acid vapor which can be used in ventilated hood,

·electrolytic cell for the electrochemical studies of lanthanide and actinide elements in various kinds of molten salt,

·analytical apparatus, which consists of continuous dissolution cell, electrolytic system, etc., for the determination of the oxidation states of the component(s) in superconducting oxide materials,

·electrolytic flow-cell with a pair of light transmission probes to investigate the redox behavior of neptunium ions by a controlled- potential electrolysis in combination with spectrophotometry,

·improved device for thermogravimetric instrument which involves a glass flange for sealing.

The new tequniques developed by the glass blowing shop in these three years are as follows;

1) Development of a gas burner made of quartz which can be used for the preparation of the sealed quartz-ampule for neutron irradiation. This burner is effectively employed to avoid contamination which usually results from metallic material of a conventional burner.

2) Development of a low-leak Teflon cock by employing a duplicate valve.

Reference

1) Department of Chemistry Progress Report, JAERI-M 85-213(1986).

Publication list

[1] K. Kimura and K. Obara, "Development of spiral glass tube with large inner surface area" (in Japanese), Honoho (Journal of the Glass Technical Society of Japan), 28(1990)7.

5. Radiochemical Studies on Iodine and Tritium

M. Saeki, T. Hirabayashi, Y. Aratono, M. Nakashima, C. Sagawa, N. M. Masaki, Y. Sun*, P.-J. Zhao*, K.-W. Sung**, M. Naritomi***, H. Nagai***, and S. Okagawa***

*Southwest Institute of Nuclear Physics and Chemistry, China

**Korea Atomic Energy Research Institute, Korea

***Fission Products Safety Laboratory, Department of Fuel Safety Research

5.1 Deposition Behavior of Radio-iodine onto SUS304 Stainless Steel and 2¼ Cr-1Mo Steel Surface

5.1.1 Introduction

Deposition behaviors of radio-iodine onto SUS304 stainless steel and $2^1/_4$Cr-1Mo steel surfaces were investigated. From the viewpoint of environmental safety, radio-iodine release from a nuclear reactor to environment is an important problem. As radio-iodine released from nuclear fuel in a gas-cooled reactor such as the High Temperature Engineering Test Reactor (HTTR) migrates in coolant gas, the interaction, such as adsorption, deposition and chemical reactions, between gaseous radio-iodine and surface of construction materials must be considered. Then we examined iodine deposition temperature by using thermochromatograph technique, in which a temperature gradient from 1173K to room temperature was held in pure He or He containing 10% of oxygen gas(10%O_2/He), and also examined the amount of iodine deposited as a function of iodine concentration in a carrier gas.

5.1.2 Deposition profile of radio-iodine

Radio-iodine molecules, $^{131}I_2$, released from iodine generator were introduced into a sample tube in the temperature gradient column through a nozzle, and were transported by a carrier gas, He or 10%O_2/He. Under flowing 10%O_2/He gas, more than 90% of iodine released was deposited on the SUS304 stainless steel surface at a temperature below 473K. On the other hand, under flowing pure He gas iodine was deposited on the surface at a temperature above 473K with the peaks at about 573K and 773K. These iodine species deposited at a higher temperature region under pure He atmosphere were easily liberated and redeposited on a lower temperature surface around 373K by subsequent flowing of 10%O_2/He gas under the same

temperature gradient condition. These results about the iodine deposition behavior indicate that the iodine species deposited are molecular iodine in $10\%O_2$/He and metal iodide in pure He atmosphere in view of the deposition temperature. Iron iodide(FeI_2) is most probable as a metal iodide[1]. It is plausible that iodine molecules migrate through micro-cracks in oxide layer, and react at a metal-metal oxide interface to form metal iodide. This metal iodide once produced will be easily oxidized under oxygen atmosphere to be liberated as molecular iodine.

In the case of $2^1/_4$Cr-1Mo steel, deposition behavior of iodine in pure He atmosphere was very similar to that in the case of SUS304 stainless steel: The iodine was deposited on the surface at a temperature between 573K and 923K with peaks at 603K and 773K. However, these iodine species was not easily liberated by subsequent flowing of $10\%O_2$/He gas: One hour flowing of the gas resulted in only a slight shift of the deposited iodine toward lower temperature region. Even after 6 hours flowing, most of the iodine was still present on the surface at a temperature above 473K. In these cases, chemical form of iodine deposited under inert atmosphere will be metal iodide as described in the case of SUS304 stainless steel. The fact that replacing He gas to $10\%O_2$/He did not much affect the iodine profile indicates that the iodide is not easily oxidized by oxygen unlike the results in the case of SUS304 stainless steel. This will be attributable to the surface property of $2^1/_4$Cr-1Mo steel which is easily oxidized as compared with SUS304 stainless steel: That is, iodine species will be incorporated into the growing oxide layer[2].

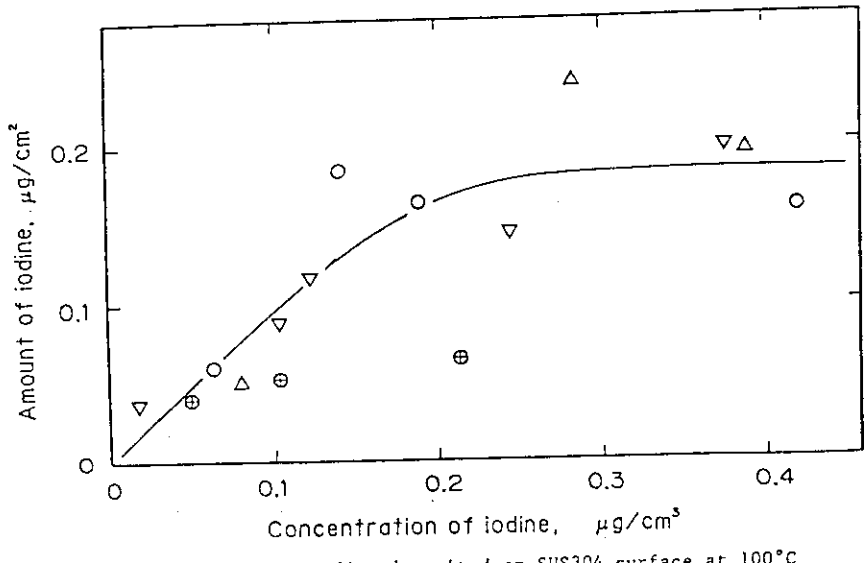

Fig. 1 Amounts of iodine deposited on SUS304 surface at 100°C as a function of iodine concentration in the stream of $10\%O_2$/He.
▽; 20ml/min: ○, ⊕; 50ml/min: △; 100ml/min.

5.1.3 Amounts of iodine deposited

Amounts of iodine deposited on the surfaces of SUS304 stainless steel at a temperature of 373K and of $2^1/_4$Cr-1Mo steel at a temperature of 823K were measured as a function of iodine concentration in 10%O_2/He gaseous phase. The results on SUS304 stainless steel were shown in Fig. 1. The amount of iodine deposited increased with increase of average iodine concentration in gaseous phase, and approached to the steady value of 0.18+0.03ug/cm^2 beyond the iodine concentration of about 0.2μg/cm^3. This value corresponds to monolayer adsorption of iodine with a value of 0.237nm^2 as the adsorption cross-sectional area of iodine molecule[3]. In the case of $2^1/_4$Cr-1Mo steel, 0.21±0.07μg/cm^2 was obtained as a average value of iodine deposition at the gaseous iodine concentration from 0.04 to 0.43μg/cm^3.

References

1) E. Hoinkis, ORNL-TM-2916(1970).

2) J. W. Tyler, J. Nucl. Mater., 161(1989)72.

3) A. L. McClellan and H. F. Harnsberger, J. Colloid and Interface Sci., 23(1967)577.

Publication list

[1] M. Nakashima, M. Saeki, C. Sagawa, N. M. Masaki, T. Hirabayashi and Y. Aratono, "Deposition Behavior of Radio-iodine onto SUS304 Stainless Steel and $2^1/_4$Cr-1Mo Steel Surface", JAERI-M 91-092, (1991).

5.2 Behavior of Radioactive Organic Iodide Under Various Reactor Accident Conditions

5.2.1 Introduction

In the Radiochemistry Laboratory, we have extensively studied iodine chemistry, especially for the mechanisms of organic iodide formation under various circumstances.[1] During last 3 years, two studies on organic iodide have been carried out. One is a study of the behavior of radioiodine in an atmosphere of the High Temperature Engineering Test Reactor (HTTR). The purpose of this study is to evaluate the formation rate of organic iodide during normal operation and under accident conditions of HTTR. The Other is a study for radioactive iodine chemistry during a severe accident of Light Water Reactor (LWR). The purpose of the latter study is to confirm the mechanism for the formation of organic iodide and to obtain the time dependent conversion rate of iodide ion in a water pool to organic iodides.

5.2.2 Behavior of Radioactive Organic Iodide in Atmosphere of HTTR

Most probable chemical form of iodine is CsI at the stage of accident of power plant from nuclear fuel into the primary coolant system. In this experiments, $Na^{125}I$ was chosen for radioactive iodine source instead of CsI, because chemical nature of NaI is very close to that of CsI. $Na^{125}I$ adsorbed on graphite was heated in pure He and He containing O_2 or H_2O atmosphere. The results obtained are as follows.

It was proved that organic iodide was formed with organic radicals released from graphite even in He atmosphere. Thus, the conversion rate of inorganic iodine into organic iodide was remarkably decreased with prolonged preheat-treatment period at 1000 °C. Organic iodide formed was easily decomposed by its recirculation into hot reaction tube kept at 900 °C. When organic iodide was passed through powdered graphite bed, more than 70% was decomposed even at 90 °C. Oxygen and water vapor intermixed in He suppressed the conversion rate of inorganic iodide into organic iodide. Figure 1 shows the effect of O_2 content in He atmosphere on conversion rate of inorganic iodide into organic iodide.

These results suggest that organic iodide rarely exists in the pressure vessel under normal operating condition of HTTR, and, under hypothetical accident condition of HTTR, organic iodide fraction never exceeds the value used for a safety assessment of light water reactor.

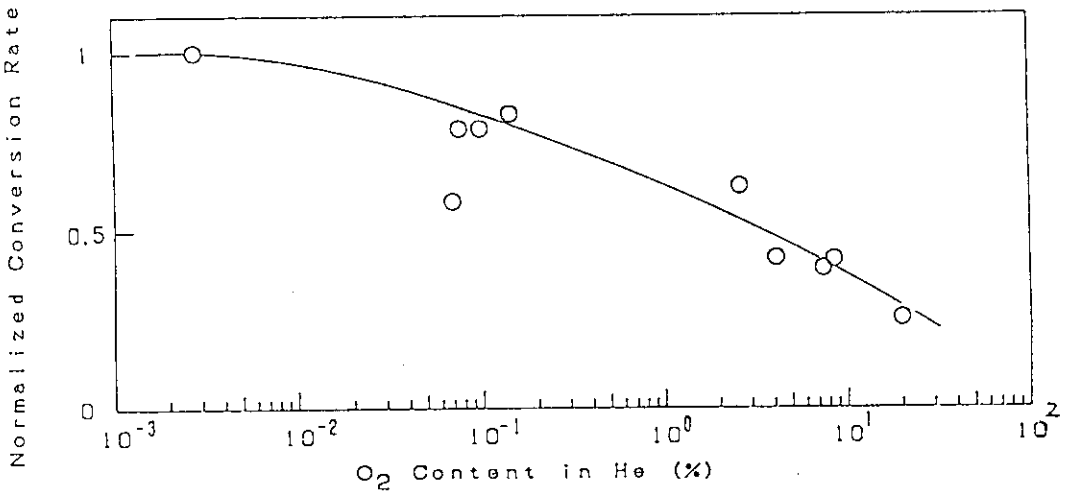

Fig. 1 Effect of O_2 content in He carrier gas on conversion rate of inorganic iodide into organic iodide

5.2.3 Studies on Formation and Transportation of Organic Iodide under Radiation Field

Radiation-induced reactions may be one of the most important factors which control the chemical forms of iodine species after CsI released from failed fuels is dissolved into water pool in containment vessel during a severe accident of LWR. In order to elucidate the relation between formation and transportation of organic iodide under natural and/or forced

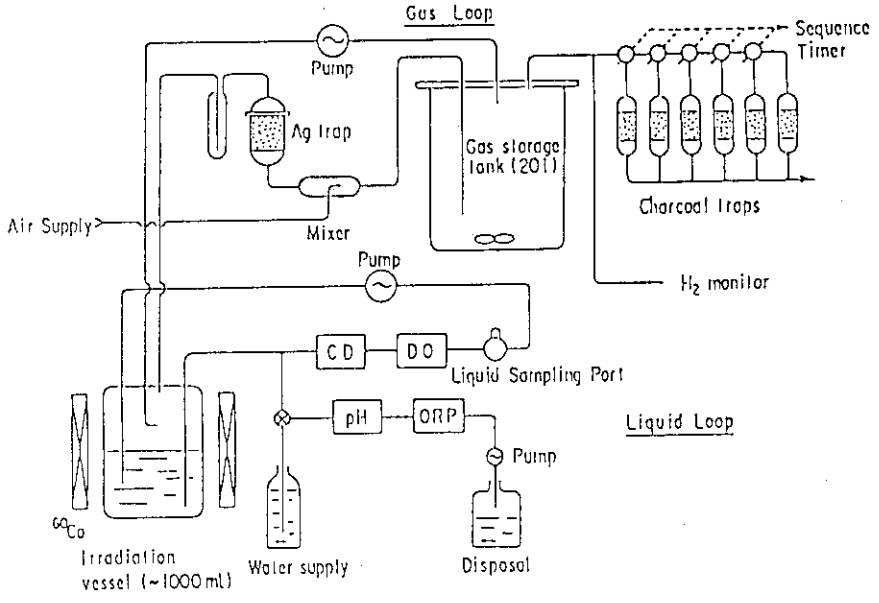

Fig. 2 VITA (Volatile Iodine Test Apparatus) System

convection condition, a test system named as VITA (Volatile Iodine Test Apparatus) has been completed by a joint development between Radiochemistry Laboratory and Fission Products Safety Laboratory.

Schematic representation of the VITA system is shown in Fig. 2. The system consists of about one litter of a main vessel (100mm in diameter x 136mm in height) which is made of Pyrex glass, and two auxiliary loops as shown in the figure. The main vessel is placed in a Gammacell-220 which contains 430 TBq (11,630Ci) of ^{60}Co, and in that test solution can be filled up to 800 ml. The solution is irradiated uniformly at an absorption dose rate of 10kGy/h (10^6 rad/h). The aqueous loop provides a pump for mixing the solution and equipment for measurements of solution pH, redox potential, dissolved oxygen concentration and electric conductivity. Small aliquot of aqueous solution can be periodically taken out in order to analyze chemical forms of iodine in the solution by ion-chromatography. The gas loop has 20 litter of a cylindrical vessel of Pyrex glass, which installs a gas mixer. The loop provides sampling systems for organic iodide and hydrogen formed. The sampling system for organic iodide consists of 6 samplers packed with 5% TEDA (Triethylenediamine) impregnated charcoal, and is sequentially used. The hydrogen gas monitor is an automatic gas sampler and a gaschromatograph with a Molecular sieve-13X column. The flow rate of the loop can be changed from 50 to 2,000 ml/min.

Several experiments were already carried out with 10^{-4} mol/dm^3 of CH_3COOH as an organic additive. Main experimental results were the following. The additive was completely decomposed within 1.5 hours by the γ-ray irradiation at the dose rate of 8 kGy/h. Dissolved oxygen was consumed rapidly in the decomposition process. The equilibrium concentrations of organic iodide and hydrogen gas released were affected by the flow rate of gaseous phase. The higher rate yielded the higher concentration, and reached its equilibrium concentration faster. However, the concentration was less than 10^{-5} (10^{-3}%) of added iodine concentration (10^{-6} mol/dm^3).

Reference

(1) M. Saeki, AERE R 11974, pp317-331, (1986).

Publication List

[1] M. Saeki, M. Nakashima, C. Sagawa, N. M. Masaki, T. Hirabayashi and Y. Aratono, " ehayior of Radioactive Organic Iodide in an Atmosphere of

High Temerature Gas-cooled Reactor", JAERI-M 90-084, (in japanease).

[2] M. Naritomi, H. Nagai, S. Okagawa and M. Saeki, "Studies on Formation and Transport of Volatile Iodine Species in Radiation Field", in : Poc. 3rd CSNI Workshop on Iodine Chemistry in Reactor Safety, Tokai, Ibaraki, Japan, 1991, in press.

5.3 Surface Interaction between Tritium and Materials - Depression of Tritium Sorbability by Surface Modification -

5.3.1 Introduction

The tritium sorbability (ad- and ab-sorbability) of material surface enhances not only the surface tritium contamination but also the tritium penetration. The tritium sorption is the first step of all elementary processes of tritium-material interaction. A considerable quantity of tritium was already reported to be sorbed on the surfaces of various materials[1-3] and to cause many problems in the course of the tritium handling due to the gradual but continuous release of tritium sorbed. The subject of surface interaction between tritium and materials, therefore, arouses much interest, and the depression of the tritium sorbability is one of the key problems to be solved. For the last several years, the surface modification of stainless steel has been studied with the intention of realizing a "tritiophobic surface", on which tritium will be hardly sorbed.

5.3.2 Change in tritium-sorption property of stainless steel by thermal surface oxidation

The surface of stainless steel was thermally oxidized at a constant temperature in the region of 293 - 1073 K and its chemical property and tritium sorbability were examined by X-ray photoelectron spectroscopy and sorption-desorption experiment, respectively. The thermal surface oxidation at 573 - 773 K was found to have a desirable effect on depressing the sorption of tritium. The stainless steel surface was constituted of an outer thin oxide layer and of an inner oxide layer; the former consisted of Fe(III) with trace amounts of Ni(II) and Cr(IV) and the latter of Fe(III)/Fe(II)/Cr(III) containing a small amount of Ni(0). From these experimental results it was inferred that the surface oxidized at several hundreds degrees Kelvin consisted of $Fe(Fe_{1-x}Cr_x)_2O_4$ (x=0-1) of inverse spinel structure covered with thin Fe_2O_3 layer containing trace amounts of CrO_2 and inverse spinel $NiFe_2O_4$ and such a stable surface layer blocked effectively the sorption of tritium onto stainless steel.

5.3.3 Surface Modification by Chromium Electrodeposition Combined with Thermal Oxidation

The surface modification of stainless steel was attempted by a method

of electrodeposition of chromium combined with thermal oxidation. The surface layer formed by the partial oxidation of chromium electrodeposited onto a stainless steel surface was found to be markedly effective in depressing tritium sorbability. The surface layer was determined to be 3 um in thickness; it was constituted of a 0.1 um thick outer layer of Cr(III) in a Cr_2O_3-like state and an inner layer of metallic Cr(0). The surface was observed to be very smooth on a nanometer scale as shown in Fig. 1. From these observations, it was inferred that the depression of tritium sorbability was attained not only by chemical stabilizing of the topmost surface due to the formation of a Cr_2O_3-like state, but also by smoothing on a nanometer scale and probably densifying of the surface layer through the partial oxidation.

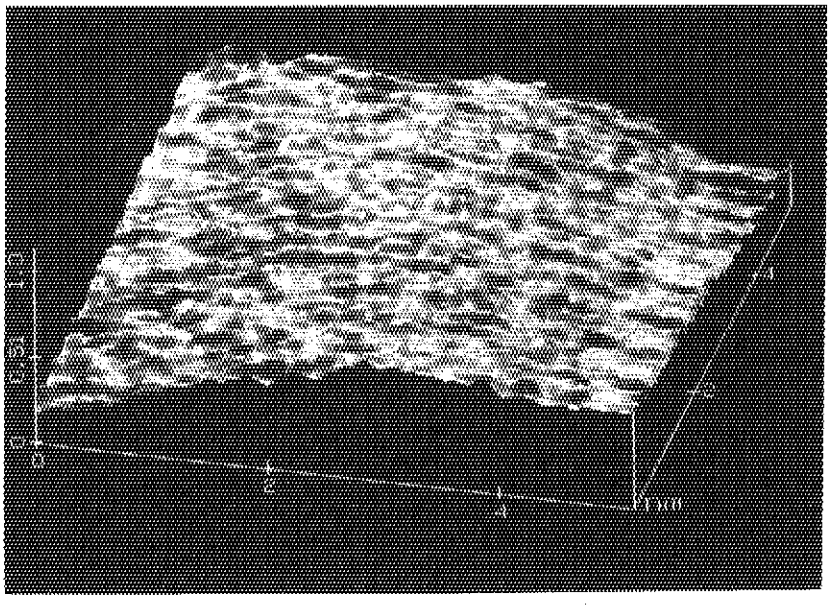

Fig. 1 Scanning tunneling microscopic image of the chromium-deposited and further thermally oxidized stainless surface.

5.3.4 Formation of a tritium-resistant surface of stainless steel by chromium diffusion coating

An attempt was made to invent a "tritiophobic surface" by a method of chromium diffusion coating, and to accomplish the prevention of tritium-contamination of stainless steel surface. The chromium layer was generated on a stainless steel surface from mixed powders of metallic Cr, NH_4Cl and Al_2O_3 in an Ar atmosphere.

The surface layer formed under an optimum condition, to provide an effective surface in suppressing the sorption of tritium, was determined to

be roughly 1.5 um in thickness. The surface layer was constituted of an outer layer of deposited chromium that was covered with very thin passive film of Cr_2O_3-like Cr(III) and an inner diffusion layer which was formed by a mutual diffusion of the deposited chromium and the constituents of stainless steel. These results led to the conclusion that the diffusion coating of the surface with chromium brought the chemical stability and probably the higher density of surface layer, and that the resulting thin stable double layer was realized as a durable and tritium-resistant surface of stainless steel.

An effective surface suppressing the tritium sorption was obtained for types 316, 304, 316L and 321. In particular, for the titanium-containing type 321 stainless steel with a high tritium sorbability, the tritium sorption was considerably reduced, although the coated surface was roughened by the chromium deposition in the form of cluster. It was found that the resistance for tritium sorption was due to the formation of the stable double layer covered with passive film of several nm thick for every type of stainless steel.

References

1) T. Hirabayashi, M. Saeki and E. Tachikawa, Proc. Inter. Symp. on Fusion Reactor Blanket and Fuel Cycle Technology, Tokai, 1986, p. 213.
2) T. Hirabayashi, M. Saeki, T. A. Sasaki and K.-W. Sung, J. Fusion. Eng. Design, 10(1989)287.
3) N. M. Masaki, T. Hirabayashi and M. Saeki, Fusion Technol., 15(1989)1337.

Publication List

[1] T. Hirabayashi, S. Poosittisak, Y. Sun and M. Saeki, "Tritium Sorption and Chemical and Topographical Properties of a Stainless Steel Surface Modified with Chromium", J. Nucl. Mater., 173(1990)26.
[2] T. Hirabayashi, T. Sato, C. Sagawa, N. M. Masaki, M. Saeki and T. Adachi, "Distribution of Radionuclides on and in Spent Nuclear Fuel Claddings of Pressurized Water Reactor", J. Nucl. Mater., 174(1990)45.
[3] T. Hirabayashi, K.-W. Sung, T. A. Sasaki and M. Saeki, "Change in Tritium-Sorption Property of Stainless Steel by Thermal Surface Oxidation", J. Nucl. Mater., 175(1990).
[4] T. Hirabayashi, Y. Sun and M. Saeki, "Formation of a Tritium-Resistant Surface of Stainless Steel by Chromium Diffusion Coating", J. Nucl.

Mater., 175(1990).

[5] T. Hirabayashi, T. Sato, C. Sagawa, N. M. Masaki, M. Saeki and T. Adachi, "Radioactivities on/in Zircaloy Claddings of PWR Spent Nuclear Fuel", The Third International Conference on Nuclear Fuel Reprocessing and Waste Management, Proceedings Vol. II, Sendai, 1991, p.903.

[6] T. Hirabayashi, Y. Sun, H. Yamamoto, Y. Toida and M. Saeki, "Chemical and Topographical Properties of Tritium-Resistant Stainless Steel Surface Formed by Chromium Diffusion Coating", J. Nucl. Mater., 182(1991)135.

[7] M. Saeki, T. Hirabayashi, Y. Aratono, M. Nakashima, N. M. Masaki and E. Tachikawa, "Chemical Behavior of Tritium in/on Various Materials", Fusion Technol., in press.

5.4 Study on chemical reactions including a tunneling effect at low temperatures

A radical appears as an intermediate in a process of chemical reactions and plays an important role in it. Because of its high reactivity, its life time is generally very short. A various experimental technique enables us to detect it, namely absorption, luminescence, etc. In this work, we adopted a method of electron spin resonance (ESR) for direct detection of radicals. Radio-gaschromatography was also adapted for analysis of products of Tritium (T) atom reactions. A reaction including thermalized radicals can not proceed quickly at low temperatures such as 4K. A radical is easily trapped in a non-reactive matrix such as rare gas solid at low temperatures. But if a radical such as a hydrogen atom has a large quantum effect, it has a large probability enough to cause a reaction even at low temperatures. Miyazaki et al. reported that an abstraction reaction of hydrogen atom occurs in the case of mixtures of H_2 and D_2 at 4K.[1] They observed an increase in the concentration of H atoms accompanied by decay of D atoms and concluded that the reaction $D + H_2 \rightarrow DH + H$ occurs in this system. A group in Moscow has studied the reaction of H(D) atoms produced by an rf discharge.[2] They observed the time evolution of the concentrations of H and D atoms in the mixture with a concentration of H_2 molecules in the range 1-4 %. Both groups explained their experimental data in terms of quantum mechanical diffusion of trapped hydrogen atoms. They concluded diffusion of H atoms in solid H_2 was due to an atom exchange reaction caused by a quantum mechanical tunneling mechanism. According to the Arrhenius rule, an ordinary chemical reaction cannot occur at low temperatures, namely 4K. The tunneling mechanism means that the reaction proceeds without overcoming an activation energy of the reaction.

The reaction $H + H_2$ has been investigated theoretically and experimentally.[3] A potential energy surface of this reaction was obtained by calculation of ab initio method. We can calculate thermal rate constants in gas phase at various temperatures on this potential energy surface including the tunneling effect.[4] On Arrhenius plot of this result, we can observe a large deviation from the linearity at low temperatures. We will select a proper matrix which can trap hydrogen atoms in it and observe the temperature dependence of the rate constant of a reaction of hydrogen atom or other radicals. Gamma-ray irradiation of hydrogen and the photolysis of hydrogen halide can produce trapped hydrogen

atoms. Tritium (T) atoms can be also produced by neutron irradiation of helium or lithium. The purposes of this study are to confirm this deviation from Arrhenius plot of experimental data of the rate constant and to investigate the process in which hot (translationally excited) atoms are deactivated by matrix.

Recoil T-atom reactions were studied in Xe-H_2-D_2 mixtures at 77K. T atoms were produced by neutron irradiation of lithium in the JRR-4 reactor. The isotope effect on the T-atom reaction with H_2 and D_2 ($k(T + H_2 \rightarrow TH + H)/k(T + D_2 \rightarrow TD + D)$) was measured on the basis of the HT and DT yields.(Fig. 1) The isotope effect($k(T + H_2)/k(T + D_2)$) is 1.1 in the range of hydrogen concentrations of 0.1 - 1.0 mol%. Since the small isotope effect (1.1) is similar to the isotope effect(1.0) for a hot T-atom reaction in the gas phase, recoil T atoms are not thermalized at these concentrations in solid xenon and form HT and DT by means of hot-atom reactions. At concentrations of hydrogen of less than 0.1 mol%, the recoil T atoms are thermalized before they encounter the solute hydrogen. The isotope effect increases with a decrease in the hydrogen concentration and amounts to 3.1 at a hydrogen concentration of 0.01 mol%. Since a large quantum effect is expected for the abstraction reaction of T atoms at 77K, the large isotope effect(3.1) at 0.01 mol% hydrogen was interpreted in terms of the reaction of thermalized T atoms due to a quantum mechanical tunneling mechanism. The present results in the solid xenon-hydrogen mixtures were compared with those in the gaseous xenon-hydrogen mixtures reported previously.[5] It was concluded that hot T atoms in the solid xenon at 77 K are deactivated much less effectively than in the gas phase and that they migrate long distances with excess kinetic energies.

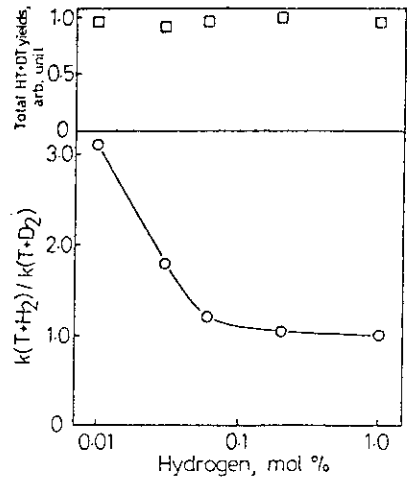

Fig.1 Concentration dependence of the isotope effect ($k(T+H_2)/k(T+D_2)$) for recoil T atom reaction in xenon-hydrogen mixture at 77 K (o). Upper figure: total yields of HT and DT (□).

Reaction of recoil T atoms were studied in solid H_2-D_2 mixtures at 4.2K. The fraction of HT in the sum of HT and DT yield, [HT]/([HT]+[DT]), is roughly equal to the mole fraction of H_2 in the H_2-D_2 mixtures.(Fig. 2) These yields were compared with the yields of H atoms produced by γ-ray radiolysis of the H_2-D_2 mixtures at 4.2K. From the comparison, it was

concluded that formation of HT could not be due to combination of thermalized T atoms with hydrogen atoms from γ-ray radiolysis of solid hydrogen during reactor irradiation but must be due to the abstraction reaction of hydrogen atom by recoil T atom from H_2 and D_2. In the abstraction reaction of hydrogen atom by thermal T atoms due to quantum mechanical tunneling, a large isotope effect, i.e., a large value of $k(T + H_2)/k(T + D_2)$, is expected at 4.2K, while $(k(T + H_2)/k(T + D_2))$ is about 1.0 in the hot T atom reaction. From the difference in isotope effects between the hot atom reaction and the thermal atom reaction it was concluded that more than 90% of recoil T atoms react with hydrogen by a hot atom reaction in solid hydrogen at 4.2K before completing their thermalization under this experimental condition.

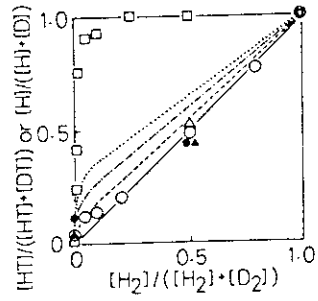

Fig.2 Fractions of HT yields produced by recoil T atom reaction and those of H atom yields produced by γ-radiolysis in the solid H_2-D_2 mixtures at 4.2 K. (○,▲,●) HT yields in the H_2-D_2 mixtures of 1.4×10^{-5} mol (○), 8.4×10^{-7} mol (▲), 1.4×10^{-7} mol (●); (△) HT yields in solid HD; (□) H atom yields in the radiolysis of H_2-D_2 mixtures. Curves are HT yields calculated for hot product yields of 1.0 (—); 0.9 (---); 0.8 (-·-), and 0.7 (···).

Miyazaki et al. have studied the effect of reagent rotational energy on the rate constant for the H + H_2 reaction at low temperatures using para and normal hydrogen.[6] They have reported that the rate constant of the H + $H_2(j = 0)$ reaction is about three times larger than that of the H + $H_2(j = 1)$ reaction at 4.2 K, where j is the rotational quantum number of the diatomic hydrogen molecule. The simplest model for the effect of rotaional energy on the reaction rate would be that the reaction barrier height of the H + $H_2(j = 1)$ reaction is smaller than that of the H + $H_2(j = 0)$ reaction by the difference in the rotational energy. It might then simply be expected that the reaction probability for H + $H_2(j = 1)$ is larger than that for H + $H_2(j = 0)$ at the same translational energy. We have calculated the reactive probabilities for the H + $H_2(j = 0, 1) \rightarrow H_2(j' = 0, 1)$ + H reactions at low rotational energies using a simplified J_z-conserving coupled-states method. Both the LSTH[7] and the PK2[8] potenial energy surfaces are used. The energy where the Wigner threshold behavior[9,10] appears is affected both by the existence of van der Waals well included in the potential surface and by the rotational state of H_2. Thermal rate constants at low temperatures are calculated for the H + para,

ortho-H_2 reactions, and the calculated values are compared with the experimental results in solid phase reported by Miyazaki et al.[6] Our computational results on the LSTH potential at 4.2K show that the rate constant calculated for H + H_2(j = 0) was larger than that for H + H_2(j = 1) at lower temperature than 4.2K.(Fig. 3) For the PK2 potential, however, this trend cannot be observed; the rate constant for the H + H_2(j = 0) reaction is smaller than that for the H + H_2(j = 1) reaction at any temperature. Thus, the present results suggest that a van der Waals well is needed for estimating the rate constants at low temperatures. At the same time, the experimental data and computational results may be viewed to be consistent. Nevertheless, the qualitative agreement obtained in the present paper is probably, in part, fortuitous since we ignored not only the effect of solid phase environment but also several other effects such as particle indistinguishability.[11]

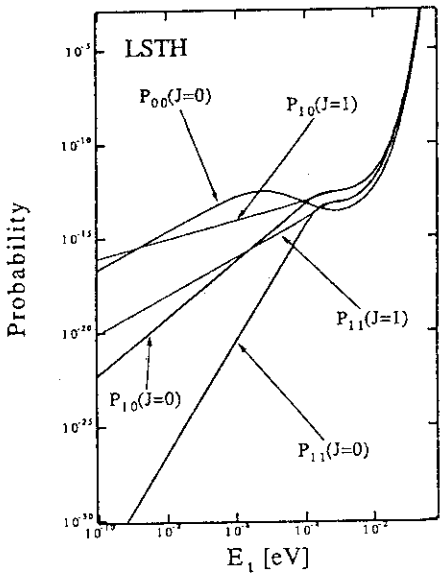

Fig.3 Temperature dependence of rotationally state-to-state thermal rate constants $k_{jj'}(T)$ for the H + H_2(v = 0,j) -> H_2(v' = 0,j') + H on the LSTH potential.

H or D atoms produced by photolysis of HI or DI have been studied in solid hydrogen(H_2 or D_2) at 4.2 K. Thermalized hydrogen atoms in solid hydrogen were observed by ESR measurement. The concentration of trapped H atoms decreased half an initial value for about 10 min in solid H_2 and did not decrease in solid D_2. The concentration of trapped D atoms did not decrease in solid D_2. The ESR signal of D atoms cannot be observed after photolysis of DI in solid H_2. Instead of D atoms, H atoms were trapped in solid H_2. The preferential formation of H atom in solid H_2 is due to the reaction D + H_2 → DH + H caused by quantum mechanical tunneling mechanism.

References

1) T. Miyazaki, K. P. Lee, K. Fueki and A. Takeuchi, J. Phys. Chem., 88(1989)4959.

2) A.V. Ivliev, A.Y. Katunin, I.I. Lukashevich, V.V. Sklyarevskii, V.V. Suraev, V.V. Filippov, N.I. Filippov and V.A. Shevtsov, Zh. Eksp. Teor. Fiz. 89 (1985) 2197.

3) G.C. Schatz, Annual Rev. Phys. Chem. 39 (1988) 317.

4) T. Takayanagi, N. Masaki, K. Nakamura, M. Okamoto, S. Sato and G.C. Schatz, J. Chem. Phys., 86(1987)6133.

5) D.J. Malcome-Lawes, "Hot Atom Chemistry," ed. by T. Matsuura, Elsevier Science Publishers and Kodansha, Tokyo(1984), p. 39, and related papers are cited therein.

6) T. Miyazaki, T. Hiraku, K. Fueki and Y. Tsuchihashi, J. Phys. Chem., 95(1991)26.

7) D.G. Truhler and C.J. Horowitz, J. Chem. Phys., 68(1978)2466.

8) R.N. Porter and M. Karplus, J. Chem. Phys., 40(1964)1105.

9) E.P. Wigner, Phys. Rev., 73(1948)1002.

10) D.W. Schwenke and D.G. Truhler, J. Chem. Phys., 83(1985)3454.

11) G.C. Schatz and A. Kuppermann, J. Chem. Phys., 65(1976)4642.

Publication list

[1] Y. Fujitani, T. Miyazaki, K. Fueki, N. M. Masaki, Y. Aratono, M. Saeki and E. Tachikawa, "The Moderation and Tunneling Reaction of Recoil T atoms in Solid Xenon-Hydrogen Mixtures at 77K," Bull. Chem. Soc. Jpn., 63(1990)520.

[2] Y. Fujitani, T. Miyazaki, K. Fueki, N. M. Masaki, Y. Aratono, M. Saeki and E. Tachikawa, "Recoil Tritium Reaction in Solid Hydrogen at Ultralow Temperatures," J. Phys. Chem., 95(1991)1651.

[3] T. Takayanagi and N. Masaki, "Dynamical calculation for the H + para, ortho-H_2 reactions at low temperatures: Effect of rotational energy of reagent H_2 molecule," J. Chem. Phys., 95(1991)4154.

6. STUDIES ON CHEMICAL REACTIONS INDUCED BY ENERGETIC PARTICLES

Y. Aratono, C. Sagawa, M. Nakashima, M. Nakada, N. M. Masaki
M. Saeki, E. Ibe*, O. Kuriyama*, S. Uchida* and T. Miyazaki**

* Energy Research Laboratory, Hitachi Ltd.
** Department of Synthetic Chemistry, Faculty of Engineering, Nagoya University

6.1 Chemical Reactions Induced by Nuclear Recoil and Ion Bombardment in Iron Oxides

6.1.1 Introduction

The chemical reactions induced by energetic particles were investigated in the solid and liquid phases.

The solid-phase experiments were performed with two purposes; (1)the understanding of the chemical reactions initiated by energetic particles in solid materials and (2)the fundamental study on the new methods for chemical energy production applying the chemical reactions induced by energetic particles. In order to meet the above two requirements, iron oxides were chosen as the samples, because Fe_3O_4 - FeO redox cycle has been considered to be the most practical one for the production of H_2 from water using D-T fusion neutron[1].

The liquid-phase experiment concerns with chemical behavior of ^{16}N formed in the light water reactors through fast neutron absorption by ^{16}O from viewpoints of radiation protection and is the cooperation study with Hitachi Ltd.. Nitrogen-16 is a radioactive nuclide with half-life of 7.1 seconds and decays to ^{16}O, emitting gamma ray of about 6 MeV. The movement of ^{16}N to a turbine system in a boiling water reactor causes an additional exposure of radiation to workers. Thus, the study was focused mainly on the clarification of formation mechanisms of ^{16}N-labeled products in order to suppress the movement of ^{16}N to the turbine system.

6.1.2 Chemical Effects of Thermal Neutron Irradiation on α-$LiFeO_2$

Chemical effects of energetic recoil particles were studied in α-$LiFeO_2$ enriched with ^6Li which served as the source of energetic

particles through $^{6}Li(n,\alpha)^{3}H$ nuclear reaction. The sample was irradiated in the S-pipe of the JRR-4 with a nominal thermal neutron flux of 5×10^{17} $m^{-2} \cdot s^{-1}$ for 3 to 12 hours at the cooling water temperature(about 320K). The Mössbauer spectra were measured at room temperature using a standard absorption method by a constant acceleration with ^{57}Co source.

The Mössbauer spectra taken before (A) and after (B) thermal neutron irradiation are shown in Fig. 1 together with the spectrum of magnetite(Fe_3O_4, (C)). From the comparison of(A), (B) and (C), it is concluded that the new peaks in (B) can be identified as Fe_3O_4. The Mössbauer spectra obtained from various irradiation fluences were almost same as (B) in peak velocity, but the relative intensity of the product against the parent material depended on the irradiation fluence, showing formation of magnetite in the entire range of the thermal neutron fluences. Four reasons will be considered for formation of Fe_3O_4. The first is the chemical effect caused by ^{3}H and ^{4}He formed with very high recoil energy from the $^{6}Li(n,\alpha)^{3}H$ reaction, the second is the effect of the FeO_2^- ion remaining after nuclear transformation of ^{6}Li, the third is the influence of the reactor radiations such as gamma rays and fast neutrons, and the fourth is a thermochemical reaction of the sample induced by heat evolved by the nuclear reaction. As the number of Fe atoms changed to magnetite is about 10^3 times that of the FeO_2^- ion, the effect of the FeO_2^- ion is considered to be negligible. No change was observed by the irradiation of α-$LiFeO_2$ having natural ^{6}Li isotopic ratio under the same irradiation condition with the ^{6}Li-doped sample and also by out-pile thermal annealing experiments. Therefore, the reaction induced by $^{6}Li(n,\alpha)^{3}H$ is mostly responsible for the formation of magnetite. The G value for the formation of magnetite, $G(Fe_3O_4)$, which is defined as the

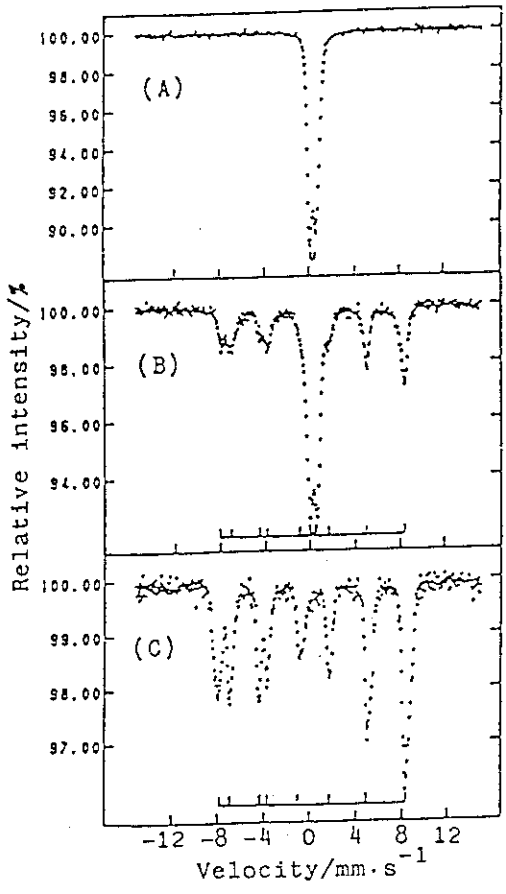

Fig. 1 Mossbauer spectra of the samples.
(A) : Before irradiation
(B) : After irradiation
(C) : Magnetite

number of magnetite formed per 100 eV of incident energy by the $^{6}Li(n,\alpha)^{3}H$ reaction(4.7 eV) is initially 10^{-2} and decreases to 10^{-3} at a fluence of 3 x 10^{22} m^{-2}.

The most interesting point of the present study is the specific formation of magnetite. Though the reaction path leading to the formation of magnetite is not clear at present, the present result may suggest that the reaction of the radiolysis products in the hot zone occurs specifically, not in a random manner, in spite of the random configuration of the radiolysis products within the hot zone immediately after formation by the energetic recoil particles.

6.1.3 Chemical Reactions Induced by 40 keV He^{+} Ions in Fe_3O_4 and α-Fe_2O_3

Chemical reactions induced by ion bombardment have been mainly studied from viewpoints of a clarification of sputtering phenomena and a modification of the surface properties by XPS, AES, etc. As for the reactions induced inside the solid, non-destructive analysis of the reaction products has not been established compared to surface analysis and which makes quantitative explanation of reaction mechanism difficult. Mössbauer spectroscopy is virtually the non-destructive analysis method and thus gives the unperturbed chemical and physical states of the reaction products. In the present experiments, conversion electron Mössbauer spectroscopy(CEMS) was applied to the study of the chemical effects of He^{+} ion bombardment on iron oxides. As the mean probing range of 7.3 keV conversion electrons is about 100 nm in the iron oxide, the results given in the present study show the chemical state of iron from the surface to about 100 nm depth, which corresponds to about 1/3 of range of 40 keV He^{+} ions.

The target grade sintered Fe_3O_4 and α-Fe_2O_3 with a purity level of more than 99.9% were bombarded from 1.9 x 10^{17} to 4.4 x 10^{18} ions·cm^{-2}(5-120 min) at 300-320 K. CEMS was carried out with a gas flow conversion electron detector at room temperature. The TRIM computer program code was used for the simulation of the slowing down and scattering of He^{+} ions in the target[2].

Magnetite was formed in case of α-Fe_2O_3, whereas no change was observed in Fe_3O_4. Fig. 2 shows the change of Mössbauer spectra of bombarded α-Fe_2O_3 as a function of fluence. The preliminary experiments on the thermochemical behavior of α-Fe_2O_3 and Fe_3O_4 showed that α-Fe_2O_3 was

reduced to Fe_3O_4 at about 1300 K, whereas Fe_3O_4 remained unchanged under about the same oxygen pressure as that under bombardment. The different behavior of α-Fe_2O_3 and Fe_3O_4 against ion bombardment agrees with the phase diagram of the Fe-O system. Though the definite explanation cannot be drawn from the thermochemical experiments alone, one of the plausible reasons for the different behavior may be ascribed to the thermal effects caused due to the hot zone created along the ion trajectory. The relative areal intensity was plotted against the fluence in Fig. 3. As is seen in the figure, the amount of Fe_3O_4 increases linearly in the initial stage and all of α-Fe_2O_3 is converted into Fe_3O_4 at the fluence of 4.4 x 10^{18} ions. The initial G value for the formation of Fe_3O_4 was calculated to be 3.5 x 10^{-4} using the linear portion of Fig. 3. The value from the present experiment is a differential one ranging from the surface to 100 nm depth in contrast with the integrated values generally obtained. As will be discussed below, the differential G value will be more useful than the integrated one for the elucidation of the reaction mechanism. According to the collision theory, the energy loss of energetic ions is controlled by two processes, the elastic collisions leading to atomic displacements and the inelastic collisions leading

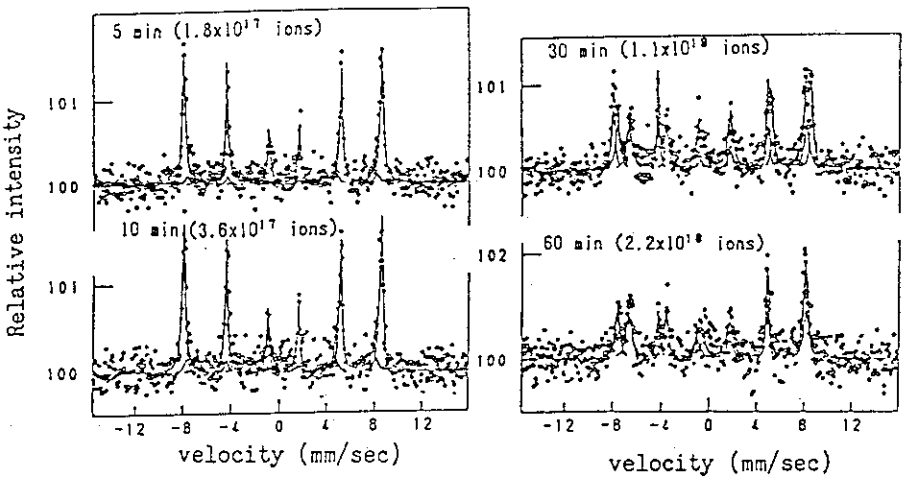

Fig. 2 Change of Mossbauer spectra with bombardment fluence.

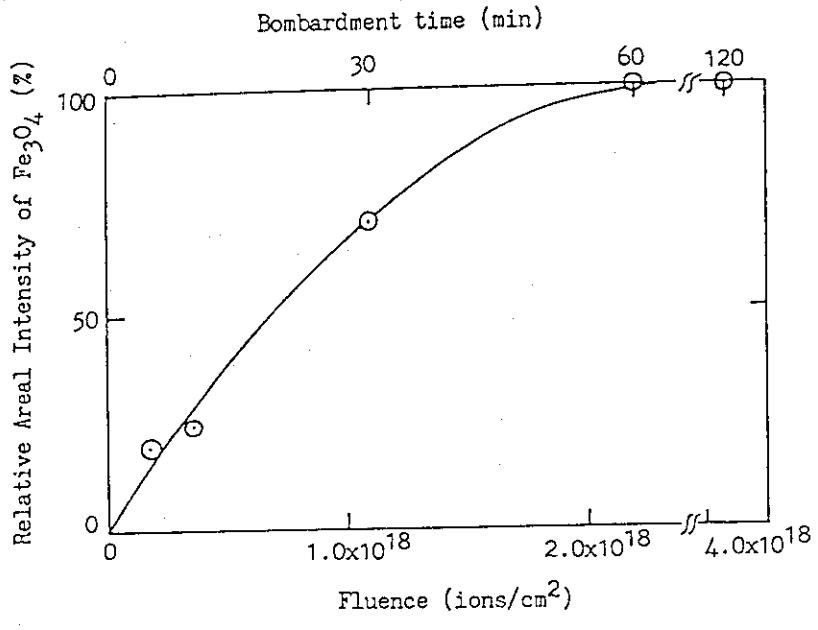

Fig. 3 Relative areal intensity of Fe_3O_4 as a function of bombardment fluence.

to electronic excitation. The relative importance of these processes for product formation has been one of the topics of radiation chemistry and the different distribution of the products has been reported as a function of the ratio$(s_e)_t/(s_n)_t$, where $(s_e)_t$ and $(s_n)_t$ mean the total stopping powers for inelastic and elastic processes[3-5]. On the other hand, as is predicted by the collision theory, the ratio $(s_e)_d/(s_n)_d$, where $(s_e)_d$ and $(s_n)_d$ are stopping powers at given depth, becomes smaller with the depth of the trajectory. This suggests that the chemical state of the product may vary with depth. The combination of CEMS with sputtering by few keV Ar^+ ions will enable the measurement of the depth profile of the products for every 100 nm. The comparison of the depth profile thus obtained with energy loss processes will give the differential G value and which will give more detailed information on the chemical reactions induced by the energetic particles. From such a point of view, the investigation is now in progress.

6.1.4 Chemical Behavior of Recoil ^{16}N Formed by Fast Neutron Irradiation on Various Aqueous Solutions

As the threshold energy of $^{16}O(n,p)^{16}N$ reaction is 9.62 MeV, the Tandem accelerator of JAERI was used to produce such high energy neutrons through $D(d,n)^3He$ reaction, where D and d indicate D_2 target gas and d^+ ion accelerated up to about 14 MeV, respectively. The estimated neutron flux was about 10^{11} $m^2 \cdot s^{-1}$. Fig. 4 shows a schematic view of the experimental set up. During the irradiation, the aqueous solution was circulated through the cell at a constant flow rate of 0.65 $ml \cdot min^{-1}$. Pure He gas was continuously bubbled through the cell at a flow rate of 2.2 $l \cdot min^{-1}$ to extract gaseous ^{16}N species into the gas phase. The γ-radioactivity of ^{16}N in the aqueous and gaseous phases was measured by conventional γ-ray spectrom-

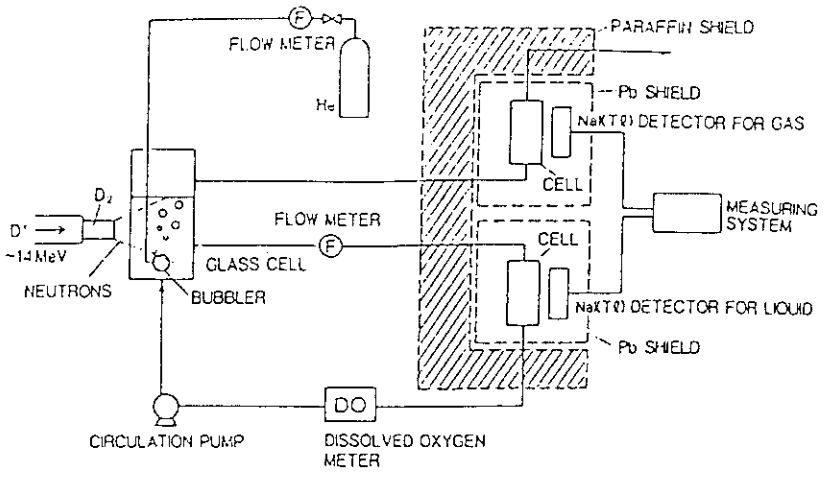

Fig. 4 Block diagram of experimental setup.

eter equipped with 3" x 3" NaI(Tl) detectors.

In Fig. 5 is shown gas to liquid partition ratio of ^{16}N against pH measured after the irradiation for various aqueous solutions (10^{-4} - 10^{-6} mol·l^{-1}). The ratios are scattered in the range between the broken lines, but obviously decrease with an increase in pH. This trend is qualitatively identical with earlier work in BORAX III[6]. These results suggest that the formation of gaseous ^{16}N can be suppressed by adjusting the cooling water to be alkaline, though the various technical difficulties must be conquered in the actual water cooled reactors.

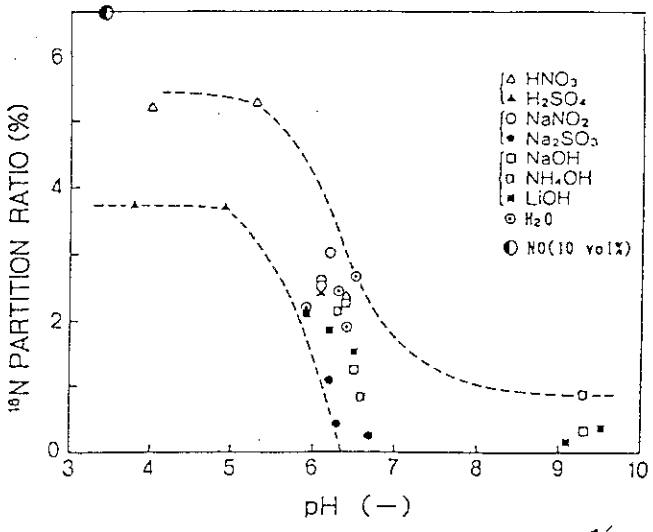

Fig. 5 Gas-to-liquid partition ratios of ^{16}N as a function of pH.

When 10 vol% of NO was added to He gas, the partition ratio increased by 30% against that from nitric acid solution. The concentration of NO_2^- in the NO-added solution is 10^3 higher than those for nitric acid solutions after bombardment. This may imply that NO_2^- is the precursor of the gaseous products. However, though the amount of NO_2^- in 10^{-4} mol·l^{-1} $NaNO_2$ solution is more than 250 times that of nitric acid solution, the partition ratios are lower than those in the nitric acid. Therefore, it is considered that the formation of the gaseous product is controlled by the synergetic effects invoked by the concentration of NO_2^- and acidity of the solutions. The numerical calculation on the formation mechanism of ^{16}N-labeled products partly supported the above consideration[7].

References

1) M. Steinberg and Vi-Duong Dang, BNL-24209(1978).
2) J. P. Biersack and L. G. Hagmark, Nucl. Instruments and Methods, 174(1980)257.
3) O. Puglisi, G. Marletta and A. Torrisi, Radn. Effects, 65(1982)11.
4) S. Ohno and K. Furukawa, Bull. Chem., Soc., Jpn., 58(1985)1100.
5) S. Ohno, K. Furukawa and T. Soga, idem., 59(1986)1947.

6) C. R. Breden, ANL-6562(1963).
7) E. Ibe, et al., J. Nucl. Sci. Technol., 26(1989)844.

Publication list

[1] Y. Aratono, C. Sagawa, M. Nakashima, M. Saeki and T. Sato, "Chemical Effects of Thermal Neutron Irradiation on α-$LiFeO_2$" Chemistry Letters, 1990, p. 35.

[2] Y. Aratono, C. Sagawa, M. Nakashima, M. Nakada, K. Hojou and M. Saeki, "Chemical Reactions Induced by 40 keV He^+ Ions in Fe_3O_4 and α-Fe_2O_3", Hyperfine Interactions, in press.

[3] E. Tachikawa, S. Ohno, M. Hoshi, M. Saeki, Y. Aratono, M. Nakashima, S. Ichikawa, N. Shinohara, Y. Yamanouchi, M. Mizumoto and S. Uchida et al(Hitachi Ltd.). "Chemical Behavior of Recoil ^{16}N Formed by Fast Neutron Irradiation on Various Aqueous Solutions", JAERI TANDEM< LINAC & V.D.G. ANNUAL REPORT, JAERI-M 90-139 (1989) p. 35.

[4] E. Ibe, O. Kuriyama, S. Uchida, Y. Aratono, N. Shinohara., M. Nakashima, S. Ichikawa, M. Saeki, M. Hoshi, Y. Yamanouchi and M. Mizumoto, "Gaseous Mass Transfer of Nitrogen-16 from Aqueous Solutions at Ambient Temperature", J. Nucl. Sci. Technol., 2(1991)162.

6.2 Aftereffects of EC decay in ^{57}Co-labeled complexes

6.2.1 Introduction

It is known that chemical environment of daughter atoms produced by nuclear transformation is frequently different from that of parent atoms[1),2)]. Emission Mössbauer spectroscopy gives us unique chemical information of ^{57}Fe-species after EC decay of ^{57}Co. The spectroscopy enable us to observe short-lived unstable species which have the mean lifetime of comparable order of magnitude to the mean lifetime of Mössbauer resonance state. The more detailed information of ^{57}Fe decayed from ^{57}Co can be obtained by emission Mössbauer spectroscopy using coincidence technique[3),4)].

6.2.2 Mixed-valence states of ^{57}Fe atoms produced in ^{57}Co-labeled $[CoFe_2O(CH_2ICO_2)_6(H_2O)_3]$ and $[CoFe_2O(CH_2BrCO_2)_6(H_2O)_3]$

Based on the studies of the temperature-dependent absorption Mössbauer spectroscopy, it has been known that the mixed-valence state of iron atoms in trinuclear iron carboxylate complexes depends on a kind of ligands, such as H_2O and pyridine derivatives, and carboxylate anions[5)-7)]. Typical absorption Mössbauer spectra are presented in Figs. 1 and 2 for $[Fe_3O(CH_2ICO_2)_6(H_2O)_3]$ and $[Fe_3O(CH_2BrCO_2)_6(H_2O)_3]$, respectively. $[Fe_3O(CH_2ICO_2)_6(H_2O)_3]$ show a temperature-dependent trapped-to-averaged valence state, while $[Fe_3O(CH_2BrCO_2)_6(H_2O)_3]$ show a temperature-independent trapped valence state. The order of the electron withdrawing property of the carboxylate groups is known, but the temperature dependence does not correspond to the order. The results indicate that the intermolecular interaction predominates rather than the electron withdrawing property of the ligand in the rate of the intermolecular electron transfer.

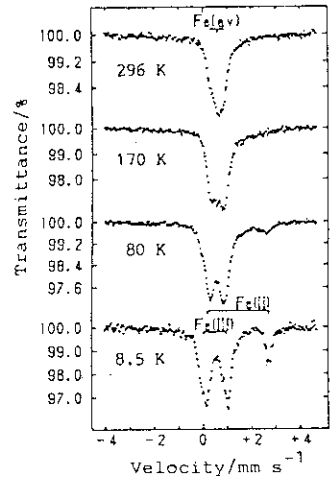

Fig.1 Absorption Mössbauer spectra of $[Fe_3O(CH_2ICO_2)_6(H_2O)_3]$.

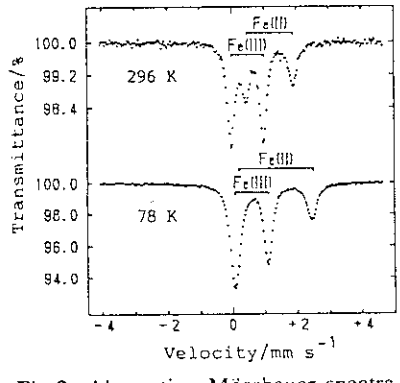

Fig.2 Absorption Mössbauer spectra of $[Fe_3O(CH_2BrCO_2)_6(H_2O)_3]$.

In the case of trinuclear cobalt-iron complexes, $[CoFe_2O(CH_2ICO_2)_6(H_2O)_3]$ and $[CoFe_2O(CH_2BrCO_2)_6(H_2O)_3]$ are isomorphous to the analogous trinuclear iron complexes $[Fe_3O(CH_2ICO_2)_6(H_2O)_3]$ and $[Fe_3O(CH_2BrCO_2)_6(H_2O)_3]$, respectively. Emission Mössbauer spectra of ^{57}Co-labeled $[CoFe_2O(CH_2ICO_2)_6(H_2O)_3]$ and $[CoFe_2O(CH_2BrCO_2)_6(H_2O)_3]$ are shown in Figs. 3 and 4, respectively. The valence

states of decayed ^{57}Fe atoms shown in Fig. 3 are found to be temperature-dependent as found in the absorption Mössbauer spectra of Fig. 1. The valence states of decayed ^{57}Fe atoms shown in Fig. 4 are found to be trapped in iron(II) and iron(III) states even at room temperature, and which are essentially different from Fig. 3. The line width of spectral components in the emission Mössbauer spectra is much broader than that found in the absorption Mössbauer spectra probably because of nucleogenic local disturbance associated with the EC decay[7]. Since the temperature dependence of the valence states observed in ^{57}Co-labeled $[CoFe_2O(CH_2ICO_2)_6(H_2O)_3]$ and $[CoFe_2O(CH_2BrCO_2)_6(H_2O)_3]$ corresponds to that observed in $[Fe_3O(CH_2ICO_2)_6(H_2O)_3]$ and $[Fe_3O(CH_2BrCO_2)_6(H_2O)_3]$, it is reasonable to conclude that the EC decay should have little after effects particularly on the mixed-valence state, although some local disturbances are produced by the nuclear transformations.

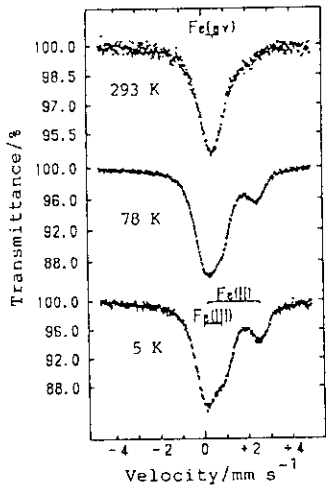

Fig.3 Emission Mössbauer spectra of ^{57}Co-labeled $[CoFe_2O(CH_2ICO_2)_6(H_2O)_3]$.

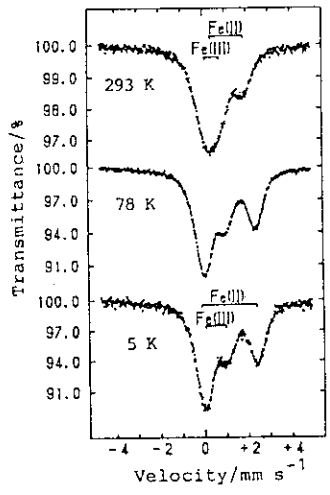

Fig.4 Emission Mössbauer spectra of ^{57}Co-labeled $[CoFe_2O(CH_2BrCO_2)_6(H_2O)_3]$.

6.2.3 Chemical states of ^{57}Fe atoms after EC decay of ^{57}Co-labeled $Co(BrO_3)_2 \cdot 6H_2O$ studied by coincidence Mössbauer spectroscopy

The time differential (delayed coincidence) Mössbauer spectroscopy shows the behavior of ^{57}Fe-species decayed from ^{57}Co in labeled compounds as a function of time[8)-10)]. As other use of coincidence technique, KX-ray gated (X,γ-ray coincidence) Mössbauer spectroscopy shows different chemical effects between the KX-ray emission and Auger electron emission during the deexcitation processes following the EC decay[11)]. The time differential X,γ-ray coincidence Mössbauer spectroscopy is used by both coincidence techniques.

The conventional emission Mössbauer spectrum of ^{57}Co-labeled $Co(BrO_3)_2 \cdot 6H_2O$ is shown in Fig.1 (a), and the X,γ-ray coincidence Mössbauer spectrum (XγMS) of the compound is shown in Fig. 2 (a). The relative area intensity of $^{57}Fe(II)$ to the sum area intensity on the XγMS was 6.6 % larger than that on the conventional spectra. The multiple ionization processes occur to a greater extent in Auger electron emission processes than in the KX-ray emission process. The redistribution of electronic states after the KX-ray emission will not cause so large a perturbation in the electronic shells of ^{57}Fe than the competitive Auger electron emission. Thus the radiation damage given by the processes of Auger electron emission will be

larger than that by the competitive KX-ray emission. This will be the reason for a larger fraction of ^{57}Fe(II)-species in KX-ray emission process than the Auger electron emission processes.

The time differential γ,γ-ray coincidence Mössbauer spectra (TDγγMS) and time differential X,γ-ray coincidence Mössbauer spectra (TDXγMS) of $Co(BrO_3)_2 \cdot 6H_2O$ are shown in Figs. 1 (b-d) and 2 (b-d), respectively. The relative area intensities of ^{57}Fe(II), ^{57}Fe(III)-1, ^{57}Fe(III)-2 and sum of ^{57}Fe(III) to the total area intensity are plotted against the mean time of the preset window in Fig. 3 and Fig. 4. The area intensity of ^{57}Fe(II) to the total area intensity decreased with a delay time. The results indicate the relaxation process of ^{57}Fe(II) to ^{57}Fe(III) by oxidation radicals formed through EC decay and Auger process. The relative area intensity of ^{57}Fe(II) estimated by TDXγMS was larger than that by TDγγMS at every time window. If the oxidation reaction can be treated as pseudo-first-order kinetics, a similar relaxation time of about 30 ns was found on the spectra of both coincidence methods[10].

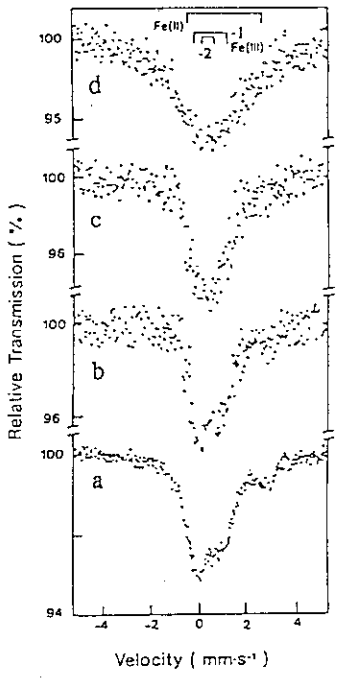

Fig.1 TDγγMS of ^{57}Co-labeled Co-$(BrO_3)_2 \cdot 6H_2O$ at room temperature. The time windows of the spectra are a) conventional, b) 150-250 ns, c) 70-130 ns, d) 0-40, respectively.

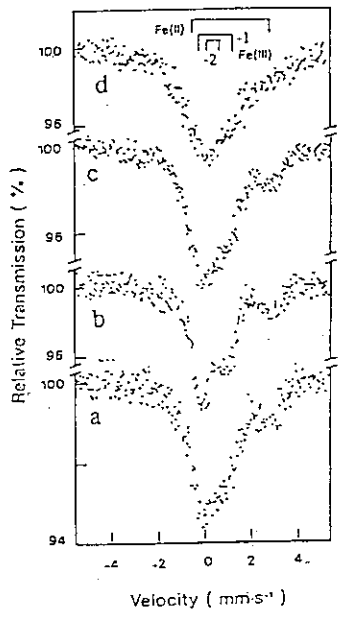

Fig.2 TDXγMS of ^{57}Co-labeled Co-$(BrO_3)_2 \cdot 6H_2O$ at room temperature. The time windows of the spectra are a) time integral, b) 120-300 ns, c) 30-130 ns, d) 0-70, respectively.

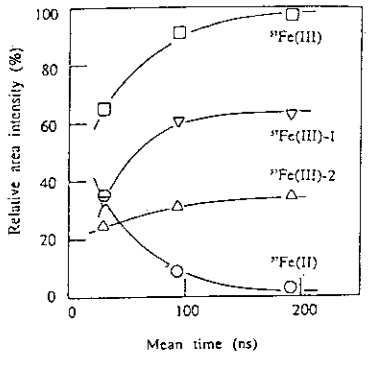

Fig. 3 Relative area intensities of ^{57}Fe(II) (○), ^{57}Fe(III)-1 (▽), ^{57}Fe(III)-2 (△), the sum of ^{57}Fe(III) (□) against the mean time of the preset time window.

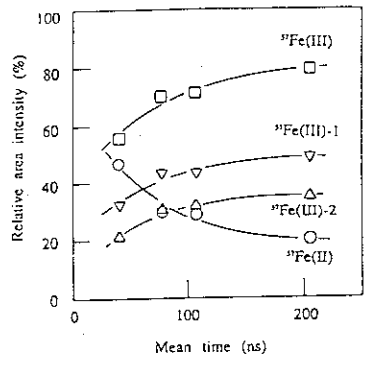

Fig. 4 Relative area intensities of ^{57}Fe(II) (○), ^{57}Fe(III)-1 (▽), ^{57}Fe(III)-2 (△), the sum of ^{57}Fe(III) (□) against the mean time of the preset time window.

References

1) T. Matsuura ed., Hot Atom Chemistry, Recent Trends and Application in the Physical and Life Science and Technology. (Kodansha,Tokyo,1984).
2) T. Tominaga and E. Tachikawa, Modern Hot-Atom Chemistry and Its Applications. (Springer-Verlag,New York,1981).
3) W. Triftsthäuser and D. Schroeer, Phys. Rev., 187(1969)491.
4) R. Grimm, P. Gütlich, E. Kankeleite and R. Link, J. Chem. Phys., 67(1977)54.
5) C. T. Dziobkowski, J. T. Wrobleski and D. B. Brown, Inorg. Chem., 20(1981)697.
6) H. G. Jang, K. Kaji, M. Sorai, R. J. Wittebort, S. J. Geib, A. L. Rheingold and D. N. Hendrickson, Inorg. Chem., 29(1990)3547, and references therein.
7) T. Sato, M. Katada, M. Nakada, K. Endo and H. Sano, J. Radioanal. Nucl. Chem. Lett., 154(1991)95.
8) Y. Watanabe, M. Nakada, K. Endo, H. Nakahara and H. Sano, J. Radioanal. Nucl. Chem. Lett., 136(1989)257.
9) M. Alflen, C. Hennen, F. Tuczec, H. Spieling and P. Gütlich, Hyperfine Int., 47(1989)115.
10)Y. Watanabe, M. Nakada, K. Endo, H. Nakahara and H. Sano, Bull. Chem. Soc. Jpn., 63(1990)2790.
11)T. Kobayashi, Bull. Chem. Soc. Jpn., 62(1989)516.

Publication List

[1] T. Sato, K. Ishishita, M. Katada, H. Sano, Y. Aratono, C. Sagawa and M.Saeki, "Mixed-valence States of ^{57}Fe Atoms Produced in ^{57}Co-labelled [$CoFe_2O(CH_2ICO_2)_6(H_2O)_3$] and [$CoFe_2O(CH_2BrCO_2)_6(H_2O)_3$]", Chem. Lett., 403(1991).
[2] T. Sato, K. Ishishita, M. Katada, M. Nakada, K. Endo and H. Sano, "Emission Mössbauer Spectroscopic Studies of ^{57}Fe Atoms Produced in ^{57}Co-labelled Trinuclear Cobalt-Iron Halogenoacetate Complexes", Hyperfine Int., in press.
[3] M. Nakada, K. Tamagaya, H. Nakahara and K. Endo, "Chemical States of ^{57}Fe-atoms after EC-decay of ^{57}Co-labelled $Co(BrO_3)_2 \cdot 6H_2O$ Studied by coincidence Mössbauer spectroscopy", Hyperfine Int., in press.

6.3 Water Splitting Catalyzed by Zeolites

6.3.1 Introduction

Zeolite is a crystalline aluminosilicate with framework structure, and its adsorption and catalytic property depends on structure, pore size, the number and position of zeolitic cations, Si/Al ratio, etc. It is well known that transition metal ion exchanged zeolites can be used as catalysts for a wide range of chemical reactions. Water splitting by such ion exchanged zeolites is one of interesting matter of research. Kasai and Bishop reported decomposition of water by Cr^{3+} or In^{3+}-exchanged mordenites in 1977[1], which undoubtfully attracted the attention of many researchers, but only a limited number of paper on water decomposition by using ion exchanged zeolites were reported in the next several years. This might be caused by lack of reproducibility in the experimental results due to difficulty in the preparation of catalysts having the same active condition. Then, it is still important to understand the mechanism of reduction and oxidation behaviors of zeolite cations and their role in various catalytic reactions. In the present study, we prepared In^{3+}-exchanged type Y zeolites and mordenites, and studied their reduction and oxidation behaviors to apply them to hydrogen production by water splitting.

6.3.2 Reduction and oxidation of In-exchanged zeolites

Indium-exchanged zeolite samples were prepared from the NaY, its H-exchanged one(HY), and two kinds of Na-mordenites with different Si/Al ratios(NaM_5 and NaM_{10}) by aqueous ion exchange in $InCl_3$ solution. After filtering, repeated rinsing and drying, portions of zeolites were made into disc shape to subject to experiments. Chemical analysis of the In-exchanged zeolites showed the chemical composition of $In_{0.21}Na_{0.54}AlO_2(SiO_2)_{2.7}$(InNaY), $H_xIn_{0.16}Na_{0.06}AlO_2(SiO_2)_{2.7}$(InHY), $In_{0.10}Na_{0.82}AlO_2(SiO_2)_{5.5}$($InNaM_5$) and $In_{0.16}Na_{0.68}AlO_2(SiO_2)_{9.2}$($InNaM_{10}$).

Temperature programmed reduction(TPR) and oxidation(TPO) experiments were conducted with Ar gas containing 2% H_2 ($Ar(H_2)$) and with He gas containing 2% O_2 ($He(O_2)$), respectively. The sample zeolite was heated from room temperature to 1123 K at a heating rate of 30 K/min with flowing the reaction gas of 30 ml/min. Figure 1 shows the TPR and TPO spectra obtained with $InNaM_5$ and $InNaM_{10}$. The TPR spectra of as-prepared samples(Run 1) showed H_2 consumption peaks, which resulted from reduction

of indium, at a temperature of 723K in both samples. Oxygen consumption peaks of the TPO spectra of these reduced samples(Run 2) were observed at 573K and 1073K in $InNaM_5$ and at 473K, 873K and 1073K in $InNaM_{10}$. Of these, the peaks at 573K and 873K resulted from oxidation of the reduced indium, because the other peaks at 473K and 1073K were also observed in TPO spectra of the original Na-mordenites. The following re-reduction(Run 3) gave H_2 consumption peaks at 723K, whose area were smaller than those in Run 1, in both $InNaM_5$ and $InNaM_{10}$. The subsequent repetition of oxidation and reduction yielded the reproducible TPO and TPR spectra, similar to those in Run 2 and 3. From these results, we can find that increase of Si/Al ratio raises oxidation temperature of indium cations sited in mordenite, but does not affect reduction behavior of them.

As shown in fig.2, H_2 consumption peaks were observed at a temperature of 723K in the TPR spectrum of as-prepared InHY(Run 1) and at 843K with two clear shoulder peaks around 693K and 973K in the TPR spectrum of as-prepared InNaY(Run 1). The subsequent oxidation of these reduced samples(Run 2) gave O_2 consumption peaks at 1023K in the TPO spectrum of InHY, which clearly consisted of at least two peaks, and at 803K in the TPO spectrum of

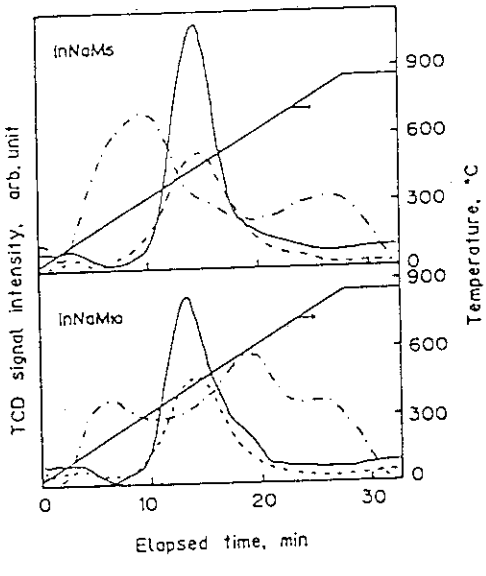

Fig.1 The TPR and TPO spectra of In-exchanged mordenites.
——— ;Run 1, — — — ;Run 2,
— · — ;Run 3.

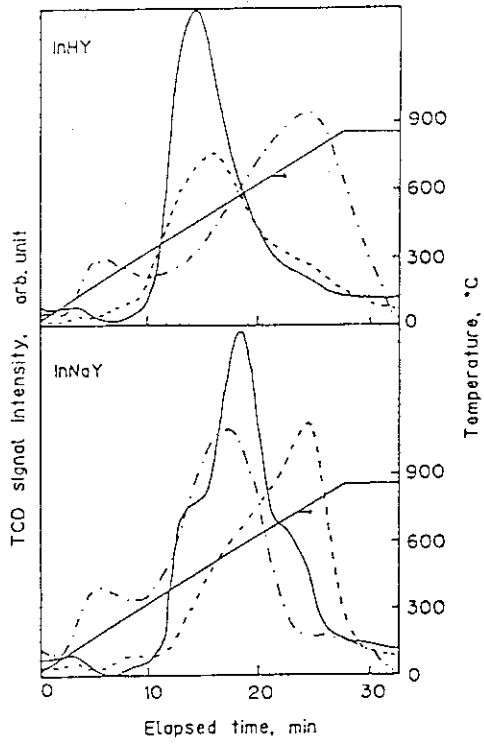

Fig.2 The TPR and TPO spectra of In exchanged type-Y zeolites.
——— ;Run 1, — — — ;Run 2,
— · — ;Run 3.

InNaY. The small peaks around 473K does not originate from indium oxidation. In the following re-reduction(Run 3), H_2 consumption peaks appeared at a temperature of 773K in the TPR spectrum of InHY and at 1023K in that of InNaY with a shoulder peak around 823K. Reproducible spectra were obtained in the subsequent repetition of oxidation and reduction. These results indicate that reduction of indium cations sited in InHY is easy compared with those in InNaY, and that, in addition, the first reduction of as-prepared samples make next re-reduction peaks shift to a higher temperature. This peak shift is more significant in InNaY than in InHY. Contrary to reduction, the oxidation of the reduced indium cations occurs at a lower temperature in InNaY than in InHY.

6.3.3 Water splitting by In-exchanged zeolites

Water splitting was attempted with In-exchanged zeolites which were subjected to the reduction treatment by Ar(H_2). The reduction of the sample is conducted as the same procedure as the TPR experiment described

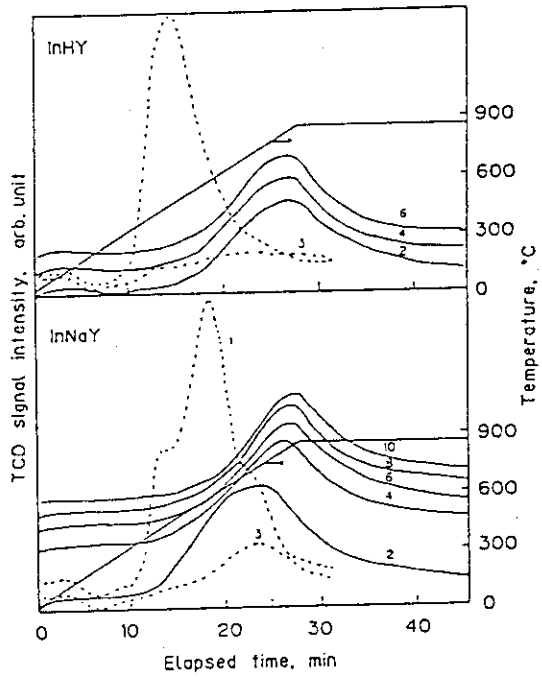

Fig.3 The temperature programmed reaction spectra of In-exchanged type-Y zeolites.
——— ;water decomposition run,
— — — ;TPR run.

above. After the reduction, the sample was heated from room temperature to 1123K at a heating rate of 30 K/min with flowing Ar gas containing water vapor(Ar(H_2O)). Hydrogen production was monitored by thermal conductivity detector. Results were shown in fig.3. Odd and even numbers respectively denote reduction run(TPR) and water decomposition run. For the reduction run, the first two curves were represented, because the H_2 consumption curves were reproduced for the subsequent reduction runs. Hydrogen production was observed in InNaY and InHY, not in $InNaM_5$ and $InNaM_{10}$. The peak area of H_2 consumption peak in the second reduction process(Run 3) was about 20% of those in the first reduction(Run 1). This means that only part of indium ions sited in these zeolites reduced water molecules to produce H_2. The amount of H_2 consumed in reduction process was two times larger than that of H_2 produced in water decomposition process. In order to clarify the reaction mechanism, further investigation is needed for the position and the oxidation state of indium ions which participate in redox reactions in zeolite cavity.

Reference

1)P. H. Kasai and R. J. Bishop, Jr., J. Phys. Chem., 81(1977)1527.

7. CHEMICAL DECONTAMINATION FOR NUCLEAR REACTORS

T.Suwa, N.Kuribayashi, T.Yasumune, Y.Ishige

7.1. Decontamination of Dismantled Components with Sulfuric Acid-Cerium(IV) Solution

Introduction

Chemical decontamination tequniques for decommissioning are divided into two groups: a predismantling system decontamination and a decontamination of dismantled components. At JAERI, efforts have been made to develop both the decontamination processes with H_2SO_4-Ce^{4+} (SC) and H_2SO_4 solutions. The SC solution was selected on the basis of the Pourbaix diagram for metal-H_2O systems and of the experimental results such as dissolution behavior of modelled cruds, decontamination effects, and corrosion rates of alloys[1-4].

The SC solution is a very effective decontamination reagent to achieve a high DF for the Cr/Ni- and Fe-rich oxides. Therefore, it is applicable to the decontamination for decommissioning of both BWRs and PWRs with a single-step process[5]. There are optimum decontamination conditions to achieve two different decontamination tasks, as shown in Table 1.

Table 1. Selection of optimum decontamination conditions for various contaminated materials

Application	Crud composition	Materials	Decontamination conditions				Treatment of waste solution
				Reagents	Temp(℃)	Time(h)	
Systems of BWR and PWR	Cr,Ni-rich	Stainless steels CrNi-alloys	A	0.25M H_2SO_4 2～5mM Ce^{4+}	80	24～72	Electrodialysis Ion-exchnge resin
Components			B	1M H_2SO_4 50 ～100mM Ce^{4+}	80	5～10	Diffusion dialysis (Reuse of H_2SO_4)
	Fe-rich	Stainless steels	C	2～3M H_2SO_4	80	1～2	
		Carbon steels	D	1～2M H_2SO_4	50～80	1	

A,B: Electrolytic oxidation of Ce^{3+} to Ce^{4+} during the decontamination.
C,D: Controlling the solution potential by electrolytic reduction.

The system decontamination using the SC solution was applied to the primary system of JPDR (Japan Power Demonstration Reactor) in 1987 [6-7].

The decontamination of dismantled components differs from the system decontamination. The radionuclides in the metallic components distribute not

only in the surface "crud" layer but also in the base metal to a certain depth. When the components need to be decontaminated to an unrestricted release level, it is required that the base metal, as well as cruds, is dissolved away to a depth (thickness) of several tens of microns beneath the surface. To achieve this objective, We have started research to achieve the following four requirements[9-10] .

(a)Achievement of unrestricted release of component materials:

β, $\gamma \leqq 0.37$ - 1Bq/g (1×10^{-5}- 2.7×10^{-5} μCi/g).

(b)To specify the amount of radioactive species in base metal:

Activity level vs. depth from base metal surface.

(c)Shortening period for decontamination time:

Higher corrosion (dissolution) rates of metals (cruds).

(d)Reduction of radioactive wastes volume:

Recycle use of decontamination reagents.

This paper describes the outline for the decontamination of dismantled components by use of the SC and H_2SO_4 alone solutions.

Corrosion Behavior

The corrosion rate of base metals is a very important factor in the SC process. It is connected with the decontamination procedure/operation such as the deontamination period, Ce^{4+} consumption rate[8] , electrolytic regenerating current of Ce^{4+} from Ce^{3+} , and treatments of the waste solutions. From the above aspects, we examined corrosion rates of typical alloys which contact with a primary cooling water in BWRs and PWRs. In addition, some alloys were examined to select corrosion resistant materials used for decontamination facility.

Table 2 summarizes the corrosion rates (mdd, mg/dm^2 · day) for typical materials in H_2SO_4 and the SC solutions. In the SC solution, the rates of SUS304, SUS316 and Inconel 600 were in the same order of ca. 10^4 mdd (5 μm/h). In H_2SO_4 solution, the rates of SUS304 and SUS316 increased with H_2SO_4 concentration, while the rate of Inconel 600 was much lower than those of stainless steels and independent of H_2SO_4 concentration.

Zircaloy-2 and -4 could be only used in both the solutions as corrosion resistant materials. Ticorex and Titanium metal were scarcely corrosive in the SC solution, but very corrosive in H_2SO_4 solution.

The stainless steels were corroded more rapidly in a certain concentration range of H_2SO_4 than in the SC solution as shown in Fig. 1. Most of metals are generally corroded at high rates within certain ranges of potential, an active region in polarization curve. For example, the corrosion rate of a SUS304 in

H_2SO_4 solution is very high in the potential range from -0.2 to -0.4 volt (vs. Ag/AgCl referece electrode)[4]. These facts provide the possibility of an effective decontamination method using H_2SO_4 solution under controlling the solution potential. This method is of interest in the following aspects compared with the SC process: (a) to make shorter an operating time in decontamination, and (b) to reduce a volume of secondary wastes, because of no use of Ce^{4+}.

Table 2. Corrosion rate of various materials (mdd, mg/dm² day)[a]

Materials	1M H_2SO_4	2M H_2SO_4	SC solution[b]
SUS304	2.0×10^4	1.0×10^5	1.0×10^4
SUS316	600	7.0×10^3	1.3×10^4
Inconel-600	300	-	2.4×10^4
Stellite D6	1.2×10^4	-	-
STPT38	2.6×10^5	-	-
Zircaloy-2	2	-	1
Zircaloy-4	2	-	1
Ticorex(Ti-Ru-Ni)	180	-	4
Titanium	1.3×10^3	3.6×10^3	1

a) Temperature: 80 ℃
b) 1M H_2SO_4-50 mM Ce^{4+} solution

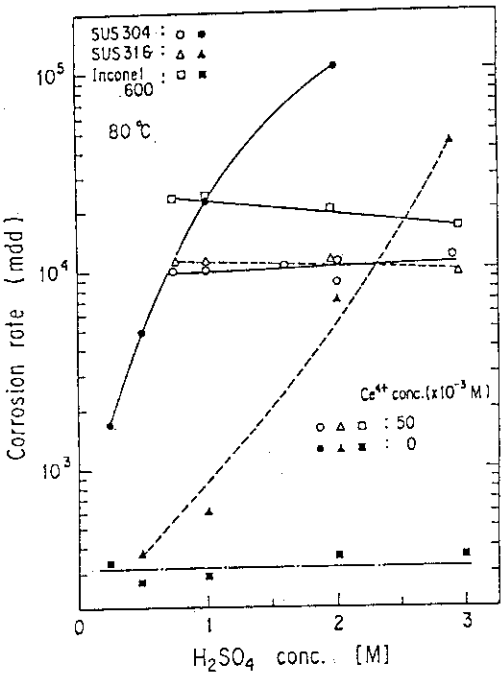

Fig.1 Effect of H_2SO_4 concentration on corrosion rates

Decontamination Process and Equipment

Optimum decontamination conditions

On selecting decontamination reagents, the type of base metals and chemical compositions of cruds are most important as shown in Table 1. For stainless steels, either the SC or H_2SO_4 solution can be applied depending on the crud compositions. The SC solution is for Inconel 600, and H_2SO_4 solution for carbon steels.

For example, in case when various contaminated specimens from JPDR are desired to dissolve up to 30 μm from the surface of the base metals, the optimum decontamination conditions are proposed as follows:

1) Carbon steels; 1M H_2SO_4, 50-80 ℃, 1 h.
2) SUS304; (a) 1M H_2SO_4, 50mM Ce^{4+}
($Ce^{4+}/Ce^{3+} \fallingdotseq 1$), 80 ℃, 6 h.
(b) 2M H_2SO_4, 80 ℃, 1 h.

A short decontamination time is attained by increasing Ce^{4+} concentration. However, since the concentration of Ce^{4+} in practical use is limited by such factor as solubility of Ce^{3+} , stability of the SC solution, and treatment of the waste solution, it should be chosen in the range of 50-100 mM

Basic procedure of SC process

Fig. 2 shows a basic procedure of the SC decontamination process. The SC process roughly divided into two steps: decontamination step and waste treatment step for the spent decontamination solution. The decontamination step can be operated with continuous electrolytic regeneration of Ce^{3+} to Ce^{4+} under the desired conditions, which are able to be changed depending upon the characteristics of the cruds on contaminated surfaces and constructual materials. After the decontamination, the decontaminated material is further washed out in water by ultrasonic cleaning.

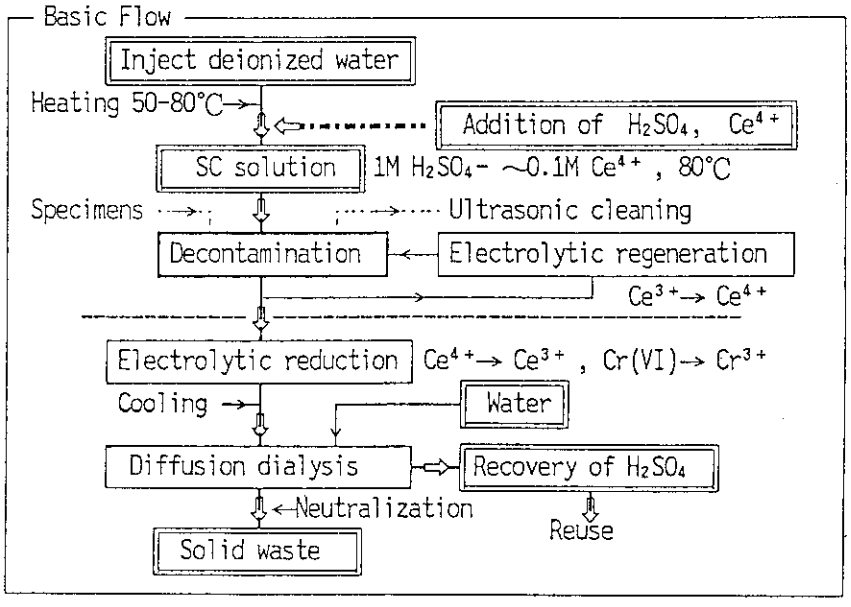

Fig.2 A basic procedure of the SC decontamination process

The solution is repeatly used until the concentration of dissolved metal ions above 1×10^4 ppm . The residual Ce^{4+} and Cr(VI) in the spent solution are electrochemically reduced to Ce^{3+} and Cr^{3+}, and the solution is then treated by diffusion dialysis to recover 70-80% of H_2SO_4 from the solution. The H_2SO_4 solution recoverd is concentrated and then reused. Finally, the diluted waste solution is solidified after being neutralized.

When the H_2SO_4 solution is used, the procedures are almost the same as the SC process except the electrolytic process. In that case, the spent solution should be directly treated by the diffusion dialysis.

The demonstration tests are in progress using an equipment as shown in Fig.

3, in which 1m² of the surface area per one batch will be treated in 1m³ of the decontamination solution.

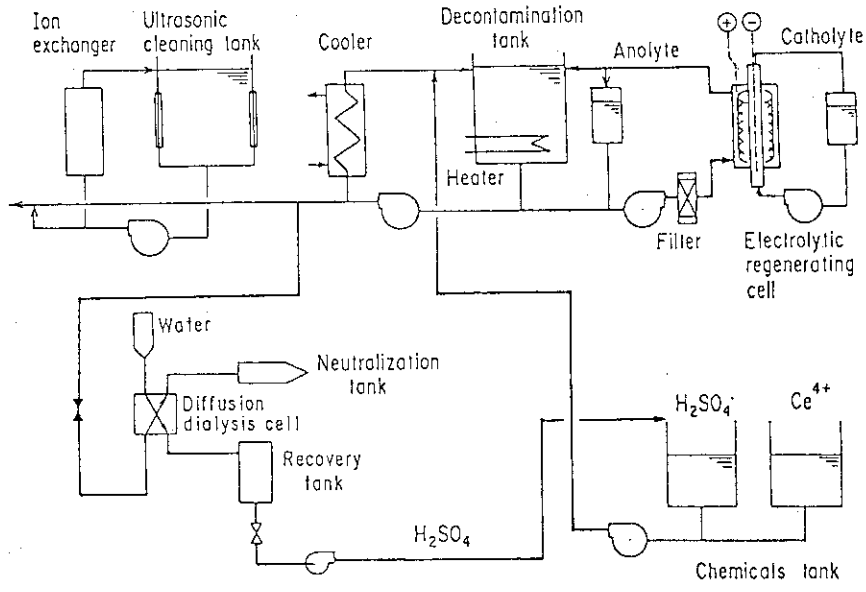

Fig.3 Schmatic diagram of the SC decontamination equipment

Capacity of electrolytic cell

The ability for the treatment of contaminated metallic components is mainly governed by the capacity of the electrolytic regenerating cell. Since the amounts of metal ions dissolved from the base metal is far larger than that of cruds, the regenerating current needed by cruds dissolution is negligible. Therefore, the regenerating current (I,Amp.) is given as[4-5] :

$$I=(1/3.73\eta_e)R_c\ S/2.4\cdot\Sigma\ Z_{Mi}a_{Mi}/M_i \qquad (1)$$

where Z_{Mi} is the ionic valence of dissolved metal ions, a_{Mi} is the content of species i in alloy, M_i is the atomic weight of species i. The value of $\Sigma Z_{Mi}\cdot a_{Mi}/M_i$ is 6.33 for SUS304. Using this value in Eq.(1),

$$I=0.707\ R_c S/\eta_e \qquad (2)$$

The calculated value of I is 200 A at S=1m², R_c =1.5x10⁴ ppm, and η_e =50%

Estimation for the amount of wastes

The amounts of the final waste can be roughly proportional to surface area of contaminated wastes (S, m²) and the depth dissolved (d, μm). For the evaluation, the following assumptions have been introduced:

- Decontamination solution; 1M H_2SO_4, 50mM Ce^{4+} ($Ce^{4+}/Ce^{3+}\fallingdotseq 1$).
- Volume of the decontamination solution; V=1 m³
- Replacement of the solution; C_M =15 kg/m³
- The total surface area (SUS304); S=100 m²
- The depth; d= 30-100 μm.

In Fig. 4, shown is the volume of the final waste vs. the dissolved amount of base metals, the latter is expressed in terms of depth from the surface. The amounts of wastes are presented as total weight of Na_2SO_4, $Ce(OH)_3$ and $M(OH)_3$ after neutralization by NaOH in the following two cases. In case A, the spent solution is directry neutralized by NaOH after decontamination. In case B, 80% of H_2SO_4 is first removed from the spent solution using diffusion dialysis and then the diluted spent solution is neutralized by NaOH. The reduction ratio of case B to case A is ca.60-70%. For example, at d= 60 μm the spent solution is 3.2m^3 in volume and contains 315kg of H_2SO_4, 45kg of Ce^{3+}, and 48kg of M^{n+}(=Fe^{3+}, Cr^{3+}, Ni^{2+}).

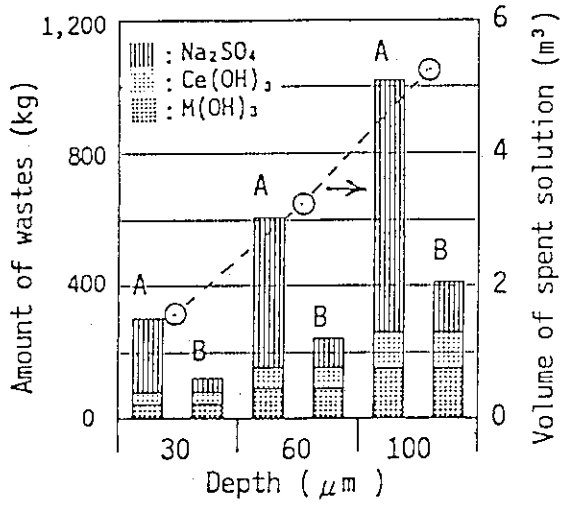

Fig.4 Estimated values of amount of decontamination wastes

We have investigated some other methods such as recovery of Ce^{3+} by ion-exchange resin and removal of dissoved metal ions and H_2SO_4 by electrodialysis. An optimum waste treatment process will be selected by combination of above methods.

The chemical decontamination processes with H_2SO_4-Ce^{4+} (SC) and H_2SO_4 solution have been developed for the decontamination of dismantled components. These processes are applicable to various types of alloys and cruds by alteration of the characteristics of decontamination solution, either oxidative or reductive. Furthermore, the treatment of both the spent solutions can be accomplished with the same system.

References

1)T.Suwa, N.Kuribayashi, E.Tachikawa: J.Nucl.Sci.Technol.,23, (1986)622.

2)T.Suwa, N.Kuribayashi, E.Tachikawa: Boshoku Gijutsu (Corrosion Eng.), 36, (1987)127, (in Japanese). → Translated to English, (1987)pp.121-128.

3)T.Suwa, N.Kuribayashi, E.Tachikawa: ibid., 36, (1987)204, (in Japanese). → Translated to English, (1987)pp.199-205.

4)T.Suwa, N.Kuribayashi, E.Tachikawa: ibid., 37, (1988)88, (in Japanese). → Translated to English, (1988)pp.73-82.

5)T.Suwa, N.Kuribayashi, E.Tachikawa: J. Nucl. Sci. Technol., 25, (1988)574.

6)E.Tachikawa, H.Yasunaka, T.Suwa, T.Gorai, M.Kawasaki: 1988 JAIF Int. Conf. on Water Chem. in Nuclear Power Plants, Proceedings Vol.2, pp.443～448, Tokyo.

7)T.Suwa, S.Goto, T.Gorai, N.Kuribayashi, E.Tachikawa, et al.: Genshiryoku -shi (J. Atomic Energy Soc. Japan), 30, (1988)1020,(in Japanese).

8)T.Suwa, N.Kuribayashi, T.Yasumune, E.Tachikawa: Denki Kagaku (Electro-chemistry), 56, (1988)722, (in Japanese).

9)T.Suwa, N.Kuribayashi, T.Yasumune: Dekomisyoningu Giho (J. of the RANDEC), No.2, (1990)29, (in Japanese).

10)T.Suwa, N.Kuribayashi, T.Yasumune, E.Tachikawa: 1991 JAIF Int. Conf. on Water Chem. in Nuclear Power Plants, pp.737- 742, Hukui City, Japan.

Publication list

[1]T.Suwa, N.Kuribayashi, T.Yasumune: Development of Chemical Decontamination Process with Sulfuric Acid-Cerium(Ⅳ) for Radioactive Contaminated Metal Wastes, Dekomisyoningu Giho (J. of the RANDEC, Research Association of Nuclear Facility Decommissioning), No.2, (1990)29, (in Japanese).

[2]T.Suwa, N.Kuribayashi, T.Yasumune, E.Tachikawa: Chemical Decontamination Process with Sulfuric Acid-Cerium(IV) for Decommissioning,－Decontamination of Dismantled Components－, 1991 JAIF Int. Conf. on Water Chem. in Nuclear Power Plants, pp.737- 742, Hukui City, Japan.

8. NUCLEAR CHEMICAL STUDIES ON TRANSURANIUM ELEMENTS

M. Hoshi, Y. Nakahara, S. Ichikawa, N. Shinohara, H. Iimura,
M. Magara, K. Tsukada*, M. Shibata**, M. Miyachi**,
A. Osa**, K. Kotani**, T. Ikuta** and M. Kubota***

* Faculty of Science, Tokyo Metropolitan University
** Faculty of Engineering, Nagoya University
***Faculty of Science, Toho University

8.1 Separation of Neutron-Rich Ruthenium Isotopes by Means of the Fast Solvent Extraction System SISAK

8.1.1 Introduction

An on-line chemical separation system, which consists of a KCl/He gas-jet recoil-transport system[1] and a continuous multistage solvent extraction system SISAK (Short-lived Isotopes Studied by AKUFVE technique),[2] has been applied for the identification of neutron-rich ruthenium isotopes produced in the spontaneous fission of ^{252}Cf. In this report, the decay data for γ-rays following the β^- decay of short-lived $^{110\text{-}112}$Ru are presented.

8.1.2 Experimental

The fission products collected with the aerosol particles in the helium gas were transferred to a static mixer, in which the activity was dissolved in 0.2M sulfuric acid containing 5x 10^{-5}M ruthenium carrier. The helium gas was separated by centrifuge, and the dissolved ruthenium was oxidized to RuO_4 by adding a solution of 0.015M $Ce(SO_4)_2$/0.2M H_2SO_4 preheated to about 90 ℃. The liquid was then contacted with CCl_4 in a second static mixer and the mixture was fed into another centrifuge to separate the organic phase with the ruthenium oxide from other fission products remaining in the aqueous phase. Gamma-ray measurements were carried out on the organic solution after the solvent extraction using a coaxial HPGe detector.

8.1.3 Results

Table 1 gives the decay data on the γ-rays following the β^- decay of ruthenium isotopes. The absolute intensities, Iγ in Table 1, were obtained by taking into account the γ-ray yields of ^{252}Cf fission given by Wilhelmy[3] and the cumulative yields for the ruthenium isotopes by Rider.[4] Very few decay data have existed in the neutron-rich ruthenium isotopes so far, but the detailed relative intensities of ^{110,111}Ru were determined in this work. The 263.5

keV γ-ray from ^{113}Ru[5] was not detected in our experiments, since the half-life of 0.8 s for ^{113}Ru is too short for our SISAK separation.

Table 1 Energies and intensities of gamma-rays following the β^- decay of 110-112Ru.[a]

Isotope	$T_{1/2}$[b] (s)	Eγ (keV)	Relative yield /fission (cps)	Relative intensity (%) this work	Ref.[6]	Iγ[c] (%)
^{110}Ru	12.0(1)	96.04(20)	1.30(34)	6.1(17)	6	
		112.51(6)	21.2(13)	100.0(61)	100	15.8(44)
		373.68(4)	2.55(36)	12.0(17)		
^{111}Ru	2.12(7)	211.61(6)	5.96(84)	54.0(82)		
		249.65(17)[d]	<1.06(30)	<9.6(28)		
		303.63(6)	8.28(66)	75.0(73)		20.7(41)
		381.40(4)	11.04(61)	100.0(55)		
^{112}Ru	1.75(7)	326.82(5)	7.2(4)			

a) Uncertainties of the values are given in parentheses.

b) Reliable half-lives taken from Ref.[7] for ^{110}Ru, and Ref.[5] for ^{111}Ru and ^{112}Ru.

c) See text for details.

d) Overlapped with the same energy γ-ray from ^{109}Ru.

References

1) K. Tsukada, T. Ohtsuki, K. Sueki, Y. Hatsukawa, H. Yoshikawa, K. Endo, H. Nakahara, N. Shinohara, S. Ichikawa, S. Usuda and M. Hoshi, Radiochim. Acta 51(1990)77.

2) G. Skarnemark, M. Skålberg, J. Alstad and T. Bjørnstad, Phys. Scr. 34(1986)597.

3) J. B. Wilhelmy, UCRL-18978 (1969).

4) B. F. Rider, NEDO-12154-3(C) (1981).

5) H. Penttilä, P.Taskinen, P. Jauho, V.Koponen, C. N. David and J. Äystö, Phys. Rev. C38(1988)931.

6) G. Franz and G. Herrmann, J. Inorg. Nucl. Chem. 40(1978)945.

7) M. Kaffrell, J. Rogowski, H. Tetzlaff, N. Trautmann, M. Skålberg, G. Skarnemark, J. Alstad and K. Wolfsberg, Institute für Kernchemie, Universität Mainz, Jahresbericht 1985, IKMz 86-1 (1986) p.7.

Publication List

[1] K. Tsukada, T. Ohtsuki, H. Yoshikawa, T. Endo, H. Nakahara, N. Shinohara, S. Ichikawa, S. Usuda and M. Hoshi, "Development of Computer-Controlled On-Line Rapid Ion-Exchange Separation System," Radiochim. Acta 51(1990)77.

[2] N. Shinohara, "Radiochemical Investigation of Transuranium Nuclides produced by Heavy Ion Reactions," Proc. of International School-Seminar on Heavy Ion Physics, JINR-D-7-90-142 (1990) p.70.

[3] N. Shinohara, S. Ichikawa, S. Baba, K. Tsukada, T. Ohtsuki and J. Alstad, "Gamma Rays of Short-Lived Ruthenium Nuclides produced in the Spontaneous Fission of ^{252}Cf," Radiochim. Acta, in press.

8.2 Mendelevium Isotopes Produced by the $^{12}C + ^{241}Am$ Reaction

8.2.1 Introduction

The heavy elements (Z>100) cannot be synthesized through multi-neutron capture of nuclear fuel followed by successive beta-decays in a reactor. The only way to produce the heavy elements is the bombardment of a suitable transuranium element with ion beams from accelerator. Synthesis of the heavy elements by heavy ion reactions proceeds through the process of compound nucleus formation, but the fission barrier of the compound nucleus with atomic number greater than 100 is so low that almost all compound nuclei compete with the fission in the every step of successive neutron evaporations. Therefore, such heavy nuclides must be synthesized to form the compound nucleus with the excitation energy as low as possible, whereas the projectile of the charged particles must overcome the coulomb barrier for the compound-nucleus formation. This report presents a result of the synthesis of mendelevium performed using the JAERI TANDEM accelerator.

8.2.2 Experimental

Target of ^{241}Am (100 $\mu g/cm^2$ in thickness) was prepared by electrodeposition from organic solution of americium nitrate.[1] The americium target was located in a reaction chamber of He-jet rapid transportation system and bombarded by ^{12}C beams of energy 80 MeV (on the target) at intensity of 600 enA. The recoiling nuclides produced in the heavy-ion reaction were caught by aerosols, transported rapidly through a capillary, and collected on a surface of tape through skimmer in a moving-tape system. The collected sample was heated in order to prepare a thin radiometric sample for alpha-ray spectrometry. The moving-tape system transferred the sample to a position of the first Si-surface-barrier detector and then to next detector successively. The duration of collection and measurement was adjusted to the same as the half-life of the aimed heavy nuclide. The cycle of collection, transfer and measurement was repeated several hundred times to accumulate the counting of alpha-ray.

8.2.3 Results

The result of the measurement of alpha-rays from ^{250}Md (half-life[2] 52s) and ^{249}Md (24s) produced by the $^{241}Am(^{12}C,3n)^{250}Md$ and $^{241}Am(^{12}C,4n)^{249}Md$ reactions respectively is shown in Fig. 1. The EC-decay daughter ^{249}Fm (2.6min) of ^{249}Md was detected, but the half-life of the daughter ^{250}Fm (30min) of ^{250}Md after EC decay is too long to be detected in this experimental condition. The accumulation of the alpha-ray counting has been continued to reveal the details of the decay schemes of ^{249}Md, ^{250}Md and ^{249}Fm and the cross sections of the formation reactions.

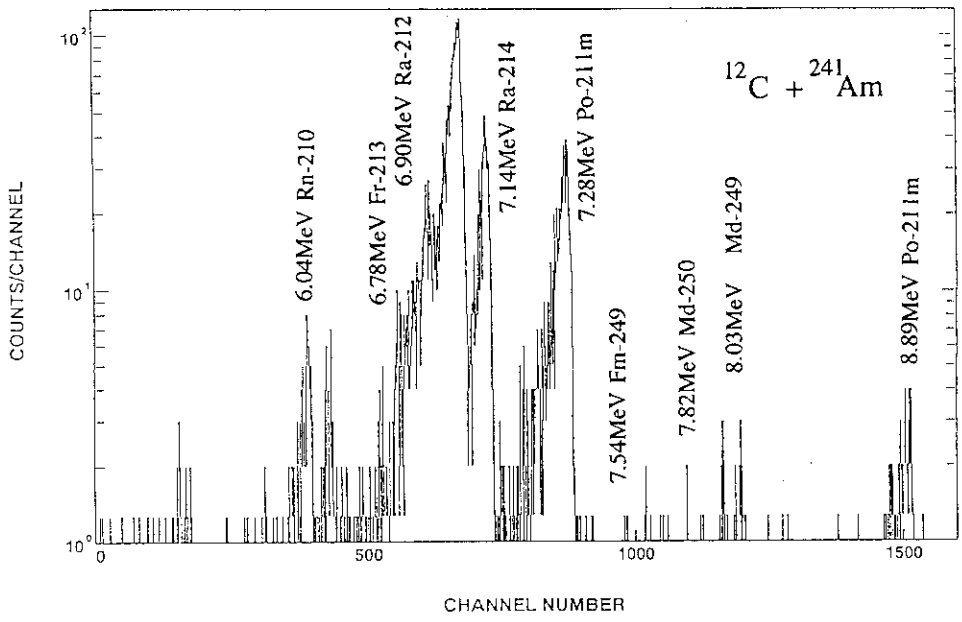

Fig. 1 Alpha-ray spectrum measured by means of a He-jet transportation and moving-tape system. The duration and the cycle for the collection of reaction products and the alpha-ray measurement were 25 s and 720 times, respectively.

References

1) N. Shinohara and N. Kohno, Appl. Radiat. Isot. 40(1988)41.

2) Table of Isotopes, 7th ed., edited by C. M. Lederer and V. S. Shirley (Wiley, New York, 1978).

Publication List

[1] I. Fujiwara, S. Shibata, H. Kudo, K. Tsukada, T. Ohtsuki, N. Shinohara, S. Ichikawa, H. Iimura, "A Research for the Production of Transuranium Elements," JAERI TANDEM, Linac & V.D.G. Annual Report 1989, JAERI-M 90-139 (1990) p.123.

8.3 A Study of Nuclides far from β-Stability by JAERI ISOL

8.3.1 Introduction

The isotope separator connected on-line to the JAERI tandem accelerator has been used for the study of unstable nuclei in the rare-earth region. So far, the decay study has focused on lanthanum isotopes by an element selective mass separation.

A study with collinear laser spectroscopy has began recently. A program of the measurement of electromagnetic moments and root-mean-square charge radii of radioactive nuclei is now in progress. The technique used and some experimental results are presented in another paper.[1)]

In this section, we describe the experimental results of decay spectroscopy together with results of hold-up times of lanthanum and cerium ions in a thermal ion source.

8.3.2 Separation efficiency and hold-up time of LaO^+ ion in a thermal ion source

For the study of neutron deficient lanthanum isotopes, the thermal ion source has been used. This is basically a surface ionization ion-source integrating a target, a recoil catcher and an ionizer; the catcher is held in the vaporizer chamber connected to the ionizer. The structure of the ion-source and its performance was reported previously[2)], in particular for element selective mass separation using monoxide ion formation.

The on-line separation efficiencies of LaO^+ ions were recently measured for $^{124,126,128}La$ isotopes at an ion-source temperature of 2400 K. This efficiency is defined as the collection rate at the tape divided by the production rate that is calculated on the basis of the cross sections predicted by ALICE code.[3)] The reaction used was a 5 MeV/u ^{32}S beam on a 3 or 4 mg/cm^2 ^{nat}Mo and/or ^{92}Mo target. For $^{126}La(T_{1/2}$=1 min) and $^{128}La(T_{1/2}$=4.9 min) isotopes, both the separation efficiencies were found to be 3% and for $^{124}La(T_{1/2}$=29 s) 1%. Although these efficiency values are not very reliable, the difference in effi-

ciency between the long-lived and short-lived isotopes is consistent with the delay characteristic of LaO^+ ions in the ion source.

Hold-up times of ions in the thermal ion source were measured for La and Ce together with neighboring elements in the periodic table.[4)]

We measured the intensity of a mass-separated beam before and after the accelerator beam stopped. It was confirmed that the intensity of a mass separated beam decreased exponentially after the accelerator beam was switched off and the production of the nuclide of interest stopped. Resultingly, a delay half-time of the radioactivity after switched off of the accelerator beam was obtained; the value $T_{1/2}^{del}/\ln 2$ should be considered a mean hold-up time in the ion source.

In an experiment, the accelerator beam bombarded the target during a period Δt_I. The accelerator beam was switched on and off by using a movable Faraday cup. Before and after the accelerator beam stopped, the mass-separated beam was collected during a period Δt_C at an Al coated Mylar tape and transferred, within a length of time Δt_T, to a detection port equipped with an HPGe detector. A γ- and/or X-ray spectrum was measured during the same period with Δt_C. The length of time Δt_T was set at 1 s, while the lengths of time Δt_I and Δt_C were changed according to the length of $T_{1/2}^{del}$ observed in a preliminary experiment. In a cycle, radioactivity measurement (and collection of the radioactivity) was repeated eight times; the measurement was two or three times before the accelerator beam stopped.

Table 1 lists reaction systems used in this study. The target foil was working as a window of the ion-source cavity. The products recoiling

Table 1 Reaction systems and measured radionuclides

Projectile Nuclide	Energy (MeV/u)	Target* Nuclide	Thickness (mg/cm^2)	Reaction channel	Measured Nuclide	Detected radiation
^{35}Cl	4.8	^{92}Mo	3.0	(3p3n)	^{121}Ba	X-ray
				(4p2n)	$^{121m,g}Cs$	X-ray
^{32}S	4.7	^{nat}Mo	4.0	(1pxn)	^{125}La	x/γ-ray
^{35}Cl	4.8	^{nat}Mo	4.0	(1pxn)	^{126}Ce	X-ray
				(2pxn)	^{126}La	X-ray
^{35}Cl	5.4	^{103}Rh	1.8	(2p4n)	^{132}Nd	γ-ray
				(3p3n)	^{132}Pr	γ-ray

*For the Rh target, recoils passed through a tantalum window of 1.5-μm thickness. For the other targets, recoils were directly implanted into a catcher.

from the target were caught by a 0.1 mm-thick tantalum foil. The vaporizer with the catcher foil and the ionizer holding inside a 0.05 mm-thick rhenium foil were heated 2400, 2500 and 2600 K.

Figure 1 shows a typical profile of a mass-separated beam of $^{125}LaO^{+}$ at 2400 K. The delay half-time obtained in the present work are plotted in Fig. 2. One can note in Fig. 2 that

1) the hold-up times of the metallic and monoxide ions of both lanthanum and cerium are much longer than those of the others
2) no differences are observed between the metallic and oxide ions of lanthanum and cerium at 2400 K.

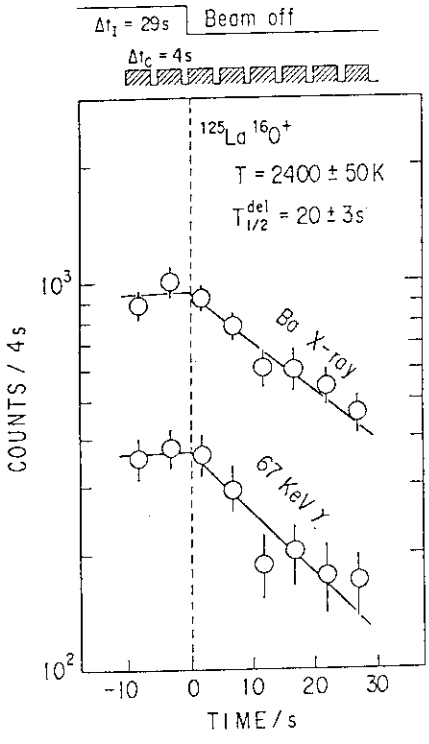

Fig. 1 A release profiles of the $^{125}LaO^{+}$ ion at an ion source temperature of 2400 K. The X-ray and γ-ray associated with the decay of ^{125}La were detected.

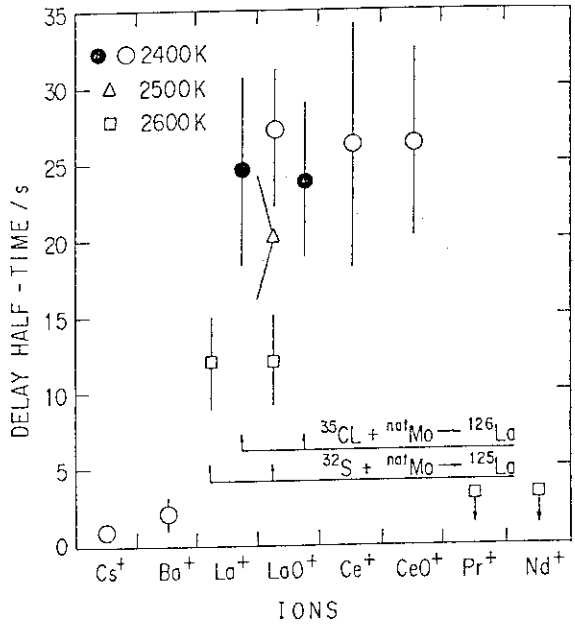

Fig .2 Delay half-times in a thermal ion source.

The above observations are discussed in the following.

The hold-up time of an ion source consists of the times in two independent steps: the diffusion of an atom in the catcher to

its surface and the subsequent effusion in the ionization cavity until emission as an ion. The time for the diffusion process and the time of sticking to the cavity wall during the effusion process are considered.

The diffusion time of the atoms depend on their implanted depth in the catcher and on the diffusion rate at a prescribed temperature. Since the nuclear reaction in our experiment almost had the same bombarding energy of 5 MeV/u, it is assumed that the mean implanted depth in the catcher was essentially the same for the nuclear reaction products studied. The diffusion constants of atom in a heated tantalum foil were experimentally determined and reported by Beyer et al.[5] Since their results indicate that rare-earth atoms diffuse more rapidly than cesium and barium atoms, it is impossible to ascribe the observed difference in the hold-up times to the difference between diffusion times of atom.

Sticking of atoms to the cavity wall was studied experimentally by Kirchner[6,7] for the FEBIAD ion source. The sticking time per collision, t_a, is given for a tantalum surface by the expression[7]

$$t_a[s] = 2.4 \times 10^{-15} \exp\{(11605\Delta H_a[ev])/T[K]\}$$

where ΔH_a denotes the adsorption enthalpy. The adsorption enthalpies determined experimentally or calculated on a semiempirical basis by Eicher and Rossback[8,9] are isted in Table 2 for cesium to neodymium on tantalum and rhenium surfaces; both tantalum and rhenium are construction materials of the ion-source cavity. If we take the semiempirical value of 5.9 eV as the adsorption enthalpy of

Table 2 Adsorption enthalpies of several elements to tantalum and rhenium surface[8,9]

Surface	Adsorption enthalphy (eV)					
	Cs	Ba	La	Ce	Pr	Nd
Ta	2.5+	4.0+	5.5(5.9+)	6.1	5.1	4.7
Re	3.4+	3.7+	6.0	6.1	5.2	4.5

+Values calculated by Rossback and Eicher.[9] The others are taken from experimental values compiled by Eicher.[8]

lanthanum onto tantalum, the adsorption enthalpies of lanthanum and cerium are large enough to explain the long hold-up times of lanthanum and cerium ions. For example, the sticking time per collision for cerium atom is calculated from above equation to be 15 ms at 2400 K for a tantalum surface. The maximum collision number n of an atoms is estimated to be 800 from that $n \sim S_{int.}/S_{exit}$, where $S_{int.}$ is the area of the wall inside the cavity, and S_{exit} the area of the exit orifice. The resulting total sticking time $nt_a \sim 10$ s is of the same order of magnitude as the experimental hold-up time.

8.3.3 Decay Study of Unstable Nuclei

Level energies and γ-transition properties in the low-lying states of ^{123}Ba have been investigated[10] through the decay of ^{123}La. The experiments were performed at the tandem accelerator, using the reaction ^{92}Mo(^{35}Cl,2p2n)^{123}La with a 180-MeV ^{35}Cl beam. The mass-separated ^{123}La activity was implanted into an aluminum-coated Mylar tape in a tape transport system and periodically transported to a measuring position, where γ-ray singles and γ-γ coincidence measurements were performed with a low-energy photon HPGe detector, a 20% HPGe detector and a 28% n-type HPGe detector. From γ-ray singles and γ-γ coincidence measurement of ^{123}La, 12 new levels have been assigned in the level scheme of ^{123}Ba. The new levels at 120.9, 153.6, 328.0, 397.5, 695.3 and 790.8 keV are expected to be the $1/2^+$, $3/2^+$, $5/2^+$, $7/2^+$, $9/2^+$ and $11/2^+$ members of a new band with $K^\pi = 1/2^+$, respectively, because the energy spacings of the six members of this band are fairly consistent with the rotational formula:

$$E_I = E_0 + A\{I(I+1)+a(-1)^{I+1/2}(I+1/2)\},$$

and give a rotational parameter A=21.9 keV and a decoupling parameter a=-0.548(Fig. 3). The bands with the same $K^\pi = 1/2^+$ have been observed in the neighboring nuclei ^{125}Ba(ref.11) and ^{127}Ba(ref.12) as the ground-state bands with the rotational parameter of A=25.5 keV and A=28.3 keV, respectively. The

decrease in the rotational parameter in the sequence ^{127}Ba, ^{125}Ba and ^{123}Ba indicates the increase in deformation.

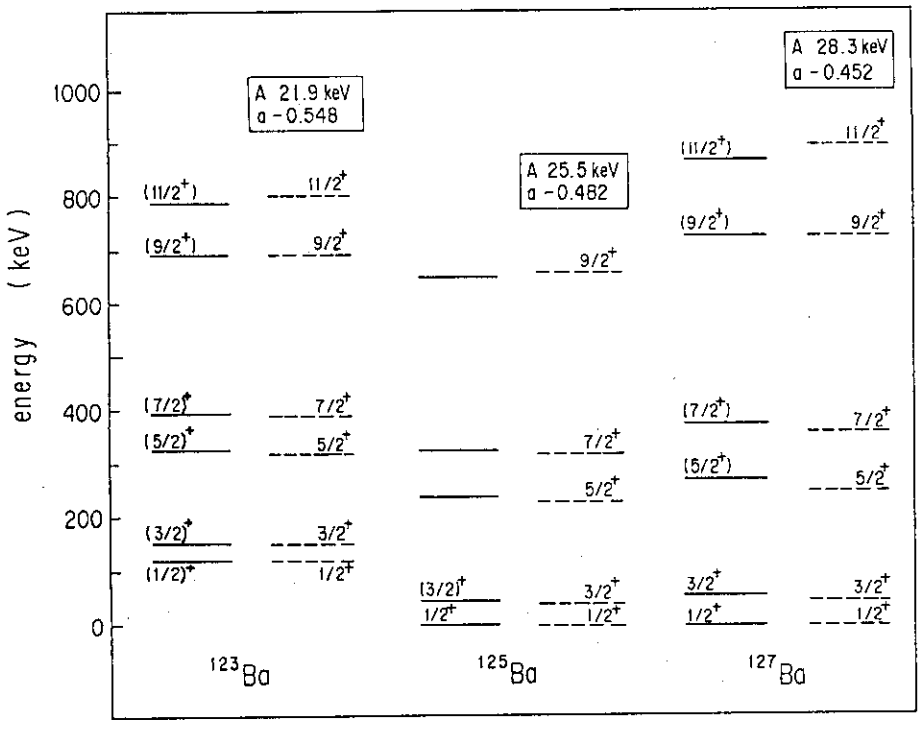

Fig. 3 Systematics of $K^{\pi}=1/2^{+}$ bands in odd-A neutron-deficient Ba isotopes. Experimental levels are indicated by solid lines. Dashed lines indicated using the rotational formura $A\{I(I+1) + a(-1)^{I+1/2}(I+1/2)\}$. The boxes contain the values of A and a parameters.

Lifetimes of excited states provides important information for the nuclear structure study. A program of the measurement of lifetimes is now in progress for the Xe-Ba-Ce transitional region of nuclear deformation.[13] A plastic scintillation detector(Pilot-U) and a BaF_2 detector are used for a $\beta-\gamma$ delayed coincidence measurement; a time resolution of 130 ps has been obtained for 1.3 MeV γ-ray. With this setup, the lifetimes of the 1st excited state(2_1^+) were measured for ^{122,124,126}Ba. The B(E2) values for $0_1^+ \rightarrow 2_1^+$ transition reduced from our experimental lifetimes were plotted against neutron number in Fig. 4 together with literature values. The B(E2) value for ^{122}Ba was found to be largest in Ba nuclei of the major shell, as expected qualitatively from the calculation by IBM-2.[14] The absolute

B(E2) value for ^{122}Ba, however, deviates from the theory, in particular from a more elaborate version of IBM-2 taking into account the Pauli blocking effect. In addition, one can note a "zigzag" pattern near N=66, which is not understandable in the framework of IBM. For better understanding of nuclear collective motion in this region, the extension of this measurement beyond N=66 is challenging.

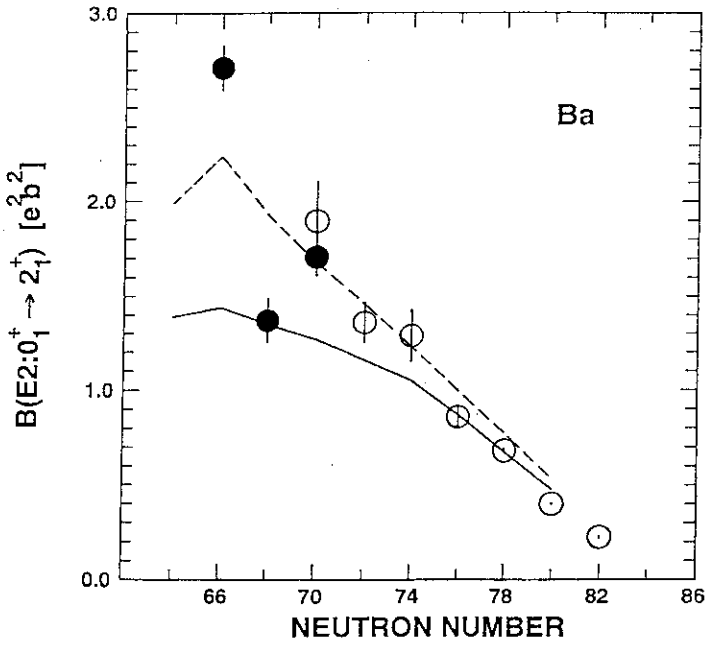

Fig. 4 B(E2; $0_1^+ \rightarrow 2_1^+$) values for neutron deficient Ba nuclei. Data obtained in the present work are indicated in solid circles. Open circles are taken from ref 15. The soild and dashed lines are results of the IBM-2 calculation by Otsuka et al. with and without the pauli blocking effect.

An experimental program of the measurement of β^+-ray maximum energy is also carried out in collaboration with Nagoya group.[16] A β^+-ray detection system free from summation of annihilation photons is constructed using an HPGe detector and two pairs of BaF_2 scintillation detectors.
The decay energy of ^{126}Cs was measured with this system. The isotope was produced by bombarding a 4.1 mg/cm^2 thick Mo foil with a 5.1 MeV/u ^{32}S beam from the tandem accelerator and separated with the JAERI-ISOL. Fermi-Kurie plot of the β^+-ray spectra observed in $\beta^+ - 2\gamma^{\pm}$ coincidence and $\beta^+ - 2\gamma^{\pm} - \gamma$ coincidence with 389 keV γ-ray are shown in Fig. 5. Closed circles correspond to the two components of β^+-rays feeding the ground state and the excited state in 389 keV of ^{126}Xe. Open circles show the second component which is obtained by subtraction of the component feeding the ground state. The endpoint energies of 3.81 ±0.04 and 3.42 ±0.07 MeV are deduced from the $\beta^+ - 2\gamma^{\pm}$

coincidence spectrum. An endpoint energy of 3.39 ± 0.16 MeV is deduced from the β^+-$2\gamma^\pm$ —γ coincidence spectrum. The mean value for Q_{EC} of ^{126}Cs derived from each spectrum is determined to 4.83 ±0.04 MeV. The accuracy of the Q_{EC}-value of ^{126}Cs has been improved.

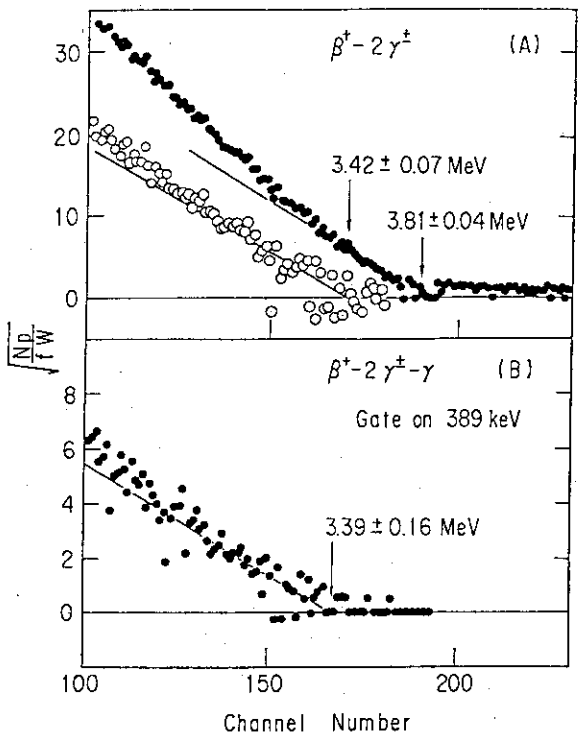

Fig. 5 (A) shows Fermi-Kurie plots of the β^+-ray spectrum of ^{126}Cs free from summation. (β^+-$2\gamma^\pm$). Open circle shows the second component which is obtained from subtraction of the component feeding the ground state. (B) shows the Fermi-Kurie polt of the β^+-ray spectrum free from summation and coincident with the γ-ray of 389 keV.

References

1)Y.Nakahara, H.Iimura, S.Ichikawa, "Laser Spectroscopy," paper in the same volume.
2)S.Ichikawa, T.Sekine, H.Iimura, M.Oshima and N.Takahashi, Nucl. Instr. Meth. **A274** (1989) 259.
3)M.Blann and J.Bisplinghoft, COO-3494-27 (1975).
4)S.Ichikawa, T.Sekine, H.Iimura and M.Oshima Nucl. Instr. Meth. **B** in press.
5)B.-J.Beyer, W-D.Fromma and A.F.Novgroadov, ZfK-309 (1976).
6)R.Kirchner, GSI 87-1, P.259 (1987).
7)R.Kirchner, GSI 88-1, P.339 and P.341 (1988).
8)B.Eicher, ZfK-396 (1979).
9)H.Rossback and B.Eicher, Zfk-527 (1984).
10)H.Iimura, M.Shibata, S.Ichikawa, T.Sekine, M.Oshima, N.Shinohara, M.Miyachi, A.Osa, H.Yamamoto and K.Kawade, J. Phys. Soci. Japan **60** (1991) 3585.

11)H.Iimura, S.Ichikawa, T.Sekine,M.Oshima, N.Shinohara, M.Miyachi, A.Osa, M.Shibata, H.Yamamoto and K.Kawade, JAERI-M 89-119 (1988) 136.
12)C.F.Liang, P.Paris, A.Peghaire, B.Weiss and A.Gizon, Proc. 4th. Int. Conf. on Nuclei far from Stability, Helsingor, 1981, P.487.
13)M.Oshima, T.Sekine, T.Morikawa, Y.Hatsukawa, S.Ichikawa, H.Iimura and M.Shibata, JAERI-M 90-139 (1990) p.161.
14)T.Otsuka, X.W.Pan and A.Arima, Private communication.
15)S.Raman, C.H.Malarkely, W.T.Milner, C.W.Nestor, Jr., and P.H.Stelson, Atomic. Data Nucl. Data tables **36** (1987) 1.
16)A.Osa, T.Ikuta, A.Taniguchi, H.Yamamoto, K.Kawade, Y.Kawase and S.Ichikawa, Nucl. Instr. Meth. **B**. in press.

Publication list

[1]H.Iimura, M.Shibata, S.Ichikawa, T.Sekine, M.Oshima, N.Shinohara, M.Miyachi, A.Osa, H.Yamamoto and K.Kawade, "Level Scheme of ^{123}Ba Fed by the ^{123}La Decay" J. Phys. Soci. Japan **60** (1991) 3585.
[2]S.Ichikawa, T.Sekine, H.Iimura, M.Oshima and N.Takahashi, "Selective Mass Separation of Light Lathanoides by means of ionization of their Monoxides" Nucl. Instr. Meth. **A274** (1989) 259.
[3]S.Ichikawa, T.Sekine, M.Oshima, H.Iimura and Y.Nakahara, "Status Report of the JAERI Isotope Separator On-line" Nucl. Instr. Meth. **B** in press.
[4]S.Ichikawa, T.Sekine, M.Oshima and H.Iimura, "Measurement of Hold-up Times in a Thermal Ion Source for Metallic and Monoxide Ions of Lanthanum and Cerim" Nucl. Instr. Meth. **B** in press.
[5]M.Oshima, T.Sekine, S.Ichikawa, Y.Hatsukawa, I.Nishinaka, T.Morikawa and H.Iimura, "Developement of a Laser-enhanced Ion-Guide ion source" Nucl. Instr. Meth. **B** in press.
[6]A.Osa, T.Ikuta, A.Taniguchi, H.Yamamoto, K.Kawade, S.Ichikawa and Y.Kawase, "Measurement of β-ray Maximum Energy with an HPGe detector by means of β^+-annihilation photons coincidence" Nucl. Instr. Meth. **B** in press.
[7]S.Ichikawa, T.Sekine, H.Iimura and M.Oshima, "Measurement of Release Speeds of La and Ce from a Thermal Ion source" KURRI-TR-333 (1990) 21.
[8]S.Ichikawa, "Status Report of the JERI-ISOL"

KURRI-TR-318 (1989) 67.

[9]H.Iimura, S.Ichikawa, M.Oshima and T.Sekine, "Identification of the New Isotope ^{121}La and Decay Spectroscopy of ^{122,124,126}La and ^{128,130}Pr" KURRI-TR-303 (1988) 30.

[10]A.Osa, M.Miyachi, M.Shibata, H.Yamamoto, K.Kawade, J-Z.Ruan, Y.Kawase, S.Ichikawa and H.Iimura, "Measurement of Beta-ray maximum energy with an HPGe Detector" in Proceeding of "The 2nd International Symposium on Advanced Nuclear Energy Research" Jan. 24-26 1990 Mito.

[11]T.Sekine, S.Ichikawa, T.Morikawa, M.Oshima, A.Osa, Y.Hatsukawa, H.Iimura and N.Shinohara, "Decay of ^{122}La" JAERI-M 91-170 (1991) P.78.

[12]H.Iimura, M.Shibata, S.Ichikawa, T.Sekine, M.Oshima, N.Shinohara, M.Miyachi, A.Osa, H.Yamamoto and K.Kawade, "A beta-decay studies of ^{123}La with an on-line Isotope Separator" JAERI-M 91-170 (1991) P.81.

[13]T.Morikawa, T.Sekine, Y.Hatsukawa, M.Oshima, S.Ichikawa, A.Osa and A.Taniguchi, "Lifetime measurement of the first 2^+ states in ^{122,124,126}Ba" JAERI-M 91-170 (1991) P.84.

[14]A.Osa, S.Ichikawa, H.Iimura, M.Miyachi, M.Shibata, H.Yamamoto, K.Kawade and Y.Kawase, "Measurement of Beta-Ray Maximum Energy with an HPGe Detector" JAERI-M 90-139 (1990) P.109.

[15]S.Ichikawa, T.Sekine, H.Iimura and M.Oshima, "Measurement of Release Speeds of La and Ce from a Thermal Ion source" JAERI-M 90-139 (1990) P.113.

[16]S.Ichikawa, H.Iimura, N.Shinohara, M.Oshima, T.Sekine and Y.Hatsukawa, "Test of an Ion Guide Method for Isotope Separator On Line" JAERI-M 90-139 (1990)P.119.

[17]M.Oshima, T.Sekine, T.Morikawa, Y.Hatsukawa, S.Ichikawa, H.Iimura and M.Shibata, "Lifetime measurement of the first 2^+ states in ^{124,126}Ba" JAERI-M 90-139 (1990) P.161.

[18]H.Iimura, S.Ichikawa, T.Sekine, M.Oshima, N.Shinohara, M.Miyachi, A.Osa, M.Shibata, H.Yamamoto and K.Kawade, "Beta-Decay studies of ^{123}La, ^{125}La and ^{127}La with an on-line Isotope Separator" JAERI-M 89-119 (1989)136.

8.4 Laser Spectroscopy

A combination of an ISOL (Isotope Separator On-Line) and a laser spectroscopy, which is so called a collinear laser-ion-beam spectroscopy, is a powerful method for measuring hyperfine structure (hfs) of atomic spectrum of a short-lived nuclide. The method provides mass separation and sub-Doppler resolution which is based on the velocity compression caused by an acceleration of the ion-beam in a separator.[1] The hfs obtained can be used for extracting nuclear structure information. In order to study electro-magnetic moments and root-mean-square charge radii of radioactive nuclei, a collinear laser-ion-beam spectroscopy system has been recently constructed at JAERI-ISOL. A progress made in our research on the laser spectroscopy from 1989 to 1991 is described here.

The first two experimets which were hfs measurements of samarium-I and europium-II were performed as a test of the instruments.[2] We have then carried out the first Doppler-free measurement of hfs on praseodymium-II by the collinear laser-ion-beam spectroscopy.[3] Presently, hfs measurement of radioactive isotope produced in neutron irradiation has being attempted.

8.4.1 Laser Instrument

A laser system consists of Ar^+-ion laser (Coherent INNOVA 100-20) and a cw ring dye laser (Coherent 699-29). The cw dye laser with wavemeter was pumped with the Ar^+-ion laser and controlled by a personal computer. As a dye we used Rhodamine 6G. The wavemeter was used to determine the absolute frequency which was calibrated by an absorption spectrum of an I_2 cell. The relative frequency of the hyperfine lines was calibrated by a confocal etalon with free spectral range of 150 MHz (Burleigh CFT-500).

8.4.2 Atomic Beam Instrument

Fig.1 shows a schematic view of the atomic beam instrument. The length of the laser beam line is about 70 cm. Atomic beam is ejected from a graphite oven which is heated with a tungsten filament. The oven temparature up to 2000 °C is easily obtained by means of an electron bombardment. The atomic- and laser-beams intersect perpendicularly in the center of the upper reaction chember. The fluorescence light generated by resonance was collected by a spherical mirror onto a photomultiplier. This experiment was done by using samarium. The spectrum obtained by scanning the laser frequency

with around 571.3 nm is shown in Fig.2 togather with the transmission spectrum of the confocal etalon. In this experiment hfs of the ^{147,149}Sm was measured with about 15 MHz of the spectral linwidth. The basic performance of the laser- and atomic-beam-instruments was confirmed.

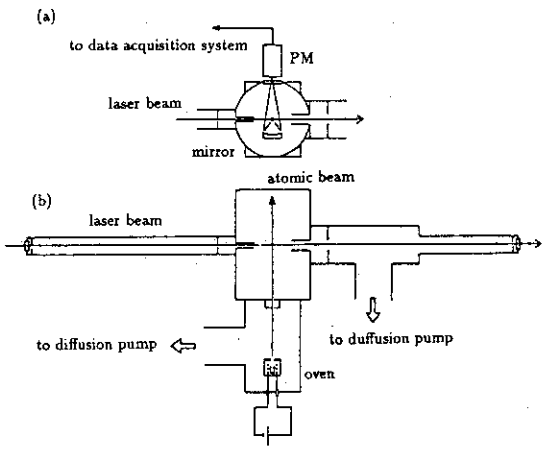

Fig. 1 Top (a) and side (b) schematic view of atomic beam instrument

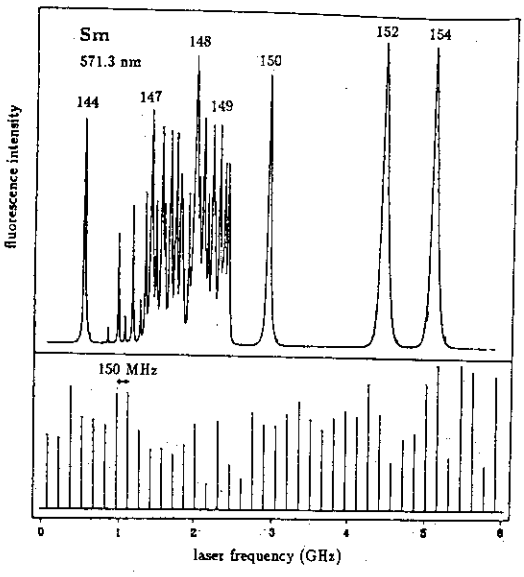

Fig. 2 Hyperfine spectrum of Sm

8.4.3 ISOL Beam Line for Collinear Laser-Ion-Beam Spectroscopy

A experimental set-up for the collinear laser-ion-beam spectroscopy is shown in Fig.3.

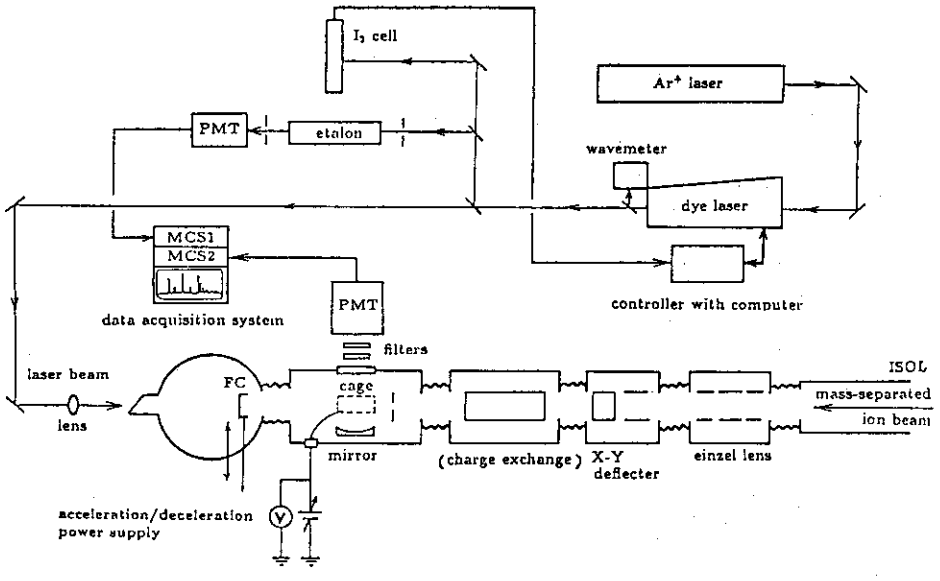

Fig.3 Experimental Setup for Collinear Laser-Ion-Beam Spectroscopy

A mass-separated ion beam is transmitted through two narrow slits (4 mmϕ) which are set upstream and down stream of the interaction region and is focused on a Faraday cup (FC) by an einzel lens. The laser beam is transported into the interaction region through a Brewster window on the axis of the counter-propagating mass-separated beam.

The interaction region was defined by a cage of 10 cm in length and 4 cm in diameter, which was kept at the potential of -3 kV. This potential ensures that the velocity of the ions is Doppler-tuned into resonance in the cage and depopulation pumping of the metastable levels does not occur far upstream from the cage. The fluorescence light after laser excitation was collected by a spherical mirror onto a cooled photomultiplier (Hamamatsu Photonics R943-02). Stray light from the laser beam was suppresed by an appropriate combination of a broad-band filter and a narrow-band interference filter. Hyperfine specra were measured by scanning the laser frequency and recorded in multi-channel scaling (MCS) mode by using a personal-computer-based data acquisition system. The observed linewidth is typically about 90MHz.

An example of measured hyperfine spectrum of $^{151}Eu^{+}$ with the intensity of 3×10^{11} ions/s in 596.6 nm transition and the results of the magnetic-dipole constant A and electric-quadrupole constant B are shown in Fig.4 and Table 1, respectively. The values of A_{151}/A_{153} and B_{151}/B_{153} are in good agreement for the those of reference values[4] of μ_{151}/μ_{153}=2.26 and Q_{151}/Q_{153}=0.391.

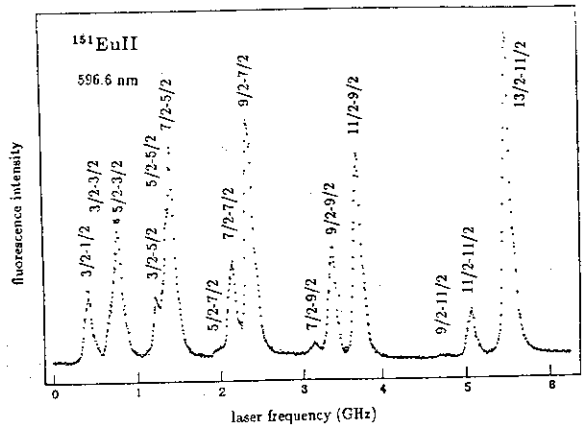

Fig.4 A Example of Measured Hyperfine Spectrum of EuII

In this experiment the basic performance of the instrument for collinear laser-ion-beam spectroscopy was satisfactorily confirmed.

Table 1 Measured A and B constants of EuII

λ(nm)	Level	A_{151}(MHz)	B_{151}(MHz)	A_{153}(MHz)	B_{153}(MHz)	A_{151}/A_{153}	B_{151}/B_{153}
596.6	$(7/2,3/2)_4$	56.0	143	23.6	346		
605.0		56.1	162	25.9	443		
Mean		56.1	152	24.7	395	2.27	0.386
596.6	$^9D^o_3$	-224	-264				
605.0	$^9D^o_4$	-112	-249				

8.4.4 Measurement of Hyperfine Structure in PrII by Collinear Laser-ion-beam Spectroscopy

The Pr-II lines show a hfs due to nuclear spin 5/2 of only the stable isotope ^{141}Pr. The spectra of PrII were investigated by using the methods of Fourier transform spectroscopy and grating photographic spectroscopy, and the results were summarized by Ginibre.[5]

However, these techniques are not sufficient to resolve the hfs because of Doppler broadening. In this work, we made the first Doppler-free measurement of the hfs in Pr-II by collinear laser-ion-beam spectroscopy in the same experimental setup as it mentioned above.

Fig.5 shows partial energy levels of PrII, in which ions in metastable $^5G^o_{2,3}$ levels were excited to the $^5H_3$ level by a laser beam and the fluorescence light from the $^5H_3$ level to the ground level was detected.

Typical hyperfine spectrum for PrII from the metastable $^5G^o_3$ level to the $^5H_3$ level (λ = 604.83 nm) is shown in Fig.6. The magnetic-dipole constant A and the electric-

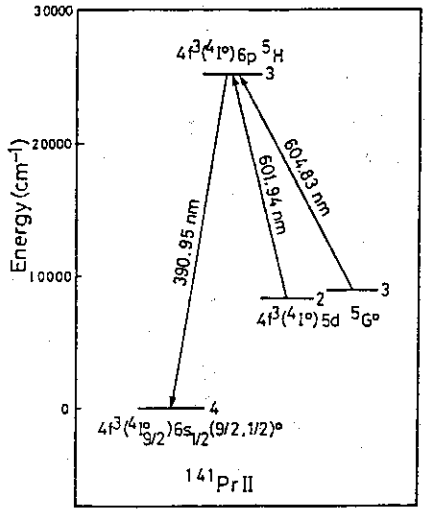

Fig.5 Partial Energy Levels of PrII

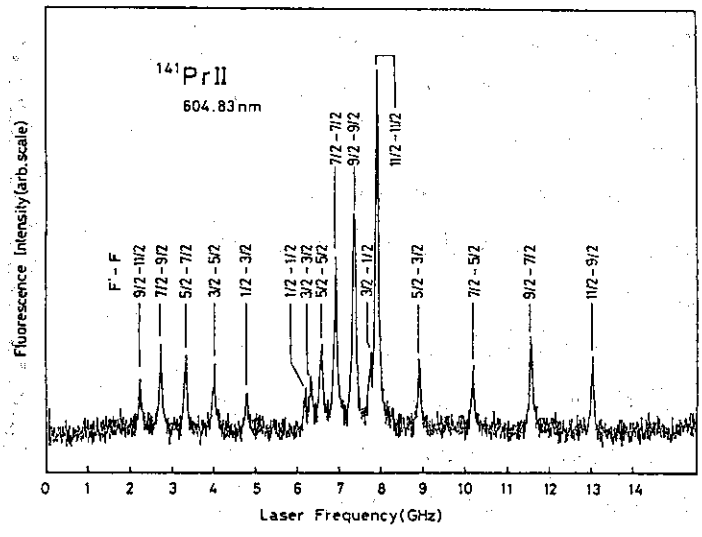

Fig.6 A Example of Measured Hyperfine Spectrum of PrII

quadrupole constant B were derived from the measured hyperfine spectra. Results are summarized in Table 2 with corresponding reference values. In the comparison between the present and reference values, the hyperfine constants A are in good agreement for the $^5G^o_{2,3}$ levels. However, there is considarable disagreement for that of the $^5H_3$ level beyond the error. Concerning the hyperfine constant B, there is no reference values to be compared. These results are consistent with the fact that the nuclear quadrupole moment of ^{141}Pr is very small.

Table 2 Measured A and B constants of PrII

λ(nm)	Level	A(MHz)		B(MHz)[b]
		Present work	Ginibre[a]	Present work
601.94	$4f^3(^4I^o)6p^5H_3$	1028.0±1.2		-16.0±12.6
604.83		1030.6±1.9		-14.2±2.5
mean		1028.7±1.0	891±17	-14.3±2.5
601.94	$4f^3(^4I^o)5d^5G^o_2$	1703.2±0.8	1614±120	-14.1±5.8
604.83	$4f^3(^4I^o)5d^5G^o_3$	932.8±2.2	942±17	-15.1±6.6

a) Ref. 5.
b) There is no reference value to be compared.

8.4.5 Improvement of Collection Efficiency of Fluorescence Photons

The overall efficiency, which is defined as a detected photons per ion, was about 5×10^{-8} in the PrII experiment mentioned above. This value is influenced by different effects such as population of metastable state used, excitation probability, collection efficiency of photons, filter transmission, photomultiplier efficiency and electric efficiency. In a experiment on unstable nuclei, the overall efficiency gives a severe limitation, because the mass-separated yield of unstable nuclei is estimated to be below 10^5 ions/s.

We tried to improve the collection efficiency of photons by changing the spherical mirror to a ellipsoidal mirror as shown in Fig.7. The solid angle of the ellipsoidal mirror is more than ten times larger than that of the spherical mirror, by which the efficiency could be improved to about 7×10^{-7} photons/ion.

Presently, hfs measurement of ^{143}PrII which is radioactive isotope ($T_{1/2}$=16.5d) produced by neutron irradiation in a rector have being attempted by using the improved photon collection system.

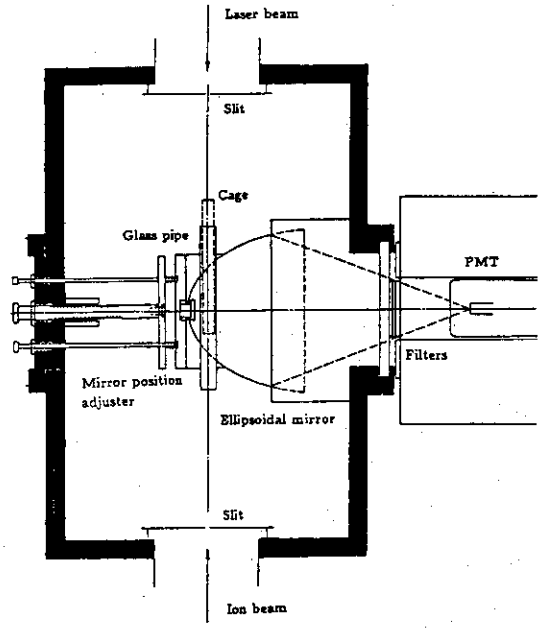

Fig.7 Schematic view of Improved Photon Collection System

References

1) R.Neugart : Nucl. Instru. Meth. **186** (1981)165.

2) H.Iimura, Y.Nakahara, S.Ichikawa, K.Kotani, T.Hasegawa, M.Wakasugi, E.Kim and T.Horiguchi : "Present Condition of Laser Spectroscopy Instrument at JAERI-ISOL", KURRI-TR-333(1990)10.

3) H.Iimura, Y.Nakahara, S.Ichikawa, K.Kotani, M.Wakasugi and T.Horiguchi : "Measurement of Hyperfine Structure of the $4f^35d^5G$-$4f^36p^5H$ in PrII by Collinear Laser-Ion-Beam Spectroscopy", J.Phys. Soci. Japan **59**(1990)4208.

4) "Table of Isotopes", 7th. ed. (1978).

5) A.Ginibre : Phys. Scr. **39**(1989)694.

Publication List

[1] H.Iimura, Y.Nakahara, S.Ichikawa, K.Kotani, T.Hasegawa, M.Wakasugi, E.Kim and T.Horiguchi : "Present Condition of Laser Spectroscopy Instrument at JAERI-ISOL", KURRI-TR-333(1990)10.

[2] Y.Nakahara, H.Iimura, S.Ichikawa, K.Kotani, M.Wakasugi and T.Horiguchi : "A Collinear Laser-Ion-Beam Spectroscopy System"", JAERI-M 91-170(1991)75.

[3] H.Iimura, Y.Nakahara, S.Ichikawa, K.Kotani, M.Wakasugi and T.Horiguchi : "Measurement of Hyperfine Structure of the $4f^35d^5G$-$4f^36p^5H$ in PrII by Collinear Laser-Ion-Beam Spectroscopy", J.Phys. Soci. Japan **59**(1990)4208.

8. 5 High Temperature Corrosion of Iron Chromium Alloys by Tellurium

8. 5. 1 Introduction

In fast breeder reactor(FBR) fuel pins, the possibility of the occurrence of the reaction between stainless steel cladding and fission products such as iodine, cesium, tellurium, etc. has been pointed out by several investigators[1, 2]. In the reactive fission products, tellurium is a corrosive fission product having the fission yield of about 1% in fast breeder reactor(FBR). The presence of tellurium in the gap between fuel and clad has been reported[3, 4]. However, the reaction of iron or iron-chromium alloys with tellurium which is the major component of stainless steel has not been studied yet. It is considered that the reaction rate between tellurium and clad made of stainless steel may be controlled by the diffusion of cations in the tellurides. However, no data for the diffusion coefficients of iron in iron tellurides have been reported.

8. 5. 2 Diffusion of Iron in Iron Tellurides by Mössbauer Spectroscopy

Singwi and Sjölander[5] have derived the relationship between line broadening $\Delta\Gamma$ and average jump frequency $\bar{\nu}$ of a diffusing atom as follows:

$$\Delta\Gamma = 2\hbar\bar{\nu}, \tag{1}$$

The observed line width Γ is the sum of the diffusional line broadening $\Delta\Gamma$ and the minimum reference line width Γ_0 where diffusion does not occur. In order to obtain the diffusional line broadening from the observed line width, we assumed that the reference line width and the activation energy ΔH_m for the atomic diffusion are constant in the temperature range studied. Hence, the relation between the observed line width and the measuring temperature T is expressed by the following equation:

$$\begin{aligned} \Gamma &= \Delta\Gamma + \Gamma_0 \\ &= (\Delta\Gamma)_0 \exp\left(-\frac{\Delta H_m}{RT}\right) + \Gamma_0, \end{aligned} \tag{2}$$

where $(\Delta\Gamma)_0$ is the pre-exponential term of the diffusional line broadening.

Figure 1 shows the full width at half maximum resonance of the spectra of β-, δ'- and ε-phases against the reciprocal of temperature. As seen in this figure, the diffusional line broadening was observed in β- and δ'-phases above 773 and 923K, respectively, but not observed in ε-phase even at temperature near the peritectic point.

The diffusional line broadening of the Mössbauer spectra of iron in β-, δ'- and ε-phases of iron telluride was studied in the temperature range from 573 to 1023K. The activation

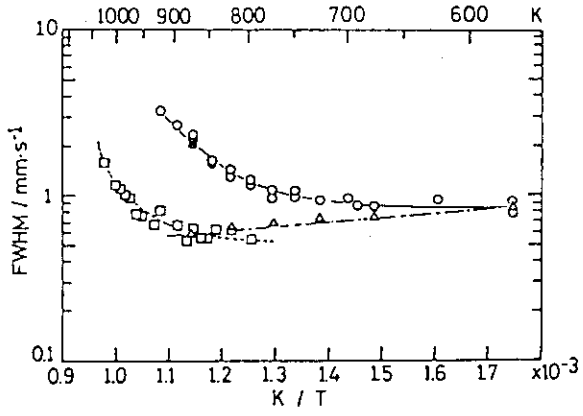

Figure 1 Observed line broadening of Mössbauer spectra in each phase against reciprocal of temperature.
○ : β-phase($Fe_{1.12}Te$)
△ : δ'-phase($Fe_{1.33}Te_2$)
□ : ε-phase($FeTe_{2.11}$)

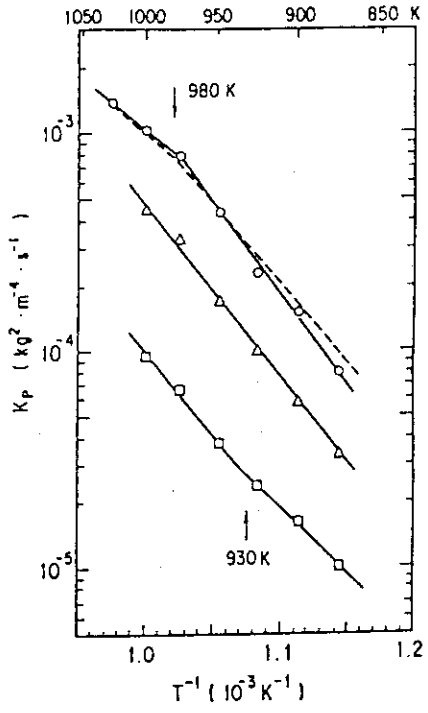

Figure 2 Dependence of reaction rate between alloys and tellurium on tellurium vapor pressure at 923K. The chromium concentrations of the alloys used are 1.17, ○, 5.65, △ and 11.96at.%Cr, □.

Table 1 Activation energies for diffusion of iron in iron tellurides

Phase	Tellurium concentration	Activation energy(kJ/mol)		
		ΔH_m	ΔH_f	$\Delta H_f + \Delta H_m$
β	47.3at.%	91.5 ± 5.4	72	164
δ'	60.1at.%	161 ± 27	-27	134
ε	67.8at.%	–	–	–

energies for atomic diffusion are summarized in table 1. The activation energy for the diffusion of iron in ε-iron telluride is probably very high, because the diffusion coefficient is too small to measure even at 873K near the peritectic point. The jump frequencies in β- and δ'-phases calculated from Mössbauer line broadening were 1.6×10^8 and $4.7 \times 10^6 s^{-1}$ at temperature of 90% of each peritectic point, respectively. The jump frequency in ε-phase was too small to measure even at 873K near peritectic point being less than $2 \times 10^6 s^{-1}$. These data indicate that the jump frequency is likely to be dependent on the distance between the iron atom and the nearest neighboring sites.

8. 5. 3 High Temperature Corrosion of Iron Chromium Alloys by Tellurium

The reaction rates of iron-chromium alloys with tellurium were measured in the temperature range from 873 to 1023K at the tellurium vapor pressure of 350Pa and in the tellurium vapor pressure range from 66.7 to 1000Pa at 923K. The rates of the reaction of the alloy with tellurium obeyed the parabolic rate law. The fact that the parabolic law

holds indicates that those reactions are controlled by the diffusion in telluride scale.

The telluride scale consisted of three types of layers: the inner, the intermediate and the outer layers. Chromium was concentrated on the inner layer which may grow by inward diffusion of tellurium. The intermediate layer consisted of mainly β-iron telluride. The outer layer consisted of both δ-and δ'-iron tellurides below 980K, and δ-iron telluride alone above 980K. The intermediate layer consisting of β-iron telluride in the telluride scale on 11.98at.%Cr alloy completely vanishes as seen from the figure. The intermediate and outer layers grew by outward diffusion of iron in iron tellurides. In the reaction between iron and tellurium, the telluride scale was observed to consist of the inner and outer layers: the inner layer is β-iron telluride grown in parallel to a and b axes, and the outer layer consists of δ and δ'-iron tellurides, but for above 980K, δ'-iron tellurides existed below 980K may be vanished in the outer layer.

Figure 2 shows the plots of the parabolic rate constant of iron-chromium alloys with various chromium concentration(1.17, 5.65 and 11.96at.%Cr) versus reciprocal temperature, in which the broken line corresponds to that for pure iron. The reaction rate decreased with increasing chromium concentration. This is explained by the fact that the iron-chromium alloy surface is protected by being covered with chromium telluride, as chromium telluride covered over the surface of alloy interrupts the outward diffusion of iron. No protection effects of chromium was observed for 1.17at.%Cr alloy, since the concentration of chromium was not enough to form a continuous chromium telluride layer.

Three activation energies for the reaction between alloy and tellurium were obtained from fig. 2 as shown in table 2. In the table, the Roman number in parenthesis shows the region which is classified from the view point of the activation energy. The activation energy ΔH for the reaction between iron-chromium alloy and tellurium at constant tellurium vapor pressure and that for the diffusion ΔH_m of iron in iron telluride at constant tellurium composition are in the following relation:

$$\Delta H = \Delta H_m + \Delta H_f, \tag{3}$$

where ΔH_f represents the formation enthalpy of point defects in iron telluride through which iron atoms diffuse. The values of ΔH_f were estimated by the present authors by using data of the vapor pressure of iron telluride reported as a function of temperature and tellurium concentration by Ipser et al.[6]. By comparison of these values with the activation energies for the diffusion of iron in iron tellurides, the rate-determining step for the reaction of scale formation is thought to be the diffusion of iron in δ'-iron telluride except the case for 1.17at.%Cr alloy above 980K and 11.96at.%Cr alloy below 930K. The former case is thought to be the diffusion of iron in δ-iron telluride while the latter may be the grain boundary diffusion of iron in δ'-iron telluride.

The slope of the plot of the reaction rate against tellurium vapor pressure is obtained to be 1/6 at 923K which is the temperature in region II for 0–5.65at.%Cr alloys and

Table 2 Activation energies for reaction between iron-chromium alloys and tellurium

Chromium composition	Activation energy(kJ/mol),ΔH		
	1023 - 980K	980 - 930K	930 - 873K
Pure Fe	115(I)	140 ± 3(II)	
1.17at.%Cr	93(I)	162 ± 13(II)	
5.65at.%Cr	–	155 ± 4(II)	
11.96at.%Cr	–	144 ± 15(II)	109 ± 3(III)

in region III for 11.96at.%Cr alloy. The slope of 1/6 may be explained by the defect structure of a doubly charged cation vacancy. The most outer layer on iron-chromium alloy as well as that on iron is consisted of δ'-iron tellurium. The defect structure of the iron telluride forming the most outer layer on iron-chromium alloys similar to that on iron can be explained as a doubly charged iron vacancy.

References

(1)M.G. Adamson, E.A Aitken, in:Proc. Intern. Conf. on Fast Breeder Reactor Fuel Performance, (Monterly CA, 1979) p.536.

(2)M.G. Adamson, E.A. Aitken, T.B. Lindemer, J. Nucl. Mater. 130(1985)375.

(3)J.W. Weber, R.D. Jensen, Trans. Am. Nucl. Soc. 14(1971)175.

(4)C.T. Walker, J. Nucl. Mater. 74(1978)358.

(5)K.S. Singwi and A. Sjölander, Phys. Rev. 120 (1960) 1093.

(6)H. Ipser, K.L. Komarek, Monatsh. Chem. 105(1974)1344.

Publication list

[1] M. Magara, T. Tsuji and K. Naito, "A Mössbauer Effect Study of Fast Ionic Diffusion of Iron Telluride", Solid State Ionics 40/41(1990)284.

[2] M. Magara, T. Tsuji and K. Naito, "Diffusion of Fe in Iron Tellurides by Mössbauer Spectroscopy", Hyperfine Int. 56(1990)1459.

[3] M. Magara, T. Tsuji and K. Naito, "High Temperature Corrosion of Iron Chromium Alloys by Tellurium", J. Nucl. Sci. Technol. 28(1991)721.

[4] M. Magara, T. Tsuji and K. Naito, "Kinetics and Mechanism of Telluride Scale Growth on Iron", J. Nucl. Sci. Technol. in print.

9. SOLUTION CHEMISTRY OF TRANSURANIUM ELEMENTS

M. Hoshi, J. Akatsu, T. Sato, C. Yonezawa and T. Kimura

9.1 Separation and Determination of Transuranium Elements Using Coprecipitation with Bismuth Phosphate

9.1.1 Introduction

The isotopic identification and determination of alpha emitting elements in radioactive wastes and environmental samples are indispensable for the waste management and environmental monitoring. The coprecipitation with bismuth phosphate have been used for the separation of plutonium from large quantities of water[1,2], bones[3], urine and faces[4,5]. However, the method required the dissolution of the precipitates and further coprecipitation with lanthanum fluoride for the measurement of alpha activity. Furthermore, little is known about information on the coprecipitation behavior of coexisting other actinide elements. The present work has been carried out to clarify the coprecipitation behavior of neptunium, plutonium, americium and curium in tracer amounts under the various chemical conditions and to establish the optimum condition of simultaneous determination of the actinide elements by coprecipitation with bismuth phosphate. On the other hand, with the knowledge that actinide elements of only in trivalent and tetravalent states are coprecipitated with bismuth phosphate, successive separation of the actinide elements can be attained by adding proper oxidizing and/or reducing agents at appropriate stages. An effective and simple method for separating the elements from each other by the coprecipitation with bismuth phosphate has also been studied.

9.1.2 Experimental

Materials and measurements

The sample solutions were prepared from radioactive tracers such as ^{237}Np, ^{239}Pu, ^{241}Am and ^{244}Cm supplied by C.E.A., France or by Amersham Radiochemical Centre, UK. These nuclides were dissolved in sulfuric acid solution for the coprecipitation study. Fission products were prepared from uranium dioxide irradiated in Japan Research Reactor 2 (JRR-2) at a thermal neutron flux of about 2×10^{13} $n \cdot cm^{-2} \cdot s^{-1}$ for 265 hours. Long-lived nuclides such as ^{90}Sr-Y, ^{95}Zr-Nb, ^{106}Ru-Rh, ^{137}Cs, ^{144}Ce-Pr and ^{147}Pm

were contained in the fission products during the experiments.

Alpha and beta activities were measured with a 2π-geometry gas flow proportional counter using PR gas (Ar 90 % and CH_4 10 %) or Q gas (He 99 % and $(CH_3)_3CH$ 1 %) as the counting gas. Alpha spectra were obtained with a 450 mm^2 silicon surface barrier detector with a 1024-channel pulse-height analyzer. A Ge detector was used to identify and determine gamma-radioactive nuclides.

Coprecipitation procedure

The procedure of coprecipitation is based on the previous method (coprecipitation with barium sulfate)[6,7] and the method was modified and applied to coprecipitation with bismuth phosphate. Filter papers (Millipore HAWP 04700, 47 mmϕ, 0.45 μm pore size) were used in all experiments. All the precipitates on the filter were dried under an infrared lamp, mounted on a stainless steel plate, and counted with similar efficiency as for the standards.

9.1.3 Results and Discussion

Effect of acid and acidity on coprecipitation

More than 98 % of Np(IV), Pu(IV), Am(III) and Cm(III) were coprecipitated with bismuth phosphate in 0.1-1.0 M phosphoric acid by adding 5 mg of bismuth. However, the coprecipitation yields considerably decreased at the phosphoric acid concentration higher than 1 M, which is due to the increase of the solubility of bismuth phosphate. More than 98 % of the elements were also coprecipitated with bismuth phosphate in sulfuric acid below 0.1 M or nitric acid below 0.05 M in the presence of 1 M phosphoric acid by adding 5 mg of bismuth. The coprecipitation yields decreased rapidly with increasing acidity. The decreases of the coprecipitation yields might be also attributed to the increase of the solubility. In sulfuric acid solution higher than 1 M, the decrease of phosphoric acid concentration brought the decrease of the coprecipitation yields of the elements. In general, the actinide ions in trivalent or tetravalent state form stable sulfate complexes as well as phosphate complexes in aqueous solution. Therefore, it is considered that the coprecipitation of the elements is depressed by the formation of sulfate complexes at lower concentration of phosphoric acid.

Effect of bismuth amount on coprecipitation

Figure 1 shows the results of the coprecipitation yields of Np(IV), Pu(IV), Am(III) and Cm(III) and of the energy resolution of the alpha-

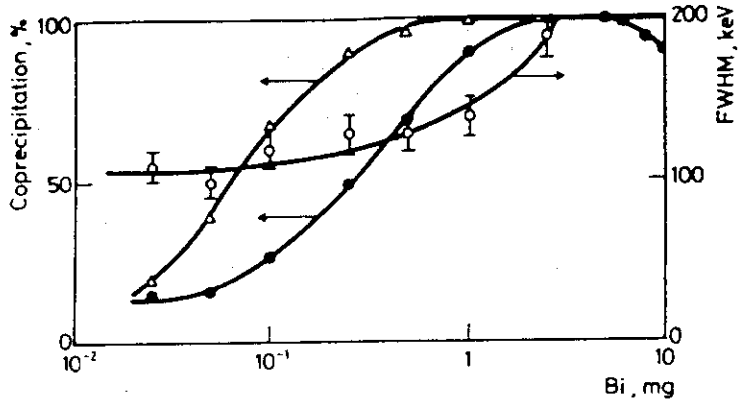

Fig. 1 Effect of bismuth amount on coprecipitation of Np, Pu, Am and Cm with $BiPO_4$; 0.013M H_2SO_4; ○ ● 1M H_3PO_4, △ 0.2M H_3PO_4

spectra at various amounts of bismuth. These actinide elements were quantitatively coprecipitated with bismuth phosphate by adding more than 1.0 or 2.5 mg of bismuth for 0.2 or 1 M phosphoric acid solution, respectively. The apparent decrease of the yields at above 6 mg of bismuth is due to the self-absorption of alpha-rays by the bismuth phosphate precipitates. At the bismuth amounts less than the value listed above the coprecipitation yields decreased gradually. The difference of the decrease in 0.2 and 1 M phosphoric acid solutions suggests that the solubility of bismuth phosphate increases with concentration of phosphoric acid, which is in agreement with the tendency described above. The energy resolution of alpha-spectra was expressed in full width at half maximum peak height (FWHM) at 5.49 MeV (^{241}Am). These results show that in 0.2 M phosphoric acid solution the addition of 1.0 mg bismuth gives both the quantitative coprecipitation of Np(IV), Pu(IV), Am(III) and Cm(III) with bismuth phosphate and the energy resolution of 140 keV which makes it possible to evaluate roughly these elements in the precipitate by direct measurement of alpha spectrum. However, the separation of the elements from each other will be required when the sample solution contains the nuclides such as ^{238}Pu and ^{241}Am which emit alpha-rays of nearly equal energy.

Reactions of neptunium, plutonium and americium with oxidizing and reducing agents

Since U(VI) and Cm(III) are stable in phosphoric acid solution, the effect of various oxidizing and reducing agents on the oxidation states of the actinide elements is studied for neptunium, plutonium and americium. In the presence of silver catalyst, $K_2S_2O_8$ rapidly oxidized Np(IV), Pu(IV)

and Am(III) to hexavalent state, which suggests that $K_2S_2O_8$ with catalyst serves as an oxidizing agent for the separation of Cm(III) from Np(VI), Pu(VI) and Am(VI). On the other hand, $KMnO_4$ rapidly oxidized Np(IV) and Pu(IV) to hexavalent state and $KBrO_3$ completely oxidized Np(IV) to Np(VI). These results suggest that $KMnO_4$ is useful oxidizing agent for the separation of Am(III) and Cm(III) from Np(VI) and Pu(VI) and that $KBrO_3$ is also useful for the separation of Pu(IV), Am(III) and Cm(III) from Np(VI).

Carboxylic acid (HCOOH, CH_3COOH) and alcohol (CH_3OH, C_2H_5OH) rapidly reduced Am(VI) to trivalent state but not Np(VI) and Pu(VI) at even 100 C with stirring for 5 min. This shows that carboxylic acid and alcohol are useful for the separation of Am(III) and Cm(III) from Np(VI) and Pu(VI). On the other hand, $NaNO_2$ reduced Np(VI), Pu(VI) and Am(VI) to Np(V), Pu(IV) and Am(III), respectively. H_2O_2 and Fe^{2+} reduced Np(VI), Pu(VI) and Am(VI) to trivalent or tetravalent state. These results suggest that $NaNO_2$ is a convenient reducing agent for the separation of Pu(IV), Am(III) and Cm(III) from Np(V) and that even if uranium might be present in the sample solution, all the transuranium elements would be separated from uranium by using H_2O_2 or Fe^{2+}.

Sequential separation of neptunium, plutonium, americium and curium

From the experimental results described above, the following procedure for sequential separation of neptunium, plutonium, americium and curium from uranium is constructed.

1) Neptunium, plutonium and americium are oxidized to hexavalent state by adding $K_2S_2O_8$-Ag^+ and Cm(III) is separated from U(VI), Np(VI), Pu(VI) and Am(VI) by coprecipitation (curium fraction).

2) Am(VI) is reduced to Am(III) by adding C_2H_5OH and Am(III) is then separated from U(VI), Np(VI) and Pu(VI) by coprecipitation (americium fraction).

3) Np(VI) and Pu(VI) are reduced to Np(V) and Pu(IV) by adding $NaNO_2$ and Pu(IV) is then separated from U(VI) and Np(V) by coprecipitation (plutonium fraction).

4) Np(V) is reduced to Np(IV) by adding H_2O_2 and Np(IV) is finally coprecipitated (neptunium fraction), while U(VI) is left in the filtrate.

The coprecipitation with bismuth phosphate is performed by adding 2.5 mg of bismuth to 40 ml of 1 M phosphoric acid solution. The experimental results of the procedure for neptunium, plutonium, americium and curium are summarized in Table 1. The results show that 95 % or more of the actinide elements are coprecipitated with bismuth phosphate of each frac-

Table 1 Distribution of Np, Pu, Am and Cm during their sequential separation on $BiPO_4$

$BiPO_4$ precipitation	Cm, %	Am, %	Pu, %	Np, %
Cm fraction	98.5 ± 1.8	1.5 ± 0.2	−	−
Am fraction	1.4 ± 0.2	97.6 ± 1.8	3.5 ± 0.3	2.7 ± 0.3
Pu fraction	<0.1	0.8 ± 0.2	94.7 ± 1.8	1.1 ± 0.2
Np fraction	−	<0.1	0.7 ± 0.2	96.0 ± 1.8
Total	>99.9 ± 1.8	>99.9 ± 1.8	98.9 ± 1.8	99.8 ± 1.8

tion and that the contamination of the other elements in each fraction is 1.5 % or less, except neptunium and plutonium in the americium fraction. On the other hand, it was confirmed experimentally that uranium was in hexavalent state during the procedure and was almost left in the filtrate.

Coprecipitation behavior of fission products

Table 2 shows the distribution of fission products during the course of sequential separation of the actinide elements on bismuth phosphate. Although the total beta activity is variable because the composition of fission products depends on a cooling time of a irradiated sample, in the case of the sample (a cooling time of 1.5 years) about 50 % of the total activity was coprecipitated with curium fraction and about 30 % of that was left in the filtrate. These results suggest that trivalent and tetravalent ions such as rare earth elements can be coprecipitated with curium fraction and the residual fission products will be left in the filtrate, though question still remains in the behavior of zirconium and niobium.

Table 2 Distribution of fission products during the course of sequential separation of actinide elements on $BiPO_4$

$BiPO_4$ precipitation	^{95}Zr, %	^{95}Nb, %	^{106}Ru, %	^{137}Cs, %	^{144}Ce, %	β-counts, %
Cm fraction	6.3 ± 1.2	40.4 ± 1.3	1.6 ± 0.4	0.1	95.5 ± 0.8	48.1 ± 0.1
Am fraction	10.3 ± 1.2	4.1 ± 0.3	0.4 ± 0.1	0.3 ± 0.1	0.1	7.5
Pu fraction	8.6 ± 1.0	2.7 ± 0.2	0.8 ± 0.2	0.2	0.4	4.6
Np fraction	7.4 ± 1.0	3.7 ± 0.2	0.4 ± 0.1	0.3 ± 0.1	−	1.4
Filtrate	68.9 ± 8.3	44.6 ± 2.4	27.0 ± 3.1	99.3 ± 3.1	0.9 ± 0.1	31.7 ± 0.1
Total	101.5 ± 8.6	95.5 ± 2.8	30.2 ± 3.1	100.2 ± 3.1	96.9 ± 0.8	93.3 ± 0.1

9.1.4 Conclusions

The coprecipitation procedure described has several advantages including simplicity, rapidity, and high reliability without tracers as yield monitors. Simultaneous and/or separate determination of transuranium elements is also possible by combination of redox reaction of the elements. Therefore, the procedures will be applicable to the determination of the alpha emitting elements in nuclear process wastes and environmental samples.

References

1) J. Kooi and U. Hollstein, Health Phys. 8(1962)41.
2) U. Hollstein, A.H.M. Hoogma and J. Kooi, Health Phys. 8(1962)49.
3) Z. Holgye, Fresenius Z. Anal. Chem. 315(1983)247.
4) Z. Holgye, Fresenius Z. Anal. Chem. 320(1985)181.
5) Z. Holgye, Appl. Radiat. Isot. 37(1986)1015.
6) T. Kimura and Y. Kobayashi, J. Radioanal. Nucl. Chem. 91(1985)59.
7) T. Kimura, Y. Kobayashi and J. Akatsu, Radiochim. Acta, 39(1986)179.

Publication List

[1] T. Kimura, "Simultaneous Determination of Neptunium, Plutonium, Americium and Curium Using Coprecipitation with Bismuth Phosphate," J. Radioanal. Nucl. Chem. 139(1990)297.
[2] T. Kimura, "Sequential Separation of Neptunium, Plutonium, Americium and Curium Using Coprecipitation with Bismuth Phosphate," J. Radioanal. Nucl. Chem. 139(1990)307.

9.2 Separation of Actinide Elements and Fission Products by Extraction Chromatography in the Bifunctional Extractant-Nitric Acid System

9.2.1 Introduction

The various nitric acid solutions containing actinide elements are generated from many stages of nuclear fuel cycle. The separation, removal and recovery of the elements from the waste solution have been an important problem in view of radioactive waste management. Bifunctional organophosphorus compounds, dihexyl-N,N-diethylcarbamoylmethylphosphonate(CMP) and octyl(phenyl)-N,N-diisobutylcalbamoylmethylphosphine oxide(CMPO), extract trivalent actinide ions as well as tetra- and hexavalent ions from moderately concentrated nitric acid[1]. Application of extraction chromatography with the bifunctional extractants, in the presence of TBP as a modifier, has then been studied for the removal and recovery of tri-, tetra- and hexavalent actinide ions from nitric acid. On the other hand, the CMP solvent extraction data of trivalent actinide and lanthanide ions suggest the possibility of mutual separation of these elements using only nitric acid[2]. Application of extraction chromatography in the CMP-HNO_3 system has also been studied for the analytical separation of the actinide elements and fission products. The present paper deals with the comparative studies of TBP-CMP/XAD-4 and TBP-CMPO/XAD-4 resins with anion and cation exchange resins on the removal and recovery of Am(III), Pu(IV) and U(VI), and the elution studies of Np(V), Am(III), Cm(III) and fission products on CMP/XAD-4 column.

9.2.2 Experimental

Materials

CMP, obtained from Occidental Chemical Corp., New York, was used without additional purification. CMPO, obtained from M&T Chemicals, Inc., New Jersey, was purified by hydrolysis with 6 M HCl and washing with 0.5 M NaOH and water. TBP, obtained from Koso Chemical Co., Tokyo, was purified by washing with 5 % Na_2CO_3 and water. Amberlite XAD-4, supplied as 20-50 mesh beads from Rohm and Haas Co., USA, was used as a support material of extractants. The preparation procedure of extractant loaded XAD-4 resin was described in the previous report[3]. The 50 wt%(1 g of extractant/g XAD-4 resin) resins in 20-50 mesh or 100-130 mesh were used for batch or column experiments, respectively.

Radioactive tracers such as ^{233}U, ^{237}Np, ^{239}Pu, ^{241}Am and ^{244}Cm were

used in the experiments. Fission products(^{90}Sr-Y, ^{137}Cs, ^{144}Ce-Pr and ^{147}Pm etc.) were prepared from uranium dioxide irradiated in Japan Research Reactor 4 (JRR-4).

Batch distribution experiments

From the radiometric analysis of aqueous phase, the distribution coefficient D as defined by Eq.(1) was calculated

$$D = \frac{C_0 - C}{C} \cdot \frac{V}{M} \quad (ml/g) \qquad (1)$$

where C_0 is initial concentration of a metal ion in the aqueous phase, C equilibrium concentration of the metal ion in the aqueous phase, V volume of the aqueous phase (ml) and M mass of the extractant/XAD-4 or ion exchange resin (g).

Column experiments

Slurry packing procedure was adopted for the column preparation. Temperature of the column was held constant by a water jacket with circulating thermostat. The eluent was supplied by a micro-tube pump and the flow rate was held constant. Fractions of 1.0 ml volume were collected by an automated fraction collector, and the element in each fraction was determined by the radiometric analysis.

9.2.3 Results and Discussion

Application of TBP-CMP/XAD-4 and TBP-CMPO/XAD-4 resins for removal and recovery of actinide elements

(i) Distribution coefficients of Am(III), Pu(IV) and U(VI).

Figures 1 and 2 show the distribution coefficients of Am(III), Pu(IV) and U(VI) between HNO_3 and 50 wt% TBP-CMP/XAD-4 and between HNO_3 and 50 wt% TBP-CMPO/XAD-4 resins, respectively. The tetravalent plutonium was prepared by the addition of 0.001 M $NaNO_2$ at the batch distribution experiments. The distribution coefficients of all three actinide ions for the TBP-CMP/XAD-4 resin increased with increasing HNO_3 concentration. The higher distribution coefficients of the actinide ions for the TBP-CMPO/XAD-4 resin were observed in the wide range of HNO_3 concentration. The effect of CMP or CMPO addition on the extraction of the actinide ions was the greatest for Am(III). A distinct synergistic interaction of the bifunctional extractant and TBP was not observed in both the TBP-CMP and TBP-CMPO systems. These results show that the TBP-CMP/XAD-4 resin makes it possible to extract tri-, tetra- and hexavalent actinide ions at higher concentration of HNO_3 and to recover the extracted actinide

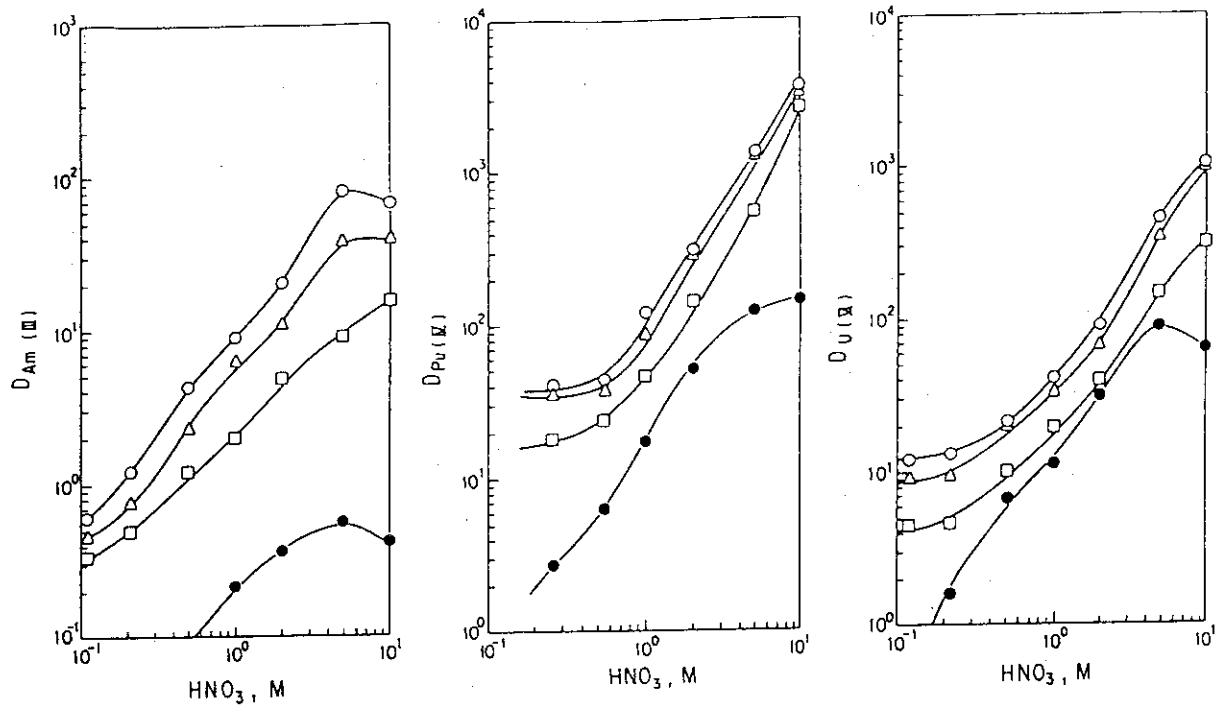

Fig. 1 Distribution coefficients of Am(III), Pu(IV) and U(VI) between HNO_3 and 50 wt% TBP-CMP/XAD-4 resin; ●, 1.88 M TBP; □, 1.25 M TBP-0.46 M CMP; △, 0.63 M TBP-0.92 M CMP; ○, 1.38 M CMP; M, mol/kg resin; 25°C.

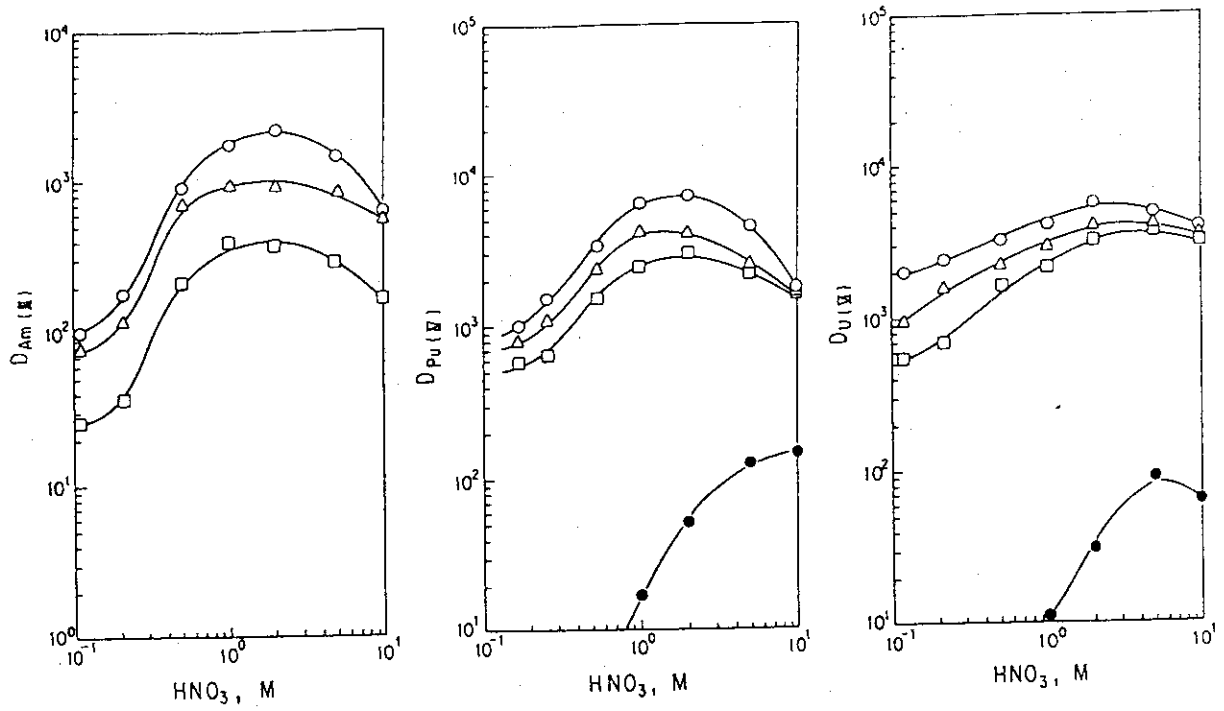

Fig. 2 Distribution coefficients of Am(III), Pu(IV) and U(VI) between HNO_3 and 50 wt% TBP-CMPO/XAD-4 resin; ●, 1.88 M TBP; □, 1.25 M TBP-0.41 M CMPO; △, 0.63 M TBP-0.82 M CMPO; ○, 1.23 M CMPO ;M, mol/kg resin; 25°C.

ions by dilute HNO_3. On the other hand, although the TBP-CMPO/XAD-4 resin is a powerful resin for the removal of the actinide ions from HNO_3, the use of complexing agents might be required for back extraction of the actinide ions from the resin at low concentration of HNO_3.

(ii) Comparison with anion and cation exchange resins.

The distribution coefficients of Am(III), Pu(IV) and U(VI) between HNO_3 and Dowex 1-X8 and 50W-X8 were also measured to compare with the results of the TBP-CMP/XAD-4 and TBP-CMPO/XAD-4 resins. The distribution coefficients obtained with the anion exchange resin (Dowex 1-X8) were more than 10^2 for Pu(IV) at above 3 M HNO_3, however those for Am(III) and U(VI) were less than 10^2 and 10^1 in the range of 0.1 and 10 M HNO_3, respectively. On the other hand, the higher distribution coefficients D were obtained with the cation exchange resin (Dowex 50W-X8) at low concentration of HNO_3, that is, $D>10^3$ for Am(III) and Pu(IV) at below 1.5 M HNO_3 and $D>10^2$ for U(VI) at below 0.5 M HNO_3. These results show that the cation exchange resin has a high ability for the removal of the actinide ions at low concentration of HNO_3, while the anion exchange resin does not have the ability except for Pu(IV).

Application of CMP/XAD-4 column for analytical separation of actinide elements and fission products

(i) Effect of temperature, flow rate and HNO_3 concentration.

In order to determine the conditions of column operation for actual separation of actinide elements and fission products, the effect of temperature of column, flow rate and HNO_3 concentration of eluent on the distribution coefficient, separation factor and resolution was studied by using Np(V), Am(III) and Cm(III). The separation factor is expressed as a ratio of the distribution coefficients. The resolution, which represents the degree of separation of two peaks in an elution chromatogram, is defined by

$$R = \frac{V_2 - V_1}{W_1 + W_2} \qquad (2)$$

where V is the total retention volume and W is the width of elution peak at the 1/e concentration of solute to the maximum. The results suggest that the CMP/XAD-4 column operation is more effective for slower flow rate of eluent and higher temperature of the column at a fixed HNO_3 concentration and that the resolution increases with increasing HNO_3 concentration, while the separation factor is held constant.

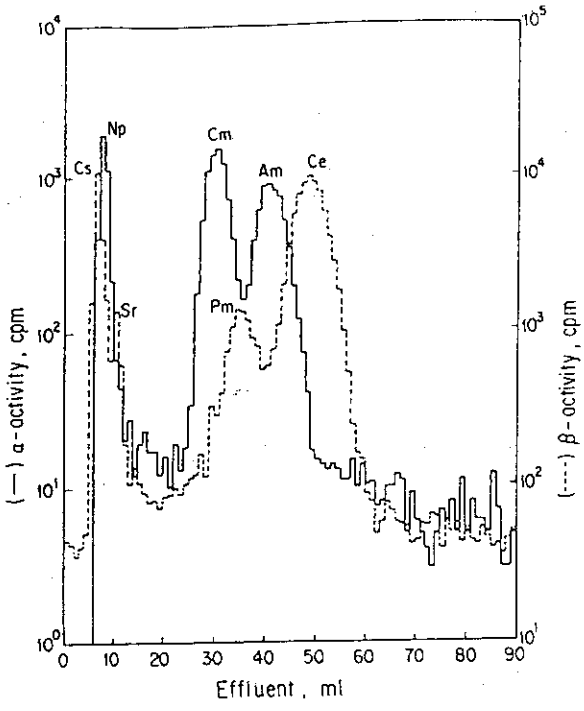

Fig. 3 Elution curves of Np, Am, Cm and fission products; Column bed, 6 mmϕx270 mm; Resin, 4.0 g of 50 wt% CMP/XAD-4; Eluent, 1.5 M HNO_3; Flow rate, 0.020 ml/cm^2min; Temperature, 40°C.

(ii) Separation of Np(V), Am(III), Cm(III) and fission products.

On the basis of the experimental results, the elution curves of Np(V), Am(III), Cm(III) and fission products were measured at the optimum condition and are shown in Fig. 3. The results indicate that Np(V) and the fission products except lanthanide elements are effectively separated from trivalent actinide and lanthanide ions, that the trivalent actinide and lanthanide ions can be separated roughly from each other by using only HNO_3 and that the order of the distribution coefficients is Ce>Am>Pm>Cm>>Sr>Np>Cs.

9.2.4 Conclusions and Future work

The TBP-CMP/XAD-4 and TBP-CMPO/XAD-4 resins were more effective than the ion exchange resins for removing tri-, tetra- and hexavalent actinide ions from moderately concentrated HNO_3. The metal ion loading capacity of the resin and the recovery of the actinide elements from the resin should be studied by both batch and column experiments.

Chromatographic separation of Np(V), Am(III), Cm(III) and fission products by the CMP/XAD-4 column was carried out by using only HNO_3 without other complexing agents. The extraction chromatography in the CMP- or CMPO-HCl and CMPO-HNO_3 with complexing agent systems should also be studied for more selective separation of the actinide elements from fission products and from each other.

References

1) E.P. Horwitz, H. Diamond and D.G. Kalina, in: Plutonium Chemistry (ACS Symposium Series 216), Eds. W.T. Carnall and G.R. Choppin, (American Chemical Society, Washington, 1983) p.443.
2) E.P. Horwitz, A.C. Muscatello, D.G. Kalina and L. Kaplan, Sep. Sci. Technol. 16(1981)417.
3) J. Akatsu and T. Kimura, J. Radioanal. Nucl. Chem. 140(1990)195.

Publication List

[1] J. Akatsu and T. Kimura, "Extraction Chromatography in a DHDECMP (XAD-4)-HNO_3 System," J. Radioanal. Nucl. Chem. 140(1990)195.
[2] T. Kimura and J. Akatsu, "Extraction Chromatography in the DHDECMP-HNO_3 System I. Extraction Behavior of Ce(III) and Am(III) with the DHDECMP/XAD-4 Resin," J. Radioanal. Nucl. Chem. 149(1991)13.
[3] T. Kimura and J. Akatsu, "Extraction Chromatography in the DHDECMP-HNO_3 System II. Characteristics of the DHDECMP/XAD-4 Resin on Separation of Trivalent Actinide Elements," J. Radioanal. Nucl. Chem. 149(1991)25.
[4] T. Kimura and J. Akatsu, "Applications of Extraction Chromatography in the Bifunctional Extractant-Nitric Acid System for Separation of Actinides in Nuclear Fuel Cycle," Proc. Int. Solvent Ext. Conf. 1990, in press.

9.3 Studies on Neutron Activation Analysis

(1) Construction of reactor neutron induced prompt gamma-ray analyzing system at the neutron beam guide of JRR-3M[1)]

A system of reactor neutron induced prompt gamma-ray analysis (PGA) is being constructed at the cold and the thermal neutron beam guides of the 20 MW upgraded research reactor JRR-3M. Owing to the high purity of the slow neutron beams, the detectors can be placed near the sample without intolerable background, so that the detection efficiency of the prompt gamma-rays is largely improved compared to the case in usual system. The present analyzing system is constructed as a permanent and stand alone instrumentation while most of the conventional systems have been used only temporarily or as a supplement to other methods.

The setup at the thermal neutron beam port is illustrated in Fig. 1. The system consists of beam guide tube, neutron beam shutter, sample box with shielding, neutron stopper and a multi-mode gamma-ray spectrometer. The whole set of the analyzing system except for the guide tube is transferred to the cold neutron beam port for the cold neutron beam experiments. The neutron beam is guided to the sample position through the neutron collimators made with LiF tiles and evacuated guide tube. The neutron intensity at the sample position is 2.0×10^8 and 1.2×10^8 n cm^{-2} s^{-1} for cold and thermal neutrons, respectively. A Teflon sample box is placed behind the beam collimator. The sample is placed and irradiated in the sample box. The sample box can be filled with He gas to reduce loss of beam intensity by neutron absorption and scattering in air and to reduce capture gamma-rays from nitrogen in air. The emitted prompt gamma-rays are detected through the windows of the sample box and through ^{6}LiF tile. The neutron beam can be absorbed by sintered B_4C and the emitted prompt gamma-rays (478 keV) are absorbed by Pb in the beam shutter and stopper.

The multi-mode gamma-ray spectrometer consists of a closed end coaxial type high purity Ge detector surrounded by a nose corn type BGO (bismuth germanate, $Bi_4Ge_3O_{12}$) scintillation detector, catcher BGO detectors and a pulse height analyzer (PHA) system controlled by a personal computer. Three modes of prompt gamma-ray measurements; single mode, Compton suppression mode, and pair spectrum mode can be performed simultaneously. The Ge detector is set with its axis perpendicular to the neutron beam at a distance 29.5 cm from the sample position. The distance

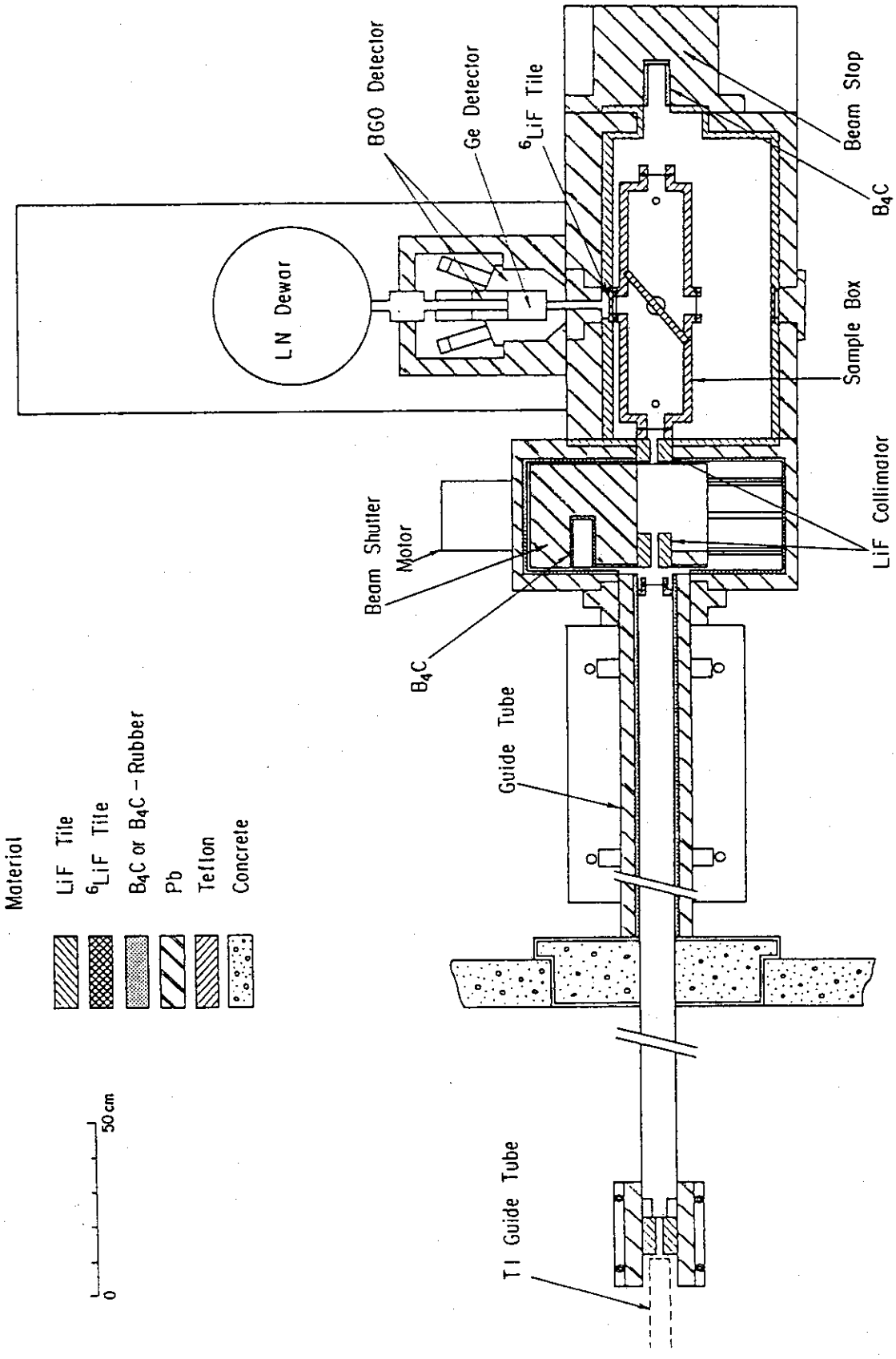

Fig. 1 Layout of JRR-3M neutron induced prompt gamma-ray analyzing system at the thermal neutron guide beam port (T1-4-1)

from the sample to the detector can be decreased to 16 cm by moving the Ge detector.

Construction of the analyzing system has been finished, and the experiment was started at the end of October 1991. The system will be used for the basic studies of elemental and isotopic analysis and then applied to various fields: environmental science, material science, geology, archeology, biology, and so on.

(2) Radiochemical neutron activation analysis of lanthanoids and uranium in geological samples[2,3]

The analysis of rock and ground water samples for lanthanoids and uranium is important for geochemical and geological research, because it allows to clarify the migration behavior of these elements in the stratum. One of the methods that allows lanthanoids and uranium determination with high sensitivity and accuracy is neutron activation analysis. However, the realization of reliable analysis for these elements is not always possible because of the low contents and the interference of fission products from uranium in the samples.

To increase the accuracy, aluminum hydroxide coprecipitation method for concentration of these element in the water sample, cation exchange procedure for lanthanoid group separation, inductively coupled plasma atomic emission spectroscopy (ICP-AES) and ^{237}Np tracer method for chemical yield determination have been developed.

Known amounts of aluminum and ^{46}Sc were added to the water samples, and lanthanoids and uranium were coprecipitated with aluminum hydroxide at pH 8.0-8.5. Chemical yield in the coprecipitation procedure was obtained by measuring gamma-ray of ^{46}Sc. The collected aluminum hydroxide precipitate and rock samples together with lanthanoids and uranium standard solutions were irradiated in JRR-4 at a thermal neutron flux of (5.5-6.0) X 10^{13} n cm^{-2} sec^{-1} for 0.5 to 6 h. After cooling for 3 days, exact amounts of lanthanoid carrier solution and ^{237}Np tracer solution were added to the samples, and then the samples were decomposed with sodium peroxide and sodium hydroxide fusion technique. The radioactive lanthanoid nuclides and $^{237,239}Np$ in the samples were separated by ion exchange methods using cation exchange resin column (AG 50W-X8, 200-400 mesh , 8 mm i.d. X 100 mm h). At first, ^{24}Na, ^{59}Fe and ^{60}Co etc. were eluted with 2M hydrochloric acid, and then $^{237,239}Np$ and ^{46}Sc were eluted with 1M sulfuric acid. Finally, lanthanoid nuclides were eluted with 50 ml of 5M hydro-

chloric acid. The eluted ^{237,239}Np together with ^{46}Sc in the 1M sulfuric acid was separated by TTA (thenoyltrifluoroacetone) liquid−liquid extraction method[4]. The separated lanthanoid and neptunium solutions were evaporated in the counting glass plate and their gamma−ray spectra were measured with coaxial and planer type Ge detectors. After measurement of the gamma−ray spectra, chemical yields of the lanthanoids and ^{237}Np were determined by ICP−AES and gamma−ray spectrometry, respectively. Accuracy and interferences of chemical yield determination of 11 lanthanoids (La, Ce, Nd, Sm, Eu, Tb, Ho, Yb, Lu, Tm) are <1 % and <8 %, respectively. Similar procedures were also applied to the uranium standard solutions. The uranium contents in the samples were calculated from the gamma−ray peak area of ^{239}Np corrected for the chemical yield. The lanthanoids contents were calculated after correcting with chemical yields and lanthanoid radionuclides produced by fission reactions of ^{235}U in the samples. Accuracy of the present methods was confirmed by satisfactory agreement between the experimental results and the values of other methods of reference rock samples (GSJ JB−1, JG−1).

References

1) C. Yonezawa, M. Hoshi, Y. Ito, E. Tachikawa, Proceedings of the 3rd Asian Symposium on Research Reactor, (1991) p.573.
2) C. Yonezawa, M. Hoshi, The 34th Symposium on Radiochemistry, Abstract of Paper, (1990) p.88.
3) C. Yonezawa, T. Kurosawa, M. Hoshi, The 35th Symposium on Radiochemistry, Abstract of Paper, (1991) p.172.
4) C. Yonezawa, M. Hoshi, E. Tachikawa, H. Kamioki, Bunseki Kagaku, 37 (1987) 7.

Publication List

[1] C. Yonezawa, G. R. Choppin, "Synergistic Extraction of Am(III), Th(IV), and U(VI) by PMBP and Crown Ethers", J. Radioanal. Nucl. Chem., 134 (1989) 233.
[2] C. Yonezawa, M. Hoshi, "Blank Analysis of Quartz Container for Instru mental Neutron Activation Analysis", Bunseki Kagaku, 39 (1990) 25.
[3] C. Yonezawa, M. Hoshi, "Reactor Neutron Activation Analysis −Review and Research Program at the Neutron Guide Beam of JRR−3 (Upgraded)−", JAERI−M 91−087 (1991).
[4] C. Yonezawa, M. Hoshi, Y. Ito, E. Tachikawa, "Construction of Reactor

Neutron Induced Prompt Gamma-ray Analyzing System at the Neutron Beam Guide of JRR-3M", Proceedings of the 3rd Asian Symposium on Research Reactor, (1991) p.573.

9.4 Volatilization Behavior of Ruthenium from Nitric Acid

9.4.1 Introduction

Ruthenium is known to volatilize from its nitric acid solution at elevated temperature. The chemical form of ruthenium volatilized from nitric acid solution appears to be ruthenium tetroxide[1]. High nitric acid concentration, high temperature, and prolonged hold up time of the solution seem to enhance the volatilization of ruthenium[2]. It has been presumed[3] that the volatilization rate of ruthenium is related to the rate of oxidation of ruthenium in a solution by nitric acid to ruthenium tetroxide. As the concentration of nitric acid increases the oxidation rate and, consequently, the volatilization rate increases.

9.4.2 Experimental

Apparatus: Apparatus used for the determination of volatilization rate of ruthenium is shown in Fig 1.

Procedures: A test solution was made by dissolving sodium nitrate into distilled water with a required amount of nitric acid. The volume of the solution was adjusted to 48ml. Two ml of a stock solution of radioactive ruthenium tracer which was prepared by dissolving crystals of the disodium hydroxotetranitronitrosylruthenate ($Na_2RuNO(NO_2)_4OH \cdot 2H_2O$) labeled with ^{106}Ru in distilled water was poured into the flask. In the solution thus obtained, air was bubbled from a nozzle at a flow rate of 10 ml/min.

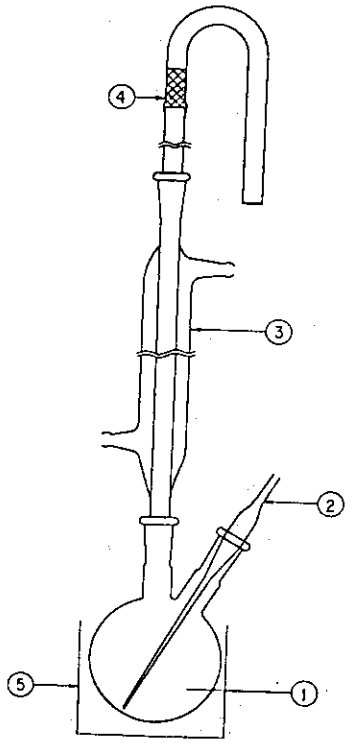

Figure 1 Schematic illustration of apparatus.
1) Reaction flask. 2) Babbling nozzle.
3) Water cooled condenser. 4) Trap
5) Mantle heater

The solution in the flask was heated by a mantle heater to maintain continuous boiling.

The nitric acid evaporated was refluxed by a water cooled condenser, in order to keep the amounts of the solution, nitric acid and sodium nitrate constant. The volatilized ruthenium was collected with a polyvinylchloride tube trap connected to the top of the condenser. The part of

polyvinylchloride tube trap blackened with ruthenium deposition near the condenser was cut off. The radioactivity of ^{106}Ru of the trap was measured by a 2"x 2" well type NaI(Tl) scintillation counter.

The ratio of ruthenium volatilized, α, at a certain time is calculated as follows:

$$\alpha = (A_t/A_0)$$

where A_t is the radioactivity found on the trap and A_0 is that of ^{106}Ru originally present in the solution.

9.4.3 Results and discussion

It has been assumed that the volatilization of ruthenium proceeds with the first order rate equation[4]:

$$d\alpha/dt = k(1-\alpha) \qquad (1)$$

where k is a rate constant. Thus, the relation between α and t is given as

$$-\ln(1-\alpha) = kt \qquad (2)$$

where t is the boiling duration of the solution.

Fig 2 shows the volatilization behavior of ruthenium as a function of boiling duration of solution for various nitric acid concentrations.

After an induction period, the volatilization of ruthenium occurred. The value $-\ln(1-\alpha)$ increases almost linearly with boiling duration as expected from Eq. (2).

It is obvious that the induction period increases with decreasing nitric acid concentration, while the volatilization rate slightly decreases as the concentration of nitric acid decreases. The slight decrease of volatilization rate would be ascribed[4] to the decrease of boiling point of nitric acid with decrease of concentration of nitric acid.

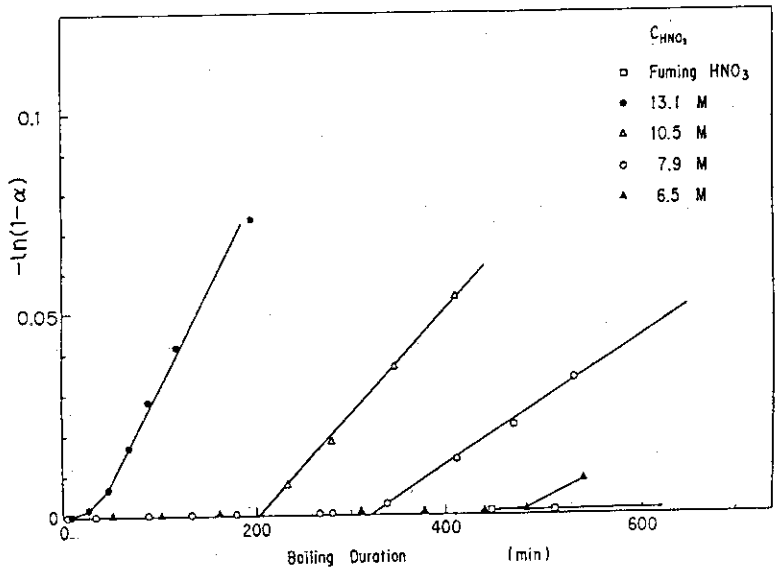

Figure 2 Effect of nitric acid concentration on the volatilization of ruthenium.

The induction perio

and the volatilization rate are tabulated[5] in Table 1 for various acidities at a constant nitrate concentration.

The volatilization rate is found to be constant within experimental error at an acidity greater than 3M, while it decreases at acidity less than 4M. The black material reported as ruthenium plating[3] is found to be deposited at acidities ranging from 1M to 3M at a lower part of the condenser where vapor refluxes into solution. The black material is not observed in 10M sodium nitrate solution. This fact suggests that volatilization of ruthenium would occur at an acidity down to 1M in the presence of an excess amount of nitrate.

Table 1 Volatilization rate and induction period at a constant nitrate concentration

Concentration, M		Volatilization rate(K), min^{-1}	Induction period, min
HNO_3	$NaNO_3$		
10	0	1.8×10^{-4}	6
9	1	1.5×10^{-4}	3
8	2	1.5×10^{-4}	9
7	3	1.6×10^{-4}	20
6	4	1.4×10^{-4}	83
5	5	1.4×10^{-4}	76
4	6	1.5×10^{-4}	110
3	7	4.4×10^{-5}	200
2	8	5.2×10^{-5}	150
1	9	$<3.4\times10^{-7}$	-
0	10	$<3.4\times10^{-7}$	-

Table 2 shows the volatilization rate and induction period of ruthenium from a mixture of nitric acid and sulfuric acid.

Although the induction periods scatter in a wide range, the volatilization rate is found to be constant within experimental condition. This fact suggests that the presence of a small amount of nitrate would cause the volatilization of ruthenium from an acidic solution with medium concentration.

Table 2 Volatilization rate and induction period from a mixture of nitric acid and sulfuric acid

Concentration, M		Volatilization rate(k), min^{-1}	Induction period, min
HNO_3	H_2SO_4		
4	3.0	5.1×10^{-5}	140
3	3.5	6.0×10^{-5}	68
2	4.0	5.5×10^{-5}	110
1	4.5	4.8×10^{-5}	170
0	5.0	$<3.0\times10^{-7}$	-

Reference

1) A. S. WILSON, HW-45620, (1956)
2) A. S. WILSON, J. Chem. Eng. Data, 5, (1960) 521
3) C. E. May, B. J. Newby, K. L. Rohde and B. D. Withrs, IOD-14448 (1958)

4) T. Sato, J. Radioanal. Nucl. Chem. 129(1989)77.
5) T. Sato, J. Radioanal. Nucl. Chem. 139(1990)25.

Publication List

[1] T. Sato, "Volatilization Behavior of Ruthenium from Boiling Nitric Acid," J. Radioanal. Nucl. Chem. 129(1989)77.

[2] T. Sato, "Adsorption and Desorption Characteristics of Silver on the Borosilicate Glass Surface," Radiochimica Acta 46(1989)101.

[3] T. Sato, "Instability of Some Nitrosylruthenium Compounds in Nitric Acid," Radiochimica Acta 46(1989)213.

[4] T. Sato," Chemical Species of Fission Product Ruthenium in the Solution of Irradiated Uranium Dioxide in Nitric Acid," Radiochimica Acta, 47(1989)219.

[5] T. Sato and R. Motoki, "Chemical Species of Ruthenium in Radioactive Aqueous waste and Decontamination Mechanism of Ruthenium with Zinc-charcoal Mixed Column," Radiochimica Acta 48(1989)101.

[6] T. Sato, "Volatilization Behavior of Ruthenium from Boiling Solutions," J. Radioanal. Nucl. Chem. 139(1990)25.

[7] T. Sato, "Cation Exchange Behavior of Some Fission Products on Strongly Acidic Cation Exchanger of Sulfonic Acid Type-Nitric Acid Media," J. Radioanal. Nucl. Chem. 139(1990)79.

[8] T. Sato, "Pressure Effect on Cation Exchange Distribution of Some Fission Products on Strongly Acidic Cation Exchanger of Sulfonic Acid Type in Nitric Acid," J. Radioanal. Nucl. Chem., in press.

[9] T. Sato, "Extraction Behavior of Yttrium with Di-isodecyl Phosphoric Acid from Nitric Acid", J. Radioanal. Nucl. Chem., in press

9.5 Determination of Plutonium Amount in a Waste Drum by Gamma Ray Assay

9.5.1 Introduction

A reliable technique for the determination of plutonium amount in a 200 liter waste drum was needed for a dismounting campaign of glove boxes used in plutonium handling at the plutonium facility in JAERI[1-4]. Four glove boxes having 5-10 m^3 were dismounted in the facility. Two were mainly made of 4 mm thick stainless steel, SUS-304, and the others made of 30 mm thick aluminum. They were cut into small pieces by a saw in a green house, sealed hermetically in polyvinyl chloride bags, and contained in drums(1.2 mm thick SUS-304, JIS-Z-1600). An attention was paid to develop a convenient technique for the plutonium assay of 200 liter waste drums.

9.5.2 Measuring system

A pair of NaI(Tl) scintillation detectors (3" x 3") face each other as shown in Fig. 1. The front and four sides of each are sealed with a lead sheet of 1 mm and lead blocks of 50 mm in thickness, respectively. They are named the first (left) and second (right), individually. A drum to be assayed is carried by its carrier to the center, and put vertically on the floor together with the carrier, keeping a given interspace between each detector and the side of the drum. The arrangement was chosen to make the counting efficiencies at all positions in the drum equal, as described later. A module counter, A_1 is connected to the first, and dual counters of A_2 and B_2 to the second. All of them operate at the same time with master-slave connection. The ^{239}Pu gamma ray (356-450 keV) is measured during 3 minutes by A_1 and A_2, and the gamma ray in the 470-790 keV region is measured by B_2 at the same time to get a substitute value for the background activity in the 356-450 keV region. The net values obtained from A_1 and A_2 are added to give the plutonium amount corresponding to that in the drum. Most of the plutonium samples used in the facility contain ^{239}Pu in the range of 84-91 atom percent.

9.5.3 Mirror image symmetrical measurement

The object to be assayed is bulky in comparison with the detectors. Plutonium also may be randomly located among the wastes in a drum. It was considered that counting efficiencies at different positions in a drum

would be made nearly equal by selecting the interspace between the side of the drum and each detector. As shown in Fig. 1, the side point, A and top point, B (and the opposite) in a drum correspond with the highest and lowest efficiencies, respectively. The efficiencies of both points are compared with that of the center as a function of the interspace R (cm) between the drum side and each detector. Both gamma ray intensities from A and B points are equal within ±25 % error to that of the center, when the interspace, R is more than 50 cm. The whole efficiency ratio compared with that of the center can be calculated from the geometrical point of view. The efficiency ratio compared with that of the center was also observed by setting 11 samples of plutonium at arbitrary positions in a drum. The whole activity can be evaluated within ±25 % error in comparison with that at the center, when R is more than 50 cm. These experiments suggest that a static measurement will be possible for the assay of a 200 liter drum. R is kept to 50 cm in the present work.

9.5.4 Gamma ray influence of ^{241}Am

A sizable amount of ^{241}Am, the decay product of ^{241}Pu (half life 14 y) always exists in plutonium bearing wastes. It emits many weak gamma rays in the 300-800 keV region as well as at 59 keV. When the ^{239}Pu activity in the 356-450 keV region is measured by A_1 and A_2, the activity of ^{241}Am in the region is also measured by the counters. The

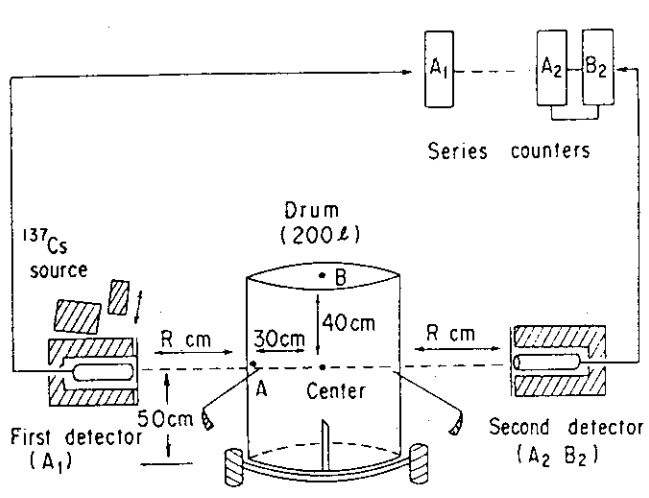

Figure 1 Schematic view of ^{239}Pu assay system

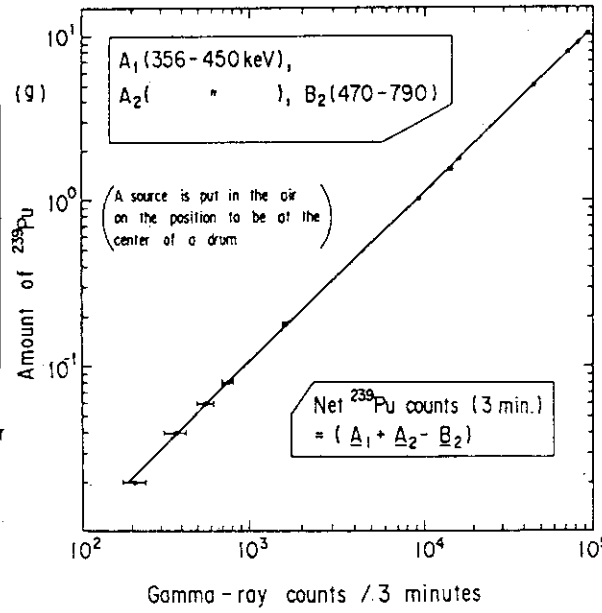

Figure 2 Calibration curve (the amount of ^{239}Pu vs. gamma ray counting value in 356-450 keV region)

third counter, B_2 was employed in order to estimate the gamma ray activity due to ^{241}Am in the 356-450 keV region. The working region, 470-790 keV was decided as follows. Using a pure source of ^{241}Am, the activity was counted for 3 minutes at the same time by A_1, A_2 and B_2. Each value stood in the relation of $\underline{A}_1 \approx \underline{A}_2 \approx (1/2)\underline{B}_2$, where $\underline{A}_1$, $\underline{A}_2$ and $\underline{B}_2$ designated the counting values obtained from the counters of A_1, A_2 and B_2, respectively. The relationship of course does not depend on the gamma ray intensity of ^{241}Am. The value obtained by B_2 counter, $\underline{B}_2$, will stand for the background values counted already in $\underline{A}_1$ and $\underline{A}_2$. On the other hand, the gamma rays from a plutonium sample are low enough in the 470-790 keV, compared with that in 356-450 keV. Hence, the net ^{239}Pu counting value can be substantially given as $(\underline{A}_1+\underline{A}_2-\underline{B}_2)/3$ min. A calibration curve is made, as is shown in Fig. 2, when plutonium samples are put in the air to be at the center position of a drum.

9.5.5 Gamma ray attenuation

Attenuation occurs in the gamma rays of ^{239}Pu passing through wastes, and must be corrected. Several drums containing materials such as rags were provided. A known amount of ^{239}Pu source was set at the center in one of them. The activity, first, was counted in the system, and compared with that of the source set in the air, in order to get a value, $(I_0/I)_{Pu-239}$, where I_0 and I are the intensities passing through air and material, respectively. Next, an external ^{137}Cs source (1 MBq, 662 keV), sealed with 50 mm thick lead blocks, is set on the top of the first detector (Fig. 1). When the front shutter was opened, the gamma

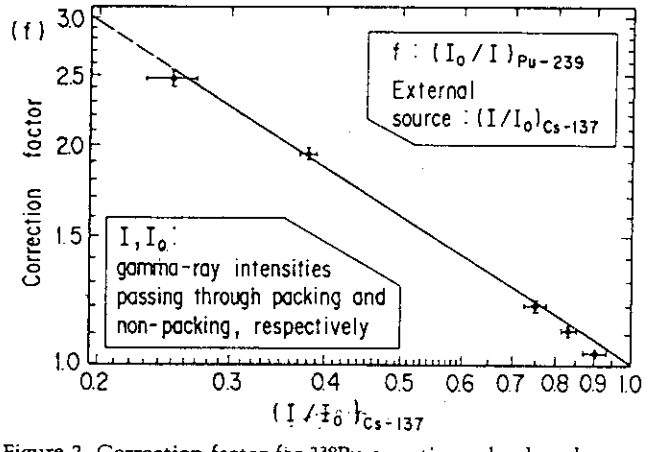

Figure 3 Correction factor for ^{239}Pu counting value based on the external source of ^{137}Cs (662 keV)

Table 1
Determination of ^{239}Pu amount in actual wastes

Drum No.	(Kg)	Cs-137 (I/I_0)	f	Counts / 3 min $(A_1+A_2-B_2)\times f$	Found ^{239}Pu(mg)	Note
1	58.8	0.58	1.45	67 x 1.45	< 20	(In a different position)
		0.74	1.22	93 x 1.22	< 20	
2	50.4	0.45	1.72	339 x 1.72	62	
		0.53	1.55	406 x 1.55	66	〃
		---	---	---		

85	11.2	0.22	2.76	355 x 2.76	110	
		0.20	2.96	385 x 2.96	123	〃
86	53.0	0.54	1.53	8,329 x 1.53	1,350	
		0.52	1.56	8,507 x 1.56	1,400	〃

ray emitted in a beam from the 8 mmϕ collimator. The gamma rays passing slopewise through the air and one of the drums provided above were counted by B_2 counter, in order to get a value of $(I/I_0)_{Cs-137}$. In this case, B2 counter worked not for measuring background activity, but for ^{137}Cs gamma ray activity. From their results, $(I_0/I)_{Pu-239}$ vs.$(I/I_0)_{Cs-137}$ is plotted in Fig.3. On the curve, a value of f is given as the correction factor of a drum. A drum assay is carried out by two successive steps. First, ^{239}Pu gamma ray from a drum to be assayed is measured for 3 min. by A_1, A_2 and B_2, keeping the shutter of the external source closed. Second, the front shutter of the external is opened. The activity is counted for 3 min. by B_2, in order to determine a f value for the drum. Hence, the ^{239}Pu counting value is corrected as,

$$\text{Net } ^{239}Pu \text{ activity (3 min.)} = (\underline{A}_1 + \underline{A}_2 - \underline{B}_2) \times f.$$

A plutonium weight corresponding to this value will be given on the curve in Fig. 2. The measuring system was verified again using with an artificial waste drum carrying a known amount of Pu sample. It was assayed repeatedly from arbitrary positions. The Pu amount in it was determined within ±25 % error.

9.5.6 Application

Waste drums generated by dismounting the glove boxes used for plutonium handling were 86 in numbers, and their weights were in the range of 40 to 175 kg. Each was assayed twice at different angle positions. The results of the first two and last two drums are shown in Table 1. The two values of each are very similar. None of the other 82 drums needed special treatment in the system.

9.5.7 Summary

Pu-bearing waste drums (each 200 liter) were assayed in a static measurement of ^{239}Pu gamma ray. The gamma ray influence of ^{241}Am coexisting with plutonium was eliminated in the measuring system. The attenuation of ^{239}Pu gamma ray passing through wastes was corrected by an external ^{137}Cs source. The drums assayed were 86 in numbers. Each weight was in the range of 40-175 kg. Plutonium could be assayed within ±25 % error for more than 0.02 g of Pu per drum in the measuring system.

References

1) J. Akatsu, J. Inst. Nucl. Mater. Manag. X(1981)22.

2) J. Akatsu, Y. Kobayashi, T. Kimura, J. Radioanal. Nucl. Chem., Letters 86(1984)159.
3) L.V. East, R. Gatti, S. Wawrowski, J. Inst. Nucl. Mater. Manag. V(1976)137.
4) R. Swennen, IAEA-R-1453-F, ETR-291, (1976).

Publication List

[1] J. Akatsu, T. Kimura and H. Mutoh, "Gamma Ray Assay of a Waste Drum for the Determination of Plutonium Amount (III)", J. Inst. Nucl. Mater. Manag. XVIII(1990)21.

10. THERMODYNAMIC STUDIES OF NUCLEAR FUEL MATERIALS

T. Muromura, A. Nakamura, K. Ohuchi, J. Tateno, T. Yamashita and Y. Hinatsu

10.1 Thermodynamic model of hyper- and hypostoichiometric actinide oxides with the fluorite structure: UO_{2+x} and PuO_{2-x}

10.1.1 Introduction

In actinide series elements, as the main and common solid oxide phase, the oxides with the fluorite structure are formed. Due to their technological importance as nuclear fuels, considerable amounts of theoretical efforts have been devoted to the thermodynamic and statistical-dynamical modellings of these actinide fluorite oxides represented by the hyperstoichiometric UO_{2+x} and the hypostoichiometric PuO_{2-x}(and its rare-earth analog CeO_{2-x}).[1-5] Unfortunately, most of those models included the most representative Atlas model[2] are more or less qualitative in nature(or the agreement with the experimental data is rather poor), suggesting the theoretical difficulties in dealing quantitatively with the complex defect structure of the widely nonstoichiometric and highly defective solid oxide phases.

In view of this situation, the present author has recently proposed a quantitative theoretical model of the oxygen excess UO_{2+x}[6] which can well describe the full set of thermodynamic data of oxygen, $\bar{g}(O_2)$, $\bar{h}(O_2)$ and $\bar{s}(O_2)$ in this system.[7] Discussions were also made on its possible extension to the oxygen deficient symmetrical counterpart PuO_{2-x}[8] based on the existing some symmetrical relationships between the thermodynamic properties of these two systems. The present report gives a brief review of their results.

10.2.2 Results and Discussion

Fig. 1 shows the experimental data of the partial molar enthalpy and entropy of oxygen, $\bar{h}(O_2)$, $\bar{s}(O_2)$ in UO_{2+x}[7] and $-\bar{h}(O_2)$, $-\bar{s}(O_2)$ in PuO_{2-x}[9], AmO_{2-x}[10], CeO_{2-x}.[11] We plotted $-\bar{h}(O_2)$ and $-\bar{s}(O_2)$ for the latter systems, because the oxygen vacancy(V_O) responsible for the hypostoichiometric (Pu,Am, Ce)O_{2-x} is thermodynamically just the negative of the oxygen interstitial(O_i) responsible for the hyperstoichiometric UO_{2+x}, that is, $(\partial G/\partial[O_i])=-(\partial G/\partial[V_O])$ $=2\bar{g}(O_2)=2(\bar{h}(O_2)-T\bar{s}(O_2))$, where G is the total Gibbs energy of the system and [ ] denotes the concentration of the chemical species. For UO_{2+x}, both the temperature T and nonstoichiometry x dependences of $\bar{h}(O_2)$ and $\bar{s}(O_2)$ are well established, as shown in Fig. 1a) for several temperatures. Whereas, for

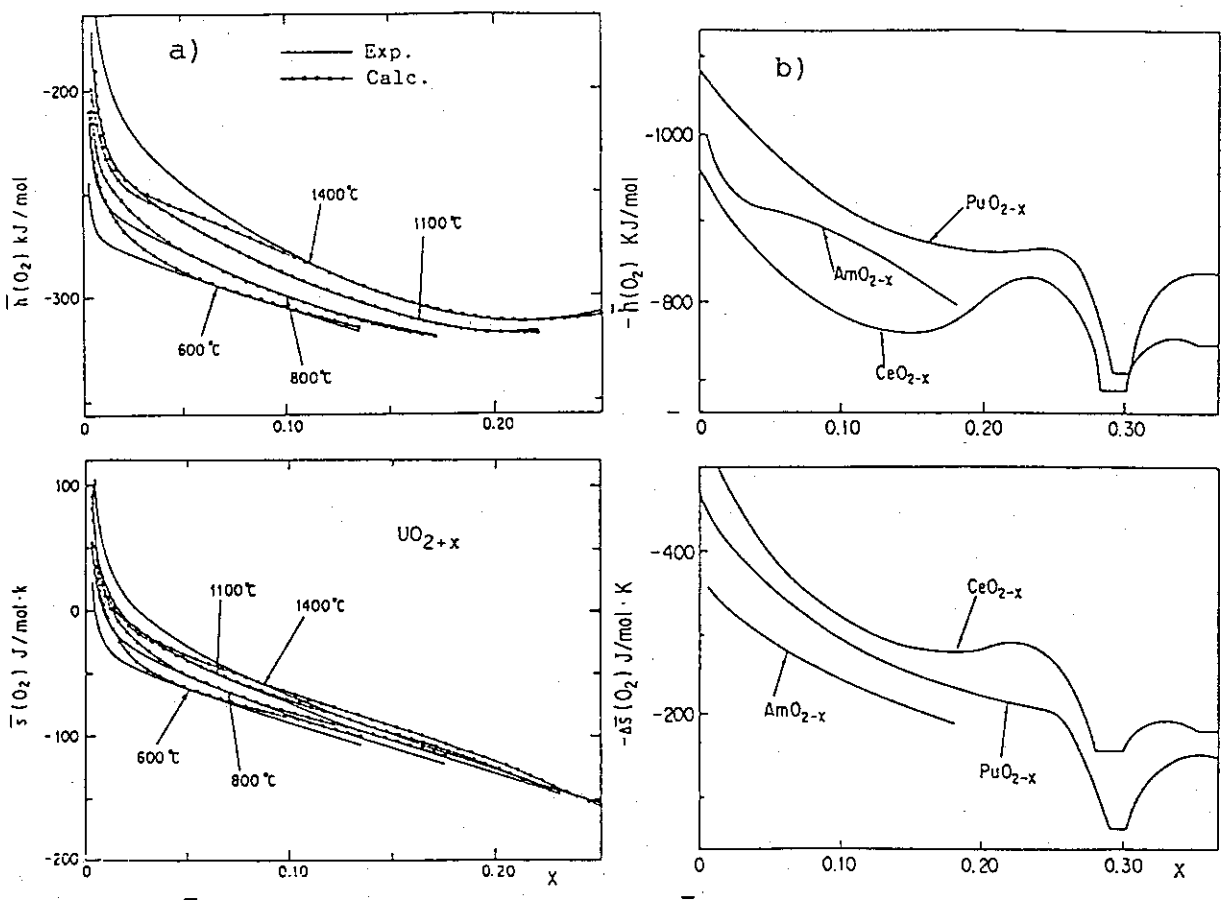

Fig. 1 a): $\bar{h}(O_2)$, $\bar{s}(O_2)$ of UO_{2+x} and b): $-\bar{h}(O_2)$, $-\bar{s}(O_2)$ of $(Pu,Am,Ce)O_{2-x}$.

$(Pu,Am,Ce)O_{2-x}$, due to the relatively large scatter of the experimental data, only the T-independent constant $\bar{h}(O_2)$ and $\bar{s}(O_2)$ are reported as a function of x. A closely symmetrical shape of these experimental data between the hyper- and hypostoichiometric systems observed in Fig. 1a) and b) are briefly summarized in Table 1, together with those of the experimental lattice constants (a(Å)) vs. x relationships reported in literatures.[12,13] These results imply that an unified thermodynamic description would be possible for these nonstoichiometric fluorite oxides $MO_{2\pm x}$ in terms of the defect chemical thermodynamics.

Results of the present quantitative defect chemical model are shown in Fig. 1a) for UO_{2+x} as the calculated curves of $\bar{h}(O_2)$ and $\bar{s}(O_2)$. The agreement with the experimental data appears satisfactory both for $\bar{h}(O_2)$ and $\bar{s}(O_2)$. As the details of the model are already given in Ref.(6), only its basic features and therefrom derived basic physical picture on the defect structure of UO_{2+x} are described here. To account for the experimentally observed strong T and x dependences of $\bar{h}(O_2)$ and $\bar{s}(O_2)$, it is necessary to incorporate properly the following two effects into the model:

(a) the coexistence of at least four kinds of oxygen interstitial clusters

$O_i^{2-}(j)(j=1,2,4,6)$, where j denotes the number of the oxide ions involved in the respective clusters, and the charge compensating hole(U^{5+}).
(b) the molar volume(V_m) dependent interactions between the above defect species.
The effect (a) is essential to mainly account for the T dependence of $\bar{h}(O_2)$ and $\bar{s}(O_2)$ and shifts them to the more negative values with decreasing T, because at lower T the relative contributions from the higher order(the enthalpically more stable) defect clusters increase. On the other hand, the effect (b) is essential to mainly account for the x dependence of $\bar{h}(O_2)$ at larger x regions: as x increases, due to the increasing electrostatic associative interactions between U^{5+} and $O_i^{2-}(j)$, the UO_{2+x} lattice contracts(see Table 1) and $\bar{h}(O_2)$ decrease at first almost linearly with x. But, when x further increases, the electrostatic repulsive interactions and also the strain effect between the oxygen interstitial clusters themselves in the too much contracted lattice become increasingly predominant, leading to the upturn of $\bar{h}(O_2)$ at the largest x region at higher T range. This also causes the instability of the UO_{2+x} lattice itself, leading further to the formation of U_4O_9 type superstructure lattice around x=0.25.

Table 1 Symmetric defect properties of actinide oxides $MO_{2\pm x}$.

$$(\partial G/\partial[O_2])=\bar{g}(O_2)=RT\cdot\ln P^{*}_{O_2}=\bar{h}(O_2)-T\bar{s}(O_2)$$
$$=+(1/2)\cdot(\partial G/\partial[O_i])$$
$$=-(1/2)\cdot(\partial G/\partial[V_O])$$

When x increases	UO_{2+x}	PuO_{2-x}
Point Defects	O_i increases	V_O increases
$\bar{g}(O_2)$	increases	decreases
$\bar{h}(O_2)$, $\bar{s}(O_2)$	decreases	increases
Lattice	contracts	expands

1 : 1 Correspondance between UO_{2+x} and PuO_{2-x}

From the above argument for UO_{2+x} and the symmetric defect dependent properties between UO_{2+x} and PuO_{2-x} in Fig. 1 and Table 1, the following basic scenario could be envisaged for the defect structure of the hypostoichiometric PuO_{2-x}:
(a) the coexistence of several kinds of oxygen vacancy(V_O) type defect clusters, and the charge compensating electron(Pu^{3+}).
(b) V_m dependent interactions between the above defect species.
As for the effect (a), at present, it is hard to judge how strong this effect may be, because as shown in Fig. 1b) T dependences of $\bar{h}(O_2)$ and $\bar{s}(O_2)$ are not at all clear for this system. As for the effect (b), this effect is certainly expected to be there from the strong x dependence of $\bar{h}(O_2)$ seen in Fig. 1b): as x increases, at first, due to the decreasing electrostatic binding of the PuO_{2-x} lattice(V_O generation and the accompanying reduction of Pu^{4+} to Pu^{3+} means the loss of the madelung energy), the lattice expands and $\bar{h}(O_2)$ increases. But, when x further increases, the too much loosened lattice tries to

reorganize itself, leading to the upturn of $-\bar{h}(O_2)$, and the PuO_{2-x} lattice is finally surrendered to the Ce_7O_{12} type superstructure lattice around x= 0.283.

References

1) Thermodynamic and Transport Properties of Uranium Dioxide and Related Phases, IAEA Technical Report No.39(1965)p.42-49.
2) L. M. Atlas, J. Phys. Chem. Solids 29(1968)91 and 29(1968)1349.
3) S. K. Mitra and A. R. Allnatt, J. Phys. C12(1979)2261.
4) L. Manes, Nonstoichiometric Oxides, Ed. T. Sørensen(Academic Press, New York, 1981)p.99-154.
5) M. Benzakour, R. Tetot and G. Boreau, J. Phys. Chem. Solids 49(1988)381.
6) A. Nakamura and T. Fujino, J. Nucl. Mater. 167(1989)36.
7) A. Nakamura and T. Fujino, J. Nucl. Mater. 149(1987)80.
8) A. Nakamura, in: Proc. Int. Symp. on Advanced Nucl. Energy - Near-future Chemistry in Nucl. Energy Field, Oarai(1989)p.173-180.
9) P. Chereau, G. Dean, M. De Franco and P. Gerdanian, J. Chem. Thermodynamics 9(1977)211.
10) T. D. Chikalla and L. Eyring, J. inorg. nucl. Chem. 29(1967)2281.
11) D. J. M. Bevan and J. Kordis, J. inorg. nucl. Chem. 26(1964)1509.
12) B. Touzelin and M. Dode, Rev. Int. Hautes Temper. et Refrac. 6(1969)267.
13) B. Touzelin, J. Nucl. Mater. 101(1981)92.

Publication List

[1] A. Nakamura and T. Fujino, "Thermodynamic Model of UO_{2+x}," J. Nucl. Mater. 167(1989)36.
[2] A. Nakamura, "Thermodynamics of Actinide Solid Oxides," in: Proc. Int. Symp. on Advanced Nuclear Energy - Near-Future Chemistry in Nuclear Energy Field, Oarai(1989)p.173-180.

10.2 Phase Relations and Thermodynamics of Ternary and Quaternary Uranium Oxides

Introduction

Several kinds of metal atoms, M, are known to substitute for uranium atom in UO_2 forming solid solutions $M_yU_{1-y}O_{2+x}$ on heating under suitable conditions. The valence of such M metals is not only +4 but also +3 or +2. Thus, in the oxide fuels during irradiation, the rare-earth and the alkaline-earth metals produced can cause some changes in the fuel properties as a result of formation of the solid solutions. The phase relation and thermodynamic studies of these oxide systems are important in view of high fission yields of some rare-earth and alkaline-earth metals.

Barium is a higher fission yield element in alkaline-earth metals. The solubility of barium was reported to be 1.2 at% in $Pu_{0.2}U_{0.8}O_2$ even above 2800°C[1] or 0.6 at% in $UO_{2.00}$ at 2000°C[2]. These low solubilities are considered to be caused from much larger crystal radius of Ba^{2+} (CN=8) viz. 1.56 Å than 1.14 Å of U^{4+} (CN=8)[3]. The larger distortion of the nearest and possibly also the next nearest atoms around a barium atom in the $(Pu,U)O_2$ or UO_2 lattice would enhanced the deformation energy which imposes restrictions on the solubility of barium. However, if the possible local expansion of the UO_2 lattice around the dissolved barium is alleviated by some of these metals with smaller crystal radii in the same lattice, the solubility of barium is expected to be increased. In this work, we took up yttrium (eight coordination crystal radius =1.159 Å[3]) as such metal, and studied the stable y range of the pseudo ternary solid solution $Ba_{y/2}U_{y/2}U_{1-y}O_{2+x}$ in relation with oxygen nonstoichiometry, x.

On account of the high neutron cross section of ^{151}Eu in the thermal and epithermal regions, UO_2 containing europium is expected to be used as a burnable poison fuel[4] for higher burnup, as well as the gadolinium uranium fuel[5]. Well defined thermodynamic data of the Eu-U-O system, especially solid solution $Eu_yU_{1-y}O_{2+x}$, are necessary in order to know the irradiation behavior of this mixed oxide. Although europium is situated between neodymium and gadolinium in the lanthanide series of the elements, it does not seem possible to forecast the thermodynamic properties of the $Eu_yU_{1-y}O_{2+x}$ only by the analogy with Nd or Gd solid solutions, since the oxidation state of Eu^{3+} rather easily turns into +2 in solids on reduction. In this work, we discuss the fluorite phase range for the specimens heated in vacuum in comparison with the reported results, and then report some

thermodynamic properties obtained from the oxygen potential measurements of this solid solution.

Experimental

Yttrium and europium sesquioxides (99.99% metallic purity) were purchased from Shinetsu Chemical Co. Ltd. Barium carbonate was precipitated from barium nitrate solution by the addition of ammonium carbonate. Triuranium octoxide U_3O_8 was prepared by oxidation of high purity uranium metal in air at 700°C[6] for one day. Uranium dioxide UO_2 was prepared by reduction of U_3O_8 in a stream of hydrogen at 1000°C for 10 hr.

Mixed oxides in the Ba-Y-U-O system were prepared by heating the mixture of barium carbonate, Y_2O_3, U_3O_8 and UO_2 in air at 1000°C. Then the products were finely ground and heated in atmosphere of hydrogen, vacuum or helium at temperature between 1250 and 1400°C. Mixed oxides in the Eu-U-O system were made by heating the mixture of Eu_2O_3, U_3O_8 and UO_2 in high vacuum (3×10^{-6} torr) at 1400°C.

Chemical analysis was carried out to determine x and y in $M_yU_{1-y}O_{2+x}$ using cerium(IV)-iron(II) back titration method[7,8].

X-ray diffraction patterns were taken for powdered specimens with a Phillips PW-1390 diffractometer using CuKα radiation monochromatized with curved pyrolytic graphite. The slit system used was 1/2°-0.1 mm-1/2°.

The thermogravimetric measurements were performed using a Cahn Model RH or Model 1000 electronic microbalance. The sintered specimen was contained in a fused silica or an alumina crucible and suspended from the balance by Pt wire. The temperature of the specimen was measured with a Pt/Pt-13%Rh thermocouple placed close to the crucible. Various heating atmospheres were obtained by adjusting the CO/CO_2 mixing ratio using calibrated mass flowmeters. The oxygen potential of the mixed gas was continuously measured with a $BaTiO_3$ oxygen monitor[9].

Results and Discussion

Ba-Y-U-O system

The phase formed, the lattice parameters of the fcc phases in relation to compositions (x and y values) and the uranium valences are summarized in table 1. In the table, the compositions of the oxides are $Ba_{y/2}Y_{y/2}U_{1-y}O_{2+x}$ (Ba:Y=1:1) unless otherwise stated. The method and condition for preparation of the solid solutions are also shown in the same table for each run. The specimens of different y values were also prepared

Table 1
Preparation methods, phases, lattice parameters, compositions and uranium valencies of solid solutions $Ba_{x/2}Y_{x/2}U_{1-x}O_{2+x}$

Method	Run [a]	y	x	Uranium valence	Phase	Lattice parameter	Remark
I	He-1	0	0.142	4.284	$(fcc)_1 + (fcc)_2$	5.4688 5.4426	Two phases almost the same amount
I	He-1	0.01	0.135	4.288	$(fcc)_1 + (fcc)_2$	5.4649 5.4438	Two phases almost the same amount
I	He-1	0.02	0.128	4.291	fcc	5.4532	Good crystallinity
I	He-1	0.05	0.156	4.407	fcc	5.4508	Good crystallinity
I	He-1	0.1	0.056	4.290	fcc	5.4516	Good crystallinity
I	He-1	0.2	0.040	4.476	fcc + another phase	5.4358	Extra-phase about 20%
I	He-1	0.5	−0.031	5.376	not single phase	–	Too broad peaks to analyse
I	He-1	0.1	0.085	4.300	fcc	5.4333	$Y_{0.1}U_{0.9}O_{2.085}$
I	He-1	0.033	0.098	4.367	fcc	5.4467	$(Ba, Y)_{0.1}U_{0.9}O_{2+x}$ with Ba : Y = 1 : 2
I	He-1	0.067	0.101	4.410	fcc + another phase (small amount)	5.4556	$(Ba, Y)_{0.1}U_{0.9}O_{2+x}$ with Ba : Y = 2 : 1
I	He-2	0	0.202	4.403	fcc	5.4520	
I	He-2	0.029	0.172	4.399	fcc	5.4512	Good crystallinity
I	He-2	0.047	0.150	4.390	fcc	5.4530	Good crystallinity
I	He-2	0.064	0.155	4.434	fcc	5.4515	Good crystallinity
I	He-2	0.094	0.140	4.466	fcc	5.4493	Good crystallinity
I	He-3	0.15	0.128	4.566	$(fcc)_1 + (fcc)_2 + BaUO_4$ + unidentified phase	5.4424	a_0 of the main fcc phase
I	He-3	0.20	0.091	4.603	$(fcc)_1 + (fcc)_2 + BaUO_4$ + unidentified phase	5.4338	a_0 of the main fcc phase
II	Vac-1	0	0.000	4.001	fcc	5.4703	Good crystallinity
II	Vac-1	0.01	−0.002	4.012	fcc	5.4695	Good crystallinity
II	Vac-1	0.02	−0.007	4.016	fcc	5.4696	Good crystallinity
II	Vac-1	0.05	0.033	4.148	$(fcc)_1 + (fcc)_2$	–	Very broad X-ray peaks
II	Vac-1	0.1	−0.077	3.996	fcc	5.4692	Good crystallinity
II	Vac-1	0.2	−0.057	4.233	not single phase	–	Too broad peaks to analyse
II	Vac-1	0.5	−0.173	4.807	not single phase	–	Too broad peaks to analyse
II	Vac-2	0.029	0.033	4.112	fcc	5.4658	Good crystallinity
II	Vac-2	0.047	0.028	4.133	fcc	5.4667	Good crystallinity
II	Vac-2	0.064	0.036	4.180	fcc	5.4654	Good crystallinity
II	Vac-2	0.094	0.021	4.202	fcc	5.4621	Good crystallinity
II	Vac-3	0.029	−0.003	4.039	fcc	5.4698	Good crystallinity
II	Vac-3	0.047	−0.012	4.049	fcc	5.4701	
II	Vac-3	0.064	−0.005	4.093	$(fcc)_1 + (fcc)_2$	5.4634	
II	Vac-3	0.094	−0.021	4.109	$(fcc)_1 + (fcc)_2$	5.4650	
II	Vac-4	0.15	−0.040	4.171	$(fcc)_1 + (fcc)_2$ + $BaUO_4$	5.4561	a_0 of the main fcc phase
II	Vac-4	0.20	−0.050	4.250	$(fcc)_1 + (fcc)_2$ + $BaUO_4$	5.4467	a_0 of the main fcc phase
III	H_2-1	0	0.000	4.000	fcc	5.4698	Good crystallinity
III	H_2-1	0.01	−0.006	4.002	fcc	5.4695	Good crystallinity
III	H_2-1	0.02	−0.009	4.011	fcc	5.4698	Good crystallinity
III	H_2-1	0.05	0.014	4.108	fcc + $BaUO_3$	–	Broad fluorite peaks
III	H_2-1	0.1	−0.083	3.982	fcc	5.4686	Good crystallinity
III	H_2-1	0.2	−0.096	4.136	fcc + $BaUO_3$	–	Broad fluorite peaks
III	H_2-1	0.5	−0.267	4.433	fcc + $BaUO_3$	–	Broad fluorite peaks
III	H_2-2	0	−0.001	4.000	fcc	5.4704	Good crystallinity
III	H_2-2	0.029	−0.010	4.024	fcc	5.4704	Good crystallinity
III	H_2-2	0.047	−0.011	4.050	fcc	5.4715	Good crystallinity
III	H_2-2	0.064	−0.013	4.076	fcc	5.4736	Good crystallinity
III	H_2-2	0.094	−0.025	4.100	fcc	5.4685	Good crystallinity
III	H_2-3	0.15	−0.056	4.133	$(fcc)_1 + (fcc)_2$ + BaU_2O_7	5.4586	a_0 of the main fcc phase
III	H_2-3	0.20	−0.079	4.178	$(fcc)_1 + (fcc)_2$ + BaU_2O_7	5.4484	a_0 of the main fcc phase

[a] Note:
He-1: He, 1350 °C, 72 h.
He-2: He, 1250 °C, 72 h.
He-3: He, 1300 °C, 48 h.
Vac-1: Vacuum, 1400 °C, 24 h.
Vac-2: Vacuum, 1250 °C, 20 h.
Vac-3: Vacuum, 1400 °C, 24 h.
Vac-4: Vacuum, 1400 °C, 24 h.
H_2-1: Hydrogen, 1250 °C, 27 h.
H_2-2: Hydrogen, 1000 °C, 24 h.
H_2-3: Hydrogen, 1000 °C, 48 h.

by heating the pellets on a Pt plate in respective runs.

In Fig.1, the mean valence of uranium in the oxides prepared are shown as a function of y in $Ba_{y/2}Y_{y/2}U_{1-y}O_{2+x}$. For yttrium solid solutions without barium, the y value is given as $Y_yU_{1-y}O_{2+x}$. The open and filled marks represent the single phase and the two- (or multi-) phase mixtures, respectively. It is seen from the figure that the mixed oxide $Ba_{y/2}Y_{y/2}U_{1-y}O_{2+x}$ crystallizes in a single phase at $y \leq 0.1$ except for a few experimental points of He-1(1300°C) and Vac-3 (1400°C). The phase splitting of the y=0 and 0.01 specimens of He-1 run is similar to that of $Ca_yU_{1-y}O_{2+x}$[10], which is considered to occur on cooling as a result of faster disproportionation of the solid solutions with lower y values. Above y=0.15, the products exist as two, three or four-phase mixtures.

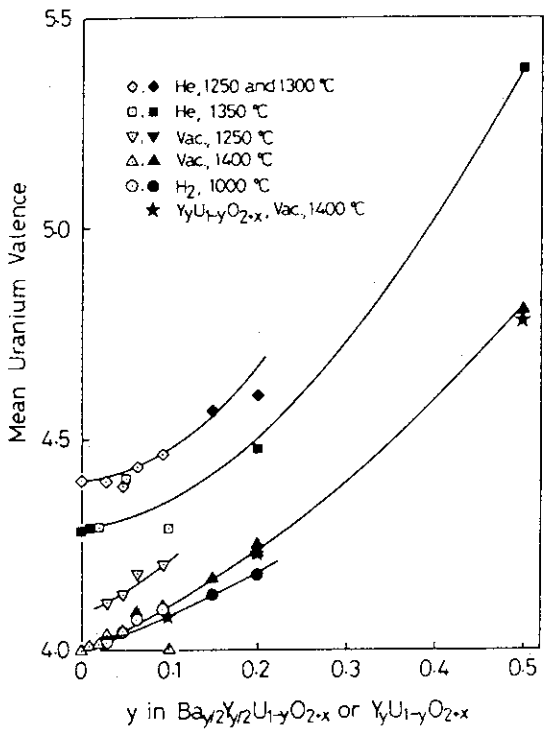

Fig. 1 Plot of mean uranium valence in the oxide(s) versus foreign metal concentration. Open and filled marks represent the single phase and the two (or more) phase mixture, respectively.

The mean uranium valence in the oxides monotonically increases with increasing y value. This fact indicates that the oxide becomes more susceptible for oxidation as more foreign cations are introduced into the crystal. The highest valency is obtained when the oxide is heated in helium. No significant anomalies in the mean uranium valence appear to exist when the oxide transforms from single phase into multiphase as the y value increases. It is interesting that the product oxides with y>0 give the mean uranium valencies of still higher than +4, even heated in a strong reducing atmosphere of hydrogen.

Figure 2 shows the lattice parameter change of the fcc solid solutions with O/(Ba+Y+U) ratio for respective y parameter. Three straight lines were obtained: The upper line represents the dependence at lower concentrations, i.e. y=0.02, 0.029, 0.047 and 0.064, and the center line for y=0.094. The lowest represents the dependence at a higher concen-

tration of y=0.1. Their respective slopes are -0.106, -0.116 and -0.128, giving an average of -0.116. This value is comparable with -0.094 of UO_{2+x}[11], -0.127 of $Pr_yU_{1-y}O_{2+x}$[12], -0.117 of $Mg_yU_{1-y}O_{2+x}$[13], -0.102 of $Ca_yU_{1-y}O_{2+x}$[10] and -0.109 of $Sr_yU_{1-y}O_{2+x}$[14] in the x>0 region. Using the above value of -0.116 and the lattice parameter of 5.4704 Å for $UO_{2.00}$[11], the least squares calculations were performed for the lattice parameter change by barium and yttrium concentrations assuming a linear relationship. Its change (in Å) was obtained as

$$a_0 = 5.4704 - 0.116x + 0.119y - 0.255z \quad (1)$$

where x, y and z are the values in $Ba_yY_zU_{1-y-z}O_{2+x}$.

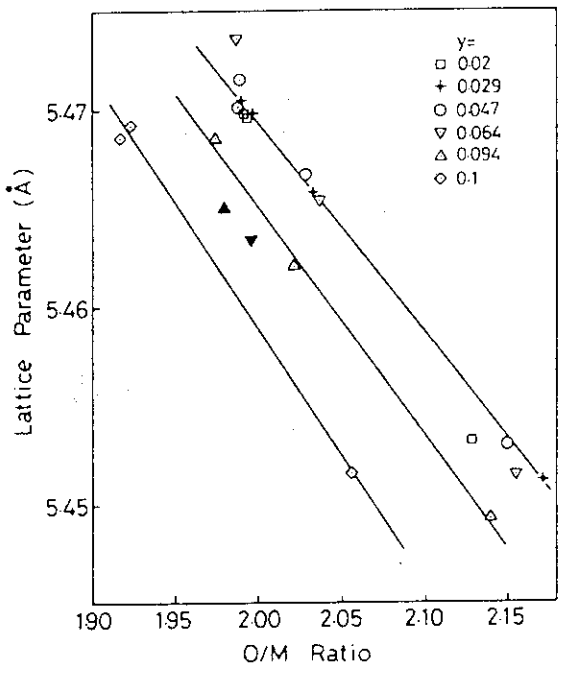

Fig. 2 Plot of fcc lattice parameter versus O/(Ba+Y+U) ratio for $Ba_{y/2}Y_{y/2}U_{1-y}O_{2+x}$. The y value is taken as a parameter.

Let us discuss about the coefficients of barium and yttrium concentrations in eq.(1). For the solid solution $Ba_yY_zU_{1-y-z}O_{2+x}$, the ionic species and their concentrations are expressed as $Ba^{2+}{}_yY^{3+}{}_zU^{4+}{}_{1-2x-3y-2z}U^{5+}{}_{2x+2y+z}O^{2-}{}_{2+x}$ if the concentrations of barium and yttrium are low enough not to yield U^{6+}. The difference of the crystal radii of Ba^{2+} and Y^{3+} from those of uranium host ions causes the change of the effective radii at cation lattice sites, but in addition, the increases in the mean valence of uranium due to the incorporation of Ba^{2+} and Y^{3+} affects the magnitude of the effective radii. On defining the mean cation radius (MCR) as the concentration weighted mean of the crystal radii in the constituent cations, the constant distance relationship for fluorite lattice[3] is also known to hold with reasonable agreement for solid solutions, i.e. $MCR+r(O^{2-})=(\sqrt{3}/4)a_0$[15], where $r(O^{2-})$ is the crystal radius of the O^{2-} ion. Since the eight coordination crystal radii for Ba^{2+}, Y^{3+}, U^{4+} and U^{5+} are 1.56, 1.159, 1.14 and 1.03 Å, respectively[3], and MCR is given as

$$MCR = 1.56y + 1.159z + 1.14(1-2x-3y-2z) + 1.03(2x+2y+z). \quad (2)$$

The change of the lattice parameter as barium concentration is obtained by

differentiating the MCR with y from the relation:

$$\frac{\sqrt{3}}{4}\frac{\partial a}{\partial y} = \frac{\partial (MCR)}{\partial y} = 1.56 - 3.42 + 2.06 = 0.20 \quad (3)$$

which yields

$$\frac{\partial a}{\partial y} = 0.462 \quad (calculated) \quad (4)$$

In a similar way, the lattice parameter change as yttrium concentration is obtained as:

$$\frac{\partial a}{\partial z} = -0.210 \quad (calculated) \quad (5)$$

The coefficient of yttrium concentration in eq.(5), -0.210, is in reasonable agreement with the observed one, -0.255 (eq.(1)). On the other hand, the coefficient of barium concentration, 0.462, given by eq.(4) is by far larger than the observed value of 0.119 in eq.(1).

There have been several studies on the solid solutions of which the $|\partial a/\partial y|$ is remarkably large. The $\partial a/\partial y$ values of $M_yU_{1-y}O_{2+x}$ solid solutions have been observed to be -0.55[13,16,17], -0.50[16], -0.44[18] for $M=Mg^{2+}$, Mn^{2+} and Sc^{3+}, respectively. On the other hand, the calculated $\partial a/\partial y$ values obtained by the above method are -0.81, -0.65 and -0.60. Here, the observed $|\partial a/\partial y|$ values are also much smaller than the calculated $|\partial a/\partial y|$ values. This disagreement is assumed to be caused by suppression of the rapid shrinkage in the real crystals through the relaxation effects[15]. It is possible that the same mechanism controls the present solid solution even in this case of $\partial a/\partial y>0$.

As another possibility, the location of barium atoms on the interstitial site of the fluorite lattice instead of the substitutional position can be considered. In the case of UO_{2+x}, the excess oxygen ions corresponding to x enter the interstitial site, which results in the change of the MCR at the metal site as:

$$MCR(UO_{2+x}) = 1.14(1-2x) + 1.03(2x)$$
$$= 1.14 - 0.22x. \quad (6)$$

Differentiation of the MCR with respect to x followed by multiplication of $4/\sqrt{3}$ yields $\partial a/\partial x$(calc.)=-0.508, which differs largely from $\partial a/\partial x$(obs.)= -0.094 for UO_{2+x}[11]. Since the effect of the crystal radius of interstitial atom on the lattice parameter of the fluorite crystal has not yet been systematically analyzed, let the difference, 0.414, be all assigned to an

electrostatic effect as a crude approximation. Then, the barium concentration dependence of the lattice parameter, $\partial a/\partial y$(calc.), for $Ba_yY_zU_{1-y-z}O_{2+x}$ would be modified by 0.462-0.414=0.048 if barium is on the interstitial position, because Ba^{2+} has the same change as O^{2-} in magnitude but opposite in sign. The above value is in reasonable agreement with the observed value, 0.119. As for the barium location in the crystal, therefore, the definitive conclusion cannot be drawn out at present.

Eu-U-O system

In Fig. 3, the lattice parameters of the fluorite solid solutions $Eu_yU_{1-y}O_{2+x}$ prepared in a $4x10^{-4}$ Pa vacuum at 1400°C are given by the filled circles. The triangles are the data of Grossman et al.[19] and the squares are those of Ohmichi et al.[20]. It is seen from the figure that the three sets of data are in accord, showing an almost linear decrease of the lattice parameter from 5.4688 Å (y=0) to 5.4045 Å (y=0.51). In this y range, although the O/(Eu+U) ratio slightly decreases from 2.0 at y=0 with increasing y, the ratio still remains 1.95 at y=0.6, as seen from the broken line in the same figure, of which the x values were determined by chemical analysis. Such low oxygen vacancy concentrations were considered to be likely to cause rather larger errors in the coefficient of x, when the least squares fit would be made for this coefficient and that of y in the representation of the lattice parameter change as a linear function of y and x. Therefore, the coefficient of x was taken from the literature for the rare-earth solid solutions in the x<0 region. The literature values are -0.285 for $La_yU_{1-y}O_{2+x}$[21], -0.321 for $Ce_yU_{1-y}O_{2+x}$[22], -0.397 for $Pr_yU_{1-y}O_{2+x}$[12], -0.30 for $Nd_yU_{1-y}O_{2+x}$[23] and -0.24 for $Gd_yU_{1-y}O_{2+x}$[20]. They are scattered to some extent, and here we have used the

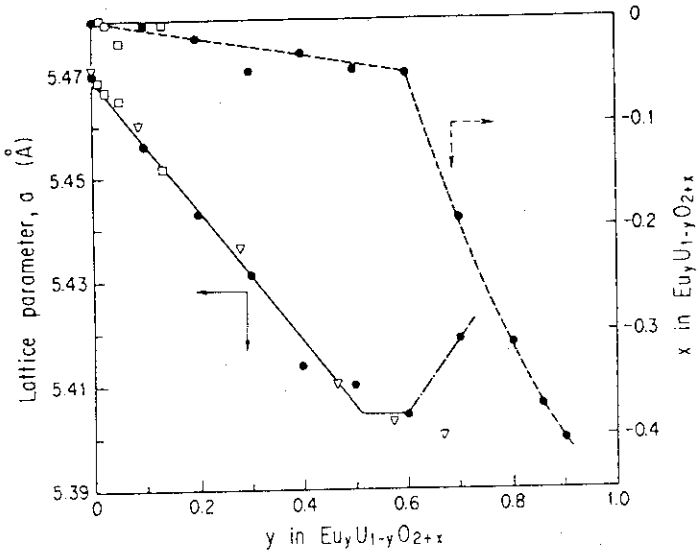

Fig. 3 Fcc lattice parameters and x values of $Eu_yU_{1-y}O_{2+x}$ prepared in $4x10^{-4}$ Pa vacuum at 1400°C. ●: Present work, ▽: Grossman et al.[19], □: Ohmichi et al.[20].

mean of these values, -0.30. The least squares calculation was carried out for the coefficient of y. The representation obtained is $a=5.4704-0.151y-0.30x$ for $x<0$. The coefficient of y in the above equation is in good agreement with -0.138[24] and -0.144[20] which have been obtained for $Eu_yU_{1-y}O_{2+x}$ ($x<0$) in the smaller y range.

Figure 4 shows a plot of the mean valence of uranium as a function of y in $Eu_yU_{1-y}O_{2+x}$. The mean valence was calculated from y and x values given in Fig. 3, assuming that europium and oxygen are in +3 and -2 oxidation states in the crystal, respectively. The uranium valence steeply increases from +4.0 at y=0 to +5.26 at y=0.6, and then sharply decreases with further increase of y forming the rhombohedral crystals.

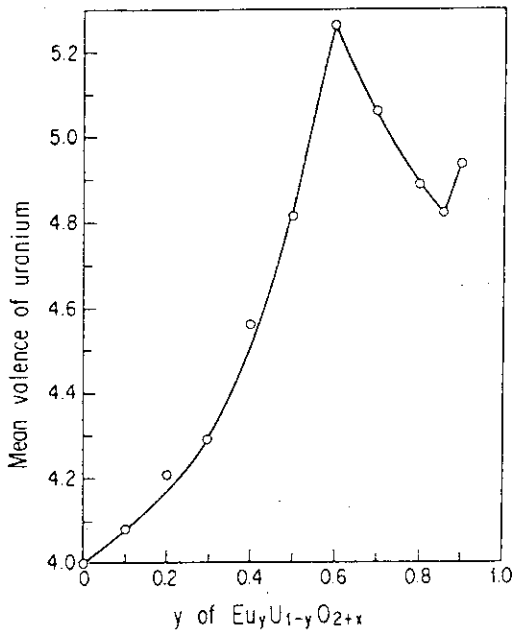

Fig. 4 Variation of mean uranium valence as a function of y in $Eu_yU_{1-y}O_{2+x}$.

The thermogravimetric measurement was performed for the solid solution $Eu_yU_{1-y}O_{2+x}$ with y=0.1 and 0.3 at 850 and 1050°C. Since the oxygen potential data have been already reported in ref. 25, results of partial molar enthalpy and entropy of oxygen for $Eu_yU_{1-y}O_{2+x}$ are discussed here and shown in Figs.5 and 6, respectively. The $\Delta\bar{S}(O_2)$ and $\Delta\bar{H}(O_2)$ values were obtained using the relations $\Delta\bar{S}(O_2)=-d(\Delta\bar{G}(O_2))/dT$ and $\Delta\bar{H}(O_2)=\Delta\bar{G}(O_2)+T\Delta\bar{S}(O_2)$ on the assumption that both $\Delta\bar{S}(O_2)$ and $\Delta\bar{H}(O_2)$ are temperature independent, as is usually made for $M_yU_{1-y}O_{2+x}$. In Figs. 5 and 6, the literature data of $M_yU_{1-y}O_{2+x}$ (M=Pu, Nd, Gd and Mg) are also given for comparison. It is interesting that the literature values of $\Delta\bar{S}(O_2)$ and $\Delta\bar{H}(O_2)$ except for neodymium solid solution[23] do not differ greatly from each other at O/(M+U) ratios larger than 2.02, independent of the charge number of the M metal ions.

Comparison of the $\Delta\bar{S}(O_2)$ curve for $Eu_yU_{1-y}O_{2+x}$ with the literature ones for other solid solutions in Fig. 5 reveals that the europium solid solution with y=0.1 exhibits much higher value of $\Delta\bar{S}(O_2)$, especially in the range of larger O/(Eu+U) ratios. The $\Delta\bar{S}(O_2)$ curve shows a broad maximum

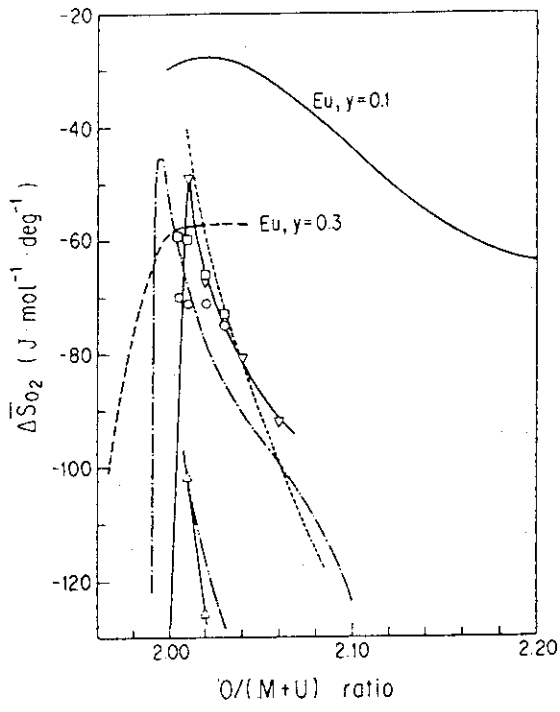

Fig. 5 Partial molar entropy of oxygen for fcc $Eu_yU_{1-y}O_{2+x}$ with y=0.1 and 0.3 compared with those of $M_yU_{1-y}O_{2+x}$ (M=Pu, Nd, Gd and Mg) solid solutions. ———: Eu, y=0.1; - - - - -: Eu, y=0.3; ○: Pu, y=0.25[27]; □: Pu, y=0.25[28]; △: Nd, y=0.2[23]; ·····: Gd, y=0.1[29]; ——··——: Gd, y=0.3[29]; ▽: Gd, y=0.1[26]; ——·—— : Mg, y=0.05[30].

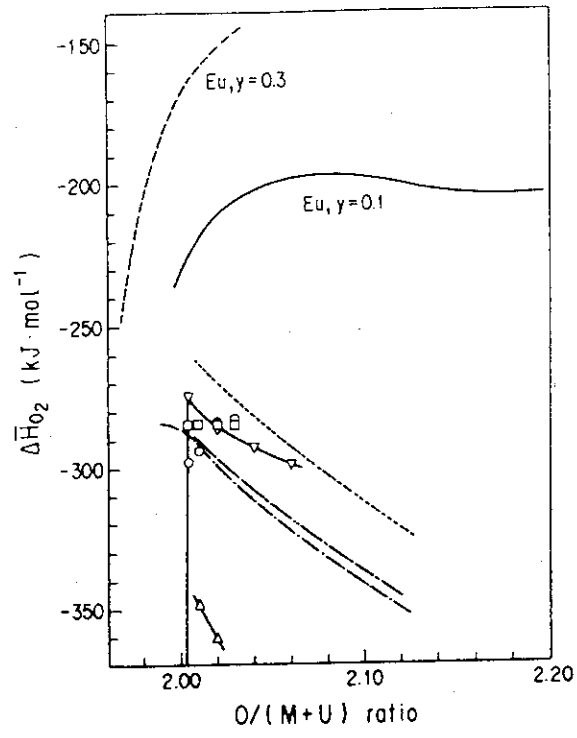

Fig. 6 Partial molar enthalpy of oxygen for fcc $Eu_yU_{1-y}O_{2+x}$ with y=0.1 and 0.3 compared with those of $M_yU_{1-y}O_{2+x}$ (M=Pu, Nd, Gd and Mg) solid solutions. ———: Eu, y=0.1; - - - -: Eu, y=0.3; ○: Pu, y=0.25[27]; □: Pu, y=0.25[28]; △: Nd, y=0.2[23]; ·····: Gd, y=0.1[29]; ——··——: Gd, y=0.3[29]; ▽: Gd, y=0.1[26]; ——·—— : Mg, y=0.05[30].

around O/(Eu+U)=2.02. This ratio is similar to that of the $\Delta\bar{S}(O_2)$ maximum point for $Gd_{0.1}U_{0.9}O_{2+x}$[26]. The europium solid solution with y=0.3, however, is found to give $\Delta\bar{S}(O_2)$ of the same order of magnitude as the literature values of the solid solutions in Fig. 5, although the x dependence of $\Delta\bar{S}(O_2)$ is greatly different. The near horizontal portion of the y=0.3 curve might be caused by the measurement error: It is possible that the actual curve should decrease with increasing O/(Eu+U) ratio in this range.

The literature values of $\Delta\bar{H}(O_2)$ shown in Fig. 6 are in relatively good agreement, except for those of neodymium solid solutions in the hyperstoichiometric composition. In contrast, the partial molar enthalpies for both $Eu_{0.1}U_{0.9}O_{2+x}$ and $Eu_{0.3}U_{0.7}O_{2+x}$ in this work are much higher than the literature values. It seems likely that the higher oxygen potentials of $Eu_yU_{1-y}O_{2+x}$ are mainly brought about by higher partial molar enthalpies.

References

1) C. Sari, C.T. Walker and G. Schumacher, J. Nucl. Mater. 79(1979)255.
2) H. Kleykamp, J. Nucl. Mater. 131(1985)221.
3) R.D. Shannon, Acta Crystallogr. A32(1976)751.
4) U. Berndt, R. Tanamas and C. Keller, J. Solid State Chem. 17(1976)113.
5) S.M. Ho and K.C. Radford, Nucl. Technol. 73(1986)350.
6) T. Fujino, H. Tagawa and T. Adachi, J. Nucl. Mater. 97(1981)93.
7) S.R. Dharwadkar and M.S. Chandrasekharaiah, Anal. Chim. Acta 45(1969)545.
8) T. Fujino and T. Yamashita, Fresenius' Z. Anal. Chem. 314(1983)423.
9) K. Naito, T. Tsuji, S. Watanabe and H. Sakai, Solid State Ionics 3/4(1981)635.
10) T. Yamashita and T. Fujino, J. Nucl. Mater. 136(1985)117.
11) H. Nickel, Nucleonik 8(1966)366.
12) T. Yamashita, T. Fujino and H. Tagawa, J. Nucl. Mater. 132(1985)192.
13) T. Fujino and K. Naito, J. Inorg. Nucl. Chem. 32(1970)627.
14) T. Fujino, T. Yamashita and H. Tagawa, J. Solid State Chem. 73(1988)255.
15) T. Fujino and C. Miyake, in: Handbook on Physics and Chemistry of the Actinides, Vol. 6 (North-Holland, Amsterdam) in press.
16) S. Kemmler-Sack and W. Ruedorff, Z. Anorg. Allg. Chem. 354(1967)255.
17) C. Keller, KFK-225 (1964)
18) Y. Hinatsu and T. Fujino, J. Solid State Chem. 62(1986)342.
19) L.N. Grossman, J.E. Lewis and D.M. Rooney, J. Nucl. Mater. 21(1967)302.
20) T. Ohmichi, S. Fukushima, A. Maeda and H. Watanabe, J. Nucl. Mater. 102(1981)40.
21) D.C. Hill, J.H. Handwerk and R.J. Beals, ANL-6711 (1963)
22) D.I.R. Norris and P. Kay, J. Nucl. Mater. 116(1983)184.
23) J.F. Wadier, CEA-R-4507 (1973).
24) S. Fukushima, T. Ohmichi, A. Maeda and M. Handa, J. Nucl. Mater. 114(1983)312.
25) T. Fujino, A. Nakamura, K. Ohuchi, J. Tateno, T. Yamashita and Y. Hinatsu, JAERI-M-89-058 (1989)
26) K. Une and M. Oguma, J. Nucl. Mater. 110(1982)215.
27) G.R. Chilton and I.A. Kirkham, in: Plutonium 1975 and Other Actinides, Eds. H. Blank and R. Lindner (North-Holland, Amsterdam, 1976) p. 171.
28) R.E Woodley and M.G. Adamson, J. Nucl. Mater. 82(1979)65.

29) T.B. Lindemer and A.L. Sutton Jr., J. Am. Ceram. Soc. 71(1988)553.
30) J. Tateno, T. Fujino and H. Tagawa, J. Solid State Chem. 30(1979)265.

Publication List

[1] T. Fujino, K. Ouchi, Y. Mozumi, R. Ueda and H. Tagawa, "Composition and oxygen potential of cubic fluorite-type solid solution $Eu_yU_{1-y}O_{2+x}$ and rhombohedral $Eu_6UO_{12+x'}$ (x'<0)", J. Nucl. Mater. 174(1990)92.
[2] T. Fujino, T. Yamashita and K. Ouchi, "Phase relation and thermodynamic properties of cubic fluorite-type solid solution, $Ba_{y/2}Y_{y/2}U_{1-y}O_{2+x}$", J. Nucl. Mater. 183(1991)46.

10.3 Formation of Lithium Plutonates by the Reaction of Lithium Nitrate and Hydroxide with PuO_2.

Introduction

Since plutonium is known as one of the most toxic substances, it is important to confine it safely and to prevent it from leaking to environment. In practice, it is essential to reduce the amount of man-made plutonium in nuclear wastes as low as possible. The poor solubility of PuO_2 in acid solution is a problem in the nuclear fuel reprocessing for $(U,Pu)O_2$ mixed oxide fuels. However, if the sparingly soluble PuO_2 can be converted into other soluble plutonium compounds, not only the reprocessing technique would be improved to a great extent, but also the plutonium content in the wastes colud be reduced significantly. Alkali metal plutonates and alkaline-earth plutonates are known to have an enhanced solubility in mineral acids[1].

As for the alkali metal-PuO_2 systems, Keller el al.[2-4] have studied the reaction between alkali oxides and PuO_2 and reported formation of the following alkali metal plutonates; Li_3PuO_4, Na_3PuO_4, Li_4PuO_5, α and ß-Na_4PuO_5, Li_5PuO_6, Li_6PuO_6 and Na_6PuO_6, together with the crystal systems and cell parameters. Reactions to form alkali plutonates from PuO_2 and alkali salts such as nitrates, hydroxides and carbonates, however, have not been well elucidated yet. In this work, the reactivity and reaction conditions to form lithium plutonates from PuO_2 and $LiNO_3$ or $LiOH\cdot H_2O$ were studied at temperatures between 773 and 1273 K; alkali metal to plutonium atom ratios between 1 and 6 were studied by means of thermogravimetry as well as X-ray diffraction.

Experimental

$LiNO_3$ and $LiOH\cdot H_2O$ used were both of reagent grade. PuO_2 was prepared by heating plutonium oxalate in air at 1273 K for 5 h. The PuO_2 yellow-buff powder thus obtained had a lattice parameter of a=5.3973(5) Å. This value is comparable with the literature value of 5.3960(3) Å[6].

PuO_2 powder was weighed in a fused quartz crucible of 15 mm outer diameter and 15 mm height. An aliquot of alkali solution was pipetted on the PuO_2 powder. The specimens were dried in a magnesium perchlorate desiccator. Several such crucibles containing the alkali salts and PuO_2 in various ratios were placed on a fused quartz boat, and heated in a stream of O_2 gas. The furnace temperature was raised at a rate of 2 K/min to a

given temperature and held at that temperature for 24 h, followed by furnace cooling to room temperature.

The thermobalance studies of the reaction of PuO_2 with $LiNO_3$ and $LiOH \cdot H_2O$ were made using a Sartorius MP8 electric microbalance (sensitivity 0.01 mg). The PuO_2 powder (about 80 mg) was weighed in a fused quartz crucible. An aliquot of lithium solution was pipetted onto the PuO_2. After the solution was dried, the crucible was suspended from the balance. The furnace temperature was raised in a stream of O_2 gas at a rate of 1 K/min to 473 K and held at that temperature for 5 h. Then, it was raised at a rate of 2 K/min to 1273 K and held for 2 h.

The X-ray diffraction patterns were taken with a Rigaku Geigerflex 2182D7 type diffractometer. The CuKα radiation was monochromatized with a curved graphite monochrometer placed between specimen and a NaI(Tl) scintillation detector.

Results and Discussion

Preparation of standard specimens of lithium plutonates

Li_4PuO_5 was prepared by heating the intimate mixture of $LiOH \cdot H_2O$ and PuO_2 (Li/Pu=4 in atom ratio) in a fused quartz crucible in a stream of O_2 at 873 K for 24h. After cooling, the brown product was ground in an agate mortar, and then it was re-heated at 973 K for 24 h. X-ray diffraction analysis showed that the product was of a single tetragonal phase with lattice parameters a=5.673(1) and c=4.416(1) Å. These values are consistent with the literature data of a=5.677(2) and c=4.421(3) Å[2]. Because no significant difference was observed between the X-ray patterns for the products heated at 973 K and 873 K, the formation reaction of the plutonates is apparently complete upon heating to 873 K.

Li_3PuO_4 was prepared as a single phase by heating the mixture of $LiOH \cdot H_2O$ and PuO_2 (Li/Pu=3 in atom ratio) in a stream of O_2 at 1173 K for 24h. The dark-brown product was subjected to X-ray diffraction analysis after cooling. The product was tetragonal with a=4.461(1) and c=8.373(1) Å, which were in good agreement with the reported lattice parameters a=4.464(2) and c= 8.367(5) Å[3]. It has been reported that in Li_3UO_4[7] the Li and U atoms are located in an ordered manner on the lattice site of the NaCl-type crystal structure. The same type of ordering can be deduced for Li_3PuO_4 from a good fit between the observed and calculated X-ray intensities obtained for space group I4/mmm (Z=2) with atom positions Pu: 2a, Li: 2b and 4d, and O: 4c and 4e with z=1/4.

The mixture of $LiOH \cdot H_2O$ and PuO_2 in an atom ratio Li/Pu=2 was heated under the same conditions as in the case of the Li_4PuO_5 preparation. Examination of the X-ray patterns revealed that the product was a mixture of the Li_4PuO_5 and PuO_2. The formation of Li_4PuO_5 instead of Li_3PuO_4 may be due to the lower heating temperature. The lattice parameter of the coexisting PuO_2 phase was 5.3956(5) Å which was significantly smaller than that of the starting PuO_2. This also occurs upon similar heating of PuO_2. The lattice contraction may be caused either by Li cations, having a smaller crystal radius, possibly substituted for Pu, or by oxygen hyper-stoichiometry of the PuO_2 phase. A similar behavior has been observed for $M_yU_{1-y}O_{2+x}$ (M=alkaline earth and rare earth elements) solid solutions[8-11].

Reactivity of lithium nitrate on PuO_2

An aliquot of $LiNO_3$ solution was pipetted on the PuO_2 powder (about 80 mg) in the crucible. The nominal Li/Pu ratios were adjusted to 1, 2 and 4. The specimens were heated at 973 K for 24 h. X-ray diffraction patterns of the products showed that they were all two-phase mixtures of Li_4PuO_5 and PuO_2 and that the peak intensities of the Li_4PuO_5 became higher as the Li/Pu ratios were higher. For the Li/Pu=4 specimen, the intensity ratio between the strongest (101) peak of Li_4PuO_5 and the strongest (111) peak of PuO_2 was 0.51.

Next, mixtures of PuO_2 powder and $LiNO_3$ with a ratio Li/Pu=4 were heated at respective temperatures of 773, 873, 1073, 1173 and 1273 K for 24 h. All the products were two-phase mixtures of Li_4PuO_5 and PuO_2 (773, 873, 973 and 1073 K) or that of Li_3PuO_4 and PuO_2 (1173 K), excluding the product heated at 1273 K for which only sharp peaks of PuO_2 phase were observed. The intensity ratio of the reflections of (101) and (111) planes of Li_4PuO_5 and PuO_2, respectively, in the product increased with increasing temperature. The ratio reached a maximum value of 0.51 at 973 K and then decreased to the value of 0.34 at 1073 K. These facts indicate that a formation reaction of Li_4PuO_5 proceeds up to 973 K and that Li_4PuO_5 begins to decompose slowly over 1073 K. The Li_3PuO_4 decomposes completely to PuO_2 and Li_2O at 1273 K.

Reactivity of lithium hydroxide on PuO_2

Lithium hydroxide solution was added to PuO_2 powder (about 80 mg) in a fused quartz crucible. Nominal Li/Pu ratios were adjusted to 1, 2, 3, 4, 4.5, 5 and 6. These specimens were heated in a stream of O_2 at 923 K for

24 h. After cooling, the X-ray diffraction patterns of the products were recorded. Subsequently, they were re-heated at 1073 K for 24 h. Figure 1 shows the X-ray diffraction patterns of the products heated at 923 K. The products with Li/Pu=1, 2, 3, and 4 are all two-phase mixtures of Li_4PuO_5 and PuO_2 and the amount of the plutonate phase becomes larger as the Li/Pu atom ratio increases.

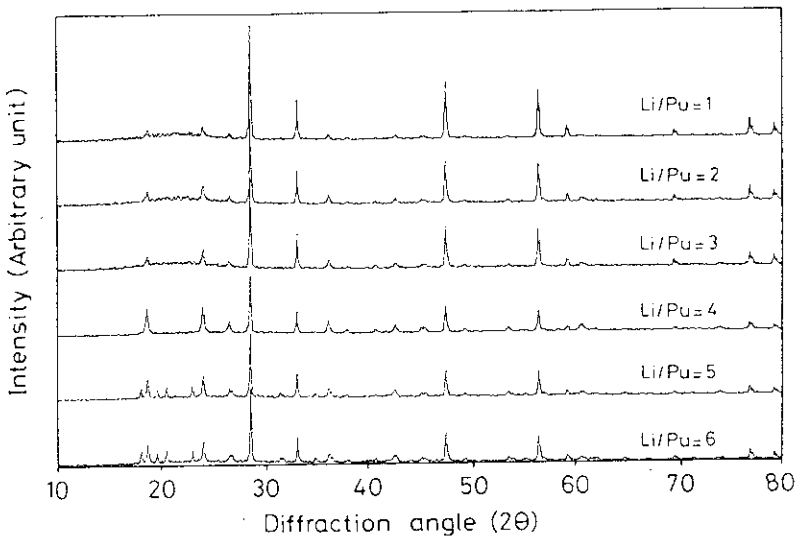

Fig. 1 X-ray diffraction patterns of the products formed by the reaction between lithium hydroxide and PuO_2 in O_2 at 923 K for 24 h: Lithium hydroxide was added to the PuO_2 powder as a solution. Heating rate: 2 K/min. The PuO_2 peaks are at 28.62, 33.17, 47.62, 56.51, 59.26, 69.63, 76.96, and 79.36°, while the primary product, Li_4PuO_5, has peaks at 18.76, 24.12, 26.68, 36.27, 38.05, 40.81, 40.93, 42.79, 45.32° etc.

In the patterns of the Li/Pu=5 and 6 products, in addition to the peaks of the Li_4PuO_5 and PuO_2 phases, those of a new phase become distinct. They appear at 18.18, 19.65, 20.57, 23.08, 26.90, 31.51, 31.77, 34.93 and 36.51° in 2-theta. When heated at 1073 K, however, these peaks vanished and only the peaks from Li_4PuO_5 and PuO_2 were evident. Keller et al. have prepared the plutonates with Li/Pu ratios higher than 4, i.e. Li_5PuO_6[4] and Li_6PuO_6[2]. The crystal of these compounds are reported to be both hexagonal with the lattice parameters a=5.19(2) and c=14.48(2) Å, and a=5.184(2) and c=14.59(5) Å for Li_5PuO_6 and Li_6PuO_6, respectively. Some of the observed peaks from the new phase could not be indexed to these compounds, which suggest either that the new phase has a lower symmetry or that the new phase is a mixture of unknown plutonates. The above experiments show that it is essential to mechanically mix the starting materials to obtain pure plutonates free from PuO_2.

Reaction of lithium nitrate and hydroxide with PuO_2 by means of the thermogravimetric method

Reactions of $LiNO_3$ and $LiOH \cdot H_2O$ with PuO_2 were studied using an

electric balance. Thermograms of the reaction between $LiNO_3$ and PuO_2 are shown in Fig. 2 together with that of the reaction of $LiNO_3$ with UO_2 and of the thermal decomposition of $LiNO_3$. The theoretical weight decrease (TWD) in the figure indicates the weight difference between the hexavalent plutonates, which should be formed as a result of reaction (1), and the sum of $LiNO_3$ and PuO_2.

$$p\cdot LiNO_3 + PuO_2 = Li_p^{+}Pu^{6+}O_{3+p/2} + \{(p-2)/4\}O_2 + p\cdot NO_2 \qquad (1)$$

where p is the mixing ratio (Li/Pu). It is seen from the figure that the curves of Li/Pu=4 and 6 (curves 1 and 2) are very close to that of the decomposition of $LiNO_3$ (curve 3). A weight decrease begins at about 720 K and it becomes rapid at above 840 K. At 910 K, curves 1 and 2 reach to 106% and 104% of TWD, respectively, and they are almost horizontal up to 1173 K, above which they again increase slightly up to 1273 K. From these observations, it can be deduced that PuO_2 reacts with Li_2O, which is formed by the decomposition of $LiNO_3$, to form plutonates. At 910 K, the reactions are nearly complete, and the curves 1 and 2 exceed 100% TWD. This fact means that the mean valency of plutonium in the product is smaller than 6+. The mean plutonium valencies are calculated to be 4.50 and 4.40 at 910 K for the Li/Pu=4 and 6 products, respectively. The products were considered to be a mixture of Li_4PuO_5 and PuO_2 from the reactivity study mentioned above. The molar ratios of the plutonate and PuO_2 are 0.25:0.75 and 0.2:0.8 in the mixtures of the Li/Pu=4 and 6 products, respectively. The weight decrease above 1173 K can be attributed to the decomposition of Li_4PuO_5 to Li_3PuO_4. The contrast between the reaction of UO_2[5] and PuO_2 with $LiNO_3$ is apparent from curve 4 in Fig. 2. Solid UO_2 is liable to become higher oxidation states upon heating in

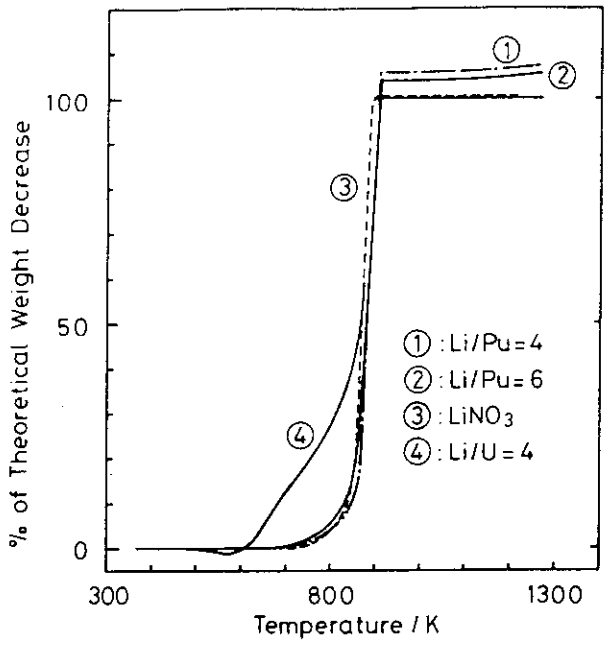

Fig. 2 Thermogravimetric curves of the reaction of lithium nitrate with PuO_2 or UO_2 in a stream of O_2: ① the ratio Li/Pu=4, ② the ratio Li/Pu=6, ④ the ratio Li/U=4. The broken line represents the thermal decomposition curve of lithium nitrate. Heating rate: 1 K/min (room temperature ~ 473 K), 2 K/min (473 ~ 1273 K).

an oxidizing atmosphere, while pure PuO_2 is known never to be oxidized to higher oxides. This difference in the oxidation character between UO_2 and PuO_2 is considered to cause the differing reactivity between them.

Reactions of $LiOH \cdot H_2O$ with PuO_2 were investigated using the specimens with the ratio Li/Pu=4 in which lithium hydroxide was added in the form of either solution (liquid samples) or powder (solid samples). The results are shown in Fig. 3 together with the thermograms of the reaction of $LiOH \cdot H_2O$ with UO_2 and of the decomposition of $LiOH \cdot H_2O$. Because the dehydration of $LiOH \cdot H_2O$ is complete at 365 K as reported by Chun[12], the actual reaction can be expressed as

$$p\text{-}LiOH + PuO_2 + (1/2)O_2 = Li_p^{+}Pu^{6+}O_{3+p/2} + (p/2)H_2O. \quad (2)$$

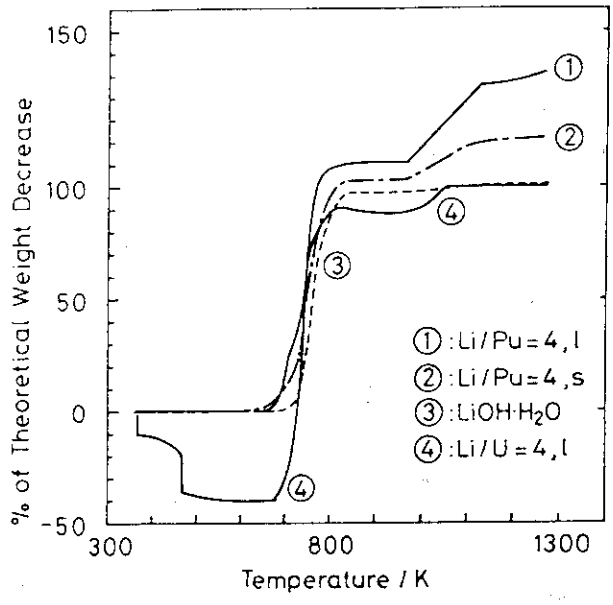

Fig. 3 Thermogravimetric curves of the reaction of lithium hydroxide with PuO_2 or UO_2 in a stream of O_2: ① the solid sample with the ratio Li/Pu=4, ② the liquid sample with the ratio Li/Pu=4, ④ the liquid sample with the ratio Li/U=4. The broken line represents the thermal decomposition curve of lithium hydroxide. Heating rate was 1 K/min to 373 K and the specimen was held at 373 K for 5 h. The specimen was again heated with a rate of 1 K/min to 473 K and held at that temperature for 2 h. After that, the heating rate was 2 K/min to 1273 K.

PuO_2 begins to react with LiOH at 660 K which is about 40 K lower than the initiation temperature of the LiOH decomposition. The weight decrease becomes rapid over 670 K, and reaches 110% and 103% TWD at 840 K for curves 1 and 2, respectively. Both curves are practically horizontal between 840 and 970 K, and then the weight decreases again at a fairly high rate to 1120 K. Above this temperature, the rate of the weight decrease slows down. From the comparison of curves 1 and 2 with curve 3, it is deduced that PuO_2 reacts with LiOH as well as with Li_2O, which is formed above 700 K. Reactions are almost complete at 840 K. The products were again a mixture of Li_4PuO_5 and PuO_2, but the amount of PuO_2 was much lower in the reaction of hydroxide. The mean valencies of plutonium in the products are 5.73 and 5.93 for the products of the liquid and solid

samples, respectively. The mole ratios of this plutonate and PuO_2 in the mixtures are calculated to be 0.86:0.14 and 0.95:0.05, respectively. That is to say, almost PuO_2 free plutonates can be obtained from the solid samples. The weight decrease observed on the curves 1 and 2 in the temperature range between 970 and 1120 K is attributed to the decomposition of Li_4PuO_5 into Li_3PuO_4, and the further weight decrease above 1120 K may be due to the vaporization of unreacted Li_2O. The reaction of LiOH with PuO_2 is very different from that of LiOH with UO_2 (curve 4) due to the differing oxidation character between PuO_2 and UO_2 as stated earlier.

Dissolution test of the plutonates in nitric acid

To a small amount of the powder products obtained by heating the liquid samples at 1073 K (Li/Pu=4 and 6) in beakers, 1-M HNO_3 was added. Most part of the specimens dissolved in two minutes, but a small quantity of residue of yellow-buff PuO_2 remained undissolved after 5 hours. For the products from the solid samples with the ratios Li/Pu=3 and 4 which contain no PuO_2, the dissolution was complete in 1-M HNO_3 in two minutes. This fact shows that the plutonates can be easily dissolved in dilute nitric acid.

References

1) F. Weigel, J.J. Katz and G.T. Seaborg: Plutonium; J.J. Katz, G.T. Seaborg and L.R. Morss, Eds; The Chemistry of the Actinide Elements (Chapman and Hall, New York, 1986) vol.1, p 711.
2) C. Keller, L. Koch and K.H. Walter, J. Inorg. Nucl. Chem. 27(1965)1205.
3) C. Keller, L. Koch and K.H. Walter, ibid. 27(1965)1225.
4) C. Keller and H. Seiffert, Angew. Chem. 81(1969)294.
5) T. Fujino, K. Ouchi, T. Yamashita and H. Natsume, J. Nucl. Mater. 116(1983)157.
6) The Thermodynamic Properties of Pu oxides; I.A.E.A., Vienna (1966).
7) G. Blasse, Z. Anorg. Allgem. Chem. 331(1964)44.
8) T. Fujino and K. Naito, J. Inorg. Nucl. Chem. 32(1970)627.
9) T. Yamashita and T. Fujino, J. Nucl. Mater. 136(1985)117.
10) T. Fujino, T. Yamashita and H. Tagawa, J. Solid State Chem. 73(1988)544.
11) T. Yamashita, T. Fujino and H. Tagawa, J. Nucl. Mater. 132(1985)192.
12) K.S. Chun, AERE-R8735 (1977).

Publication List

[1] T. Yamashita, K. Ohuchi, K. Takahashi and T. Fujino, "Formation of Litium Plutonates by the Reaction of Litium Nitrate and Hydroxide with PuO_2", Proc. Symp. to Commemorate the 50th Anniversary of the Discovery of Transuranium Elements, Washington D.C., August, 1990.

10.4 Analysis of the Optical Spectra and Magnetic Susceptibilities of Ternary Actinide Oxides

10.4.1 Introduction

Contrary to the situation for the $4f^n$ configurations of rare earths, it is usually impossible to treat the crystal-field acting on $5f^n$ configurations of actinide compounds as a small perturbation of atomic levels. In many cases, the crystal field interaction, spin-orbit coupling interaction, and electronic repulsion interaction are of comparable magnitude, which makes the analysis of the experimental results complicated. However, for the actinide ions having the $[Rn]5f^1$ electronic configuration, the situation is considerably simplified, because there is no electron-electron repulsion interaction.

Kanellakopulos et al.[1] measured optical spectra and magnetic susceptibilities for a number of uranates (U^{5+}), neptunates (Np^{6+}), and one plutonate (Pu^{7+}), and fitted their data to the theory developed by Eisenstein and Pryce[2] with an additional parameter to account for a tetragonal distortion of the crystal field. However, an added empirical temperature-independent paramagnetic susceptibility was necessary in order to obtain a satisfactory fit of the magnetic susceptibility data as a function of temperature. Edelstein and Goffart[3] questioned the use of a spin-orbit coupling constant by Kanellakopulos et al. which was almost constant for U^{5+}, Np^{6+}, and Pu^{7+} (1800∼1900 cm^{-1}), because the spin-orbit coupling constant is known to increase markedly with higher atomic number and higher charge on the ions[4]. For some compounds, the orbital reduction factors obtained show the relation $k < k'$, which is an improbable result[5] because the orbital reduction factor k is associated with overlap of the t_{2u} orbitals of the 5f electrons with p_π electrons on the oxygen; on the other hand the orbital reduction factor k' is related to the anti-bonding of the $5f\delta$ orbitals (t_{1u}) with $2p_\sigma$ electrons on the oxygen atoms. Eisenstein and Pryce pointed out that k should be very nearly unity[2].

We focus our attention on the magnetic and optical properties of Li_7UO_6, Ba_3NpO_6, and Li_5UO_6 in which the actinide ions are nearly octahedrally coordinated by six oxygens. Although electron paramagnetic resonance (EPR) measurements have not been carried out yet for Ba_3NpO_6 and Li_5PuO_6, we may obtain the ground state g-values from their magnetic susceptibilities, because the susceptibilities are linear against

reciprocal temperature over the temperature range from 4.2 K to 300 K[1].

In this report, we will obtain the crystal field parameters of Li_7UO_6, Ba_3NpO_3, and Li_5PuO_6 by fitting the calculations not only to the transition energies but also to the ground state g-values on the basis of an octahedral crystal field model with/without a small tetragonal distortion.

Details of the calculation methods are described in our earlier paper[6].

10.4.2 Results and Discussion

The transition eneregies, and all the crystal field parameters and the orbital reduction factors, are listed in Tables 1 and 2, respectively. The transition energies calculated are well fitted to those obtained

Table 1
Electronic transition energies.

Compound	Assignment	Transition energies (cm^{-1}) Experiment	Calculation
Li_7UO_6	$\Gamma_7'(\Gamma_7) \rightarrow \Gamma_6'(\Gamma_6)$	15,468	15,475
	$\Gamma_7'(\Gamma_7) \rightarrow \Gamma_7'(\Gamma_8')$	13,871	13,264
	$\Gamma_7'(\Gamma_7) \rightarrow \Gamma_6'(\Gamma_8')$		13,102
	$\Gamma_7'(\Gamma_7) \rightarrow \Gamma_7'(\Gamma_7')$	7,439	7,435
	$\Gamma_7'(\Gamma_7) \rightarrow \Gamma_7'(\Gamma_8)$	5,972	5,961
	$\Gamma_7'(\Gamma_7) \rightarrow \Gamma_6'(\Gamma_8)$	5,416	5,409
Ba_3NpO_6	$\Gamma_7 \rightarrow \Gamma_6$	>16,500	19,077
	$\Gamma_7 \rightarrow \Gamma_8'$	>16,500	17,018
	$\Gamma_7 \rightarrow \Gamma_7'$	9,390	9,390
	$\Gamma_7 \rightarrow \Gamma_8$	7,690	7,580
Li_5PuO_6	$\Gamma_7'(\Gamma_7) \rightarrow \Gamma_6'(\Gamma_6)$	18,519	18,511
	$\Gamma_7'(\Gamma_7) \rightarrow \Gamma_7'(\Gamma_8')$	15,873	15,758
	$\Gamma_7'(\Gamma_7) \rightarrow \Gamma_6'(\Gamma_8')$	14,350	14,347
	$\Gamma_7'(\Gamma_7) \rightarrow \Gamma_7'(\Gamma_7')$	10,256	10,214
	$\Gamma_7'(\Gamma_7) \rightarrow \Gamma_7'(\Gamma_8)$	8,818	8,772
	$\Gamma_7'(\Gamma_7) \rightarrow \Gamma_6'(\Gamma_8)$	6,623	6,632

experimentally. As expected from the crystal structures of Li_7UO_6 and Li_5PuO_6[7], both the quartets Γ_8 and Γ_8' are split into two doublets Γ_7 and Γ_6 (Fig. 1). Since the splitting of the quartet Γ_8' level is not experimentally observed for Li_7UO_6, the degree of tetragonal distortion is considered to be fairly small, which is clearly shown in the tetragonal distortion parameter τ. The spin-orbit coupling constants (ζ) obtained for Li_7UO_6, Ba_3NpO_6, and Li_5PuO_6 are all reasonable values for U^{5+}, Np^{6+}, and Pu^{7+}, and increase with atomic number and/or oxidation state, which is consistent with the results of the theoretical calculations[4]. In this study, we have taken into account the covalency effect in chemical bonding, i.e., introduced the orbital reduction factors (k and k') in the calculation of energy levels and magnetic susceptibilities. Although the orbital reduction factors determined

here (Table 2) may not be the unique values for each compound, the results indicate that k' should be much smaller than k, which is consistent with the theoretical view[2,5]. To obtain a satisfactory fit of the magnetic susceptibility data as a function of temperature, an added empirical temperature-independent paramagnetic (TIP) susceptibility was needed for all of the compounds. We suggest the reduced actinide ions with $[Rn]5f^2$ configuration, i.e., U^{4+}, Np^{5+}, and Pu^{6+} are responsible for this extra TIP. These ions in octahedral coordination are known to show a temperature-independent paramagnetism over a wide temperature range[3]. With this hypothesis and from the comparison of the extra TIP between compounds, it was found that a considerable amount of Pu^{6+} ions which are much more stable than Pu^{7+} ions exist in Li_5PuO_6. The crystal field splitting Δ which is very sensitive to the magnetic properties of the compounds increases with atomic number (from U^{5+} to Np^{6+} to Pu^{7+}), as expected.

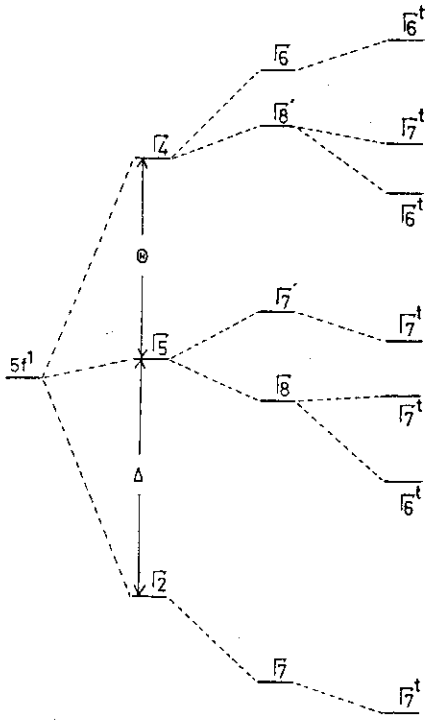

Fig. 1
f^1 orbital energy splitting perturbed by octahedral crystal field, spin-orbit coupling, and tetragonal crystal field distortion.

Table 2
Crystal-field parameters and orbital reduction factors.

	free ion	Oh	Oh+spin-orbit	+tetragonal distortion		
Compound	ζ (cm^{-1})	Δ (cm^{-1})	Θ (cm^{-1})	τ (cm^{-1})	k	k'
Li_7UO_6	1868	4604	6600	140	1.0	0.8
Ba_3NpO_6	2378	5695	8800	0	1.0	0.6
Li_5PuO_6	2520	6700	5600	480	1.0	0.6

References

1) B. Kanellakopulos, E. Henrich, C. Keller, F. Baumgärtner, E. König, and V.P. Desai, Chem. Phys. 53(1980)197.
2) J.C. Eisenstein and M.H.L. Pryce, Proc. Roy. Soc., Ser A, 255(1960)181.
3) N.M. Edelstein and J. Goffart, in: The Chemistry of the Actinide Elements, Eds. J.J. Katz, G.T. Seaborg, and L.R. Morss, 2nd edn, (Chapman and Hall, London/New York, 1986) Chap.18.
4) W.B. Lewis, J.B. Mann, D.A. Liberman, and D.T. Cromer, J. Chem. Phys. 53 (1970)809.
5) H.G. Hecht, W.B. Lewis, and M.P. Eastman, Adv. Chem. Phys. 21(1971)351.
6) Y. Hinatsu and N. Edelstein, J. Solid State Chem. 93(1991)173.
7) C. Keller, in MTP International Review of Science, Vol.7, "Lanthanides and Actinides" Ed. K.W. Bagnall, Series I (Butterworths, London, 1972) p.47.

Publication List

[1] Y. Hinatsu and T. Fujino, "Studies on Magnetic Properties of UO_2-CeO_2 Solid Solutions: III. Magnetic Susceptibilities of Solid Solutions with High Cerium Concentrations," J. Less-Common Metals 149(1989)197.
[2] Y. Hinatsu and T. Fujino, "Magnetic Susceptibilities of $M_yU_{1-y}O_{2+x}$ (M = Th, Zr, Ce, La, Y, Sc, Ca) Solid Solutions," J. Less-Commom Metals 155(1989)347.
[3] Y. Hinatsu and T. Fujino, "Study of Electron Paramagnetic Resonance on $Ce_{0.1}U_{0.9}O_2$ Solid Solution," Chem. Phys. Lett. 172(1990)131.
[4] Y. Hinatsu and N. Edelstein, "Analysis of the Optical Spectra and Magnetic Susceptibilities of Li_7UO_6, Ba_3NpO_6, and Li_5PuO_6," J. Solid State Chem. 93(1991)173.
[5] Y. Hinatsu, "Magnetic Susceptibilities of $Y_yU_{1-y}O_{2+x}$ Solid Solutions," J. Solid State Chem. 94(1991)163.
[6] Y. Hinatsu and N. Edelstein, "Electron Paramagnetic Resonance Studies of Cm^{3+} in Single Crystals of YPO_4," J. Atom. Ener. Soc. Japan 33(1991)994.
[7] Y. Hinatsu, "Magnetic Studies on $(U,La)O_{2+x}$ Solid Solutions II. Magnetic Susceptibilities of Solid Solutions with High Lanthanum and Oxygen Concentrations," J. Solid State Chem. 95(1991)300.
[8] Y. Hinatsu, "Magnetic Susceptibilities of $Mg_yU_{1-y}O_{2+x}$ Solid Solutions," J. Solid State Chem. 95(1991)430.

10.5 Microwave Properties of High-T_c Superconductors and Related Material

10.5.1 Microwave Properties of Inhomogeneous $YBa_2Cu_3O_7$ [1]

The RF properties of High T_c superconducting material in the microwave region have been investigated mainly by the cavity method, from which one can obtain some parameters of the superconductors such as surface impedance and energy gap. Here we report an analysis of the experimental results with the standing-wave method in terms of the propagation constant under the assumption that superconductivity coexists with dielectricity.

The preparation method of $YBa_2Cu_3O_7$ is described elsewhere.[1)] The prepared powder specimen was investigated by the standing-wave method, the fundamentals of which are shown in Fig. 1. The powder specimen (thickness d and density ρ) was packed into an end section of the X-band waveguide which was terminated by a reflecting plane. The standing waves occur by the interference between incident and reflecting waves in the waveguide. The voltage standing-wave ratio, $(VSWR)=V_{max}/V_{min}$, and the distance between the first voltage minimum and the surface of the specimen, y, were determined with a standing-wave detector. The specimen was cooled in liquid helium and the temperature of the specimen in a cryostat was varied within ± 0.1K.

In the normal state, the complex dielectric permittivity, $\varepsilon=\varepsilon_o(\bar{\varepsilon}'-i\bar{\varepsilon}'')$ where ε_o is the dielectric constant of vacuum, can be calculated from the experimental result using the following equations:[2)]

$$\bar{\varepsilon}'=(\lambda/\lambda_c)^2-(\lambda/2\pi)^2(\alpha^2-\beta^2), \tag{1}$$

$$\bar{\varepsilon}''+(\sigma/\omega\varepsilon_o)=2(\lambda/2\pi)^2\alpha\beta\ , \tag{2}$$

$$\gamma=\alpha+i\beta, \tag{3}$$

and

$$\frac{\tanh(\gamma d)}{\gamma d}=\frac{\lambda_g}{2\pi d}\left\{\frac{\tan(2\pi y/\lambda_g)+ir}{ir\tan(2\pi y/\lambda_g)-1}\right\}, \tag{4}$$

where λ and λ_g are the wavelength in the free space and that in the air inside the waveguide, respectively, and λ_c is the cut-off wavelength (λ_c =4.58cm for X-band waveguide) and $r=(VSWR)^{-1}$. The symbol γ stands for the propagation constant of microwaves in the specimen, while σ is the

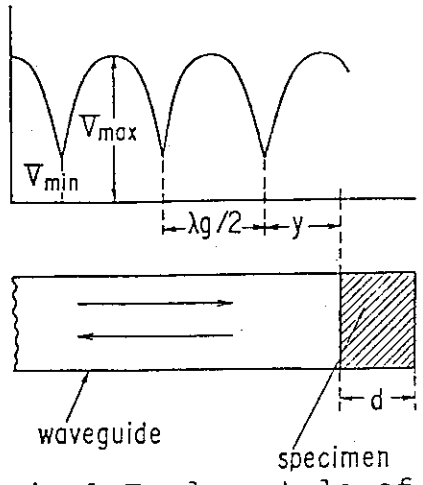

Fig.1 Fundamentals of standing-wave method.

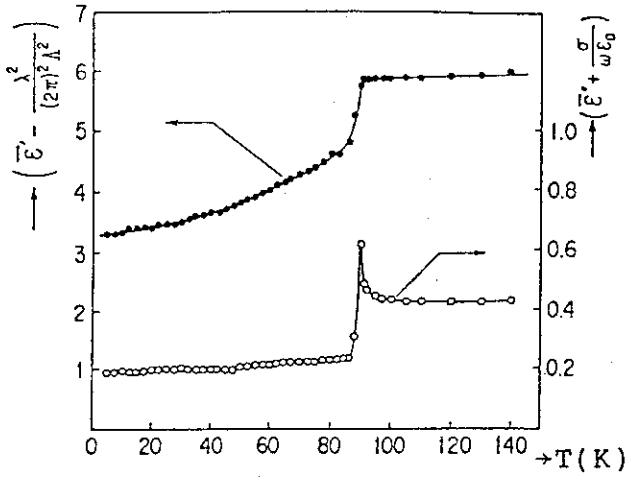

Fig.2 Complex dielectric permittivity of $YBa_2Cu_3O_7$.

conductivity of the specimen. The term ($\sigma/\omega\varepsilon_o$), which can be neglected in the case of dielectrics with low conductivity, is retained here. Thus, the calculated complex dielectric permittivity for the specimen with d=0.36cm and ρ=4.22g/cm^3 (packing factor=0.65), at 9.12GHz, is shown in Fig. 2. Of course, the above equations are not valid for superconducting state. Thus they must be modified.

To obtain the propagation constant in the superconducting state, we use the Maxwell equations in conjunction with the London equation.[3] We start with two of the Maxwell equations in the following form,

$$\mathrm{rot}H=J+(\partial D/\partial t)\ , \tag{5}$$

$$\mathrm{rot}E=-(\partial B/\partial t)\ . \tag{6}$$

Taking the rotation of Eq. (5), we have

$$\nabla^2 H=-\mathrm{rot}J-\varepsilon\mathrm{rot}(\partial E/\partial t)\ . \tag{7}$$

Here we use the identities as $\mathrm{rot}(\mathrm{rot}H)=\nabla(\mathrm{div}H)-\nabla^2 H$ and $\mathrm{div}H=0$. By using Eq. (6), Eq. (7) can be rewritten as

$$\nabla^2 H=-\mathrm{rot}J+\mu\varepsilon(\partial^2 H/\partial t^2)\ . \tag{8}$$

In the superconducting state, the total current is given by

$$J=J_n+J_S\ , \tag{9}$$

where J_n and J_s express the normal and superconducting currents, respectively. For the superconducting current, we can use London equation as

$$\mathrm{rot}J_S=-H/\lambda_L^2\ , \tag{10}$$

where λ_L is the London penetration depth. In the following discussions we

postulate that this equation is also valid for an inhomogeneous superconductor such as powder specimen if we use Λ instead of λ_L, where Λ is the phenomenological penetration depth. For normal current, we use Ohm's law,

$$J_n=\sigma E . \tag{11}$$

Then we have

$$\mathrm{rot}J=-\Lambda^{-2}H-\mu\sigma(\partial H/\partial t) . \tag{12}$$

From Eqs. (8) and (12), we have

$$\nabla^2 H=\Lambda^{-2}H+\mu\sigma(\partial H/\partial t)+\mu\varepsilon(\partial^2 H/\partial t^2) . \tag{13}$$

Suppose a superconductor occupies a half-space Z>0 and the electric field E, the current J and the magnetic field H are all parallel to the surface of the superconductor, the z=0-plane, and are directed along the x-, X- and y-axes, respectively. It is reasonable to assume that H_y as a function of time can be expressed as $H_y(z)\exp(i\omega t)$: then Eq. (13) becomes

$$\frac{\partial^2 H_y(z)}{\partial z^2}=\frac{H_y(z)}{\Lambda^2}+i\omega\mu\sigma H_y(z)-\omega^2\mu\varepsilon H_y(z) . \tag{14}$$

Furthermore we assume that the electromagnetic wave attenuates as it penetrates into the superconducting material according to the equation $H_y(z)=H_o\exp(-kz)$, where k is the propagation constant in superconducting materials. Then we have

$$k^2=\Lambda^{-2}+i\omega\mu\sigma+\omega^2\mu\varepsilon . \tag{15}$$

Here k is the superconducting counterpart of γ of the normal phase. If the superconductivity is dominant in the material ($J_s>>J_n$), Λ is small and the second and the third terms become negligible in Eq. (15). Conversely, if the normal state is dominant, Λ is large and the first term becomes negligible. We can put $\mu=\mu_o$ in Eq. (15) because the terms which contain the quantity μ are only important when the normal state is dominant.

The propagation constant k is given only by the first and second terms of Eq. (15) in the conventional superconductor, while it is so supplemented by the third term as to reflect the coexistence of the dielectricity and the superconductivity in the high-T_c superconductors. Eq. (15) is rewritten in the term of the complex dielectric permittivity as

$$k^2=-\omega^2\mu_o\varepsilon_o\bar{\varepsilon}'+\Lambda^{-2}+i(\omega^2\mu_o\varepsilon_o\bar{\varepsilon}''+\omega\mu_o\sigma). \tag{16}$$

Taking account of the relation between the propagation constant in free space and that in the waveguide, we can write the propagation constant of the superconducting material in the waveguide k_g as

$$k_g=\left(\frac{2\pi}{\lambda_c}\right)^2+\left(\frac{2\pi}{\lambda}\right)^2\left\{\left(\frac{\lambda^2}{(2\pi)^2\Lambda^2}-\varepsilon'\right)+i\left(\bar{\varepsilon}''+\frac{\sigma}{\omega\varepsilon_o}\right)\right\}. \tag{17}$$

By putting the following equation into Eq. (17)

$$k_g=\alpha_{gs}+i\beta_{gs}\ , \tag{18}$$

and writing down the real and imaginary components in Eq. (17) separately, we have

$$\bar{\varepsilon}'-\frac{\lambda^2}{(2\pi)^2\Lambda^2}=\left(\frac{\lambda}{\lambda_c}\right)^2-\left(\frac{\lambda}{2\pi}\right)^2(\alpha_{gs}^2-\beta_{gs}^2), \tag{19}$$

$$\bar{\varepsilon}''+\frac{\sigma}{\omega\varepsilon_o}=2\left(\frac{\lambda}{2\pi}\right)^2\alpha_{gs}\beta_{gs}\ . \tag{20}$$

Eq. (19) clearly shows that $\bar{\varepsilon}'$ in Eq. (1) must be replaced by $\bar{\varepsilon}'-\lambda^2/(2\pi)^2\Lambda^2$ in the superconducting state.

The values of α_{gs} and β_{gs} in the right-hand side of Eqs. (19) and (20) are obtained from the experiment, so we can plot the real and imaginary parts of the permittivity as a function of temperature as shown in Fig. 2. The decrement of $\bar{\varepsilon}'-\lambda^2/(2\pi)^2\Lambda^2$ below T_c with decreasing temperature in Fig. 2 should correspond to the diminution of the penetration depth in the powder specimen, suppose that $\bar{\varepsilon}'$ remains constant in the superconducting state. From this point of view, Λ can be deduced with the use of Eq. (19) and the values are plotted as a function of temperature in Fig. 3. This reveals that the penetration depth is as large as $\Lambda=0.32$cm at T=5K in the powder specimen. The temperature dependence of the London penetration depth of $YBa_2Cu_3O_7$ with higher density has been investigated by several authors.[4-7] From these

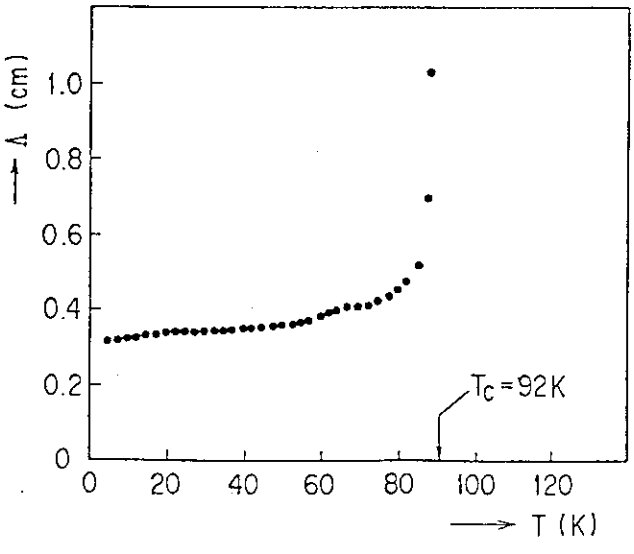

Fig.3 Penetration depth of powder specimen of $YBa_2Cu_3O_7$.

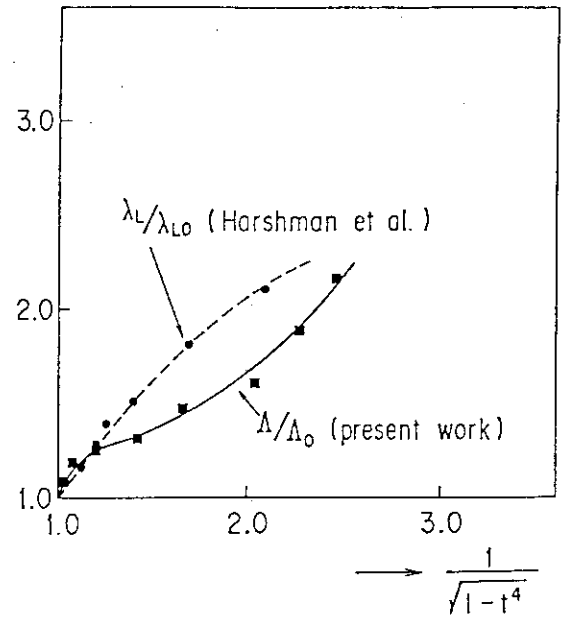

Fig.4 London penetration depth by Harshman et al. and the phenomenological penetration depth in $YBa_2Cu_3O_7$.

result, it has been concluded that the London penetration depth of sintered $YBa_2Cu_3O_7$ was approximately expressed by $\lambda_L=\lambda_{Lo}Z(t)$ where t and λ_{Lo} are the reduced temperature (T/T_c) and the London penetration depth at the low temperature limit, respectively. The function Z(t) based on the two-fluid model is due to Gorter and Casimir and is given by,

$$Z(t)=(1-t^4)^{-1/2}. \qquad (21)$$

In Fig. 4, λ_L/λ_{Lo} and Λ/Λ_o are plotted against Z(t), where Λ_o is the value of Λ at the low temperature limit. The temperature dependence of λ_L by Harshman et al.[5] is well described by Eq. (21). The phenomenological penetration depth seems to have similar temperature dependence on that of λ_L. although it is 10^4 times as large as Λ_L. According to the theoretical analysis by taking account of Josephson effect by Rosenblatt et al.[8], the penetration depth of an inhomogeneous system should be expressed by const. $\times\lambda_L/I_J^{1/2}$, where I_J is the critical current of a junction. Under the condition of $T<<T_c$, I_J is independent of temperature.[9] Thus the experimental result could be explain by taking account of the Josephson effect. However, further quantative comparison seems to be difficult at present.

10.5.2 Electronic properties of La_2CuO_4 at Low Temperature [2]

La_2CuO_4 is the mother compound of the superconducting oxides with high-T_c. We measured the dielectric permittivity at 9GHz and the dc resistivity in La_2CuO_4, and we discussed electronic properties of La_2CuO_4 as the precursor of the superconducting state in the present report.

The prepared powder of La_2CuO_4 was examined with a dielectric measurement apparatus by the standing-wave method described already.

dc resistivity measurements were also performed using La_2CuO_4 ceramics which were prepared by sintering the pressed powder at 950C for 15h. A standard four-probe method was used for the resistivity measurement of sheet-shaped specimen of 10x1.2x0.1mm^3. The measuring current was about 1mA/cm^2 and the accuracy is about 10^{-3}ohm cm.

$\bar{\varepsilon}'$ and $\bar{\varepsilon}''$ of the La_2CuO_4 powder measured at 9.12GHz are plotted against temperature in Fig. 5. The packing factor of the specimen is 0.40. From this figure the temperature dependence of dielectric constant is found to be classified into two regions, lower or higher than about 25K. In the high temperature region the curves of $\bar{\varepsilon}'$ and $\bar{\varepsilon}''$ versus T are characteristic of Debye

relaxation. For this mechanism we introduce the following quantities,

$$\varepsilon' = \varepsilon_\infty + \frac{\Delta\varepsilon}{1+(\omega\tau)^2} , \qquad (22)$$

$$\varepsilon'' = \frac{\Delta\varepsilon\omega\tau}{1+(\omega\tau)^2} , \qquad (23)$$

$$\Delta\varepsilon = \varepsilon_0 - \varepsilon_\infty , \qquad (24)$$

$$\tau = \tau_0 \exp(E_a/kT), \qquad (25)$$

where ε_0 is the static dielectrc constant, ε_∞ the dielectric constant at high frequency, τ the relaxation time and ω the measurement frequency. By fitting the above equations to the curve in Fig. 5, we have obtained τ as a function of T. In Fig. 6 $\ln(\omega\tau)$ is plotted against 1/T, where the activation energy is obtained as E_a=0.024eV. This Debye type relaxation should be related to the electronic polarization due to hopping of localized carriers. The obtained E_a should be the activation energy of hopping. The nature of the carriers in the low temperature region cannot be discussed from the dielectric data alone.

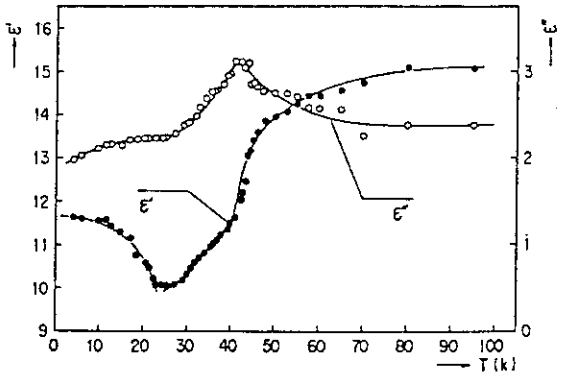

Fig.5 Temperatur dependence of ε' and ε" of La_2CuO_4 at 9.12GHz.

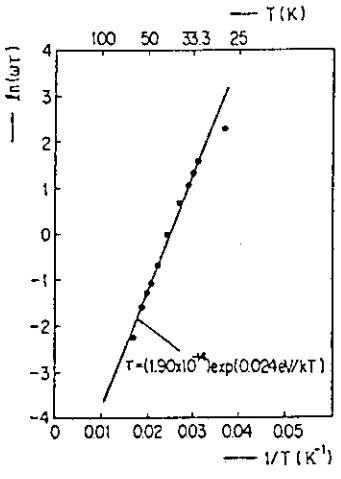

Fig.6 Plot of $\ln(\omega\tau)$ vs. 1/T.

The dc resistivity is also analyzed as a function of temperature. In Fig. 7. $\ln\rho$ is plotted against $T^{-1/4}$. The temperature dependence on the resistivity is also divided into two regions. In the low temperature region (4-25K) dc resistivity is expressed as

$$\rho = 0.133\exp[(26700/T)^{1/4}] \text{ ohm cm.} \qquad (26)$$

In the high temperature region (40-100K) the resistivity seems rather to obey an ordinary activation process. The plotting of $\ln(\rho/T)$ versus 1/T is shown in Fig. 8. The activation energy is 0.024eV, which agrees fairly well with that

obtained in the dielectric measurement.

The dc resistivity of La_2CuO_4 has been studied by some authors,[10, 11] and the result for Eq. (26) shows that variable-range hopping (VRH) takes place. VRH is explained by the localization of electron (or hole) due to the random potential, that means the Anderson localization[12]. The density of state in La_2CuO_4 is given thematically in Fig. 9, where E_c and E'_c are the mobility edges, and the Anderson-localized states are shown shaded.

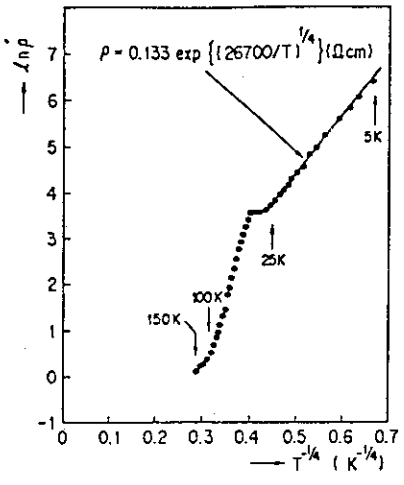

Fig.7 Plot of ln ρ vs. $T^{-1/4}$.

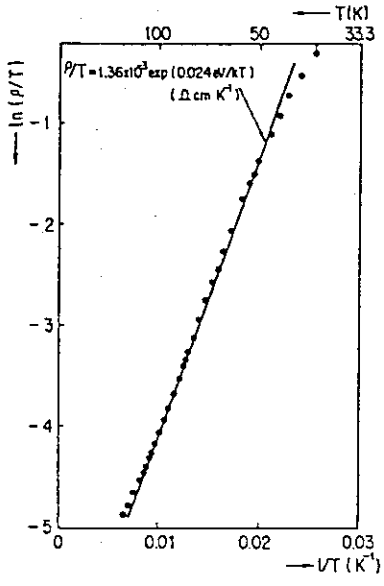

Fig.8 Plot of ln(ρ/T) vs. 1/T.

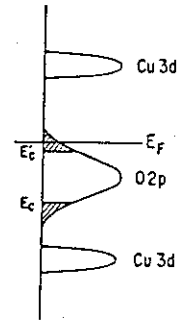

Fig.9 Schematic diagram of the density of states in La_2CuO_4.

References

1) J. Tateno and N. Masaki, Jpn. J. Appl. Phys. 26 (1987) L1654.

2) S. Robert and A. J. von Hippel, J. Appl. Phys. 17 (1964) 616.

3) R. F. Soohoo, Microwave Magnetics (Harper & Row, New york, 1985) Chap. 10.

4) S. Sridhar, C. A. Shiffman and H. Hamdeh, Phys. Rev. 36B (1987) 2301.

5) D. R. Harshman et al., Phys. Rev. 36B (1987) 2386.

6) H. Wiesman et al., High-Temperature Superconductors (eds. M. B. Brodsky et al., Material Research Soc., Pittsburgh, 1989) p. 387.

7) S. Ahmed et al., Supercond. Sci. Technol., 1 (1989) 281.

8) J. Rosenblatt, P. Peyral and A. Raboutou, Inhomogeneous Superconductors-

1979 (eds. D. U. Gubser et al., American Institute of Physics, New York, 1980) p. 33.

9) M. Tinkham, Introduction to Superconductivity (McGraw-Hill, New York, 1979) p. 217.

10) M. Oda et al., Solid State Commun. 76 (1988) 257.

11) M. A. Kastner et al., Phys. Rev. B37 (1988) 111.

12) N. F. Mott and E. A. Davis, Electronic Process in Noncrystalline Materials, 2nd Ed. (Clarendon, Oxford, 1979).

Publication List

[1] J. Tateno and N. Masaki, "Microwave Properties of Inhomogeneous $YBa_2Cu_3O_7$", Jpn. J. Appl. Phys., 29 (1990) 2407.

[2] J. Tateno, N. Masaki and A. Iwase, " Electronic Properties in La_2CuO_4 at Low Temperatures", Phys. Lett. A138 (1989) 313.

10.6 A new chemical approach to high T_c superconductivity

10.6.1 Introduction

In this report, the author gives a brief review of a new chemical approach to high T_c superconductivity, the Multi-Valence Resonance-Condensation model(the MVRC model)[1-3], and demonstrates its practical applicability to various high T_c oxide systems and A-15 type intermetallic Nb_3Ge[4,5].

In contrast to the conventional phonon-mediated BCS mechanism of superconductivity[6] in the MVRC model, the origin of superconductivity is sought in the more fundamental and universal nature of matter, i.e., the chemical bond, more specifically, the microscopic quantum chemical resonances inside the tri-cation crystal molecule of the appropriate chemical species Cu (Bi, Nb etc.) shown in Fig. 1. Adopting the formal valence representation for various cations[7,8], two modes of these resonance hybrids are possible in principle, which have either the higher or lower average cation valence than the intermediate valence state ⊕ denoted here as ORH and RRH respectively. Of course, in the oxides, though not depicted in this figure, the Cu-Cu(Bi-Bi) bond is an indirect one via the oxide ion(O^{2-}). So, depending on the nature of the hybrid molecular orbital(MO) bond between the cations and the oxygen, holes(or electrons) in the ORH(or RRH) type normal state conductors should exhibit a variable character ranging from the cation d(s)- to the oxygen 2p orbitals' character. But, the essential point here is that such hybrid MO bonds exist and the charge transfer process of $\underline{Cu}^{3+} + O^{2-} \rightarrow Cu^{2+} + \underline{O}^{-}$ takes place between them.

These microscopic resonances(ORH and RRH) in Fig. 1 are attained by the simultaneous and symmetrical paired motion of two electrons having opposite spin in opposite directions. So, if these microscopic resonances indeed exist there and extend throughout the whole crystal, the system is expected to be in the macroscopically coherent quantum-chemical resonating state with a real-space electron pair, that is, the MVRC state of superconductivity.

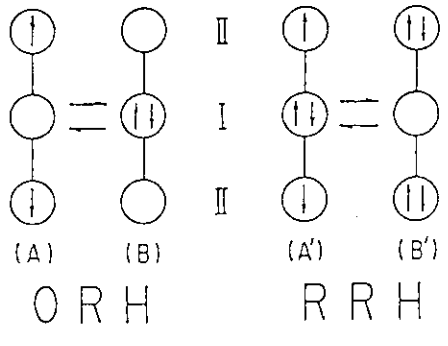

Fig. 1 Oxidized and Reduced type Resonance-Hybrids(ORH and RRH) inside the tri-cation crystal molecule.

Spin state(electron number):

○(0), ⊕(1), ⊕⊕(2).

This is demonstrated in the following for various superconductors.

10.6.2 Results and Discussion

The 90K high T_c superconductor $YBa_2Cu_3O_7$[9] with a tri-layered perovskite structure at the average Cu valence of 2.33+ offers the best example of the present model: The (b-c) plane of this system shown in Fig. 2 is apparently nothing but the interconnected quasi-one-dimensional(1D') array of ORH in Fig. 1. Thus, the microscopic intra-molecular resonance(A⇌B), provided now with the inter-molecular resonance, is considered to manifest itself as the macroscopic MVRC state of superconductivity(ABAB····⇌BABA····), in which every electron moves as half of a real-space electron pair. We may regard the MVRC state more straightforwardly as a Bose-condensate of two bosons(A and B) strongly interacting in real space.

It is well recognized that $YBa_2Cu_3O_{7-y}$ also exhibits the second superconductive plateau of T_c=55-60K around $0.25 \leq y \leq 0.50$[10] with quasi-two-dimensional superconductivity which is similar to that of single-layered $La(Sr)_2CuO_4$[11] and multilayered Tl(Bi)-Cu-O systems[12,13]. Further extension of the trilayer structure in Fig. 2 in the upper and lower directions as IIIIIIIII···· provides the required two-dimensional Cu-O square planes((a-b) planes) responsible for their two-dimensional(2D) superconductivity. This is the isotropic 2D array of A and B of ORH in Fig. 1 with the overall optimum average Cu valence of 2.25+. As its symmetrical counterpart, 2D superconductivity of RRH in Fig. 1 is also realized in the so-called electron type $Nd_{2-x}Ce_xCuO_{4-y}$[14] with its optimum average Cu valence of 1.75+. A 3D network system is obtained by combining these 2D square planes as (a-b), (b-c) and (a-c) planes in the 3D manner.

Results of the present analysis are briefly summarized in Table 1 in order of increasing dimensionality of the system, where 1-, 2- and 3D exten-

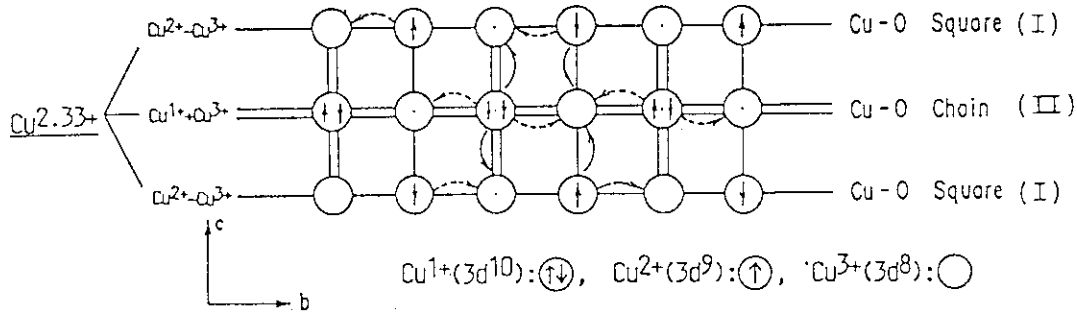

Fig. 2 (b-c) plane of $YBa_2Cu_3O_7$; tri-layer type quasi-one-dimensional(1D') superconductivity(ORH).

Table 1 Brief summary of the present analysis on various superconductors.

Dimension	Systems (Electron Conf.)	T_c(max) (K)	Cation orbital	Cation Valence (ORH or RRH)	Valence State ⇅ ↑ ○
1D Chain	$\underline{Nb}_3Ge(4d^45s^1)$	23.7	d_{z^2} σ	2.25+(ORH)	$Nb^{1,2,3+}(4d^{4,3,2})$
1D' Chain	$YBa_2\underline{Cu}_3O_7(3d^{10}4s^1)$	92	$3d_{x^2-y^2}$ σ*	2.33+(")	$Cu^{1,2,3+}(3d^{10,9,8})$
2D Square Plane	$La_{1.75}Sr_{0.25}\underline{Cu}O_4$	37	"	2.25+(")	" (")
	Tl(Bi)-Cu-O Systems	130	"	" (")	" (")
	$Nd_{1.85}Ce_{0.15}\underline{Cu}O_{3.95}$	20	"	1.75+(RRH)	" (")
2- to 3D' Network	$Li_{0.8}\underline{Ti}_{2.2}O_4(3d^{2}4p^{2})$	12.2	" σ	3.25+(ORH)	$Ti^{2,3,4+}(3d^{2,1,0})$
	$K_{0.75}\underline{Mo}O_3(4d^55s^1)$#	4.3	$4d_{x^2-y^2}$ σ	5.25+(")	$Mo^{4,5,6+}(4d^{2,1,0})$
	$K_{0.75}\underline{W}O_3(5d^46s^2)$#	1.5	5d " "	" (")	$W^{4,5,6+}(5d^{2,1,0})$
	$K_{0.25}\underline{Re}O_3(5d^56s^2)$#	3.6	5d " "	5.75+(RRH)	$Re^{5,6,7+}$(")
	$Ag_7O_8\underline{N}O_3(4d^{10}5s^1)$#	1.0	4d " σ*	2.25+(ORH)	$Ag^{1,2,3+}(4d^{10,9,8})$
	$Ba\underline{Pb}_{3/4}Bi_{1/4}O_{3.935}(6s^26p^2)$	13	6s σ	3.25+(")	$Pb^{2,3,4+}(6s^{2,1,0})$
3D Network	$Ba_{3/4}K_{1/4}\underline{Bi}O_3(6s^26p^3)$	30	"	4.25+(")	$Bi^{3,4,5+}$(")

Underlined cationic species denote those responsible for their superconductivity.
#: For these systems, theoretically most optimized compositions(cation valence) shown in this table are not realized experimentally.

sions of ORH and RRH of Fig. 1 provide the most optimum valence state(chemical compositions) of various superconductors with at least nine kinds of multi-valent type 'soft valence' cations by including also a non-oxide system, i.e., the A-15 type intermetallic Nb_3Ge with a true 1D Nb-Nb chain type direct d-d HOMO bond. For full details, see Refs.(1) and (4).

As for the nature and mechanism of the superconductive transition, the present model suggests the following qualitative scenario: The system may approach these particular valence states either from the magnetic insulator side(La_2CuO_4, $YBa_2Cu_3O_6$) or from the metallic oxide side($BaPbO_3$, ReO_3). Then, their electronic states would be significantly destabilized, driven just to the middle of the metal/insulator transition region, and totally perturbed from the initial stable chemical state in either the magnetic order or the metallic covalent bond. To restabilize the system, the electron system first exerts the dynamic valence exchange A(A') → B(B') or vice versa and generates the multi-valence state. Thereafter, using the induced electron ⇅-hole ○ attractive interactions inside and between the chains(planes) as ordering energy of the process, this high temperature disordered multi-valence state with lots of unsymmetrical electron and spin configurations(valence fluctuation) will start to order gradually with decreasing temperature(valence ordering), competing against the thermal agitation of the system. As the temperature is further lowered, the ordering reaches a critical level around which the system can no longer sustain its A(A')-B(B') type compressed state. The system drops almost spontaneously into the most stable macroscopically coherent MVRC state(resonance-condensation), thereby changing the nature of the chemical

bond from the electrostatically bound excitonic and CDW type to the completely uniform strong resonance type.

To conclude, the answer of the present model to our basic question on high T_c superconductivity(What is high T_c superconductivity and how can this state be realized?) is briefly summarized as follows: The MVRC state of superconductivity is a Bose-condensate of two bosons(A(A') and B(B')) shown in Fig. 1 strongly interacting in real space. This state is realized through the self-organization process of the electron system as the fundamental chemical bonding force, that is, valence fluctuation → valence ordering → resonance-condensation.

References

1) A. Nakamura, Proc. Tsukuba Seminar on High T_c Superconductivity, eds. K. Masuda et al.(Tsukuba Univ., Tsukuba, 1989)P.85-90.
2) A. Nakamura, Jpn. J. Appl. Phys. 28(1989)2468.
3) A. Nakamura, Springer Proceedings in Physics, Vol.51: "The Physics and Chemistry of Organic Superconductors," eds. G. Saito and S. Kagoshima (Springer-Verlag, Berlin, 1990)P.457-460.
4) A. Nakamura, Studies of High Temperature Superconductors, Vol.4, ed. A. V. Narlikar(Nova Science Publishers, New York, 1990)P.311-337.
5) A. Nakamura, Solid State Ionics, in press.
6) J. Bardeen, L. N. Cooper and J. R. Schrieffer, Phys. Rev. 108(1957)1175.
7) A. W. Sleight, Science 242(1988)1519.
8) J. A. Wilson, J. Phys. C21(1988)2067.
9) M. K. Wu, J. R. Ashburn, C. J. Torg, P. H. Hor, R. L. Gao, Z. J. Huang, Y. Q. Wang and C. W. Chu, Phys. Rev. Lett. 58(1987)908.
10) R. J. Cava, B. Batlogg, A. P. Ramirez, D. Weder, C. H. Chen, E. A. Rietman and S. M. Zahurak, High Temperature Superconductors, eds. M. B. Brodsky et al.(MRS, Pittsburgh, 1988)P.19.
11) J. G. Bednorz and K. A. Müller, Z. Phys. B64(1986)189.
12) Z. Z. Sheng and A. M. Hermann, Nature 332(1988)55.
13) H. Maeda, Y. Tanaka, Y. Fukutomi and T. Asano, Jpn. J. Appl. Phys. 27(1988) L209.
13) Y. Tokura, H. Takagi and S. Uchida, Nature 337(1989)345.

Publication List

[1] A. Nakamura, "A Possible Novel and Universal Origin of Superconductivity: Multivalence Resonance-Condensation Model," in: Proc. Tsukuba Seminar on

High T_C Superconductivity, eds. K. Masuda et al.(Tsukuba Univ., Tsukuba, 1989)P.85-90.

[2] A. Nakamura, "Multivalence Resonance-Condensation Model for Electron Pairing and Superconductivity in High T_C Superconductors: A Possible Novel and Universal Origin of Superconductivity," Jpn. J. Appl. Phys. 28(1989)2468.

[3] A. Nakamura, "Multi-Valence Resonance-Condensation Model: A Possible Novel and Universal Origin of Superconductivity," in: Springer Proceedings in Physics, Vol.51; The Physics and Chemistry of Organic Superconductors, eds. G. Saito and S. Kagoshima(Springer-Verlag, Berlin, 1990)P.457-460.

[4] A. Nakamura, "A New Theoretical Approach to Electron Pairing and Superconductivity in High T_C Superconductors," in: Studies of High Temperature Superconductors, Vol.4, ed. A. V. Narlikar(Nova Science Publishers, New York, 1990)P.311-337.

[5] A. Nakamura, "A Chemical Approach to High T_C Superconductivity," Solid State Ionics, in press.

11. Solid-State Chemistry of Radiation Damage

T.A. Sasaki, S. Furuno, K. Hojou, Y. Baba, H. Yamamoto,
H. Ohtsu and T. Soga

11.1. Studies of Chemical Reactions Induced by Energetic Beams

11.1.1. Trapping of Atmospheric Gases on Metal Surfaces under Ion Bombardment

Introduction

Bombardment of energetic ions on a compound generally induces a decomposition of the compound. For example, the bombardment of rare-gas ions on a metal oxide leads to the reduction of the oxide due to a preferential sputtering of the oxygen atoms. Such decomposition reactions essentially occur through physical processes, which are specified by the mass and energy of the bombarding ions, the mass of the target, and so forth.[1] While, there have been some thermochemical approaches to explain the mechanism of these decomposition reactions at the ion-bombarded surfaces.[2-6] One of the widely accepted theories is the localized thermal equilibrium (LTE) model, proposed by Andersen et al.[3,4] The products of the decomposition reaction in the ion-bombarded surface are fairly well estimated by this model, supposing that the reaction occurs in the thermal equilibrium region around the track of the ion at quite high temperature.[8,9] This thermochemical treatment has been so far also applied to the sputtering of oxides by rare-gas ion bombardments.[6,9,10]

In contrast to such decomposition of compounds by ion bombardments, there has been few approaches about thermochemical explanations regarding synthesis reactions induced by ion beams. Experimentally, it has been recently observed that the bombardments of rare-gas ions on some metals in the atmosphere of oxygen or nitrogen promote the incorporation of the gases in the surface layer of the metals.[11-21] From the physical viewpoint, these phenomena have been attributed primarily to the formation of defects by the ion bombardment.[15] The radiation enhanced diffusion[22] may further promote the incorporation.

This section deals with the trapping of atmospheric oxygen and nitrogen on metal surfaces under rare-gas ion bombardments. The mechanism of the incorporation reaction will be discussed, mainly based on the thermodynamical

parameters of the metal oxides and nitrides, respectively.

Experimental

The targets used were high-purity transition metals (>99.9 %) of 10 mm ϕ x 0.2 mm. The metals were polished with diamond paste of 1/4 μm before the introduction into the vacuum chamber.

The metal was annealed at 600℃ in vacuum, and sputtered with 8-keV Ar^+ ions until the surface oxygen and carbon contaminations were completely removed. Then, the sample was bombarded with 8-keV Ar^+ ions, produced in a duoplasmatron ion source, at room temperature. The bombarding angle was 25° from the surface normal. The typical flux of the Ar^+ beam was 2.5 x 10^{13} atoms $\cdot$ $cm^{-2} \cdot sec^{-1}$ (4 $\mu A/cm^2$), monitored with a Faraday cup. The partial pressure of argon during the bombardment was 8 x 10^{-5} Pa. During the bombardment, high-purity oxygen was introduced into the bombarding chamber to a pressure of 1 x 10^{-3} Pa.

The surface chemical states and O/Me or N/Me (Me:metal) ratios were measured by XPS at a pressure of 3 x 10^{-8} Pa, using an Mg Kα X-ray (1253.6 eV) as an excitation source. The binding energy was calibrated using the $4f_{7/2}$ line of metallic gold, assumed to be 84.0 eV.

Results and Discussion

Fig.1 shows the XPS spectra in Ti2p region for titanium before (a) and after (c) Ar^+-ion bombardment in oxygen atmosphere for 4 min. For comparison, the spectrum for the oxygen-adsorbed sample without Ar^+-ion bombardment is also shown as spectrum (b). Although the appreciable amount of oxygen is adsorbed on titanium without bombardment, the metallic phase still remains in spectrum (b). On the other hand, the metallic phase completely disappears with the bombardment of Ar^+ ions (spectrum (c)). The binding energy of the most intense peak in spectrum (c) is consistent with that of the standard TiO_2.

The time dependences of the surface O/Ti ratio, determined by XPS, for both with and without Ar^+-ion bombardments are shown in fig.2. The O/Ti ratio is normalized such that the O1s/Ti2p ratio of the standard TiO_2 is 2.0. In the case of the oxygen-adsorbed sample, the O/Ti ratio saturates to be about 1.3 after 4 min. In this region, the rate of adsorption and desorption becomes equal. The ratio for the Ar^+-ion bombarded sample saturates to be 1.96. The difference from 2.0 is due to the existence of a small amount of Ti_2O_3.

In order to investigate the depth profile of the oxide layers, titanium samples oxidized for 4 min with (a) and without (b) the Ar^+-ion bombardment were sputtered with 8-keV Ar^+ ions of 10 $\mu A/cm^2$. The fluence dependences of the O1s/Ti2p ratio are indicated in fig.3. The O1s/Ti2p ratios exponentially decrease with the fluence of Ar^+ ions. It is observed that the oxide layer with Ar^+-ion bombardment extends deeper in the target than that without bombardment. Estimated from the sputtering yield of TiO_2 by the 8-keV Ar^+ ion bombardment[24] and the density of TiO_2, the approximate thicknesses of the oxide layers are determined to be 5.0 nm for the line (a) and 0.8 nm for the line (b). The range of 8-keV Ar^+ ion in titanium, which is perpendicular to the surface, is calculated to be 6.1 nm using TRIM code.[25] The result suggests that the oxide layer produced by the Ar^+-ion bombardment is formed around the track of the implanted Ar^+ ions.

For the purpose of sputter cleaning, the surface of titanium was bombarded with Ar^+ ions. Thus, there are already appreciable amount of defects in the surface before the oxygen exposure. However, the amount of the surface oxide and its thickness produced by the adsorption is much smaller than those produced by the Ar^+-ion bombardment. Therefore, such promotion of oxidation is caused by the simultaneous bombardment during the oxygen exposure. This finding indicates that the defects or excited states, having short life time, play important roles in the oxidation reaction.

Such a promotion of oxidation reactions is also observed for other transition-metal targets, as listed in Table 1. In this table, the surface O/Me ratios for the samples exposed to oxygen for 4 min are indicated, because the ratios become almost saturated by 4 min-exposure. Among the metals examined, promotions of the oxidation reactions for copper, silver and gold are negligibly small, but appreciable promotion is observed for the other metals.

The stability of the reaction products is one of the essential factors to discuss the gas trapping process. Such stability is inferred by the Gibbs energy of formation (ΔG) of the compounds between target metals and atmospheric gases. In the case of titanium target, it has been observed that the atmospheric nitrogen is trapped under the same condition as the present experiment.[20] For comparison, trappings of hydrogen and carbon were investigated using hydrogen and methane, respectively, as atmospheric gases under the same experimental condition. However, the formation of titanium hydride or carbide was not observed. The ΔG values of titanium compounds, TiH_2, TiN, TiO_2 and TiC are -37 kcal/mol, -93 kcal/mol, -229

kcal/mol and -46 kcal/mol, respectively.[26] The difference in the behavior of trapping among four kinds of gases suggests that the increase in the stability of the reaction product leads to the high trapping efficiency. This relation will be discussed more quantitatively for the oxygen trapping as follows.

In the case of chemical adsorption, the rate of the oxide formation is simply expressed as,

$$dx/dt = k_1(1-x)-k_2x \tag{1}$$

where x ($0 \leqq x \leqq 1$) is surface coverage of oxide, t (sec) the time for the oxygen exposure, and k_1 and k_2 (sec^{-1}) the rate constants of adsorption and desorption, respectively. The ratio of k_1/k_2 is proportional to the sticking coefficient of oxygen at the metal surface. Note that the above equation only expresses the average value in the surface region, detected by XPS, i.e., about 1.5 nm from the surface. By solving equation (1), we can obtain the coverage of oxide at t sec,

$$x(t) = [k_1/(k_1+k_2)]*[1-\exp(-(k_1+k_2)t)] \tag{2}.$$

At the steady state, the saturated value of x is expressed by setting $t \to \infty$ in the equation (2),

$$x(\infty) = k_1/(k_1+k_2) \tag{3}.$$

Although a chemical adsorption of oxygen on a metal surface is essentially based on the chemical reactivity of the metal with oxygen, it also depends on the crystal structure of the surface, surface roughness, and so forth. In the case of thermal process, the reaction of the oxide formation is expressed as the following equation,

$$xMe + (y/2)O_2 \rightarrow Me_xO_y + \Delta G \tag{4}.$$

The value of ΔG is related to the pressure of oxygen as

$$\begin{aligned}\Delta G &= -RT\ln(1/[O_2]^{y/2}) \\ &= (y/2)RT\ln[O_2]\end{aligned} \tag{5}.$$

In order to compare the chemical reactivity of various metals with oxygen at the same pressure, we may compare the $\Delta G/y$ values among the oxides.

Fig.4 shows the relation between the saturated elemental ratio of surface O/Me and Gibbs energy of oxide formation, $\Delta G/y$, for various metals. The O/Me ratio is obtained by dividing the observed O1s/(Me2p,3d or 4f) value with that calculated using the theoretical photoionization cross sections.[23] Oxygen hardly adsorbs on the metals with the $\Delta G/y$ value of the oxide larger than -50 kcal/mol.

When Ar^+ ions are bombarded during the oxygen exposure, we assume that rate constant of oxide formation increases to $k_1+\alpha$ $(\alpha \geqq 0)$, where α (sec^{-1}) is the number of oxides produced by Ar^+-ion bombardment, depending on the flux of Ar^+-ion beam. It should be noted that the rate constant of the decomposition of oxides also increases to $k_2+\beta$ $(\beta \geqq 0)$ due to the preferential sputtering of oxygen atoms. The value of β is related to the sputtering yield Y and the flux of the incident ion f as $\beta=Yf$. Thus, the equation (3) can be rewritten as

$$x(\infty) = (k_1+\alpha)/(k_1+\alpha+k_2+\beta) \qquad (6).$$

If the promotion of oxidation reaction by Ar^+ ions is observed, it is obvious that the value of α is much larger than that of β for those metals. In addition, the sputtering yields of the present oxides by 8-keV Ar^+ ions range from 0.2 to 1.7.[25] This means that the large variation of the saturated O/Me ratio for various metals is mainly due to the difference in the value of α.

With regard to the physical process, the promotion of oxide formation by Ar^+-ion bombardment can be primarily attributed to the knock-on collision by Ar^+ ions at the surface. However, the contribution of chemical reaction must be considered in order to interpret the large difference in the reaction rate of the oxide formation among various metals.

Kim et al. have found the relation between the sputtering behavior and the thermodynamical parameters for various oxides sputtered by rare-gas ions, supposing that the sputtering occur in thermal equilibrium region.[9] They have indicated that the standard Gibbs energy of formation of oxide, ΔG, is related to the reduction of the oxide. In our case, both the formation and decomposition simultaneously occur.

The relation between the saturated value of the surface O/Me ratio and the $\Delta G/y$ for various metals bombarded with Ar^+ ions are shown in fig.5.

Compared with the result for the oxygen-adsorbed samples (fig.4), the relation between two values is clearly observed. There exists a threshold at about -70 kcal/mol. The oxides with the $\Delta G/y$ value higher than -60 kcal/mol are hardly produced under the present condition, while most of the ratios of those with the $\Delta G/y$ value lower than -80 kcal/mol are close to 1.

Regarding the decomposition of oxides, the threshold of ΔG of the oxide for the reduction by Ar^+-ion bombardment ranges from -60 kcal/mol to -118 kcal/mol [9]. In this case, the threshold of thermodynamical parameters exists, because the sputtering occurs in the local thermal equilibrium region produced around the track of the Ar^+ ions, and we can assume that the sputtering occurs through thermal reaction at quite high temperature. The present results of the threshold for the oxide formation, ranging from -60 kcal/mol to -80 kcal/mol, is close to those for the reduction. This finding suggests that such formation of compounds by Ar^+-ion bombardment also occurs through thermochemical reaction near the thermal equilibrium region. Therefore, it can be concluded that the trapping of atmospheric gases in the surface induced by ion bombardment occurs through chemical reaction at quite high temperature near the track of the bombarding ions, rather than through physical processes such as knock-on collisions. Similar results was also obtained for nitridation reaction induced at transition-metal surfaces by Ar^+-ion bombardments. The obtained relation between the thermochemical parameter of the reaction product and the trapping of atmospheric gas will be useful to estimate the extent of gas trapping reaction by the ion bombardment for the other gas-solid systems.

Table 1
Saturated ratios of O1s/(Me2p, 3d or 4f)

Target	Main product	Saturated O1s/(Me2p, 3d or 4f) ratio			
		Line	With bombardment	Without bombardment	Theoretical ratio
Ti	TiO_2	O1s/Ti2p	0.71	0.48	0.72
V	V_2O_5	O1s/V2p	0.55	0.30	0.74
Cr	Cr_2O_3	O1s/Cr2p	0.36	0.15	0.37
Fe	Fe_2O_3	O1s/Fe2p	0.26	0.22	0.27
Ni	NiO	O1s/Ni2p	0.095	0.077	0.14
Cu	CuO	O1s/Cu2p	0.005	0.005	0.12
Y	Y_2O_3	O1s/Y3d	0.60	0.56	0.69
Zr	ZrO_2	O1s/Zr3d	0.63	0.41	0.78
Nb	Nb_2O_5	O1s/Nb3d	0.56	0.19	0.84
Mo	MoO_3	O1s/Mo3d	0.32	0.10	0.88
Ag	Ag_2O	O1s/Ag3d	0.004	0.003	0.079
W	WO_3	O1s/W4f	0.13	0.072	0.83
Au	Au_2O_3	O1s/Au4f	0.005	0.000	0.24

The metal targets were exposed to 1×10^{-3} Pa O_2 for 4 min with and without bombardment of 8 keV Ar^+ ions at a fluence of 4 $\mu A/cm^2$. The theoretical ratios are calculated using photoionization cross-sections [23].

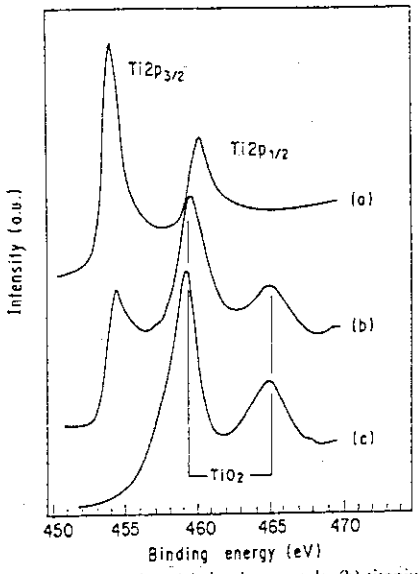

Fig. 1. XPS spectra in the Ti2p region: (a) titanium metals, (b) titanium metal exposed to oxygen at a pressure of 1×10^{-3} Pa for 4 min, and (c) titanium metal bombarded with 8 keV Ar^+ ions of 4 $\mu A/cm^2$ in oxygen at a pressure of 1×10^{-3} Pa for 4 min.

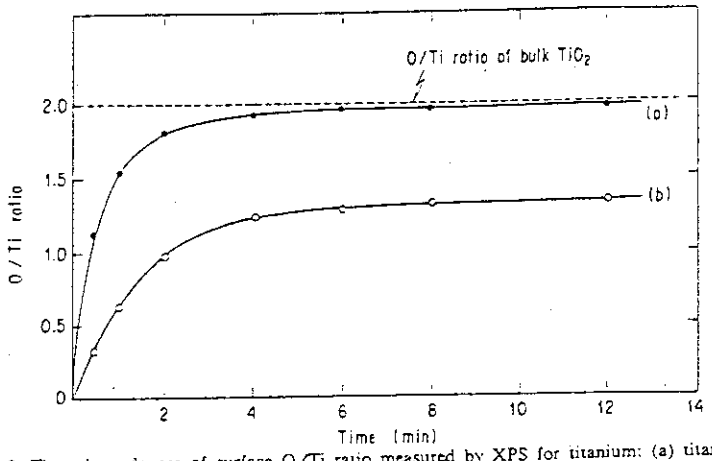

Fig. 2. Time dependences of surface O/Ti ratio measured by XPS for titanium: (a) titanium bombarded with 8 keV Ar^+ ions at 4 $\mu A/cm^2$ in oxygen at a pressure of 1×10^{-3} Pa, and (b) titanium exposed to oxygen at a pressure of 1×10^{-3} Pa without bombardment.

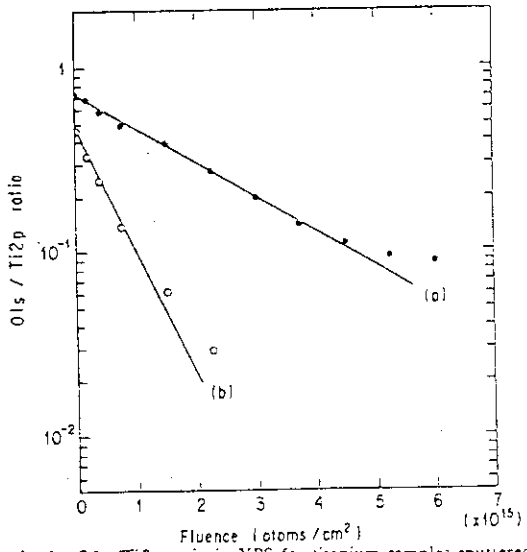

Fig. 3. Changes in the O1s/Ti2p ratio in XPS for titanium samples sputtered with 8 keV Ar^+ ions of 10 $\mu A/cm^2$: (a) titanium metal bombarded with 8 keV Ar^+ ions of 4 $\mu A/cm^2$ in oxygen at a pressure of 1×10^{-3} Pa for 4 min, and (b) titanium exposed to oxygen at a pressure of 1×10^{-3} Pa for 4 min without bombardment.

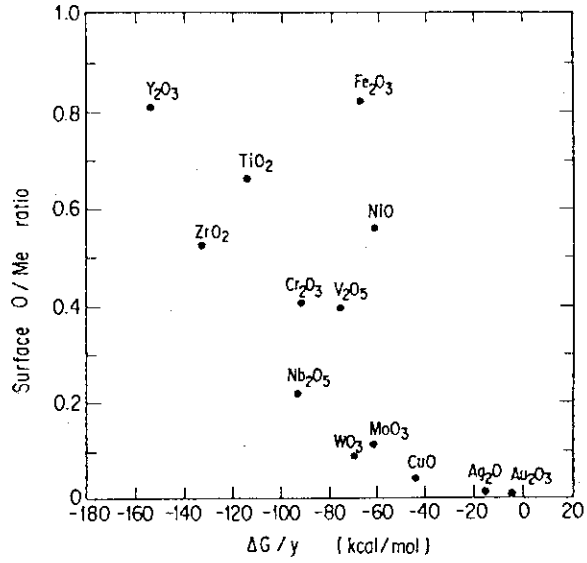

Fig. 4. Relation between saturated ratio of O/Me for metals exposed to oxygen at a pressure of 1×10^{-3} Pa and Gibbs free energy of oxide formation at 298 K. The O/Me ratio is represented as the O1s/(Me2p, 3d or 4f) value in XPS divided by the theoretical ratio calculated using photoionization cross sections. The Gibbs free energy of formation is divided by y, assuming that the composition of the oxide is Me_xO_y.

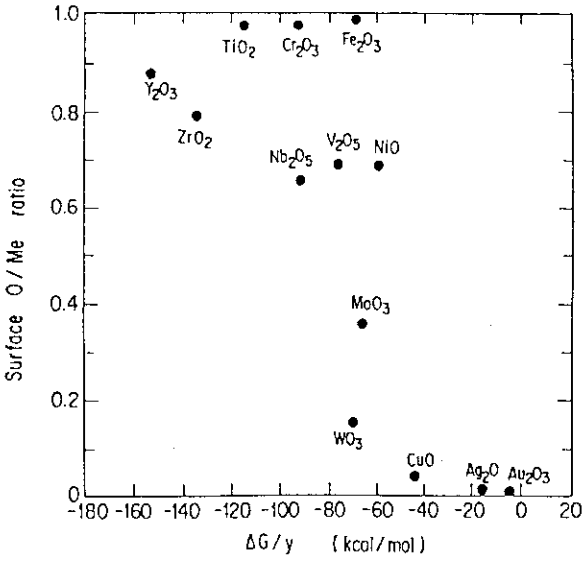

Fig. 5. Relation between saturated ratio of O/Me for metals bombarded with 8 keV Ar^+ ions in oxygen at a pressure of 1×10^{-3} Pa and Gibbs free energy of oxide formation at 298 K. The O/Me ratio is represented as the O1s/(Me2p, 3d or 4f) value in XPS divided by the theoretical ratio calculated using photoionization cross sections. The Gibbs free energy of formation is divided by y, assuming that the composition of the oxide is Me_xO_y.

11.1.2. Desorption of Ions from Rare-Gas Solids by Electronic Transition

Introduction

The desorption mechanisms of atomic and cluster ions from adsorbed rare gases, i.e., rare-gas solids (RGSs) by electron impact are not well understood. In an investigation aimed at progress in this respect, we have found evidence for novel excitations in solid argon, exciton pairs $[(Ar^*)_2]$ on neighboring atoms in the bulk or at the surface. These results also make conclusions about the acting desorption mechanisms possible.

All processes of DIET (desorption induced by electronic transition) involve a stage where part of the electronic excitation energy is transferred to nuclear motion. For DIET of neutrals from RGSs, two basic processes are considered to be important at present. The so-called molecular mechanism involves the formation, the vibrational relaxation, of a molecularly self-trapped exciton near the surface; desorption occurs either directly or due to sputtering of neighboring atoms by the fragments of this dissociating excimer.[27] The second process is the so-called cavity mechanism which is a consequence of atomic self-trapping of excitons on the surface of the RGS. Desorption of electronically excited excimers and monomers via this process has been observed for the light RGSs. Ar and Ne, where the interaction between the lattice and the inflated electron distribution of these particles is repulsive, but not for heavy rare gases Kr and Xe.[28] For both reaction types, the primary electronic excitations are of the exciton type; for Ar, the thresholds are at 11.8 eV (surface) and 12.2 eV (bulk).[28] The relative contribution of both mechanisms to the total desorption yield of neutrals depend on the thickness of the film.[29]

Studies on stimulated desorption of ions from RGSs are less numerous. Desorption of singly charged ions has been observed to be caused by the primary excitation of electronically excited ions X^{+*}, and primary double ionization X^{2+},[30] DIET of singly and doubly charged ions was obtained for core ionization from solid Ar as well as Kr.[31] The processes supplying kinetic energy have been interpreted as Coulomb repulsion of ion pairs which are formed by curve crossing from the initially multiply excited particles and their ground-state neighbors,[30] or by the radiative or recombinative decay of doubly charged ionimers.[31] From the comparison of the ion yields for excitonic and continuum-type core excitations it was concluded that the ion signal is at least partly due to Coulomb repulsion of pairs of ions, one partner of which is created in a secondary, electron-impact, ionization step

by fast electrons originating from the Auger or autoionization decay of the core excitation, which itself supplies the second particle of the pair.[32] Precise data on the regime of the primary threshold for DIET of ions from RGSs, however, are missing. In this section, the elucidation of this energy range is described.

Experimental

The experiments were performed in a ultra-high vacuum (UHV) system with a base pressure of 4 x 10^{-9} Pa. The system contained a cryomanipulator for the sample, equipped with a temperature controller (temperature range 10-1600 K), a quadrupole mass spectrometer for the detection of neutrals (n-QMS), a second QMS without ionizer for the detection of ions (i-QMS), and a hemispherical analyzer for electron spectroscopy. A ring shaped thoria-coated tungsten filament located between the sample and the i-QMS. was used to irradiate the sample with electrons. The energy of the emitted electrons was set by negatively biasing the filament. The sample itself was always grounded. The spread of the kinetic energy of the electrons was approximately ±0.3 eV; it was mainly due to the voltage drop across the filament. A retardation grid between the filament and the i-QMS prevented electrons from entering the detector. The Ar and Kr films were dosed onto a Pt(111) single crystal by a microchannelplate doser. The thickness of the films was derived from temperature-programmed-desorption spectra taken with the n-QMS. It is given in multiples of the amount adsorbed in the first layer on the metal substrate. The substrate itself was cleaned by Ar^+ sputtering and heating in 10^{-4} Pa of oxygen. Its periodicity and cleanliness were checked by LEED and X-ray photoemission spectroscopy (XPS) (Al/Mg Kα source with hemispherical electron energy analyzer). Dosing and measurements were done at 10 K.

The work function of the filament was obtained by measuring the kinetic energy of the emitted electrons referred to the vacuum level by the hemispherical analyzer; the work functions of the samples, the knowledge of which was necessary for the evaluation of the precise values of the electron energies at the surface of the films, were derived from the cutoff of the secondary electron peak in XPS. Because of the very low mobility of holes, charging is always a severe problem in electron and ion spectroscopy on RGSs. Here, we observed strong dependences of the threshold energies on beam current for electron fluxes in the microamp regime, especially for thick layer. For beam currents lower than 10^{-9} A, however, the energetic

position of the thresholds became independent of the primary electron flux. Therefore, all data presented here are recorded with such low primary electron currents.

Results and Discussion

The Ar_2^+, Ar^+, Ar^{2+}, and Kr^+ electron-stimulated-desorption (ESD) signals obtained from solid Ar and Kr, respectively, are shown in Fig.6. The traces for the singly charged species (which we consider first) are apparently a superposition of (a) distinct resonances, and (b) a background increasing with energy. The branching, however, varies. The resonant features are strong for the Ar ionimer, and weak for Ar^+ ESD. For Kr^+, no such resonant maxima are visible. The onsets of these resonances T_1 and T_2 for argon (taken from the Ar_2^+ trace) are at 24.2, 34, and 50 eV. Closer inspection exhibits fine structure of the first maximum. The primary threshold at 24.2 eV is followed by a second step at 25.4 eV (see the inset in Fig.6; for clarity, we label these onsets as T_{11} and T_{12}, respectively). Data for films of different thicknesses clearly discriminate T_{11} as a surface, and T_{12} as a bulk excitation (Fig.7). The contribution of T_{11} to the desorption yield saturates at about 10 layers, whereas T_{12} increases with film thickness up to more than 100 layers. For Ar, no ESD of ions was obtained for excitation energies below T_{11}. For Kr, where such resonant peaks are not present, the onset of ionic ESD was found at 30 eV, see Fig.6.

In a previous photon-stimulated study, the primary excitation of electronically excited singly charged ions as well as the creation of doubly charged ions was identified as the stimulus for DIET of ions.[30] The interpretation given in Refs.30 and 31 imply that these multiply excited particles cause desorption either by the formation of ion pairs by curve crossing, $X^{+*}X, X^{2+} \rightarrow X^+X^+$, and subsequent Coulomb repulsion of the constituents of these,[30] or by formation of excited excimers which decay after vibrational relaxation.[31] For Ar, the thresholds for Ar^{+*} and for Ar^{2+} formation were obtained at 32 and 40 eV, respectively.[30] For stimulation by electron impact as in this study, however, these excitations should be visible as broad maxima similar to the ionization-cross-section curves obtained in the gas phase, and not as narrow resonances as seen in Fig.6. They certainly do contribute to the smooth background of the signals in Fig.6, but they cannot be the cause of the resonances because the convoluted densities of states of the two free electrons in the final state should lead to maxima with widths similar to those obtained for the ionization cross section, i.e., about 80

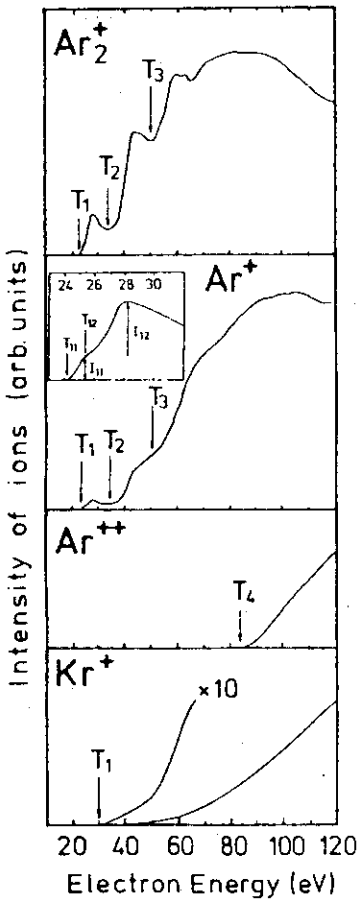

FIG. 6 Ar_2^+, Ar^+, Ar^{2+}, and Kr^+ ESD yields vs electron energy from 40-layer-thick Ar and Kr films. Inset: The first resonance on an expanded energy scale.

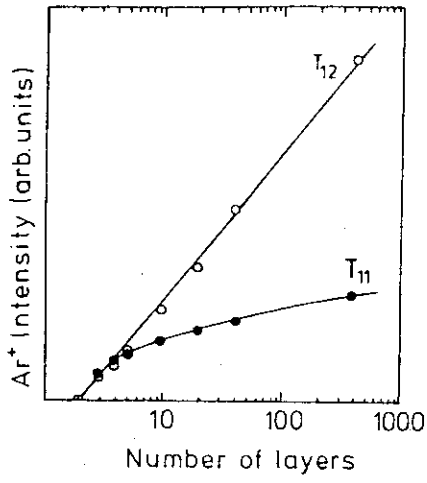

FIG. 7 Dependence of the Ar^+ signals I_{11} and I_{12} which are correlated to T_{11} and T_{12} (see inset of Fig. 1) on film thickness.

eV for Ar.[34] Another contribution to the background presumably stems from ion pairs which are created by one single electron (see above). Utilizing gas-phase ionization cross sections,[34] we derived similar probabilities for (a) the creation of doubly charged ions, and (b) ionization of adjacent atoms by the same electron. For Ar, scenario (b) gives a broad maximum at 100 eV, in very good agreement with the trace for Ar^+ in Fig.6. The background of the Ar_2^+ curve with its maximum at 80 eV resembles more closely the energy dependence observed for single ionization.[34] Coulomb repulsion of ion pairs apparently is not the prevalent process for desorption of ionimers. This indicates that for these species a DIET mechanism is necessary, which acts between the excited molecule and the lattice and not between separate particles.

This mechanism can be clarified by identifying the nature of the

resonant excitations seen for the ion traces in Fig.6. Focusing on the features T_{11} and T_{12}, we emphasize that these cannot be assigned to electronic excitations of one single Ar atom, since they are observed between the excitation energies for Ar3p ionization and Ar3s exciton.[28,35] Even the possibility of multiple bound electronic excitations of one atom is ruled our for energy reasons (for Ar gas, the lowest excitation of this type is beyond the threshold for 3s excitations).[36] However, considering the excitation energies for n=1 surface and bulk excitons of 11.8 eV and 12.2 eV in argon, we can explain these maxima as due to the excitation of two 3p excitons on neighboring atoms. On the surface, desorption of such a doubly excited excimer Ar_2^{**}, which resembles an alkali molecule, is expected to rapidly proceed as in the previously described cavity mechanism for Ar, but not for Kr (see above), in agreement with our findings. The appearance of ionic molecules can be explained by autoionization of the highly excited entities in the gas phase after their desorption, either into Ar_2^+ in its stable ground state, or into a dissociative excited state $(Ar\text{-}Ar)^+$ leading to Ar^+ detection.

The most striking result is that these exciton pairs apparently have a lifetime as "free" excitations which is sufficiently long to enable their diffusion through the solid to the surface, as the data from Fig.7 unambiguously indicate. The barrier against delocalization into separate excitons must be due to the mutual interaction energy $\Delta E \sim 1$ eV for the bulk species), which is comparable to the width of the exciton bands, i.e., arguments similar to those used for the interpretation of the long lifetimes seen for multiply excited states in Auger spectroscopy can be applied here.[37] To our knowledge, this is the first observation of such an exciton dressed by an exciton in RGSs (however, holes dressed by an exciton have observed before in electron-scattering experiments).[38]

The dependence of the ESD yield on film thickness has not been recorded in detail for T_2 and T_3 at 34 eV and 50 eV. Because of their resonant shape and their energetic positions we tentatively assign them to multiple (n) excitonic excitations at $n(12\text{ eV})+\Delta E$, for n=3 and 4. The driving force for the desorption process would then be identical for T_2 to T_3. The visibility of these features in the ionimer and, though depleted, in the ion yield apparently reflects different branching ratios in the autoionization process. The large nonresonant backgrounds obtained for Ar^+ and Ar_2^+ ESD, however, are indicative of other desorption mechanisms, probably proceeding via the creation of Ar^{2+}, Ar^+Ar^+, and Ar^*Ar^+ excitation.

The threshold at 83 eV for the desorption of Ar^{2+} (see Fig.6) is in good agreement with the threshold for the formation of Ar^{3+} in the gas phase.[34] Obviously, DIET of this species is initiated by curve crossing from $Ar^{3+}Ar$ to $Ar^{2+}Ar^{+}$ or $Ar^{2+*}Ar^{+}$, and Coulomb repulsion. It is, however, still an open question why no ions are seen at the threshold for the creation of adjacent pairs of doubly and singly charged particles by one electron at about 54 eV. The probability for such an excitation should be comparable to primary triple ionization.

In summary, our threshold investigation of ionic ESD from condensed Ar and Kr have clarified the mechanisms of ion desorption and have led to the identification of new RGS excitations, exciton pairs (surface and bulk), which show up because of selective expulsion of dimers. The bulk species can migrate over more than 100 layers spacing.

The work summarized in this section has been done when one of the authors was studying in Germany. The authors would like to thank Professor D. Menzel and Dr. P. Feulner of Technical University Munchen, and Dr. G. Dujardin of Orsay of Paris University for the cooperation and valuable discussions throughout the work.

11.1.3. Other works

The other works on chemical reactions induced by energetic beams, which have been done in these three yeas, are summarized as follows:

1) Nitrogenation of various transition metals by N_2^{+}-ion implantation has been investigated by means of X-ray photoelectron spectroscopy.[39] It was found that the saturated values of surface N/Me (Me:metal) ratio for various metal targets are related to the Gibbs free energy of nitride formation. It was concluded that the nitrogenation of the metals by ion implantation is influenced by the chemical reactivity between the metal and nitrogen.

2) A dynamic mixing method has been applied to the preparation of TiN thin films using an N_2^{+} ion beam of 1 keV.[40] The optimum condition for making the TiN films was established.

3) In 1987, research and development activity for a new large-scale synchrotron radiation facility (SPring-8) had started. The institute of Physical and Chemical Research (RIKEN) and JAERI have been participating in this project. The research and development activities for the construction of beam lines in SPring-8 have been presented.[41]

4) The structure of physisorbed and chemisorbed O_2 on Pt(111) has been in-

vestigated by near-edge X-ray-absorption fine-structure spectroscopy (NEXAFS) using synchrotron beam.[42] The electronic structure and geometry of adsorbed oxygen was clarified.

References

1) P. Sigmund, Phys. Rev. 184 (1969) 383.
2) Z. Jurela, Int. J. Mass Spectrom. Ion Phys. 12 (1973) 33.
3) C.A. Andersen and J.R. Hinthorne, Anal. Chem. 45 (1973) 1421.
4) C.A. Andersen, Proc. Workshop on SIMS and IMMA, NBS Special Publication 427 (1975) 79.
5) R. Kelly, Rad. Effects 32 (1977) 91.
6) R. Kelly, Surf. Sci. 90 (1979) 280.
7) T. Ishitani, H. Tamura and T. Kondo, Anal. Chem. 47 (1975) 1294.
8) D. Newbury, US-Japan Joint Seminor, Oct. 12-17, Honolulu, Hawai (1975).
9) K.S. Kim, W.E. Baitinger, J.W. Amy and N. Winograd, J. Electron Spectrosc. Relat. Phenom. 5 (1974) 351.
10) K.S. Kim, W.E. Baitinger and N. Winograd, Surf. Sci. 55 (1976) 285.
11) K. Wittmaack, Surf. Sci. 68 (1978) 118.
12) J. Hrbek, Thin Solid Films 42 (1977) 185.
13) W.O. Hofer, H.L. Bay, P.J. Martin, J. Nucl. Mater. 76/77 (1978) 156.
14) G.I. Grigorov, I.N. Martev and K.K. Tzatzov, C.R. Acad. Bulg. Sci. 32 (1979) 1069.
15) W. Wach and K. Wittmaack, J. Appl. Phys. 52 (1981) 3341.
16) G.I. Grigorov, I.N. Martev and K.K. Tzatzov, Thin Solid Films 76 (1981) 269.
17) H. Oechsner and A. Wucher, Appl. Surf. Sci. 10 (1982) 342.
18) M. Saidoh, J. Nucl. Mater. 128/129 (1984) 540.
19) M. Saidoh, H. Gnaser and W.O. Hofer, Nucl. Instrum. Methods Phys. Res. B28 (1987) 540.
20) Y. Baba, T.A. Sasaki and I. Takano, J. Vac. Sci. Technol. A6 (1988) 2945.
21) Y. Baba and T.A. Sasaki, Mater. Sci. Eng. A 115 (1989) 203.
22) P.S. Ho, Surf. Sci. 72 (1978) 253.
23) J.H. Scofield, J. Electron Spectrosc. Relat. Phenom. 8 (1976) 129.
24) J. Bohdansky, J. Nucl. Mater. 93/94 (1980) 44.
25) J.P. Biersack and L.G. Haggmark, Nucl. Instrum. Methods 174 (1980) 257.
26) I. Bartin and O. Knacke, Thermochemical Properties of Inorganic Substances (Springer, Berlin, 1973).

27) R.E. Johnson and M. Inokuti, Nucl. Instrum. Methods 206 (1983) 289.
28) F. Coletti, J.M. Debever and G. Zimmerer, J. Phys. (Paris) Lett. 45 (1984) 467.
29) P. Feulner, T. Müller, A. Puschmann and D. Menzel, Phys. Rev. Lett. 59 (1987) 791.
30) G. Dujardin, L. Hellner, M.J. Besnard-Ramage and R. Azria, Phys. Rev. Lett. 64 (1990) 1289.
31) G. Rocker, P. Feulner, R. Scheuerer, L. Zhu and D. Menzel, Phys. Scr. 41 (1990) 1014.
32) R. Scheuerer, P. Feulner, G. Rocker, L. Zhu and D. Menzel, in: DIET IV edited by G. Betz and P. Varga (Springer, Berlin, 1990) p235.
33) R. Treichler, W. Wurth, W. Riedl, P. Feulner and D. Menzel, Surf. Sci. in press.
34) L.J. Kiefer and G.H. Dunn, Rev. Mod. Phys. 38 (1966) 1.
35) R. Hansel, G. Keitel, C. Kurz and P. Schreiber, Phys. Rev. Lett. 25 (1970) 208.
36) R.P. Madden, D.C. Ederer and K. Codling, Phys. Rev. 177 (1969) 136.
37) M. Cini, Solid State Commun. 24 (1977) 681.
38) H. Moller, R. Brodmann, G. Zimmerer and U. Hahn, Solid State Commun. 20 (1976) 401.
39) I. Takano, S. Isobe, T.A. Sasaki and Y. Baba, Appl. Surf. Sci. 37 (1989) 25.
40) I. Takano, S. Isobe, T.A. Sasaki and Y. Baba, Thin Solid Films 171 (1989) 263.
41) T. Watanabe, H. Ohno, H. Iwasaki, T. Sasaki and RIKEN-JAERI Joint Users Group, Proceedings of International Symposium on Advanced Nuclear Energy Research -Evolution by Accelerators-, Mito, p 267 (1990).
42) W. Wurth, J. Stöhr, P. Feulner, X. Pan, K.R. Bauchspiess, Y. Baba, E. Hudel, G. Rocker and D. Menzel, Phys. Rev. Lett. 65 (1990) 2426.

Publication list

[1] T.A. Sasaki, "Chemical Reactions Induced on Solid Surface by Low Energy Ions," Proceedings of International Symposium on Advanced Nuclear Energy Research -Near-Future Chemistry in Nuclear Energy Field-, Oh-arai, p.37 (1989).
[2] Y. Baba, H. Yamamoto and T.A. Sasaki, "Photoelectron Spectroscopic Analysis of Rare-gas Atoms Implanted in Metals," Proceedings of International Symposium on Advanced Nuclear Energy Research -Near-

Future Chemistry in Nuclear Energy Field-, Oh-arai, p.414 (1989).

[3] Y. Baba, "Surface Chemical Reaction Induced by Ion Beam," Kagaku to Kogyo (in Japanese), 42 (1989) 200.

[4] I. Takano, S. Isobe, T.A. Sasaki and Y. Baba, "Nitorgenation of Various Transition Metals by N_2^+-ion Implantation," Appl. Surf. Sci. 37 (1989) 25.

[5] I. Takano, S. Isobe, T.A. Sasaki and Y. Baba, "Preparation of TiN Thin Films by the Dynamic Mixing Method Using an N_2^+ Ion Beam of 1 keV," Thin Solid Films 171 (1989) 263.

[6] Y. Baba and T.A. Sasaki, "Nitride Formation at Metal Surfaces by Ar^+ Ion Bombardment in Nitrogen Atmosphere," Mater. Sci. Eng. A 115 (1989) 203.

[7] Y. Baba, T.A. Sasaki and I. Takano, "Trapping of Atmospheric Oxygen on Metal Surfaces under Ar^+ Ion Bombardment," Surf. Sci. 221 (1989) 609.

[8] Z. Lin, P. Feulner, G. Rocker, R. Scheuerer, Y. Baba, E. Hudel, W. Wurth and D. Menzel, "NEXAFS von Van-der-Waals Gebundenen Kondensaten: Hinweise auf Resonante Anregung in Molekülartige Endzustände bei Mischungen von CO und H2," BESSY Jahresbericht 1989 p.163 (1989).

[9] A. Sagara, K. Kamada, T.A. Sasaki and Y. Baba, "Measurements of Evaporation Rate of Lithium from Al-Li Alloy by Depth Profiling with an Ion Beam," Nucl. Instrum. Methods Phys. Res. B 44 (1990) 373.

[10] T.A. Sasaki, Y. Baba and H. Yamamoto, "Nitridation Induced on Metal Surface by Ar^+-ion Impact under N_2 Atmosphere," Vacuum 41 (1990) 185.

[11] W. Wurth, J. Stöhr, P. Feulner, X. Pan, K.R. Bauchspiess, Y. Baba, E. Hudel, G. Rocker and D. Menzel, "Bonding, Structure, and Magnetism of Physiorbed and Chemisorbed O_2 on Pt(111)," Phys. Rev. Lett. 65 (1990) 2426.

[12] Y. Baba, E. Hudel, T. Schwabenthan, G. Rocker, R. Scheuerer, W. Wurth, P. Feulner and D. Menzel, "Photonenstimulierte Ionen-Desorption von Edelgas-Kondensaten," BESSY Jahresbericht 1990 p.289 (1990).

[13] W. Wurth, J. Stöhr, Y. Baba, E. Hudel, G. Rocker, P. Feulner and D. Menzel, "Resonante Rumpfanregung und Augerzelfall beim Übergang von Physisorption zu Chemisorption," BESSY Jahresbericht 1990 p.337 (1990).

[14] T. Hirabayashi, K.W. Sung, T.A. Sasaki and M. Saeki, "Change in Tritium-sorpiton Property of Stainless Steel by Thermal Surface Oxidation," J. Nucl. Mater. 175 (1990) 78.

[15] T. Watanabe, H. Ohno, H. Iwasaki, T. Sasaki and RIKEN-JAERI Joint Users Group, "Research and Development Activity for the Construction of

Beam Lines in SPring-8 (A New 8 GeV SR Ring)," Proceedings of International Symposium on Advanced Nuclear Energy Research -Evolution by Accelerators-, Mito, p 267 (1990).

[16] Y. Baba, G. Dujardin, P. Feulner, and D. Menzel, "Formation and Dynamics of Exciton Pairs in Solid Argon Probed by Electron-Stimulated Ion Desorption," Phys. Rev. Lett. 66 (1991) 3269.

[17] T. Hirabayashi, Y. Sun, H. Yamamoto, Y. Toida and M. Saeki, "Chemical and Topographical Properties of Tritium-resistant Stainless Steel Surfaces Formed by Chromium Diffusion Coating," J. Nucl. Mater. 182 (1991) 135.

[18] Y. Baba, H. Yamamoto and T.A. Sasaki, "XPS and XAES Measurements on Trapped Rare Gases in Transition Metals," Nucl. Instrum. Methods Phys. Res. B, in press.

[19] Y. Baba, H. Yamamoto and T.A. Sasaki, "Trapping of Low-energy Xenon Ion in Surfaces of Transition Metals," Nucl. Instrum. Methods Phys. Res. B, in press.

11.2 In-situ observation of structural and chamical changes in metals and ceramics irradiated with ion and electron beams

11.2.1 In-situ Observation of the Dynamic Behavior of Bubbles in Aluminum during 10keV H_2^+ Ion Irradiation and Successive Annealing

Introduction

Aluminum is one of the candidate materials for a fusion reactor constituent because of its low atomic number and low activation [1,2]. In order to simulate the structural and chemical changes due to plasma-wall interactions, ion irradiation experiments have been widely performed. Among these activities [3,4,5], in-situ observation of dynamic process of damage evolution is a unique technique to establish a reliable physical model.

In a previous paper [4], we reported the results of the dynamic behavior of bubbles and blisters in helium ion irradiated aluminum observed by using the equipment recently developed in our laboratory [5].

The present paper reports the results of in-situ observation on dynamic behavior of bubbles in aluminum during 10 keV H_2^+ ion irradiation and successive annealing steps.

Experimental procedure

Specimens were zone refined aluminum of 99.9999 % purity [6]. Thin films suitable for electron microscope observation were made by electropolishing in a mixed solution of ethanol and perchloric acid in the ratio of 4:1.

The in-situ observation and parallel-EELS analysis system during ion irradiation were made by combining an 100kV transmission electron microscope of the JEM-100C type (JEOL) with both an ion accelerator and a parallel-EELS (GATAN model 666), which is shown schematically in fig.1 [4]. The energy resolution of parallel-EELS was 0.6-1.0 eV. Results of in-situ observation during ion irradiations were recorded with a VTR through a TV camera and a monitor TV.

The 10 keV H_2^+ ion irradiation was performed at 113-373 K with the flux of 6×10^{17}-1.2×10^{18} ions/m^2s. After irradiation at 113 K, the specimens were annealed from 113 K to 300 K in the electron microscope. After the annealing mentioned above, the same specimen was annealed from 300 K to

498 K. The temperature was raised stepwise, 25 K steps for 10 min intervals.

Results of in-situ observation during ion irradiation and successive annealing steps were recorded with a VTR through a TV camera.

Results and discussion

Formation of bubbles and dislocation loops during irradiation at various temperatures

In the case of irradiation at 300 K with the flux of 1.2×10^{18} ions/m^2s dislocation loops were produced at the initial stage and then small bubbles were formed. These bubbles grew without appreciable increase in number and slowly coalesced, keeping a dumb-bell shape for a long time after coalescence as shown in figs. 2(a) to (h). This was in contrast to the case of He^+ ion irradiation at 573 K, where violent coalescence of bubbles was observed [2]. The reason for this slow coalescence is considered to be due to both lower inner pressure and lower temperature in comparison with the case of He^+ ion irradiation. No bubbles were observed during irradiation at 373 K and 113 K respectively, but dislocation loops were formed at the initial stage, and then grew and increased in number leading to tangling. It was revealed also that dislocation loops not only grew, but some shrank and disappeared.

Behavior of bubbles and dislocation loops during annealing up to room temperature after the irradiation at 113 K

Bubbles were found to be formed during annealing up to 300K after the irradiation to a fluence of 2.1×10^{21} ions/m^2 , as shown in fig.3. Vacancies and hydrogen atoms accumulated in the specimen during irradiation at 113K would migrate during annealing up to 273K, resulting in the formation of bubbles.

Behavior of bubbles during annealing from room temperature to 498 K

The specimen where the bubbles were formed by rapid annealing as described in section 3.2. was aged at 300 K for three days. Then the

annealing experiment was performed up to 498 K. The temperature was raised stepwise, 25 K steps for 10 min intervals. The typical results of this in-situ observation are shown in the series of photos of figs. 4 (a)-(h). The small bubbles of about 2.5 nm in radius began to shrink initially and disappeared at low temperatures near 330 K, and then larger bubbles began to shrink and vanished at higher temperatures. All the bubbles disappeared at 498 K. Another interesting thing seen in these figures is that the bubbles exhibiting a round shape at room temperature turned to have facets at 323 K and then turned roundish again with increasing temperatures. This change to roundish shape in the bubbles is considered to correspond to the change in the inner pressure of bubbles due to partial emission of hydrogen.

From the shrinkage curve of the radius of the bubbles plotted against time at fixed temperature, it is possible to estimate roughly the activation energy for the bubble shrinkage. The shrinkage curves at 498 K for some bubbles are shown in fig. 5. This figure shows that the gradient of each curve becomes nearly equal after the radii of each bubble reach about 10 nm. From the gradient of each curve at this point of radius, the activation energy E_{act} was estimated to be about 1 eV. The nearly equal values for E_{act} were obtained at other lower temperatures for the values of the radius smaller than 10 nm. Therefore the value of 1 eV for E_{act} is general for bubble shrinkage observed in the present experiment. The E_{act} can be expressed by $E_{act}=E_b+E_m-(P_{eq}-P_{in})$, where E_b is binding energy of a vacancy to a bubble, E_m is migration energy of a vacancy, P_{eq} is outer pressure due to a surface tension of bubble, P_{in} is inner gas pressure and is atomic volume. P_{eq} and P_{in} are estimated to be two orders of magnitude less than 1 eV for a bubble with a radius larger than 10 nm and can be neglected. Accordingly E_b is roughly estimated to be about 0.4 eV, because E_m is known to be about o.66 eV [7].

Conclusion

The results of in-situ observation of the dynamic behavior of bubbles in aluminum during 10 keV H_2^+ ion irradiations and successive annealing were as follows.

(1) Bubbles were formed during irradiation at 300 K, but no bubbles were

observed by irradiation at 113K and 373 K respectively.

(2) Annealing experiments from 113 K to 300 K after 113 K irradiation revealed that rapid annealing resulted in bubble formation, while slow annealing resulted in no bubble formation.

(3) By successive annealing from 300 K to 498 K,the smaller bubbles began to shrink initially and disappeared at lower temperatures, and then larger bubbles began to shrink and vanished at higher tempera tures. All the bubbles disappeared at 498 K.

(4) The activation energy for bubble shrinkage was estimated to be about 1eV from the bubble shrinkage curve and consequently the binding energy of a vacancy to a bubble was inferred to be about 0.4 eV.

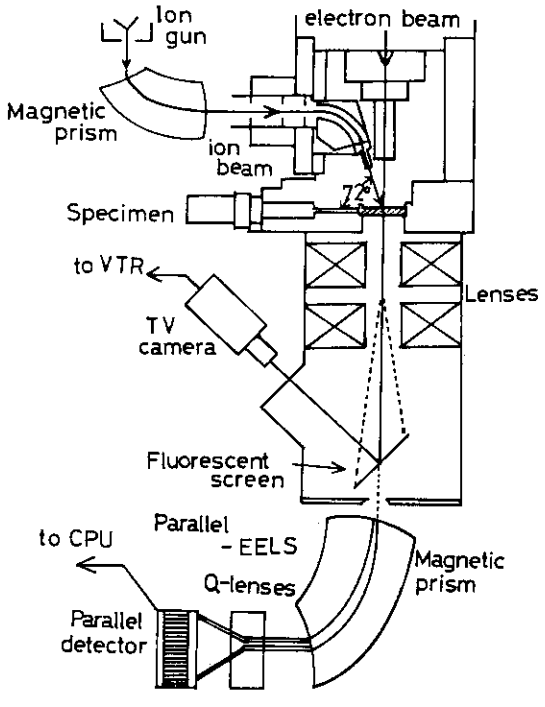

Fig.1 Schematic diagram of equipment of in-situ observation and EELS analysis.

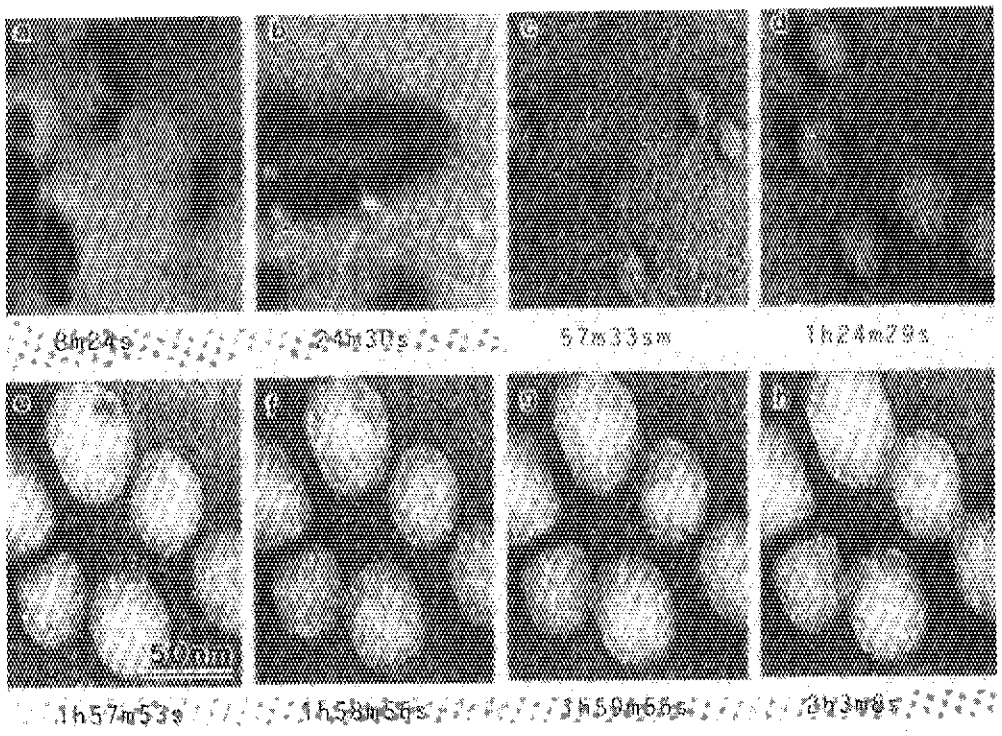

Fig.2 Formation, growth and coalescence of dislocation loops and bubbles during 10 keV H_2^+irradiation at 300 K with the flux of 1.2×10^{18} ions/m^2s.

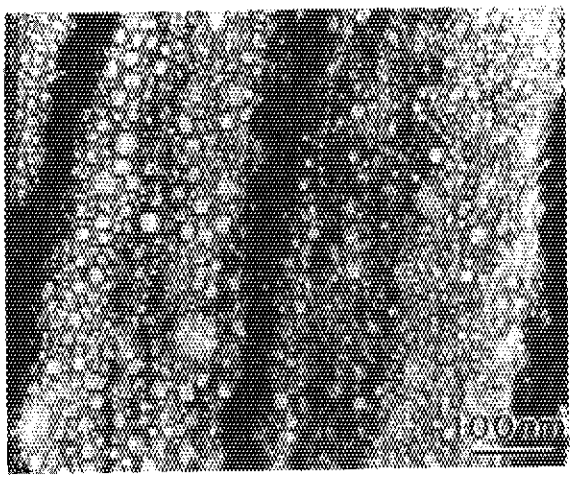

Fig.3 Bubbles formed by rapid annealing from 113 K to 300 K (5.3K/min) after 10 keV H_2^+irradiation at 113 K to a fluence of 2.2×10^{21}ions/m^2.

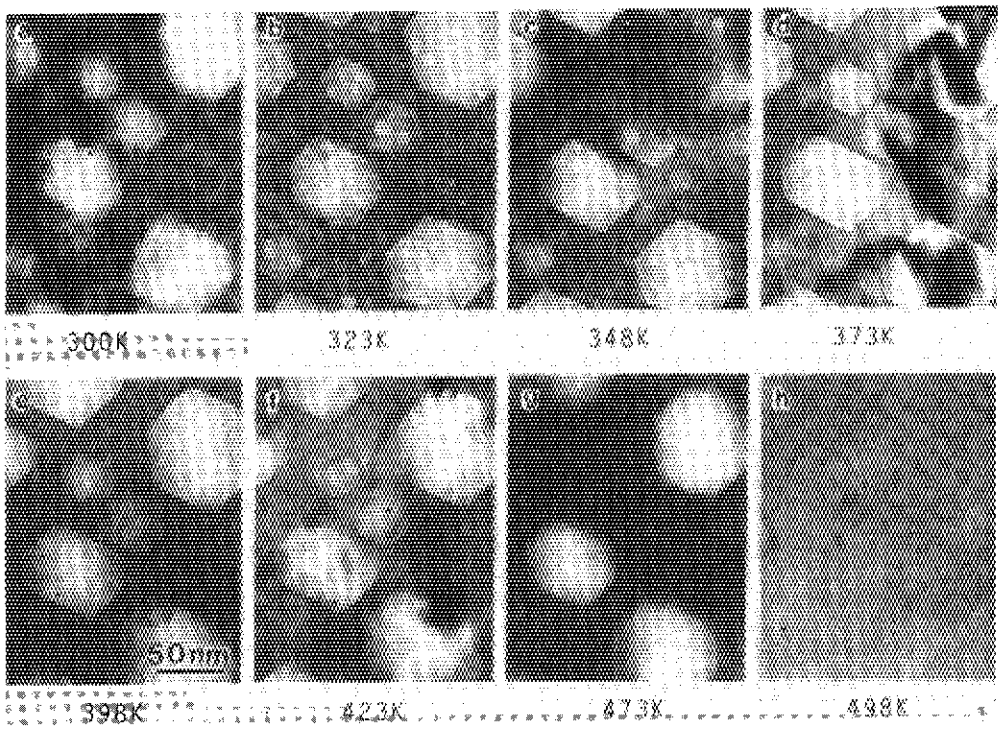

Fig.4 Behavior of bubble shrinkage and disappearance during annealing from 300 K to 498K after 10 keV H_2^+ irradiation at 113 K.

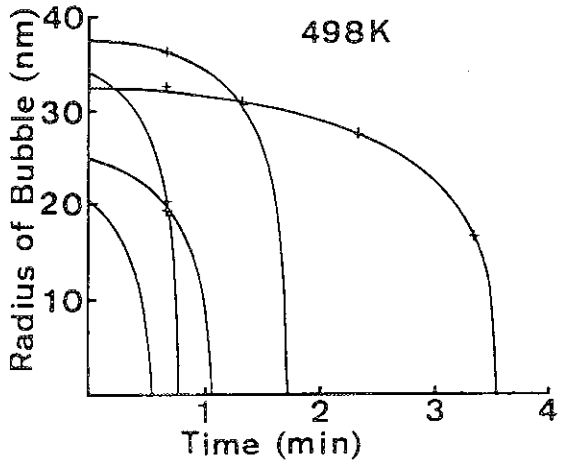

Fig.5 Variation of the radius of some bubbles with time during annealing at 498 K.

11.2.2 Parallel-Detection Electron Energy-Loss Spectroscopic Analysis of SiC Crystals Irradiated with Hydrogen Ions

Introduction

Hydrogen recycling and permeation of the first wall of fusion devices are strongly influenced by the surface condition of first-wall materials. One of the important problems is the behavior of hydrogen in the surface materials. However, there are only a few papers on the structural and chemical changes due to the hydrogen atoms implanted in the first wall materials[8,9,10].

Recently, we have developed a new in-situ observation system consisting of a 100 keV transmission electron microscope linked with an ion beam of relatively low energy and of high current density[4]. Using this system, we studied dynamical behavior of growth, coalescence, burst and disappearance of helium bubbles and blisters in aluminum [5] and SiC and TiC crystals [4] during helium ion irradiation. Furthermore, it was observed by EELS measurement that a large amount of helium was contained in the bubbles in the aluminum and SiC crystals produced by the helium ion irradiation[11,12].

The present paper reports the results of in-situ observation and the analysis by Parallel-EELS (electron energy loss spectroscope) on structural and compositional change in SiC crystals irradiated with 10 keV H_2^+-ions at room temperature(RT).

Experimental procedures

The specimens were SiC sintered polycrystals containing beryllia (BeO) powder less than 1%wt. supplied from Hitachi Research Ltd.. The structure of SiC crystals was of the hexagonal 6H type. The thin disks with about 3 mm diameter were cut out from plates by ultrasonic machining and the central part of disk was polished to a thickness of about 20 um with dimple grinder to form concave lens shape. Thin films suitable for electron microscopy were made by Ar^+ ions bombardment at room temperature. Very thin amorphous layer was produced in the surface of SiC crystals by ion beam etching and annealing was performed to make this amorphous layer crystallized at 1000 to 1200 C in vacuum for one hour prior to irradiation.

In the present experiments, 10 keV H_2^+ ions were used for the irradiations with the flux of 6×10^{18} ions/m^2/sec under the pressure of 1×10^{-5} Pa at room temperature.

Experimental results and discussions

Electron microscopic observation

Thin films of SiC crystals made by ion thinning and successive annealing treatment were observed before ion irradiation. Fig. 6 shows a general aspect of unirradiated SiC crystals, which were wedge shaped and had a small grain size of 2 to 10 um with various orientation.

Amorphous zones were observed in SiC crystals irradiated with 10 keV H_2^+-ions to a fluence higher than 3×10^{21} ions/m^2 at RT,as shown in fig.7. Amorphization phenomena due to ion irradiation have been already observed in the case of He^+ ion irradiation [13]. The damage density in the SiC amorphous structure and the depth distribution of ions were calculated by the TRIM-8 code for 10 keV H_2^+ ions of a fluence of 1×10^{21} ions/m^2, as shown in fig.8. Hydrogen atoms were distributed within a depth of about 100nm and average range was about 60nm. The damage density was estimated to be about 1 dpa in this case. This value is considered to be critical for amorphization. For a fluence larger than 1×10^{22} ions/m^2, bubbles were found to be produced[14].

EELS of irradiated SiC crystals

The plasmon energy, Ep is sensitive to the chemical composition and the density of a material[15] . Then, if structure of SiC crystals was changed during H_2^+-ions irradiation, the lattice parameter and composition may alter, leading to a change in the density of outer-shell electron and a corresponding change in plasmon energy.

Fig.9(a),(b) and (c) show the change of the plasmon loss spectrum of SiC crystals with the hydrogen ion fluences. The first and secondary plasmon peaks are found to shift to the lower energy side for the fluence of about 1.5×10^{21} ions/m^2. Fig.9(a) shows the EELS spectrum from unirradiated SiC crystals, exhibiting first and secondary plasmon loss peaks at 22.7 eV and 45.5 eV, respectively. Fig.9 (b) and (c) show EELS spectra

obtained after irradiation to the fluences of 6.5×10^{21} ions/m^2 and 8.6×10^{21} ions/m^2, respectively. From the shift of the plasmon loss peak seen in these figs., it is possible to estimate the ratio of composition, Si/C based on the data by Sabatini et al.[16] using amorphous specimens. Fig.10 shows the relationship between plasmon energy,Ep and composition. The values of opened circles are the data due to parallel-EELS obtained by the authors and the value of filled circles were obtained by Sabatini et al.[16]. The ratio of Si/C was found to become about 1.2 after irradiation with 8.6×10^{21} ions/m^2.

Another interesting point is a shoulder appearing at about 13 eV,which is shown in fig.9 (b)and(c) . This shoulder seems predominant with increasing H_2^+ ion fluences. This tendency is more clearly shown in the differential curves in fig.11 (a),(b) and (c). The origin of this peak is considered to occur in the following two ways: one is due to C-H bonding, which exhibits rather broad spectra around 13 to 14 eV[19]. ESCA data on SiC irradiated with 6 keV H_2^+ ions, clearly showed a chemical shift of the C_{1s} line which was identified to be due to C-H bonding [3]. Another possibility is due to hydrogen molecule which exhibits also a EELS peak at 13.6 eV [13]. From the EELS data of hydrogen absorbed in tantalum, platinum and silicon, the peak located at 13 eV was attributed to the excitation of molecular hydrogen bond [19].

In the present experiment, hydrogen atoms implanted in SiC crystal are considered to be trapped in both Si and C-sites. Hydrogen atoms trapped in a Si-site are surrounded by C atoms and may easily form C-H bonding. Hydrogen atoms trapped in a C-site are surrounded by Si atoms, but it may be difficult to form chemical bond with Si atoms [10]. In fact, a EELS peak of Si-H bond at 3.3 eV was not observed in the present experiment. Accordingly, as the irradiation proceeds, some of the impinging hydrogen atoms may migrate to the hydrogen atoms previously trapped in C-sites , and form hydrogen molecules. Accordingly, it is considered that hydrogen implanted into SiC crystals exist in the form of both hydrogen molecule and C-H compounds.

Conclusion

(1) Amorphization was found to occur in SiC crystal at a fluences exceeding 3×10^{21} ions/m^2 at RT.

(2) The plasmon loss spectrum was found to shift to the lower energy side for fluences above 1.5×10^{21} ions/m^2. From this shift, the ratio of Si/C was found to become about 1.2 after irradiation with 10 kev H_2^+-ions to a fluence of 8.6×10^{21} ions/m^2.

(3) Hydrogen ions implanted into SiC crystals are considered to exist in the form of both hydrogen molecule and C-H compound judging from the shoulder peak at about 13.6eV.

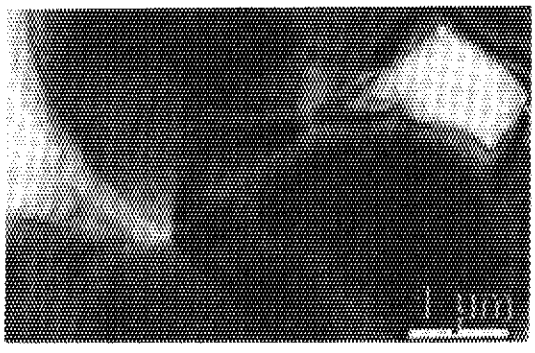

Fig.6 The general aspect of a sintered SiC polycrystal before irradiation.

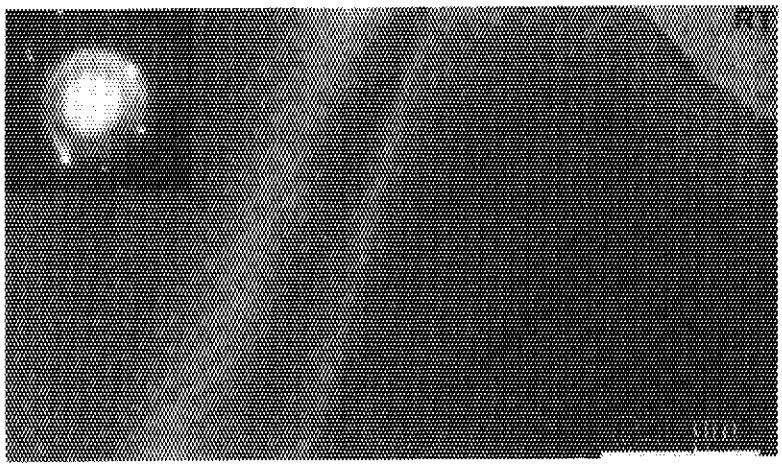

Fig.7 An amorphous zone produced in SiC crystals irradiated with 10 keV H_2^+ ions to a fluence of 3×10^{17} ions/cm^2 at RT.

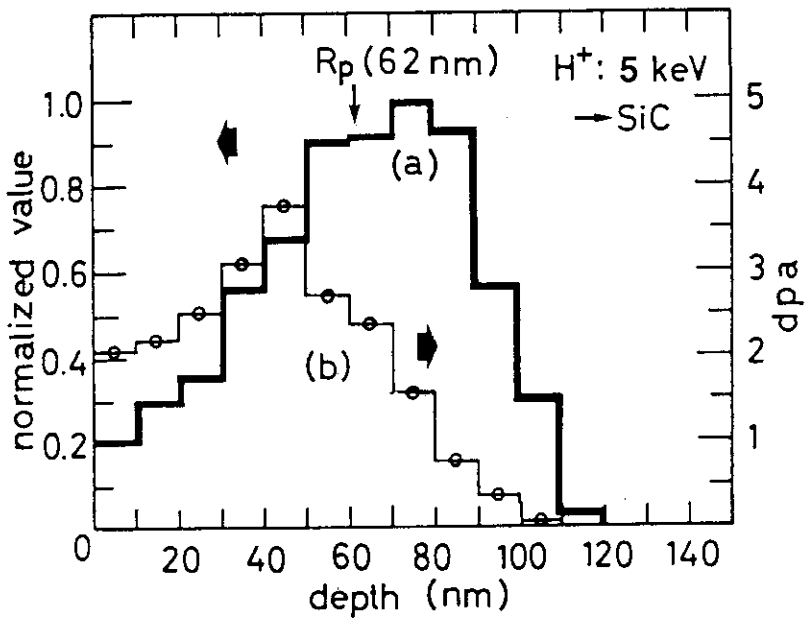

Fig.8 Results of the TRIM code calculation for the fluence of 1×10^{21} ions/m^2.
(a): Depth distribution of implanted hydrogen atoms
(b): Damage density due to hydrogen atoms

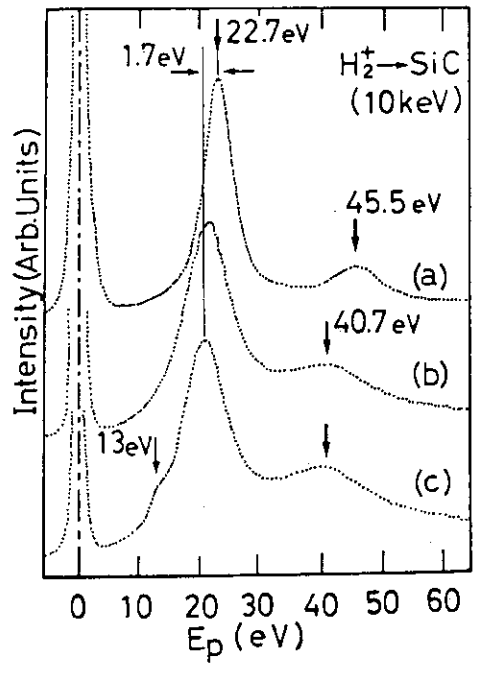

Fig.9 Parallel-EELS spectra from unirradiated SiC crystals (a) and from an amorphous zone produced by irradiation to fluences of 6.5×10^{21} ions/m^2 (b) and 8.6×10^{21} ions/m^2 (c).

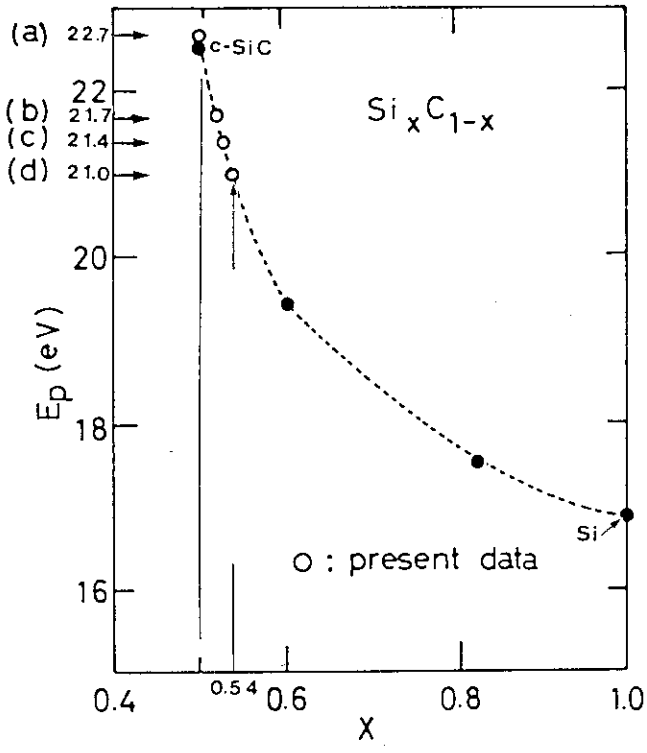

Fig.10 Relationship between plasmon loss energy, Ep and composition, X. Opened circled: present data. Filled circles: amorphous Si_xC_{1-x} from ref.16

fluences ;
(a): unirradiation,(b):1.5×10^{21}ions/m^2
(c): 4.3×10^{21} ions/m^2,(d): 6.5×10^{21} ions/m^2,(e): 8.6×10^{21} ions/m^2.

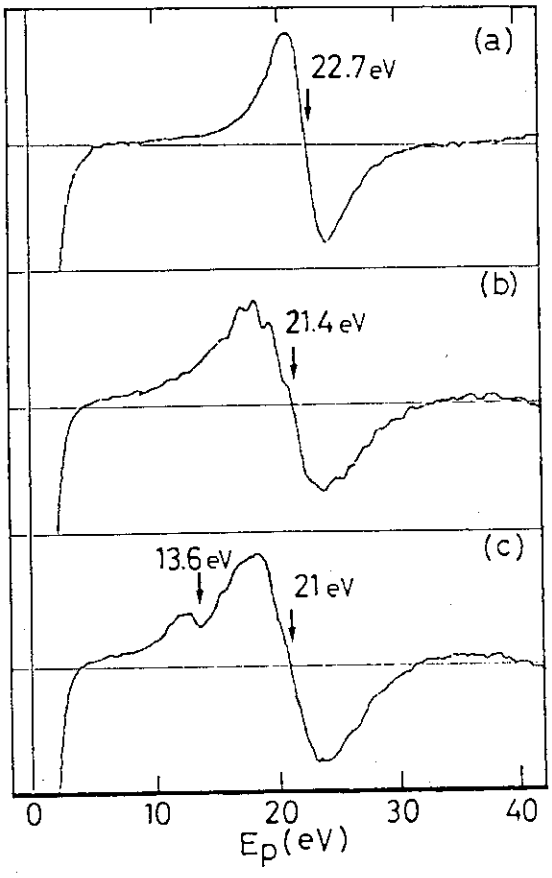

Fig.11 First differential curves obtained from the plasmon loss spectra shown in Fig.9

11.2.3 In-situ observation of structural damages in SiC crystals induced by hydrogen ion irradiation and successive electron irradiation

Introduction

The fusion reactor materials are exposed to 14MeV neutrons as well as various ions such as helium due to (n,) reaction, hydrogen and other gases coming from (n,p) reaction and plasma gases. Recently, in order to simulate the surface damage due to plasma wall interaction, the effects of helium or hydrogen ions on the evolution of structural changes in materials have been investigated by electron microscopy[20,21].

In those materials, silicon carbide is one of the candidate materials for use in the first wall of a fusion reactor. We have observed the damage structures in silicon carbide (SiC) crystals irradiated with helium ions at various temperature below 1300 C, and found that amorphization, recrystallization and bubble growth occurred by irradiation at room temperature, 800 C and 1000 C , respectively[12,22]. Furthermore, the internal pressure of helium bubbles in SiC crystals formed by helium ion irradiation was found to be the order of 10^8 Pa. from electron energy loss spectroscopy measurement [12].

Recently, we have developed an in-situ observation system consisting of a 100 keV transmission electron microscope linked with both an ion accelerator[5] and a parallel electron energy loss spectrometer (parallel-EELS)[23]. Using this system, we studied dynamical behavior of growth, coalescence, blisters, burst and disappearance of helium bubbles in aluminum [4], SiC and TiC[5] crystals during helium ion irradiation.

In the case of hydrogen ion irradiation at room temperature, the plasmon loss peaks of SiC crystals were found to shift to the lower energy side after hydrogen ion irradiation at room temperature by use of parallel-EELS and it was concluded that this shift resulted from the decrease in the ratio of composition of C/Si[23].

It was also reported that amorphization occurred but bubbles were not observed by hydrogen ion irradiation for the fluence less than 2.4×10^{22} atoms/m^2at room temperature[23].

In this paper, the possibility of hydrogen bubble formation is examined in more detail under high fluence irradiation or by successive electron irradiation after hydrogen ion implantation.

Experimental procedures

The specimens used in the present work were SiC sintered polycrystals containing beryllia(BeO) powder less than 1wt%, which were supplied from Hitachi Research Ltd.. The structure of SiC crystals was hexagonal 6H type. Thin disks with about 3mm in diameter were cut out from a plate by a ultrasonic machining and a central part of the disk was polished to a thickness of about 20 um with a dimple grinder to form concave lens shape. Thin films suitable for electron microscopy were then made by 2-4 keV Ar^+ ion etching at room temperature.

In the present experiments, 10keV H_2^+ ions were used for the irradiations with the flux of 3.6×10^{18}atoms/m^2/sec under the pressure of 1×10^{-5}Pa at room temperature . A 100keV electron irradiations after hydrogen ion implantation at room temperature were performed with the flux of above 6×10^{20} electrons/m^2/sec at room temperature.

Results and discussion

Bubbles formation by heavy irradiation at room temperature(RT.)

Thin films of SiC crystals before ion irradiation consisted of small grains of 2 to 10 um in size, and were very homogeneous in appearance within the grains, as shown in Fig.12(a). Amorphization occurred by irradiation with 10 keV H_2^+ions to a fluence higher than 3×10^{21} atoms/m^2 at room temperature, as shown in Fig.12(b) From the calculation using the TRIM-code[24], it is revealed that implanted hydrogen atom are distributed within a depth of about 100nm. Therefore, almost all implanted atoms are considered to stop within the specimen used in the present experiment.

As the irradiation proceeded to a fluence above 4.8×10^{22} atoms/m^2 at room temperature, bubbles were formed, as shown in Fig.13. This phenomenon is very similar as those already observed in the case of He ions irradiation[12]. It had been considered that it was difficult for the bubbles to be formed in amorphous structure because the most of hydrogen atoms were trapped in the various sites of dangling bonds in the amorphous structure and became immobile. However, the present experiment clearly shows that bubbles were formed even in the amorphous structure of SiC, when subjected

to heavy irradiation, as described above.

Bubble formation by 100keV electron irradiation after hydrogen ion implantation

It was found that a number of small bubbles were formed by 100keV electron irradiation in the amorphous SiC specimen which had exhibited no bubble formation after 10keV H_2^+ ion implantation to a fluence of 6.6×10^{21} atoms/m^2 at room temperature. The electron flux required for this bubble formation was above 1×10^{17} electrons /cm^2/sec at room temperature.. Fig.14 and 15 show dynamic behaviors of bubble growth by coalescence in amorphous SiC during irradiation with 100keV electrons at room temperature after 10keV H_2^+ ion implantation. Such an effect of electron irradiation on the formation of bubbles, shown in Fig.14, was not observed in a amorphous SiC in the case of 10keV helium ion irradiation[5]. Fig.14 and 15 show also the electron flux dependence on the formation and growth of bubbles. That is, the growth of bubbles was more predominant with increasing the electron flux. The present experiment mentioned above clearly shows that hydrogen ion irradiation to the fluence less than about 2.4×10^{22} atoms/m^2 is unable to form visible bubbles, unless successive electron irradiation is performed. It is considered that hydrogen atoms implanted are trapped in various sites of the dangling bonds in an amorphous structure of SiC, and these trapped hydrogen atoms are able to be knocked out to the neighboring hydrogen atom sites by electron irradiation successively. Resultantly electron irradiation would cause short range diffusion of these hydrogen atoms by knock-on effect leading to their clustering to form bubbles. This interpretation is supported by another annealing experiment after hydrogen ion implantation. It was found that electron irradiation could not cause the bubble formation for the specimens annealed at 300 C for 20 min after hydrogen ion implantation at room temperature., as shown in Fig.16. By annealing at 300 C a large part of hydrogen atoms trapped are considered to be released from the trapped sites and escape away from the surface by long range diffusion, resulting in no bubble formation.

Conclusions

The results of the in-situ observations of SiC crystals irradiated with H_2^+ ion irradiation and successive electron irradiation are summarized as follows.

(1) Bubble formation was not observed for the fluence below 4.8×10^{22}atoms/m^2, while bubbles were formed for the fluence above this value.

(2) Electron irradiation performed successively after H_2^+ ion irradiation at room temperature. gave rise to bubble formation even in an amor phous structure of SiC. It is considered that implanted hydrogen atoms trapped in dangling bonds in an amorphous structure are knocked out by electron irradiation and coagulate with each other to form bubbles.

(3) Electron irradiation after annealing at 300 C of hydrogen ion im planted SiC caused no bubble formation. In this case, it is consid ered that a large part of implanted hydrogen atoms had been released from the trapped sites and escaped away from the surface by long rang diffusion at high temperatures.

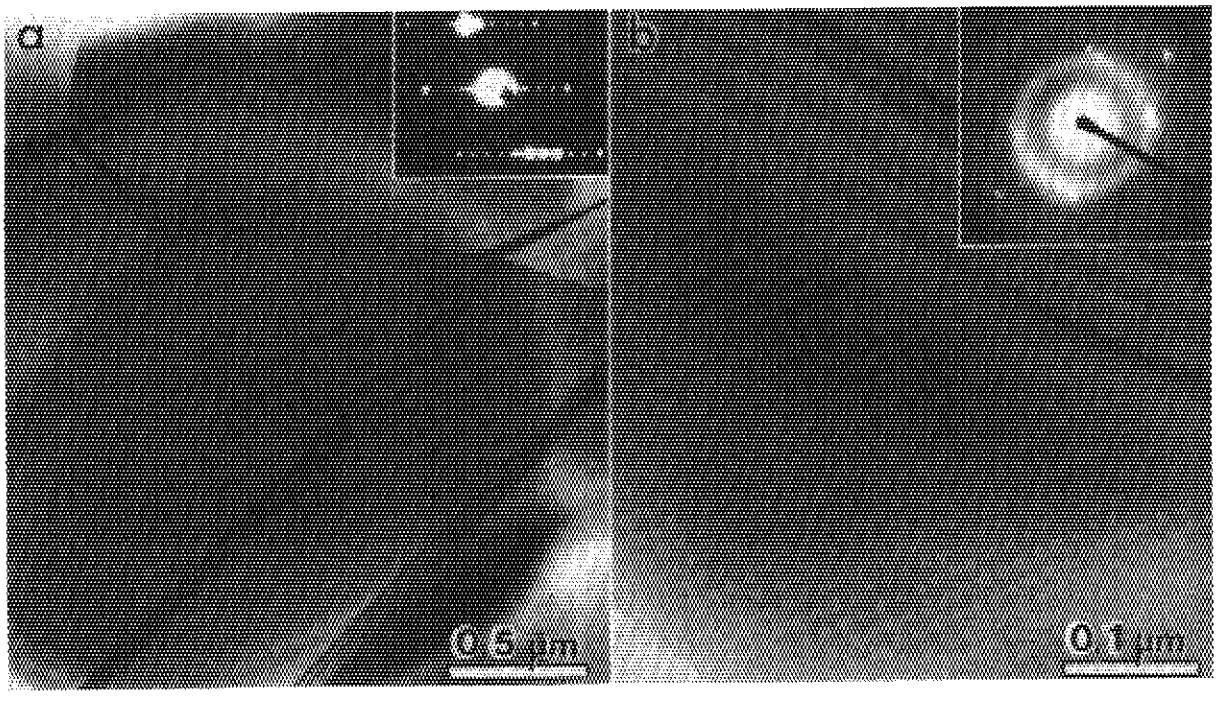

Fig.12 The general aspect of a sintered SiC polycrystal before irradiation (a) and an amorphous area produced in SiC crystals irradiated with 10 keV H_2^+ions to a fluence of 6.6×10^{21}atoms/m^2at RT.(b).

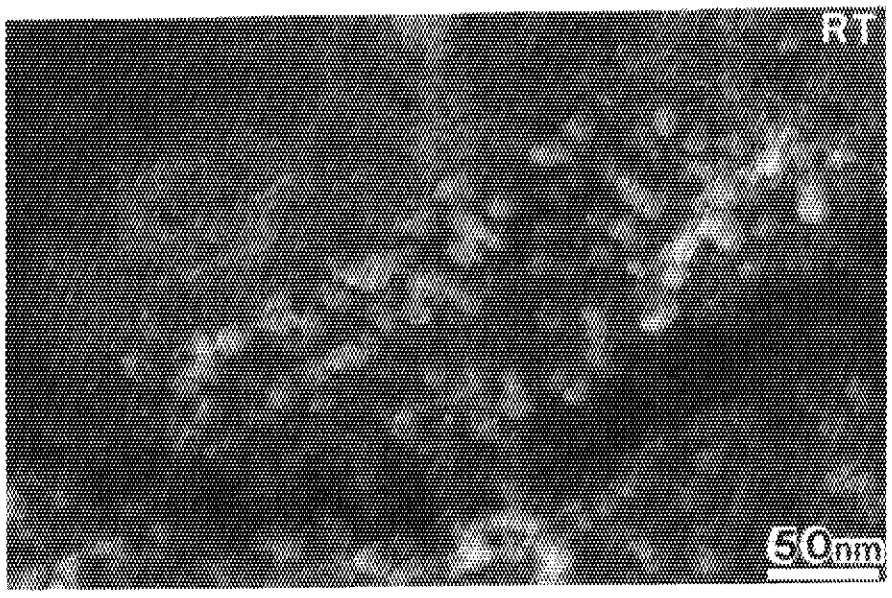

Fig.13 Bubbles produced in SiC crystal with 10keV H_2^+ ions to a fluence of 4.8×10^{22} atoms/m^2 at RT.

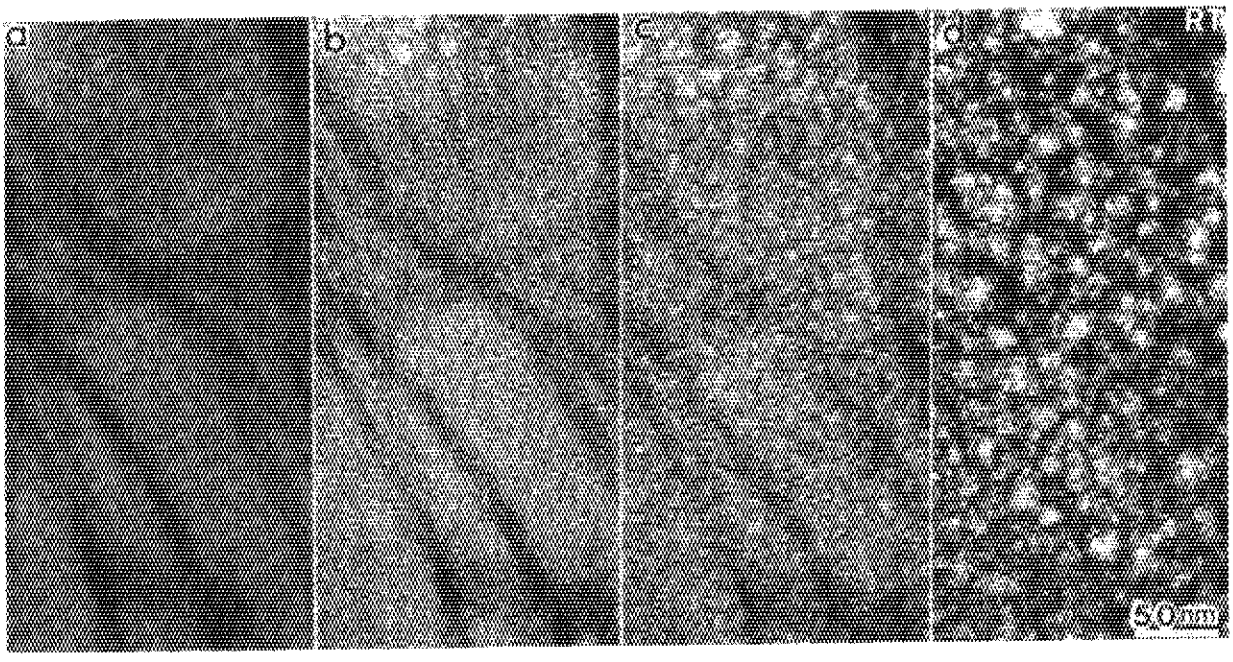

Fig.14 Evolution of bubbles in SiC crystal during irradiation with 100keV electrons of 4.2×10^{21} electrons/m^2/sec after 10 keV H_2^+ ion implantation to a fluence of 6.6×10^{21} atoms/m^2 at RT.. Fluences :(a) no electron irradiation; (b)3.8×10^{24}electrons/m^2;(c) 7.6×10^{24} electrons/m^2; (d)1.5×10^{25}electrons/m^2

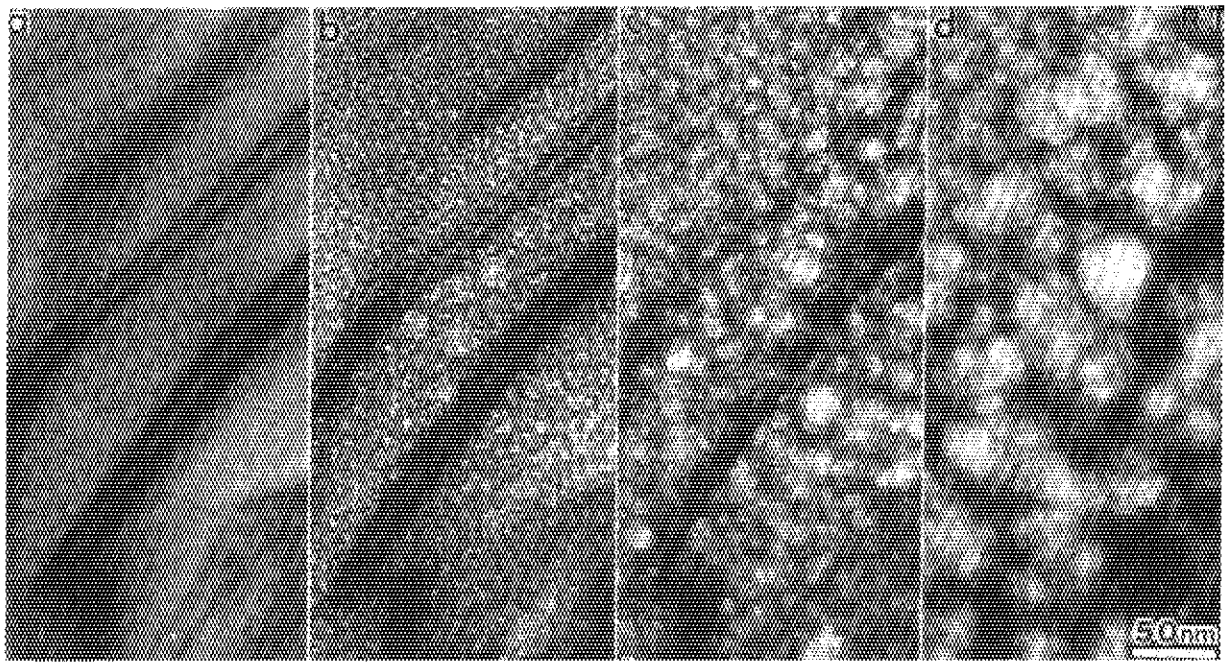

Fig.15 Evolution of bubbles in SiC crystal during irradiation with 100keV electrons of 8.4×10^{21} electrons/m^2/sec after 10keV H_2^+ ion implantation to a fluence of 6.6×10^{21} atoms/m^2 at RT.. Fluences:(a) 3.4×10^{23} electrons/m^2; (b)1×10^{24} electrons/m^2; (c) 2×10^{24} electrons/m^2; (d) 3.5×10^{24} electrons/m^2.

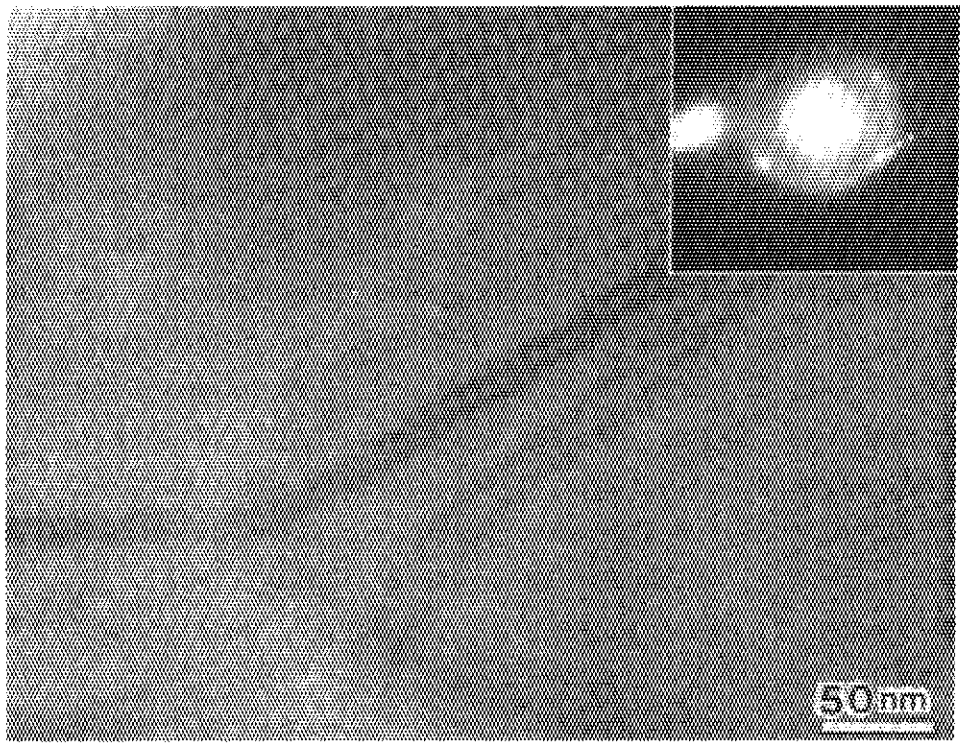

Fig.16 No bubbles in the SiC specimen annealed at 300 C after H_2^+ ion implantation and then irradiated with 100keV electrons.

References

1) R.A. Kramer, E.C. Franz, R.H. Wagner, R.R. Guerra, S.P. Ray and W.E. Wahnsiedler, Low-Activation Structural Materials for Fusion Reactors; Extreme Purity Base Al Alloy, (Alcoa Technical center) EPRI report AP-2220(1982).

2) T. Noda, F. Abe, H. Araki and M. Okada, J. Nucl. Mater. **155-157** (1988)581.

3) S. Furuno, K. Izui, K. Ono and T. Kino, J. Nucl. Mater.**133-134** (1985)400.

4) S. Furuno, K. Hojou, K. Izui, N. Kamigaki and T. Kino, J. Nucl. Mater. **155-157**(1988)1149.

5) K. Hojou, S. Furuno, H. Otsu, K. Izui and T. Tsukamoto, J. Nucl. Mater. **155-157**(1988)298.

6) T. Kino, E. Hashimoto, N. Kamigaki, K. Kiso and R. Matsushita, Trans. Jpn. Inst. Met. **18**(1977)305.

7) K. Ono and T. Kino, J. Phys. Soc. Jpn. **44**(1978)875.

8) M. Mohri, K. Watanabe and T. Yamashina, J. Nucl. Mater. **93&94**(1980)28.

9) S. Fukuda, M. Mohri and T. Yamashina, 9th Int. Vacuum Congr. and 5th Int. Conf. on Solid Surfaces, Madrid(1983)p.192.

10) T.A. Sasaki and Y. Baba, J. Nucl. Mater. **138** (1986)145.

11) K. Izui, K. Hojou, S. Furuno, K. Ono and T. Kino, J. Electron Microsc. **33** (1984)381.

12) K. Hojou and K. Izui, J. Nucl. Mater. **160** (1988)147.

13) K. Hojou and K. Izui, J. Nucl. Mater. **133 & 134** (1985)709.

14) K. Hojou, S. Furuno and K. Izui, J. Electron Microsc.,**40** (1991)157.

15) R.F. Egerton," Electron Energy-Loss Spectroscopy in the Electron Microscope", Plenum Press, New York and London (1986).

16) R.L. Sabatini, J. Tafto, F.J. Kampas and G. Rajeswaran, Ann.in 42th Ann. Proc. EM Soc. Am. San Francisco, CA, (1984)562.

17) A.D. Baker and D. Betteridge, "Photoelectron Spectroscopy; Chemical and Analytical Aspects", Pergamon Press,Oxford(1972).

18) C.C. Ahn and O.L. Krivanek, "EELS Atlas", Gatan (1983).

19) D. Massignon, F. Pellerin and C.LE Gressus, J. Nucl. Mater.**93 & 94** (1980)871.

20) H. Kusanagi, H. Kimura, M.Tokiwai and T. Suzuki, J.Nucl.Mater. **133&134** (1985)473.

21) D.B. Bullen , G.L. Kulcinski and R.A. Dodd, J.Nucl. Mater. **133&134** (1985)455.

22) K. Hojou and K. Izui, Proc. XIth Int.Cong. on Electron Microscopy, Kyoto: (1986)1301.

23) K.Hojou, S.Furuno, T. Soga and K. Izui , J. Nucl. Mater. **179-181** (1991)411.

24) J.P. Biersack and L.G. Haggmark , Nucl. Instrum. Methods. **174** (1980)257.

Publication List

[1] K. Hojou, S. Furuno, H. Maeta, H. Otsu and T. Soga, "In situ observation of ion irradiation damage in material and ceramics", Pro. Inter. Symp. on Advanced Nuclear Energy Research, Ooarai (1989) p.353.

[2] D. Shindo, K. Hiraga, S. Nakajima, M. Kikuchi, Y. Syono, N. Kobayashi, K. Hojou, T.Soga, S. Furuno and H. Otsu, " Oxygen-edge fine strucure of $TlBa_2Ca_{1-x}Y_xCu_2O_7$ studied by electron energy loss spectroscopy" Phsica **C159** (1989)794.

[3] D. Shindo, K. Hiraga, M. Hirabayashi, M. Kikuchi, Y. Syono, S. Furuno, K.Hojou, T. Soga and H. Otsu, " In situ obserbation of oxygen K-edge fine structure of $YBa_2Cu_3O_{7-y}$by EELS" J. Electron Microsc., **38**(1989)155.

[4] D. Shindo, H. Sato, G.L.Liedl, D. Perry, K. Hiraga, S. Nakajima, M. Kikuchi, Y. Syono, K. Hojou and T. Soga," Oxygen K-edge fine structure of $Tl_1Ba_2Ca_{n-1}Cu_nO_{2n+3}$ studied by electron energy loss spectroscopy" Japan J. Applied Physics, **28**(1989)L955.

[5] D. Shindo, K. Hiraga, A. Tokiwa, T. Soga, K. Hojou, S. Furuno, H. Otsu, S. Nakajima, M. Hirabayashi, M. Kikuchi and Y. Syono, " Electron Enelgy loss spectroscopy on oxygen K-edge fine structure of $YBa_2Cu_3O_y$ containing dopants(La,Ca,Co), Japan J. Applied Physics, **28**(1989)L1197.

[6] S. Furuno, K. Hojou, H. Otsu, K. Izui, T. Sasaki, T. Tsukamoto and T. Hata, "A new system for in-situ observation of dynamic process of structural and chemical changes during ion beam irradiation in a 400kV electron microscope." Electron microscopy, vol.3 (1990)p.538

[7] K. Hojou, S.Furuno, H.Otsu and K.Izui, " In-situ electron energy loss spectroscpy of silicon carbide crystals during electron

irradiation after hydrogen ion implantation." Electron Microscopy, vol.4 (1990)p.124.

[8] K. Kushita and K. Hojou, " Structure change of crystalline graph ite due to hydrogen ion irradiation observed by in-situ electron energy loss spectroscopy" Electron Microscopy,vol.4 (1990)p.126.

[9] K. Hojou, S. Furuno, H. Ostu and T. Soge, " In-situ observation and EELS analysis of materials during ion irrdiation", The 2nd Inter. Symp.on Advanced Nuclear Energy Reseach, Mito,(1990)p.413.

[9] K. Hojou, S.Furuno, T soga and K. Izui, " New in-situ parallel-detection electron energy-loss spectroscopy of SiC crystals irradiated with hydrogen ions.", J.Nucl.Mater., **179-181**(1991)411.

[10] K. Hojou, S. Jitsukawa, M. Suzuki, S. Hamada and A. Hishinuma," Application of electron energy loss spectroscopy to microchemical analysis of Ti-modified austenitic stainless steel irradiated in HFIR." J. Nucl.Mater., **179-181**(1991)496.

[11] S. Jitsukawa, K. Hojou and A. Hishinuma, "Effect of phosphorus and boron additions on helium bubble microstructure in titanium-modified austenitic stainless steels." J.Nucl.Mater.,**179-181**(1991)538.

[12] N. Kamigaki, S.Furuno, K. Hojou, K. Izui and T. Kino, " Evolution of structural damage in high-purity aluminum alloys during ion irradiation and the following heat treatments.", J. Nucl.Mater.,**179-181** (1991)970.

[13] K. Ono, T. Kino, S. Furuno, K. Hojou, K. Izui, K. Mizuno and K.Ito, " Effect of hydrogen on the formation of interstitial loops in hydrogen-irradiated aluminum.", J. Nucl. Mater., **179-181** (1991)978.

[14] H. Maeta, S.Furuno, K. Hojou, H. Otsu and M. Watanabe, " In-situ observation of bubble formation in superconducting YBa2Cu3O7-y during He-ion irradiation in an electron microscope.", J. Nucl. Mater., **179-181**(1991)1003.

[15] S. Furuno, K. Hojou, H. Otsu, K. Izui, N. Kamigaki and T. Kino, " In-situ observation of the dynamic behavior of bubbles in alumi num during 10keV H2+ ion irradiation and successive annealing.", **179-181**(1991)1011.

[16] K. Hojou, S. Furuno and K. Izui, " In-situ observation of structural damage in SiC crystals induced by hydrogen ion irradiation and successive electron irradiation." J. Electron Microsc.,**40** (1991)157.

[17] K. N. Kushita and K. Hojou, " In situ EELS observation of graph ite structure modification due to hydrogen ion irradiation."

Ultramicroscopy, **35**(1991)289.

[18] K. Ono, T. Kino, S. Furuno, K. Hojou, K. Izui, K. Mizuno and K. Ito, " Conversion of hydrogen bubbles to disk-shaped defects in hydrogen irradiated aluminum." J. Nucl. Mater., **183**(1991)154.

[19] E.A. Kenik and K. Hojou, " Radiation-induced segergation in austenitic stainless steels" Pro. 49th AMSA (1991)556.

[20] K. Ono, T. Kino,S. Furuno, K. Hojou, K. Izui, K. Mizuno and K. Ito, "Conversion of hydrogen bubbles to disk-shaped defects in hydrogen irradiated aluminum." J. Nucl. Mater., **183**(1991)154.

12. SERVICE WITH Co-60 IRRADIATION FACILITY AND ANALYTICAL EQUIPMENTS

T. A. Sasaki, H. Nagayama, T. Ohkubo, H. Ohtsu, T. Soga and K. Furukawa

12.1 Outline

Co-60 irradiation facility in Tokai Research Establishment was completed in August, 1958. Since the starting of irradiation service in September 1958 thirty-three years have passed. The services have been performed for demands in various research fields such as electronics, superconductivity, biotechnology, space science, surface science and radiation chemistry in and outside the Institute.

The improvement of the facility building and repair of its equipments were often carried out and Co-60 gamma-ray source was renewed several times for its reinforcement. The number of achievement in the irradiation service until now has exceeded 38,000 for applied experiments and 1,200 for fundamental experiments. In this report, an outline of the business in last three years is given(the fiscal 1989, 1990 and 1991).

12.2 Co-60 Gamma-ray Source

In order to satisfy requirements for reinforcement of the gamma-ray source a new 4.1 PBq(nominal 110 kCi) source was installed in 1987. The services have been performed by the use of the new source and 0.22 PBq(nominal 45 kCi) source which was purchased in June, 1972. Table 1 shows the dose rates of these sources measured on 18th October, 1991.

Table 1 Dose rates of gamma-ray sources measured on 18th October, 1991.

Distance(cm)	Dose rates(C/kg.hr)	
	4.1 PBq	0.22 PBq
0	2200	150
10	1000	64
20	330	18
30	160	8.8
50	58	3.4
70	29	1.7

12.3 Maintenance and Management of Facility

A cave consists of three cells. A cell and B cell of the right and left sides are used for irradiation experiments, and center C cell for the stor[illegible] of the sources. There are a stepping back door in each cell and a interval partition door(lift door) between the cells. A chain block is installed in the ceiling of the cell for transportation of the sources and specimens. In order to operate them safely, radiation monitors and interlock circuits are set in the cells.

A driver mechanism of the lift door in the cell was changed into a ball screw jack type screw from the old simple screw. For the convenience of the maintenance over the cells a new hoist(1t) was installed in the ceiling of the cave. The water pipelines in the Facility were replaced with new ones under the cooperation of the Technical Department(JAERI), because they were worn out by the use of the last 33 years.

Measurements of dose rates have been carried out for the nominal 110 kCi and nominal 45 kCi in April and October every year, and the results were announced to the users and persons concerned.

12.4 Irradiation Application Achievement

For a survey of recent tendency in the irradiation application the theme and purpose of the in-situ experiment are shown in Tables 2(fiscal 1989), 3(fiscal 1990) and 4(April-December 1991). In these tables number of the application and days required for the in-situ experiment a year are also included. Figure 1 represents bar diagrams for total number of application and total days required for the in-situ experiments in recent three years.

Table 2 Theme and purpose of application (A), and number of applocation and days spent by users (B) (April 1989-March 1990)

(A)

Name of users	Theme and purpose of application
JAERI users	
Nuclear Engineering School	Radiation damage of thymine
JMTR Project Engineering Division	Irradiation effects of shieling material, lead glass and furon gas
Department of Research, Takasaki Research Establishment	Radiolysis of gaseous carbon dioxide
Fission Products Safety Lab.	Preparation of volatile iodine by gamma-rays
Radiochemistry Lab. I	Radiolysis of mixed oxides of lithium and iron, adsorbed water, SF_6, and complexes containing iron
Material Innovation Lab.	Measurements of electric properties of ceramics under gamma irradiations
Reactor Instrumentation Lab.	Radiation resistance of glassy materials Radiation resistance test of fiber cables under the irradiation
Solid State Chemistry Lab.	Radiation resistance test of lubricants Cleaning of container for dosimetry Irradiation test of alanin dosimeter
Physical Chemistry Lab.	Probable enhancement for radiation damage of polymers
Shielding Lab.	Irradiation test of $Li_2B_4O_7$ TLD
Materials Processing and Qualification Lab.	Irradiation effects of gamma-rays on ionic conductivity of Li_2O
Production Division	Radiation resistance test of materials for RI production
Outside users	
National Lab. for High Energy Physics	Research of some compounds resistible to intense radiation Gamma rradiation effects of liquid crystal

Asahi Chemical Industry Co. Ltd.	Post-polymerization of gamma irradiation
Kyowa Gas Chemical Co. Ltd.	Radiation resistance test of ion-exchange resin
Q. I. Co. Ltd.	Irradiation test of IC for radiation resistance
Fuji Electric Co. Ltd.	Irradiation test of motor for radiation resistance
Fujitsu Co. Ltd.	Examination of radiation durability of IC circuits
NEC Co. Ltd.	Evaluation of gamma irradiation of IC circuits
Hitachi Cable Co. Ltd.	Irradiation test of optical fiber
Faculty of Engineering, Kumamoto University	Gamma-ray induced chemical reactions of radicals Irradiation effect of polypeptide Absorption and desorption of metal ions from gamma-irradiated resin Study of radiation resistance of dye
Faculty of Engineering, Ehime University	Preparation of new carbon material by gamma irradiation Effects of irradiation on electricity of polymerized materials
University of Tsukuba	Gammma-irradiation effects of unstable cation radical Measurements of radiation damages of scintilation counter and optical fiber
Faculty of Agriculture, Hokkaido University	Gamma-irradiation effect of casein on formation of gel
Kumamoto Institute of Technology	Radiation chemistry of biomaterials
Faculty of Agriculture, Kagoshima University	Irradiation effects of pollen
Hachinohe Institute of Technology	Irradiation effects of polyethylene Irradiation effects of organic materials

Faculty of Engineering, University of Tokyo	Gamma radiation effect of polyethylene
Kyoto Prefectural University	Gamma-ray irradiation effects of natural polymer
Faculty of Science, Kochi University	Lattice defects and ionic conductivity of irradiated ionic crystals
Faculty of Science, Osaka University	Experiment of transmission change by gamma irradiation
Tokyo Institute of Technology	Radiation damage study of fusion reactor materials

(B)　(1989)

Name of user	Number of applications	Days spend by user
JAERI users		
Nuclear Engineering School	63 (9.48%)	
JMTR Project Engneering Division	61 (9.18%)	3 (4.05%)
Department of Research, Takasaki Research Establishment	39 (5.87%)	
Fission Products Safety Lab.	28 (4.21%)	
Radiochemistry Lab. I	27 (4.06%)	
Material Innovation Lab.		15 (20.27%)
Reactor Instrumentation Lab.	6 (0.84%)	7 (9.45%)
Solid State Chemistry Lab.	20 (2.8%)	6 (8.1%)
Physical Chemistry Lab.	6 (0.84%)	
Shielding Lab.	10 (1.4%)	
Material Processing and Qualification Lab.	5 (0.7%)	
Production Division	3 (0.42%)	
Outside users		
National Lab. for High Energy Phsics	52 (7.83%)	
Asahi Chemical Indutry Co. Ltd.	5 (0.75%)	
Kyowa Gas Chemical Co. Ltd	4 (0.6%)	
Q.I Co. Ltd.	4 (0.6%)	
Fuji Electronic Co. Ltd.	3 (0.45%)	
Fujitsu Co. Ltd.		20 (27.06%)

NEC Co. Ltd.		4 (5.4%)
Hitachi Cable Co. Ltd.		2 (2.7%)
Universities(Total)	328 (49.44%)	17 (22.97%)
Total	664	74

Table 3 Theme and purpose of application (A), and number of applocation and days spent by users (B) (April 1990-March 1991)

(A)

Name of users	Theme and purpose of application
JAERI users	
Nuclear Engineering School	Radiation damage of thymine /ascorbic acid
Radiochemistry Lab. I	Radiolysis of water and SF_6
JMTR Project Engineering Division	Irradiation effects of shieling material, lead glass and furon gas
Shielding Lab.	Irradiation test of TLD
Reactor Instrumentation Lab.	Radiation resistance of optical fiber cables Sensitivity of neutron detector to gamma
Department of Nuclear Ship Engineering, Reactor Engineering Division	Adjustment of dosimeter elements Irradiation test of cables and connectors for nuclear instrumentations
Solid State Chemistry Lab.	Radiation resistance test of monitor cables Cleaning of container for dosimetry Dosimetry by Fricke dosimeter
Physical Chemistry Lab.	Probable enhancement for radiation damage of polymers
Materials Processing and Qualification Lab.	Irradiation effects of gamma-rays of lead fluoride Measurement of electric conductivity of ceramics during gamma irradiation
Solid State Physics Lab. II	Gamma irradiation effects of high Tc super-conductor
Department of Research, Takasaki Research Establish-ment	Radiolysis of gaseous carbon dioxide
Nuclear Fuel Chemistry Lab.	Irradation test of window material for nuclear fusion vessel
JMTR Irradiation Division I Lab.	Measurement of electric properties of A1203 during irradiation

Material Innovation Lab.	Measurements of electric properties of ceramics under gamma irradiations
Engineered Barrier Materials Lab.	Effects of gamma irradiation on corrosion of metals
Fuel Processing Lab.	Examination of cleaning of solvens for fuel processing
Outside users	
National Lab. for High Energy Physics	Research of some compounds resistible to intense radiation Gamma rradiation effects on transmission coefficient Radiation damages of scintilator, diodes and adhesive reagents
Hitachi Nuclear Engineering Ltd.	Polymerization of polyethylene Hardening test of WPC
Central Research Institute of Electric Power Industry	Radioactive dating of quartz
Asahi Chemical Industry Co. Ltd.	Post-polymerization of gamma irradiation of diacethylene
Hitachi Ltd.	Evaluation of radiation resistivity of semi-conductor Test for radiation resistivity of detector for electromagnetic flowmeter
Hitachi Installation Engineering Co. Ltd.	Radiation resistance test of position-sensitive electric switch
Fujitsu Co. Ltd.	Examination of radiation durability of IC circuits
NEC Co. Ltd.	Evaluation of gamma irradiation of IC circuits
Nihon Texas Instrument Ltd.	Examination of radiation durability of LSI devices
Faculty of Engineering, Kumamoto University	Gamma-ray induced chemical reactions of radicals Irradiation effect of polypeptide Study of floating and cleaning of metal ions by surfactants

	Gamma-irradiation effects of resin on abilities of adsorption and desorption
Faculty of Engineering, Ehime University	Preparation of new carbon material by gamma irradiation Preparation of new materials for gas sensor by gamma irradiation
University of Tsukuba	Study of structure of unstable cation radical Measurements of radiation damages of scintilation counter and optical fiber
Faculty of Agriculture, Hokkaido University	Gamma-irradiation effect of casein on formation of gel
Faculty of Agriculture, Kagoshima University	Irradiation effects of pollen
Faculty of Education, Yamaguchi University	Spin trapping in biomaterials irradiated with gamma rays
Faculty of Engineering, University of Tokyo	Gamma radiation effect of organic solid
Kyoto Prefectural University	Gamma-ray irradiation effects of natural polymer
Faculty of Science, Kochi University	Lattice defects and ionic conductivity of irradiated ionic crystals
Faculty of Engineering, Ibaraki University	Trapping state and stability of electron produced in propylene
Faculty of Science, Yamagata University	Radiation damage study of simple solid substances

(B) (1990)

Name of user	Number of applications	Days spent by users
Nuclear Engneering School	138 (17.05%)	
Radiochemistry Lab. I	131 (16.19%)	
JMTR Project Engneering Division	42 (5.19%)	4 (3.25%)
Shielding Lab.	11 (1.35%)	
Reactor Insrumentation Lab.	8 (0.98%)	11 (8.94%)
Department of Nuclear Ship Engineering. Reactor Engineering Division	7 (0.86%)	
Solid State Chemistry Lab.	5 (0.61%)	6 (4.87%)
Physical Chemistry Lab.	4 (0.49%)	
Material Processing and Qualification Lab.	4 (0.49%)	4 (3.25%)
Solid State Physics Lab. II	4 (0.49%)	
Department of Research. Takasaki Research Establishment	3 (0.37%)	
Nuclear Fuel Chemistry Lab.	2 (0.24%)	
JMTR Irradiation DIvision I Lab.	1 (0.12%)	5 (4.06%)
Material Innovation Lab.		23 (18.69%)
Engineered Barrier Materials Lab.	1 (0.12%)	11 (8.94%)
Fuel Reprocessing Lab.		4 (3.25%)
Outside users		
National Lab. for High Energy Physics	73 (9.02%)	

Hitachi Nuclear Engineering Ltd.	40 (4.94%)	
Central Research Institute of Electric Power Industry	12 (1.48%)	
Asahi Chemical Industry Co. Ltd.	10 (1.23%)	
Hitachi Ltd.	4 (0.49%)	11 (8.94%)
Hitachi Installation Engineering Co. Ltd.	1 (0.12%)	
Fujitsu Co. Ltd.		24 (19.57%)
NEC Corporation		3 (2.43%)
Nihon Texas Instrument Ltd.		1 (0.81%)
Universities (Total)	308 (38.13%)	16 (13.0%)
Total	809	123

Table 4 Theme and purpose of application (A), and number of application and days spent by users (B) (April 1991-December 1991)

(A)

Name of users	Theme and purpose of application
JAERI users	
Nuclear Engineering School	Radiation damage of thymine /ascorbic acid
Mutsu Establishment, Marine Technical Services Division	Irradiation test of cables and connectors for nuclear instruments
Reactor Instrumentation Lab.	Radiation resistance tests of optical fiber cables, insulating wires and optical ceramics
Shielding Lab.	Irradiation test of TLD($Li_2B_4O_7$, LiF)
JMTR Irradiation Division I Lab.	Measurement of properties of magnetic probe during irradiation
Solid State Chemistry Lab.	Radiation resistance test of thermostat Cleaning of container for dosimetry Dosimetry by Fricke dosimeter
Production Division	Radiation resistance test of line tubes of apparatus for RI preparation
Engineered Barrier Materials Lab.	Effects of gamma irradiation on corrosion of metals
Material Innovation Lab.	Measurements of electric properties of ceramics under gamma irradiations
Outside users	
National Lab. for High Energy Physics	Research of some compounds resistible to intense radiation Gamma rradiation-effects on transmission coefficient of lead fluoride Radiation damages of inorganic scintilators
Fuji Photo Optical Co. Ltd.	Irradiation test of TV lenses
Tohyoh Ink Production Ltd.	Polymerization of diacethylene resin
Fujitsu Co. Ltd.	Examination of radiation durability of IC circuits

Nihon Texas Instrument Ltd.	Examination of radiation durability of LSI devices
Faculty of Engineering, Kumamoto University	Polymerization of organic monomers Radiation resistance test of surfactants
Faculty of Engineering, Ehime University	Preparation of new carbon material by gamma irradiation Preparation of new materials for gas sensor by gamma irradiation
University of Tsukuba	Radiation damage of scintilator by gamma radiations Measurements of optical properties of scintilation counter and optical fiber during gamma irradiation
Faculty of Agriculture, Hokkaido University	Gamma-irradiation effect of casein on formation of gel
Faculty of Agriculture, Kagoshima University	Irradiation effects of seed
Faculty of Engineering, University of Tokyo	Gamma radiation-effect of polyethylene
Faculty of Science, Showa College of Pharmaceutical Sciences	Examination of radiolyses by EC decay and gamma irradiation

(B)(1991)

Name of user	Number of applications	Days spent by users
Nuclear Engneerinng School	240 (37.32%)	
Mutsu Establishment Marine Technical Services Division	34 (5.27%)	
Reactor Instrumentation Lab.	14 (2.17%)	10 (11.36%)
Shielding Lab.	13 (2.01%)	
JMTR Irradiation Division I	7 (1.08%)	6 (6.81%)
Solid State Chemistry Lab.	6 (0.93%)	8 (9.09%)
Production Division	4 (0.62%)	
Engineered Barrier Materials Lab.	1 (0.15%)	24 (27.3%)
Material Innovation Lab.		9 (10.22%)
Outside users		
National Lab. for High Energy Phisics	123 (19.09%)	
Fuji Photo Optical Co. Ltd.	2 (0.31%)	
Toyo Ink Production Ltd.	1 (0.15%)	
Fujitsu Co. Ltd.		11 (12.5%)
Nihon Texas Instrument Ltd.		2 (2.27%)
Universities(Total)	199 (30.9%)	18 (20.45%)
TOtal	644	88

1) Number of applications

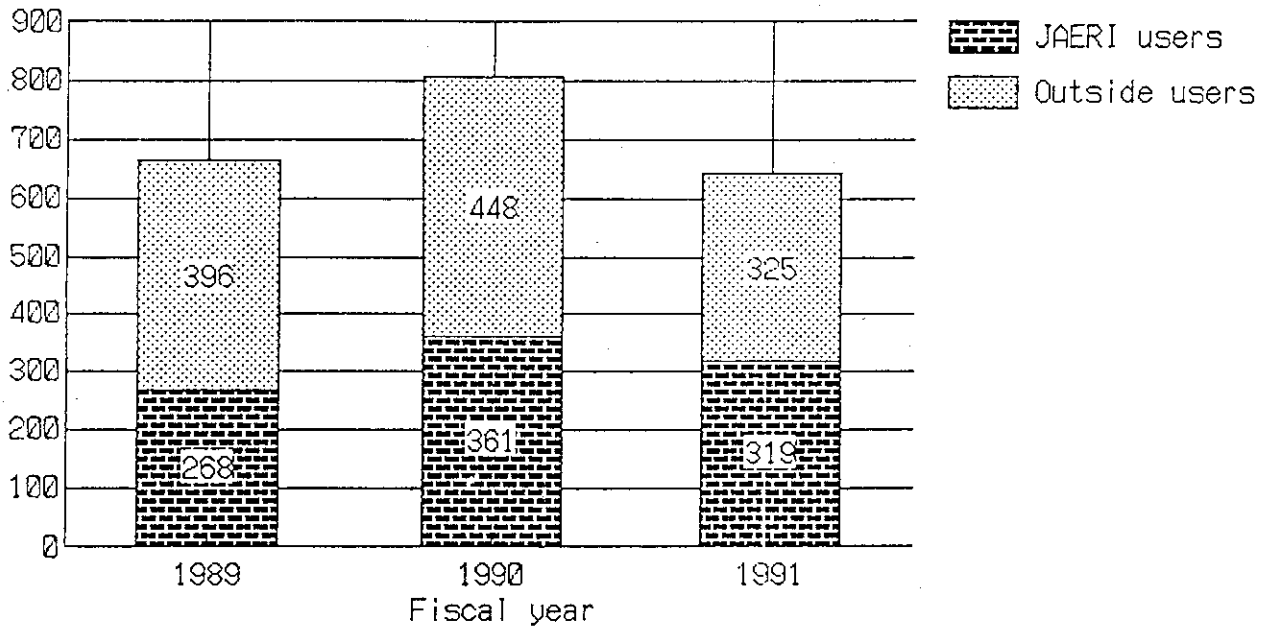

2) Days spent by users

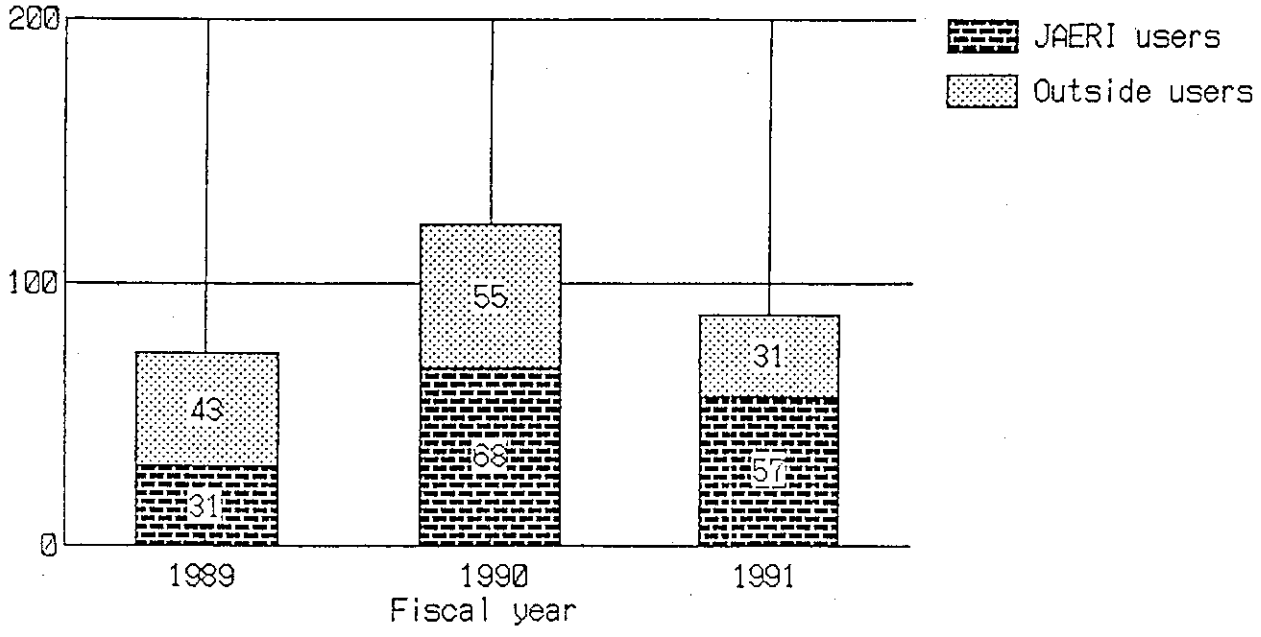

Fig.1 Number of applications and days spent by users (depending on the fiscal years).

13. STUDIES ON SEPARATION AND FIXATION OF VOLATILE RADIONUCLIDES

G. Fujisawa, N. Ishikawa, Y. Komaki, T. Sakurai, A. Takahashi,
S. Suzuki, A. Yokoyama, K. Yokoyama, M. Ohnuki, and T. Adachi

13.1 Distribution of iodine in the dissolution of spent PWR-fuel pellets

13.1.1 Introduction

Radioiodine ^{129}I, the longest lived of the volatile radionuclides, has a high potential to leak to the environment through natural paths, so that it is necessary to properly control it in reprocessing. It is especially important to understand the behavior of iodine in the dissolution, because this step determines the method and quantity of iodine distribution within reprocessing plants. However, the literature treating dissolution of actual spent fuel is not much.

According to experimental data so far presented,[1,2] more than 99% of the iodine volatilizes into dissolved off-gas and only less than one percent remains in the fuel solution. In addition to these two, however, there may be other paths to which iodine is distributed, i.e., insoluble residue, hull, and the wall of dissolved; the foregoing reports said nothing about this point. Of these, the insoluble residue deserves special attention because its amount tends to increase with increasing burnup of fuels. Its interaction with iodine is one of our concerns.

We are also concerned with iodine species remaining in the fuel solution. Extremely high radioactivity of the solution and weak radioactivity of ^{129}I make it difficult to directly identify them in the solution. The main component has been postulated to be iodate (IO_3^-) and NOx sparge through the solution has been proposed for its expulsion by earlier workers.[3] In our previous work,[4] however, colloid of AgI and PdI_2 constituted the main part of iodine quantity in a simulated spent-fuel solution. There is, thus, an uncertainty for iodine species remaining in the fuel solution.

The present work intended to clarify the behavior of iodine in the dissolution, especially its interaction with the insoluble residue as well as iodine species in the fuel solution. Besides dissolution of actual spent-fuel pellets, amounts of iodide (I^-) was added to a simulated spent-fuel solution to obtain back-up data for those purposes.

13.1.2 Experimental

1) Dissolution of spent-fuel specimens and analysis of ^{129}I.

Spent-fuel specimens of 1 to 3 g was put in a 100 ml-Pyrex flask together with their hull and was dissolved in 4 M HNO_3 (30 ml) at 100 °C. Helium flow bubbled the solution at a flow rate of 40 ml/min to carry the volatilized iodine to a iodine filter consisting of a silver-impregnated paper filter and a triethylenediamine-impregnated charcoal filter. Iodine trapped there was determined by gamma spectrometry using a multichannel pulse height analyzer (Canberra Series 35 plus) with a germanium detector.

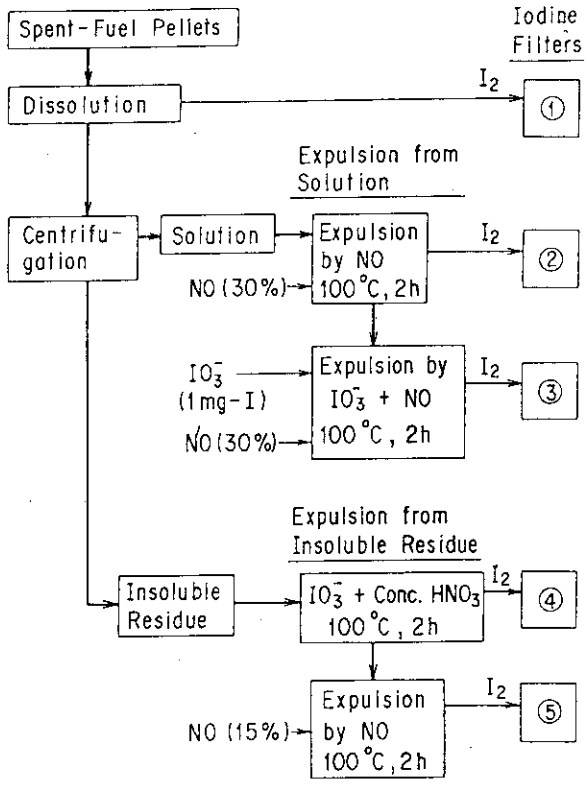

Fig. 1 Analytical process of determining iodine (^{129}I) quantity in spent-fuel pellets.

The dissolution was followed by centrifugation to separate the insoluble residue from the solution, and the expulsion of iodine was carried out for both of them for determination of iodine (^{129}I). Figure 1 illustrates the analytical procedure. Iodine in the solution was first expelled by passing a gas flow of 30% NO plus 70% N_2 (total flow rate, 20 ml/min) through the solution at 100 °C for 2 h; the iodine expelled was collected on a renewed iodine filter. (30% NO was equivalent to 10% NO_2 in its efficiency of expelling iodine from 3 to 4 M HNO_3.) To further expel remaining iodine,[3,4] 1 ml of potassium iodate solution including 1 mg-I/ml was put in the solution, and after heated at 100 °C for 1h, the solution was again bubbled with the NO flow for 1h. In the case of the simulated spent-fuel solution, this expulsion process removed 55 to 98% of iodine in the solution, depending upon the composition of iodine species in it.[4]

Expulsion of iodine from the insoluble residue was carried out in the

same way as in our previous work.[5] The residue was first heated in 30 ml of a concentrated nitric acid solution including IO_3^- (6 mg-I) at 100 °C for 2h to elute iodine from residue to solution. Then, the solution was bubbled with a NO flow for 2h to transfer iodine from solution to the iodine filter. These procedures can transfer 70±20% of iodine in the residue onto the filter.[5] After every experimental step shown in the figure, the iodine filter was replaced by new one; so, five sets of the filter were used in an experimental run. A film of polyacetal was placed upstream of the iodine filter to remove preliminarily aerosol including strong gamma-emitter such as ^{137}Cs and ^{106}Ru which might interfere with gamma-spectrometry of ^{129}I collected on the iodine filter.

2) Supplemental experiments using simulated spent-fuel solution.

To understand the iodine species in the actual fuel solution, an amount of iodine (I^-) labeled with ^{131}I was added into a simulated spent-fuel solution at 100 °C and its behavior was examined. This solution was prepared so as to be equivalent to the dissolution of spent fuels with a burnup of 40 GWD/t; it contained uranium with concentration of 50 g-U/l and corresponding amounts of several fission-product elements, i.e., Pd, Ag, Sr, Ba, La, Ce, Ru, Zr, Nd, and Mo.[4] Iodine species produced in the solution was analyzed by a carbon tetrachloride (CCl_4) extraction method which identified dissolved iodine, I_2(aq), organic iodine, I^-, IO_3^-, and colloidal iodine in this order with the aid of gamma spectrometry.[4,5]

Table 1 The amount of iodine (^{129}I) volatilized in the analytical process for spent-fuel pellets. The numbers 1 to 5 correspond to those in Fig. 1.

Type of Fuel Sample (burnup) Weight	Wt. of Insoluble Residue mg	Iodine (^{129}I) volatilized, Bq/g-U_0 (%)						Ⓑ Calculation by ORIGEN II Bq/g-U_0	Ⓐ/Ⓑ x 100
		① Dissolution	From Solution		From Residue		Ⓐ Total		
			② NO	③ IO_3^- + NO	④ IO_3^- + HNO_3	⑤ NO			
UO_2 (39.7 GWD/t) 2.250g (No.87H02)	7.8	968 (98.1)	8.5 (0.9)	3.2 (0.3)	N.D. (0.0)	6.8 (0.7)	986.5 (100.0)	1388	71.7
Gd_2O_3-UO_2 (21.2 GWD/t) 1.382g (No.89G05)	4.3	583 (88.1)	35.7 (5.4)	28.2 (4.3)	N.D. (0.0)	15.0 (2.3)	661.9 (100.0)	1000	66.2

N.D. --- not detected.

13.1.3 Results and discussion

1) Distribution of ^{129}I in the dissolution of spent-fuel specimen.

Table 1 shows the results of two experimental runs so far performed.

The one (87H02) is for 2.250 g of spent PWR-fuel pellets with burnup of 39.7 GWD/t, and the other (89G05), for 1.382 g of gadolinium-added PWR-fuel pellets with burnup of 25.7 GWD/t. In the former, the insoluble residue of 7.8 mg (0.35 wt.%) retained 0.7% of the total ^{129}I quantity collected on the iodine filters, while in the latter 2.3% of the total iodine quantity came form the insoluble residue of 4.3 mg (0.31 wt.%). Although the amounts vary between the two runs, the present work has revealed that part of iodine in spent fuels can be conveyed to the insoluble residue produced in the dissolution.

2) Iodine species in the insoluble residue.

As already described in our previous work,[6] the dissolution of simulated spent-fuel pellets also conveyed 2 to 5% of iodine in the pellets to the insoluble residue. This phenomenon was ascribable to the formation of slightly soluble iodides such as AgI and PdI_2, because heating the insoluble residue in nitric acid solution (100 °C) resulted in the release of elemental iodine (I_2) and the presence of Ag^+ and Pd_2^+ was necessary for iodine to be incorporated in the insoluble residue. The iodine which was found in the insoluble residue produced in the dissolution of actual spent-fuels, is considered to be the same as those described above, i.e., AgI and PdI_2.

3) Iodine species in the fuel solution.

Table 1 also shows that NO sparge still leaves a considerable amount of iodine in the solution; addition of excess amount of IO_3^- plus NO sparge was needed to further expel the remaining iodine. These finding suggest the presence of other iodine species besides IO_3^-. To understand these species, supplemental experiments were carried out using simulated spent-fuel solution.

Figure 2 shows the iodine species generated by addition of iodide (1 mg-I^-) to the solution at 100 °C; NO_2 (3% in N_2) was supplied to it to simulate dissolution of the fuels.

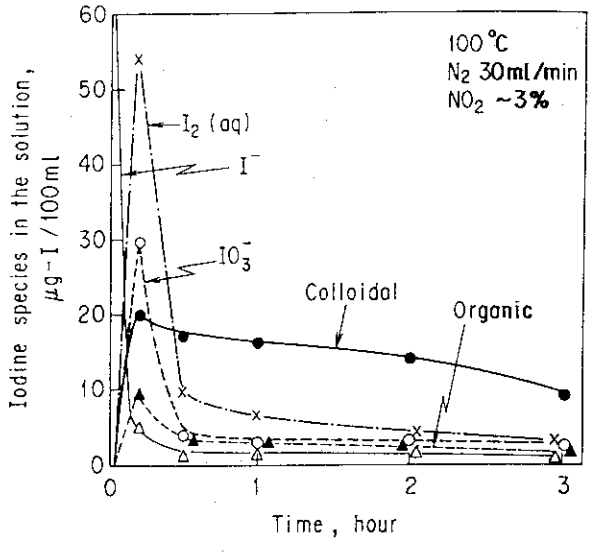

Fig. 2 Change of iodine (I^-) added to a simulated spent-fuel solution at 100 °C. One milligram of iodine (I^-) was added to 100 ml-simulated spent-fuel solution including uranium of 50 g-U/l and the corresponding amounts of fission product elements.

During 3h of heating, 98.5% of the added iodine volatilized into off-gas, and the main iodine species in the solution was not IO_3^- but colloidal iodine; presence of NO_2 interferes with formation of IO_3^-. To examine the behavior of colloidal iodine, I_2(aq) and IO_3^- in the expulsion process, iodide (1 mg-I^-) was heated in the solution without NO_2 supply in order to increase IO_3^- quantity, and then the expulsion of iodine was carried out in the same manner as that for actual spent-fuel solution shown in Table 1. During the expulsion process, iodine species in the solution have changed in their amounts as Figure 3 shows. While I_2(aq) and IO_3^- have been removed from the solution easily by the first NO sparge alone, colloidal iodine needs the second expulsion for its effective removal from the solution. Comparison of these results with those shown in Table 1 suggests that colloidal iodine constitutes the major part of iodine remaining in the actual spent-fuel solution.

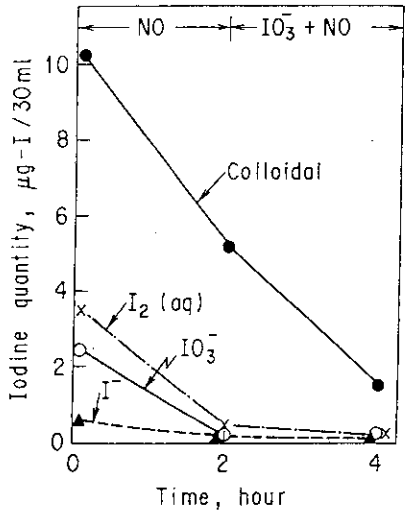

Fig. 3 Decrease in amount of iodine species in a simulated spent-fuel solution during the expulsion process consisting of the 'NO sparge' and the addition of excess IO_3^- plus NO sparge.

For the colloidal iodine produced in the simulated spent-fuel solution, the following results have been obtained:

(1) Heating the solution without NO_2 supply results in the decrease of colloidal iodine and volatilization of I_2. When a simulated spent-fuel solution (50 ml) including 8.3 μg of colloidal iodine was heated at 100 °C for 6h at N_2 flow rate of 20 ml/min, 4.2 μg of the iodine was trapped on the iodine filter as I_2, and 3.2 μg was oxidized into IO_3^-. At 30 °C, the colloid was decreased to 5.1 μg in 166h.

(2) The amount of the colloid increases with increasing concentrations of Ag^+ and Pd_2^+ in the solution. The results are the same as those obtained for the iodine in the insoluble residue,[5] and, hence, the colloidal iodine would be microparticles of AgI and PdI_2. The same colloid is expected to be formed in the dissolution of actual spent-fuels.

13.1.4 Conclusions

(1) The dissolution of spent PWR-fuel specimens at 100 °C can distribute

iodine(^{129}I) into the insoluble residue besides off-gas and solution.

(2) The dissolution leaves considerable amount of iodine in the solution, and its complete expulsion cannot be accomplished by NO or NO_2 sparge alone. The cause seems to be that colloid of AgI and PdI_2 constitutes the major part of the iodine species.

References

1) W. Hebel and G. Cottone (Eds.),"Management Modes of Iodine-129," (Harwood academic publishers, Brussels, 1981), p. 71.
2) A. Leudet, P. Miquel, P.J. Goumondy and G. Charrier, CONF-820833-V1, M.W. First Ed., Boston, 1983), p.639.
3) E. Henrich, R. Hufner and A. Sahm, IAEA-SM-245/16, (International Atomic Energy Agency, Vienna, 1980), p. 139.
4) T. Sakurai, A. Takahashi, N. Ishikawa and Y. Komaki, Nucl. Technol. **85**(1989)206.
5) A.W. Castleman, Jr., I.N. Tang and H.R. Munkelvitz, J. Inorg. Nucl. Chem. **30**(1968)5.
6) T. Sakurai, A. Takahashi, N. Ishikawa and Y. Komaki, Nucl. Technol. **94**(1991)99.

Publication list

[1] T. Sakurai, A. Takahashi, N. Ishikawa,and Y. Komaki,"The Behavior of Iodine in a Simulated Spent-Fuel Solution," Nucl.Tecnol. **85**(1989)206.
[2] T. Sakurai, A. Takahashi, N. Ishikawa, Y. Komaki, M. Ohnuki, and T. Adachi, "Behavior of Iodine in the Dissolution of Spent PWR-Fuel Pellets," (Proc. 3rd Int. Conf. Reprocessing and Waste Management, Vol. II, Sendai, 1991), p. 678.
[3] T. Sakurai, A.Takahashi, N. Ishikawa, and Y. Komaki, "The Interaction of Iodine with Insoluble Residue in the Dissolution of Simulated Spent-Fuel Pellets," Nucl. Technol. **94**(1991)99.

13.2 I_2 Monitoring in N_2 by Laser Induced Fluorescence Method

13.2.1 Introduction

A real-time, on-line monitoring of iodine-129 in spent fuel reprocessing off-gas streams would be required to monitor the flow of iodine in the process, to observe accidental large release of radioiodine and so on.[1,2] However, the on-line monitoring of the iodine-129 by conventional counting techniques is difficult because of its low specific activity and low energy decay products. A detection technique using laser such as a laser induced fluorescence and intracavity absorption laser spectroscopy is a promising candidate for the on-line monitoring of the iodine-129.[1] The studies on the monitoring I_2 using a visible CW laser[1-5] show that the detection techniques using laser are sensitive even in air or N_2 at atmospheric pressure. However, further work on the effects of gasses in the reprocessing off-gas stream on the monitoring I_2 are needed to apply such a technique to an on-line monitoring of I_2 in the reprocessing off-gas stream. For example, the reprocessing off-gas contains other molecules than I_2, and these may interfere with the detection of I_2 in the reprocessing off-gases. Especially NO_2, whose fraction is a few percent of total off-gases, has absorption bands in visible region. In some studies,[3,4] the isotopically selective detection of I_2 has been accomplished for neat I_2 sample. However, the isotopic selectivity of the absorption lines may be lost at atmospheric off-gas pressure because of the collisional broadening of the absorption lines. Moreover, the I_2 fluorescence is quenched by the reprocessing off-gases. So, it is important to know the gas pressure effects on the quenching and the isotopic selectivity.

In this work, the effects of the N_2 gas pressure (or concentration) to the isotopic selectivity and the I_2 fluorescence intensity are studied by measuring high resolution fluorescence excitation spectra of $^{127}I_2$ for the $B^3\Pi(0_u^+) \leftarrow X^1\Sigma(0_g^+)$ electronic band system near ^3He-^{20}Ne laser frequency at various concentrations of N_2. The possibility of interference from NO_2 is also examined. Moreover, the fluorescence from $^{127}I_2$ molecules in N_2 flow at atmospheric pressure was detected at various concentrations of $^{127}I_2$ molecules as a test of feasibility of on-line I_2 monitoring by a ^3He-^{20}Ne laser-induced fluorescence technique.

13.2.2 Experimental

An experimental apparatus for continuous monitoring of $^{127}I_2$ is shown in Fig. 1. Iodine molecules flowed with the N_2 carrier gas at a flow rate of 50

ml/min through a fluorescence cell, made of monel metal and having brewster-angle sapphire windows. I_2 samples at various concentrations in the carrier gas were prepared by passing the carrier gas saturated with I_2 at room temperature through a cold glass tube maintained at desired temperatures from −60 to 0 °C. The I_2 concentration was calculated from the relationship between the vapor pressure and temperature in ref. 6. The 632.8 nm radiation from a ^3He−^{20}Ne laser (Nihon Kagaku Engineering NEO−50MS; 50mW) was mechanically chopped, typically at 854Hz, by a slotted wheel, and then passed through the fluorescence cell to excite I_2. Fluorescence from $^{127}I_2$ was observed at right angle to the direction of the He−Ne laser beam by a photomultiplier (PM; Hamamatsu R649). A long-pass wavelength filter was placed in front of the PM to eliminate the scattered He−Ne laser radiation. Output from the PM was analyzed by a lock-in amplifier (NF Electronic Instruments 5610B) synchronized with the chopping frequency and recorded by a strip-chart recorder.

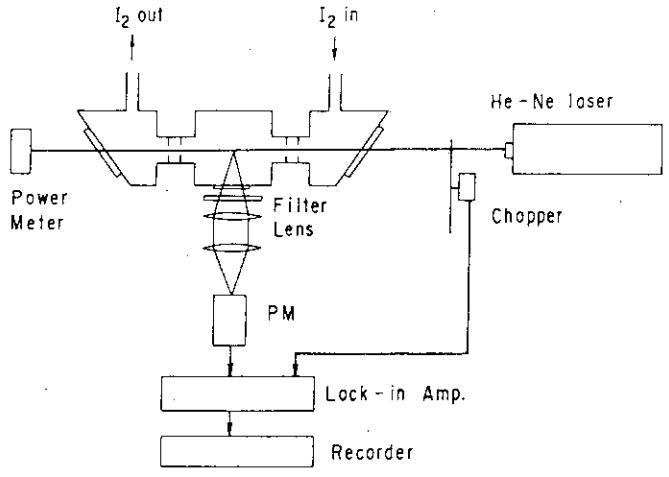

Fig.1 Experimental Apparatus for continuous monitoring of I_2.

High resolution fluorescence excitation spectra of $^{127}I_2$ and were measured using the apparatus shown in Fig. 1 with small change described below; the He−Ne laser was replaced by a ring dye laser (Spectra Physics 380A) pumped by an argon-ion laser (Spectra Physics 168). A part of the laser radiation was split into a Fabry−Perot interferometer with a free spectral range of 2 GHz (Spectra Physics 450−03) to monitor the laser frequency. The fluorescence excitation spectra of both isotopic molecules were measured simultaneously by placing in a line the fluorescence cell filled with $^{127}I_2$.

The $^{127}I_2$ was supplied by Junsei Pure Chemical Co. and used without further purifications. Nitrogen dioxide, supplied by Matheson Co., was purified by oxidizing impurity N_2O_3 to NO_2 by bubbling oxygen gas into the NO_2.[7)]

13.2.3 Results and Discussion

Figure 2 shows the N_2 concentration dependence of the $^{127}I_2$ fluorescence

excitation spectra near the $^{3}He-^{20}Ne$ laser frequency (15797.998 cm^{-1}) at a constant I_2 concentration of 7×10^{15} molecules/cm^3. As a result of the collisional broadening of the absorption lines, each vibrational-rotational line broadened with increasing the N_2 concentration and only the unresolved spectrum could be observed at the N_2 concentration of 2.4×10^{19} molecules/cm^3. Since the similar behavior on buffer gas concentration is expected to the $^{129}I_2$ and $^{127}I^{129}I$ fluorescence excitation spectra, the isotope selective excitation of iodine molecules cannot be expected at the atmospheric buffer gas pressure. In fact, the fluorescence intensity from the $^{129}I_2$ excited by the $^{3}He-^{20}Ne$ laser was the same as that from the $^{127}I_2$ at the atmospheric air pressure[5], although the fluorescence intensity from the $^{129}I_2$ is larger than that from the $^{127}I_2$ at zero N_2 pressure.

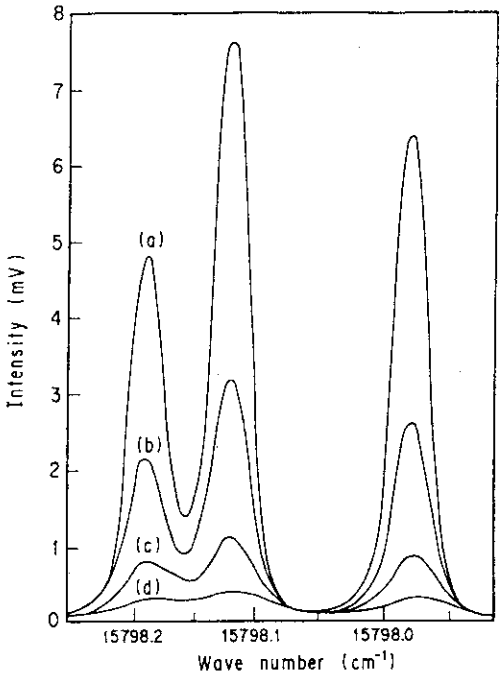

Fig.2 Fluorescence excitation spectra of $^{127}I_2$ at N_2 concentration of (a) 6.8×10^{17}, (b) 1.3×10^{18}, (c) 2.7×10^{18} and (d) 5.2×10^{18} molecules/cm^3. The concentration of I_2 is constant at 7×10^{15} molecules/cm^3.

The fluorescence intensity, $I_f(\nu,[I_2],[N_2])$, at the excitation frequency ν is written by the equation;

$$I_f(\nu,[I_2],[N_2]) = \frac{A\sigma(\nu,[I_2],[N_2])I[N_2]}{\tau_0^{-1} + k_{I_2}[I_2] + k_{N_2}[N_2]} \qquad (1)$$

where $\sigma(\nu,[I_2],[N_2])$ is the absorption cross section as a function of ν, $[I_2]$ and $[N_2]$, I is the laser intensity, k_{I_2} and k_{N_2} are the electronic quenching rate constants of the B $^{3}\Pi(0_u^{+})$ state by the collision with I_2 and N_2 molecules, respectively, τ_0 is the lifetime of the B $^{3}\Pi(0_u^{+})$ state and A is proportional constant. From the values of τ_0, k_{I_2}[8] and k_{N_2} obtained by the kinetic plot of the N_2 concentration dependence of the peak intensity for the P(33) line of the 6-3 band, the fluorescence intensity is approximated by the equation

$$I_f(\nu,[I_2],[N_2]) = \frac{A\sigma(\nu,[I_2],[N_2])I[I_2]}{k_{N_2}[N_2]} \qquad (2)$$

at the N_2 concentration above 6×10^{17} molecules/cm^3. Since the ratio of $[I_2]$ to

$[N_2]$ is independent of the gas pressures in the fluorescence cell, the fluorescence intensity is proportional to the absorption cross section. The relative absorption cross sections were calculated by using the absorption lineshape which consists of the doppler and collision broadened hyperfine structures and the collision broadening constant obtained by fitting the absorption lines to a analytical expression for the lineshape. The relative absorption cross sections at the peak frequency of the P(33) line of the 6−3 band and the He−Ne laser frequency are plotted as a function of $[N_2]$ in Fig 3. The cross section at the peak frequency of the P(33) line of the 6−3 band monotonically increases with decreasing N_2 concentration. Therefore, the I_2 detection limit will be improved by reducing the sample gas pressure. On the other hand, the fluorescence intensity is not so much improved by reducing sample gas pressure in the case of exciting $^{127}I_2$ by the $^3He-^{20}Ne$ laser, because the absorption cross section decreases with decreasing the concentration at low N_2 concentration. Since absorption line width decreases with decreasing N_2 pressure, reducing sample gas pressure in the fluorescence cell improves both the I_2 detection limit and the isotopic selectivity.

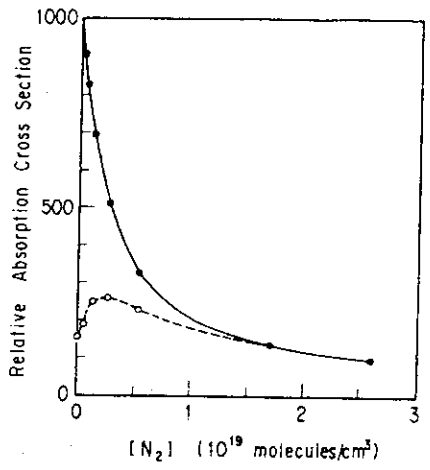

Fig.3 N_2 concentration dependence of the absorption cross sections at the peak frequency of the P(33) line of the 6−3 band (●) and the $^3He-^{20}Ne$ laser frequency (○).

The fluorescence intensity of $^{127}I_2$ excited by the $^3He-^{20}Ne$ laser in the N_2 at atmospheric pressure are plotted as a function of the I_2 concentration in Fig. 4. The error bars associated to each

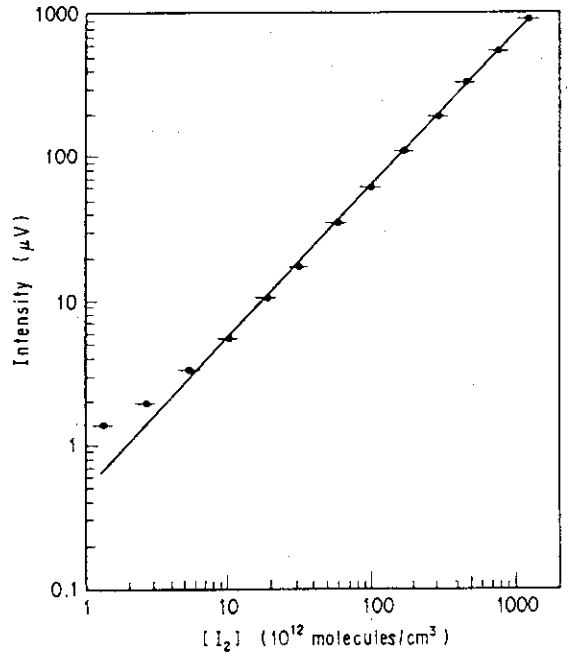

Fig.4 I_2 concentration dependence of the fluorescence intensity of I_2 excited by the $^3He-^{20}Ne$ laser at a constant N_2 pressure of 101 kPa and room temperature.

plot represent the fluctuation of the I_2 concentration which is due to the variation of the temperature of the cold glass tube. The fluorescence intensity is almost linear with the I_2 concentration, and the I_2 detection limit of 5×10^{12} molecules/cm^3 was achieved. Although this value is about 10 times as high as the reported detection limits,[2,5] the detection limit will be further improved by using the intracavity configuration of the fluorescence cell. Because a few percent NO_2 is contained in reprocessing off-gas and has weak absorption at the He-Ne laser frequency, we measured the NO_2 fluorescence intensity by exciting 1.4 % NO_2 in N_2 at atmospheric pressure by the ^{3}He−^{20}Ne laser in order to clarify whether NO_2 interferes with the detection of I_2. Since the NO_2 fluorescence intensity is 60 times as high as the I_2 fluorescence intensity at the detection limit, NO_2 in the off-gases should be removed before monitoring small concentration of I_2.

13.2.4 Conclusions

Reducing the sample gas pressure in the fluorescence cell of an on-line I_2 monitor based on the laser induced fluorescence method was found to improve both the I_2 detection limit and the isotopic selectivity because of the decrease in the quenching rate by N_2 and in the absorption line widths. Since a few percent NO_2 molecules in the reprocessing off-gasses was found to interfere with the detection of trace amount of I_2 molecules, the NO_2 molecules should be removed from the off-gasses before detecting I_2 molecules. Finally, $^{127}I_2$ in N_2 at atmospheric pressure were detected down to 5×10^{12} molecules/cm^3 by a ^{3}He−^{20}Ne laser induced fluorescence technique with extracavity configuration of the fluorescence cell.

References

1) J. Dube and Y. Zabaluev, Proc. 15th DOE Nuclear Air Cleaning Conference **1**(1979)971.
2) A. P. Baronavski and J. R. McDonald, Proc. 15th DOE Nuclear Air Cleaning Conference **1**(1979)901.
3) J. P. Hohimer and P. J. Hargis, Jr, Anal. Chem. **51**(1979)930.
4) R. W. Goles, R. C. Fukuda, M. W. Cole and F. P. Brauer, Anal. Chem. **53**(1981)776.
5) A. C. Vikis and R. MacFarlane, in Gaseous Effluent Treatment in Nuclear Installations (Proc. Conf. Luxembourg, 1985), EUR 10580, CEC, Brussels, 686 (1986)
6) Kagakukougakubinran, p.26 (Maruzen, 1978) (in Japanese)

7) I. R. Beattie, Mellor's Comprehensive Treatise in Inorganic and Theoretical Chemistry Vol. 8, suppl. 7, p. 247 (Longmans, 1967)
8) K. C. Shotton and G. D. Chapman, J. Chem. Phys. **56**(1972)1012.

Publication list

[1] A. Yokoyama, G. Fujisawa, T. Sakurai and K. Suzuki, "Buffer gas effect on monitoring I_2 by a laser induced fluorescence method", Spectrochimica Acta, **47A**(1991)567.

13.3 Development of Two Frequency (CO_2-N_2O) Laser

13.3.1 Introduction

For exciting a molecule vibrationally, the first barrier is anharmonicity of vibration. It is estimated that difference between energy levels of vibration in higher vibrational state is much narrower than that in lower state. Generally, a molecule can be vibrationally excited to v=2-3 state by single-frequency laser and excitation up to the higher levels is difficult due to deviation of the difference of energy levels of vibration from laser frequency.

In case of comparatively large molecule like SF_6, quasi-continuum state begins at v=3-4 and multi-photon excitation and dissociation of the molecule is possible. But, in case of the smaller molecule like BCl_3 and BBr_3, the quasi-continuum state begins at about v=8-9 and it is difficult to excite those molecules to the quasi-continuum state by single-frequency laser. It has been reported that strong laser field of 1G watt/cm^2 is necessary for dissociation of BCl_3 molecule by single-frequency CO_2 laser[1].

We have proved that excitation by multifrequency laser is effective for the molecule consisting of small number of atoms[2]. We have constructed multifrequency NH_3 laser[3] for excitation and dissociation of BBr_3 and have shown that in addition to the first laser frequency to excite ground state BBr_3, the second laser frequency to excite BBr_3 in excited state is necessary for effective sequential excitation. For example, the excitation of $^{10}BBr_3$, whose peak frequency in the infrared absorption spectrum is at 857 cm^{-1}, by the NH_3 laser with the two frequencies 854 cm^{-1} and 828 cm^{-1} is effective for the dissociation of the molecules. The $^{11}BBr_3$ with the peak absorption frequency of 821 cm^{-1} are also effectively dissociated by the NH_3 laser with the two frequencies of 816 and 781 cm^{-1}. The frequencies 828 and 781 cm^{-1} are estimated to serve for exciting $^{10}BBr_3$ and $^{11}BBr_3$ in excited

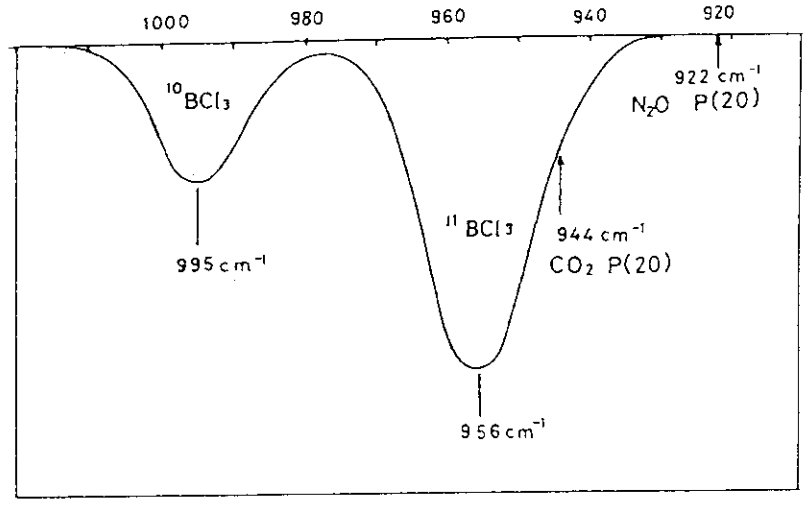

Fig. 1 Infrared spectrum of natural BCl_3 and positions of typical N_2O and CO_2 laser lines.

state, respectively.

To develop the above multi-frequency excitation method, irradiation of BCl_3 by CO_2-N_2O laser is planned. In Fig. 1, infrared absorption of BCl_3 and typical (P(20) line) frequency of CO_2 laser and N_2O laser is shown . It is expected that the frequency 922 cm^{-1} of N_2O laser is effective for excitation of the $^{11}BCl_3$ in excited state.

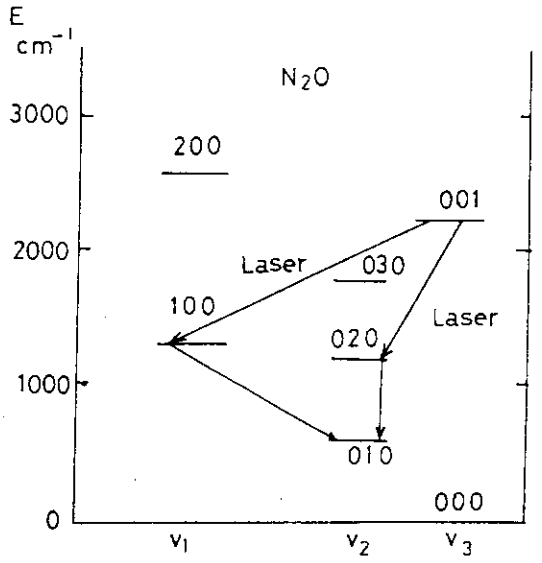

Fig. 2 Vibrational energy level of N_2O molecule.
ν_1; symmetric stretching
ν_2; bending
ν_3; antisymmetric stretching

13.3.2 Experimental and results

Energy levels of vibration of N_2O is shown in Fig. 2. The wavelength of N_2O laser is slightly longer than that of CO_2 laser. Because of lack of symmetry of N_2O molecule, oscillation of odd number P line, for example P(19) line etc., is also possible and fine tuning of the N_2O laser is useful for far-infrared laser.

The CO_2-N_2O laser was made by modifying the CO laser.[4] The laser tube is made of pyrex with the dimension of 140mmϕ x 1600mmL. The resonator consists of gold-coated mirror and ZnSe output mirror with 90% reflectivity at 10.6 μ. Capacity of the main discharge capacitor is 0.05 μF and that of preionizer capaci-

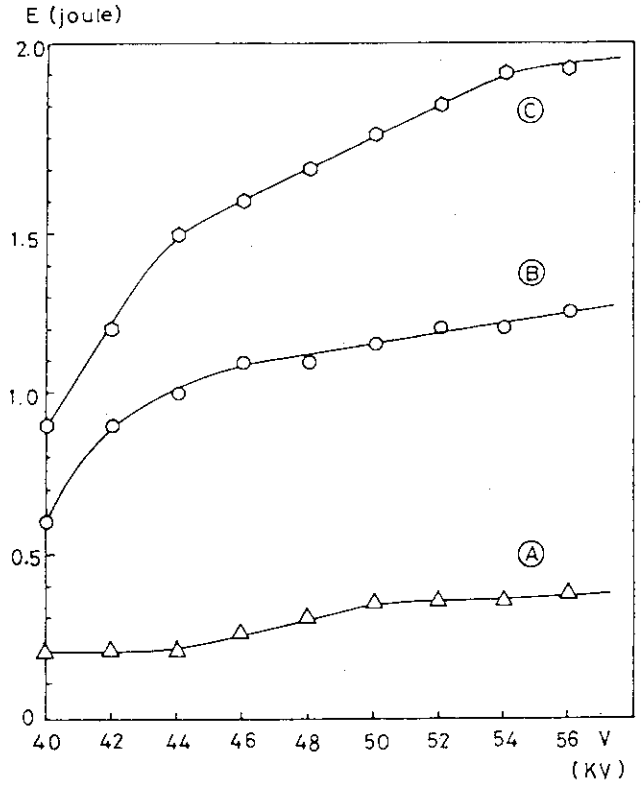

Fig. 3 Discharge voltage V and gas consumption dependence of output of N_2O laser E.
A) N_2O : N_2 : He = 1 : 0 : 9
B) N_2O : N_2 : He = 1 : 1 : 8
C) N_2O : N_2 : He = 1 : 2 : 7

tor is 20 nF. The size of output laser beam is 60 x 60 mm^2. The maximum discharge voltage is about 60 KV. The pulse energy of the laser was measured by ED 500 energy meter (Gentec). The energies of CO_2 P(20)line and N_2O P(20) line of the CO_2N_2O laser pulse were measured by combining CT−10 spectrometer (JASCO) and ED 200 energy meter (Gentec). The pulse form of the laser was measured by HgCdTe detector (Labimex) in room temperature and oscilloscope.

One of difficulties of N_2O laser excited by discharge is electron attachment to N_2O molecule,

$$N_2O + e^- \rightarrow N_2O^-$$

which hinders homogeneous discharge in high concentration of N_2O. Usually, to cancel this effect, H_2 and CO gas are added to N_2O gas[5].

$$N_2O^- + H_2 \rightarrow H_2O + N_2 + e^-$$

But, in our experiment, H_2 or CO were not added because of some fear of the explosion. The output of N_2O laser can be increase by vibrational energy transfer. In Fig. 3, the output of N_2O laser increases markedly by addition of N_2 gas due to energy transfer from excited N_2 to N_2O molecule. But, addition of N_2 brings about the increase

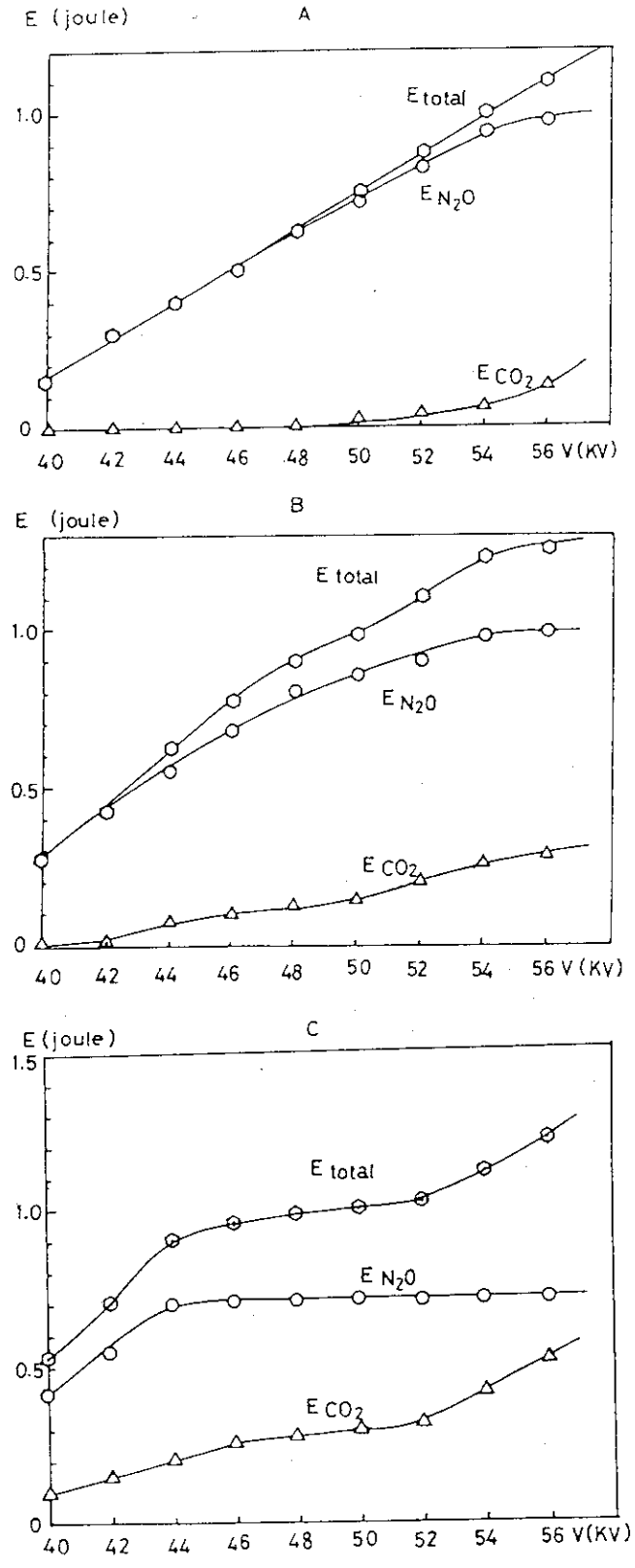

Fig.4 Discharge voltage V and total pressure of working gas dependence of output of N_2O laser. Gas composition is N_2O 10.52%, CO_2 5.26%, N_2 5.26%, He 78.96%. Total pressure A) 285torr, B) 250torr, C) 200torr

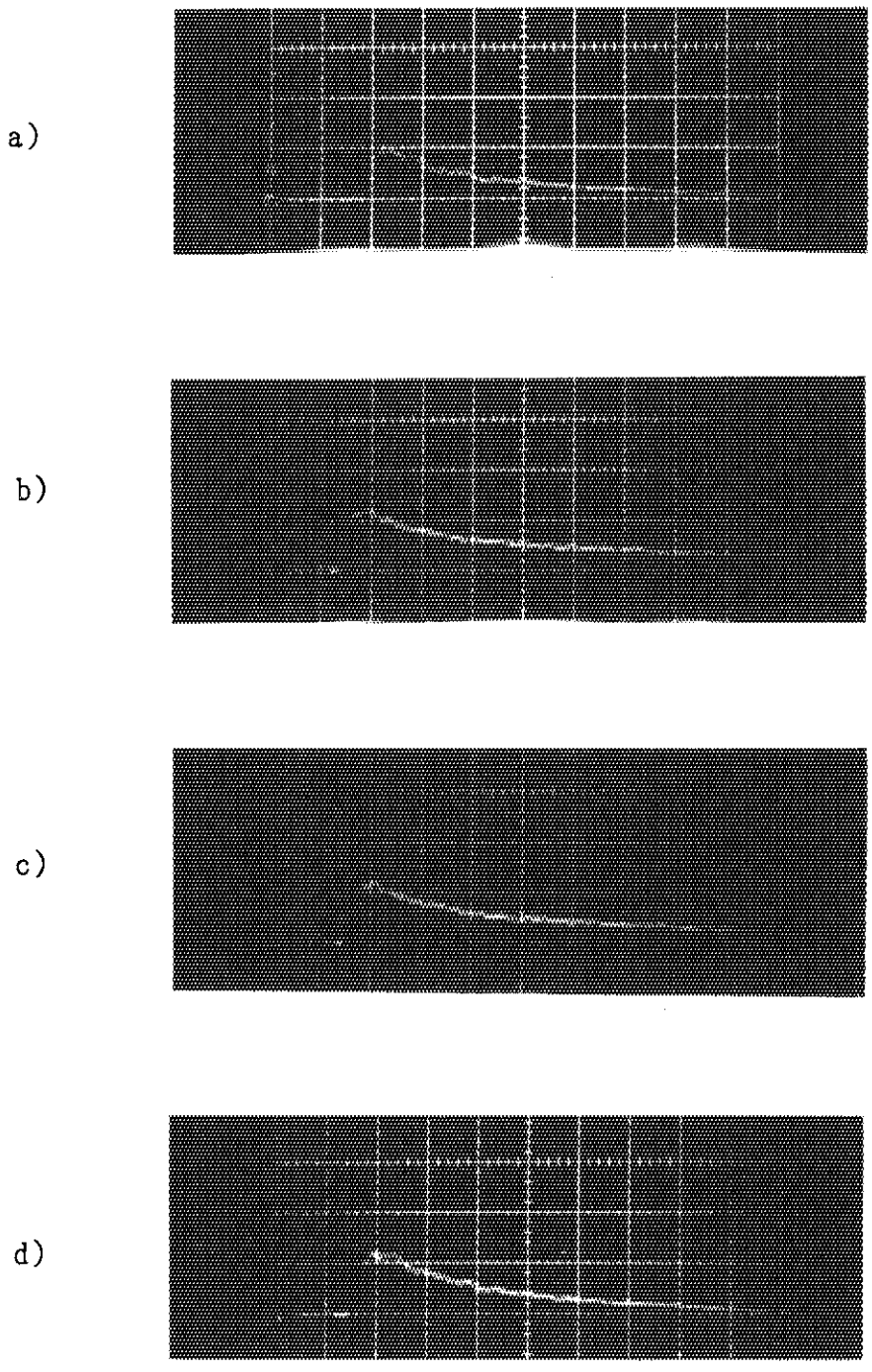

Fig. 5 Pulse form of N_2O laser of various gas composition. Horizontal line; 0.5 μsec/div.
a) N_2O 30 torr + He 225torr b) N_2O 30torr + N_2 15torr + He 225torr
c) N_2O 30torr + CO_2 15torr + He 225torr d) N_2O 30torr + CO_2 15torr + N_2 5torr + He 225torr

of the laser pulse width. Laser oscillation of CO_2–N_2O system is complicated, depending on the total gas pressure. In Fig. 4, the outputs of CO_2 P(20) and N_2O P(20) as a function of total gas pressure are shown. The variation of the outputs has not been analyzed due to lack of relaxation data of excited N_2O and the other gases.

The laser pulse forms of N_2O, N_2O–N_2, N_2O–CO_2 and N_2O–CO_2–N_2 systems are shown in Fig. 5. Both the peak and the tail of the laser pulse increase by addition of N_2 and CO_2 gas. It seems that energy transfer from excited CO_2 to N_2O occurs and it is estimated from pulse width that intermolecular rotational energy transfer by collisions of N_2O molecules is comparatively slow.

Kinetic modeling of N_2O laser will be possible by the calculation of the optical gain for the rotation-vibration transition of N_2O.

References

1) R.V. Ambartsumyan, V.S. Letkov, E.A. Ryabov and N.V.Chekalin, JETP Lett., **20**(1974)273
2) K. Suzuki, G. Fujisawa, A. Yokoyama, US Patent No 4, 775, 453(1989)
3) K. Suzuki, A. Yokoyama, G. Fujisawa, N. Ishikawa, M. Iwasaki, JAERI-M 88-168(1988)
4) "Department Chemistry Progress Report" p258, JAERI-M 89-058(1989)
5) V.V. Apollonov, G.G. Baitsur, G. Kononov, A.M. Prokhorov, S.K. Semenov, K.N. Firsov and V.A. Yamshchikov, Sov.J.Quatum Electron. **19**(1989)839

Publication List

[1] K. Suzuki, G. Fujisawa and A. Yokoyama, "Separation Method of Boron Isotopes" US Patent No 4,775,453 (1989)
[2] Y. Ikezoe, S. Soga, K. Suzuki and S. Ohno, "CO_2 Laser Photolysis of Clustered Ion (1)" JAERI-M 90-141(1990)

13.4 Molecular beam study on infrared multiphoton dissociation of 1,2-dichlorotrifluoroethane

13.4.1 Introduction

Photofragmentation translational spectroscopy (PTS) is an experimental method for studying dynamics of elementary photodissociation processes and elucidating pathways of photodissociation by measuring time-of-flight (TOF) spectrum of photoproducts under collision free conditions. If a mass spectrometer with an electron impact ionizer is used as a detector of neutral products, daughter ions of the products are easily produced through ionization-fragmentation processes of the products. This may cause the difficulties of the identification of neutral photoproducts produced through several competitive photodissociation pathways and sequential secondary photodissociation processes. Since kinetic energy distributions for different dissociation processes and velocity of photoproducts are , however, usually different, signals from different products shows different peak arrival times on the TOF spectrum and these can be distinguished.[1] For example, when benzene (C_6H_6) is irradiated at 193 nm, three competitive dissociation channels as one photon processes are open[2]:

$$C_6H_6 \rightleftharpoons C_6H_5 + H \quad (1)$$
$$C_6H_4 + H_2 \quad (2)$$
$$C_5H_3 + CH_3 \quad (3)$$

Moreover, C_6H_5 and C_6H_4 dissociate through secondary dissociation channels:

$$C_6H_5 \rightleftharpoons C_4H_3 + C_2H_2 \quad (4)$$
$$C_6H_4 + H \quad (5)$$
$$C_6H_4 \longrightarrow C_6H_3 + H \quad (6)$$

Although signals at m/e 62 ($C_5H_2^+$) come not only from the daughter ion of C_5H_3 produced through reaction (3) but also from daughter ions of C_6H_5, C_6H_4 and C_6H_3 produced through other channels, the C_5H_3 shows the fastest peak on the TOF spectrum at m/e 62 and can be easily distinguished from the daughter ions of other products.

Infrared multiphoton dissociation (IRMPD) of halogenated hydrocarbons are attractive for laser isotope separation because of its intrinsic high isotopic selectivity, and were widely studied for its application to the laser isotope separation.[3] Moreover, since IRMPD occurs under collision free conditions, this is powerful excitation tool for studying unimolecular dissociation without interference of collisional effects. The PTS technique has been successfully applied to the studies on the IRMPD of many molecules by Lee et al.[4] In this

paper, the IRMPD of 1,2-dichloro-trifluoroethane (DCTFE) is presented.

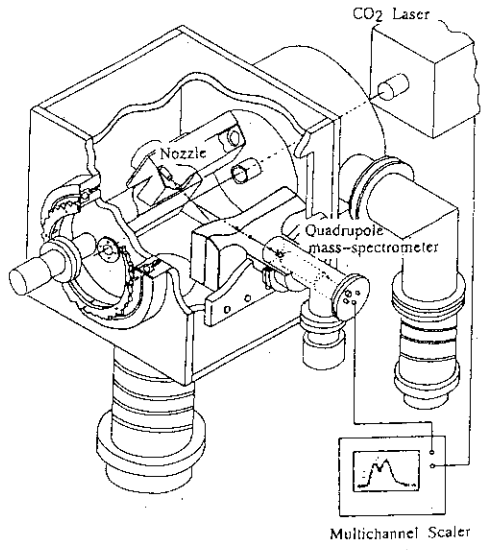

Fig. 1 Molecular beam machine for the photo-fragmentation translational spectroscopy

13.4.2 Experimental

A molecular beam machine for the PTS is shown in Fig. 1. This machine consists of three parts; i.e., a source region where a continuum molecular beam is formed, a main region where the molecular beam and a laser beam crosses and detector region where dissociation products are detected with a quadrupole mass spectrometer with an electron impact ionizer. The molecular beam was formed by expanding 200torr of DCTFE into the source region through a 0.1 mm diam nozzle. The nozzle was heated at 280 °C to enhance multiphoton absorption and prevent from the formation of clusters. The pressure in the source region was maintained at $\sim 10^{-4}$ torr by pumping it with a combination of a 6" diffusion pump and a 1500 l/sec turbomolecular pump while the beam was running. The molecular beam was collimated by being passed through two skimmers and crossed with the laser beam at the center of the main region. The main region was pumped to $\sim 10^{-7}$ torr by a 10" diffusion pump. A copper panel cooled at 77 K with liquid nitrogen are located in the main region to aid pumping capability. A differential pumping region was located between the source and main region and pumped with a 200 l/sec magnetically suspended turbomolecular pump. The laser beam from a TEA CO_2 laser (Lumonics TEA-841) was focus with a 30 cm focal length ZnSe lens. The size of laser spot was 3×3 mm^2 at the interaction region of the laser and the molecular beam. The DCTFE was excited at 9.504μm and 6 - 12 J/cm^2. The neutral fragments flying into the detector region through three slits was ionized with electron bombardment at 90 eV of the electron energy, mass-selected by a quadrupole mass spectrometer and detected by a secondary electron multiplier. The source region was pumped to $\sim 10^{-10}$ torr with a magnetically suspended turbomolecular pump. The wall surrounding the detector region was cooled at 77 K. Two differential pumping regions were located between the main and detector region and pumped with two 200 l/sec magnetically suspended turbomolecular pumps. The TOF spectra of the fragments were obtained by recording pulses due to the fragments on a

multichannel scaler, triggered with a pulse synchronized with the laser pulse, as a function of those flight time from the interaction region and the detector. Each TOF spectrum was obtained by accumulating signals for 400000 − 1000000 laser shots. The source region can be rotated with respect to the laser beam axis, and the spectra were obtained at 10° of the detector angle which is defined as the one between the molecular beam direction and the direction from the interaction region to the detector. The velocity distribution of the molecular beam was measured by a conventional TOF method. The molecular beam was chopped to ca. 12 μsec pulse by a slotted wheel and the TOF spectra of the molecular beam was measured at the detector angle of 0°.

13.4.3 Results and Discussion

For the primary photodissociation process, the following HCl and Cl elimination reaction occurs competitively:

$$CF_2ClCFClH \rightarrow CF_2CFCl + HCl \qquad \Delta H^\circ_0 = 32.5 \text{ kcal/mol} \quad \text{(Ia)}$$

$$\rightarrow (CF_2ClCF + HCl \qquad \Delta H^\circ_0 = 76.2 \text{ kcal/mol}) \quad \text{(Ib)}$$

$$\rightarrow CF_2ClCFH + Cl \qquad \Delta H^\circ_0 = 83.5 \text{ kcal/mol} \quad \text{(IIa)}$$

$$\rightarrow (CF_2CFClH + Cl \qquad \Delta H^\circ_0 = 85.1 \text{ kcal/mol}) \quad \text{(IIb)}$$

Hydrogen chloride from the concerted reaction I was observed in the TOF spectrum at m/e 36 (HCl^+) shown in Fig. 2(a). Although the heat of reaction calculated by *ab initio* molecular orbital calculations[5] is much higher for the four center elimination reaction Ia than for the three center elimination reaction Ib, the exit barrier is generally much higher for the four center elimination than for the three center elimination. Therefore, although the TOF spectra show only one peak, the activation energy for the reaction Ib may be comparable to that for the reaction Ia and both reaction may occur competitively. The TOF spectrum at m/e 82 ($C_2F_3H^+$), shown in Fig. 2(b), shows the fragment C_2F_3ClH produced by the simple bond rupture reaction II. Although the primary ion of C_2F_3ClH could not be observed, this must be due to the fragmentation of the radical by the electron bombardment, because the fragment was internally excited. The counter part of this fragment, Cl, is observed as the slow component in the TOF spectrum at m/e 35 (Cl^+) shown in Fig. 2(c). The fast component in the spectrum is the daughter ion of HCl. The linear momentum matching between the Cl and C_2F_3ClH assures the assignment for the reaction II. The primary ion of the counter part of HCl could not be observed. This is again due to the fragmentation in the ionizer by electron bombardment. The counter part C_2F_3Cl appears in the TOF spectra at m/e 31 (CF^+) and 66 ($CFCl^+$) as shown in Fig. 2. The fast parts of these spectrum cannot be fit by only the

reaction I. This indicates that the other reactions also occur. As a result of IRMPD, CF_2CFCl dissociates to CF_2 and CFCl[6]:

$$CF_2CFCl \rightarrow CF_2 + CFCl \quad (III)$$

Therefore, we tentatively assigned the fast component in the TOF spectra to the secondary products CF_2 and CFCl produced by the reaction III, in which the reactant CF_2CFCl was the product of the primary process Ia.

The distributions of the center of mass translational energies released from the reaction I and II, which are obtained by fitting the TOF spectra in Fig. 2, are shown in Fig. 3. The distribution for the reaction II shows that the peak of the distribution appears almost 0 kcal/mol and that the average translational energy release is low (1.6 kcal/mol). This character is typical for simple bond rupture reactions with very small exit barrier, because the excess energy distributes statistically in the internal mode of freedom of reacting molecules. On the other hand, the distribution for the reaction I shows that the peak translational energy is ca. 2 kcal/mol and that the average energy (5.6 kcal/mol) is larger than that for the reaction II. In the case of the concerted reaction like the reaction I with some extent of exit barrier, there are two types of internal energy to be released to the translational energy of the products: the excess energy above the activation energy will be distributed among internal modes of the reactant and only the

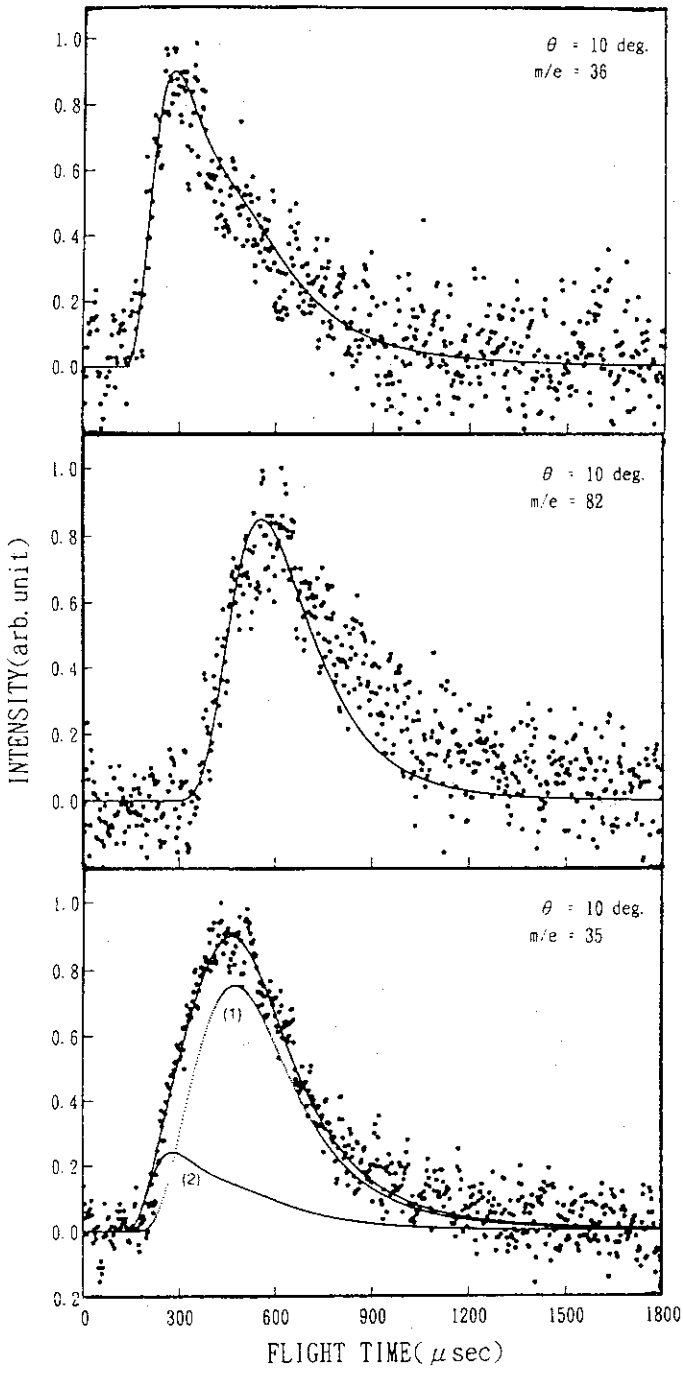

Fig. 2 TOF spectra observed at m/e 36 (a), 82 (b) and 35 (c). Curve (1) in (c) indicates the contribution from reaction (I), and curve (2) indicates the contribution from reaction (II).

energy distributed in the reaction coordinate will be released to the translational energy of the products. On the other hand, exchange of the exit barrier to the translational energy depends on the dynamics of the dissociation along the potential energy surface beyond the transition state. Therefore, it is reasonable that the average translational energy for the reaction I is larger than that for the reaction II.

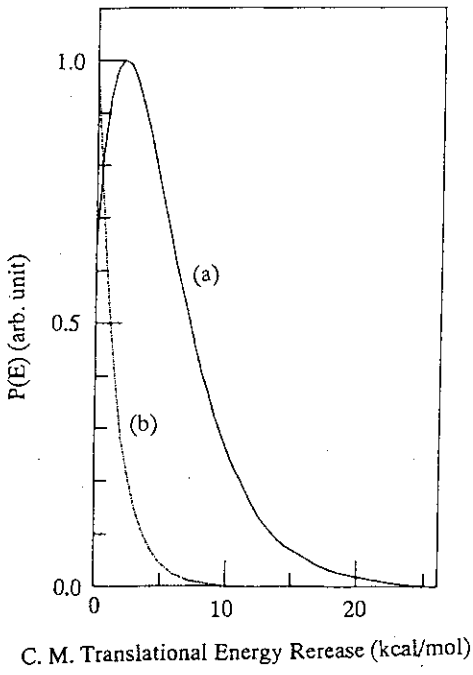

Fig. 3 Translational energy distributions for reaction I (a) and reaction II (b)

Acknowledgement

The authors would thank Professor Y. T. Lee for his kind advice on the construction of the molecular beam machine used in this experiment.

References

1) A.M. Wodtke and Y.T. Lee, in Advances in Gas Phase Photochemistry and Kinetics, J. Baggott and M. Ashfold, Eds. (Royal Society of Chemistry, London, 1987)
2) A. Yokoyama, X. Zhao, E.J. Hintsa, R.E. Continetti and Y.T. Lee, J. Chem. Phys. **92**(1990)4222
3) R.D. McAlpine and D.K. Evans, Adv. Chem. Phys. **60**(1985)31
4) P.A. Schulz, Aa.S. Sudbo, D.J. Krajnovich, H.S. Kwok, Y.R. Shen and Y.T. Lee, Ann. Rev. Phys. Chem. **30**(1979)379 and reference therein
5) See section 13.5 of this report
6) J.C. Stephenson, S.E. Bialkowski and D.S. King, J. Chem. Phys. **72**(1980)1161

Publication Lists

[1] M. Iwasaki, T. Sakka, S. Ohashi, H. Matsushita, A. Yokoyama and K. Suzuki, "H/D exchange reaction between $CHCl_3$ and D_2O in two-liquid-phase-system", J. Phys. Chem. **93**(1989)5139
[2] X. Zhao, R.E. Continetti, A. Yokoyama, E.J. Hintsa and Y.T. Lee, "Dissociation of cyclohexene and 1,4-cyclohexadiene in a molecular beam", J. Chem. Phys. **91**(1989)4118

[3] A. Yokoyama, X. Zhao, E.J. Hintsa, R.E. Continetti and Y.T. Lee, "Molecular beam studies of photodissociation of benzene at 193 and 248 nm", J. Chem. Phys. **92**(1990)4222

[4] M. Iwasaki, T. Sakka, A. Yokoyama and K. Suzuki, "Frequency dependence of CO_2 laser photolysis of $CClF_2CH_2Cl$ and $CClF_2CHCl_2$", Chem. Phys. Letters, in press.

13.5 Theoretical study on the unimolecular decomposition of 1,2-dichlorotrifluoroethane $CHClFCClF_2$

13.5.1 Introduction

There is no thermochemical data available for the unimolecular decomposition of 1,2-dichlorotrifluoroethane(DCTFE). Therefore, it is worthwhile to investigate the energetics, theoretically. Computations involving *ab initio* molecular orbital(MO) calculation will provide thermochemical properties with enough accuracy to discuss reaction mechanisms and, hopefully, to support experimental results.

The mechanism deduced from the experimental obsevation is briefly represented below.

$CHClFCClF_2$ (DCTFE)	→	$CHFCClF_2$ (or $CHClFCF_2$) (MCTFE) + Cl	(1)
	→	$CClF=CF_2 + HCl$	(2)
	⇏	$CHClF + CClF_2$	(3)
$CClF=CF_2$	→	$CClF + CF_2$	(4)
	⇏	$CFCF_2 + Cl$	(5)
MCTFE	⇏	$CHF=CF_2 + Cl$	(6)

(a) C-Cl bond fission (1) and HCl molecular elimination (2) occur comparablly. (b) C-C bond fission (3) is not important as expected. (c) Secondary multiphoton absorption of chlorotrifluoroethene($CClF=CF_2$) results in C=C double bond cleavage (4) instead of C-Cl bond fission (5). (d) Monochlorotrifluoroethyl(MCTFE) radical formed by reaction (1) doesn't seem to decompose via further multiphoton absorption (6). The results are expected to be confirmed through the computation.

13.5.2 Calculation technique

In *ab initio* MO studies for the purpose of evaluating bond dissociation energies, there are two approaches to more reliable outputs. One is the adoption of larger basis sets and the other is that of more sofisticated theory to include electron correlation energies. The effects of these two approaches are not independent of each other. If you use a much larger basis set, you can expect larger correlation energy included by the same method than the case smaller basis set is used. The selection of a combination of those approaches would be, thus, not unequivocal and, usually, determined by available computer resources, i.e., disk space, memory size and cputime.

We used Dunning's double zeta plus polarization(DZP) basis sets[1] for the first row atoms and Wadt & Hay's effective core potential(ECP)[2] with valence DZP basis set for chlorine atom. All *d*-functions used were consist of six members with exponents $\zeta_d(Cl) = 0.5$. The ECP was used to reduce the number of basis functions and then to

save the disk space and cputime needed. The basis set includes 108 basis functions for DCTFE and will be designated by ECPDZP in this report.

Only self-consistent field(SCF) calculation was employed to find equilibrium structure of each species and for vibrational analyses at those structures. We have selected the restricted Hartree Fock(RHF) calculation and the unrestricted HF(UHF) calculation for closed shell systems and open shell systems, respectively. Of course, little correlation energy is included at this level of theory, that is, within HF appoloximation electron correlation is to be ignored. But, in general, more sofisticated beyond-HF calculations, such as configuration interaction, hardly cause considerable change onto the structures of stable molecules in spite of bond dissociation energies[3]. Since we used ECPDZP basis in the geometry optimization, the procedure is conventionally designated by HF/ECPDZP. For example, a vibrational analysis of DCTFE took a memory size of 250 *MB* and a cputime of ca.9 *h* on FACOM VP-2600 at Computing and Information Systems Center in Tokai Research Establishment.

For the purpose of evaluating enthalpy changes, the second order Møller Plesset (MP2) perturbation theory was involved at each equilibrium geometry (designated by MP2/ECPDZP//HF/ECPDZP). The MP calculation requires less cputime than the other beyond-HF calculations, therefore being almost only way to include correlation energies in large systems as treated here on our accessible hardware. It took about 300 *MB* in the disk space and a cputime of 9 *h* on MIPS RS3230 workstation to calculate a total energy of DCTFE at a single geometry.

All calculations were carried out using HONDO7 and *Gaussian 90* [4].

13.5.3 Performance of calculation

Reliability of such calculation has been checked in some cases of chlorinated hydrocarbons, for which the thermochemical data are aveilable in literature. We took up two types of reactions, i.e., simple C-Cl bond rupture and HCl molecular elimination. The calculations were carried out at the MP2/ECPDZP//MP2/ECPDZP and MP2/ECPDZP// HF/ECPDZP levels for C_1 compounds and for C_2 compounds, respectively. To correct zero point energies, unknown vibrational frequencies have been calculated at the same level of theory as is used in the geometry optimizations.

The enthalpy changes ΔH_0° calculated are listed in Table 1 with literature values[5-10]. The C-Cl bond energies are underestimated by about 2 kcal/mol, while ΔH_0° for the HCl eliminations are in good agreement with the experimental values. Especially, in the latter case effects of substitutions by other halogen atoms are well represented.

13.5.4 Results and Discussion

We have found an equilibrium structure of DCTFE in *anti* structure with respect to

Table 1 Enthalpy changes for simple C-Cl bond rupture and HCl molecular elimination. (kcal/mol)

Reaction			ΔH_0° Calc.	ΔH_0° Expt.
CH_3Cl	⟶	$CH_3 + Cl$	78.1	82.3
CH_2ClF	⟶	$CH_2F + Cl$	82.0[a]	84.7
$CClF_3$	⟶	$CF_3 + Cl$	82.9	84.9
CCl_2F_2	⟶	$CClF_2 + Cl$	79.0[a]	80.5
CCl_4	⟶	$CCl_3 + Cl$	67.7	70.1
CH_3CH_2Cl	⟶	$CH_3CH_2 + Cl$	84.3[a]	84.1[b]
CH_3CH_2Cl	⟶	$CH_2=CH_2 + HCl$	20.2	19.0
CH_2ClCH_2Cl	⟶	$CH_2=CHCl + HCl$	18.2	17.5[b]
CH_3CClF_2	⟶	$CH_2=CF_2 + HCl$	26.2[a]	25.9[b]

a) Zero point energies used were theoretical values. b) ΔH_{298}°

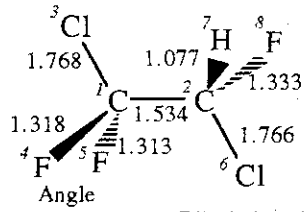

Angle

	Dihedral angle
3-1-2 = 109.8°	4-1-2-3 = 119.0°
4-1-2 = 109.3°	5-1-2-3 = 121.0°
5-1-2 = 111.4°	6-2-1-3 = 178.8°
6-2-1 = 110.5°	7-2-1-6 = 119.0°
7-2-1 = 109.6°	8-2-1-6 = 120.5°
8-2-1 = 109.1°	

Fig. 1 Equilibrium geometry of *anti* DCTFE .(distance in Å)

the Cl-C-C-Cl framwork. The geometric parameter are shown in Fig. 1. Presumablly, there exist two conformers in *gauche* structure, but steric repulsion between two Cl atoms may let these conformers somewhat unstable compared to the *anti* structure. At any rate, in the later part of this report all relative energies are measured from the *anti* structure and DCTFE will denote *anti* DCTFE.

Four types of reactions have been considered as the primary fragmentaions and three as the secondary. The primary fragmentations considered are C-Cl bond fissions (1), a four center HCl elimination (2a), a three center elimination (2b), and a C-C bond fission (3) of DCTFE. The secondary are a C-C bond fission (4) and a C-Cl bond fission (5) of $CClF=CF_2$ and C-Cl bond fission (6) of MCTFE. Relative energies ΔE and enthalpy changes ΔH_0° are listed in Table 2 and an energy diagram is shown in Fig. 2. In Table 2 ΔE are defined by the difference of the total energies between products and reactans and ΔH_0° are defined by zero point energy-corrected ΔE. As mentioned before, the calculation carried out at the MP2/ECPDZP//HF/ECPDZP level.

Energetically most favorable fragmentation is four center HCl elimination (2a). Since an exit barrier should exist in this process, searching for the transition state is need ed to evaluate the threshold

Table 2 Relative energies ΔE and enthalpy changes ΔH_0 relevant for the fragmentation of DCTFE. (kcal/mol)

No.	Reaction		ΔE	ΔH_0°
(1a)	$CHClFCClF_2$	⟶ $CHFCClF_2 + Cl$	83.5	80.2
(1b)		⟶ $CHClFCF_2 + Cl$	85.1	
(2a)		⟶ $CClF=CF_2 + HCl$	37.7	32.5
(2b)		⟶ S-$CFCClF_2 + HCl$[a]	82.9	76.2
(2c)		⟶ T-$CFCClF_2 + HCl$[b]	96.1	
(3)		⟶ $CHClF + CClF_2$	94.6	90.1
(4)	$CClF=CF_2$	⟶ $CClF + CF_2$	87.0	81.7
(5)		⟶ $CFCF_2 + Cl$	100.6	97.8
(6)	$CHFCClF_2$	⟶ $CHF=CF_2 + Cl$	27.1	23.6

a) S-CFCClF2 : singlet CFCClF2. b) T-CFCClF2 : triplet CFCClF2.

energy. Calculation for the barrier height is currently in progress. The experimental result has suggested that the transition state lies near the MCTFE + Cl asymptote (80.2 kcal/mol). The result consists with the fairly large value of ΔH_0° for reaction (2a), provided that the reverse activation energy is infered from analogy with the case of CH_3CCl_3 and CH_3CH_2Cl, in which the barrier heights have been reported to be 41.6 and 45 kcal/mol [11,12], respectively. Thus, competetion between reaction (2a) and (1) seems quite reasonable in this case.

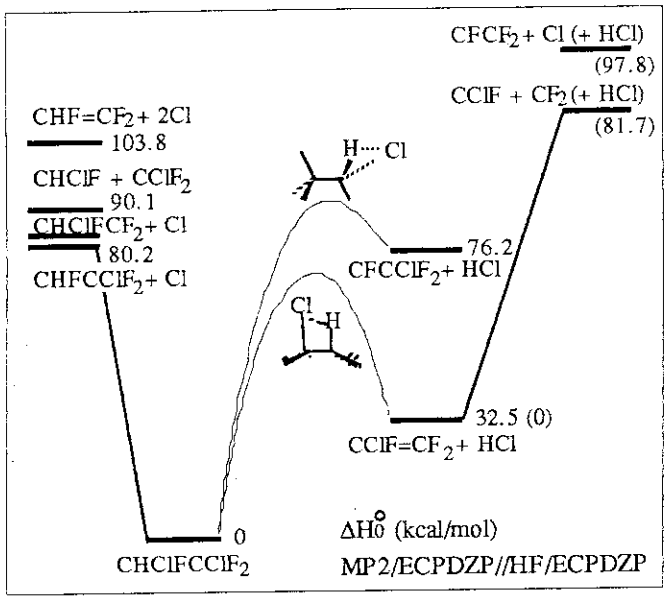

Fig. 2 Energy diagram for the fragmentation of DCTFE.

Cl atom fragment observed in the IRMPD experiment probably arises from both reaction (1a) and (1b). The energy difference is less than 2 kcal/mol. The slight favor of (1a) would be explained by the number of F atoms connected to α-carbon of MCTFE. F atoms tend to destabilize methyl radical substituted by them as shown in Table 1. Two conformations with respect to the rotation around the C-C bond are possible in MCTFE because the three bonds connecting to the carbon atom are not in the same plane. The *gauche* structure with respect to ClCCH skelton has been found to be only 0.2 kcal/mol stabler than the *anti* structure.

Three center HCl eliminations (2b) and (2c) form a singlet carben and a triplet carben, respectively. The singlet is lower than the triplet by ca. 13 kcal/mol. Although the enthalpy change for reaction (2b) is marginally lower than reaction (1), reaction (2b) may not contribute to the HCl formation due to an exit barrier with significant reverse activation energy.

The secondary photofragmentation reaction obserbed are somewhat curious. The C=C double bond is broken in preference to the C-Cl single bond in the fragmentation of $CClF=CF_2$. Stephenson et al. have reported the identical result through a static cell experiment using $CClF=CF_2$ as a sample gas. In the theoretical calculation presented here, the observations have been clearly confirmed. As shown in the right hand side in Fig. 2, the C=C double bond energy of 81.7 kcal/mol is extremely small compared to ethylen double bond of 169 kcal/mol[5]. To the contrary, The C-Cl bond is stronger than the corresponding bond of ethenyl chloride CH_2CHCl by about 9 kcal/mol [8,14]. After all, the C=C double bond is weaker than the C-Cl single bond by 16.1 kcal/mol.

The difference is large enough for reaction (4) to be a predominant process as has been observed in the experiments.

In conclusion, *ab initio* MO calculations for energetics of framentation reactions of DCTFE has revealed that C-Cl simple bond rupture and four center HCl molecular elimination can compete with each other and that the secondary fragmentation of $CClF=CF_2$ proceeds predominantly through C=C double bond cleavage.

References

1) T. H. Dunning, Jr. and P. J. Hay, in: Modern Theoretical Chemistry, Ed. H. F. Schaefer III (Plenum Press, NewYork, 1977) Vol.3, Chapter 1.
2) W. R. Wadt and P. J. Hay, J. Chem. Phys., 82 (1985) 284.
3) W. J. Hehre, L. Radom, P. v.R. Schleyer and J. A. Pople, in: Abinitio Molecular Orbital Theory (Wiley-Interscience Publication, NewYork, 1986) p. 133.
4) (a) M. Dupuis, J. D. Watts, H. O. Villar and G. J. B. Hurst, HONDO7, QCPE #544, Indiana University. (b) M. J. Frisch, M. Head-Gordon, G. W. Trucks, J. B. Foresman, H. B. Schlegel, K. Raghavachari, M. A. Robb, J. S. Binkley, C. Gonzalez, D. J. Defrees, D. J. Fox, R. A. Whiteside, R. Seeger, C. F. Melius, J. Baker, R. L. Martin, L. R. Kahn, J. J. P. Stewart, S. Topiol, J. A. Pople, *Gaussian 90*, Gaussian Inc., Pittsburgh PA, 1990.
5) M. W. Chase, Jr., C. A. Davies, J. R. Downey, Jr., D. J. Frurip, R. A. McDonald and A. N. Syverud, in: JANAF thermochemical Tables 3rd ed., (National Bureau of Standards, Washington, D. C., 1985).
6) H. Okabe, in: Photochemistry of Small Molecules (Wiley-Interscience Publication, NewYork, 1978) p. 171.
7) J. Chao, A. S. Rodgers, R. C. Wilhoit and B. J. Zwolinski, J. Phys. Chem. Ref. Data, 3 (1974) 141.
8) J. L. Franklin, J. G. Dillard, H. M. Rosenstock, J. T. Herron, K. Draxl and F. H. Field, NSRDS-NBS26(1969).
9) E. Tschuikow-Roux and S. Paddison, Int. J. Chem. Kinett., 19 (1987) 15.
10) E. Tschuikow-Roux and D. R. Salomon, J. Phys. Chem., 91 (1987) 699.
11) A. S. Sudbø, P. A. Schulz, Y. R. Shen and Y. T. Lee, J. Chem. Phys., 69 (1978) 2312.
12) P. C. Hiberty, J. Am. Chem. Soc., 97 (1975) 5975.
13) J. C. Stephenson, S. E. Bialkowski and D. S. King, J. Chem. Phys., 72 (1980) 1161.
14) S. W. Benson, in: Thermochemical kinetics Second Ed. (Wiley-Interscience, NewYork, 1976).

14. PHYSICO-CHEMICAL STUDIES ON FLUORINE COMPOUNDS

Y. Komaki, H. Shinohara, G. Fujisawa, N. Ishikawa, and K. Ohwada

14.1 Vibrational Studies on Actinide and Fission Products Compounds

14.1.1 Optically Active Vibrations of Alkali Metal Actinide(V) Hexafluoride Complexes[1,2]

The study of vibronic structures of pentavalent actinide halide complexes provides significant information on the typical electronic transitions and energy levels of 5f electrons. Therefore, it is valuable to analyze in detail electronic absorption spectra of various pentavalent actinide halide complexes prepared so far.[3-17] Recently, Hecht et al.[17] have measured the electronic absorption spectra of complex pentavalent uranium halides such as $LiUF_6$, α−$NaUF_6$, and $CsUF_6$ at low temperatures, and have systematically interpreted their spectra as consisting of sequences of vibronic transitions coupled to well-defined electronic excited states. In addition, crystal-field calculations have been carried out successfully. However, it seems that there are a few unsatisfactory spectral assignments of the observed bands. For instance, the mode labeled ν_c(340 cm^{-1}), only found in the excited state of $LiUF_6$, is not assigned clearly; furthermore, the assignment of the low-frequency mode at 53 cm^{-1} is obscure. In order to remove such ambiguities, it would be better to perform a group theoretical analysis as well as a normal coordinate treatment of optically active lattice vibrations as a whole crystal. In the present study, we take up three complexes of $LiUF_6$, α−$NaUF_6$, and $CsUF_6$ and assume, to a first approximation, two idealized structures for such crystals, to which the GF matrix method[18] developed for analyzing the optically active lattice vibrations of a crystal is applied.

The crystal structure of $LiUF_6$ and α−$NaUF_6$, which has been determined by Penneman and co-workers,[5,7] is rhombohedral (space group R3). Each uranium is comprised of six octahedrally bonded fluorine atoms (sixfold coordination) at a distance U−F = 1.98 A. The alkali metal ion M^+ (Li, Na) is surrounded with six UF_6^- units in MUF_6 (distorted NaCl-type structure). In this case, we assume an idealized structure (face-centered cubic type) in which each UF_6^- is a regular octahedron (Oh-symmetry) and M^+ is also coordinated, as a regular octahedron, by six UF_6^- units. On the other hand, the crystal structure of $CsUF_6$ has been determined by Penneman et al.[5] and Rosenzweig and Cromer[19] and is similar to that of $LiUF_6$ and α−$NaUF_6$. Each uranium

consists of six octahedrally bonded fluorine atoms (sixfold coordination) at a distance U-F = 2.057 A.[4,19] However, Cs^+ is surrounded with eight UF_6^- units in $CsUF_6$ (distorted CsCl type structure). For this case, we may assume a body-centered cubic type structure in which each UF_6^- is a regular octahedron (Oh-symmetry) and Cs^+ is coordinated by eight UF_6^- units. Here, it should be noted that these models are somewhat different from the actual crystal structures. Nevertheless, such modelings may be allowed, as a first step in exact analyses of vibronic structures, when one takes into account (1) simplification of group theoretical and normal coordinate analyses and (2) reasonable assignments of observed bands.

A group theoretical consideration shows that for the model structures described above there should be eight optically active fundamental vibrations, i.e., one A_{1g} (Raman-active), one E_g (Raman-active), one F_{1g} (Raman-active), three F_{1u} (infrared-active), one F_{2g} (Raman-active), and one F_{2u} (both-inactive) vibrations. It is found at first sight that two vibrational modes are added anew to six fundamental modes of the UF_6^- unit alone. One is the Raman-active F_{1g} vibration expressing the rotational lattice vibration, and the other is the infrared-active F_{1u} vibration corresponding to the translational lattice vibration.

The normal coordinate analyses of optically active vibrations of the complexes under consideration have been carried out with the assumption of two idealized structural models as described above. On the basis of these treatments, all of the observed bands so far reported have been successfully assigned to the intramolecular vibrations (UF_6^-) as well as the optically active lattice vibrations [M^+(Li, Na, Cs)...UF_6^-]. The results are listed in Tables 1, 2, and 3. The potential (force) constants concerning U-F and M-F bonds have been obtained within the framework of the modified valence force field. One finds from these tables that the agreement between the calculated and observed frequencies is very good for the complexes under consideration. This fact supports the supposition that the present vibrational assignments made under the assumption of two

Table 1 Observed[a] and calculated vibrational frequencies (in cm^{-1}) of $LiUF_6$.

Mode (Symm. species)	Observed		Calculated
	Fund.[b]	Excit.[c]	
ν_1 (A_{1g})	622	626	622
ν_2 (E_g)	439	461	439
ν_3 (F_{1g})	–	53	53
ν_4 (F_{1u})	515	510, 582	515
ν_5 (F_{1u})	–	340	340
ν_6 (F_{1u})	152	152, 183	152
ν_7 (F_{2g})	222, 232	240	222
ν_8 (F_{2u})	–	107	107

[a] Data taken from Ref.17.
[b] Observed infrared- and Raman-active vibrational frequencies of fundamental modes.
[c] Deduced from measurements in excited-state spectra.

idealized structures are adequate. Therefore, we may conclude that the normal coordinate analysis of the optically active lattice vibrations is suitable for the theoretical interpretation of the vibronic structures of crystals such as $LiUF_6$, α-$NaUF_6$, and $CsUF_6$.

The series of six-coordinated actinide(V) fluoride complexes $CsUF_6$, $CsNpF_6$, and $CsPuF_6$ have been found to be isostructural one another (space group R3).[8,9] This suggests that the optically active vibrations of $CsNpF_6$ and $CsPuF_6$ may be estimated by applying the same analytical method that was used for the case of $CsUF_6$. Such a prediction is valuable not only for knowledge of the fundamental frequencies of $CsNpF_6$ and $CsPuF_6$ but also for the theoretical interpretation of their vibronic structures in electronic excited states. Interestingly, the prediction of fundamental frequencies of the complexes in question is equivalent to that of their force constants. In the present effort, the force constants of $CsUF_6$ have been transferred, after some revision, to predict the fundamental vibrational frequencies of $CsNpF_6$ and $CsPuF_6$. The calculated results show that the An-F (An = U, Np, Pu) stretching vibrations corresponding to the $\nu_1(A_{1g})$, $\nu_2(E_g)$ and $\nu_4(F_{1u})$ modes regularly decrease by 5 - 8 cm^{-1}, in the order U > Np > Pu. Although the calculated fundamental frequencies of $CsNpF_6$ and $CsPuF_6$ are somewhat arbitrary, one may expect that such data would be useful in preliminary descriptions of vibronic structures in electronic excited states. It goes without saying that, to confirm the correctness of the calculated

Table 2 Observed[a] and calculated vibrational frequencies (in cm^{-1}) of α-$NaUF_6$.

Mode (Symm. species)	Observed		Calculated
	Fund.[b]	Excit.[c]	
ν_1 (A_{1g})	621	618	621
ν_2 (E_g)	449	-	449
ν_3 (F_{1g})	-	48	48
ν_4 (F_{1u})	520	512	520
ν_5 (F_{1u})	-	-	190
ν_6 (F_{1u})	-	122, 132	122
ν_7 (F_{2g})	206, 209	-	206
ν_8 (F_{2u})	-	72	72

[a] Data taken from Ref.17.
[b] Observed infrared- and Raman-active vibrational frequencies of fundamental modes.
[c] Deduced from measurements in excited-state spectra.

Table 3 Observed[a] and calculated vibrational frequencies (in cm^{-1}) of $CsUF_6$.

Mode (Symm. species)	Observed		Calculated
	Fund.[b]	Excit.[c]	
ν_1 (A_{1g})	608	605	608
ν_2 (E_g)	452	470	452
ν_3 (F_{1g})	-	25	31
ν_4 (F_{1u})	505	505	505
ν_5 (F_{1u})	-	37	33
ν_6 (F_{1u})	-	126-183	126
ν_7 (F_{2g})	190, 213	-	190
ν_8 (F_{2u})	-	60	60

[a] Data taken from Ref.17.
[b] Observed infrared- and Raman-active vibrational frequencies of fundamental modes.
[c] Deduced from measurements in excited-state spectra.

frequencies, it is very desirable to perform infrared and Raman spectral measurements in addition to the measurement of electronic absorption spectra at low temperatures.

14.1.2 Application of Potential Constants[20-23]

In studies of molecular force fields, one of the most significant problems is to determine the reliable general valence force (potential) constants such as bond stretching, angle deformation, bond-bond interaction, and bond-angle interaction in polyatomic molecules. As is well known, this problem has been approached from various points of view by many investigators, and relatively sufficient data on it now exist. The next problem is to make the best use of these potential constants for an understanding of physical and chemical properties of molecules. For this purpose, we have recently developed the methods[20-22] of determining empirically diatomic molecular energy components (electronic kinetic energy, total electrostatic potential energy, electron-nuclear attraction energy, electron-electron repulsion energy, and Hartree-Fock eigenvalue sum) by making use of harmonic and anharmonic potential constants spectroscopically available. The methods are based on the inhomogeneous linear second- and third-order differential equations[24-27] which are derivable from the quantum-mechanical virial theorem[28] that is theoretically exact to all intents and purposes. It has been shown that the methods are simple and powerful in calculating the molecular energy components of various diatomic molecules.

In the subsequent effort, the harmonic and anharmonic potential constants of heteronuclear diatomic molecules have been applied to problems of determining the number of electrons transferred (charge transfer) and electric dipole moment functions of such molecules.[23] This study is of practical importance from the point of view that the electric dipole moments as functions of the internuclear distance provide the basis for the calculation of transition probability coefficients and radiative life-times in vibration-rotation states. The approach developed here is mainly based on the Slater's orbital expansion method[29], that is, in a non-spin-polarized calculation atomic energies in a molecule are expanded with respect to the occupation number of electrons of atomic orbitals. To confirm the accuracy and the reliability of the approach, we have calculated the number of electrons transferred and electric dipole moments for alkali halides and other heteronuclear diatomic molecules. Specially, detailed analyses of electric dipole moment functions have been carried out on hydrogen fluoride (HF) and hydrogen oxide (OH) for which

reliable experimental dipole moment functions are presently known over a wide range of internuclear distances. These analyses show that the present approach is very useful in evaluating the charge transfer and the electric dipole moment change on formation of heteronuclear diatomic molecules.

References

1) K. Ohwada, Appl. Spectrosc. **43**(1989)714.
2) K. Ohwada, Appl. Spectrosc. **44**(1990)844.
3) R.A. Penneman, L.B. Asprey, and G.D. Sturgeon, J. Am. Chem. Soc. **84**(1962)4608.
4) M.J. Reisfeld and G.A. Crosby, J. Mol. Spectrosc. **10**(1963)232.
5) R.A. Penneman, G.D. Sturgeon, and L.B. Asprey, Inorg. Chem. **3**(1964)126.
6) M.J. Reisfeld and G.A. Crosby, Inorg. Chem. **4**(1965)65.
7) G.D. Sturgeon, R.A. Penneman, F.H. Kruse, and L.B. Asprey, Inorg. Chem. **4**(1965)748.
8) L.B. Asprey, T.K. Kennan, R.A. Penneman, and G.D. Sturgeon, Inorg. Nucl. Chem. Lett. **2**(1966)19.
9) R.A. Penneman, G.D. Sturgeon, L.B. Asprey, and H.F. Kruse, J. Am. Chem. Soc. **87**(1965)5803.
10) J. Selbin and J.D. Ortego, Chem. Rev. **69**(1965)657.
11) J.L. Ryan, J. Inorg. Nucl. Chem. **33**(1971)153.
12) A.F. Leung, J. Phys. Chem. Solids, **38**(1977)529.
13) E. Soulie, J. Phys. Chem. Solids, **39**(1978)695.
14) Y.M. Poon and D.J. Newman, J. Chem. Phys. **77**(1982)1077.
15) H.G. Hecht, L.P. Varga, W.B. Lewis, and A.M. Boring, J. Chem. Phys. **70**(1979)101.
16) L.R. Morss, C.W. Williams, and W.T. Carnall, Am. Chem. Soc. Symp. Ser. **216**(1983)199.
17) H.G. Hecht, J.G. Malm, J. Foropoulos, and W.T. Carnall, J. Chem. Phys. **84**(1986)3653.
18) T. Shimanouchi, M. Tsuboi, and T. Miyazawa, J. Chem. Phys. **35**(1961) 1597.
19) A. Rosenzweig and D.T. Cromer, Acta Cryst. **23**(1967)865.
20) K. Ohwada, Spectrochim. Acta, **45A**(1989)487.
21) K. Ohwada, Spectrochim. Acta, **46A**(1990)1461.
22) K. Ohwada, Chem. Phys. Res. **1**(1990)21.
23) K. Ohwada, Spectrochim. Acta, in press (1991).

24) W.L. Clinton, J. Chem. Phys. **36**(1962)556; **38**(1963)2339.
25) R.G. Parr and R.F. Borkman, J. Chem. Phys. **46**(1967)3683; **48**(1968)1116.
26) K. Ohwada, J. Chem. Phys. **87**(1987)4727.
27) K. Ohwada, Spectrochim. Acta, **44A**(1988)809.
28) J.C. Slater, Quantum Theory of Molecules and Solids, Vol. 1 (McGraw-Hill, New York, 1963); J. Chem. Phys. **1**(1933)687.
29) J.C. Slater, Quantum Theory of Molecules and Solids, Vol. 4 (McGraw-Hill, New York, 1974).

Publication List

[1] K. Ohwada, "Application of Potential Constants: Empirical Determination of Molecular Energy Components for Diatomic Molecules. I," Spectrochim. Acta, **45A**(1989)487.
[2] K. Ohwada, "Optically Active Vibrations of Lithium and α-Sodium Uranium Hexafluoride Complexes ($LiUF_6$ and α-$NaUF_6$)," Appl. Spectrosc. **43**(1989)714.
[3] K. Ohwada, "Optically Active Vibrations of Lanthanum Copper Oxide Compound (La_2CuO_4)," Spectrochim. Acta, **45A**(1989)1137.
[4] K. Ohwada, "Optically Active Vibrations of Cesium Actinide(V) Hexafluoride Complexes ($CsUF_6$, $CsNpF_6$, and $CsPuF_6$)," Appl. Spectrosc. **44**(1990)844.
[5] K. Ohwada, "Application of Potential Constants: Empirical Determination of Molecular Energy Components for Diatomic Molecules. II," Spectrochim. Acta, **46A**(1990)1461.
[6] K. Ohwada, "Application of Potential Constants: Empirical Determination of Molecular Energy Components for Diatomic Molecules. III," Chem. Phys. Res. **1**(1990)21.
[7] K. Ohwada, "Application of Potential Constants: Charge Transfer and Electric Dipole Moment Change on Formation of Heteronuclear Diatomic Molecules. IV," Spectrochim. Acta, in press (1991).

14.2 Pattern formation on polyimide using irradiation by heavy ion and the subsequent etching.

14.2.1 Introduction

Polyimide(PI) has superior characteristics of heat-resistance, radiation-resistance[1], and chemical-resistance among lots of polymers, and so has been expected for uses of various applications. Authors have studied the microfilters of polymers by using bombardments of heavy ions and the chemical etching method, for instance the microfilters of polyesters,[2,3] fluoropolymers,[4] and polyimide.[5] Etched tracks of heavy ions in polymers have been pay an attention in detection of heavy ions and its energies, and so some relations have been found to exist between a heavy ion with an incident energy and its feature of an etched track.[6] Etching the overlapping tracks can make channels of a certain depth in the polymer.[7]

Here, authors have studied the formation of etched picture in the layer of PI coated on the copper substrate by using the overlapping bombardments of heavy ions over the mask of the picture on PI, followed by etching. We have achieved the selective removal of PI layer from the copper substrate by the track etching method. We also have found that the etching ratio, the track etching rate to the bulk etching rate increases by etching with the additional surfactant and by the post-irradiation with gamma ray.

14.2.2 Experimental

PI specimen consists of double layers structure of PI layer and the copper substrate, where about 30 μm thick PI is coated on the one side of copper. The C(110 MeV), the Si(140 MeV), the Ni(200 MeV), the Br(130 MeV), and the Ag(200 MeV) ions were irradiated over the specimen at room temperature in the dose of 10^8 to 10^{11}p/cm^2 from Tandem accelerator. The region irradiated along the pattern by the overlapping tracks is completely dissolved in a 10% NaClO solution with 0.01% fluoro-surfactant at 60°C. Figure 1 shows the original pattern of PI layer irradiated by the Ag ion at the dose of 10^{10} ions/cm^2 before etching. The reduced thickness of the etched layer was examined using an optical microscope and a scanning microscope. In this experiment, the depth reduced to the bottom from the surface of PI per time is defined to be the track

Fig. 1 Pattern of PI layer irradiated by the Ag ion at the dose of 10^{10}ions/cm^2

etching rate V_t, and the bulk etching rate is V_g.

In order to influence additionally the degraded region in the polymer irradiated by heavy ions the suitable post-irradiation with gamma ray or u.v. light were carried out. The dose of gamma ray used was up to 1 MGy in the atmosphere of oxygen of 7 kg/cm^2 and u.v. light by XeCl laser in the range of 85-175 mJ/cm^2 in air.

14.2.3 Results and Discussion

(a) *Selection of etchant*

Although several kinds of etchants, $KMnO_4$, $K_2Cr_2O_7$ in H_2SO_4, NaOH, and NaClO solutions were examined for development of tracks in PI, 10% NaClO solution was found the most suitable etchant, because of no swelling of PI and none of the copper corrosion. Etching was carried out in 10% NaClO solution at 60°C for 7.5 hours.

(b) *Effect of additional surfactant on etching sensitivity*

Addition of the surfactant to the etchant results in the increase in V_t but the small decrease in V_g. Addition of the surfactant increases the effect of wettability to the surface of PI and consequently increase in V_t, while V_g remains small.

(c) *Ion species dependence of etching sensitivity*

In cases of the Ag and Ni ions, the etching rate for the Ag ion is larger than that for the Ni ion, and at the

Table 1 Ion species dependence of etching ratio (V_t/V_g)

Ions	Energy (Mev)	V_t (μm/hr)	V_g (μm/hr)	V_t/V_g
$^{109}Ag^{12+}$	200	1.1	0.1	11
$^{79}Br^{9+}$	130	1.0	0.1	10
$^{58}Ni^{12+}$	200	0.4	0.1	4.0
$^{28}Si^{8+}$	140	0.17	0.1	1.7
$^{12}C^{6+}$	90	0.1	0.1	1.0

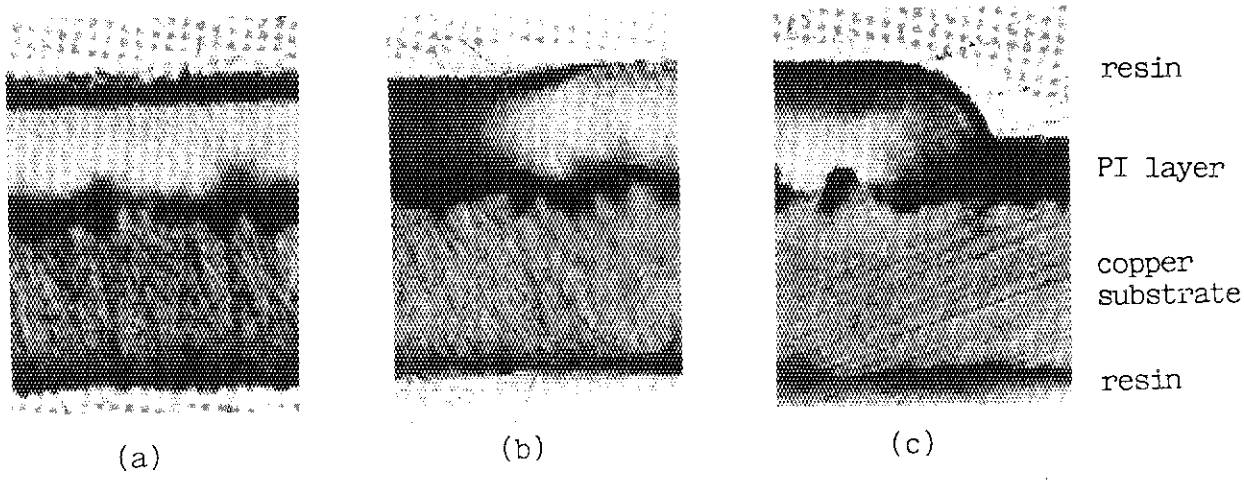

Fig. 2 Etched patterns on PI layers irradiated by the Ni(b) and the Ag(c) ions and on the virgin PI layer(a) × 630

same dose, the etching ratio is higher for the heavy ions than for the light ions, as shown in Table 1 and in Fig. 2.

Figure 3 shows the track etching rate, V_t versus the Z^*/β ratio, where Z^* is the effective charge and β the velocity of the ion. The data were fitted with the following relation within the experimental condition.

$$V_t = a(Z^*/\beta)^b$$

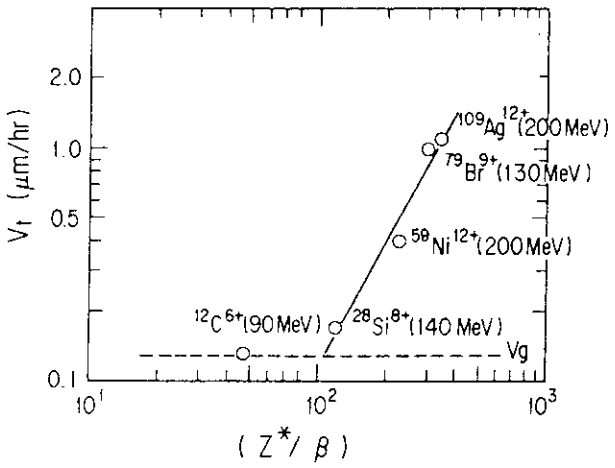

Fig. 3 V_t versus (Z^*/β) in etching of PI irradiated by various ions

The values of a and b equal $10^{-4.61}$ and 1.83[8], respectively. Consequently, under the same etching condition for such a specimen, the etching rate was found to determine only by the function of Z^* and β. Namely, the track etching rate (V_t) is closely related to the mass, charge and energy of the ion. No etched tracks revealed on PI irradiated with the C ion.

(d) *Postirradiation effect on etching ratio*

Each postirradiation by gamma ray and laser u.v.light is expected to influence the chemical bonding in the damaged molecule induced by the ion beam. Postirradiation was carried out on the PI film which had been previously irradiated by the Ag or the Ni ions to the dose of 10^{10} p/cm^2. In case of the Ag ion, we found that gamma ray postirradiation to the dose of 1 MGy increases the etching rate by a factor of 1.5, as shown in Fig. 4, but the effect of oxygen during irradiation remains obscure, and

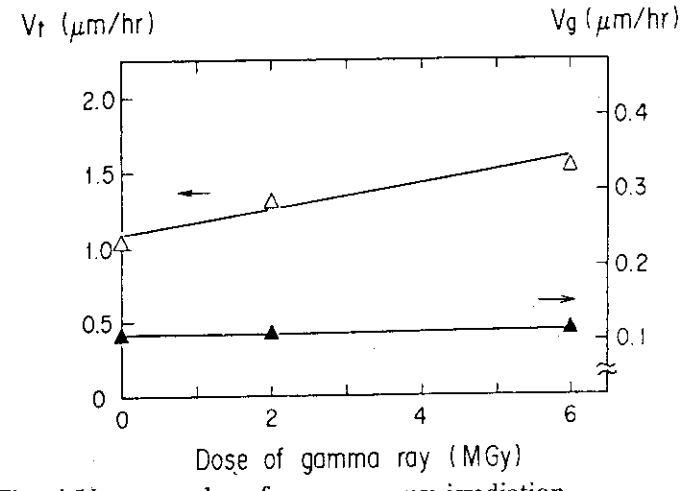

Fig. 4 V_t versus dose for gamma ray irradiation

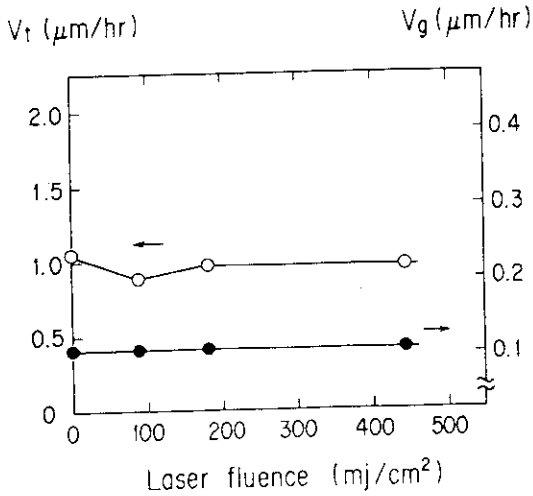

Fig. 5 V_t versus laser fluence for XeCl (309 nm) excimer laser

XeCl excimer laser changes a little as shown in Fig. 5.

It has been found that molecular structures in the damaged region are unstable for gamma ray, and u.v. light does not penetrate the film so deep as to effect on the damaged region.

14.2.4 Conclusions

After irradiation by the heavy ions followed by exposing to gamma ray or u.v. light from excimer laser, the PI film coated on the copper substrate was developed in 10% NaClO solution with the negligible corrosion of copper.

The etching ratio V_t/V_g, was evaluated from the decrement of the film thickness. Addition of the surfactant to the etchant results in increasing the etching ratio about two times. It seems that the etchant with the surfactant efficiently attacks on the PI film to increase the track etching rate V_t.

At the same dose, the ratio is larger for the heavy ions than for the light ions. These results were related to the function of Z^* and β. We have found that a constant thickness of layer of PI is removed by bombardment of arbitrary heavy ions whose mass, charge, and energy are decided.

Gamma ray postirradiation to the dose of 1 MGy increases the etching ratio by a factor of 1.5, but XeCl excimer laser changes a little. It may be concluded that molecular structures in the damaged region are unstable for gamma ray, but u.v. light does not penetrate the film thickness so deep as to effect on the damaged region.

References

1) T. Sasuga, N. Hayakawa, K. Yoshida, and M. Hagiwara, POLYMER, **26**(1985)1039
2) Y. Komaki, H. Otsu, K. Izui, and S. Tsujimura, J.Appl.Phys, **46**(1975)1155
3) Y. Komaki and S. Tsujimura, J.Appl.Phys, **47**(1976)1355
4) Y. Komaki, N. Ishikawa, T. Sakurai, N. Morishita, and M. Iwasaki, Nucl. Instrum. and Meth., **B34**(1988)332
5) Y. Komaki ,Y. Matsumoto, N. Ishikawa, and T.Sakurai, POLYMER Comm., **30**(1989)43
6) R.L. Fleischer, P.B. Price, and R.M. Walker, Nuclear Tracks in Solids: Principle and Applications (University of California, Berkeley, 1975)
7) B.E. Fischer and R. Spohr, Nucl.Tracks Radiat.Meas., **15**(1988)75
8) B. Grabez, P. Vater, and R. Brandt, GSI Scientific Report, (1987)253

Publication lists

[1] Y. Komaki, Y. Matsumoto, N. Ishikawa, and T. Sakurai, POLYMER Comm., **30**(1989)43

[2] Y. Matsumoto, Y Matsuura, Y. Hibino, K. Iwata (Sumitomo electric industries); Y. Komaki, N. Ishikawa, T. Sakurai, and E. Tachikawa, Proc. Int. Conf. on Evolution by Beam Applications, Takasaki, Nov. 5(1991) in press.

[3] Y. Komaki, N. Ishikawa, A. Takahashi, A. Yokoyama, T. Sakurai, M. Ohnuki, Y. Kobayashi, and T. Adachi, J. Atom. Energy Soc. Japan, **33**(1991)489 in Japanese

[4] M. Kumakura, I. Kaetsu, Y. Komaki, T. Sakurai, R. Arai, Y. Sejima, and T. Ohno, Proc. the 2 nd Int. Symp. on Advanced Nucl. Energy Res. -Evolution by Accelerator-, p 674, Jan 24, 1990, Mito

[5] M. Kumakura, I. Kaetsu, Y. Komaki, T. Sakurai, R. Arai, Y. Sejima, and T. Ohno, "Contact lens of fine holes and its manufacturing method" Japan patent, H1-268312(1989)

[6] Y. Komaki, N. Ishikawa, T. Sakurai, and Y. Matsumoto, "Manufacturing method of microporous polyimide film", Japan patent H2-47141(1990)

14.3 Reaction Behavior of Poly(vinylidene Fluoride) Films with Elemental Fluorine.

14.3.1 Introduction

Although Polyethylene (PE) film is easily perfluorinated by the use of elemental fluorine at room temperature, poly(vinylidene fluoride) (PVdF) film or poly(trifluoroethylene) (PTrFE) film scarcely react with fluorine at the same condition. It can be seen that these poly(hydrofluoroethylene)s (PHFE) are rather special polymer which do not appear in the course of fluorination of PE. We are intending to explain these differences in reactivity with elemental fluorine experimentally. In our earlier article[1] on the perfluorination of PHFE films by direct fluorination, we have pointed out that the increases in mass of these polymer films caused by fluorination were useful measure of the degree of fluorination, especially in case of PVdF films at which the values were 99−100% of the theoretical value. The situation described above has suggested that a gas−solid reaction of PVdF films with elemental fluorine fits to a kinetic study of the reaction.

Changes in mass and size, IR spectra, XPS, and action of a solvent of PVdF on the polymer caused by the direct fluorination were investigated to analyze the reaction behavior of the polymer.

14.3.2 Experimental

The PVdF films, kindly supplied from Kureha Chemical Industry Co., Ltd., were uniaxially oriented (u.o.) crystal form I, about 10 μm and 30μm thick, and biaxially oriented (b.o.) crystal form II, about 9μm and 50μm thick, free from any plasticizer or stabilizer, and their fluorine contents were identical to the theoretical value of 59.3%. The fluorine, >98% purity and O_2<0.5%, and argon used were identical to that described in the earlier article[2]. Outline of the apparatus and the method of fluorination has been described earlier[2]. Each unfluorinated film was treated with fluorine for a definite time, 10min−200h, according to the batch procedure. The reaction vessel, 0.38dm^3, was kept in an air thermostat of ±0.2°C.

Apparent IR absorbance was standardized in the following equation;

$$D_0 = DMA_2 / W_1 \qquad (1)$$

where D_0 is the standardized absorbance (mole^{-1}cm^2), D is the apparent absorbance (logarithm of transmittance), M is the formula mass of PVdF monomer unit, A_2 is the area of the film after the reaction, W_1 is the mass of the film before the reaction.

Degree of fluorination of the film and the number of H−F exchanges per unit surface area of the film were calculated by the equations:

$$\bar{R} = (W_2 - W_1)M / 2W_1(F - H) \quad (2)$$

$$n = (W_2 - W_1)N_0 / 2A_1(F - H) \quad (3)$$

where $\bar{R}$ is the degree of fluorination ($\bar{R}$ = 1 for the perfluorination), W_1 and W_2 are the mass of the film before and after the reaction, F and H are the atomic mass of fluorine and hydrogen, n is the number of H−F exchanges per unit surface area of the film, N_0 is the Avogadro number, and A_1 is the area of the film (surface area is $2A_1$) before the reaction.

14.3.3 Results and Discussion

1) Reaction rate

Numbers of H−F exchanges per unit area of polymers, n, at 90.3 °C and 1.03×10^5 Pa fluorine were plotted as a function of time, t, for 4 kinds of films. In the case of thin film, b.o.−form II, 9μm thick, a strongly oriented film, the n−t plot showed that n was a parabolic function of time in the early stage of the reaction (stage I, $0<\bar{R}<0.2$) and the n^2−t plot at 50.4−90.3°C gave straight lines and the Arrhenius plot gave an apparent activation energy of 18.5kcal/mole. In the case of thick film, b.o.−form II, 50μm thick, and u.o.−form I, 30μm thick, not so strongly oriented, the n's in the early stage of the reaction were the same linear function of time. The n−t plot for u.o.−form I, 30μm thick film from 40.9−90.3°C gave straight lines and the Arrhenius plot gave an apparent activation energy of 15.4kcal/mole.

Through a transient stage (stage II, $0.2<\bar{R}<0.3-0.4$ in b.o.−form II, 9μm thick film), the n changed to exponential function of time in the later stage of fluorination and the n−*ln*t or $\bar{R}$−*ln*t plots gave straight lines till the completion of perfluorination for all polymers (stage III, $0.3-0.4<\bar{R}$ in b.o.− form II, 9μm thick film).

The rate determining steps in the gas−solid reactions which follow the parabolic or the exponential rate equation are known to be the diffusion processes in the product layer[3,4]. Appearance of the reaction rate following the linear rate equation in this work suggests that the rate determining step in this case is not a diffusion process but a chemical reaction process. Effect of the partial pressure of fluorine and hydrogen fluoride on the reaction rate in this case was investigated and it was found that the rate was proportional to the fluorine pressure and not affected by the existence of hydrogen fluoride even at equal partial pressure with that of fluorine. The radical chain mechanism for gas−gas halogenation[5] cannot explain our results and a new mechanism with the

molecular initiation[6] directly followed by the termination (The molecular initiation-termination pair mechanism) was proposed:

$$RH + F_2 \rightarrow R\cdot + HF + F\cdot \quad (4)$$

$$R\cdot + F\cdot \rightarrow RF \quad (5)$$

$$d[RF]/dt = k[RH][F_2] \quad (6)$$

A weak absorption band at around 1330cm^{-1} assigned[7] to abnormal tail-to-tail polymerization of monomers, $-CH_2-CH_2-$, disappeared within very early period in the reaction stage I and a new absorption appeared at around 1350 m^{-1}. This implies that these groups exist in the polymer where fluorine can access easily, i.e., in the amorphous region.

In the reaction stage I, broad absorption band appeared at around 1100cm^{-1} and gradually increased. This can be explained as the accumulation of reaction intermediate, $(-CF_2-CHF-)_n$. The intensity of the absorption band at around 531cm^{-1}, assigned[7] as CF_2 bending mode in the form II crystalline PVdF, remained constant to the near end of this stage and no absorption band appeared at around 553cm^{-1}, assigned[8] to bending mode of CF_2 in PTFE. This implies that the fluorination is in progress exclusively in an amorphous region of the polymer and perfluorinated sites dose not exist in this reaction period.

In the reaction stage II, the intensities of 976cm^{-1}-band, assigned[7] as CH_2 twisting mode in the form II crystalline PVdF, and 531 cm $^{-1}$-band, decreased linearly with $\bar{R}$ and the 553cm^{-1}-band appeared. This implies that the fluorination is in progress at both the amorphous region and the crystal region of the polymer and some PTFE-like product is formed.

In the reaction stage III, the linear decrease in intensity of the 976cm^{-1}- and 531cm^{-1}-band and the linear increase of the 553cm^{-1}-band with $\bar{R}$ continued. The absolute values of the gradients of decreases for the 976cm^{-1}- and 553cm^{-1}- band suddenly increased at $\bar{R}$ nearly equal to 0.55, and these gradients were held constant till the finish of the perfluorination. These sudden changes of the gradients at around $\bar{R}$=0.55 implies that the fluorination in the amorphous region has completed at this point and thereafter the reaction is in progress exclusively in the crystal region of the polymer. This point of view was supported by the IR spectral measurement with polarized light for the fluorinated u.o.-form I, 30μm thick film in which the absorption band at around 598cm^{-1}, assigned[7] to the amorphous region of PVdF, decreased linearly with $\bar{R}$ and almost disappeared at around $\bar{R}$=0.5.

3) XPS spectral change

Electron spectra from C1s of PVdF film, b.o.-form II, 9μm thick, $\bar{R}$=0 (unfluorinated), 0.07, 0.16, 0.46, and 0.65, PTrFE film, and PTFE plate were

measured by courtesy of Shimadzu Corporation. Comparison of these spectra revealed that $-CH_2-$ in $(-CF_2-CH_2-)_n$ and $-CHF-$ in $(-CF_2-CHF-)_n$ remained in the fluorinated polymer even at $\bar{R}$=0.46 while not observed at $\bar{R}$=0.65. This implies that the surface layer of the polymer within 100Å thick is still not perfluorinated in the reaction stage III at $\bar{R}$=0.46 and unfluorinated PVdF and PTrFE−like reaction intermediates are remaining in the surface region and the perfluorination of the surface layer has finished in the polymer at $\bar{R}$=0.65. Hence an attempt to form PTFE−like corrosion resistant layer on the surface of PVdF by a slight fluorination will not succeed.

4) Action of solvent of PVdF

Fluorinated PVdF films, u.o.−form II, 9μm thick, $\bar{R}$=0.14, 0.41, and 0.77, were dipped in dimethyl acetamide, a solvent of PVdF, at 90°C for 2h and change in IR spectra were observed. In the case of reaction stage I, $\bar{R}$=0.14, all sharp absorption bands which are characteristic of crystalline PVdF disappeared, in the case of beginnings of the reaction stage II, $\bar{R}$=0.41, very little part of the crystalline band remained, and in the case of the reaction stage II, $\bar{R}$=0.77, any change in the IR spectra and the mass of the film was not observed. This observation implies that the residual crystalline PVdF in the reaction stage III at $\bar{R}$=0.77 is covered with PTFE−like protective layer.

14.3.4 Conclusion

A reaction behavior of PVdF film of 9μm to 50μm thick with elemental fluorine till perfluorination has been studied on the whole and the following results were obtained: (1) The progress of the reaction could be separated into three periods with respect to the type of reaction rate equation which the reactions follow, i.e., the stage I where the rates obey the linear or parabolic function of time, the stage II which is the transient region, and the stage III where the rates obey exponential function; (2) In case of 9μm thick film the stage I ranged from 0% to about 20% of perfluorination, the stage II from 20% to 30−40% of perfluorination, and the stage III from 30−40% to 100% of perfluorination; (3) In the stage I the reaction proceeded exclusively in the amorphous region of the polymer and produced $(-CF_2-CHF-)_n$−type intermediates with no $(-CF_2-CF_2-)_n$−type products; (4) The rate determining step in the region where the rates follows the linear equation which gave apparent activation energy of 15.4kcal/mole was explained as a chemical reaction with the molecular initiation[6] which is followed by the direct combination of the resultant radicals; (5) The rate determining step in the region where the rates follows the parabolic equation with the apparent activation energy of

18.5kcal/mole was explained as the diffusion process in the polymer; (6) In the stage II the reaction giving $(-CF_2-CHF-)_n$ groups and very little $(-CF_2-CF_2-)_n$ groups proceeded both in an amorphous region and a crystal region of the polymer ; (7) In the stage III the reaction proceeded both in an amorphous region and a crystal region of the film till the amorphous region had been perfluorinated and after that the reaction proceeded in the residual crystal region; (8) The polymer in the stage III after amorphous region had been perfluorinated contained crystalline PVdF covered with crystalline PTFE-like substance and the film was resistant to corrosive chemicals; (9) Some $(-CF_2-CH_2-)_n$ and $(-CH_2-CHF-)_n$ groups remained in the surface layer of the polymer even in the stage III till the amorphous region of the polymer had been perfluorinated so that very little fluorination of the polymer surface was proved to be not effective to form PTFE-like corrosion resistant surface layer.

Acknowledgment

The author wishes to thank Dr. H. Imoto of Kyoto University for his help in XPS spectral measurements.

References

1) K. Ohwada, Y. Komaki, and H. Shinohara, JAERI-M 89-058(1989)294.
2) H. Shinohara, J. Polym. Sci. Polym. Chem. Ed., 17(1979)1543.
3) G. Tammann, Zeit. anorg. Chem., 111(1920)78.
4) B. Lustman and R. F. Mehl, Trans. Amer. Inst. Min. Eng., 143(1941)246.
5) P. C. Anson, P. S. Fredricks, and J. M. Tedder, J. Chem. Soc., (1959)918.
6) W. T. Miller, Jr., S. D. Koch, Jr., and F. W. McLafferty, J. Am. Chem.Soc., 78(1956)4992
7) S. Enomoto, Y. Kawai, and M. Sugita, J. Polym. Sci. A-2, 6(1968)861.
8) C. Y. Liang and S. Krimm, J. Chem. Phys., 25(1956),563.

15. STUDIES ON CHEMICAL REACTIONS INDUCED BY LASER EXCITATION

S. Ohno, H. Shiraishi, K. Furukawa, Y. Yamada, and T. Takayanagi

15.1 Photoreduction and Emission of Solid Europium Chloride in KBr by Laser Irradiation at 308 nm

15.1.1 Introduction

The lanthanide elements have complicated optical spectra because of the 4f shell and their absorption and fluorescence properties have been studied extensively.[1,2] Photochemical partitioning of lanthanide elements in solution has been studied by some workers.[3,4] Since most of the lanthanide elements are stable in the trivalent state in a solution, separation may be possible by stabilizing divalent lanthanides. Europium is unique in that it is stable in divalent state in addition to the trivalent state. Eu^{2+} produced by photoreduction can be stabilized by using SO_4^{2-} [3] or 18-crown-6 ether.[4]

The optical absorption, emission and Zeeman splitting have been studied for Eu^{2+} doped in NaCl, KCl and KBr crystals.[5,6] We report here on the effect of laser irradiation (308 nm) of solid trivalent europium chloride $EuCl_3 \cdot 6H_2O$ in KBr. The aim of the present series of investigation is to study photochemical process which may be applicable to elemental partitioning.

15.1.2 Experimental

We employed a XeCl excimer-laser (Lambda Physik EMG201MSC) for irradiation of ultra-violet light at 308 nm (output energy: 400mJ/pulse, pulse width: 20 ns). Emission at a desired delayed time after laser pulse was measured by a diode array multichannel detector (Princeton Instruments SMA) with 120 nm wavelength width and 50 ns detection time width. These signals were accumulated for several hundreds pulses to obtain a time-resolved emission spectrum. We also employed a photomultiplier (Hamamatu R928), a monochromater (ISA HR-320) and a fast transient digitizer (Tektronix 7912HB) to detect the single emission signal at a wavelength induced by pulsed irradiation.

For the detection of transient absorption, the probing light from a

pulsed high-pressure xenon flash lamp (Tokyo Instruments XF-150) traversed the sample at right angles to the excitation laser light. The transient absorbance at various wavelengths was measured with a photomultiplier placed in the analyzing beam behind the sample disk. To eliminate the emission of sample by laser irradiation, the emission signal obtained without probing light was subtracted from the observed with laser irradiation. The transient absorbance was calculated from this signal and the reference signal of probe light without laser irradiation. A spectrophotometer (JASCO Ubest-30) was used to measure ordinary UV-visible absorption spectra.

As the sample disk, $EuCl_3 \cdot 6H_2O$ was ground and mixed with KBr, and then pressed to form a 1cm diameter disk. Thick sample ($EuCl_3 \cdot 6H_2O$: 0.04 g, KBr : 0.10 g) for emission measurements and thin sample ($EuCl_3 \cdot 6H_2O$: 0.005 g, KBr : 0.10 g) for absorption measurements. The laser light was slightly focussed by a convex lens (f=150 mm) and the spot at the sample disk was 0.1 cm^2.

15.1.3 Results and Discussion

Time resolved emission spectra induced by 308 nm irradiation is shown in Fig. 1. The decaying part of these signals can be fitted by a single exponential curve to obtain emission lifetime. $EuCl_3$ has a broad absorption band assigned to f-d or charge-transfer band in the ultraviolet region. Excitation to this broad absorption band is followed by deexcitation to lower f-f excited levels; sharp emissions from Eu^{3+} (assigned to f-f transition) were thus observed (Fig.1a). The emission agrees with those previously observed with direct excitation of f-f transition in Eu^{3+} ($^7F_0 \rightarrow {}^5D_2$) at 465 nm. The lifetimes of these transition $^5D_1 \rightarrow {}^7F_j$ and $^5D_0 \rightarrow {}^7F_j$ are 6.9 and 120 μs, respectively, and are the same as those obtained from the 465 nm excitation. Apart from the emission due to the f-f transitions, a broad intense emission band at 420 nm assignable to transition of Eu^{2+} ($4f^6 5d \rightarrow 4f^7$) was observed (Fig 1b). The lifetime measured from the time-resolved emission spectra was 1.0 μs. When a disk sample of pure $EuCl_3 \cdot 6H_2O$ without KBr was irradiated by 308 nm laser light, the emissions due to the f-f transitions of Eu^{3+} were only observed with no emission at 420 nm. It thus appears that the KBr matrix temporarily donates an electron to reduce $EuCl_3 \cdot 6H_2O$ in the KBr disk upon laser irradiation.

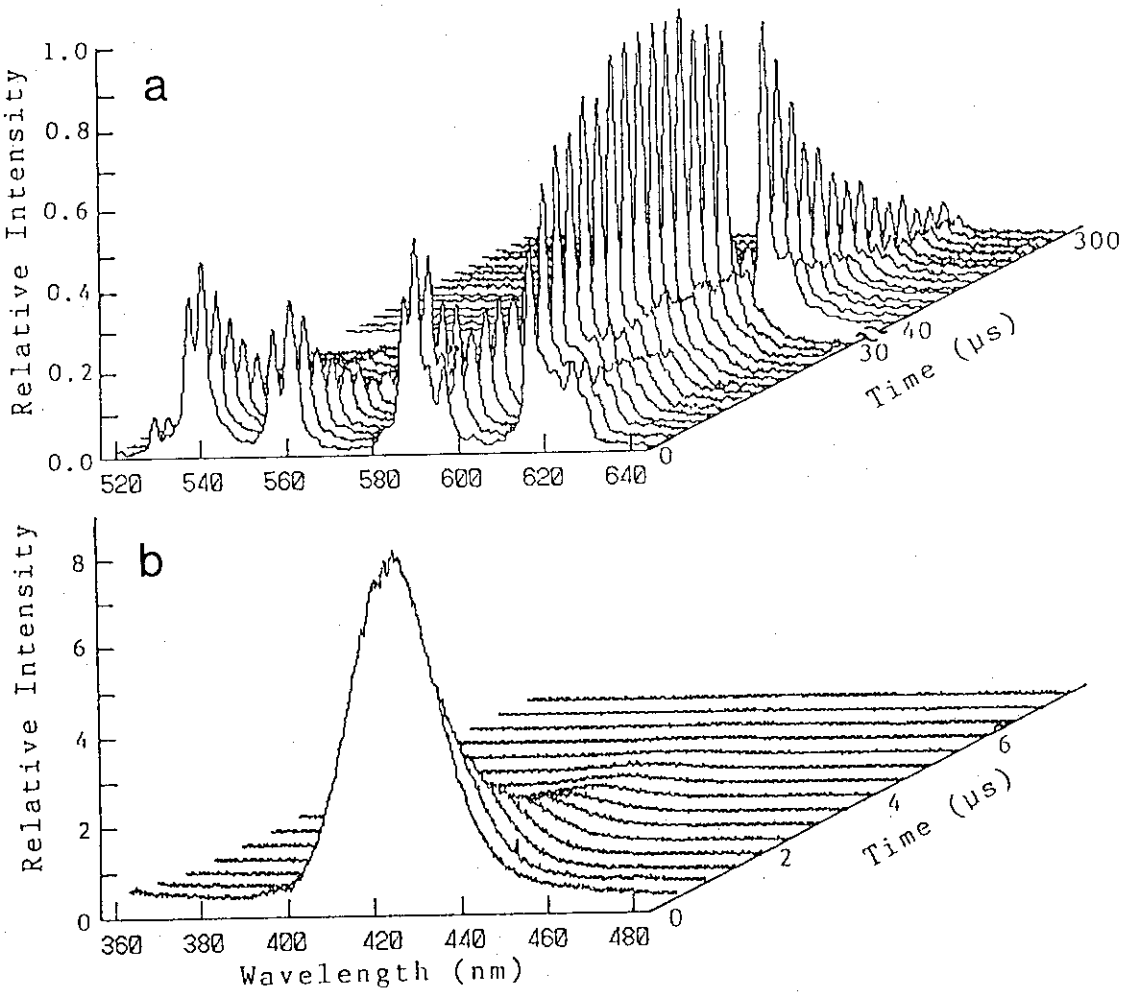

Fig. 1 The time-resolved emission spectra observed by irradiating $EuCl_3 \cdot 6H_2O$ in KBr disk with 308 nm laser light. (a) spectrum assigned to f-f transitions ($^5D_1, ^5D_0 \rightarrow {}^7F_j$); (b) that assigned to transition in Eu^{2+} ($4f^6 5d \rightarrow 4f^7$).

Transient absorbance of Eu^{2+} produced by photoreduction was observed by using a photomultiplier and transient digitizer at some wavelengths at room temperature (Fig. 2). The spectrum of this transient absorption signal is shown in Fig. 3. This absorption spectrum is consistent with the absorption spectrum of Eu^{2+} given in literature[5,6] the absorption being observed at wavelength shorter than 410 nm with a maximum near 320 nm. The decay lifetimes of these signals was very short, 1.0 ±0.2 μs. The produced Eu^{2+} appears, therefore, to be oxidized rapidly after deexcitation to the ground state.

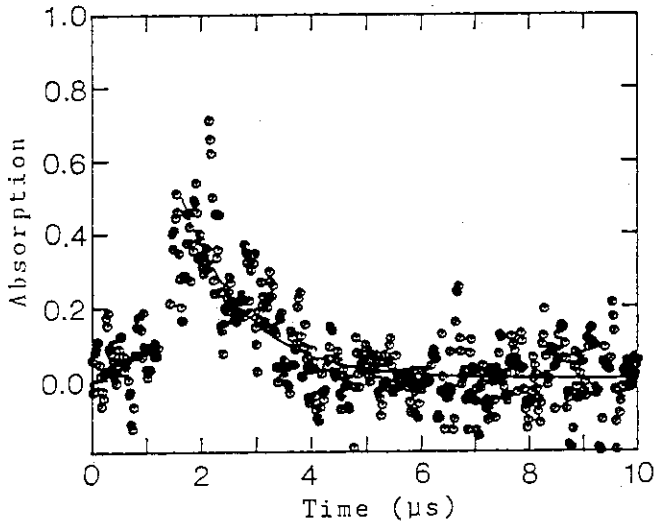

Fig. 2 Time profile of the transient absorption at 340 nm observed for $EuCl_3 \cdot 6H_2O$ in KBr disk irradiated by 308 nm laser light.

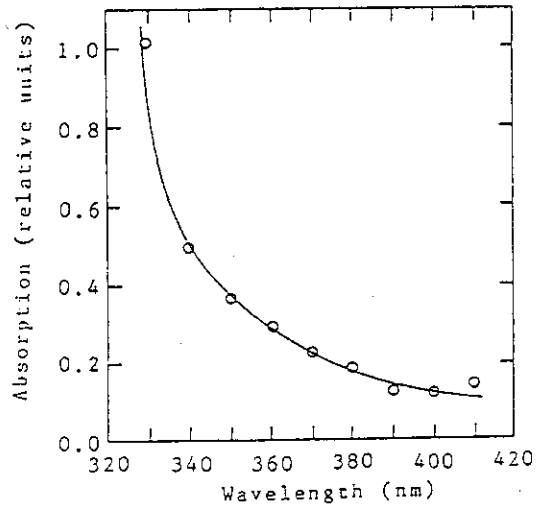

Fig. 3 The transient absorption spectrum of $EuCl_3 \cdot 6H_2O$ in KBr disk irradiated by 308 nm laser light.

The production mechanism of excited Eu^{2+} that radiates fluorescence at 420 nm may occur in two ways: 1) the excited Eu^{2+} is produced directly after photoreduction of Eu^{3+} or 2) the ground state Eu^{2+} produced by the photoreduction of Eu^{3+} is further excited. To examine which process is actually taking place, we observed the relationship between laser energy and emission intensity, so that the number of photon responsible for the process may be determined. The laser energy was varied by use of beam splitters and the emission at 420 nm was detected at various laser intensity. In Fig. 4 a linear relation between the laser energy and the emission intensity of Eu^{2+} is seen at a lower laser energy less than 0.5 J cm^{-2} $pulse^{-1}$. Therefore, Eu^{2+} is produced by one photon absorption. At

higher laser energy, the emission intensity saturates, probably because the rate of excitation and that of deexcitation of Eu^{3+} become comparable.

To confirm the instability of the photoreduced Eu^{2+}, the ordinary absorption spectrum of the disk sample was measured both before and after photoirradiation and no change due to the production of Eu^{2+} was observed. It was also noticed that the intensity of 420 nm emission during laser pulse-irradiation did not change with the number of pulses. Thus it was clear that the photoreduced Eu^{2+} was not stable in the present system but was oxidized to reform Eu^{3+} rapidly. A gross kinetic scheme may be depicted as in Fig. 5. The levels are designated as follows: Level 1 is the ground state of Eu^{3+}; 2 is the excited f-d or charge-transfer state of Eu^{3+}; 3 is the fluorescence level of Eu^{3+}; 5 is the excited and fluorescence level of Eu^{2+}, assigned to $4f^6 5d$; and 4 is the ground state of Eu^{2+}, assigned to $4f^7$.

Transition rates are also indicated in Fig 5: I is the irradiation laser energy; σ is the absorption cross section of Eu^{3+}; k_{21} is the radiationless deexcitation rate; k_{23} and k_{31} are the transition rates for radiationless and radiative deexcitation for Eu^{3+}; k_{25} is the transition probability to produce the excited level of Eu^{2+} ($4f^6 5d$); k_{54} is the transition probability for fluorescence of the excited level to the ground level of Eu^{2+}; and k_{41} is the rate for oxidation of the ground state of Eu^{2+}. The real energetic scheme is naturally more complicated by the presence of a number of f-electron excited states.

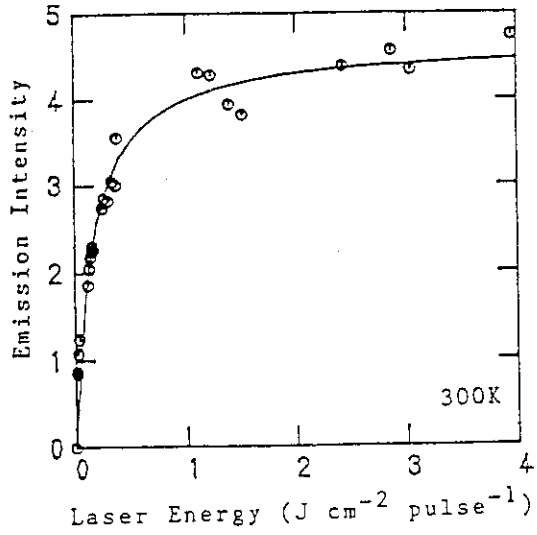

Fig. 4 The dpendence of the emission intensity at 420 nm upon the irradiating laser energy (308 nm). The sample is $EuCl_3 \cdot 6H_2O$ in KBr disk at 300 K.

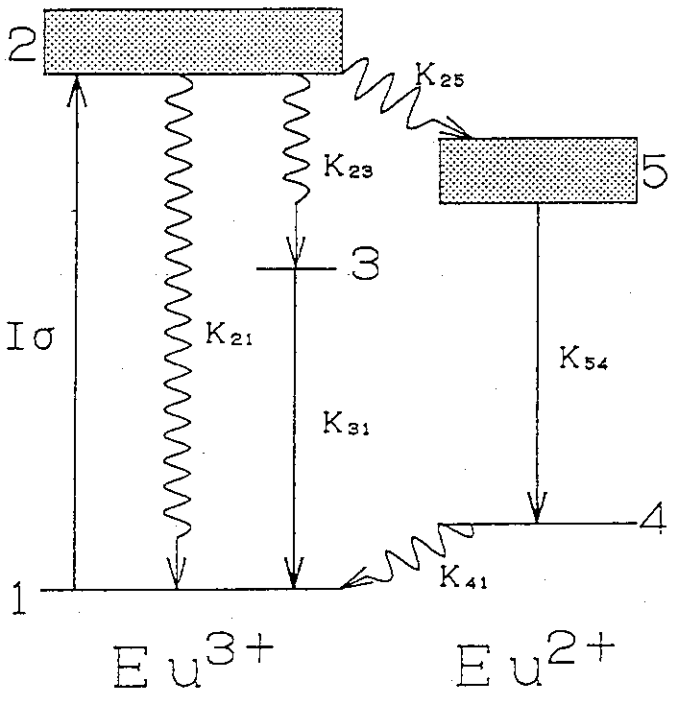

Fig. 5 The energy diagram of the system.

References

1) K. A. Gschneidner, Jr. and L. Eyring, "Handbook on the Physics and Chemistry of Rare Earths", North-Holland Publishing Company, (1979), p.171.

2) F. S. Richardson, Chem. Rev. **82**, (1982) 541.

3) T. Donohue, J. Chem. Phys. **67**, (1977) 5402.

4) T. Donohue, Chem. Biochem. Appl. Lasers, **5**, (1980) 239.

5) R. Reisfeld and A. Glasner, J. Opt. Soc. Am. **54**, (1964) 331.

6) J. Hernandez A., W. K. Cory, and J. Rubio O., J. Chem.Phys. **72**, (1980) 198.

7) T. H. Maiman, Phys. Rev. **123**, (1961) 1145.

Publication List

[1] Y. Yamada and S. Ohno, "Photoreduction and Emission of Solid Europium(III) Chloride in KBr by Laser Irradiation at 308 nm," Bull. Chem. Soc. Jpn. **64** (1991) 926.

15.2 Photoreduction of Solid Europium Chloride in KBr by Visible Two-photon Excitation

Two-photon excitation of Eu^{2+} ions in CaF_2, SrF_2 and alkali halide crystals has been studied [1-5] to investigate the aggregation kinetics of Eu^{2+} in single crystals. Two-photon luminescence excitation spectra of Eu^{3+} in CaF_2 and YAG were measured.[6,7] We have reported that Eu^{3+} was reduced to form excited Eu^{2+} which emitted at 420 nm ($4f^65d \rightarrow 4f^7$) by irradiating $EuCl_3 \cdot 6H_2O$ in KBr sample with ultraviolet light (308 nm).[8] Here, we report that Eu^{3+} is also reduced to form Eu^{2+} by two-photon excitation with visible laser light.

We employed a pulsed laser for irradiation; a dye-laser (FL3002 Lambda Physik; coumarin-2-dye) pumped with an excimer-laser (EMG201MSC Lambda Physik pulse-width; 20 ns). The direct output beam of the laser was of 2 mm diameter and its energy was 0.3-3.2 mJ/pulse depending on wavelength. For detection, a diode array multichannel detector (SMA Princeton Instruments) and a photomultiplier (R928 Hamamatu) connected to a fast transient digitizer (7812HB Tektronix) were employed.

In order to observe multiphoton absorption, the sample was irradiated by laser condensed by a lens; the intensity of the irradiating light was adjusted by varying the distance (x) between the lens and a sample. The focal length of the convex lens was 330 mm. When solid $EuCl_3 \cdot H_2O$ mixed in KBr was irradiated at 465 nm without focusing, emission assigned to f-f transition of Eu^{3+} (520-640 nm) was observed ($x < 250$ mm in Fig.1). As the distance between the lens and the sample approaches the focal distance ($x \geq 250$ mm), broad emission at 420 nm, assignable to emission of Eu^{2+} ($4f^65d \rightarrow 4f^7$), is observed. In the previous section, it was reported that $EuCl_3 \cdot 6H_2O$ in KBr disk was photoreduced by 308 nm laser light to form excited Eu^{2+} and that the emission from the excited Eu^{2+} was observed directly after reduction of Eu^{3+}. Here, it is demonstrated that the visible multiphoton excitation also induces the emission from Eu^{2+} formed by the reduction of Eu^{3+}. When the distance between the lens and the sample was very close to the focal length ($x \geq 290$ mm), sharp emission lines were observed. These emissions are attributable to atomic emission of Eu and K. For comparison a pure KBr disk and a pure $EuCl_3 \cdot 6H_2O$ disk were also irradiated by condensed light. Emissions due to atomic spectra of K (KI; 344.6, 344.7, 404.4, 404.7 nm) and Eu (EuI; 459.4, 462.7, 466.2 nm and EuII; 382.0, 390.7, 393.1, 397.2, 413.0, 420.5 nm) were observed.

The solid sample was sputtered by ablation and the vaporized atoms or molecules were further excited to emit atomic spectra. Also was found the continuum spectrum with short lifetime due to the plasma state produced by laser ablation. The broad emission centered at 420 nm was not observed in these pure samples.

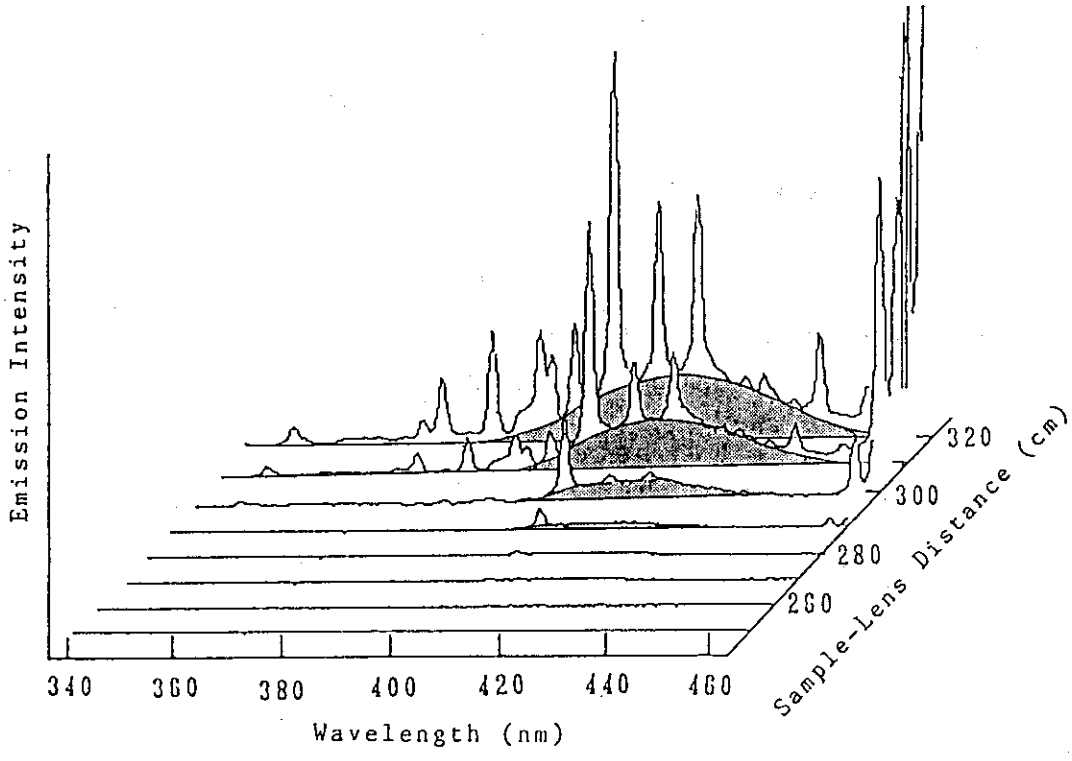

Fig. 1 The emission spectra of $EuCl_3 \cdot 6H_2O$ in KBr irradiated by 465 nm laser light with varying distance between sample and the convex lens (f=330 mm); measured at 2 μs (gate time: 100 ns) after the laser irradiation. The marked area corresponds to the emission of Eu^{2+}.

Time dependence of these emissions was measured. The emission at 416 nm, which is due to excited Eu^{2+} ($4f^6 5d \rightarrow 4f^7$), had a lifetime of 0.9 μs, the estimation being made from the slow component of the decay curve as shown in Fig. 2. This value is in good agreement with the lifetime of the emission observed with 308 nm irradiation.[8] Time dependence of the emission at 459.4 nm (EuI) and 404.4 nm (KI) was quite different from that at 416 nm (Eu^{2+}). The emission due to the plasma state disappeared rapidly (< 0.2 μs), and the atomic spectra grew slightly (~ 1 μs) and then decayed slowly (1-2 μs).

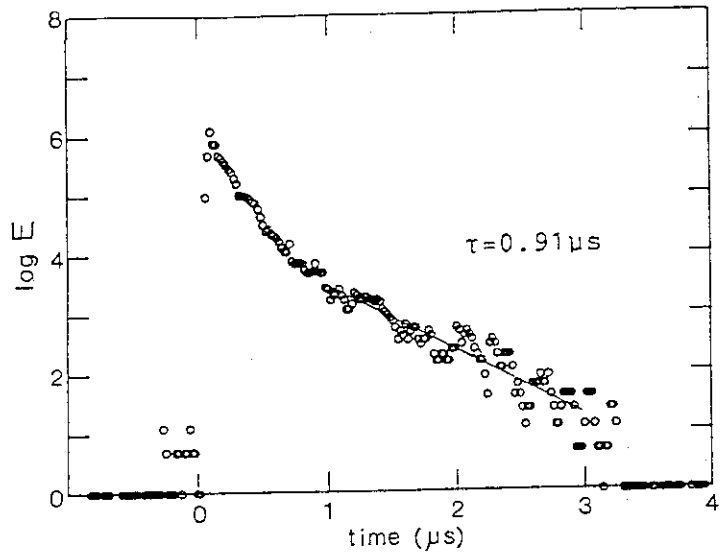

Fig. 2 Transition of the emission intensity at 416 nm from $EuCl_3 \cdot 6H_2O$ in KBr irradiated by condensed 465 nm laser light (solid line indicates the decay curve for lifetime of 0.91 μs).

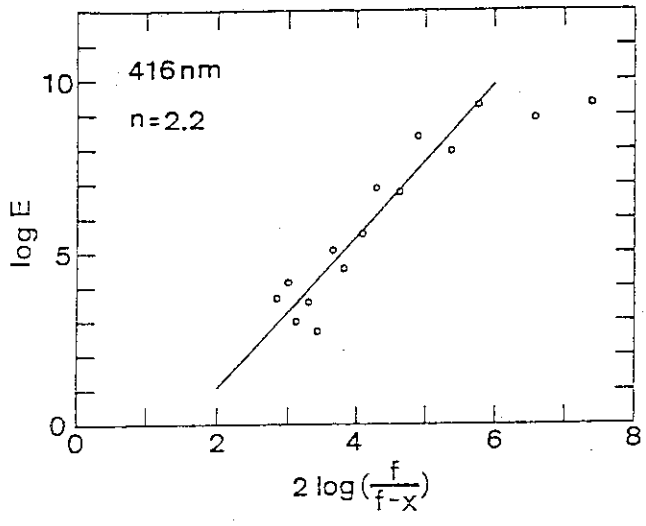

Fig. 3 Dependence of the emission intensity (E_{obsd}) at 416 nm from $EuCl_3 \cdot 6H_2O$ in KBr on the distance (x) between the lens and the sample (irradiated by condensed 465 nm laser light; f=330 mm).

The relationship between the observed intensity, E_{obsd}, and the distance, x, may be expressed as $E_{obsd} = k \cdot I_0^n \cdot (f/(f-x))^{2n}$,where I_0 is the intensity of laser output, f is the focal length of the lens, k is a constant and n is the number of photons needed to induce the emission. The laser intensity at the sample is $I_0 \cdot (f/(f-x))^2$. It can be seen from Fig. 3 that the emission from Eu^{2+} is induced with two photons (n=2) from the experimental results (Fig. 3), and that the excited Eu^{2+} is produced directly following the photoreduction of Eu^{3+}. The atomic emissions of Eu and K were analyzed to be characterized by a larger n of about 3.

It was also examined how the emission from Eu^{2+} depended on the

wavelength of laser light. In Fig. 4, the observed emission intensity was normalized with respect to the laser intensity on the bases that the emission from Eu^{2+} is caused by two-photon absorption. As seen in the figure, the stronger emission was observed at the shorter wavelength. While Eu^{3+} has absorption at 465 nm corresponding to $^7F_0 \rightarrow {}^5D_2$ transition, the emission induced by 465 nm irradiation was no stronger compared to the cases of excitation at other wavelengths. Therefore, the two-photon excitation observed in the present study must be a nonresonant transition.

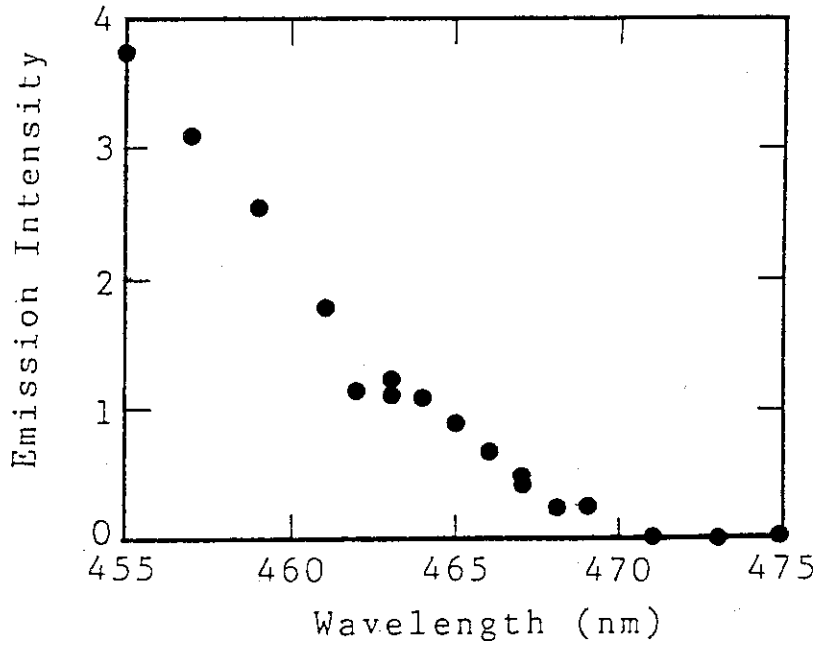

Fig. 4 The dependence of the emission intensity of Eu^{2+} at 416nm upon laser wavelength (455-475 nm). The distance between lens (f=330 mm) and sample is 280 mm.

References

1) Y. Yamada and S. Ohno, Bull. Chem. Soc. Jpn. **64** (1991) 926.

2) W. Kaiser and C. G. B. Garrett, Phys. Rev. Lett. **7**, 229 (1961).

3) U. Fritzler and G. Schaack, J. Phys. C: Solid State Phys.,**9**, L23 (1976).

4) U. Fritzler, *Z. Phys. B*, **27**, 289 (1977).

5) L.A.O. Nunes, F.M. Matinaga, and J.C. Castro, Phys. Rev.B, **32**, 8356 (1985).

6) F.M. Matinaga, L.A.O. Nunes, S.C. Zilio, and J.C. Castro, Phys. Rev. B, **37**, 993 (1988).

7) L.E. Kholodenkov and A.G. Makhanek, Phys. Status Solidi B, **112**, K149 (1982).

8) L. E. Kholodenkov and A.G. Makhanek, Phys. Status Solidi B, 125, 365 (1984).

Publication List

[1] Y. Yamada and S. Ohno, "Photoreduction of Solid Europium Chroride in KBr by Visible Two-photon Excitation," Chem. Lett. (1991) 465.

15.3 Metastable Dissociation of Multiphoton ionized Xenon Clusters

15.3.1 Introduction

Clusters have been studied by many workers from a viewpoint that they may relate properties of isolated molecular or atomic systems and those of the condensed phase.[1] The development of the inert-gas adiabatic-expansion technique together with TOF (Time of Flight) mass spectroscopy has provided a method of studying small clusters. The chemical and physical properties of clusters vary with the size, and clusters of some particular numbers of atoms, called "magic number", possess particular stability. It is important to measure metastable decomposition of clusters in order to understand their dynamics. A useful method to observe this unimolecular decomposition was demonstrated using a reflectron TOF mass spectroscopy technique. Both parent and daughter cluster ions were measured in the study of evaporative unimolecular dissociation of ammonia cluster ions[2-4] and other cluster ions.[5-7]

Xenon cluster ions have been studied experimentally in relation to the magic number; mass spectra of xenon cluster ions have strong peaks at certain cluster sizes, magic numbers being at n=13 and 19.[8-10] Calculations such as molecular dynamics have been performed to predict the magic numbers or stability of clusters.[11-13] The structure and stability of xenon cluster ions have been calculated theoretically,[14] and their thermochemical values have been measured experimentally.[15] The metastable dissociation rates of xenon cluster ions hve been measured on a microsecond time scale for clusters containing 10 to 79 atoms with the help of a double-focusing TOF mass spectrometer.[16] Quantitative analysis on the dissociation of small xenon cluster ions containing less than 10 atoms has not been reported because of their small dissociation probabilities.

We report here rates of metastable dissociations of Xe_n^+ ($Xe_n^+ \rightarrow Xe_{n-1}^+ + Xe$, where n = 2-19) observed using an angular reflectron TOF mass spectrometer. The highest dissociation rate was found for Xe_{14}^+. In addition there was a general trend that the larger cluster ions have the higher dissociation rates.

15.3.2 Experimental

The experimental apparatus is illustrated in Fig. 1. Xe gas (293K,

2.0×10^5 Pa) was introduced to the evacuated chamber (10^{-1} Pa) through a pulsed nozzle of 0.5 mm diameter (Jordan PSV) and pulse width of about 200 ms. Neutral Xe clusters formed in supersonic expansion were introduced to the ionization region through the skimmer. These neutral clusters were ionized by 266 nm light from a frequency-quadrupled Nd:YAG laser (Lumonics HY750) synchronized to the pulsed nozzle. The laser pulses of approximately 7 ns duration with intensity of 53 mJ per pulse were condensed by a convex lens (f = 80 mm) onto the ionization region. An angular reflectron (Jordan AREF) was employed to measure the cluster ions. Ions formed by multiphoton ionization were accelerated in a double electrostatic field to about 1.0 keV and travelled through a 100 cm-long field-free (10^{-4} Pa) region toward a reflection mirror. In a linear TOF measurement, the voltage of the grids of the reflection mirror were set to ground or lower potential, so that the ions passed through a reflection mirror and were detected by a microchannel plate detector placed behind the reflection mirror (MCP_1). In a reflection TOF measurements, ions were reflected and then travelled a further 80 cm through another field-free region. The cluster ions were then detected by another microchannel plate detector (MCP_r). The TOF signal through a fast preamplifier (Ortec 9305) was recorded by a digital oscilloscope (LeCroy 9400A) using a starting-trigger signal from a pin-photodiode detecting the laser pulse. The experiments were made at 10 Hz and TOF spectra were accumulated for 1000 laser shots.

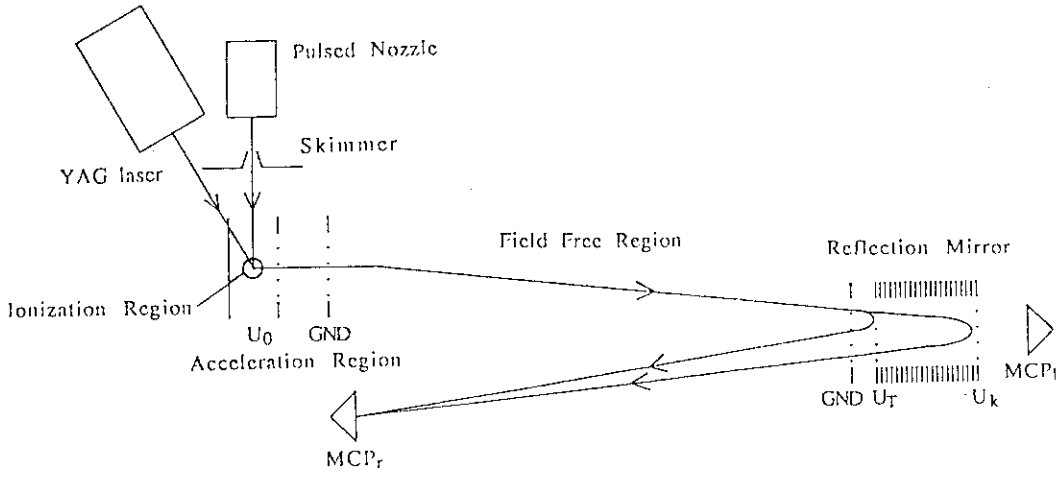

Fig. 1 Schematic of the experimental setup. The neutral cluster beam crosses with the laser beam in the ionization region. Arrowed lines indicate the trajectory of cluster ions in the reflectron made which is used to separate the daughter and parent cluster ions.

15.3.3 Results and discussion

Neutral Xe clusters are photoionized by multiphoton excitation using 266 nm laser light. Since the ionization potential of Xe is 12.13 eV, at least three photons are used for the ionization. In a TOF mass spectra, a variety of Xe_n^+ cluster ions with sizes up to n = 22 were observed. The most intense signal is assigned to monomer Xe^+ ion and cluster ions of larger mass have weaker intensities. A spectrum obtained with the linear TOF setup has low mass resolution and the differences between the flight times for the different isotopes were not observed. In the reflection mode the mirror is used to improve the time resolution. We can make the peaks in a TOF spectrum sharp by adjusting the voltage of the reflection mirror properly[17] and correcting the distribution of initial energy of the ions. Then the splitting due to the difference in masses of the isotopes can be observed for the Xe^+ ions (128, 129, 130, 131, 132, 134, and 136 amu) and the splinting of the larger cluster ions up to Xe_4^+ are observed.

The cluster ions produced by multiphoton ionization may undergo rapid fragmentation in the TOF region. As they grow evaporatively cool, dissociation extends to longer time, and the metastable dissociation process of cluster ions in the field-free region is observed. The reflectron is also employed to measure fractions of dissociating cluster ions by separating daughter and parent ions.[2] The initial parent ion energy (U_0), determined by the potential applied to the TOF lens elements and the position of the ionization point, is measured by using the reflection as an energy analyzer. When a metastable parent ion decomposes to a daughter ion, the daughter ion has an energy of $U_d = (M_d/M_p)U_0$, where M_d and M_p are masses of daughter and parent ions, respectively.

By setting the voltages on the second grid (U_t) and the last grid (U_k) of the refection mirror so that $U_d<U_t<U_0<U_k$, a daughter cluster ion and the corresponding parent ion are reflected separately. Daughter cluster ions then reach the microchannel plate before their parent cluster ions reach it. The metastable decomposition process can be studied in this way. Daughter cluster ions with larger masses are detected separately from their parent cluster ions by setting larger voltage at U_t. When $U_0<U_t$, both daughter and parent cluster ions are reflected in the first reflective field of the reflectron and they appear in the same peak on a spectrum.

The TOF mass spectrum of daughter plus parent cluster ions measured at U_0 = 1000 V, U_t = 980 V and U_k = 1200 V is given in Fig 2b. Daughter

and parent ion cluster ions are reflected in the first and second field, respectively. By setting U_t = 980 V and U_k=0 V, only daughter cluster ions are detected as shown in Fig. 2a. The peaks of daughter cluster ions detected in Fig. 2a precisely correspond to their peaks observed in Fig 2b. While some parent and daughter cluster ions overlap with each other in Fig 2b, the proper signals of parent cluster ions are estimated by subtracting the spectrum of daughter cluster ions (Fig. 2a) from that of daughter plus parent cluster ions (Fig. 2b). From the calculation of flight time, one can identify the daughter cluster ions produced by the metastable dissociation. In these case, the dissociation process can be expressed as

$$Xe_{n+1}^{+} \rightarrow Xe_n^{+} + Xe.$$

The dissociation process involves loss of only one neutral atom for every cluster ion. The fractions are estimated from the integrated peak intensities of these spectra. Though the small decay fractions are measured sensitively in this method, this operational mode leads to different flight paths and different collection efficiencies for the daughter and parent cluster ions.[2,3] Therefore, only the relative dissociation probabilities can be estimated in this operational mode.

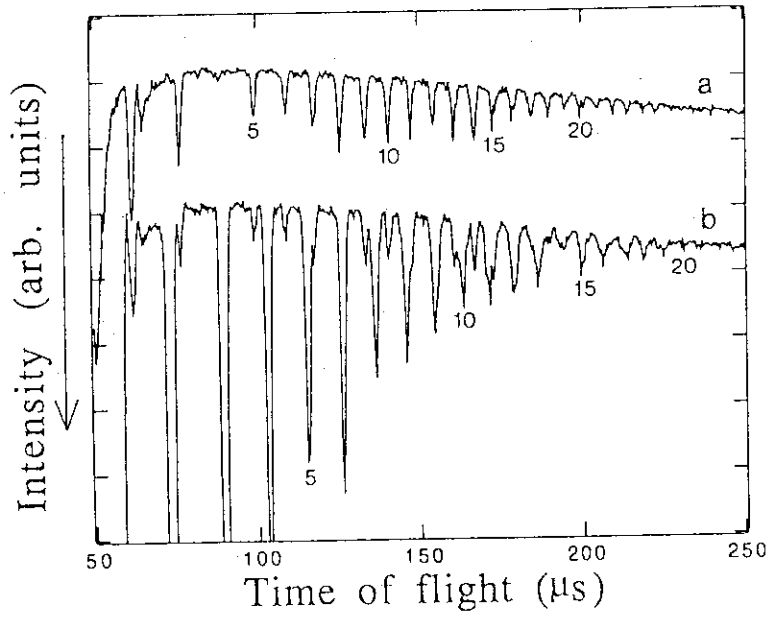

Fig. 2 TOF mass spectra taken using the reflectron. a) daughter cluster ions (U_0=1000 V, U_t=980 V and U_k=1200 V) and b) daughter and parent cluster ions (U_0=1000 V, U_k=980 V and U_k=0 V). Indicated numbers correspond to n for $Xe_n^{+} \rightarrow Xe_{n-1}^{+} + Xe$.

One can also measure decay fractions in a linear TOF setup. In this operational mode, a reflection grid is employed as a retarding grid. Without the retarding voltage ($U_t = U_k = 0$), flight times of fragments are determined by the energy at the exit of the accelerating region, and the decay fractions cannot be observed separately. When a retarding grid is employed, daughter cluster ions having less energy than retarding grid do not reach the multichannel plate ($U_d < U_t$, $U_k = 0$). While we cannot determine the daughter cluster ions, the decay fractions are estimated from the differences in intensities of parent cluster ions for the same flight path. The TOF spectra measured in this operational mode are given in Fig.3. The dissociation probabilities are estimated from the small differences of the large intensities of the signals, so the errors may be large in contrast to those estimated in the reflection mode. The dissociation probabilities for small Xe cluster ions Xe_n^+ (n = 2-13) are less than 0.2 and are too small for quantitative evaluation. Fortunately, however, Xe_{14}^+ has an exceptionally large decay fraction which is estimated to be 0.52 ± 0.08. Using the decay fraction at Xe_{14}^+ measured in this linear TOF mode as standard, one can estimate absolute dissociation probabilities measured in the reflection mode. By this method the measured intensities of daughter cluster ions in the reflection mode are corrected by a factor 0.36.

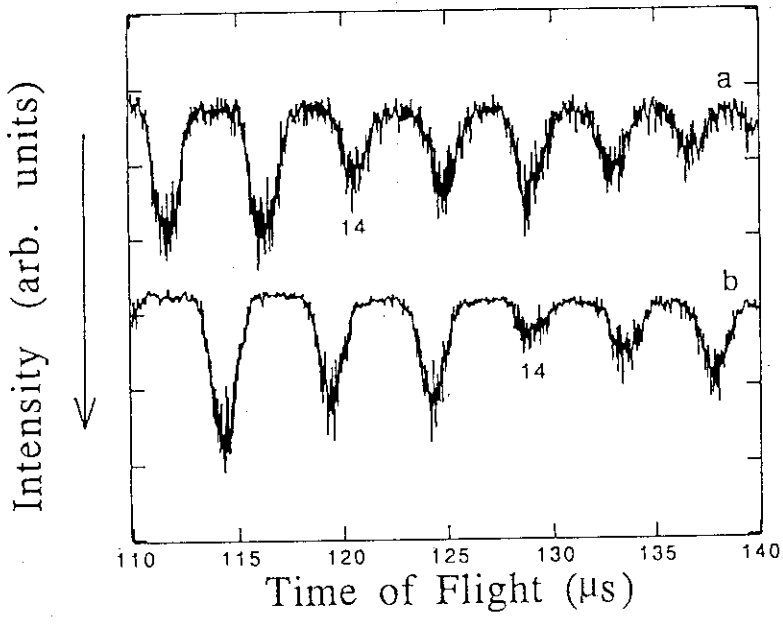

Fig. 3 TOF mass spectra taken in the linear TOF mode. a) daughter and parent cluster ions (U_0=1000 V, U_k=0 V and U_t=0 V) and b) parent cluster ions in the case where daughter cluster ions are excluded (U_0=1000 V, U_k=0 V and U_t=980 V).

From the dissociation probability of cluster ions, we can estimate the rate of metastable dissociation assuming an exponential decay: these cluster ions travelling the flight tube do not collide with each other. The rate constant k is:

$$k = -\ln(1-d/(d+p))/t_w, \qquad (1)$$

where d and p are the fractions of the daughter and parent cluster ions, respectively, t_w is the time window of dissociation (in this case the flight time of the cluster ion from the exit of the acceleration region to the reflection region). The rate constants k for cluster sizes from 2 to 19 are given in Fig. 4. For the large cluster ions (n = 20, 21 and 22), only the daughter cluster ions are observed because of high dissociation rates. Therefore dissociation rates for large cluster ions could not be estimated here.

The dissociation rates for these cluster ions show a maximum at n=14 and minima at 4, 13 and 19. These numbers correspond to the magic numbers reported in the literature.[8-10] The structure and energy of Xe cluster ions were calculated,[14] and it has been shown that Xe_4^+ has a linear core and that Xe_{13}^+ and Xe_{19}^+ have compact structures. These compact structures result in increased binding energy, and the differences in the dissociation rates are taken to reflect the stability of these ions.

A general trend is seen in Fig. 4 that the larger cluster ions have the higher dissociation rates in the size range studied. Klots' evaporative ensemble[18-20] predicts this tendency very well. In this theory the normalized population of daughter ions is given by

$$d/(p+d)=(C_n/g^2)\ln\{t/[t_0+(t-t_0)\exp(g^2/C_n)]\}, \qquad (2)$$

where t_0 is the flight time of the parent cluster ion before entering the field-free region, and t is the flight time of the parent cluster ion from the last TOF lens to the first grid of the reflection unit. t_0 and t are calculated from the voltages and configurations of the grids. C_n is the heat capacity of the cluster ion of size n ($C_n = c \cdot n$). g is the Gspann parameter which is nearly independent of the size, composition of the aggregate, and the time (g = 25). From the least square fitting of our experimental results, c = 2.62 is obtained (Fig. 4). Klots fitted this equation to the experimental data of Xe_n^+ (n = 10-79) as measured by

Kreusle[16] and obtained c = 2.79.[20] Our experimental data on small cluster ions are in good agreement with this value.

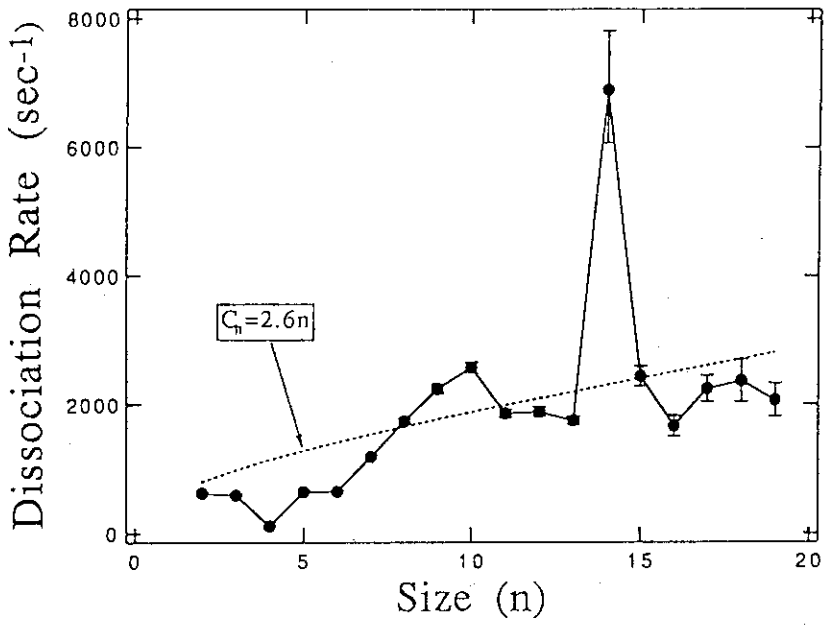

Fig. 4 The dissociation rates for xenon cluster ions in the field-free drift tube. The dotted line indicates the estimated value using the evaporative ensemble.

References

1) J.P. Maier, "Ion and Cluster Ion Spectroscopy and Structure", (Elsevier, Amsterdam, 1989).

2) O. Echt, P.D. Dao, S. Morgan, and A.W. Castleman, Jr., J. Chem. Phys. **82** (1985) 4076.

3) S. Wei, W.B. Tzeng, and A.W. Castleman, Jr., J. Chem. Phys. **92** (1990) 332.

4) S. Wei, W.B. Tzeng, and A.W. Castleman, Jr., J. Chem. Phys. **93** (1990) 2506.

5) W.B. Tzeng, S. Wei, and A.W. Castleman, Jr., J. Am. Chem. Soc. **111** (1989) 6035.

6) S.Wei, W.B. Tzeng, and A.W. Castleman, Jr., J. Phys. Chem. **94** (1990) 6927.

7) R.J. Stanley, M. Cook, and A.W. Castleman, Jr., J. Phys. Chem. **94** (1990) 3668.

8) O. Echt, K. Sattler, and E. Recknagel, Phys. Rev. Lett. **47** (1981)

1121.

9) O. Echt, A.Reyes Flotte, M. Knapp, K. Sattler, and E. Recknagel, Ber. Bunsenges. Phys. Chem. **86** (1982) 860.

10) A. Ding and J. Hesslich, Chem. Phys. Lett. **94** (1983) 54.

11) J.J. Saenz, J.M. Soler, and N. Garcia, Chem. Phys. Lett. **114** (1985) 15.

12) J.M. Soler, J.J. Saenz, and N. Garcia, Chem. Phys. Lett. **109** (1984) 71.

13) E.E. Polymeropoulos and J. Brickmann, Surface Science **156** (1985) 563.

14) M. Amarouche, G. Durand, and J. P. Malrieu, J. Chem. Phys. **88** (1988) 1010.

15) K. Hiraoka and T. Mori, J. Chem. Phys. **92** (1990) 4408.

16) D. Kreisle, O. Echt, M. Knapp, and E. Recknagel, Phys. Rev. A **33** (1986) 768.

17) V.I. Karataev, B. A. Mayrin, and D. V. Shmikk, Sov. Phys. Tech. Phys. **16** (1972) 1177.

18) C.E. Klots, J. Chem. Phys. **83** (1985) 5864.

19) C.E. Klots, Z. Phys. D **5** (1987) 83.

20) C.E. Klots, J. Phys. Chem. **92** (1988) 5864.

Publication List

[1] Y. Yamada, T. Takayanagi, K. Furukawa, and S. Ohno, "Metastable Dissociation of Multiphoton-ionized Xenon Clusters," Rapid Comm. in Mass Spectometry, **5** (1991) 303.

15.4 Microdosimetry of High-Energy Heavy Ions

15.4.1 Introduction

In microdosimetry of high-energy heavy ions, two kinds of information are of fundamental importance; (1) the ratio of the deposited energy going into kinetic energy of atoms to that going into electronic excitations or ionizations, and (2) the spatial distribution of the deposited energy around the track of an incident heavy ion.

It is well-known that the W-value, mean energy required to produce an ion-electron pair, has little dependence on energy at very high energies. This is because the amount of energy converted into kinetic energy of gas atoms is negligible.[1] For heavy or low-energy incident particles, this fraction become large due to "nuclear collision", resulting in an increase of W. Thus, we aim at experimental determination of W for Ar gas as a function of primary energy of the incident particle. Then, we try to compare the results with those obtained from the LSS theory concerning the partitioning of energy into electronic processes and the kinetic energy of gas atoms.[2]

As to information on the spatial distribution of the deposited energy, we employ the method by Wingate and Baum[3] who measured radial distribution of ionization current in a small wall-less ionization chamber.

15.4.2 Experimental

A collimated beam of heavy ion of the energy range 100-150 MeV from the JAERI Tandem accelerator is introduced in the vacuum vessel through a set of aperture which serves also for differential pumping system.

A schematic view of the apparatus used in the present work is shown in Fig. 1. A large cylindrical ionization chamber (of diameter 180 mm, length 900 mm) made of Al (a) is used for measurements of W. Details of this chamber were reported previously.[4] Spatial distribution of the deposited energy was measured with the small wall-less ionization chamber (b). It consisted of two cylindrical meshes and a central wire supported by Teflon insulator, respectively. The wall-less ionization chamber itself is placed in large vacuum vessel filled with an Ar gas at variable pressure and it is movable by remote operation. The radial distance from the beam track was adjusted by changing either the gas pressure or the radial

position of the wall-less ionization chamber.

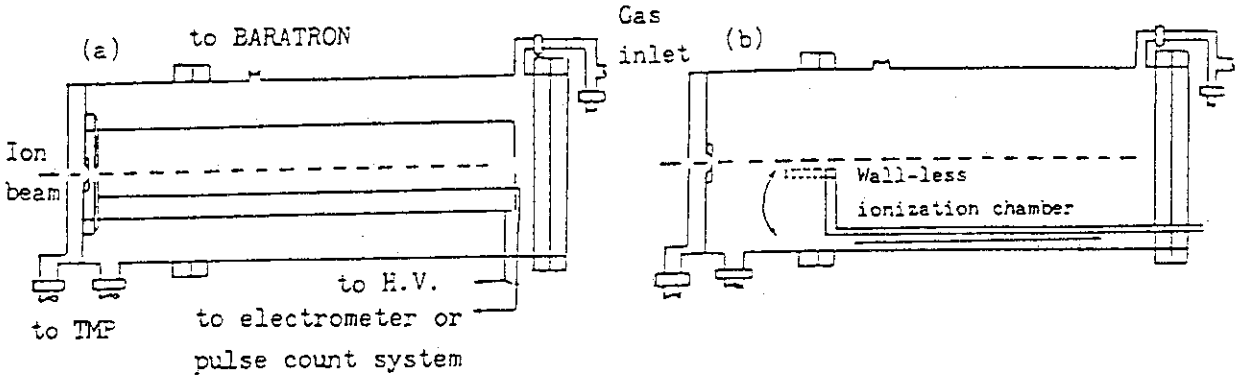

Fig. 1 A schematic view of the ionization chamber.

15.4.3 Results and Discussion

The saturation curves were obtained for the 23.0 and 86.7 MeV S^{10+} and 90.9 MeV I^{7+} ions incident on the chamber containing Ar gas at pressure ranging from 0.45 to 100 Torr. The saturation currents obtained at the pressure of 50 and 100 Torr are nearly the same, indicating that the incident ions are completely stopped within the chamber.

W value is the mean energy required to create an ion-electron pair when an incident ion is stopped in the gas. Thus if N ions of energy E lose all their energy in the gas and produce ionization current I, then W is given by

$$W = E N e / I,$$

where e is the electronic charge. In Fig. 2 we plot the W values as a function of the reduced energy. The figure also shows the curve calculated by using LSS theory.

The agreement between the experimental and the theoretical results is reasonable in that the fraction of the energy that goes into kinetic energy of gas atoms becomes larger as the incident particle is heavier in mass and lower in energy. However, it is noticed that the experimental results showed a significant deviation from the theory.

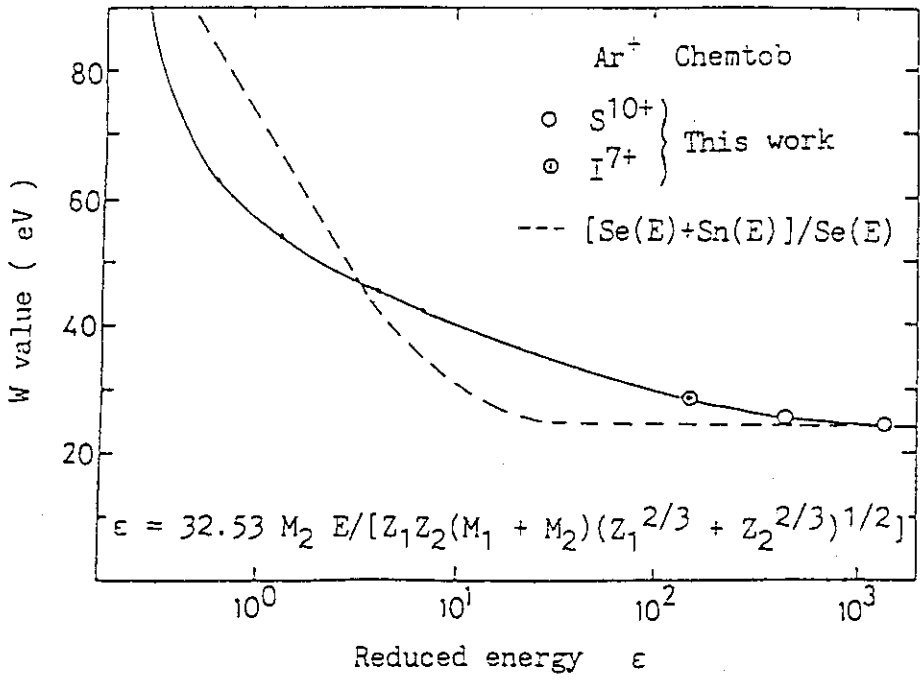

Fig.2 W as a function of reduced energy for Ar gas.

Fig. 3 shows the radial distribution of absorbed dose obtained in Ar gas by a small wall-less ionization chamber at various distances from the path of the incident 200 MeV Ni ion. In this measurement the mesh chamber was placed at the radial distance of 35 ~ 70 mm from the beam path. The pressure in the chamber was varied from 0.25 to 40 Torr. The radial distance is all normalized to the density of 1 g/cm3, i.e., simulated radial distance R is given by

$$R = R_{gas}\ (d_{gas}/d_{water}),$$

where R_{gas} is the observed distance. d_{gas} and d_{water} are the density of Ar gas used and that of liquid water, respectively. Dose in eV/g at the distance of R is:

$$\text{Dose} = (I_p/I_i)(ZW_e/v\ d_{gas}))(d_{water}/d_{gas})^2,$$

where I_p and I_i are the ionization current in the small wall-less chamber and the incident ion-beam current, respectively. Z is the charge of the incident ion, W_e is W-value of the gas for electron (=26.2 eV), and v is the volume of the small wall-less ionization chamber. The results indicate that the radial distribution of the normalized absorbed dose decreases with 1/2.5 power of the normalized radial distance.

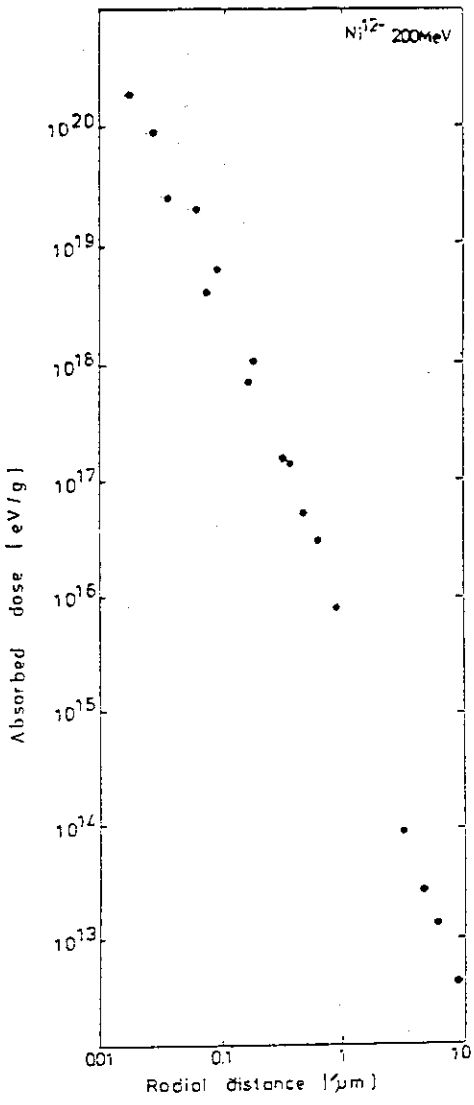

Fig.3 Absorbed dose as a function of simulated radial distance.

References

1) "Average Energy Required to Produce An Ion Pair", ICRU Report 31 (1979).

2) J.F. Ziegler, "Handbook of Stopping Cross-Section for Energetic Ions of All Elements", Pregamon Press, NY., (1979).

3) C.L. Wingate and J.W. Baum, Radiat. Res. **65** (1976) 1.

4) K. Furukawa, S. Ohno, Y. Komaki, H. Namba, Y. Aoki, and Y. Nakai, JAERI-M89-119 (1989) 83.

5) M. Chemtob, B. Lavigne, J. Chary, V.D. Nguyen, N.Parmentier, J.P. Noel, and C. Fiche, Phys. Med. Biol. **22** (1977) 208.

16. Studies on Dissolution of High-Burnup Fuels

E. Tachikawa, T. Adachi, Y. Aratono, K. Gunji,
T. Hirabayashi, K. Hojou, J. Ishikawa, Y. Kato,
T. Kimura, K. Kohno, M. Komaki, M. Magara,
N. M. Masaki, Y. Meguro, H. Muto, Y. Nakahara,
M. Nakashima, K. Obara, M. Ohnuki, H. Ohtsu, M. Saeki,
C. Sagawa, T. Sakurai, T. Sato, T. Sonobe, T. Suzuki,
A. Takahashi, H. Takeishi, Y. Toida, Z. Yoshida

To obtain quantitative data relating to the dissolution of high burnup spent nuclear fuel, dissolution study has been carried out at the Department of Chemistry from 1984 under the contract with Science and Technology Agency entitled "Reprocessing Test Study of High Burnup Fuel"[1]. PWR spent fuels of 8,400 to 36,100 MWd/t in assemblywise averaged burnup in which UO_2 and UO_2-Gd_2O_3 fuels were involved were dissolved and the chemical composition and distribution of radioactive nuclides were measured for insoluble residue, cladding material(hull), off-gas and dissolved solution. With these analyses basic data concerning the dissolution and clarification process in the reprocessing plant were accumlated. The schematic diagram of the study is shown in Fig. 1, and the characteristics of samples in Table 1.

Table 1 Samples for dissolution study

Sample No.	11	12	13	14	15	16	17
Cycle of irrad.	3	2	2	2	2	2	3
Type of fuel	UO_2	UO_2-Gd_2O_3	UO_2	UO_2-Gd_2O_3	UO_2-Gd_2O_3	UO_2	UO_2
Measured Burnup (MWd/t)	39,700	25,700	30,800	21,900	29,400	39,300	(32,100)
U Enrichment(%)	3.42	1.7	3.2	1.7	1.7	3.2	3.24
Pellet Weight(g)	2.250	1.382	1.302	1.659	1.742	2.008	2.008
Hull Weight(g)	0.425	0.347	0.347	0.379	0.405	0.369	0.369

16.1 Dissolution behavior[2)]

Spent fuel rods from 800MWe class PWR nuclear power plants were cut into pieces, and the specimens with ca. 3mm in length (2-3 g as UO_2) were obtained. They were dissolved in a batchwise together with Zircaloy cladding in ca. 30 ml of 4M nitric acid at 100 ℃ with stream of helium gas(Fig. 2). The rate of dissolution was observed by krypton monitor. Dissolution was almost completed within 2 h. The dissolution rates of UO_2-Gd_2O_3 fuels were a little slower than those of UO_2 fuel[3)].

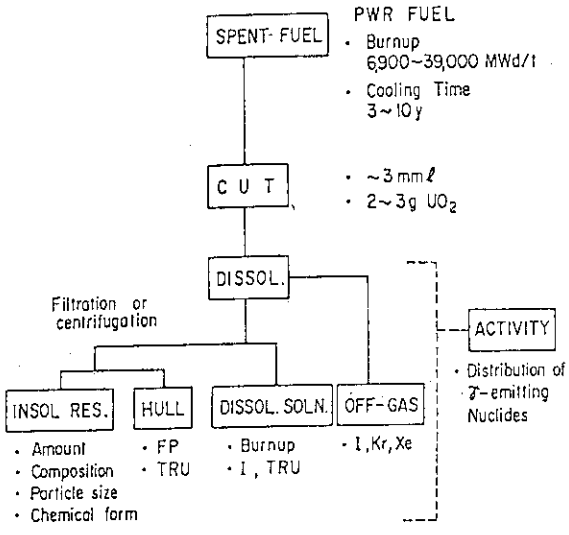

Fig. 1 Overview of the dissolution test study.

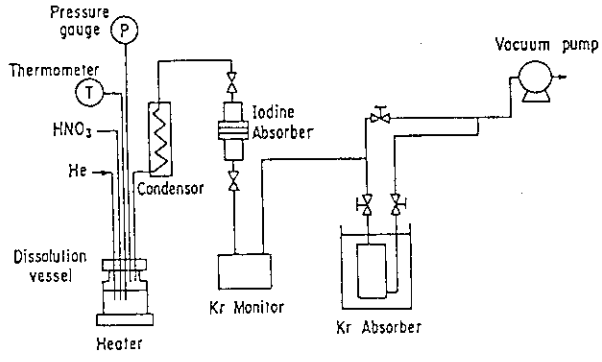

Fig. 2 Schematic diagram of dissolution apparatus.

16.2 Analysis of volatile radionuclides in the dissolver-off-gas

During dissolution of the specimen, the amounts of iodine (^{129}I) and krypton (^{85}K) in the dissolver-off-gas were measured together with isotope compositions of krypton and xenon. The dissolution was followed by the expulsion of iodine from fuel solution, insoluble residue and fuel cladding in order to obtain its material balance. A similar apparatus(Fig. 2) was used in the expulsion processes.

(1) Analysis of iodine-129 in the fuel solution, insoluble residue and fuel cladding

After dissolution, the insoluble residue was separated from the fuel solution by centrifugation, and the expulsion of iodine

was carried out for both of them.

Iodine in the solution was first removed by NO gas sparge at 100℃. For the further removal of a small amount of iodine remaining in the solution, excess amount of potassium iodate was added to the solution as the carrier of original iodate present in the solution, and after heating at 100℃ for 1 h, the solution was again bubbled with the NO flow[4]. The iodine volatilized in each step was trapped separately on the iodine absorber (Fig. 2) and analyzed by gamma ray spectrometry.

In the case of the expulsion of iodine from insoluble residue, the residue was first heated in 30 ml of concentrated nitric acid solution including excess inactive iodate to elute iodine from the insoluble residue to the solution[5]. Then, the solution was bubbled with a NO gas flow to transfer the iodine from the solution to the iodine absorber. Expulsion of iodine from the fuel cladding was also carried out in the same way as the insoluble residue.

Table 2 shows the result of several experimental runs for UO_2 fuels and UO_2-Gd_2O_3 fuels with the weight of specimens and their measured burnup. It was found that a small part of iodine in the fuel was able to be distributed to the insoluble residue, besides dissolver-off-gas and solution. For the UO_2 fuels, its amount was around 1% or less of the total I-129. For the gadolinium-added fuels, it ranged up to 2.3%.

In the solution iodine was involved up to 10%. In the fuel cladding iodine was not retained.

From the comparison of total amounts of iodine obtained in the experiments with those calculated from ORIGEN2 code, it was found that the total amount of iodine collected on the iodine absorber was approximately 60 to 70% of the calculated values.

(2) Analyses of krypton and xenon

Besides Kr and Xe, He, O_2, N_2 and NOx were also trapped in the Kr absorber shown in Fig. 2. Before analyses of Kr and Xe, their separation from these impurities was carried out. Oxygen, nitrogen and NOx were removed by passing repeatedly the gaseous mixture through a column filled with titanium sponge at high temperatures (500 to 800℃). The residual gas was then

Table 2 Amounts of iodine-129 volatilized from the fuel pellets

Fuels	UO_2		UO_2		UO_2		UO_2		UO_2-Gd_2O_3		UO_2-Gd_2O_3		UO_2-Gd_2O_3	
Sample No.	11		13		16		17		12		14		15	
Burnup (MWd/t)	39,700		30,800		39,300		(32,100)		25,700		21,900		29,400	
Initial uranium amount [U_e]g	2.036		1.172		1.572		(1.804)		1.154		1.366		1.430	
Amount of insoluble residue (mg)	7.8		3.2		8.5		5.9		4.3		4.0		14.7	
Amount of iodine	Bq/g-U_e	%	Bq/g-U_e	%	Bq/g-U_e	%	Bq/g-U_e	%	Bq/g-U_e	%	Bq/g-U_e	%	Bq/g-U_e	%
During Dissolution	968	98.1	707.3	96.8	789.0	97.2	787.1	98.9	583	88.1	497.6	93.4	727.14	100
Expulsion from the solution	11.7	1.2	23.6	3.3	9.6	1.2	2.1	0.3	63.9	9.7	34.8	6.6	N.D.	
Expulsion from the insoluble residue	6.8	0.7	-	-	13.3	1.6	6.1	0.8	15.0	2.3	N.D.		N.D.	
Expulsion from the fuel cladding	N.D.		-	-	-	-	-	-	-	-	N.D.		-	
Total	986.5	100	730.9	100	811.9	100	795.3	100	661.9	100	532.4	100	727.1	100
Calculation by ORIGEN-2 code	1388	-	1090	-	1400	-	1130	-	1000	-	910	-	1260	-
A/B %	71.1	-	67.1	-	58.0	-	70.4	-	66.2	-	58.5	-	57.7	-

N.D. ; not detected

evacuated through a column charged with zeolite at -196℃ to remove He. The krypton and xenon thus purified was subjected to mass spectrometry to obtain their isotope compositions. ^{85}Kr was also determined by gamma ray spectrometry.

Table 3 shows the isotope compositions of krypton and xenon, and Table 4 the amount of ^{85}Kr. The isotope ratio of ^{85}Kr averaged about 6.4%.

Table 3 Isotope composition of krypton and xenon in the dissolver-off-gas

Unit:atom%

Sample No.	13	14	15	16
Burnup(MWd/t)	30,800	21,900	29,400	39,300
Kr-82	0.4(5)	0.6(4)	0.6(2)	0.6(1)
Kr-83	14.7(15)	14.0(7)	12.6(5)	11.4(4)
Kr-84	34.1(12)	34.4(17)	32.6(8)	32.6(8)
Kr-85	5.9(3)	7.7(6)	6.1(4)	6.1(4)
Kr-86	41.0(10)	39.3(18)	48.1(9)	49.6(8)
Xe-130	N.D.	N.D.	N.D.	0.3(1)
Xe-131	10.0(4)	7.0(2)	6.6(3)	6.3(1)
Xe-132	21.2(6)	21.4(7)	21.1(3)	20.6(6)
Xe-134	27.7(6)	27.9(13)	28.1(3)	28.1(3)
Xe-136	41.1(8)	43.6(5)	44.4(2)	44.5(7)

"0.4(5)" mean 0.4±0.5 N.D. ; not detected

Table 4 Radioactivity of ^{85}Kr in the dissolver-off-gas

Sample No.	11	12	13	14	15	16
Burnup (MWd/t)	39,700	25,700	30,800	21,900	29,400	39,300
Initial uranium amount (U_e,g)	2.036	1.154	1.172	1.366	1.430	1.572
Kr-85 Bq/U_e-g	1.66×10^8	7.74×10^7	2.31×10^8	1.05×10^7	1.75×10^8	2.28×10^8

16.3 Analysis of insoluble residue[2)]

(1) Amount of insoluble residue

The relation between the amount of insoluble residue and

burnup of the fuel is shown in Fig. 3. The amount of insoluble residue obtained from UO_2-Gd_2O_3 fuel was about two times larger compared with that from UO_2 fuel. This may be resulted from the fact that the UO_2-Gd_2O_3 fuel has lower initial enrichment for U-235(1.7%) than that of the UO_2 fuel (3.2%)[3]. Owing to the low enrichment, such noble element nuclides as Ru-104, Rh-103, Pd-105, and Pd-106 are much more produced because contribution of Pu-239 and -241 to total fission is increased.

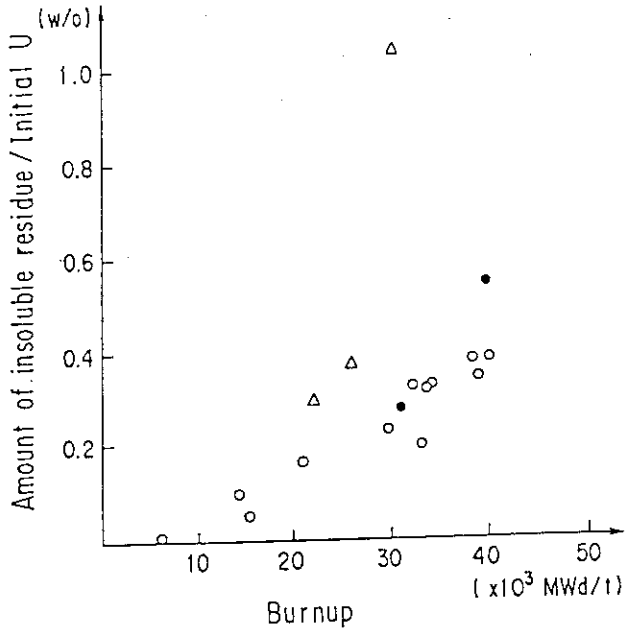

Fig. 3 Relation betwen amount of insoluble residue and burnup of PWR fuel.

○ : UO_2
● : UO_2, in Gadolinia-Assembly
△ : $UO_2-Gd_2O_3$, in Gadolinia Assembly

(2) Composition of insoluble residue

The typical example of the composition of the insoluble residue is shown in Table 5. for UO_2 fuel(NO. 8) and for UO_2-Gd_2O_3 fuel(No. 12). More than 70 % of the insoluble residue is noble elements such as ruthenium, rhodium and palladium together with molybdenum and technetium. The amount of molybdenum largely depends upon the composition of fuels. This again may be related to the lower enrichment of U-235 in UO_2-Gd_2O_3 fuel. Fission yields of molybdenum isotopes for U-235 and Pu-239, -241 are not greatly changed, but those of ruthenium, rhodium and palladium for Pu-239, -241 are much higher than for U-235.

The crystal structure of the insoluble residue was identified as rurhenium alloy(hexagonal, ε -phase) by X-ray diffractometry as suggested in the studies of the simulated fuel[6].

Table 5 Analytical results of insoluble residue

Element	Sample number 8(UO_2) mg	8(UO_2) %	12(UO_2-Gd_2O_3) mg	12(UO_2-Gd_2O_3) %
Mo	1.16	21.6	0.24	6.9
Tc	0.05	1.0	0.082	2.4
Ru	2.84	53.0	1.74	50.1
Rh	0.41	7.6	0.13	3.7
Pd	0.43	8.1	0.36	10.4
Cr	0.027	0.5	0.08	2.3
Fe	0.14	2.6	0.17	4.9
Ni	< 0.01	-	< 0.01	-
Zr	0.29	5.5	0.67	19.3
Total	5.36	100	3.47	100
Measured burnup(MWd/t)	34100		25700	
Insoluble residue weighed(mg)	7.0		4.3	
Initial U(g)	2.153		1.154	

16.4 Analysis of spent fuel claddings

In the study of spent fuel claddings, the radioactivities from β , γ , and α -emitters were examined as a function of burnup in the range of about 7,000 to 40,000 MWd/t.

(1) β , and γ -emitters in cladding

Figure 4 shows the activities of representative β and γ -emitters in spent nuclear fuel claddings as a function of burnup. The radioactivity of fission products Cs-137, Ru-106, H-3 and the activation product Co-60 increase proportionately with burnup of fuel, whereas the radionuclides Cs-134 and Eu-154 increase with the second power of burnup. These results suggest that, although single event such as fission reaction of U-235 produced directly the former radionuclides, the successive reaction with neutron, that is, the neutron capture after fission reaction, participated in the formation process of the latter radionuclides. Consequently, the formation of Cs-134 and Eu-154 appears to show second-order dependence on the burnup of fuel.

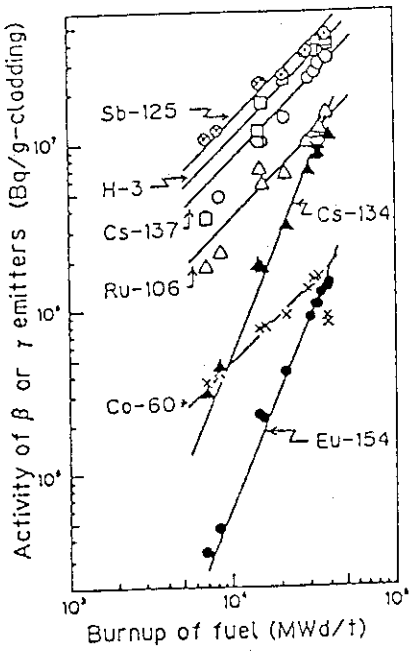

Fig. 4 Activity of β or γ emitters in the spent fuel claddings.

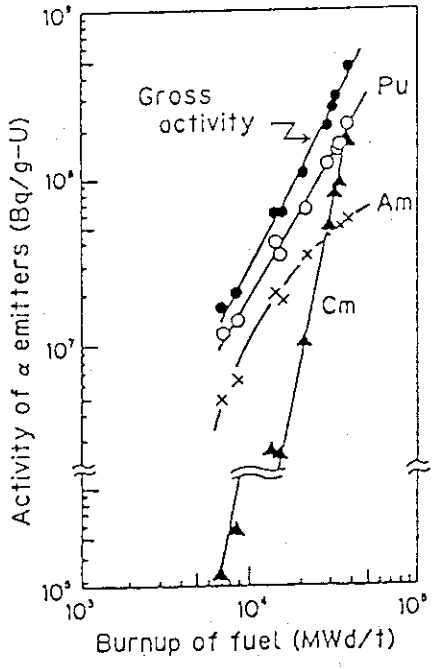

Fig. 5 Elemental contribution to α -ray activity in the spent nuclear fuel as a function of fuel burnup.

(2) α -Emitters on and in Cladding

The gross activities of α -emitters on the inner and outer surfaces of cladding were given in the previous report as a function of burnup[7]. The activity of α -emitters on the inner surface increased with the 3.1 power of fuel burnup, while that on the outer surface increased with the 1.3 power. On the other hand, the gross α -ray activity of the fuel, as shown in Fig. 5, increased with the second power of the burnup. These results indicated that the accumulation of α -emitters on the inner surface was enhanced by the fuel burnup, whereas the accumulation on the outer surface was less than that expected from Fig. 5. The enhancement of the accumulation of α -emitters on the inner surface appears to be eventually caused by the occulusion of the actinoids through the repetition of the adsorption and/or adhesion of fuel and the oxidation of inner surface during irradiation.

The distribution of α -emitters in the spent fuel cladding of 24,900 MWd/t is shown in Table 6. They are principally present on the inner and the outer surfaces and only small amount distributes in the interior of the cladding. The α -emitters concentration ranged from 1.3 to 36 kBq/g, except for

the inner (3.7 μm in depth) and the outer (617 μm in depth) surface layer of the cladding and the weighed average concentration was found to be about 2 kBq/g (about 50 nCi/g) in the interior of cladding.

Table 6 Distribution of α-emitters in the spent fuel cladding of 29,400 MWd/t burnup at 5 years cooling

Depth (μm)	Radioactivity (Bq/g cladding)					
	Gross α	U	Np	Pu	Am	Cm
0 - 3.7	1.97×10^{6}	1.6×10^{1}	6×10^{0}	9.7×10^{5}	3.93×10^{5}	5.12×10^{5}
3.7- 5.4	3.6×10^{4}	4×10^{0}	$<4\times10^{0}$	1.48×10^{4}	7.43×10^{3}	8.7×10^{3}
5.4- 6.8	3.03×10^{4}	$<1.6\times10^{0}$	$<5\times10^{0}$	1.38×10^{4}	4.7×10^{3}	7.6×10^{3}
6.8- 10	7.6×10^{3}	-	-	-	-	-
10 - 20	8.7×10^{3}	-	-	-	-	-
20 - 80	3.5×10^{3}	-	-	-	-	-
80 - 135	2.06×10^{3}	-	-	-	-	-
135 - 189	1.52×10^{3}	-	-	-	-	-
189 - 241	1.47×10^{3}	-	-	-	-	-
241 - 385	1.39×10^{3}	$<5\times10^{-2}$	$<5\times10^{0}$	6.1×10^{1}	2.69×10^{2}	3.15×10^{2}
385 - 524	1.49×10^{3}	-	-	-	-	-
524 - 617	1.61×10^{3}	-	-	-	-	-
617 - 620*	2.20×10^{5}	5×10^{1}	$<2\times10^{0}$	1.45×10^{5}	2.60×10^{4}	3.33×10^{4}

*:Outer surface layer

16.5 Analysis of dissolved solution

Knowing the composition of spent nuclear fuel as accurately as possible is essential in several fields of nuclear technology as reactor operation, spent fuel reprocessing, waste disposal management and safegurds. The purpose of the analysis is not only to supply a accurate burnup value but also to get a more information on fission products and actinides in the fuel for better understanding of irradiation behavior and isotope correlation of a spent fuel. And using the measured values one can improve the calculation method and nuclear data for the prediction of amounts of FPs and actinoids constituting nuclear fuels.

FPs and actinides in the dissolved solution were determined by the procedure shown in the previous report[8]. In Tables 7 to 9, isotope composition of uranium and plutonium are shown with burnup.

Tables 7 Isotopic composition of uranium in dissolved solution

Unit:atom%

Sample No.	11	12	13	14	15	16
Type of fuel	UO_2	UO_2-Gd_2O_3	UO_2	UO_2-Gd_2O_3	UO_2-Gd_2O_3	UO_2
Measured Burnup (MWd/t)	39,700	25,700	30,800	21,900	29,400	39,300
U-234	0.0183(1)	0.0088(2)	0.0185(1)	0.0094(1)	0.0083(1)	0.0164(1)
U-235	0.831(1)	0.465(2)	0.961(2)	0.572(1)	0.386(1)	0.654(14)
U-236	0.494(2)	0.224(4)	0.404(1)	0.206(1)	0.235(1)	0.450(2)
U-238	98.658(2)	99.302(4)	98.617(2)	99.213(1)	99.371(1)	98.80(2)

Cooling time:5 y, 1.234±(5) means 1.234±0.005.

Tables 8 Isotopic composition of plutonium in dissolved solution

Unit:atom%

Sample No.	11	12	13	14	15	16
Type of fuel	UO_2	UO_2-Gd_2O_3	UO_2	UO_2-Gd_2O_3	UO_2-Gd_2O_3	UO_2
Measured Burnup (MWd/t)	39,700	25,700	30,800	21,900	29,400	39,300
Pu-238	2.40(2)	1.08(2)	1.35(1)	0.871(9)	1.35(1)	2.03(2)
Pu-239	55.07(2)	56.32(2)	58.50(2)	59.53(2)	53.69(2)	52.74(3)
Pu-240	24.48(2)	24.57(2)	24.16(2)	23.73(3)	25.35(2)	25.85(3)
Pu-241	11.68(2)	11.95(2)	11.11(2)	11.19(1)	12.33(1)	12.05(4)
Pu-242	6.37(1)	6.08(1)	4.89(1)	4.69(1)	7.29(1)	7.35(2)

Cooling time:5 y, 1.234±(5) means 1.234±0.005.

Table 9 Burnup and amounts of plutonium and Nd-148 in dissolved solution

Sample No.	11	12	13	14	15	16
Type of fuel	UO_2	UO_2-Gd_2O_3	UO_2	UO_2-Gd_2O_3	UO_2-Gd_2O_3	UO_2
Measured Burnup (%FIMA)	4.135	2.680	3.205	2.283	3.060	4.098
Measured Burnup (MWd/t)	39,700	25,700	30,800	21,900	29,400	39,300
Pu/U atom ratio	1.162×10^{-2}	1.015×10^{-2}	9.206×10^{-3}	9.265×10^{-3}	1.066×10^{-2}	1.060×10^{-2}
Nd-148/U atom ratio	7.305×10^{-4}	4.685×10^{-4}	5.597×10^{-4}	3.949×10^{-4}	5.344×10^{-4}	7.231×10^{-4}

Cooling time:5 y.

[This work was performed under the auspieces of Science and Technology Agency of Japan.]

References

1) Department of Chemistry Progress Report(Jan. 1986 - Dec. 1988), JAERI-M 89-058, p.321(1989).
2) T. Adachi, M. Ohnuki, N. Yoshida, T. Sonobe, W. Kawamura, H. Takeishi, K. Gunji, T. Kimura, T. Suzuki, Y. Nakahara, T. Muromura, Y. Kobayashi, H. Okashita, and T. Yamamoto, J. Nucl. Mter. 174(1990)60.
3) T. Adachi, M. Ohnuki, H. Takeishi, K. Gunji, and W. Kawamura, in:Proceedings of the Third International Conference on Nuclear Fuel Reprocessing and Waste Management (RECOD' 91, 1991)p.675.
4) T. Sakurai, A. Takahashi, N. Ishikawa and Y. Komaki; Nucl. Technol. 85(1989)206.
5) T. Sakurai, A. Takahashi, N. Ishikawa and Y. Komaki; ibid., 94(1991)99.
6) T. Muromura, T. Adachi, H. Takeishi, Z. Yoshida, T. Yamamoto, K. Ueno, J. Nucl. Mater. 151(1988)318.
7) Department of Chemistry Progress Report(Jan. 1986 - Dec. 1988), JAERI-M 89-058(1989) p.324.
8) ibid, p.325.

Publication list

[1] Dissolution Study Group in the Department of Chemistry, "Dissolution Studies of Spent Nuclear Fuels," JAERI-M 91-010(1991).
[2] T. Adachi, M. Ohnuki, N. Yoshida, T. Sonobe, W. Kawamura, H. Takeishi, K. Gunji, T. Kimura, T. Suzuki, Y. Nakahara, T. Muromura, Y. Kobayashi, H. Okashita, T. Yamamoto, "Dissolution study of spent PWR fuel:Dissolution behavior and chemical properties of insoluble residues," J. Nucl. Mater. 174(1990)60.
[3] T. Adachi, M. Ohnuki, H. Takeishi, K. Gunji, W. Kawamura, "Dissolution behavior and characteristics of fission product insoluble residues of PWR spent nuclear fuel, "Proceedings of the Third International Conference on

Nuclear Fuel Reprocessing and Waste Management(RECOD ' 91), April 14-18, 1991, Sendai, Japan, p.675.

[4] T. Sakurai, A. Takahashi, N. Ishikawa, Y. Komaki, M. Ohnuki, and T. Adachi, "Behavior of Iodine in the Dissolution of Spent PWR-Fuel Pellets," Proceedings of the Third International Conference on Nuclear Fuel Reprocessing and Waste Management (RECOD ' 91), April 14-18, 1991, Sendai, Japan, p. 678.

[5] Y. Komaki, N. Ishikawa, A. Takahashi, A. Yokoyama, T. Sakurai, M. Ohnuki, Y. Kobayashi, and T. Adachi,"Analytical Method and Behavior of Volatile Nuclides in Dissolution of of Spent LWR Fuels," J. At. Energy Soc. Jpn., 33(1991)489.

[6] T. Hirabayashi, T. Sato, C. Sagawa, N. M. Masaki, M. Saeki and T. Adachi, "Distribution of radionuclides on nd in spent nuclear fuel claddings of pressurized water reactors," J. Nucl. Mater. 174(1990)45.

[7] T. Hirabayashi, T. Sato, C. Sagawa, N. M. Masaki, M. Saeki and T. Adachi, "Radioactivities on/in Zircaloy claddings of PWR spent nuclear fuel, " Proceedings of the Third International Conference on Nuclear Fuel Reprocessing and Waste Management(RECOD ' 91), April 14-18, 1991, Sendai, Japan, p.903.

[8] Y. Nakahaa, T. Suzuki, K. Gunji, N. Kohno, H.Takano, Z. Yoshida and T. Adachi, "Amount of Nuclides Constituting PWR Spent Fuels: Comparison of Observed with Calculated Values," Radiochim. Acta 50(1990)141.

17. JAERI UNIVERSITIES CO-WORKING PROJECT ON CHEMISTRY OF ACTINIDES

M. Hoshi, Y. Nakahara, S. Ichikawa, N. Shinohara, H. Iimura, M. Magara, T. Fujino*, T. Muromura, T. Yamashita, K. Ohuchi, Z. Yoshida, T. Kimura, Y. Meguro, H. Aoyagi and C. Yonezawa, and H. Nakahara(1), K. Sueki(1), T. Kobayashi(1), T. Tsukada(1), I. Nishinaka(1), T. Horiguchi(2), M. Wakasugi(3), H. Katsuragawa(4), T. Minowa(4), M. Kubota(4), K. Kawade(5), H. Yamamoto(5), A. Taniguchi(5), T. Ikuta(5), K. Naito(5), T. Tsuji(5), M. Oda(5), S. Taguchi(5), M. Amaya(5), S. Kihara(6), S. Umetani(6), M. Matsui(6), T. Tominaga(7) and Y. Minai(7)

* Research Institute of Mineral Dressing and Metallurgy, Tohoku University
(1) Faculty of Science, Tokyo Metropolitan University
(2) Faculty of Science, Hiroshima University
(3) The Institute of Physical and Chemical Research (RIKEN)
(4) Faculty of Science, Toho University
(5) Faculty of Engineering, Nagoya University
(6) Institute for Chemical Research, Kyoto University
(7) Faculty of Science, University of Tokyo

17.1 Fission Yields of Rare Earth Elements in the p + ^{244}Pu Reaction

Detailed features of mass yield curves are necessary for the study of fission mechanism, but the yields in the rare earth region have scarcely been reported[1,2] because of the short half-lives of the nuclides to be measured. A computer-controlled rapid ion-exchange separation system[3] has been applied to the measurements of the fission yields in the region of the rare earth elements in the proton-induced fission of ^{244}Pu.

The mass yield distributions of fragments in the proton energy range 11-16 MeV have been measured by gas-jet transport method and catcher-foil method. The cross section of each fission product was determined from the observed γ-ray intensities, followed by the correction with the chemical yields and/or the transport efficiencies of the gas-jet. Correction with the charge distribution was also done by assuming a Gaussian distribution with the most probable charge of the unchanged charge division model.[4] The mass yield distribution obtained is shown in Fig.1. Mechanism of the asymmetric mass division in this region is

now contemplating from the energy dependence of the yields.

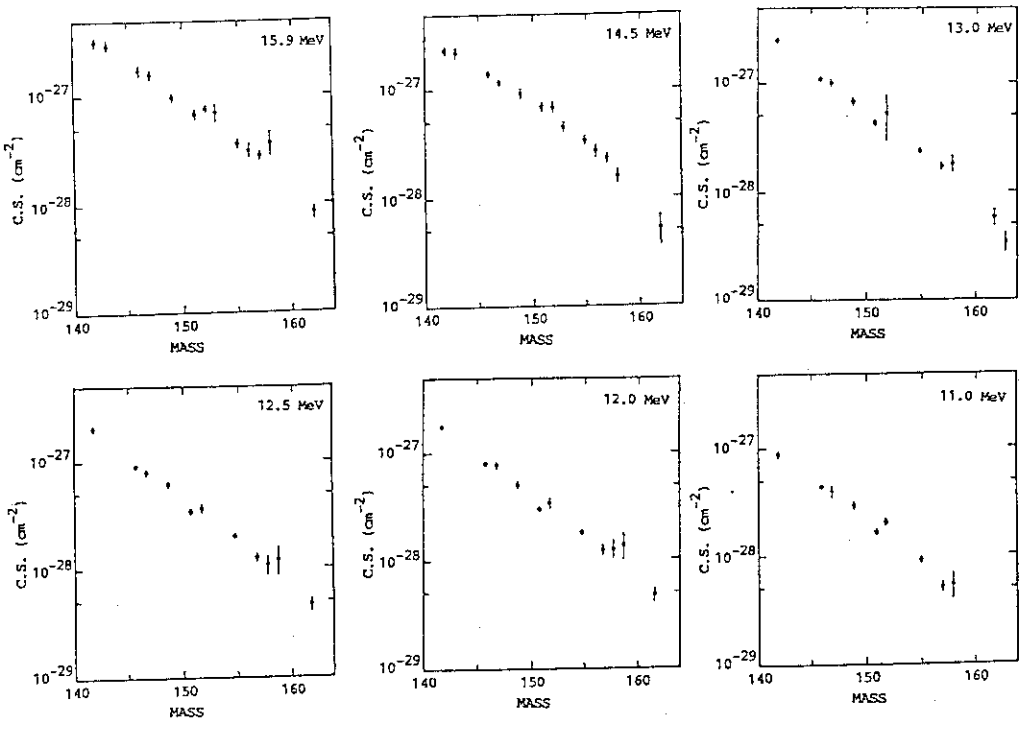

Fig. 1 Mass yield distribution of the fragments produced by the 11-16 MeV proton-induced fission of ^{244}Pu.

References

1) V.K. Rao, V.K. Bhargava, S.G. Marathe, S.M.Sahakundu and R.H. Iyer, Phys. Rev. C19(1979)1372.

2) A.C. Wahl, Atom. Data and Nucl. Data Tables 39(1988)1.

3) K. Tsukada, T. Ohtsuki, K. Sueki, Y. Hatsukawa, H. Yoshikawa, K. Endo, H. Nakahara, N. Shinohara, S. Ichikawa, S. Usuda and M. Hoshi, Radiochim. Acta 51(1990)77 .

4) A.C. Wahl, R.L. Freguson, D.R. Nethaway, D.E. Troutner and K. Wolfsberg, Phys. Rev. 126(1962)1112.

Publication List

[1] T. Ohtsuki, Y. Hamajima, K. Sueki, H. Nakahara, Y. Nagame, N. Shinohara, H. Ikezoe, "Systematic Analysis of Mass Yield Curves in Low Energy Fission of Actinides," Phys. Rev. C40(1989)2144.

[2] K. Tsukada, T. Ohtsuki, K. Sueki, Y. Hatsukawa, H. Yoshikawa, K. Endo, H. Nakahara, N. Shinohara, S. Ichikawa, S. Usuda and M. Hoshi, "Development of

Computer-Controlled On-Line Rapid Ion-Exchange Separation System," Radiochim. Acta 51(1990)77.

[3] T. Ohtsuki, Y. Nagame, K. Tsukada, N. Shinohara, S. Baba, K. Hashimoto, I. Nishinaka, K. Sueki, Y. Hatsukawa, K. Hata, T. Sekine, I. Kanno, H. Ikeoze, H. Nakahara, "Mass Yield Curves in Low-Energy Proton-Induced Fission of ^{233}U, ^{235}U, ^{236}U, ^{237}Np, ^{239}Pu, ^{242}Pu, ^{244}Pu, ^{241}Am and ^{243}Am," Phys. Rev. C44(1991) 1405.

17.2 Measurement of Hyperfine Structure in PrII by Collinear Laser-Ion-Beam Spectroscopy

Collinear laser-ion-beam spectroscopy is superior to the conventional spectroscopic methods, because it provides mass separation and sub-Doppler resolution. This technique has been used to study hyperfine structure (hfs) in some rare earth ions. Nevertheless, experimental data still far from complete. The PrII lines show a hfs due to nuclear spin 5/2 of only the stable isotope ^{141}Pr. The spectra of PrII were investigated by using the methods of Fourier transform spectroscopy and grating photographic spectroscopy, and the results were summarized by Ginibre.[1] However, these techniques are not sufficient to resolve the hfs because of Doppler broadning. In this work, we made for the first time Doppler-free measurement of the hfs in PrII by collinear laser-ion-beam spectroscopy.

Experimental set-up was as follows. A beam of 40 keV Pr^+ ions was produced by the isotope separator[2] at the tandem accelerator facility in JAERI. The metastable ions were excited from metastable levels to high-lying levels by a counter-propagating laser beam. The interaction region was defined by a cage of 10 cm in length and 4 cm in diameter, which was kept at the potential of -3kV. This potential ensures that the velocity of the ions is Doppler-tuned into resonance in the cage and depopulation pumping of the metastable levels does not occur far upstream from the cage. Resonance was observed by detecting the fluorescence light, which was collected by a spherical mirror onto a cooled photomultiplier. Hyperfine spectra were measured by scanning the laser frequency. The observed linewidth was typically about 90 MHz (FWHM).

The magnetic-dipole constant A and electric-quadrupole constant B were derived from the measured spectra. The results are consistent with the fact that the nuclear quadrupole moment of ^{141}Pr is very small.

References

1) A. Ginibre : Phys. Scr. **39**(1989)694.

2) S.Ichikawa, T.Sekine, H.Iimura and M.Oshima : Nucl. Instr. and Meth. **A274**(1989)259.

Publication List

[1] H.Iimura, Y.Nakahara, S.Ichikawa, K.Kotani, M.Wakasugi and T.Horiguchi : "Measurement of Hyperfine Structure of the $4f^35d^5G$-$4f^36p^5H$ in PrII by Collinear Laser-Ion-Beam Spectroscopy", J.Phys. Soci. Japan **59**(1990)4208.

17.3 Beta-Decay Studies of Mass Separated ^{123,125}Ba

The feature of low-lying states of Cs(Z=55) nuclei are clearly dependent on the neutron number N.[1,2,3] Information of these levels from β-decay of Ba is, however, very scarce in the neutron deficient region. In the present work, we studied β-decay of ^{123,125}Ba using the JAERI-ISOL.[4]

The experiments were performed at the tandem accelerator in JAERI, by using the reaction ^{nat}Mo(^{32}S,2pxn)^{123,125}Ba with a 5.1MeV/u ^{32}S beam. The thickness of the molybdenum targets was about 4.1 mg/cm^2. The reaction products were ionized in a surface-ionization ion source and mass-separated. The mass-separated reaction products were implanted into an aluminum coated Mylar tape in a tape transport system and periodically transported to a measuring position, where γ-ray singles and γ-γ coincidence measurements were performed with a low-energy photon HPGe(LEPS) and a 27% X-γ HPGe detector. Gamma-ray multi-spectrum were measured with the LEPS and HPGe detector. The decays of each γ-rays were traced by taking consecutively 16 spectra. In order to measure half-lives of excited states, β-γ delayed coincidence were observed with a plastic scintillator and the LEPS. Coincidence events were recorded in list mode on a magnetic tape by means of multi-parameter system(AMS-1600) controlled by a personal computer(NEC PC-9800).

The β^+-ray maximum energies of ^{123,125}Ba were also measured. Singles γ-ray and β^+-γ coincidence measurements were performed with the LEPS and the x-γ HPGe detector. Energy calibration of the LEPS was made up to 6MeV with prompt γ-rays from the thermal neutron capture of ^{56}Fe(n,γ) and ^{35}Cl(n,γ). Thermal neutrons were generated by a ^{252}Cf neutron source of 3.5MBq.

Decay curves of intense γ-ray measured at the mass A=123 are shown in Fig. 1. The analysis of the data on the decay of each photopeak gave a half-life of 2.4 ± 0.1 min for ^{123}Ba. This value is in agreement with the previous one.[5,6] There are 17 new γ-rays with 2.4 ±0.1 min half-life identified from

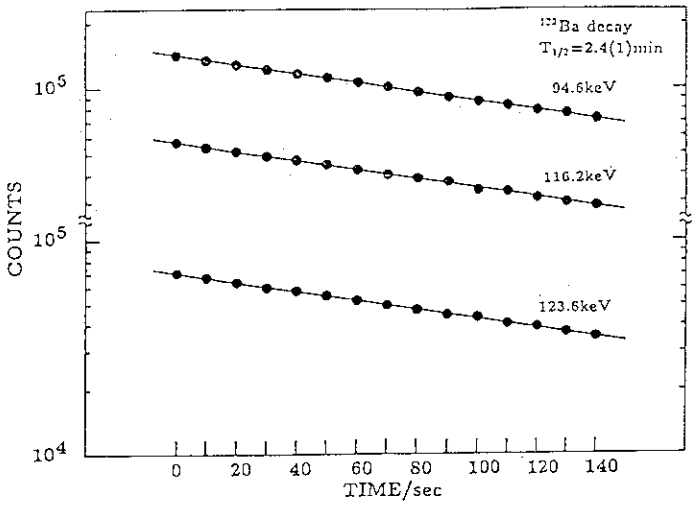

Fig. 1 Decay curves of intense γ-rays assigned to ^{123}Ba.

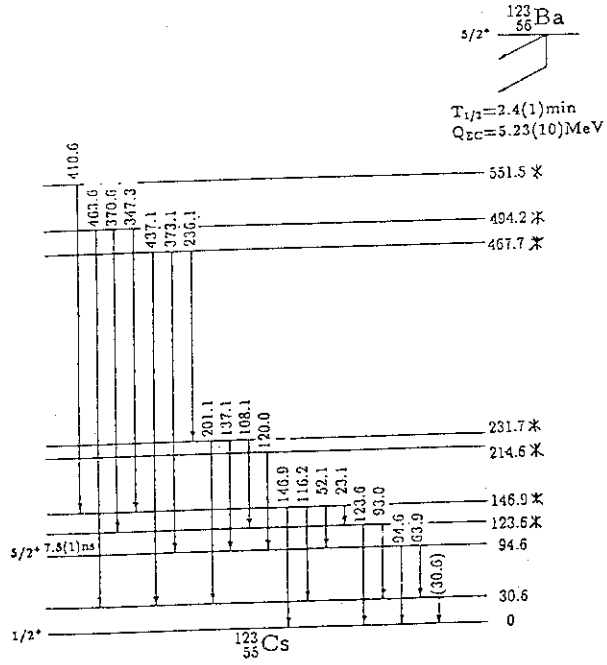

Fig. 2 Decay scheme of ^{123}Ba.

multispectrum analysis to belong to the decay of ^{123}Ba.

Figure 2 shows a decay scheme of ^{123}Ba obtained from present measurement. It is constructed on the basis of the energies and the coincidence relations of the γ-rays assigned to the decay of ^{123}Ba. We have derived 7 new levels, the energies of which are indicated with an asterisk. The present results are consistent with the results reported by Marguier et al.[7] The Fermi-Kurie plot of the β^+-ray spectrum observed in coincidence with 94.6 keV γ-ray of ^{123}Ba is shown in Fig. 3. The Q_{EC}-value for ^{123}Ba was determined to be 5.23 ± 0.10MeV, which was the first experimental value.

A decay scheme for ^{125}Ba was also constructed and 20 new levels were derived. The half-life and Q_{EC}-value for ^{123}Ba and ^{125}Ba found in this study are summarized in Table 1.

Further investigation including the measurements of relative intensities of the γ-rays is in progress to obtain more complete decay schemes of the isotopes.

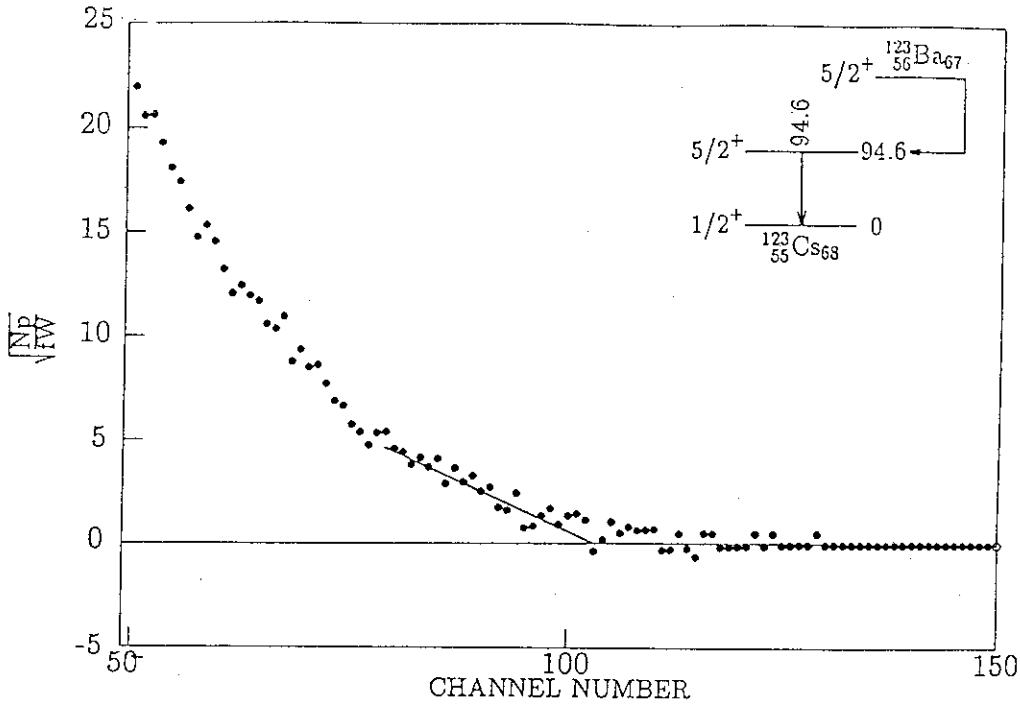

Fig. 3 Fermi-Kurie plot of the β^+-ray spectrum observed in coincidence with 94.6keV γ-ray of ^{123}Ba. The simplified decay scheme is shown in the inset.

Table 1. Half lives and Q_{EC}-values obtained in the present work.

Nuclide	$T_{1/2}$ (min)		Q_{EC}-value (MeV)	
	present work	other results	present work	other results
^{123}Ba	2.4±0.1	2.7±0.4[a)] 2.0±0.5[b)]	5.23±0.10	5.50(syst.)[d)]
^{125}Ba	3.6±0.3	3.5±0.4[a)] 3.0±0.5[c)]	4.41±0.07	4.51±0.25[d)]

a) R.Arlt et al.:Acta.Phys.Pol. B6 (1975) 433.
b) I.L.Preiss et al.:J.Inorg.Nuclear Chem. 24 (1962) 589.
c) J.M.D'Auria et al.:Phys. Rev. 172 (1968) 1176.
d) A.H.Wapstra et al.:Nucl.Phys. A432 (1985) 1.

References

1)K.Sofia, B.P.Pathak and S.Das Gupta, Phys. Rev.**C14**(1976)1277.
2)U.Garg, T.P.Sjoreen and D.B.Fossan, Phys. Rev. **C19**(1979)217.
3)G.Beyer, A.Jasinski, O.Knotek, H.G.Ortlepp, H.U.Siebert, R.Arlt, E.Herrmann, G.Musiol and H.Tyrroff, Nucl. Phys. **A260**(1976)269.
4)S.Ichikawa,T.Sekine, M.Oshima, H.Iimura and Y.Nakahara, Nucl. Instr. Meth. **B** in press.
5)R.Arlt, A.Jasinski, W.Neubert and H.G.Ortlepp, Acta. Phys. Pol. **B6**(1975)433.
6)I.L.Preiss and P.M.Sturdler, J.Inog. Nuclear Chem. 24(1962)589.
7)G.Marguier, A.Charvet, J.Genevey, C.Richard-Serre, A.Knipper, G.Walter and ISOLDE Collaboration, J.Phys. G:Nucl. Phys. **7**(1981)101.

Publication list

[1]A.Osa, T.Ikuta, A.Taniguchi, H.Yamamoto, K.Kawade, S.Ichikawa and Y.Kawase, "Measurement of β-ray Maximum Energy with an HPGE detector by means of β^+-annihilation photons coincidence" Nucl. Instr. Meth. **B** in press.
[2]A.Osa, S.Ichikawa, H.Iimura, M.Miyachi, M.Shibata, H.Yamamoto, K.Kawade and Y.Kawase, "Measurement of Beta-Ray Maximum Energy with an HPGe Detector" JAERI-M 90-139 (1990) 109.
[3]A.Osa, M.Miyachi, M.Shibata, H.Yamamoto, K.Kawade, J-Z.Ruan, Y.Kawase, S.Ichikawa and H.Iimura, "Measurement of Beta-Ray Maximum Energy with an HPGe Detector" in Proceeding of "The 2nd International Symposium on Advanced Nuclear Energy Research" Jan. 24-26 1990 Mito.

17.4 Nonstoichiometry and Thermodynamic Properties of MOX fuels doped with Lanthanides.

Introduction

Plutonium-uranium mixed oxides (MOX), $(U,Pu)O_2$, are promised to be used in modern thermal fission reactors as well as in fast breeder reactors. Because of the technical importance of this material, physical, chemical and thermodynamic properties of MOX have been studied extensively, and their data have been accumulated in these days[1]. However, few thermodynamic studies of MOX fuels containing fission product elements have carried out, which serve important information for evaluation of the irradiation behavior of the fuels. In this work, we chose lanthanum as a fission product element and studied electrical properties of La doped $(Pu,U)O_2$ solid solutions in order to evaluate the effect of dopant on the defect structures and electrical properties. The composition of specimens studied were $La_{0.01}(Pu_{0.2}U_{0.8})_{0.99}O_{2+x}$ and $La_{0.1}(Pu_{0.2}U_{0.8})_{0.9}O_{2+x}$. Details of sample preparation and experimental procedures are given in ref. 2.

Results and Discussion

Figure 1 shows the oxygen partial pressure dependence ($P(O_2)$) of the electrical conductivity (σ) of the $La_z(Pu_{0.2}U_{0.8})_{1-z}O_{2+x}$ (z=0.01 and 0.1) solid solutions measured at 1273 K, together with that of $Pu_{0.2}U_{0.8}O_{2+x}$[1] (a solid line) for comparison. Since the electrical conductivities of all specimens were reversible for increasing (filled marks) and decreasing (open marks) oxygen partial pressure from 10^{-15} to $10^{-1.5}$ Pa, it is considered that the equilibrium was reached for each specimen. In the figure, three different dependencies of σ upon $P(O_2)$ for $La_z(Pu_{0.2}U_{0.8})_{1-z}O_{2+x}$ are distinguished: (1) In low $P(O_2)$ region below $10^{-11.5}$ Pa, the electrical conductivity of z=0.1 spec-

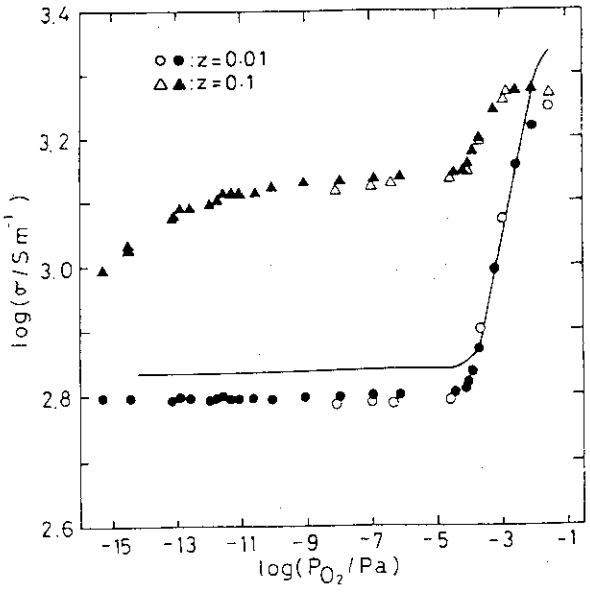

Fig. 1 The oxygen partial pressure dependencies of the electrical conductivity for $La_z(Pu_{0.2}U_{0.8})_{1-z}O_{2+x}$ (z=0.01 and 0.1) at 1273 K.

imen increases with increasing $P(O_2)$. Similar behavior was also observed for $La_{0.05}U_{0.95}O_{2-x}$ below 10^{-9} Pa[3], and therefore, the present that specimen is considered to become hypostoichiometric composition. (2) In the intermediate $P(O_2)$ region between about 10^{-11} and 10^{-4} Pa, the electrical conductivity is independent of $P(O_2)$. (3) In high $P(O_2)$ region above 10^{-4} Pa, the electrical conductivity increases with increasing $P(O_2)$ and the $P(O_2)$ dependence of σ decreases with increasing z. Further increase of $P(O_2)$ causes the decrease of the electrical conductivity, presumably due to the onset of the phase transformation from a single phase MO_{2+x} to two-phase MO_{2+x} and M_4O_{9-y} region.

The $P(O_2)$ dependence of σ for MO_{2+x} at constant temperature is usually expressed as $\sigma \propto P(O_2)^{1/n}$. The defect structure can be determined from the value of n. In the high $P(O_2)$ region above 10^{-4} Pa, the slopes of $La_z(Pu_{0.2}U_{0.8})_{1-z}O_{2+x}$ in Fig. 1 are 1/4.1, 1/5.1 and 1/9.9 for z=0, 0.01 and 0.1, respectively. Based on the values of n, the defect structures of $La_z(Pu_{0.2}U_{0.8})_{1-z}O_{2+x}$ are discussed by considering the complex defect model proposed by Willis[4-7], which consists of the oxygen vacancies (V_o) at normal lattice sites and two kinds of interstitial oxygens (O_i^a and O_i^b), and also by considering the electroneutrality condition between the concentrations of the complex defect and hole. Using Kröger-Vink notation[8], the formation of the complex defect is represented by eq.(1),

$$O_2(g) + 2V_i^a + 2V_i^b + 2O_o = (2(O_i^a O_i^b V_o))^{m'} + mh^{\cdot} \qquad (1)$$

where h is a electron hole and m is the charge of the complex defect. Then, $\sigma \propto 1/(m+1)$. The dependence of n=4.1 and 5.1 observed for z=0 and 0.01 of $La_z(Pu_{0.2}U_{0.8})_{1-z}O_{2+x}$ specimens, respectively, from the log σ vs log $P(O_2)$ relation in the high $P(O_2)$ region at 1273 K can be interpreted from eq.(1) by taking the values for m=3 and 4, respectively. For the z=0.1 specimen, another complex defect formation can be considered. The complex defect formation is expressed as eq.(2),

$$(1/2)O_2(g) + 2V_i^a + V_i^b + 2O_o = (2O_i^a O_i^b 2V_o))^{m'} + mh^{\cdot}. \qquad (2)$$

Then, $\sigma \propto 1/2(m+1)$. The dependence of n=9.9 observed for z=0.1 specimen can be interpreted from eq.(2), taking the value for m=4.

In the intermediate $P(O_2)$ region between 10^{-11} to 10^{-4} Pa, the slopes of $La_z(Pu_{0.2}U_{0.8})_{1-z}O_{2+x}$ in Fig. 1 are zero, irrespective of z. It is considered that the neutral defect is predominant in this region. It is also seen from the figure that the value of electrical conductivity of z=0.01 specimen in this region is almost same as that of z=0 but that of z=0.1 increases by about factor two. Since doped lanthanum of which the

oxidation state is +3 substitute for U^{4+} in the solid solution, the same concentration of U^{4+} are oxidized to U^{5+}, which serve a carrier for electrical conductivity, then the electrical conductivity of z=0.1 specimen increases in this region.

References

1) K. Naito, T. Tsuji, T. Fujino and T. Yamashita, J. Nucl. Mater. 169(1898)329.
2) T. Fujino, A. Nakamura, K. Ohuchi, T. Tateno, T. Yamashita and Y. Hinatsu, JAERI-M-89-058.
3) T. Matsui and K. Naito, J. Nucl. Mater. 138(1986)19.
4) B.M.T. Willis, Proc. Roy. Soc. London, A274(1963)122.
5) B.M.T. Willis, Proc. Roy. Soc. London, A274(1963)134.
6) B.M.T. Willis, J. de Phys. 25(1964)431.
7) B.T.M. Willis, Nature 197(1963)755.
8) F.A. Kröger and V.J. Vink, in: Solid State Physics, Vol.3 (Academic Press, New York, 1965) p.307.

Publication List

[1] K. Naito, T. Tsuji, T. Fujino and T. Yamashita, "Electrical Conductivity and Defect Structure of $(U,Pu)O_{2+x}$." J. Nucl. Mater. 169(1989)329.
[2] K. Naito, T. Tsuji, T. Matsui, T. Fujino, T. Yamashita and K. Ohuchi, "Defect Chemistry of Plutonium Oxides." Proc. Symp. to Commemorate the 50th Anniversary of the Discovery of Transuranium Elements, Washington D.C., August, 1990.

17.5 Formation of americium and europium humate complexes

Binding of actinide elements with organic or inorganic ligands is of importance for understanding their behaviors in environments. In particular, humic acid, a naturally-derived polyelectrolyte, has been demonstrated by experimental studies on interaction with actinides as an important material potentially controlling the actinide behavior[1]. In this study, binding constants of americium and europium with a humic acid were determined to know if complex formation of trivalent actinice-humates affects dissolved species of the actinides in hydrosphere.

Binding constants of americium and europium humates were determined in the range of pH = 4.5 - 6.0 by solvent extraction using di(2-ethylhexyl)phosphoric acid(DEHP)[2]. Assuming the presence of 1:1 and 1:2 complex, dependence of the distribution coefficient on the humic acid concentration was analyzed to obtain apparent binding constants. The binding constants of Am^{3+} and Eu^{3+} for humic acid were plotted against pH in Fig. 1. The binding constants of Am^{3+} are nearby identical to those of Eu^{3+}

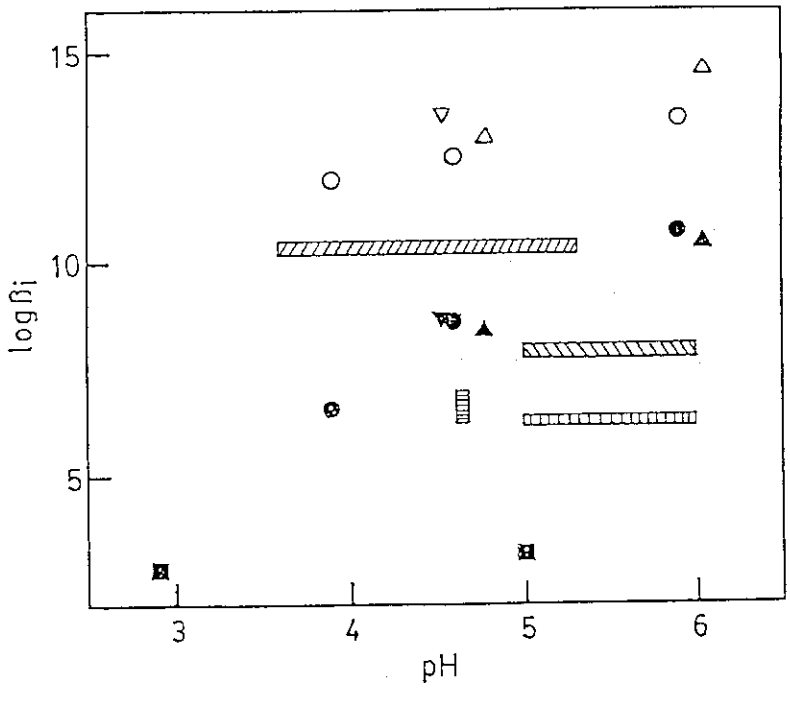

Fig. 1. Comparison of the determined binding constants with several reported values (2,3-7) for trivalent actinides and lanthanides with humic substances: (▲) - $\log\beta_1$ for Am^{3+} (this work), (△) - $\log\beta_2$ for Am^{3+} (this work), (▼) - $\log\beta_1$ for Eu^{3+} (this work), (▽) - $\log\beta_2$ for Eu^{3+} (this work), (❂) - $\log\beta_1$ for Am^{3+} (2), (○) -$\log\beta_2$ for Am^{3+} (2), (▨) - $\log\beta_1$ for Eu^{3+} determined with ultrafiltration (3), (▤) - $\log\beta_1$ for Am^{3+} determined with spectrophotometry (4), (▨) - $\log\beta_1$ for Eu^{3+} with ion exchange (5), (■) - $\log\beta_1$ for Pu^{3+} with solvent extraction (6), and (▥) - $\log\beta_1$ for Am^{3+} with spectrophtometry and ultrafiltration (7).

obtained in this study. The difference in ionic radius between two ions is so small that the binding constants obtained are similar. In Fig. 1 the binding constants of trivalent actinides and lanthanides with humic substances recently reported[3-7] are also shown. The binding constants obtained in this study were mostly in agreement with those determined previously by the same procedures but with humic acids of different origin and composition. However, the binding constants reported in literatures were largely different among them depending on the methods and humic acids employed. Further development of analytical techniques to determine binding constants for actinides at tracer level is necessary for the estimation of actinide behavior in environments.

References

1) G. R. Choppin, B. Allard,: A. J. Freeman, C. Keller, ed. "Handbook on the Physics and Chemistry of Actinides, Vol. 3", Elsevier Pib., New York, 1985, Chap. 11.
2) G. R. Choppin, R. A. Torres, Radiochim. Acta, 35(1984)143.
3) M. S. Caceci, Radiochim. Acta, 39(1985)51.
4) V. Moulin, P. Robouch, P. Vitorge, B. Allard, Inorg. Chim. Acta, 140(1987)303.
5) J. H. Ephraim, J. A. Marinsky, S. J. Cramer, Talanta, 36(1989)437.
6) G. R. Mahajan, V. K. Rao, P. R. Natarajan, J. Radioanal. Nucl. Chem., 137(1989)219.
7) J. I. Kim, G. Buckau, E. Bryant, R. Klenze, Radiochim. Acta, 48(1989)135

Publication List

[1] Y. Minai, Y. Meguro, T. Tominaga, "Formation of Americium and Europium Humate Complexes," The 3rd Internat. Symp. Adv. Nucl. Ener. Res., Mito March(1991), p229.

17.6 Electrochemical Studies of State of Actinide Ions in Solutions

Oxidation state of such actinide elements as U, Np, and Pu in solutions are liable to vary by oxidation-reduction and/or disproportionation reactions, and complex formation of individual ions afford various chemical forms. To elucidate and control complicated chemical behaviors of actinide ions, e. g., their transport or retention in the natural environment or their distribution in wet-chemical process, fundamental and systematic informations on redox, dispropotionation, and complex formation reactions are indispensable. Cooperative work has been performed to obtain fundamental data of solution chemistry and to develope new methods for the determination and speciation of actinide ions by electrochemical methods.

(i) Fundamental data on redox and complex formation reactions of actinide ions at various oxidation states were obtained. Flow-coulometry with column electrode(s) of glassy carbon fibers as working electrode material, conventional voltammetry with rotating disc electrode, and polarography with dropping mercury electrode were employed for the measurement. Coulopotentiograms, i.e., coulomb-potential curves observed by flow-coulometry, for the redox of U, Np, and Pu ions in perchloric, nitric, hydrochloric, sulfuric, and phosphoric acid solutions were obtanied (cf. chapter 3.1). From results obtained by flow-coulometry together with those by voltammetry and polarography the redox process, the number of electron involved in the process, reversibility of the process, the shift of the redox potential due to the complex formation, and the species participating in the process were determined. Flow-coulometric methods for the electrolytic preparation and the speciation of the actinide-ion species at various states, which includes such fairly unstable species as U(IV), Np(III), or Pu(V), were developed on the basis of the results of coulopotentiograms.

(ii) It was confirmed that U(IV)-hydroxide generated through the reduction of U(VI) in aqueous solution of pH 2 to 6 deposit at the surface of the glassy carbon electrode whose surface had been pretreated by the anodic polarization. Based on this principle, procedure for the quantitative preconcentration of trace quantity of uranium in solutions was developed by means of flow-coulometry. Recommended procedure was applied to the determination of uranium in envionmental solutions such as sea water and ground water.

(iii) The ion transfer polarography and voltammetry at the interface between two immiscible solutions, i.e., aqueous/organic solutions interface,

has been developed. The current-potential ralation obtained by ion-transfer voltammetry gives fundamental information on the state of metal ion in the solution phase, i.e., the solvation of the ion, and valency and size of the ion, complex formation, etc. This novel electrochemical technique is promising to elueidate the mechanism of ion transfer process which is involved in the solvent extraction reaction, ion-transport through the membrane, etc. Study on the transfer of actinide ions at various states through aqueous/organic solutions interface is now in progress by using ion-transfer voltammetry.

Publication List

[1] Z. Yoshida, H. Aoyagi, and S. Kihara, "State Analysis of Ions in Solutions", Proc. Intern. Symp. Adv. Nucl. Energ. Res., Oarai, 398(1989).

[2] S. Kihara, M. Suzuki, K. Maeda, K. Ogura, M. Matsui, and Z. Yoshida, "Voltammetry for the Charge Transfer at Two Immiscible Electrolyte Solutions Interface; A New Branch of Electroanalytical Chemistry", Proc. Intern. Symp. Adv. Nucl. Energ. Res., Oarai, 428(1989).

[3] S. Kihara, Z. Yoshida, H. Aoyagi, "Analytical Chemical Study on Actinide Ions by Column Electrode Electrolysis", Bunseki Kagaku, 40, (1991)309, (in Japanese).

[4] S. Kihara, M. Suzuki, K. Maeda, K. Ogura, M. Matsui, and Z. Yoshida, "The Electron Transfer at a Liquid/Liquid Interface Studied by Current-scan Polarography at the Electrolyte Dropping Electrode", J. Electroanal. Chem., 271(1989)107.

18. In Search of Cold D-D Nuclear Fusion

E. Tachikawa, T. Hirabayashi, Z. Yoshida, Y. Aratono, T. Kimura, H. Aoyagi, R. Sato, K. Obara, Y. Yamanouti, M. Sugimoto, E. Minegara, M. Oshima, T. Hunahashi, H. Motohashi, N. Sikazono, M. Tanase, and M. Katoh

Since the success of "Cold Nuclear Fusion by the Electrolysis of D_2O" was reported in March, 1989[1,2], the experiments for confirming the phenomena have been carried out by the cooperative team of Departments of Chemistry, Physics, and Radioisotopes in JAERI. The following items have been studied;

(i) The measurements of the neutron emission rate, neutron energy spectrum, tritium yield, and excess heat generation rate during the electrolysis of D_2O using various palladium cathodes,[1,2]

(ii) The measurements of neutron emission rate from titanium and titanium alloy sponge in pressurized D_2 gas,[3]

(iii) The measurements of the neutron emission rate from the palladium rods stimulated with a high voltage discharge between the rods,[4]

(iv) The structural analysis of palladium with deuterium loaded electrolytically by X-ray diffraction and neutron diffraction methods ,

(v) The determination of α-emitting nuclides contained in the materials used for the experiments.

The results proved are as follows;[5,6]

1. The neutron emission rate was less than 0.1/sec in both the D_2O-electrolysis and the gas type experiment,
2. The burst emission of neutron was not observed ,
3. The excess heat generation as well as tritium production were not observed,
4. The β-phase is formed in the palladium by the D_2O-electrolysis and the ratio of the β-phase increases with increasing electrolysis time, and
5. The concentrations of U and Th as impurities in palladium and titanium materials were less than the lower detection limit, i.e., 20-30ppb, by the neutron activation analysis.

The production behavior and rates of neutrons induced by cosmic rays in a material have then been studied quantitatively[7]. The gross (G) and coincidence (C) neutron counting rates were measured by MCS analysis and by the multichannel time spectra obtained by using PIA, respectively, in the presence

of various materials with similar dimensions in the center hole of polyethylene moderator with 32 ^{3}He counters.

Figure 1 shows bilogarithmic plots of G and C($n.s^{-1}.mol^{-1}$) per mole of the material vs. mean atomic weight A of the material. The values G and C calculated by the data from Pb through Al were proportional to $A^{1.80}$ and $A^{2.11}$, respectively.

The multiple production of neutrons induced by cosmic rays are observed in the materials in wide range of the periodic table, although the production rates are low and about 10^{-3}-$10^{-2}n.kg^{-1}.s^{-1}$. The neutron production in D_2O is exceptionally higher than that expected from the above relationship. The multiple production of neutrons should be taken into account to evaluate the background neutron on the low level neutron measurements, especially in cold fusion research.

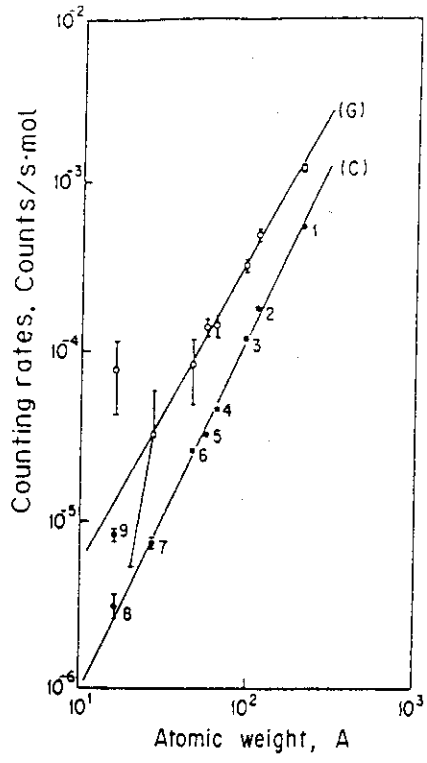

$G=e^{-(16.3\pm0.3)}A^{1.80\pm0.06}$, $C=e^{-(18.8\pm0.2)}A^{2.11\pm0.06}$
1: Pb; 2: Cd; 3: Nb-Mo; 4: Cu-Zn; 5: Fe; 6: Ti-Al-V-Sn; 7: Al; 8: H_2O; 9: D_2O

Fig. 1 Atomic weight dependence of *G* and *C* neutron counting rates

Reference

1) M. Fleischmann, S. Pons, M. Hawkins, J. Electroanal, Chem., 261(1989)301.
2) S. E. Jones, E. P. Palmer, J. B. Czirr, D. L. Decker, G. L. Jensen, J. M. Thorne, S. F. Taylor, J. Rafelski, Nature, 338(1989)737.
3) H. O. Menlove, et. al., LA-UR89-1974(1989).
4) N. Wada, et. al., Jpn. J. Appl. Phys., 28(1989)2017.
5) E. Tachikawa, et. al., JAERI-M89-42(1989).
6) E. Tachikawa, et. al., JAERI-M90-134(1990).
7) Kimura, J. Nucl. Sci. Tech., 27(1990)1147.

Publication list

[1] E. Tachikawa, T. Hirabayashi, Z. Yoshida, Y. Aratono, T. Kimura, H. Aoyagi, R. Sato, K. Obara, Y. Yamanouti, M. Sugimoto, E. Minahara, M. Oshima, T. Hunahashi, H. Motohashi, N. Sikazono, M. Tanase, and M. Katoh, "In Search of Cold D-D Nuclear Fusion (I)", JAERI-M 89-42(1989).

[2] E. Tachikawa, T. Hirabayashi, Z. Yoshida, Y. Aratono, T. Kimura, H. Aoyagi, C. Yonezawa, R. Sato, K. Obara, M. Tanase, and M. Katoh, "In Search of Cold D-D Nuclear Fusion (II)", JAERI-M 90-134(1990).

[3] T. Kimura, "Quantitative Evaluation of Multiple Production of Neutrons Induced by Cosmic Rays in Materials", J. Nucl. Sci. Tech., 27(1990)1147.

[4] E. Tachikawa, Z. Yoshida, T. Hirabayashi, Y. Aratono, T. Kimura, and T. Takeda, "Whole Aspect of Cold D-D Nuclear Fusion", Genshiryoku Kougyou, 37(1991)11, (in Japanese).

19. COOPERATION BETWEEN ININ AND JAERI IN THE AREA OF BASIC RESEARCH ON ACTINIDE CHEMISTRY

J. Serrano G.*, L.A. Fucugauchi*, T. Kimura, Z. Yoshida and E. Tachikawa
*Division of Research and Development, National Institute for Nuclear Research (ININ), MEXICO

19.1 Application of Extraction Chromatography in the TBP-HNO_3 System for Analytical Separation of Actinide Elements

In the previous work,[1] the characteristics of the TBP/XAD-4 resin on the separation of the actinide elements and fission products were studied and a separation procedure of the elements was suggested. Preliminary experiments have shown that the recommended procedure was not satisfactory because of the behavior of neptunium, plutonium and some fission products and that additional studies were necessary to develop a quantitative separation of the actinide elements and fission products.

In the present cooperation, as an application of the TBP/XAD-4 column for the analytical separation of uranium, neptunium, plutonium and americium, the elution behavior of these elements as a function of their redox reagents was thoroughly studied. Subsequently, two effective procedures to carry out a quantitative separation of the actinide elements from each other were established by combining extraction chromatography in the TBP-HNO_3 system and the redox reactions of the actinide elements. Figures 1 and 2 show the flow diagrams of the procedures.

References

1) T. Kimura, J. Radioanal. Nucl. Chem. 141(1990)307.

Publication List

[1] T. Kimura, "Extraction Chromatography in the TBP-HNO_3 System I. Extraction Behavior of Th(IV) and U(VI) with the TBP/XAD-4 Resin," J. Radioanal. Nucl. Chem. 141(1990)295.

[2] T. Kimura, "Extraction Chromatography in the TBP-HNO_3 System II. Characteristics of the TBP/XAD-4 Resin on Separation of Actinide Elements," J. Radioanal. Nucl. Chem. 141(1990)307.

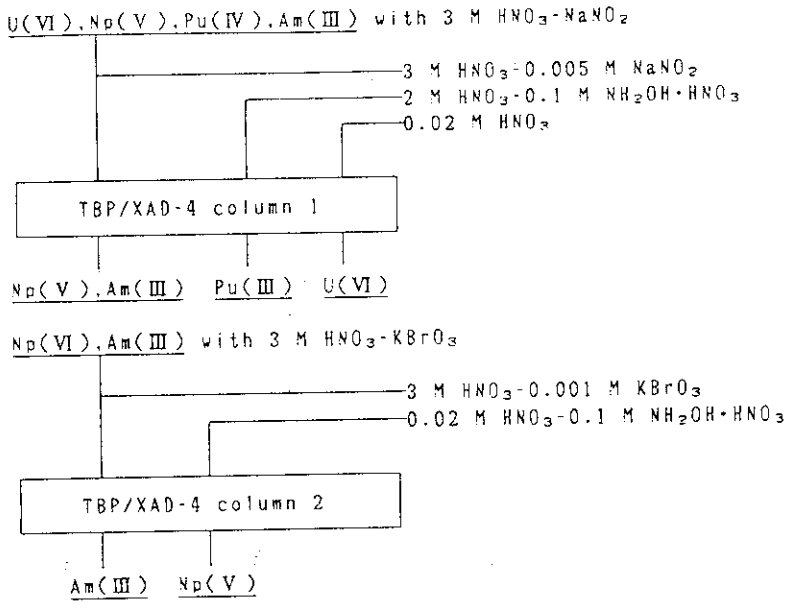

Fig. 1 Separation procedure of U, Np, Pu and Am

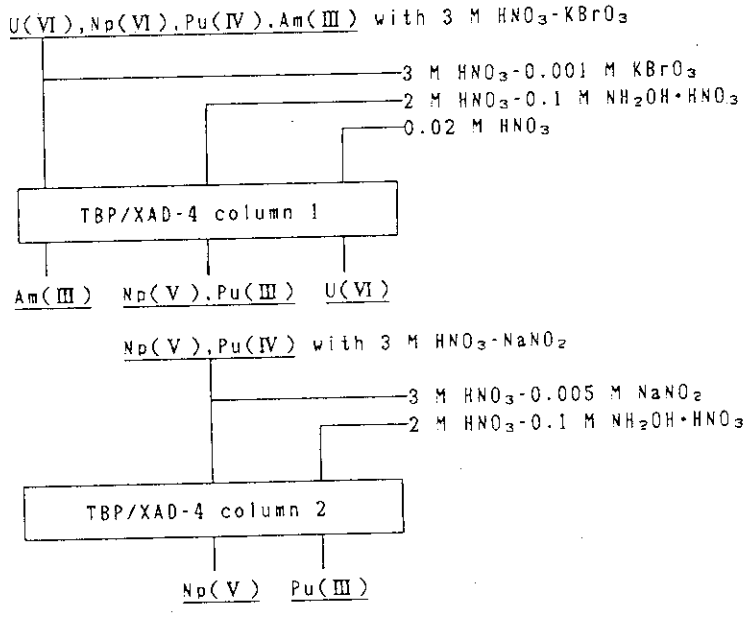

Fig. 2 Separation procedure of U, Np, Pu and Am